OPEN ACCESS
OPUS AUGSBURG

Universität Augsburg
Universitätsbibliothek

Impact of decontamination and recultivation of agricultural soils on sediment and radiocaesium transfers in Fukushima rivers

Thomas Chalaux-Clergue

Angaben zur Veröffentlichung / Publication details:

Chalaux-Clergue, Thomas. 2024. Impact of decontamination and recultivation of agricultural soils on sediment and radiocaesium transfers in Fukushima rivers. Online-Ressource. Gif-sur-Yvette: Université Paris-Saclay. https://theses.fr/2024UPASJ037.

Nutzungsbedingungen / Terms of use: **licgercopyright**

Dieses Dokument wird unter folgenden Bedingungen zur Verfügung gestellt: / This document is made available under these conditions:
Deutsches Urheberrecht
Weitere Informationen finden Sie unter: / For more information see:
https://www.uni-augsburg.de/de/organisation/bibliothek/publizieren-zitieren-archivieren/publiz/





Impact of decontamination and recultivation of agricultural soils on sediment and radiocaesium transfers in Fukushima rivers

Thomas Chalaux

▶ **To cite this version:**

Thomas Chalaux. Impact of decontamination and recultivation of agricultural soils on sediment and radiocaesium transfers in Fukushima rivers. Continental interfaces, environment. Université Paris-Saclay, 2024. English. NNT : 2024UPASJ037 . tel-04975039

HAL Id: tel-04975039

https://theses.hal.science/tel-04975039v1

Submitted on 3 Mar 2025

HAL is a multi-disciplinary open access archive for the deposit and dissemination of scientific research documents, whether they are published or not. The documents may come from teaching and research institutions in France or abroad, or from public or private research centers.

L'archive ouverte pluridisciplinaire **HAL**, est destinée au dépôt et à la diffusion de documents scientifiques de niveau recherche, publiés ou non, émanant des établissements d'enseignement et de recherche français ou étrangers, des laboratoires publics ou privés.

université PARIS-SACLAY

Impact of decontamination and recultivation of agricultural soils on sediment and radiocaesium transfers in Fukushima rivers

Impact de la décontamination et de la remise en culture des sols agricoles sur les transferts de sédiments et de radiocésium dans les rivières de Fukushima

Thèse de doctorat de l'université Paris-Saclay

École doctorale n° 579,
Sciences mécaniques et énergétiques, matériaux et géosciences (SMEMaG)
Spécialité de doctorat : Géosciences
Graduate School : Géosciences, climat, environnement et planètes
Référent : Université de Versailles-Saint-Quentin-en-Yvelines (UVSQ)

Thèse préparée dans les unités de recherche **Laboratoire des Sciences du Climat et de l'Environnement (LSCE ; Université Paris-Saclay - CEA - CNRS - UVSQ, France)** et **Laboratory of Soil Chemistry (Kyoto Prefectural University, Graduate School of Life and Environmental Sciences, Japan)**, sous la direction de **Olivier EVRARD**, directeur de recherche CEA, et la co-direction de **Atsushi NAKAO**, associate professor at Kyoto Prefectural University.

Thèse soutenue à Paris-Saclay, le 16 décembre 2024, par

Thomas CHALAUX-CLERGUE

Composition du jury

Membres du jury avec voix délibérative

Cécile QUANTIN Professeure, Université Paris-Saclay	Présidente
Frédérique EYROLLE Chercheure HDR, Institut de Radioprotection et de Sûreté Nucléaire (IRSN)	Rapporteur & Examinatrice
Takuro SHINANO Professor, Hokkaido University, Graduate School of Agriculture	Rapporteur & Examinateur
David MONTAGNE Maître de conférence, AgroParisTech - Institut national de recherche pour l'agriculture, l'alimentation et l'environnement (INRAE)	Examinateur

THESE DE DOCTORAT
NNT : 2024UPASJ037











This PhD was funded and hosted by the *Commissariat à l'Energie Atomique et aux Energies Alternatives* (CEA) at the *Laboratoire des Sciences du Climat et de l'Environnement* (LSCE) in France, to which I am deeply grateful. This research has been conducted with the support of Short-term Fellowship (Grant number PE22708) by Japan Society for the Promotion of Science (JSPS). I am grateful to the JSPS for offering me an opportunity to conduct part of my research in Japan, and to Kyoto Prefectural University for hosting me during the second year of my PhD.

本研究は、日本学術振興会外国人特別研究員（欧米短期）（PE22708）の支援を受け実施しました。日本での活動の機会を与えてくださった日本学術振興会、博士後期課程二年時の一年間、温かく受け入れてくださった京都府立大学の皆様にもこの場を借りて厚く御礼申し上げます。

Tu as pouvoir sur ton esprit - non sur les événements extérieurs. Réalise cela, et tu trouveras la force.

You have power over your mind - not outside events. Realize this, and you will find strength.

Marc-Aurèle

Pensées pour moi-même - Meditations

なぜだろう、
この世に執着する
死に来るために生まれてきたのに。
夏目漱石

"Sans savoir pourquoi
j'aime ce monde
où nous venons pour mourir"

Natsume Sōseki

八百万の神あらゆるものに神は宿る。

"Les huit millions de divinités
habitent toutes choses."

Proverbe shintoïste

Acknowledgements - Remerciements

Nous y sommes, et lorsque j'écris ces mots, la fin de cette thèse approche à grands pas. Après trois années qui m'ont semblé passer à toute vitesse et qui, en même temps, ont duré une vie, j'en arrive au bout. Mais voilà, c'est la fin de ce chapitre, le début de beaucoup d'autres, mais la fin de celui-ci. Avant cela, j'aimerais remercier toutes les personnes que j'ai rencontrées au cours de cette thèse ou auparavant et qui m'ont accompagné dans cette aventure.

Je tiens tout d'abord à remercier mes encadrants de thèse, Olivier Evrard et Atsushi Nakao, qui m'ont accordé leur confiance pour mener à bien ce projet. Merci à toi, Olivier, d'avoir réussi à obtenir ce financement du CEA, et d'avoir vu le processus de sélection et d'obtention ; j'en entrevois la complexe réalité. Je vous remercie également pour le soutien que vous avez apporté pour obtenir une bourse de la JSPS et pouvoir passer un an à la Kyoto Prefectural University de Kyoto (avec, sans l'ombre d'un doute, l'existence du Mitate Lab qui a dû jouer en ma faveur). Cette année au Japon, dans ce pays qui m'inspirait depuis si longtemps, même si elle fut difficile, a marqué profondément et durablement qui je suis, et rien que pour ça, je vous suis infiniment reconnaissant.

Olivier, je te remercie pour ton accompagnement en douceur dans le métier de chercheur, pour toutes nos discussions scientifiques et la confiance que tu m'as accordée, même dans mes bouillonnements d'idées, parfois trop ambitieux, mais que tu m'as laissé explorer. Je ne saurais non plus oublier tous les autres moments, et nos autres discussions au LSCE, dans le bus 9, le RER B, durant les missions au Japon, à l'IER, dans les temples, les cafés japonais, les izakaya, les restaurants à Tokyo, les beer shops, les restaurants européano-japonais que tu affectionnes tant, et dont je ne saisi toujours pas très bien cet intérêt, qui font une multitude de bons souvenir.

Nakao, of all our discussions, I remember the one we had in the KPU cafeteria, the one in the basement, right next to the laboratory building. During this discussion, where it was difficult to understand each other behind these large sheets of Plexiglas, you quoted this sentence to me: "Because we love what we know, and we are careful about what we love", before adding: "Please explain to people so that they protect what is around us". It was just a simple refectory discussion, but those words still have resonance. I also remember particularly well that mission in December 2022 to Mount Aso, Kyushu, with Nanami and Shinji. Alongside the beauty of the scenery, I remember the delicious Kumamoto ramen and, in a different category, the sazae, but above all I had the pleasure of sharing a moment around the floors, between "true pedologists kana".

Je remercie aussi les membres du jury pour avoir accepté d'évaluer mon travail, Pr Cécile Quantin, Dr Frédérique Eyrolle, Pr Takuro Shinano, et Pr David Montagne.

J'adresse également mes remerciements à l'ensemble des personnes avec qui j'ai échangé ou collaboré dans le cadre de ma thèse, et avec qui j'ai toujours eu le sentiment d'être placé sur un pied d'égalité. Je remercie plus particulièrement Pedro Batista, Nuria Martinez-Carreras et Patrick Laceby pour leur accompagnement et leurs précieux conseils lors de ce travail sur la sélection des traceurs, étalé sur la première et la deuxième année. Cécile Asanuma-Brice, lors de nos échanges dans le cadre du Mitate Lab, lors des visites des villages de la zone contaminée, à l'ambassade de France à Tokyo, à Hiroshima, ainsi que lors de la visite de l'île d'Odaiba sous une pluie torrentielle. Jean-Christophe Bodineau, lors de cette mission à Modane, en première année, où nous avons déplacé 14 tonnes de briques de plomb et des détecteurs gamma, et où nous avions eu droit à plusieurs cours de spectrométrie gamma, plus interessants les uns que les autres. Rosalie Vandromme et Olivier Cerdan pour nos discussions, vos connaissances du bassin versant du Mano

Dam et vos précieux conseils. Oldrich Navratil, Arthur Gaillot et David Montagne pour nos échanges sur l'utilisation de la spectroscopie infrarouge. Sujet avec lequel j'embête Olivier depuis le début de ma thèse, et que j'apprécie voir prendre de l'ampleur. Sylvain Huon, pour ton expertise et ta bienveillance lors de mes visites à Jussieu, où nos discussions ont toujours été très instructives et m'ont toujours donné envie d'explorer et d'expérimenter de nouvelles choses. Enfin, nos collègues japonais, Y. Wakiyama-sensei de l'Insitute of Environmental Radioactivity (IER) de l'université de Fukushima, S. Hayashi-sensei et H. Tsuji-sensei du National Institute for Environmental Studies (NIES), qui ont toujours montré de l'intérêt pour mon travail, m'ont toujours aiguillé sur des points que j'avais pu omettre, et avec qui j'ai toujours pris plaisir à échanger.

Je remercie aussi les membres du commité de suivi, Dr Pedro Batista, Dr Seiji Hayashi, Dr Yoshifumi Wakiyama et Pr Edwige Pons-Branchu, pour leurs conseils tout au long de ma thèse.

Je tiens également à remercier l'équipe Géochimie des Impacts du LSCE (GeDI) du LSCE, plus précisément Sophie Ayrault, Anthony Foucher et Irène Lefèvre, pour leur soutien, les échanges enrichissants et l'ambiance de travail stimulante. Anthony pour toutes les connaissances que tu m'as transmises sur les carottes sédimentaires, et pour le plaisir que j'ai eu à partager cette dernière mission au Japon avec toi. Irène, pour toutes tes explications sur la spectrométrie gamma et ton exigence sur le sujet, ainsi que pour toutes nos discussions où l'on refaisait le monde. Le quatuor initial, Camille Asselin, Jean-Sébastien Barbier et Rémi Bizeul, pour l'ambiance de travail et le soutien. Sans oublier nos rendez-vous hebdomadaires à Hall of Beer tout au long de notre première année, pour décompresser, discuter, refaire le monde, rire et découvrir de nouvelles bières (grâce aux conseils de Bryan). Aurélie Diacre, pour nos discussions interminables à chaque fois que tu passais au LSCE. Romain Ducruet, Amaury Bardelle, Paul Hazet, Nicolas Tenaud et Yangjunjie Xu, avec qui il était tout aussi agréable de discuter et d'aller boire des verres, au point que nous avons fini par déplacer notre rendez-vous hebdomadaire du jeudi au mercredi, du Hall of Beer au O'Massy Pale. Merci encore à toi, Nicolas, pour ton investissement et ta curiosité qui nous ont permis de réaliser mes envies de mesures, quelque peu ambitieuses, lors de ma troisième année. Amanda Diacre, j'ai apprécié nos discussions, qui elles aussi s'éternisaient après la pause café, mais aussi ton honnêteté et tes remarques sur ce qui nous entoure.

During my year in Japan, and especially at KPU, I had the chance to immerse myself in Japanese culture and meet some truly wonderful people, Bich-san, Yanai-san, Kohei, Toshiki, Miku, Nanami, Shinji, Ayumi, Ayano, Seki-san, Eika and all the students in the soil chemistry lab. I know that the language barrier was a limiting factor in getting to know each other better, but I have precious memories of the exchanges I had with each and every one of you. I have fond memories of the hikes, the trips to Mount Aso, northern Kyoto or Nara, the meals we shared, whether it was at the Izakaya sharing dashiyaki or the various types of ramen - although I still can't recognise the different types, I remember their taste - the parties that punctuated the year following the various events in the Japanese students' lives. Bich-san, I am so grateful to you for welcoming me into your home just before I left, and I cherish the memories of those moments. I hope to see you again.

L'année au Japon m'a aussi fait vivre trois rencontres inoubliables, Chiara Raponni, Pierre-Alexis Chaboche et Jérôme Arnaud. Sans avoir à forcer, nous nous sommes immédiatement entendus. Notre week-end à Tsuchi-yu, entre balade sous le feuilles d'automnes des érables, les onsen et les temples, est un doux souvenir suspendu. Tout comme votre séjour à Kyoto. Les innombrables discussions et débats que nous avons eus, ont fait germer des envies de podcasts, et c'est une idée qui ne m'a pas quittée.

Merci à mes proches, Charlotte, Victor, Aude, tata et tonton, ainsi qu'à mes amis, Alexandre, Alix, Mathias, Thomas et Éléonore, pour nos discussions et débats passionnés sur tous les sujets du monde. Merci pour

vos encouragements et pour m’avoir donné l’énergie de faire toujours plus. Mes sœours, Inès et Léa, qui me rappellent à quoi ressemble la détermination. Enfin, je remercie mes parents de m’avoir appris à voir le monde différemment et de m’avoir incité à remettre et me remettre en question sans cesse. c’est grâce à toi que j’ai ce goût pour la science et cet amour de la nature. Papa, merci pour toutes nos discussions, plus ou moins philosophiques, sur la manière de voir les choses et de s’écouter. Merci pour votre folie, elle rend mon monde plus beau et plus atteignable.

Mais surtout, car je pense que, parce que "nous sommes l’ensemble de toutes les personnes que l’on a aimées, de tous les livres qu’on a lu, de tous les films que l’on a regardés, de tous les voyages que l’on a faits, de tous les amours que l’on a eus" (Renzo Piano) je suis qui je suis, car vous êtes vous. Merci pour ça.

Table of Contents

General Introduction **35**

I Sediment Source Fingerprinting: Concept, Techniques & Usages **55**

I.1 Introduction . . . 57

I.2 Materials and methods . . . 60

I.2.1 Catchment description . . . 60

I.2.2 Soil and sediment sampling and processing . . . 61

I.2.3 Laboratory analysis . . . 61

I.2.4 Virtual mixtures . . . 62

I.2.5 Tracer selection . . . 62

I.2.5.1 Three-step method . . . 62

I.2.5.2 Consensus method . . . 64

I.2.6 Source contribution modelling . . . 65

I.2.6.1 Un-mixing model . . . 65

I.2.6.2 Accuracy assessment . . . 65

I.3 Results . . . 67

I.3.1 Tracer selection . . . 67

I.3.1.1 Selection of tracers . . . 67

I.3.2 Prediction accuracy and tracer selection methods . . . 69

I.3.3 Source contribution predictions . . . 74

I.4 Discussion . . . 76

I.4.1 Conservative behaviour assessment . . . 76

I.4.2 Tracer selection and contribution modelling . . . 77

I.4.3 Assessing modelling prediction accuracy . . . 78

I.5 Conclusion . . . 79

I.6 Supplementary materials . . . 82

I.6.1 Laboratory analysis . . . 82

I.6.1.1 Organic matter . . . 82

I.6.1.2 Geochemistry . . . 82

I.6.1.3 Visible colorimetry . . . 83

I.6.2 Figures . . . 84

I.6.3 Tables . . . 87

II Decontamination and Radiocesium Transfer: Sediment Core Insights **107**

II.1 Introduction . . . 109

II.2 Materials and methods . . . 112

II.2.1 Study site . . . 112

II.2.2 Catchment management after FDNPP accident . . . 114

II.2.3 Sediment core and soil sampling and processing . . . 114

II.2.4 Laboratory analysis . . . 114

II.2.5 Sediment source fingerprinting . . . 115

II.2.5.1 Tracer selection . . . 115

II.2.5.2 Virtual mixtures . . . 115
II.2.5.3 Un-mixing modeling . . . 116
II.2.5.4 Accuracy assessment . . . 116
II.2.6 Identifying and dating sedimentation associated to extreme precipitation events . . . 117
II.2.7 Extreme events averaged properties . . . 118
II.3 Results . . . 118
II.3.1 Identifying sedimentation events . . . 118
II.3.1.1 Sediment core description . . . 118
II.3.1.2 Radiocesium activities . . . 120
II.3.1.3 Elemental geochemistry . . . 120
II.3.1.4 Organic matter . . . 120
II.3.1.5 Grain size and specific surface area . . . 120
II.3.1.6 Identifying sedimentation events along the sediment core . . . 121
II.3.2 Dating of events . . . 121
II.3.2.1 Identification of extreme precipitation events . . . 121
II.3.2.2 Extreme precipitation events and reservoir management . . . 121
II.3.2.3 Deposited sediment flux to the reservoir . . . 123
II.3.2.4 Decontamination progress and extreme rainfall events . . . 123
II.3.2.5 Dating of identified sedimentation events . . . 124
II.3.3 Source sediment fingerprinting . . . 126
II.3.3.1 Origin of organic matter . . . 126
II.3.3.2 Tracer selection . . . 127
II.3.3.3 Sediment source fingerprinting modeling . . . 128
II.3.4 Evolution of sediment transfers and sources throughout time . . . 129
II.3.5 Evolution of ^{137}Cs transfers through time . . . 130
II.4 Discussion . . . 131
II.4.1 Identifying and dating sedimentation events along the sediment core . . . 131
II.4.2 Evolution of sediment source contributions and ^{137}Cs transfers through time . . . 132
II.4.3 Perspectives and management implications . . . 133
II.5 Conclusions . . . 135
II.6 Supplementary materials . . . 137
II.6.1 Laboratory analysis methodology . . . 137
II.6.1.1 Radiocesium analysis . . . 137
II.6.1.2 Organic Matter . . . 137
II.6.1.3 Elemental geochemistry . . . 137
II.6.1.4 Visible colorimetry . . . 138
II.6.1.5 Particle sizes . . . 139
II.6.1.6 Bulk density . . . 139
II.6.2 Figures . . . 140
II.6.3 Tables . . . 142

III Decontamination and Radiocesium Transfer: Flood Deposits Insights 163
III.1 Introduction . . . 164
III.2 Materials and Methods . . . 167
III.2.1 Study site . . . 167

III.2.2 Catchment management after FDNPP accident . . . 169
III.2.3 Sediment and soil sampling and processing . . . 169
III.2.4 Laboratory analyses . . . 170
III.2.5 Sediment connectivity . . . 170
III.2.5.1 Contributing area . . . 171
III.2.5.2 Distance in downslope direction . . . 172
III.2.5.3 Slope gradient . . . 172
III.2.5.4 Cover factor . . . 172
III.2.5.5 Surface roughness index . . . 173
III.2.5.6 Precipitation intensity and erosivity factors . . . 173
III.2.6 Sediment source fingerprinting . . . 177
III.2.6.1 Tracer selection . . . 177
III.2.6.2 Source contribution modeling . . . 178
III.2.6.3 Modeling accuracy assessment . . . 178
III.3 Results . . . 179
III.3.1 Rainfall erosivity throughout time . . . 179
III.3.2 Evolution of sediment connectivity through time . . . 186
III.3.3 Impact of erosive events on sediment connectivity . . . 186
III.3.4 Evolution of ^{137}Cs transfers in space and time . . . 192
III.3.5 Sediment source fingerprinting . . . 194
III.3.5.1 Tracer selection . . . 194
III.3.5.2 Sediment source fingerprinting modelling accuracy . . . 195
III.3.5.3 Sediment source contribution through space and time . . . 196
III.4 Discussion . . . 200
III.4.1 Rainfall erosivity and mapping . . . 200
III.4.2 Evolution of the index of connectivity under land use changes and the occurrence of erosive events . . . 201
III.4.3 Dynamic of ^{137}Cs transfer and sediment sources . . . 203
III.5 Conclusions . . . 204
III.6 Supplementary materials . . . 206
III.6.1 Laboratory analysis methodology . . . 206
III.6.1.1 Radiocesium analysis . . . 206
III.6.1.2 Organic Matter . . . 206
III.6.1.3 Elemental geochemistry . . . 206
III.6.1.4 Visible colorimetry . . . 208
III.6.2 Figures . . . 210
III.6.3 Tables . . . 211

IV Radiocesium and Sediment Transfers: Perspectives on Decontamination Timing 235
IV.1 Introduction . . . 236
IV.2 Materials and Methods . . . 238
IV.2.1 Study sites . . . 238
IV.2.2 Sampling and processing of sediment cores and potential sources . . . 240
IV.2.3 Laboratory analyses . . . 241
IV.2.4 Energy Dispersive X-ray Fluorescence (ED-XRF) core scanner . . . 241

IV.2.5 Initial deposition density of ^{137}Cs . . . 242
IV.2.6 Sediment source fingerprinting . . . 243
IV.2.6.1 Tracer selection . . . 243
IV.2.6.2 Source contribution modeling . . . 243
IV.2.6.3 Modelling accuracy assessment . . . 244
IV.3 Results . . . 244
IV.3.1 Initial deposition density and transfers of ^{137}Cs . . . 244
IV.3.2 Evolution of properties along the sediment cores . . . 247
IV.3.2.1 Validity and comparison of ED-XRF core scanner data with ED-XRF concentration data . . . 247
IV.3.2.2 High-resolution proxy-based event identification . . . 247
IV.3.3 Sediment source fingerprinting . . . 249
IV.3.3.1 Origin of organic matter . . . 249
IV.3.3.2 Tracer selection . . . 249
IV.3.3.3 Sediment source fingerprinting modelling accuracy . . . 250
IV.3.3.4 Evolution of sediment source contribution . . . 251
IV.4 Discussion . . . 253
IV.4.1 Challenges in combining ED-XRF core scanner analyses with sediment source fingerprinting techniques . . . 253
IV.4.2 Evolution of sediment source contribution and ^{137}Cs transfers . . . 254
IV.4.3 Perspectives on decontamination timing and management implications . . . 256
IV.5 Conclusions . . . 257
IV.6 Supplementary materials . . . 259
IV.6.1 Laboratory analysis methodology . . . 259
IV.6.1.1 Radiocesium analysis . . . 259
IV.6.1.2 Organic Matter . . . 259
IV.6.1.3 Elemental geochemistry . . . 259
IV.6.1.4 Bulk density . . . 260
IV.6.2 Figures . . . 261
IV.6.3 Tables . . . 264

General Discussion, Perspectives and Conclusions **281**

Appendix **301**

A fingR package: A Support for Sediment Source Fingerprinting Studies **303**
A.1 Installation . . . 304
A.2 Usage . . . 304
A.2.1 Data preparation . . . 304
A.2.1.1 Database construction . . . 305
A.2.1.2 Selecting properties vectors . . . 306
A.2.1.3 Evaluation of measurement quality . . . 307
A.3 Tracer selection . . . 308
A.3.1 Conservative behaviour . . . 308
A.3.2 Discriminant power . . . 310
A.3.3 Identified tracers: conservative and discriminant properties . . . 312

A.3.4 Discriminant Function Analysis stepwise selection . . . 313
A.4 Source Contribution Modelling . . . 314
A.4.1 Virtual Mixtures Generation . . . 314
A.4.2 Un-Mixing models . . . 316
A.4.2.1 Bayesian Mean Model - BMM . . . 316
A.4.2.1.a Run BMM . . . 316
A.4.2.1.b Collect and organise BMM contributions . . . 317
A.4.2.2 MixSIAR model . . . 319
A.4.2.2.a Generate data for MixSIAR . . . 319
A.4.2.2.b Load mixture, source and discrimination data . . . 320
A.4.2.2.c Write JAGS model file . . . 321
A.4.2.2.d Run MixSIAR . . . 322
A.4.2.2.e Collect and organise MixSIAR contributions . . . 323
A.4.3 Modelling accuracy statistics calculation . . . 324
A.4.3.1 General accuracy metrics . . . 325
A.4.3.2 Continuous ranked probability score . . . 326
A.4.3.3 Prediction interval width . . . 326
A.4.3.4 Encompassed sample predictions . . . 327
A.5 Citation . . . 328

B A unified template for sediment source fingerprinting databases 331

C Analyses for Conducting Sediment Fingerprinting Approaches in the Mano Dam Reservoir (Hayama Lake) Catchment (Fukushima Prefecture, Japan) 335

D Diagnostic Properties of River Flood Deposit Sediment Collected Annually from 2011 to 2023 at Ten Sites across a Water Reservoir Catchment Contaminated after the Fukushima Daiichi Nuclear Accident Radiocesium Fallout (Mano Dam) 337

E Diagnostic properties of three sediment cores collected in 2021-2022 from Three water reservoirs draining contaminated catchments after the Fukushima Daiichi Nuclear Power Plant accident (Mano dam, Ogaki dam, and Yokokawa dam) 339

Résumé général 345

List of Figures

GI.1 (A) Map of the ^{137}Cs deposition on soils across Northeastern Japan following FDNPP (after Kato et al. (2019)); (B) – (C) delineation of the areas where decontamination works have been conducted following the FDNPP accident in Japan including the Intensive Contamination Survey Areas – ICAs (40 municipalities; 24,000 km^2), the Special Decontamination Zone – SDZ (parts of the 11 municipalities; 1,150 km^2) and the DTRZ – Difficult to Return Zone (parts of 8 municipalities; 335 km^2) (Source: Japanese Ministry of Environment). Realised for Evrard et al. (2023). 36

GI.2 Evolution of the areas and locations where protective actions and evacuation were ordered or recommended from the FDNPP accident on 11 March 2011 until Spring 2022 (adapted from IAEA (2015) for 2011 and updated onwards). 38

GI.3 Flood deposits collection during a post-typhoon 2022 and 2023 sampling campaigns (© Olivier Evrard). 41

I.1 Map of the main land uses in the Hayama Lake catchment area over the 2014-2016 period with location of source samples and the sediment core (cartographic data: GSI and JAXA). FDNPP: Fukushima Daiichi nuclear power plant. 61

I.2 Tracer selection using the three-step method (TSM) according to different range test criteria. Green filled circles indicate a property that passed the conservative behaviour (i.e. range test) or the discriminant power (Kruskal-Wallis H test) tests. Blue filled diamonds indicate selected tracers (i.e. properties that passed both conservative behaviour and discriminant power tests) and blue diamonds with white points indicate tracers retained by the discriminant function analysis (DFA) forward stepwise selection based on Wilk's lambda criterion. Kruskal-Wallis H test's *p* value significance: "***" *p* value < 0.001; "**" *p* value < 0.01; "*" *p* value < 0.05; "." *p* value < 0.1; " " *p*-value < 1. OM: organic matter; Min-Max: minimum to maximum; SD: standard deviation. 67

I.3 Tracer selection using the consensus method (CM). Green filled circles indicate properties selected by the conservativeness index (i.e. CI = 0.0). The value in the circle refers to the number of sediment samples (out of 32) that obtained a Consensus Raking score above the threshold (i.e. CR $\geq$ 70). Blue filled diamonds indicate selected tracers. OM: organic matter. 68

I.4 Summary of MixSIAR accuracy statistics calculated on virtual mixtures (n = 138) for each tracer selection method: three-step method (TSM) range test criteria and consensus method (CM) for each individual soil source and average of all three sources for each method. Tracers selected by each method are listed in Table I.III. Model accuracy statistics were shown by darker bar plots for each selection approach. W50*: prediction interval width; ME: mean error; RMSE: root mean square error; r^2: squared Pearson's correlation coefficient; NSE: Nash-Sutcliffe modelling efficiency coefficient; CRPS: continuous ranked probability score. Note that symbol $*$ indicates mean values per source . 69

I.5 Relationship between theoretical virtual mixture source contributions and prediction interval width (W50) across sources (cropland, forest and subsoil) according to each tracer selection approach: three-step method (TSM) range test criteria, which are minimum-maximum (red circle), minimum-maximum ± 10 % (brown crossed circle), whiskers (yellow/orange diamond), hinge (green square), and mean ± SD (blue triangle point down) - filled and empty symbols correspond to the selection before DFA (no DFA) and after DFA respectively, except for mean (blue triangle) and median (blue crossed square) criteria for which empty symbols correspond to the same selection of tracers before and after DFA - and consensus method (CM; purple circle plus). 70

I.6 Relationship between theoretical and predicted virtual mixture source contributions (cropland, forest, subsoil), according to each tracer selection approach: three-step method (TSM) range test criteria, which are minimum-maximum (red circle), minimum-maximum ± 10 % (brown crossed circle), whiskers (yellow/orange diamond), hinge (green square), and mean ± SD (blue triangle point down) - filled and empty symbols correspond to the selection before DFA (no DFA) and after DFA respectively, except for mean (blue triangle) and median (blue crossed square) criteria for which empty symbols correspond to the same selection of tracers before and after DFA - and consensus method (CM; purple circle plus). 72

I.7 Relationship between theoretical virtual mixture source contributions and continuous ranked probability score (CRPS) across sources: three-step method (TSM) range test criteria which are minimum-maximum (red circle), minimum-maximum ± 10 % (brown crossed circle), whiskers (yellow/orange diamond), hinge (green square) and mean ± SD (blue triangle point down) - filled and empty symbols correspond to the selection before DFA (no DFA) and after DFA respectively, except for mean (blue triangle) and median (blue crossed square) criteria for which empty symbols correspond to the same selection of tracers before and after DFA - and consensus method (CM; purple circle plus). 73

I.8 Predicted source contributions for the sediment core samples according to each tracer selection approach. The different range test criteria of the three-step method (TSM) are the following: minimum-maximum (red circle), minimum-maximum ± 10 % (brown crossed circle), whiskers (yellow/orange diamond), hinge (green square), mean (blue triangle), mean ± SD (light blue triangle point down), and median (purple crossed square); the consensus method (CM; light purple circle plus) is also shown. Empty and filled symbols correspond to the use of DFA or not. The error buffer ribbons around the plotted values correspond to the respective RMSE values calculated on virtual mixtures. 74

I.9 Log-transformed values of selected tracers along the sediment core (black dot; measurement uncertainty is represented with a grey buffer) and in the potential source signatures (vertical line represents mean value, and the buffer zone along each line represents the standard deviation). 75

I.SM-1 Sediment core and source samples δ^{13}C and TOC/N and typical ranges for organic inputs to lacustrine environments (thresholds from Lamb et al. (2006)). 82

I.SM-2 Map of the main land uses in the study area over the 2014-2016 period with location of the source samples and the sediment core (cartographic data: GSI and JAXA). FDNPP: Fukushima Dai-ichi Nuclear power plant. 84

I.SM-3 Map of the main geology types in the study area with location of the source samples and the sediment core (cartographic data: GSI). FDNPP: Fukushima Dai-ichi Nuclear power plant. 85

I.SM-4 Map of the main soil types in the study area with location of the source samples and the sediment core (cartographic data: GSI and NARO). FDNPP: Fukushima Dai-ichi Nuclear power plant. 86

II.1 Mano Dam reservoir catchment map of the main (a) land uses over the 2014-2016 period, (b) geological, and (c) pedological types with the location of source samples and sediment core sampling. Cartographic data from the Geospatial Information Authority of Japan (GSI), JAXA High-Resolution Land-Use and Lad-Cover Map Products 2014-2016 (ver. 18.03), and NARO). 113

II.2 Mano Dam reservoir (a) sediment core log and analysed properties, from left to right: colour indices: (b) L* and (c) b*, (d) $^{134}Cs/^{137}Cs$ ratio decay-corrected to 11 March 2011 along with the 1.06 $\pm$ 0.04 (standard deviation) range attributed to material exposed to Fukushima fallout (blue area) (Kobayashi et al., 2013), (e)^{137}Cs activity, elemental geochemistry of: (f) Al, (g) Si, (h) Ti, (i) total organic carbon (TOC) content, and granulometry: (j) frequency of grain size from 0.1 to 2500 μm along with the D10, D50 and D90 (white dashed lines) and (k) specific surface area (SSA), and (l) identified extreme precipitation events. Measurement uncertainties are displayed as a grey ribbon. 119

II.3 (a) Mean daily precipitation at the four precipitation monitoring AMeDAS stations surrounding the Mano Dam reservoir catchment between March 2011 and June 2021, reservoir dam (b) water level and (c) water discharge between January 2014 and June 2021, (d) suspended sediment flux at the hydrological station upstream the reservoir, and (e) the progress of decontamination as of cumulative proportion of the total decontaminated area under contrasted land uses (cropland, grass border, grassland, forest border). Extreme precipitation events ranked as extra-tropical cyclone (solid), typhoon (dash), severe tropical storm (dot-dash) and tropical storm (dot) that generated more than 60 or 100 mm of daily precipitation (horizontal dotted lines, Evrard et al. (2014)) are identified by their international number ID. The progress of the total decontaminated surface area with the successive levels of 10 %, 20 % and 30 % are indicated. The grey bar in sub-figure (a) represents the time frame displayed in sub-figure (b). 122

II.4 (a) Identification of extreme precipitation events-associated deposits and (b) dating of these identified deposits by comparing ^{137}Cs distribution along the sediment core, progress of decontamination, and the extreme precipitation events that occurred since the Fukushima Daiichi Nuclear Power Plant (FDNPP) accident in March 2011. Decontam. stands for decontamination. Extreme precipitation events ranked as extra-tropical cyclone (solid), typhoon (dash), severe tropical storm (dot-dash) and tropical storm (dot) that generated more than 60 mm of daily precipitation (horizontal dotted line, Evrard et al. (2014)) are identified by their international number ID and named when associated with a deposit. . 125

II.5 Signatures of δ^{13}C and TOC/TN in potential sources and in sediment core samples along with typical ranges for organic inputs to clay-sized dominant terrestrial environments (according to Lamb et al. (2006) and Amorim et al. (2022)). Sediment core samples showing values lying outside of the range found in potential sources are indicated by their depth intervals (cm). TOC stands for total organic carbon; TN for total nitrogen; POC for particulate organic matter; DOC for dissolved organic matter. 126

II.6 Tracer selection according to the Three-Step Method using range test hinge criteria. Green filled circles and portions indicate a property that passed the conservativity (i.e. range test) and the discriminant power (i.e. Kolmogorov-Smirnov two-samples test p value < 0.01) tests, respectively. Blue filled diamonds indicate selected tracers (i.e. properties that passed both conservativity and discriminant power tests) and blue diamonds with white dots indicate tracers retained by the discriminant function analysis (DFA) forward stepwise selection based on Wilk's lambda criterion. TOC stands for total organic carbon. 127

II.7 Relationship between theoretical and predicted contributions of the virtual mixtures (blue diamond) for each source: (a) undecontaminated cropland, (b) forest, (c) subsoil, of the multiple model (blue line) as the average of MixSIAR (red line) and Bayesian Mean Model (orange line) predictions along with actual Mano Dam sediment core samples predicted contributions (green circle). (d) Ternary plot of the theoretical (light blue diamond) and predicted (blue diamond) contributions of the virtual mixtures and predicted contributions of the Mano Dam sediment core samples (green dot). Mano Dam sediment core samples with predicted contributions outside of the range/space defined by the predicted contributions of the virtual mixtures are circled in red. 128

II.8 Evolution of the (a) mass accumulation rate (MAR) as a function of the contribution of each sedimentary source (%), ^{137}Cs (b) activity and (c) cumulative deposition flux per extreme precipitation event identified along the sediment core sampled in the downstream part of the Mano Dam reservoir. 130

II.SM-1 Comparison of sediment cores collected at the downstream location of the Mano Dam reservoir in June 2021 and in November 2014 (DD1 and DD2) in Huon et al. (2018) study. 140

II.SM-2 Mano Dam Reservoir management and metrics during extreme precipitation events, as hourly observations over nine-days of water inflow (red) and outflow (green) and dam water level (dark) along with water flow (red dot-dashed) and suspended sediment flux (orange) at the reservoir inlet river monitoring station. The black dashed line marks the dam management water level threshold at 176 *m*. Crossed circles denote damaged monitoring stations during (d) Etau & Kilo and (i) Hagibis. 141

III.1 Mano Dam reservoir catchment map of the main (a) land uses over the 2018-2020 period, (b) geological substrates, and (c) soil types, with the location of the ten lag deposit sampling sites (pink octagon) and potential source samples. Cartographic data from the Geospatial Information Authority of Japan (GSI), JAXA High-Resolution Land-Use and Lad-Cover Map Products 2018-2020 (ver. 21.11), and NARO). 168

III.2 Location of the 58 weather stations within a 110 km buffer zone around the Fukushima Daiichi Nuclear Power Plant (FDNPP) over the ^{137}Cs deposition on soils across north-eastern Japan after Kato et al. (2019), and location of the Mano Dam reservoir catchment (white line). Cartographic data available from the Geospatial Information Authority of Japan (GSI). 174

III.3 Predicted rainfall erosivity (EI_{30} in MJ mm ha^{-1} h^{-1}) for the last erosive events that occurred prior to each November sediment sampling campaign from 2011 to 2023 across the Mano Dam reservoir catchment. 185

III.4 Evolution of the index of connectivity (IC) in the Mano Dam reservoir catchment based on topographical and contextual information at the time of the annual November flood deposit sampling campaign from 2011 to 2023. White and empty octagons indicate the occurrence or the absence of sediment when conducting sampling, respectively, and blue octagons indicate those sites where water level was too high during the campaign. *This graph is composed of two sub-figures.* 189

III.5 Evolution of the index of connectivity (IC) in the Mano Dam reservoir catchment based on topographical and contextual information and the intensity of the last erosive event at the time of the annual November sampling campaign from 2011 to 2023. White and empty octagons indicate the occurrence or the absence of sediment when conducting sampling, respectively, and blue octagon indicates those sites where water level was too high during the campaign. *This graph is composed of two sub-figures.* 191

III.6 Annual evolution of ^{137}Cs activities in flood deposits collected in November across the Mano Dam reservoir catchment from 2011 to 2023. Orange solid and dotted lines indicate annual mean and median values, respectively, with the standard deviation around the mean indicated by the light orange ribbon. Number in brackets indicates the number of samples collected during each campaign. Dotted line indicates the occurrence of the decontamination period that took place from June 2014 to December 2016. 192

III.7 Annual evolution of ^{137}Cs activity in flood deposits collected annually from 2011 to 2023 during the November sampling campaign at ten sampling sites across the Mano Dam reservoir catchment. Cartographic data available from the Geospatial Information Authority of Japan (GSI) and JAXA High-Resolution Land-Use and Lad-Cover Map Products 2018-2020 (ver. 21.11). 193

III.8 Tracer selection according to the three-step method. Green filled circles and sections indicate a property considered conservative according to the range test based on the mean $\pm$ one standard deviation of the log-transformed values and the discriminant power test (two-sample Kolmogorov-Smirnov test p value < 0.01), respectively. Blue filled diamonds indicate selected tracers (i.e. properties that passed both the conservative behaviour and discriminant capacity tests). TOC stands for total organic carbon, TN stands for total nitrogen, CN stands for TOC/TN ratio. 194

III.9 Relationship between theoretical and predicted contributions of the 231 virtual mixtures (blue diamond) for each source: (a) farmland, (b) forest, (c) subsoil, of the MixSIAR model (blue line) predictions along with the 101 lag deposit samples predicted contributions (orange dot). (d) Ternary plot of the theoretical (light blue diamond) and predicted (blue diamond) contributions of the virtual mixtures and predicted contribution of the lag deposit samples (orange dot). 196

III.10 Annual evolution of sediment source contribution from three potential sources, among farmland (brown), forest (green), subsoil-"fresh soil" (yellow), in flood deposits collected annually from 2011 to 2023 during the November sampling campaign at ten sampling sites across the Mano Dam reservoir catchment. Cartographic data available from the Geospatial Information Authority of Japan (GSI) and JAXA High-Resolution Land-Use and Lad-Cover Map Products 2018-2020 (ver. 21.11). 197

III.SM-1 Comparison of the element concentrations of Mg, Al, K, Ca, Ti, Cr, Mn, Fe, Co, Ni, Cu, Zn, Rb, Sr, Ba, and Pb measured using quadrupole inductively coupled plasma mass spectrometry (TQ-ICP-MS) and X-ray florescence (XRF) on 34 Saharan dust samples collected throughout Europe. 207

III.SM-2 Distribution of potential sources among forest (green), Farmland (brown), and Subsoil - Fresh soil (yellow), and lag sediment samples (blue dots) values for the tracers retained for sediment source fingerprinting. Kolmogorov-Smirnov two-samples tests for source groups significance of the *p* value. "***" *p* value $\leq$ 0.001; "**" *p* value $\leq$ 0.01; "*" *p* value $\leq$ 0.05; "." *p* value $\leq$ 0.1; " " *p* value $>$ 0.1. 210

IV.1 Main land uses over the 2006-2011 period in the (a) Mano Dam, (b) Ogaki Dam, and (c) Yokokawa Dam reservoir catchments. Cartographic data from the Geospatial Information Authority of Japan (GSI), and JAXA High-Resolution Land-Use and Lad-Cover Map Products 2006-2011 (ver. 16.09). 239

IV.2 Rasterized map of the reconstructed initial ^{137}Cs fallout map (decay corrected to July 2011) after the Fukushima Daiichi Nuclear Power Plan (FDNPP) from Kato et al. (2019), with a minimum threshold of 1 kBq m^{-2}.
The map raster is available online at https://zenodo.org/records/7827616 (Evrard et al., 2023) 245

IV.3 Evolution of analysed properties along the (a) Mano Dam, (b) Ogaki Dam, and (c) Yokokawa Dam sediment cores, from left to right: previously identified extreme precipitation events in the Mano Dam sediment core in Chalaux-Clergue et al. (2024c), ^{137}Cs activity and ED-XRF terrigenous proxy represented by the Al and Fe elemental profile, the Compton/Rayleigh scattering ratios (Mo inc:coh), the Al elemental geochemistry measured by quantitative ED-XRF, total organic carbon (TOC) content analysed by EA-IRMS (light grey) (measurement uncertainties are displayed as a grey ribbon). 'cps' stands for count-per-second. 248

IV.4 Signatures of δ^{13}C and TOC/TN in potential sources and in Mano (blue dot), Ogaki (pink dot) and Yokokawa (Green dot) Dam reservoir sediment core samples along with typical ranges for organic inputs to clay-sized dominant terrestrial environments (according to Lamb et al. (2006) and Amorim et al. (2022)). TOC stands for total organic carbon; TN for total nitrogen; POC for particulate organic matter; DOC for dissolved organic matter. 250

IV.5 Relationship between theoretical and predicted contributions of the 41 virtual mixtures (blue diamond) for each source: (a) topsoil, and (b) subsoil, for the MixSIAR model (blue line) predictions obtained for each individual sediment core 1-cm layer samples predicted contributions (orange dot) collected in Mano Dam (n = 38), Ogaki Dam (n = 16) and Yokokawa Dam reservoirs (n = 35). 251

IV.6 Evolution of the quantitative source contributions between topsoil and subsoil sedimentary sources (in g cm^{-3}) and radiocesium activity (in Bq kg^{-1}) along the sediment core collected in the downstream part of reservoir of the (a) Mano Dam (June 2021), (b) Ogaki Dam (September 2022) and (c) Yokokawa Dam (August 2022). FDNPP stands for Fukushima Daiichi Nuclear Power Plant accident 252
IV.SM-1 Main geological substrate in the (a) Mano Dam, (b) Ogaki Dam, and (c) Yokokawa Dam reservoir catchments. Cartographic data from the Geospatial Information Authority of Japan (GSI). 261
IV.SM-2 Main soil types over the 2006-2011 period in the (a) Mano Dam, (b) Ogaki Dam, and (c) Yokokawa Dam reservoir catchments. Cartographic data from the Geospatial Information Authority of Japan (GSI), and NARO). 262
IV.SM-3 Evaluation of the validity of the analyses realised by the Itrax Energy-Dispersive X-ray Fluorescence (ED-XRF) every 1 mm on the (a) Ogaki and (b) Yokokawa Dam reservoir sediment cores. 263
IV.SM-4 Comparison of the calibrated total organic carbon (TOC) from Energy-Dispersive X-ray Fluorescence (ED-XRF) and EA-IRMS measured TOC on the sediment layer of the (a) Ogaki and (b) Yokokawa Dam reservoir sediment cores. r^2 stands for the Pearson squared correlation. 264

GD.1 Damaged concrete river bank after the occurrence of the Typhoon Etau in September 2015 at the inlet of the Mano Dam reservoir (© Olivier Evrard - 2 November 2015). . . . 288

R.1 (A) Carte des dépôts de ^{137}Cs dans la région du nord-est du Japon suite à l'accident de la FDNPP (d'après Kato et al. (2019)); (B) - (C) délimitation des zones où des travaux de décontamination ont été menés, comprenant les zones d'étude intensive de la contamination (*Intensive Contamination Survey Areas* - ICAs) (40 municipalités; 24 000 km^2), la zone de décontamination spéciale (*Special Decontamination Zone* - SDZ) (11 municipalités; 1 150 km^2) et la zone difficile au retour (*Difficult-to-Return Zone* - DTRZ) (tout ou partie de 8 municipalités; 335 km^2) (Source : Ministère japonais de l'environnement). Cartes réalisée dans le cadre de Evrard et al. (2023). 346
R.2 Évolution des zones où les mesures de protection et d'évacuation ont été ordonnées ou recommandées depuis l'accident de la centrale nucléaire de Fukushima, le 11 mars 2011, jusqu'au printemps 2022 (adapté de IAEA (2015) pour l'année 2011 et mis à jour depuis lors). 348
R.3 Prélèvement de laisses de crue lors des campagnes de prélèvement d'automne des années 2022 et 2023 (© Olivier Evrard). 351

List of Tables

I.I Equations of the common range test criteria used in the literature to test the conservative behaviour in the three-step method (TSM). s_i is the source group i from 1 to n, the number of source groups; t_j is the target sample j value with j from 1 to m, the number of samples; and μ is the mean and σ is the standard deviation (SD). Symbol * indicates statistics calculated on log-transformed values. 63

I.II Formula of model prediction accuracy metrics. With z_i and $\hat{z}_i$, respectively, the measured and predicted contributions for the sample i; $\bar{z}$ and $\bar{\hat{z}}$ the measured and predicted mean contribution of all samples; and n the number of samples. 66

I.III Tracers selected by the three-step method (TSM) according to the range test criteria and the consensus method (CM). Tracers underlined and written in bold were retained by the discriminant function analysis (DFA) forward stepwise selection based on Wilk's lambda criterion. Min-Max = minimum to maximum. 68

I.SM-I Summary of MixSIAR accuracy statistics calculated on virtual mixtures (n = 138) for each tracer selection method: three-step method (TSM) range test criteria and consensus method (CM) for cropland course. W50*: prediction interval width; ME: mean error; RMSE: root mean square error; r^2: squared Pearson's correlation coefficient; NSE: Nash-Sutcliffe modelling efficiency coefficient; CRPS*: continuous ranked probability score. Note that * indicates mean values per source. 87

I.SM-II Summary of MixSIAR accuracy statistics calculated on virtual mixtures (n = 138) for each tracer selection method: three-step Method (TSM) range test criteria and consensus method (CM) for forest course. W50*: prediction interval width; ME: mean error; RMSE: root mean square error; r^2: squared Pearson's correlation coefficient; NSE: Nash-Sutcliffe modelling efficiency coefficient; CRPS*: continuous ranked probability score. Note that * indicates mean values per source. 87

I.SM-III Summary of MixSIAR accuracy statistics calculated on virtual mixtures (n = 138) for each tracer selection method: three-step method (TSM) range test criteria and consensus method (CM) for subsoil course. W50*: prediction interval width; ME: mean error; RMSE: root mean square error; r^2: squared Pearson's correlation coefficient; NSE: Nash-Sutcliffe modelling efficiency coefficient; CRPS*: continuous ranked probability score. Note that * indicates mean values per source. 88

I.SM-IV Summary of MixSIAR accuracy statistics calculated on virtual mixtures (n = 138) for each tracer selection method: three-step method (TSM) range test criteria and consensus method (CM) averaged on the three sources (i.e. cropland, forest and subsoil). W50*: prediction interval width; ME: mean error; RMSE: root mean square error; r^2: squared Pearson's correlation coefficient; NSE: Nash-Sutcliffe modelling efficiency coefficient; CRPS*: continuous ranked probability score. Note that $*$ indicates mean values per source. 88

I.SM-V Selected tracer Pearson correlation coefficients. The symbol · represents correlation with significance test *p* value lower than 0.05. 89

I.SM-VI Number of sediment samples that fell inside of the space of the virtual mixture predicted contributions for each tracer selection method out of 32. 89

II.SM-I Kolmogorov-Smirnov two-samples tests for source groups significance of the *p* value. "***" *p* value $\leq$ 0.001; "**" *p* value $\leq$ 0.01; "*" *p* value $\leq$ 0.05; "." *p* value $\leq$ 0.1; " " *p* value $>$ 0.1. 142

II.SM-II Summary mean and standard deviation values of analysed properties for each potential source group: forest (n = 24), undecontaminated cropland (n = 24), remediated cropland (n = 10) and subsoil (i.e. channel bank or landslide, n = 10). 142

II.SM-III Summary of the 27 extreme precipitation events that occurred between March 2011 and June 2021 and were recorded by the four precipitation monitoring AMeDAS stations surrounding the Mano Dam reservoir catchment located in Fukushima City, Hippo, Iitate and Soma. The dash indicates missing data. 143

II.SM-IV Summary of management and metrics during extreme precipitation events between 2014 and 2019, of the maximum water flow and suspended sediment flux at the reservoir inlet river monitoring station, maximum dam water flow metrics (inflow and outflow) and dam water level (maximum and level range). The KO indicates damaged river monitoring station during the event; max. stands for maximum; n.a. stands for not applicable; dash indicates missing data. 144

II.SM-V Summary of sediment source fingerprinting modeling prediction accuracy statistics calculated on virtual mixtures predictions (n = 138) for each model (i.e. MixSIAR, BMM, and Multiple-model). ME: mean error; RMSE: root mean square error; r^2: squared Pearson's correlation coefficient; NSE: Nash-Sutcliffe modeling efficiency coefficient; W50: prediction interval width; CRPS: continuous ranked probability score; ESP: encompassed sample predictions expressed as number of sample within the range out of 38 (n) and as percentage (%). BMM stands for bayesian mean model. Note: * indicates the mean values per source. 145

II.SM-VI Summary of predicted source contributions by each model for each potential source (in %). MM: Multiple-model. 146

II.SM-VII Characteristics of each extreme events identified along the Mano Dam reservoir sediment core with the sediment source contributions, ^{137}Cs activity and flux. MAR = mass accumulation rate, FDNPP = Fukushima Daiichi Nuclear Power Plant. Average per event apart from 23$-$28 event are indicated as mean $\pm$ standard deviation. 147

III.I Annual statistics of erosive events, erosive energy (EI_{30}) and associated precipitation and annual R factor, at each 58 weather stations within a radius of 110 km around the Fukushima Daiichi Nuclear Power Plant (FDNPP) for the period 2011-2023. Prefecture and stations are ordered from North-West to South-East. SD stands for standard deviation, * indicates that 2012 was missing, ** indicates that 2022 and 2023 were missing, *** indicates that the period 2019-2023 was missing. 180

III.II Annual Erosive events mean R factor and standard deviation (SD) for 58 weather stations within a radius of 110 km around the Fukushima Daiichi Nuclear Power Plant (FDNPP) for the period 2011-2023. 181

III.II Monthly Erosive events mean R factor and standard deviation (SD) for 58 weather stations within a radius of 110 km around the Fukushima Daiichi Nuclear Power Plant (FDNPP) for the period 2011-2023. 181

III.III Observed cumulative precipitation and rainfall erosivity (EI_{30}) of the erosive events that occurred before the annual November sampling campaign from 2011 to 2023 within a 110 km radius area around the Fukushima Daiichi Nuclear Power Plant (FDNPP), along with maximum EI_{30} observed at a weather station. 'Cumulative' line in bold corresponds to the event statistics for the year summed by station. Extreme precipitation event intensity classification grades stand for: 2 = tropical depression, 3 = tropical storm, 4 = severe tropical storm, 5 = typhoon, 6 = extra-tropical cyclone. 182

III.IV Observed and predicted rainfall erosivity mean and standard deviation (SD) (EI_{30} in MJ mm ha^{-1} h^{-1}) for the last(s) erosive events that occurred before the November sampling campaign from 2011 to 2023 over 58 weather stations located within a 100 km radius around the Fukushima Daiichi Nuclear Power Plant (FDNPP), along with the generalised additive models (GAMs) accuracy metrics. ME stands for mean error, RMSE for root mean square error, r^2 for squared Pearson's linear correlation, R^2 for coefficient of determination, R^2_{adj} for adjusted coefficient of determination. The covariates used to fit each model are listed in Supplementary Materials Table III.SM-V. 183

III.V Summary of predicted rainfall erosivity (EI_{30} in MJ mm ha^{-1} h^{-1}) across the Mano Dam reservoir catchment areas for the last erosive events that occurred before the sampling campaign from 2011 to 2023. SD stands for standard deviation. '*' indicates years with cumulative of events. 184

III.VI Annual statistics of the index of connectivity in the Mano Dam reservoir catchment at the time of the annual November flood deposit sampling campaign, from 2011 to 2023. SD stands for standard deviation. Years annotated with * and ** were generated with identical C-factor and JAXA Land Use layers respectively. Note: These statistics were computed using the 'zonal statistics' tool in QGIS [ver. 3.34.8] on the maps presented in figure III.4. 186

III.VII Annual statistics of the index of connectivity in the Mano Dam reservoir catchment at the time of the annual November sampling campaign considering the impact of the last erosive event before each campaign, from 2011 to 2023. SD stands for standard deviation. Note: These statistics were computed using the 'zonal statistics' tool in QGIS [ver. 3.34.8] on the maps presented in figure III.5. 187

III.VIII Summary of sediment source fingerprinting MixSIAR modeling prediction accuracy statistics calculated on virtual mixtures (n = 231). W50 stands from prediction interval width; ME stands for mean error; RMSE stands for root mean square error, r^2 stands for squared Pearson's correlation coefficient, NSE stands for Nash-Sutcliffe modeling efficiency coefficient; CRPS stands for continuous ranked probability score; ESP stands from encompassed sample predictions expression as the number of samples within the range of source out of 101 (n) and as a percentage (%). The * indicates mean value per source. 195

III.SM-I Location of flood deposit sampling sites and annual sampling during the annual sampling campaign after typhoon season from 2011 to 2023. The collected sediment samples are indicated with their label, "n.d." stands for no deposit, "flood" for site under a flood event at the time of the sampling campaign, and "-" for sites that have not been visited. 211

III.SM-II Weather stations information (prefecture, name, number, coordinates) along with the morphometric attributes (elevation,

. 212

III.SM-III Kolmogorov-Smirnov two-samples tests for source groups significance of the *p* value. "***" *p* value $\leq$ 0.001; "**" *p* value $\leq$ 0.01; "*" *p* value $\leq$ 0.05; "." *p* value $\leq$ 0.1; " " *p* value $>$ 0.1. 214

III.SM-IV Summary mean and standard deviation values of analysed properties for each potential source group: forest (n = 24),farmland (n = 24), "fresh soil" (n = 10), subsoil (i.e. channel bank or landslide, n = 10), and merged subsoil - fresh soil (n = 20). 214

III.SM-V Effective degree of freedom (EDF) values of the covariates of the generalised additive models (GAM) fitted on the last erosive events before sampling campaign measured intensity (EI_{30}) from 2011 to 2023. '-' indicates covariates that prevented model convergence and that were removed. 215

III.SM-VI Annual statistics of the P factor in the Mano Dam reservoir catchment at the time of the last erosive events before each sampling campaigns, from 2011 to 2023. SD stands for standard deviation. 216

III.SM-VII The annual statistics of the ^{137}Cs activity of the flood deposits in flood deposit sediments sampled in November across the catchment of the Mano Dam reservoir. 216

III.SM-VIII Median of the predicted source contributions predicted by MixSIAR of the flood deposits sampled from 2011 to 2023 at ten sampling sites within the Mano Dam reservoir catchment. "n.d." stands for no deposit, "-" for sites that have not been visited. 217

III.SM-IX Observed cumulative precipitation and rainfall erosivity (EI_{30}) of the erosive events that occurred before the annual November 2013 sampling campaign within a 110 km radius area around the Fukushima Daiichi Nuclear Power Plant (FDNPP), along with maximum EI_{30} observed at a weather station. 'Cumulative' line in bold corresponds to the event statistics for the year summed by station. Extreme precipitation event intensity classification grades stand for: 2 = tropical depression, 3 = tropical storm, 4 = severe tropical storm, 5 = typhoon, 6 = extra-tropical cyclone. 218

III.SM-X Observed cumulative precipitation and rainfall erosivity (EI_{30}) during the Phanfone and Vonfong events within a 110 km radius area around the Fukushima Daiichi Nuclear Power Plant (FDNPP), along with maximum EI_{30} observed at a weather station, and compared Chartin et al. (2017). 'Cumulative' line in bold corresponds to the event statistics for the year summed by station. Extreme precipitation event intensity classification grades stand for: 2 = tropical depression, 3 = tropical storm, 4 = severe tropical storm, 5 = typhoon, 6 = extra-tropical cyclone. 218

IV.I Summary of the initial deposition density and stock of ^{137}Cs following the Fukushima Daiichi Nuclear Power Plant (FDNPP) accident in March 2011 (decay-corrected to July 2011) within the Mano Dam, Ogaki Dam and Yokokawa Dam reservoir catchments. In addition, the catchment stock is compared to the initial deposition of $2.7 \cdot 10^{15}$ Bq on the terrestrial surface of Japan (in %). Note: These statistics were computed using the "zonal statistics" tool in QGIS [ver. 3.34.8] on the map presented in Supplementary Materials Fig. IV.2 and available online at (Evrard et al., 2023). 246

IV.SM-I Kolmogorov-Smirnov two-samples tests for topsoil (n = 59) and subsoil (n = 24) groups and for reservoir sediment cores: Mano Dam (n = 38), Ogaki (n = 16), and Yokokawa Dam (n = 35), significance of the *p* value. "***" *p* value $\leq$ 0.001; "**" *p* value $\leq$ 0.01; "*" *p* value $\leq$ 0.05; "." *p* value $\leq$ 0.1; " " *p* value $>$ 0.1. 264

IV.SM-II Summary mean and standard deviation values of analysed properties for each potential source group: topsoil (n = 59) and subsoil (n = 24), and reservoir sediment core layer samples: Mano Dam (n = 38), Ogaki (n = 16), and Yokokawa Dam (n = 35). 264
IV.SM-III Summary of sediment source fingerprinting MixSIAR modeling prediction accuracy statistics calculated on virtual mixtures (n = 41). W50 stands from prediction interval width; ME stands for mean error; RMSE stands for root mean square error, r^2 stands for squared Pearson's correlation coefficient, NSE stands for Nash-Sutcliffe modeling efficiency coefficient; CRPS stands for continuous ranked probability score; ESP stands from encompassed sample predictions expression as the number of samples within the range of source out of 89 (n) and as a percentage (%). The * indicates mean value per source. . 265
IV.SM-IV Evolution of the relative source contributions between two potential sources (i.e. Topsoil and subsoil; in %) predicted by the MixSIAR un-mixing model along the sediment cores collected in (a) Mano Dam, (b) Ogaki Dam, and (c) Yokokawa Dam reservoirs.. 266
IV.SM-V Evolution of quantitative source contributions between two potential sources (i.e. Topsoil and subsoil; in g cm^{-3}) predicted by the MixSIAR un-mixing model along the sediment cores collected in (a) Mano Dam, (b) Ogaki Dam, and (c) Yokokawa Dam reservoirs. . . 267

B.I Summary of CSV Files 331

General Introduction

General Introduction

Context

On 11 March 2011, Japan was affected by a series of events that resulted in the worse nuclear accident since Chernobyl. At 14:46 local time, Japan was struck by the "Great East Japan Earthquake" (東日本大震災 - '*higashi nihon daishinsai*' in Japanese) with a magnitude Mw of 7.3, although the main earthquake occurred about 130 km off the northeast coast of Honshū island - the main island of Japan - with a magnitude Mw of 9.0 (Simons et al., 2011). It was the strongest earthquake ever recorded in the country (Yagi and Fukahata, 2011; Zhao, 2015). Less than one hour after the main earthquake, a powerful tsunami with a height ranging from 4.1 m in Kamaishi City (釜石市) to 40.5 m in Miyako City (宮古市), both located in Iwate Prefecture (岩手県), hit about 2000 km of Japanese coasts and travelled up to 10 km inland, flooding around 561 km^2 (JMA, 2011; NOAA, 2015). The prefectures of Iwate, Miyagi (宮城県) and Fukushima (福島県) were severely affected, with the Miyagi Prefecture being the hardest hit. The Japanese government reported 19,579 deaths, 6,242 injured and 2,553 people missing (Fire and Disaster Management Agency, 2021; Emergency Disaster Preparedness Headquarters, 2021).

The Fukushima Daiichi Nuclear Power Plant (FDNPP), owned by the Tokyo Electric Power Company (TEPCO) and located on the coast line of Fukushima Prefecture, which was operating on emergency generators after the earthquake, was flooded by a tsunami wave of 14-15 m, which largely overflew the 5.5 m height tsunami wall (IAEA, 2015). The flooding of the emergency generators deprived the four operating reactors of their cooling systems. This led to an increase in temperature and hydrogen pressure inside the reactors. For pressure control in the reactors, the operators carried out depressurisation operations, which resulted in the release of hydrogen and radioactive elements within the reactor buildings. The presence of hydrogen in the buildings led to explosions in reactors 1 and 3 and to fires in reactor 4. These events resulted in the release of large quantities of radioactive elements into the environment, estimated to 520 PBq without considering noble gases (Chino et al., 2011; Kobayashi et al., 2013; Steinhauser, 2014; Yamamoto, 2015), of which 20 % deposited over the northeastern part of Honshū island, and the rest was blown out towards the Pacific Ocean (Morino et al., 2013; Onda et al., 2020). The severity of the event was ultimately categorised as a Major Accident on the International Nuclear and Radiological Event Scale (INES Level 7) (IAEA, 2015).

Among the radionuclides released into the environment, two major radioactive elements have been widely deposited over Japan, iodine (^{131}I) and radiocesium (^{134}Cs and ^{137}Cs) (Kato et al., 2012; Hashimoto et al., 2012). Because of their respective half-lives of 8 days, 2 years and 30 years, contamination related to radiocesium, and especially ^{137}Cs, leads to a long-standing problem for Japan as it may represent a current and future health risk for the local population, which is still the case, more than 10 years after the accident. Of the 2.7 PBq of ^{137}Cs that deposited onto inland Japan, most of it, 2.0 PBq, deposited within the Fukushima Prefecture (74 %) (Fig. GI.1.A) (Kato et al., 2019; Taniguchi et al., 2019). Within the Fukushima Prefecture, 83 % of the Prefecture area has received at least 5 kBq m^{-2} of ^{137}Cs (11,430 km^2), and 26 % has received at least 100 kBq m^{-2} (3,520 km^2) (Kato et al., 2019). The inhabitants living within a 20-km radius around FDNPP (Evacuation Zone) and those who could be exposed to a radioactive dose rate exceeding 20 mSv yr^{-1} in 2011 (Planned Evacuation Zone) were evacuated as a matter of priority (Fig. GI.2). A total of eleven municipalities located within the Fukushima Prefecture, with a population of about 80,000 inhabitants and

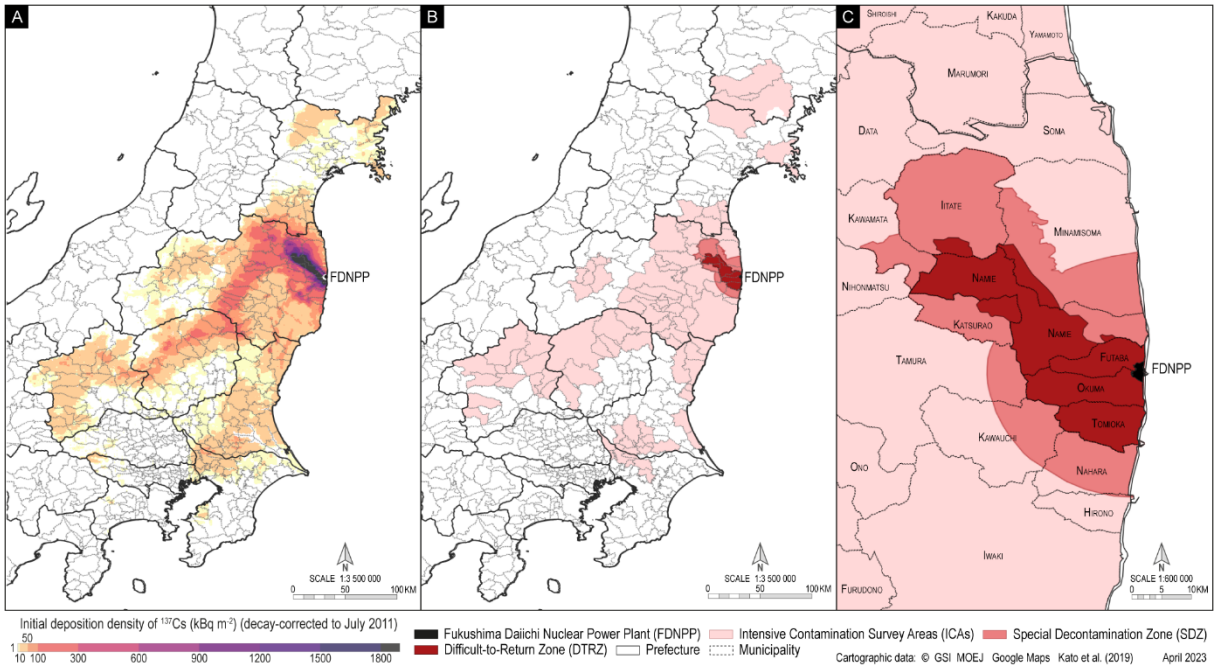


Figure GI.1: (A) Map of the ^{137}Cs deposition on soils across Northeastern Japan following FDNPP (after Kato et al. (2019)); (B) – (C) delineation of the areas where decontamination works have been conducted following the FDNPP accident in Japan including the Intensive Contamination Survey Areas – ICAs (40 municipalities; 24,000 km^2), the Special Decontamination Zone – SDZ (parts of the 11 municipalities; 1,150 km^2) and the DTRZ – Difficult to Return Zone (parts of 8 municipalities; 335 km^2) (Source: Japanese Ministry of Environment). Realised for Evrard et al. (2023).

covering 1,150 km^2, were under evacuation orders and classified as a Residence Restriction Area (Futaba Town - 双葉町, Iitate Village - 飯舘村, Katsurao Village - 葛尾村, Kawamata Town - 川俣町, Kawauchi Village - 川内村, Minamisōma City - 南相馬市, Namie Town - 浪江町, Naraha Town - 楢葉町, Ōkuma Town - 大熊町, Tamura City - 田村市, Tomioka Town - 富岡町). To enable the rapid return of the population and the resumption of economic activities and especially agriculture, the Japanese government initiated an unprecedented large-scale decontamination programme to remediate ^{137}Cs-contaminated soils in residential and cultivated areas affected by the main radioactive plume (Yasutaka and Naito, 2016). In relation to the initial radioactive contamination and the resulting exposition of inhabitants and workers to radiation dose rates, different zones were delineated. The long-term objective of the decontamination programme was to reach individual exposure doses below 1 mSv yr^{-1} or 0.23 μSv h^{-1}, assuming that people spend 8 hours outside and 16 hours in a wooden house with a low shielding rate in a day (reference level of exposure dose in normal conditions by the International Commission on Radiological Protection - IRCP) (MoE, 2013). Any areas where the radiation dose rate was higher than this threshold, were considered as "Intensive Contamination Survey Area" (ICAs; 汚染状況重点調査地域) by the Ministry of the Environment of Japan (MoE) (MoE, 2013), which impacted a width area over Japan (24,000 km^2) and a population of 6,9 million of inhabitants (Fig. GI.1.B) (MoE, 2018), and where the inhabitants were not evacuated. In immediate post-accidental conditions, higher dose exposure was allowed, with a maximum threshold of 20 mSv yr^{-1} or 3.8 μSv h^{-1} was set to allow residence. The eleven municipalities where the exposure dose rate exceeded this threshold at the time of the accident, were classified as "Special Decontamination Zone" (SDZ; 除染特別地域), and the areas where the exposure dose rate was expected to still exceed this threshold even five years after the accident (i.e., by 2016) were classified as "Difficult-to-Return Zone" (DTRZ; 帰還困難区域) (Fig. GI.1.B and C).

After deposition, ^{137}Cs strongly and quasi-permanently binds to fine soil particles (such as silt or clays; Sawhney (1972); He and Walling (1996)), leading to 90-99 % of the ^{137}Cs to accumulate within the uppermost 5 cm of undisturbed soil (Kato et al., 2012; Lepage et al., 2015), allowing for potential decontamination of contaminated soil to target this layer only. In December 2011, the MoE issued the decontamination guidelines (MoE, 2011) (revised in 2013 MoE (2013)), outlining the methods for decontamination in residential and cultivated areas as well as the protocols for the collection, transportation, and storage of removed soil. Then, in January 2012, the MoE published the "Policy for Decontamination in the Special Decontamination Area", which presents the roadmap for decontamination activities (Yasutaka and Naito, 2016).

In farmland areas (i.e. paddy fields or other arable land), the decontamination procedure depended on the initial ^{137}Cs activity in the soil (MoE, 2013, 2015, 2023). On the one hand, inversion tillage to a depth of 30-45 cm was carried out on farmland soils with activities below 5 kBq kg^{-1}. On the other hand, for farmland soils with activities above 5 kBq kg^{-1}, the following four steps were carried out: (1) removal of the upper 5 cm layer of soil, (2) addition of saprolite - derived from granite or sandstone - from local quarries opened for this purpose (55.5 m^3 per 1,000 m^2), referred to as "fresh soil", (3) restoration of soil fertility with amendments, either carbonate (as needed) and phosphorus silicate (about 0.8 t ha^{-1}) or zeolite amendments (about 0.5 t ha^{-1}), and (4) mixing of the 'fresh soil' layer with the underlying soil layer by double deep-ploughing (25-30 cm). The decontamination of the forest was limited to the forested areas within 20-m of residential settlements and along roads, and consisted of removing litter and fallen organic material (leaves, branches) - called "sediment" by the Japanese authorities - to a depth of about 5 cm, without reaching the "mineral soil" layer. The forests were also cleared of underbrush and shrubs. In addition, conifers were pruned to a height of about 4 m from the ground if they were within about 5 m of the forest edge, and the pruned branches were collected. The decontamination of grassland and grass strips located around agricultural areas, residential settlements or along the roads consisted of cutting and removing weeds and bushes.

All organic material collected during the decontamination has been transported to special facilities for processing. By March 2020, within the SDZ, 87 km^2 of farmland, 78 km^2 of forest, and 15 km^2 of road were decontaminated, accounting for about 16 % of the SDZ area (MoE, 2023). Nevertheless, decontamination involved a large number of workers and generated a significant quantities of waste, with 13.43 million m^3 of waste transported to interim storage facilities by 2020. Over the period from 2011 to 2020, 16 % of the total cost of recovery and reconstruction from the Great Tohoku Earthquake and FDNPP accident, amounting to JPY 6,122.3 billion, was spent on the "Nuclear Recovery Policy", including approximately JPY 1,500 billion and JPY 1,400 billion for the decontamination in the SDZ and ICAs, respectively (MoE, 2018; Board of Audit of Japan, 2023; Evrard et al., 2023).

The progress of decontamination, which was completed between 2017 and 2020 in the ICAs and the SDZ, together with physical radioactive decay, actively reduced the ambient air dose rates as well as individual exposure levels, allowing the evacuation orders to be gradually lifted between April 2014 in Tamura City and March 2020 in Futaba Town (Fig. GI.2) (MoE, 2023; Evrard et al., 2019) (Fig. GI.2). Indeed, soil decontamination has resulted in a reduction of 20 to 70 % in ambient air dose rates compared to the 2011 levels (MoE, 2018; Onda et al., 2020), which also led to a reduction in individual radiation exposure (Tsubokura et al., 2019). Conversely, the evacuation order was maintained in the DTRZ, as these were the areas with the highest radiation doses and they were not initially targeted for decontamination. However, after a partial reopening of the DTRZ in the Spring of 2022, the DTRZ was gradually reopened from 2023 without mandatory decontamination, except in "special reconstruction and revitalisation zones" (特定復興再生拠点区域), which are mainly areas located in the vicinity of residential settlements or agricultural areas. However, despite this workforce and

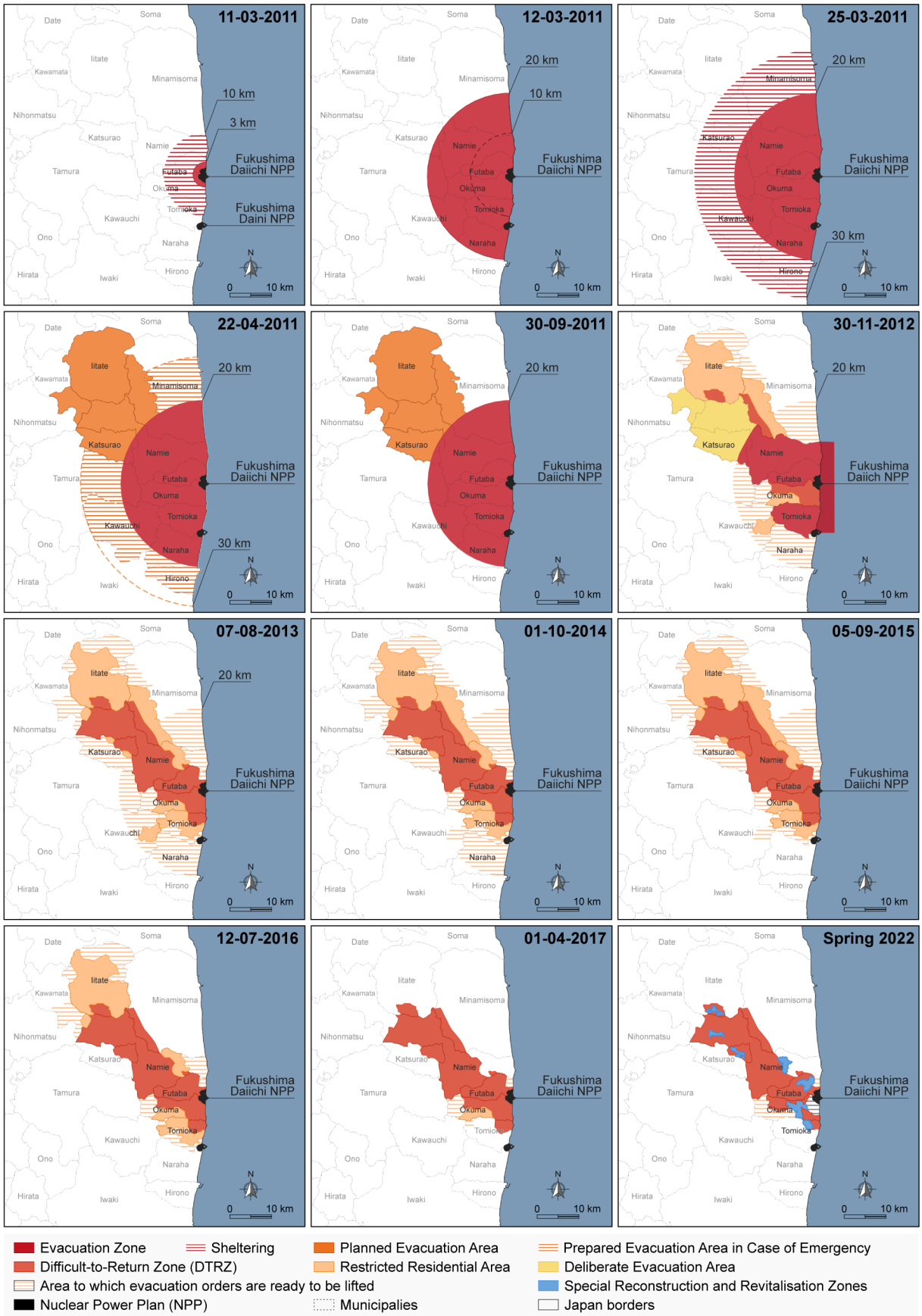


Figure GI.2: Evolution of the areas and locations where protective actions and evacuation were ordered or recommended from the FDNPP accident on 11 March 2011 until Spring 2022 (adapted from IAEA (2015) for 2011 and updated onwards).

financial investment, only a small proportion of evacuated residents had returned, estimated to reach about 30 % by 2020 (Taira et al., 2020; Asanuma-Brice et al., 2023). Multiple factors have contributed to the low return rate, including changes in living conditions (such as family separations and loss of community life), the lack of infrastructure and public services, concerns over radiation exposure, and restrictions on outdoor activities like hiking, freshwater fishing, and traditional harvesting of wild vegetables (山菜 - 'sansai') or mushrooms.

As the decontamination programme mainly targeted residential and agricultural areas, decontamination was restricted to a limited proportion of the overall region, mainly covered by forest (70-80 %). In addition, while only 19 % of the ^{137}Cs deposition occurred over farmland, 74 % of the initial deposition occurred over forested areas, which were almost not decontaminated (Kato et al., 2019). According to Yasutaka et al. (2013), the decontamination of the 20-m buffer zone of forest around residential areas and along roads was estimated to correspond to about 5 % of the overall forested areas within the SDZ.

In addition, this region of Japan is annually affected by at least one extreme precipitation event, such as typhoons or tropical storms, between July and October. These heavy precipitation events have been identified as the main driver of sediment transfer across landscapes (Laceby et al., 2016; Chartin et al., 2017). As a consequence, the vast majority of ^{137}Cs transfers occurs during these extreme precipitation events (82 to 99 %; Yamashiki et al. (2014); Sakaguchi et al. (2015); Iwagami et al. (2017); Osawa et al. (2018)) along the transfer of fine material of soil such as its silt-sized fraction (3-63 μm) (Sakaguchi et al., 2015). Therefore, under the influence of these events, the areas that have not been decontaminated, including forests or the DTRZ, could act as a long-term source of contaminated sediment, which could lead to the recontamination of previously decontaminated areas downstream.

Nevertheless, in parallel with the progress of decontamination, a decrease in particle-bound ^{137}Cs activities in river sediment has been observed, and various factors have been proposed to explain this decrease, including physical radioactive decay, reduced ^{137}Cs inventories due to repeated erosion events, progress of decontamination, and reduced erosion as a result of spontaneous vegetation regrowth following land abandonment. From the time of the FDNPP accident in March 2011 to the present day, significant changes in radiocesium and sediment transfers along with variations in sediment source contributions have been expected as a result of the drastic and rapid changes in land uses and covers recorded following the evacuation of the contaminated areas, the implementation of the decontamination programme, and the resumption of agricultural activities in decontaminated farmlands.

Objectives and general approach

The main research objective of this thesis is to investigate the impact of decontamination and recultivation of agricultural soils on sediment and radiocesium transfers in the coastal rivers draining the main radioactive plume generated by the FDNPP accident, through the compared analysis of contrasted catchments draining this zone characterised by different land covers and post-accidental management strategies.

This research focuses on the upper part of three coastal rivers (i.e., Mano - 真野川, Ukedo - 請戸川 et Ota - 太田川), located in the Northeastern part of Fukushima Prefecture and draining the main radiocesium plume resulting from the FDNPP accident. These catchments share similar topographical characteristics and can be divided into two main sections: an upstream mountainous area and a downstream coastal area, with a steep transition zone between them. The mountainous sections of these catchments are drained by reservoir dams built for agricultural irrigation purposes located on the edge of the mountainous plateau. The Mano Dam reservoir is located on the Mano River, the Ogaki Dam reservoir on the Ukedo River, and the Yokokawa

(横川) Dam reservoir on the Ota River. Therefore, these three catchments are typical mountainous catchments representative of those found in the Northeastern part of the Fukushima Prefecture, in terms of environmental conditions and topography. However, the catchments of the Mano and Ogaki Dams drain mixed agricultural and forested catchments, with forests covering about 90 % of their surface area, while the Yokokawa Dam catchment area can be considered as exclusively forested (99 %). In the Mano and Ogaki Dam catchments, due to the overall steep topography, farmland (i.e. cropland, grassland and paddy fields - about 10 %) is concentrated in the valley bottoms. The farmland areas, due to their location in the valley bottoms and through the creation of irrigation/drainage systems especially for paddy fields, were highly connected to the river system. Built-up areas consist mainly of isolated houses or hamlets and cover a very small part of the catchment areas (about 1 %). The mixed agricultural/forested catchments of the Mano and Ogaki Dams, mainly differed in their post-accidental decontamination strategies and timing. Within the Mano Dam catchment area, which is located in the Northern part of Iitate village within the SDZ, the decontamination was initiated in June 2014 and completed in December 2016, whereas the Ogaki Dam catchment, located in Namie Town within the DTRZ, was initially not included in the decontamination programme. The decontamination of the Ogaki Dam catchment area was initiated in Spring in 2022, along with the reopening of the DTRZ, with the mandatory decontamination of the "Special Reconstruction and Revitalization Zones" mainly concentrated in the vicinity of the Namie Town and the agricultural valley of the upstream Koidetani River (小出谷川).

This thesis is a continuation of the research initiated by the *Laboratoire des Sciences du Climat de l'Environnement* (LSCE - *Laboratory of Climate and Environmental Sciences*) between 2011 and 2013 with the TOFU project ("*Tracing the environmental consequences of the tsunami caused by the Tokohu earthquake and the Fukushima accident*"). It was followed by the AMORAD project ("*Amélioration des MOdèles de prévision de la dispersion et d'évaluation de l'impact des RADionucléides au sein de l'environnement*" - Improving models for predicting the dispersion and assessing the impact of radionuclides in the environment) coordinated by the *Institut de Radioprotection et de Sûreté Nucléaire* (IRSN -French Institute for Radioprotection and Nuclear Safety) and funded as part of the programme of *Investissement d'Avenir en RadioProtection et Sûreté Nucléaire* (RPSN - investment for the future of RadioProtection and Nuclear Safety) from 2014 to 2021, in which LSCE coordinated the "continental radionuclide transfer" axis aiming to improve radionuclide erosion modelling in continental landscapes based on feedbacks and measurements carried out in the region affected by the FDNPP accident.

As from the first field campaign organised in 2011 as part of the TOFU project, river sediment deposited after a flood event, referred to as "flood deposits" (see picture GI.3), was collected during two sampling campaigns organised each year during the immediate post-accidental phase (2011-2016), with one campaign taking place in spring after the snowmelt (April-May) and one campaign in autumn after the typhoon season (October-November). Then, from 2017 onwards, the sampling of flood deposits was restricted to the annual autumn campaign. In addition, soil samples corresponding to the potential sources of sediment, such as abandoned farmland, decontaminated farmland, 'fresh soil', grassland, forest, landslide, riverbank, and subsoil, were collected during three dedicated sampling campaigns organised in 2011, 2015 and 2019. By 2021, a total of 19 sampling campaigns had been carried out. At the begging of this thesis, all the physico-chemical analyses carried out on soil and lag deposit samples (i.e., gamma spectrometry, elemental geochemistry, organic matter properties, and visible spectrocolourimetry) were compiled into a single comprehensive database related to 159 soil and 911 lag deposit samples. From this database, soil and sediment samples considered to be relevant for the current research were selected. This included soil samples collected in the Yokokawa Dam (n = 14) and in Mano Dam (n = 34) reservoir catchments, as well as from the neighbouring upper Niida



Figure GI.3: Flood deposits collection during a post-typhoon 2022 and 2023 sampling campaigns (© Olivier Evrard).

River catchment (n = 34; 新田川), which is highly similar to the Mano catchment. In addition, lag deposit samples from the Mano Dam catchment, collected annually from 2011 to 2021 after the typhoon season in October-November (n = 91), were also selected. As the original database did not include soil samples from the Ogaki Dam catchment because of its location in the DTRZ where access was strongly restricted before the pandemic, a dedicated field campaign was organised in April 2022 to identify potential sources of sediment in the area, and samples were collected to this end in June/July 2022 along the Ukedo River (n = 36). Then, two additional post-typhoon sampling campaigns were also conducted in November 2022 and in November 2023, with the respective collection of 33 and 35 lag deposit samples, incorporating 68 additional lag deposit samples into the global database. Among these, 18 samples were collected in the Mano Dam reservoir catchment (total = 109). In addition, following the lessons learnt from the analysis of sediment cores collected at upstream, midstream and downstream locations of the Mano Dam reservoir in November 2014 (Huon et al., 2018), two additional sediment cores were collected at the midstream and downstream locations of this reservoir in June 2021. In addition, two other sediment cores were collected in the downstream sections of the Ogaki Dam and Yokokawa Dam reservoirs in September and August 2022, respectively.

In the first part of the PhD, the methodology of the sediment source fingerprinting was reviewed. The methodology of the sediment source fingerprinting consists of two stages, including the selection of tracers among the analysed physico-chemical properties, followed by the modelling of the sediment source contributions through their deconvolution in a sediment mixture. To be selected as a tracer, a property must meet two criteria: it must remain stable during the erosion process, which is referred to as the "tracer conservative behaviour", and it must allow to differentiate between the potential sources, which is referred to as the "tracer discriminant power". The correct identification of the tracers represents a critical step for the subsequent accurate prediction of sediment source contributions. These are several tracer selection methods, the most common method, referred to as the "three-step method", and the recently introduced method proposed by Lizaga et al. (2020), which is called the "consensus method". As these different tracer selection methods were used in parallel as they had never been compared until then in the scientific literature, it was chosen to compare their respective tracer selections on a single actual sample dataset (i.e. the successive sedimentation layers of a core collected in the Mano Dam reservoir). These two methods were investigated and compared regard-

ing their selection of tracers. Then, the impact of these contrasted tracer selections on the prediction of the sediment source contributions was assessed. In addition, the use of virtually generated mixtures, defined mathematically, to evaluate the contribution modelling accuracy has been formalised and discussed. In parallel to this work, an R package was developed and published. The package, fingR, was developed to provide a facilitated and convenient implementation of the most common approach (i.e. the three-step method) along with tools for assessing prediction accuracy.

In the second phase of the PhD, the impact of soil decontamination on sediment and radiocesium transfers was investigated in one to three of the above-mentioned contrasted catchments. Sediment source fingerprinting techniques were developed to support this analysis and to assess in particular their potential impact on changes in sediment source contributions. This approach was also applied on different sediment matrices depending on the study site:

- The impact of farmland decontamination was investigated using two types of sediment matrices: reservoir sediment cores and flood deposits. These sediment samples were collected in the Mano Dam reservoir catchment, which is an early decontaminated mixed agricultural/forested catchment. On the first hand, sediment cores provided a continuous record of the sediment transfers that have taken place in the catchment before, during and after the accident. The deposition sequence was identified and dated, using a range of diagnostic properties and contextual information. Then, the sediment and the associated radiocesium fluxes were reconstructed over the period from the FDNPP accident in 2011 to the collection of the sediment core (June 2021). On the other hand, flood deposits collected annually at ten sites across the Mano Dam reservoir catchment, allowed to investigate the spatial variations and the temporal evolution of sediment and radiocesium transfers across the catchment.
- The difference in the dominant land uses and management after the FDNPP accident between the Mano, Ogaki and Yokokawa dam catchments, were investigated to assess the impact of the timing of decontamination on the sediment and radiocesium transfers across the river systems.

The combination of sediment core and lag deposit sampling strategies provides a more comprehensive dataset allowing to improve our spatially-distributed understanding of erosion processes occurring across catchments in the context of those major land use and cover changes that have occurred during the successive phases of abandonment, decontamination and resumption of agricultural activities from the FDNPP accident until nowadays.

Manuscript structure

The research presented in this manuscript is organised in four chapters, the content of which is described as follows:

- In Chapter I, the sediment source fingerprinting technique is introduced, with a focus on its background methodology and the impact of tracer selection on sediment source contribution modelling. The sensitivity of source contributions to different tracer selection methods is examined by comparing the tracer selections of seven variations of the three-step method and of a consensus approach using a single actual dataset. The implications of these different tracer selections for modelling sediment source contributions are discussed. This chapter also explores the use of virtual mixtures to assess the accuracy of the modelling approach and the transferability of the calculated accuracy metrics to actual sediment samples. The

results of this research have been published in the Copernicus journal *SOIL*, and an R package developed in the framework of this work, which was continuously updated until the current 2.1.1 version, is available on *Github*, while all previous versions are archived on *Zenodo*.

- Chapter II focuses on the retrospective assessment of the impact of farmland decontamination on the sediment and particle-bound ^{137}Cs transfers in the Mano Dam reservoir catchment, based on the detailed investigation of a sediment core collected in the downstream section of the reservoir in June 2021. The sequence of sediment deposition resulting from extreme precipitation events, such as typhoons or tropical storms, and its chronology were reconstructed through the analysis of several diagnostic properties (i.e., radionuclide gamma spectrometry, organic matter content and stable isotopes, element geochemistry, visible spectrocolourimetry, and granulometry and other contextual information. The relative contributions of the potential sources, among farmland, forest and subsoil, and their changes with time, were determined using a sediment source fingerprinting approach developed using the tools and following the recommendations made in Chapter I. The findings of this work have been published in the *Science of the Total Environment* journal.

- Chapter III investigated the impact of decontamination on the transfers of sediment and ^{137}Cs in terms of both their temporal and spatial variations, using 101 flood deposits collected annually between 2011 and 2023 after the typhoon season, in October-November, from ten sampling sites distributed across the entire Mano Dam reservoir catchment. In order to better understand the impact of spatial heterogeneity across the catchment and the influence of changes in farmland cover following the abandonment of agricultural activities due to the evacuation, an index of connectivity was calculated annually by combining topographical and land cover information during the post-accidental period. In addition, rainfall erosivity was calculated using the data from 58 weather stations operated by the Japanese Meteorological Agency and located within a 110 km radius around the FDNPP site. Subsequently, the erosivity associated with the major events that occurred prior to each sampling campaign was calculated and spatialised across the investigated area. The impact of the last erosive events that occurred prior to the sampling campaign on the sediment connectivity was assessed. The spatial and temporal evolution of the sediment source contributions as well as evolution of ^{137}Cs activities in sediment were discussed at light of the progress of decontamination and the intensity of the last erosive events, which is reflected in values of the connectivity index.

- Chapter IV investigates the impact of decontamination timing on sediment and radiocesium transfers through the study of three sediment cores collected from the reservoirs of the three above-mentioned catchments. To this end, several diagnostic properties (similar to those listed in Chapter I) were analysed in core 1 cm depth increments, in addition to the high-resolution energy dispersive X-ray fluorescence (ED-XRF) core scanning at 1 mm resolution, as discussed in Chapter II. The potential of high-resolution ED-XRF core scanner data for both sediment fingerprinting studies and for reconstructing the chronology of extreme erosion/sedimentation events is explored. The evolution of sediment source contributions and ^{137}Cs deposition fluxes from the FDNPP accident until nowadays was reconstructed and compared, highlighting the differences and similarities between these contrasted catchments, their land uses and the contrasted management strategies.

Finally, the results obtained during this research are put into perspective to discuss the impacts of soil decontamination and its timing on sediment and radiocesium transfers in the region of the Fukushima Prefecture affected by the FDNPP accident. The general discussion of this manuscript deals with the use of lacus-

trine sediment cores and flood deposits for investigating sediment and contaminant transfers in river systems. Then, the use of high-resolution ED-XRF core scanner analysis for sediment source fingerprinting studies is discussed, and novel approaches are explored to further develop its application for sediment source fingerprinting. Finally, the limits associated with current techniques are discussed and potential perspectives for the evolution of the sediment source fingerprinting approach are put forward. The discussion is followed by conclusive remarks on the implementation of a decontamination programme in the context of the Fukushima accident and the wider application of the lessons learned from this decade of research on sediment and pollutant transfers in river systems by water erosion.

References

Asanuma-Brice, C., Evrard, O., Chalaux, T., 2023. Why did so few refugees return to the Fukushima fallout-impacted region after remediation? An interdisciplinary case study from Iitate village, Japan. International Journal of Disaster Risk Reduction 85, 103498. URL: https://linkinghub.elsevier.com/retrieve/pii/S2212420922007178, doi:10.1016/j.ijdrr.2022.103498.

Board of Audit of Japan, 2023. Status of Implementation of Projects Related to Recovery from the Great East Japan Earthquake. Technical Report. Board of Audit of Japan. URL: https://www.jbaudit.go.jp/pr/kensa/result/5/pdf/050203_01_zenbun.pdf.

Chartin, C., Evrard, O., Laceby, J.P., Onda, Y., Ottlé, C., Lefèvre, I., Cerdan, O., 2017. The impact of typhoons on sediment connectivity: Lessons learnt from contaminated coastal catchments of the Fukushima Prefecture (Japan): Typhoon Impact on Sediment Connectivity - Fukushima, Japan. Earth Surface Processes and Landforms 42, 306–317. URL: https://onlinelibrary.wiley.com/doi/10.1002/esp.4056, doi:10.1002/esp.4056.

Chino, M., Nakayama, H., Nagai, H., Terada, H., Katata, G., Yamazawa, H., 2011. Preliminary Estimation of Release Amounts of ^{131}I and ^{137}Cs Accidentally Discharged from the Fukushima Daiichi Nuclear Power Plant into the Atmosphere. Journal of Nuclear Science and Technology 48, 1129–1134. URL: http://www.tandfonline.com/doi/abs/10.1080/18811248.2011.9711799, doi:10.1080/18811248.2011.9711799.

Emergency Disaster Preparedness Headquarters, 2021. Police Activities and Damage from the 2011 Tohoku Earthquake. Technical Report 1. Emergency Disaster Preparedness Headquarters, Police Agency. URL: https://www.npa.go.jp/news/other/earthquake2011/pdf/higaijokyo.pdf.

Evrard, O., Chalaux-Clergue, T., Chaboche, P.A., Wakiyama, Y., Thiry, Y., 2023. Research and management challenges following soil and landscape decontamination at the onset of the reopening of the Difficult-To-Return Zone, Fukushima (Japan). SOIL 9, 479–497. URL: https://soil.copernicus.org/articles/9/479/2023/, doi:10.5194/soil-9-479-2023.

Evrard, O., Laceby, J.P., Nakao, A., 2019. Effectiveness of landscape decontamination following the Fukushima nuclear accident: A review. SOIL 5, 333–350. URL: https://soil.copernicus.org/articles/5/333/2019/, doi:10.5194/soil-5-333-2019.

Fire and Disaster Management Agency, 2021. 2011 Tohoku-Pacific Ocean Earthquake (Great East Japan Earthquake). Technical Report 161. Disaster Management Headquarters, Fire and Disaster Management Agency. Japan. URL: https://www.fdma.go.jp/disaster/higashinihon/items/161.pdf.

Hashimoto, S., Ugawa, S., Nanko, K., Shichi, K., 2012. The total amounts of radioactively contaminated materials in forests in Fukushima, Japan. Scientific Reports 2, 416. URL: https://www.nature.com/articles/srep00416, doi:10.1038/srep00416.

He, Q., Walling, D., 1996. Interpreting particle size effects in the adsorption of 137Cs and unsupported 210Pb by mineral soils and sediments. Journal of Environmental Radioactivity 30, 117–137. URL: https://linkinghub.elsevier.com/retrieve/pii/0265931X96892757, doi:10.1016/0265-931X(96)89275-7.

Huon, S., Hayashi, S., Laceby, J.P., Tsuji, H., Onda, Y., Evrard, O., 2018. Source dynamics of radiocesium-contaminated particulate matter deposited in an agricultural water reservoir after the Fukushima nuclear accident. Science of The Total Environment 612, 1079–1090. URL: https://linkinghub.elsevier.com/retrieve/pii/S0048969717319083, doi:10.1016/j.scitotenv.2017.07.205.

IAEA, 2015. The Fukushima Daiichi Accident. Non-Serial Publications, International Atomic Energy Agency, Vienna, Austria. URL: https://www-pub.iaea.org/MTCD/Publications/PDF/SupplementaryMaterials/P1710/Languages/French.pdf.

Iwagami, S., Onda, Y., Tsujimura, M., Abe, Y., 2017. Contribution of radioactive 137Cs discharge by suspended sediment, coarse organic matter, and dissolved fraction from a headwater catchment in

Fukushima after the Fukushima Dai-ichi Nuclear Power Plant accident. Journal of Environmental Radioactivity 166, 466–474. URL: https://linkinghub.elsevier.com/retrieve/pii/S0265931X16302557, doi:10.1016/j.jenvrad.2016.07.025.

JMA, 2011. Information on the 2011 Geart East Japan Earthquake. URL: https://www.jma.go.jp/jma/en/2011_Earthquake/Information_on_2011_Earthquake.html.

Kato, H., Onda, Y., Gao, X., Sanada, Y., Saito, K., 2019. Reconstruction of a Fukushima accident-derived radiocesium fallout map for environmental transfer studies. Journal of Environmental Radioactivity 210, 105996. URL: https://linkinghub.elsevier.com/retrieve/pii/S0265931X18303308, doi:10.1016/j.jenvrad.2019.105996.

Kato, H., Onda, Y., Teramage, M., 2012. Depth distribution of 137Cs, 134Cs, and 131I in soil profile after Fukushima Dai-ichi Nuclear Power Plant Accident. Journal of Environmental Radioactivity 111, 59–64. URL: https://linkinghub.elsevier.com/retrieve/pii/S0265931X11002426, doi:10.1016/j.jenvrad.2011.10.003.

Kobayashi, T., Nagai, H., Chino, M., Kawamura, H., 2013. Source term estimation of atmospheric release due to the Fukushima Dai-ichi Nuclear Power Plant accident by atmospheric and oceanic dispersion simulations: Fukushima NPP Accident Related. Journal of Nuclear Science and Technology 50, 255–264. URL: http://www.tandfonline.com/doi/abs/10.1080/00223131.2013.772449, doi:10.1080/00223131.2013.772449.

Laceby, J.P., Chartin, C., Evrard, O., Onda, Y., Garcia-Sanchez, L., Cerdan, O., 2016. Rainfall erosivity in catchments contaminated with fallout from the Fukushima Daiichi nuclear power plant accident. Hydrology and Earth System Sciences 20, 2467–2482. URL: https://hess.copernicus.org/articles/20/2467/2016/, doi:10.5194/hess-20-2467-2016.

Lepage, H., Evrard, O., Onda, Y., Lefèvre, I., Laceby, J.P., Ayrault, S., 2015. Depth distribution of cesium-137 in paddy fields across the Fukushima pollution plume in 2013. Journal of Environmental Radioactivity 147, 157–164. URL: https://linkinghub.elsevier.com/retrieve/pii/S0265931X15001484, doi:10.1016/j.jenvrad.2015.05.003.

Lizaga, I., Latorre, B., Gaspar, L., Navas, A., 2020. Consensus ranking as a method to identify non-conservative and dissenting tracers in fingerprinting studies. Science of The Total Environment 720, 137537. URL: https://linkinghub.elsevier.com/retrieve/pii/S0048969720310482, doi:10.1016/j.scitotenv.2020.137537.

MoE, 2011. Basic Principles on the Act on Special Measures Concerning the Handling of Environment Pollution by Radioactive Materials Discharged by the Nuclear Power Station Accident Associated with the Tohoku District-Off the Pacific Ocean Earthquake That Occurred on March 11, 2011. Technical Report. Ministry of the Environment. Japan. URL: https://josen.env.go.jp/en/framework/pdf/basic_principles.pdf.

MoE, 2013. Decontamination Guidelines. Technical Report 2. Japanese Ministry of Environment. Japan.

MoE, 2015. Decontamination Report - A Compilation of Experiences to Date on Decontamination for the Living Environment Conducted by the Ministry of the Environment. Technical Report. Japanese Ministry of Environment. Japan. URL: http://josen.env.go.jp/en/policy_document/.

MoE, 2018. Decontamination Projects for Radioactive Contamination Discharged by Tokyo Electric Power Company Fukushima Daiichi Nuclear Power Station Accident. Technical Report. Japanese Ministry of Environment.

MoE, 2023. Decontamination status. URL: http://josen.env.go.jp/area/.

Morino, Y., Ohara, T., Watanabe, M., Hayashi, S., Nishizawa, M., 2013. Episode Analysis of Deposition of Radiocesium from the Fukushima Daiichi Nuclear Power Plant Accident. Environmental Science & Technology 47, 2314–2322. URL: https://pubs.acs.org/doi/10.1021/es304620x, doi:10.1021/es304620x.

NOAA, 2015. Great Tohokun Japan Earthquake and Tsunami, 11 March 2011. URL: https://www.ngdc.noaa.gov/hazard/11mar2011.html.

Onda, Y., Taniguchi, K., Yoshimura, K., Kato, H., Takahashi, J., Wakiyama, Y., Coppin, F., Smith, H., 2020. Radionuclides from the Fukushima Daiichi Nuclear Power Plant in terrestrial systems. Nature Reviews Earth & Environment 1, 644–660. URL: https://www.nature.com/articles/s43017-020-0099-x, doi:10.1038/s43017-020-0099-x.

Osawa, K., Nonaka, Y., Nishimura, T., Tanoi, K., Matsui, H., Mizogichi, M., Tatsuno, T., 2018. Quantification of dissolved and particulate radiocesium fluxes in two rivers draining the main radioactive pollution plume in Fukushima, Japan (2013–2016). Anthropocene 22, 40–50. URL: https://linkinghub.elsevier.com/retrieve/pii/S2213305418300262, doi:10.1016/j.ancene.2018.04.003.

Sakaguchi, A., Tanaka, K., Iwatani, H., Chiga, H., Fan, Q., Onda, Y., Takahashi, Y., 2015. Size distribution studies of 137Cs in river water in the Abukuma Riverine system following the Fukushima Dai-ichi Nuclear Power Plant accident. Journal of Environmental Radioactivity 139, 379–389. URL: https://linkinghub.elsevier.com/retrieve/pii/S0265931X14001519, doi:10.1016/j.jenvrad.2014.05.011.

Sawhney, B.L., 1972. Selective Sorption and Fixation of Cations by Clay Minerals: A Review. Clays and Clay Minerals 20, 93–100. URL: https://doi.org/10.1346/CCMN.1972.0200208, doi:10.1346/CCMN.1972.0200208.

Simons, M., Minson, S.E., Sladen, A., Ortega, F., Jiang, J., Owen, S.E., Meng, L., Ampuero, J.P., Wei, S., Chu, R., Helmberger, D.V., Kanamori, H., Hetland, E., Moore, A.W., Webb, F.H., 2011. The 2011 Magnitude 9.0 Tohoku-Oki Earthquake: Mosaicking the Megathrust from Seconds to Centuries. Science 332, 1421–1425. URL: https://science.sciencemag.org/content/332/6036/1421, doi:10.1126/science.1206731.

Steinhauser, G., 2014. Fukushima's Forgotten Radionuclides: A Review of the Understudied Radioactive Emissions. Environmental Science & Technology 48, 4649–4663. URL: https://pubs.acs.org/doi/10.1021/es405654c, doi:10.1021/es405654c.

Taira, Y., Matsuo, M., Yamaguchi, T., Yamada, Y., Orita, M., Takamura, N., 2020. Radiocesium levels in contaminated forests has remained stable, even after heavy rains due to typhoons and localized downpours. Scientific Reports 10, 19215. URL: https://www.nature.com/articles/s41598-020-75857-1, doi:10.1038/s41598-020-75857-1.

Taniguchi, K., Onda, Y., Smith, H.G., Blake, W., Yoshimura, K., Yamashiki, Y., Kuramoto, T., Saito, K., 2019. Transport and Redistribution of Radiocesium in Fukushima Fallout through Rivers. Environmental Science & Technology 53, 12339–12347. URL: https://pubs.acs.org/doi/10.1021/acs.est.9b02890, doi:10.1021/acs.est.9b02890.

Tsubokura, M., Murakami, M., Takebayashi, Y., Nomura, S., Ono, K., Ozaki, A., Sawano, T., Kobashi, Y., Oikawa, T., 2019. Impact of decontamination on individual radiation doses from external exposure among residents of Minamisoma City after the 2011 Fukushima Daiichi nuclear power plant incident in Japan: A retrospective observational study. Journal of Radiological Protection 39, 854–871. URL: https://iopscience.iop.org/article/10.1088/1361-6498/ab280e, doi:10.1088/1361-6498/ab280e.

Yagi, Y., Fukahata, Y., 2011. Rupture process of the 2011 Tohoku-oki earthquake and absolute elastic strain release: RUPTURE PROCESS OF TOHOKU-OKI EARTHQUAKE. Geophysical Research Letters 38, n/a–n/a. URL: http://doi.wiley.com/10.1029/2011GL048701, doi:10.1029/2011GL048701.

Yamamoto, M., 2015. Overview of the Fukushima Dai-ichi Nuclear Power Plant (FDNPP) accident, with amounts and isotopic compositions of the released radionuclides. Journal of Radioanalytical and Nuclear Chemistry 303, 1227–1231. URL: http://link.springer.com/10.1007/s10967-014-3639-3, doi:10.1007/s10967-014-3639-3.

Yamashiki, Y., Onda, Y., Smith, H.G., Blake, W.H., Wakahara, T., Igarashi, Y., Matsuura, Y., Yoshimura, K., 2014. Initial flux of sediment-associated radiocesium to the ocean from the largest river impacted by Fukushima Daiichi Nuclear Power Plant. Scientific Reports 4, 3714. URL: https://www.nature.com/articles/srep03714, doi:10.1038/srep03714.

Yasutaka, T., Iwasaki, Y., Hashimoto, S., Naito, W., Ono, K., Kishimoto, A., Yoshida, K., Murakami, M., Kawaguchi, I., Oka, T., Nakanishi, J., 2013. A GIS-based evaluation of the effect of decontamination on effective doses due to long-term external exposures in Fukushima. Chemosphere 93,

1222–1229. URL: https://linkinghub.elsevier.com/retrieve/pii/S0045653513009405, doi:10.1016/j.chemosphere.2013.06.083.

Yasutaka, T., Naito, W., 2016. Assessing cost and effectiveness of radiation decontamination in Fukushima Prefecture, Japan. Journal of Environmental Radioactivity 151, 512–520. URL: https://linkinghub.elsevier.com/retrieve/pii/S0265931X15001575, doi:10.1016/j.jenvrad.2015.05.012.

Zhao, D., 2015. The 2011 Tohoku earthquake (Mw 9.0) sequence and subduction dynamics in Western Pacific and East Asia. Journal of Asian Earth Sciences 98, 26–49. URL: https://linkinghub.elsevier.com/retrieve/pii/S1367912014004799, doi:10.1016/j.jseaes.2014.10.022.

Chapter I

Sediment Source Fingerprinting: Concept, Techniques & Usages

Chapter I

Sediment Source Fingerprinting: Concept, Techniques & Usages

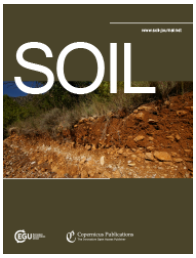
In recent decades, the field of sediment fingerprinting has gained significant interest as a method to understand and quantify sediment sources in catchments, particularly in the context of accelerated soil erosion and sediment delivery to aquatic systems. This approach appears to be essential for implementing effective soil and water conservation strategies, as it helps to quantify the relative contributions of different sediment sources to water bodies. A key step in sediment fingerprinting is the selection of appropriate tracers to identify and quantify sediment sources. The accuracy of this process is highly dependent on the methods used for tracer selection and their ability to reflect the actual sediment dynamics. Traditionally, the three-step method (TSM) has been the most commonly used approach for tracer selection, in which potential tracers are identified based on their ability to discriminate between sediment sources, their discriminant power, and their ability to remain unchanged during the erosion process, i.e. their conservative behaviour. In addition, several variations of the parameters used to assess conservative behaviour have been described in the literature. Recently, the consensus method (CM) has been proposed as an alternative, offering a potentially more robust approach to tracer selection. Despite these advances, the effectiveness and reliability of these methods in practice have not been compared yet on a single real sample dataset.

This chapter investigates and compares the TSM and CM methods by analysing their selection of tracers and the impact of this selection on the prediction of sediment source contributions. The study uses a dataset consisting of properties analysed on soil and sediment core layer samples, coupled with virtual mixtures with known source proportions, to evaluate the modelling accuracy and consistency of each method. By examining the selection of conservative properties, model predictions and the discrepancies of results obtained with virtual mixtures and actual sediment samples, this research aims to provide a comprehensive understanding of the strengths and limitations of the current tracer selection methods. The findings of this study are expected to provide valuable insights into the effectiveness of different tracer selection techniques and highlight the need for improved methods to better replicate real-world sediment dynamics. Future research directions will focus on refining tracer selection criteria and developing novel metrics to improve the reliability of sediment fingerprinting approaches. This is essential to improve our understanding of sediment transport processes and to support the implementation of effective environmental management practices.



In parallel to the work presented above, a R package was developed and published. The fingR package is a practical implementation of the most conventional method, the TSM. It provides a convenient, non-directed environment, taking into account existing variations of the methods, to identify discriminant and conservative properties, generate virtual mixture contributions and properties based on the user's potential sources, run the Bayesian Mean Model (BMM), extract and order MixSIAR and BMM model predictions, assess modelling accuracy metrics using virtual mixture predictions, without requiring any changes to the loaded dataset by the user. The main functions, their purpose and usage are presented following their usage in a conventional sediment tracing study on the fingR Github page (https://github.com/tchalauxclergue/fingR, see Appendix A) (Chalaux-Clergue and Bizeul, 2023). In addition, a database template was proposed and uploaded on Zenodo (Chalaux-Clergue et al., 2024a) (see Appendix B).

Sensitivity of source sediment fingerprinting to tracer selection methods



Thomas Chalaux-Clergue [a,*], Rémi Bizeul [a,*], Pedro V. G. Batista [b], Núria Martínez-Carreras [c], J. Patrick Laceby [d] and Olivier Evrard [a]

[a] *Laboratoire des Sciences du Climat et de l'Environnement (LSCE-IPSL), Université Paris-Saclay, UMR 8212 (CEA-CNRS-UVSQ), Gif-sur-Yvette 91190, France*

[b] *Water and Soil Resource Research, Institute for Geography, Universität Augsburg, Alter Postweg 118, 86159 Augsburg, Germany*

[c] *Environmental Research and Innovation Department (ERIN), Catchment and Eco-Hydrology Research Group (CAT), Luxembourg Institute of Science and Technology (LIST), Belvaux, Luxembourg*

[d] *Environment and Protected Areas, 3535 Research Rd NW, Calgary, Alberta, T2L 2K8, Canada*

ABSTRACT

In a context of accelerated soil erosion and sediment supply to water bodies, sediment fingerprinting techniques have received an increasing interest in the last 2 decades. The selection of tracers is a particularly critical step for the subsequent accurate prediction of sediment source contributions. To select tracers, the most conventional approach is the three-step method, although, more recently, the consensus method has also been proposed as an alternative. The outputs of these two approaches were compared in terms of identification of conservative properties, tracer selection, modelled contributions and performance on a single dataset. As for the three-step method, several range test criteria were compared, along with the impact of the discriminant function analysis (DFA).

The dataset was composed of tracer properties analysed in soil (three potential sources; n = 56) and sediment core samples (n = 32). Soil and sediment samples were sieved to 63 μm and analysed for organic matter, elemental geochemistry and diffuse visible spectrometry. Virtual mixtures (n = 138) with known source proportions were generated to assess model accuracy of each tracer selection method. The Bayesian un-mixing model MixSIAR was then used to predict source contributions on both virtual mixtures and actual sediments. The different methods tested in the current research can be distributed into three groups according to their sensitivity to the conservative behaviour of properties, which was found to be associated with different predicted source contribution tendencies along the sediment core. The methods selecting the largest number of tracers were associated with a dominant and constant contribution of forests to sediment. In contrast, the methods selecting the lowest number of tracers were associated with a dominant and constant contribution of cropland to sediment. Furthermore, the intermediate selection of tracers led to more balanced contributions of both cropland and forest to sediments.

The prediction of the virtual mixtures allowed us to compute several evaluation metrics, which are generally used to support the evaluation of model accuracy for each tracer selection method. However, strong differences or the absence of correspondence were observed between the range of predicted contributions obtained for virtual mixtures and those values obtained for actual sediments. These divergences highlight the fact that evaluation metrics obtained for virtual mixtures may not be directly transferable to models run for actual samples and must be interpreted with caution, to avoid over-interpretation or misinterpretation. These divergences may likely be attributed to the occurrence of a not (fully) conservative behaviour of potential tracer properties during erosion, transport and deposition processes, which could not be fully reproduced when generating the virtual mixtures with currently available methods.

Future research should develop novel metrics to quantify the conservative behaviour of tracer properties during erosion and transport processes. Furthermore, new methods should be designed to generate virtual mixtures closer to reality and to better evaluate model accuracy. These improvements would contribute to the development of more reliable sediment fingerprinting techniques, which are needed to better support the implementation of effective soil and water conservation measures at the catchment scale.

Received: 29 August 2023 - Discussion started: 8 September 2023 - Revised: 8 December 2023 - Accepted 29 December 2023 - Published: 13 February 2024.
Published in SOIL, 10, 109-138, 2024, by Copernicus Publications on behalf of the European Geosciences Union.
* indicates corresponding authors - DOI: https://doi.org/10.5194/soil-10-109-2024

I.1 - Introduction

During the last several decades, an acceleration of soil erosion has been observed in response to land use changes or farming-practice modifications in several regions around the world (Poesen, 2018; Pennock, 2019). Moreover, global warming will likely further increase the frequency of erosive storms and the associated soil losses (OCC, 2015; Li and Fang, 2016). This acceleration of soil erosion leads to an increase of on-site and off-site negative socio-environmental impacts (Lal, 1998, 2001), including the deterioration of soil agronomic properties (Pimentel, 2006; Montgomery, 2007), the transfer of pollutants associated with soil particles (e.g. pesticides, herbicides, chemical fertilisers, heavy metals, radionuclides) (Lal, 1998; Bing et al., 2013; Debnath et al., 2021), the alteration of soil organic carbon stocks (Olson et al., 2016; Lal, 2019), the degradation of aquatic ecosystems (e.g. eutrophication, increased turbidity) (Kemp et al., 2011; Issaka and Ashraf, 2017) and an increased sediment supply to waterbodies (e.g. reservoir and bay siltation) (Collins et al., 2020). The identification of soil erosion sources is therefore essential to prevent water-erosion-induced land degradation and its associated effects.

The sediment source fingerprinting technique was initially developed to determine the origin of sediment (Wall and Wilding, 1976; Peart and Walling, 1986; Loughran et al., 1987). After initial qualitative studies (Wall and Wilding, 1976; Loughran et al., 1987), the subsequent development of quantitative un-mixing models (Peart and Walling, 1986; Walling and Woodward, 1992; Collins et al., 1997a) made it possible to estimate the contributions of different sources to target sediment samples. Since then, the technique has received increasing attention (Collins et al., 2020; Batista et al., 2022). Overall, the goal of sediment tracing studies has been to improve our understanding of sediment transfer processes and to guide landscape management (Laceby et al., 2015; Owens et al., 2016). However, in practice, the technique has mainly been used by scientists as a research tool, and few direct applications by landscape managers have been reported (Minella et al., 2008; Collins et al., 2020; Xu et al., 2022). This likely demonstrates that, despite some homogenisation and simplification efforts (Mukundan et al., 2012; Collins et al., 2017; Evrard et al., 2022), the technique remains too complex, and the development of simpler and more robust procedures would allow for its wider application (Xu et al., 2022).

In the last few years, there has been a renewed interest among the sediment fingerprinting community in methodological issues associated with the technique, such as the tracer selection methods (i.e. the identification of fingerprint properties suitable for source discrimination and apportionment) (Collins and Walling, 2004; Laceby et al., 2017; Collins et al., 2020; Evrard et al., 2022). This stems from the large diversity of properties that are currently used in sediment fingerprinting studies, e.g. radionuclides (Collins et al., 1997b;

Evrard et al., 2020a), elemental geochemistry (Collins et al., 1997b; Blake et al., 2006; Laceby and Olley, 2015), magnetic susceptibility (Lizaga et al., 2019), organic matter and stable isotopes ($\delta^{13}C$, $\delta^{15}N$) (Laceby et al., 2016b; Huon et al., 2018). Collins et al. (2020) listed properties that have recently gained attention, such as compound-specific stable isotopes (CSSIs) (Gibbs, 2008), environmental DNA (eDNA) (Evrard et al., 2019), the stable oxygen isotope ratio with the oxygen isotopic composition of phosphate ($\delta^{18}O_p$) (Mingus et al., 2019), and diffuse reflectance spectroscopy in the visible (Martínez-Carreras et al., 2010; Summers et al., 2011; Tiecher et al., 2015), near-infrared (Summers et al., 2011) or mid-infrared range (Brosinsky et al., 2014; Farias Amorim et al., 2021). Theoretically, a larger number of measured properties should raise the probability of identifying robust tracers (Laceby et al., 2017; Collins et al., 2020; Evrard et al., 2022). Indeed, tracer selection has a fundamental impact on model predictions and their interpretation (Laceby and Olley, 2015; Laceby et al., 2015; Gaspar et al., 2019), as the inclusion of non-conservative properties in models was shown to strongly decrease the overall model quality (Sherriff et al., 2015; Smith et al., 2018; Vale et al., 2022).

The most conventional approach of tracer selection is a three-step method (TSM) (Collins et al., 2010; Wilkinson et al., 2013; Laceby et al., 2015; Sherriff et al., 2015). The first step assesses the conservative behaviour of each property, and the second step determines their capacity to discriminate between sources. The joint use of both tests allows us to select tracers from a potentially wide suite of measured properties. The third step of this approach consists of selecting optimal tracers for modelling.

Conservative behaviour refers to the absence of changes in the property between sources and targets. Sources correspond to materials that may have contributed to the formation of the target sediments (e.g. land uses, land covers, river banks, roads, landslides). The nature of the target sediments can vary, as it may include material as different as lag sediment, lake sediments, suspended matter, etc. The non-conservative behaviour of a tracer can be mainly attributed to two phenomena. The first is that particle size sorting may occur along the transport pathway (Walling et al., 2000). Sediment transport is a physical mechanism which, depending on runoff magnitude, rainfall intensity, river discharge, and other hydro-sedimentary components, will transport specific particle size fractions, weights and compositions (i.e. mineral or organic fractions) (Viparelli et al., 2013; Gateuille et al., 2019). In general, the average size of particles decreases with the distance travelled (Laceby et al., 2017). Fine particles with a higher specific surface area are generally associated with higher tracer concentrations than coarser material fractions (Horowitze, 1991; Collins et al., 1997a). In order to reduce the impact of particle size sorting on sediment properties, the $< 63\ \mu m$ fraction is commonly analysed after sieving both source and target material to this threshold when studying properties preferentially enriched in or sorbed onto fine particles (i.e. clays or silts) (Collins et al., 1997a; Gellis and Noe, 2013; Laceby et al., 2017) such as radionuclides, heavy metals or pesticides (Collins et al., 2020; Evrard et al., 2022). The second phenomenon is related to tracer concentration changes due to biogeochemical processes occurring during particle transport (Koiter et al., 2013). The changes depend on how tracers are affected by biogeochemical processes, such as dissolution, sorption, oxidation and reduction. Highly reactive elements, such as Na, Ca and Mg, show a high water-solubility and tend to dissolve when the sediment is immersed. Other elements, such as Ti, Al, and Si, are, in contrast, less susceptible to react in changing conditions (i.e. redox conditions), which makes them more suitable tracers (Meybeck and Helmer, 1989; Phillips and Greenway, 1998).

To assess the conservative behaviour of the property, in the first step of the TSM, the range of property values in source and target samples are compared. The objective of the range test is to assess whether the range of source values includes all individual target sediment sample values (Wilkinson et al., 2013). Various range tests based on source group statistics are commonly used in the literature: minimum-maximum (Smith

and Blake, 2014; Sellier et al., 2021), minimum-maximum ± 10 % (as measurement error) (Gellis and Noe, 2013; Gellis and Gorman Sanisaca, 2018; Dabrin et al., 2021), boxplot examination (whiskers and hinge box) (Sellier et al., 2020; Batista et al., 2022), mean (Wilkinson et al., 2013; Nosrati et al., 2021), mean plus/minus standard deviation (SD) (Evrard et al., 2020b; Laceby et al., 2021), and median (Collins et al., 2013; Batista et al., 2022). In these range tests, the source property range is defined as the highest and lowest values of the chosen statistics among the source groups. However, range tests do not quantify or confirm the complete absence of non-conservative behaviour (Collins et al., 2017; Sherriff et al., 2015).

The property's ability to differentiate between sources, originally proposed by Collins et al. (1997b), determines whether a property is a discriminant tracer or not. This second step of the TSM allows for the selection of tracers that maximise source discrimination. To assess the discrimination power of a given property, the conventional tracer selection approach relies on the non-parametric Kruskal-Wallis H test (Hollander et al., 2013). The result of the Kruskal-Wallis H test indicates that at least one of the groups differs from the other for a given property. Other tests, such as Dunn's, Mann-Whitney U or Kolmogorov-Smirnov tests, can be used to determine the discriminatory power of a given property for each individual source (e.g. forest versus cropland versus subsoil).

Conventionally, after assessing the tracer's conservative behaviour and discrimination capacity, the third step of the TSM is to conduct a discriminant function analysis (DFA) or a principal component analysis (PCA). When applying the DFA, a subset of tracers is selected using a forward stepwise selection procedure based on Wilk's lambda criterion (Collins et al., 1997b). This step aims at selecting the lowest number of tracers that maximises sample source discrimination, in order to avoid selecting redundant tracers (Small et al., 2004). However, this practice is currently debated, as some authors argue that a higher number of tracers can improve source dimensionality and definition, as well as alleviate the impact of non-conservative tracers (Martínez-Carreras et al., 2008; Sherriff et al., 2015).

Another tracer selection method, the consensus method (CM), was developed by Lizaga et al. (2020). It is based on the information provided by single tracers in an un-mixing context. The CM selects tracers combining the identification of non-conservative behaviour and conflicting tracers. It consists of two tests: the conservativeness index (CI) and the consensus ranking (CR). The CI is based on the results of the predictions from single-tracer models to identify non-conservative and dissenting tracers, whereas the CR is a scoring function based on debates aimed at discarding the properties that prevent consensus. The CI is applied to all target sediment samples and provides unique results for the entire study, whereas the CR is applied to each individual target sediment sample, which may result in the selection of different lists of tracers for different target samples.

Selected tracers are then used in un-mixing models to assess the contribution of sources to the target samples. After the use of simple (Peart and Walling, 1986) and quantitative un-mixing models (Collins et al., 1997a), earlier modelling approaches were based on deterministic optimisation procedures (Walden et al., 1997), and, more recently, more advanced approaches have moved towards stochastic procedures using Bayesian and/or Monte Carlo methods (Small et al., 2002; Martínez-Carreras et al., 2008; Nosrati et al., 2014; Laceby and Olley, 2015). In order to assess the overall reliability of the study, it is important to assess the predictive accuracy of the un-mixing models. Stochastic models produce a distribution of source contributions for which a prediction interval can be determined, which provides an indicator of modelling accuracy (Batista et al., 2022). The use of artificial mixtures allows prediction accuracy to be assessed in more diverse ways by using them as target mixtures with known contributions. It is then possible to calculate various statistics to describe and evaluate the prediction uncertainty. Although these mixtures were initially prepared in the

laboratory (Martínez-Carreras et al., 2010; Haddadchi et al., 2014; Huangfu et al., 2020), the development of virtually generated mixtures (Laceby et al., 2015; Palazón et al., 2015; Sherriff et al., 2015) appears as a relevant alternative (Batista et al., 2022). However, when artificial mixtures are produced, their properties are not affected by erosive processes and are therefore perfectly conservative.

The objectives of the current study are therefore to: (1) compare the tracer selections given by the two approaches (i.e. three-step method and consensus method), (2) assess the impact of the stepwise selection on the TSM selections of tracers, (3) evaluate the impact of these different selections of tracers on sediment source apportionment prediction accuracy using virtual mixtures and (4) draw general recommendations from this evaluation for future sediment fingerprinting studies.

I.2 - Materials and methods

I.2.1 - Catchment description

The Hayama Lake catchment (67 km^2), located in the upper part of the Mano River in northeastern Japan (Fukushima Prefecture, Tōhoku region), is a typical mountainous agricultural catchment of the eastern edge of Fukushima Prefecture. Due to the steep topography, cropland is located at the bottom of valleys and in the vicinity of rivers, and it is bordered by forest on steep mountainous hillslopes. Forestry is the main land use, which covers 91 % of the catchment, while cropland represents 7 % and, urban settlements and bare soil less than 2 % (Fig. I.1 and Supplementary Materials Fig. I.SM-2; data are from JAXA (2016, 2018, 2022)). However, cropland is located in places with a high hydro-sedimentary connectivity (Chartin et al., 2013). The Hayama Lake catchment area is located within the main inland radioactive contamination plume resulting from the Fukushima Daiichi Nuclear Power Plant accident in March 2011 (Kato et al., 2019). Once deposited, ^{137}Cs strongly and quasi-permanently binds to fine soil particles such as silts and clays (Sawhney, 1972; He and Walling, 1996), which has been confirmed in the soils of Fukushima Prefecture (Saito et al., 2014; Nakao et al., 2014).

Catchment altitude ranges from 170 m to 700 m above sea level. The climate is continental (Dfa), with no dry season and hot summer, and it is bordered to the east by a Cfa temperate climate with no dry season and hot summer according to Köppen's climatic classification (Beck et al., 2018). The regional hydrological year runs from November to October (Laceby et al., 2016a; Whitaker et al., 2022). Over the 2006 to 2021 period, the mean annual temperature was 13.6 $\pm$ 0.4 °C yr^{-1} (standard deviation), with mean monthly values ranging from -1.5 °C in January to 31.1 °C in August. The mean annual precipitation was 1220 $\pm$ 189 mm yr^{-1} (SD), some of which falls as snow in winter. The majority of precipitation occurs between June and October, representing 60 % of the annual rainfall and 86 % of the rainfall erosivity (Laceby et al., 2016a). This period corresponds to the Japanese typhoon season with a peak of intensity in September in Fukushima Prefecture. Major typhoons were shown to be the main drivers of sediment production (Chartin et al., 2017), as they can generate 40 % of the annual rainfall erosivity within a very short period (Laceby et al., 2016a).

The Hayama Lake catchment is mainly underlain by non-alkaline mafic volcanic rocks (42 %), granite (31 %) granodiorite (17 %) and sedimentary rocks (7 %) (Supplementary Materials Fig. I.SM-3). Main soil groups, according to the Comprehensive Soil Classification System of Japan (Obara et al., 2011, 2015, and equivalent soil types according to the World Reference Base for Soil Resources (WRB)), are the following: Brown Forest soils (37 %; WRB: Cambisols/Stagnosols), Allophanic Andosols (36 %; Silandic Andosols), Cambic Red-

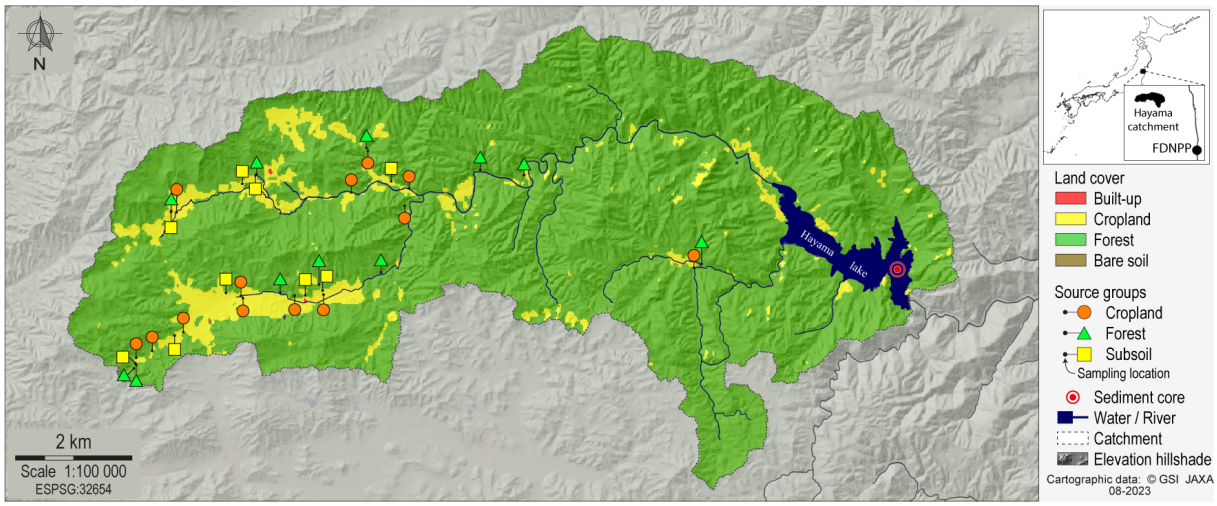


Figure I.1: Map of the main land uses in the Hayama Lake catchment area over the 2014-2016 period with location of source samples and the sediment core (cartographic data: GSI and JAXA). FDNPP: Fukushima Daiichi nuclear power plant.

Yellow soils (9 %; WRB: Cambisols) and Lithosols (9 %; WRB: Leptosols) (Supplementary Materials Fig. I.SM-4) (data from NARO (2011)).

All maps and geographical processing were performed using the QGIS software (QGIS Development Team, 2022).

I.2.2 - Soil and sediment sampling and processing

All sediment targets were taken from one sediment core sampled on 8 June 2021 in the downstream part of Hayama Lake (Mano dam lake) at 42 m depth (Fig. I.1) by the National Institute of Environmental Studies (NIES) (Japan). The core was 38 cm long with a diameter of 11 cm. It was sectioned into 38 increments of 1 cm in order to achieve a high-resolution investigation of the sediment core. A group of 32 layers were selected for this study, from 6 cm to 38 cm depths, which corresponds to a stable land use period (i.e. prior to decontamination work; Chalaux-Clergue et al. (2024b)). Sediment samples were dried at 40 °C for 96 hours.

Soil samples (n = 56) were collected in areas representative of the main potential sediment sources to Hayama Lake, including 24 cropland, 22 forest and 10 subsoil (i.e. channel bank or landslide) samples. Some source soils were sampled in the adjacent Niida River catchment, which is similar to the Hayama Lake catchment. Particular care was taken to ensure that these samples were representative of the Hayama Lake catchment characteristics, in terms of land use, geology and pedology (see Supplementary Materials I.SM-2, I.SM-3 and I.SM-4) (Williamson et al., 2023). The similarity of soil sample properties from both catchments was tested using the Kolmogorov-Smirnov test (not shown). Soils were sampled with a plastic trowel and consisted of 10 composited sub-samples of topsoil (1-2-cm uppermost layer). All soil samples were dried at 40 °C for about 48 hours and then sieved to 63 μm to isolate the fraction concentrating ^{137}Cs (i.e. to silt and clay minerals (Sawhney, 1972; He and Walling, 1996)).

I.2.3 - Laboratory analysis

Various analyses were conducted to characterise sediment and soil properties: organic matter composition determined by the combustion method (i.e. total organic carbon (TOC) and total nitrogen (TN)), elemental

geochemistry analysed by X-ray fluorescence (XRF) for 17 elements (i.e. Al, Ca, Co, Cr, Cu, Fe, K, Mg, Mn, Ni, Pb, Rb, Si, Sr, Ti, Zn, and Zr), visible colour indices by diffuse reflectance (i.e. CIE Lab, CIE LCh), geothite peak intensities (445 and 525 nm; Tiecher et al. (2021)), the ratio between the % reflectance at 700 nm and 400 nm (Q7/4; Debret et al. (2011)) and iron oxide-associated parameters (A1, A2, A3, Gt; (Tiecher et al., 2015)). All analysis methods and calculations are described in Appendix C.

Only properties for which the measurement uncertainty is too large were removed from further analysis. The following criterion has been set: if obtaining, considering the measurement uncertainty, a majority or the totality of the sample values was virtually impossible (e.g. when the measurement uncertainty is subtracted from the property measurement and results in a negative value), then the corresponding property was discarded.

I.2.4 - Virtual mixtures

Virtual mixtures were generated in order to assess model prediction accuracy (Palazón et al., 2015; Smith et al., 2018; Gaspar et al., 2019; Farias Amorim et al., 2021; Batista et al., 2022). They were shown to provide a reliable alternative to laboratory mixtures (Batista et al., 2022). Their ease of generation allows the model to be evaluated under a wide range of source contributions. For a given source, virtual mixture contributions were designed to range from 0 to 100 %, with 5-percent increments. The contributions of the other sources to the mixtures were then determined as fractions of the remaining contribution (i.e. $1 - \text{source A contribution}$), the fractions being in turn determined by the number of sources. The denominators were defined as $(\text{n} - 1) \cdot 2$ with n the number of source. The numerators were set to 3 and 1 as three sources were considered in the current research ($3/4$ and $1/4$). Theoretical source contributions for the virtual mixtures were determined as follows:

$$(C_A,\ C_B,\ C_C) = \begin{cases} C_A \in \{0,\ 5, \ldots 100\} \\ C_B = (1 - C_A)\ \cdot\ \frac{3}{(n-1)\ \cdot\ 2} \\ C_C = (1 - C_A)\ \cdot\ \frac{1}{(n-1)\ \cdot\ 2} \end{cases} \tag{I.1}$$

with C_A, C_B and C_C being the contributions of sources A, B and C, and n is the number of sources.

Permutations were then determined following this contribution scale, which generated a total of 138 virtual mixtures for the three source groups. For every source group, the mean and SD of each property were calculated. For each virtual mixture, each source group mean value was multiplied by the corresponding group contribution (e.g. cropland 0.40, forest 0.45, subsoil 0.15). Then, all source group values were summed to provide the virtual mixture property value.

I.2.5 - Tracer selection

I.2.5.1 - Three-step method

The TSM (Mukundan et al., 2010; Sellier et al., 2020; Batista et al., 2022) is based on three steps: (1) a range test to identify conservative properties (Martínez-Carreras et al., 2010; Wilkinson et al., 2013; Gellis and Walling, 2013), (2) a Kruskal-Wallis H test to identify discriminant properties (Collins et al., 1997b), and then (3) a discriminant function analysis (DFA) or a principal component analysis (PCA) with forward stepwise selection based on Wilk's lambda criterion to identify the best subset of predictors among the identified tracers

(i.e. conservative and discriminant properties) (Collins and Walling, 2002).

Conservative behaviour.

The conservative behaviour of properties was assessed using a range test. Within a range test, the range of sources is defined as the highest and lowest values of a criterion of the property among source groups. To be conservative, all the sample property values should lie within the source range.

$$\text{conservative if } \{ \text{ sources lower bound } \leq \text{ target value } \leq \text{ sources upper bound } \} \tag{I.2}$$

Several range test criteria are found in the literature, and these were all applied to identify conservative properties as an alternative to the TSM: minimum-maximum (Smith and Blake, 2014; Sellier et al., 2021), minimum-maximum ± 10 % (as measurement error) (Gellis and Noe, 2013; Gellis and Gorman Sanisaca, 2018; Dabrin et al., 2021), boxplot whiskers interpretation (i.e. outlier thresholds) (Sellier et al., 2020) and boxplot hinge interpretation (i.e. also referred to as interquartile range (IQR)) (Batista et al., 2022), mean (Wilkinson et al., 2013; Nosrati et al., 2021), mean plus/minus 1 standard deviation (mean ± SD) (Evrard et al., 2020b; Laceby et al., 2021), and median (Collins et al., 2013; Batista et al., 2022) are detailed in Table I.I.

Table I.I: Equations of the common range test criteria used in the literature to test the conservative behaviour in the three-step method (TSM). s_i is the source group i from 1 to n, the number of source groups; t_j is the target sample j value with j from 1 to m, the number of samples; and μ is the mean and σ is the standard deviation (SD). Symbol * indicates statistics calculated on log-transformed values.

Criterion	Range test equation
Minimum-maximum	$min(min_{s_i}) \leq t_j \leq max(max_{s_i})$
Minimum-maximum ±10 %	$min(min_{s_i} \cdot 0.9) \leq t_j \leq max(max_{s_i} \cdot 1.1)$
Hinge	$min(Q_{s_i}(0.25)) \leq t_j \leq max(Q_{s_i}(0.75))$
Whiskers	$min(max(min_{s_i}, Q_{s_i}(0.25) - 1.5\ \text{IQR}_{s_i})) \leq t_j \leq max(min(max_{s_i}, Q_{s_i}(0.75) + 1.5\ \text{IQR}_{s_i}))$
Mean	$min(\mu^*_{s_i}) \leq t_j \leq max(\mu^*_{s_i})$
Mean ± SD	$min(\mu^*_{s_i} - \sigma^*_{s_i}) \leq t_j \leq max(\mu^* s_i + \sigma^*_{s_i})$
Median	$min(median_{s_i}) \leq t_j \leq max(median_{s_i})$

Discriminant power.

The ability of the property to discriminate between source groups is assessed using a Kruskal-Wallis H test (Hollander et al., 2013). This is a non-parametric test that checks whether two or more samples originate from the same distribution, and it represents an extension of the Mann-Whitney U test that compares two samples. The test hypotheses are the following.

- The null hypothesis (H_0): the median across the three groups are equal.
- The alternative hypothesis (H_1): at least one of the group medians is different from the others.

The test statistic is given by

$$H = (N-1)\frac{\sum_{i=1}^{g} n_i\ (\overline{r}_i - \overline{r})^2}{\sum_{i=1}^{g}\sum_{j=1}^{n_i}(r_{ij} - \overline{r})^2}, \tag{I.3}$$

with n being the total number of observations across all groups, g the number of groups, n_i the number of observations in group i, r_{ij} the rank of observation j from group i, $\overline{r}_i$ the mean rank of all observations for

group i and $\overline{r}$ the mean of all r_{ij}.

Kruskal-Wallis H tests were performed using the function 'kruskal.test' from the stats package (R Core Team, 2022). For properties with a *p* value below α = 0.05, the null hypothesis is rejected, which means that at least one of the source groups is different from the others and that the property is therefore discriminant.

Discriminant function analysis.

A discriminant function analysis (DFA) stepwise selection is carried out to identify a subset of predictors among the identified tracers (Collins and Walling, 2002; Collins et al., 2010). A forward stepwise variable selection based on Wilk's lambda criterion was performed using the function 'greedy.wilks' from the klaR package (Weihs et al., 2023). The function first initiates a model with the variable that discriminates groups. Then, the model is extended by including other variables based on Wilk's lambda criterion: the one variable that minimises the Wilk's lambda is only included if the model's *p* value remains statistically significant after its inclusion. Wilk's lambda statistic approaches zero when the variability between groups is higher than the variability within each group; then this criterion maximises the difference between groups. As the use of the DFA stepwise selection has been criticised because some studies showed that the use of a higher number of tracers decreases the sensitivity of the results to non-conservative tracers (Martínez-Carreras et al., 2008; Sherriff et al., 2015), we used the list of identified tracers before ("no DFA") and after the stepwise selection procedure ("DFA") in order to assess its potential impact on the calculation of source contributions.

I.2.5.2 - Consensus method

The approach by Lizaga et al. (2020) to select properties, referred to as the consensus method (CM), is based on two tests: the conservativeness index (CI) and the consensus ranking (CR). In the CM, tracers are selected by identifying non-conservative behaviour (using the CI test) and dissenting tracers (CR test). The CI of each property is calculated for all target samples simultaneously, while the CR is calculated for each target sample independently. As a result, a set of tracers is selected for each target sample. Tests were performed using the 1.3 version of FingerPro (Lizaga et al., 2022) under the R ver. 4.1.2 (R Core Team, 2021) environment.

Conservativeness index.

The CI quantifies how conservative a property is based on the result of a single-tracer model. To be considered conservative, the CI should be strictly equal to 0. A single-tracer model is a standard linear un-mixing model with only one true analysed property and n $-$ 2 virtual properties (n the number of source groups). The model is solved to obtain the source contributions. This process is repeated 2000 times, which creates a distribution of predictions. The prediction couples (i.e. $w_1, w_2, ..., w_n$) are sorted according to the Euclidean distance to a perfectly balanced mixture (i.e. $\frac{1}{\mathrm{n}}$). A percentile of the sorted prediction couple is chosen to compute the CI as the root mean square error (RMSE) of the non-conservative part (nc) of the contribution, as follows:

$$\mathrm{CI} = -\sqrt{\sum_{j=1}^{n}\left(\mathrm{nc}(w_j) - \frac{1}{n}\right)^2} \text{ ; with } nc(w) = \begin{cases} -w & \text{if } w < 0 \\ 0 & \text{if } 0 \leqslant w \leqslant 1 \\ w-1 & \text{if } w > 1 \end{cases} \tag{I.4}$$

with w_j being of the j^{th} source group predicted contribution of the selected percentile, and n is the number of

source groups.

A property is considered conservative if the CI values are strictly equal to zero.

Consensus ranking.

CR is an index that quantifies the relevance of each property for the prediction based on a debate agreement for a single target sample. In each debate, a subset of n $+ 1$ randomly selected properties is built and several rounds of debates are performed excluding one property each time. The consensus of each debate is measured through the quality of the mass balance equations. When the exclusion of a property leads to an increase of the subset consensus score (i.e. higher RMSE of the mass balance equations), the property is considered dissenting and "lost a debate". The CR of a property is the ratio between the number of attended debates (set at 2000) and the number of lost debates, and it is calculated as follows:

$$\text{CR} = 100\left(1 - \frac{\text{lost debates}}{\text{attended debates}}\right) \tag{I.5}$$

Properties with a CR score above a certain threshold are considered relevant and are selected. Lizaga et al. (2020) recommended to select properties with a CR score above 70.

I.2.6 - Source contribution modelling

I.2.6.1 - Un-mixing model

An un-mixing model was run on actual sediment samples and virtual mixtures using the tracers selected by the TSM without and with DFA and the CM. To do so, the widely used Bayesian un-mixing model MixSIAR was employed using the R package MixSIAR (Stock et al., 2020, ver. 3.1.12) with JAGS (Stock et al., 2022, ver. 4.3.1) (Collins et al., 2020; Evrard et al., 2022; Lizaga et al., 2020; Batista et al., 2022). To quantify the contributions of n sources, the model requires n-1 tracers. The model was run with a "long" Markov Chain Monte Carlo sampling algorithm (i.e. chain length = 300,000, burn-in = 200,000, thin = 100 and chains = 3) with a process error structure. Model convergence was determined by the Gelman-Rubin diagnostic using the 'output_JAGS' function from the 'MixSIAR' package, and none of the tracer selection approaches tested had a value greater than 1.05. The median value of the distribution predicted by MixSIAR was reported as the source contribution for each sediment target and virtual mixture.

I.2.6.2 - Accuracy assessment

For each tracer selection approach, MixSIAR prediction accuracy was assessed using virtual mixture contribution predictions, for which theoretical source contributions were known a priori. Each model's prediction accuracy was evaluated based on different criteria: uncertainty (prediction interval width (W50)), residual error or bias (mean error (ME)), performance (squared Pearson correlation coefficient (r^2)), root-mean-square error (RMSE), Nash-Sutcliffe modelling efficiency coefficient (NSE), and continuous ranked probability score (CRPS). A summary of the metrics, with their formula, unit, range and ideal values, is provided in Table I.II (Matheson and Winkler, 1976; Bennett et al., 2013; Batista et al., 2022).

Table I.II: Formula of model prediction accuracy metrics. With z_i and $\hat{z}_i$, respectively, the measured and predicted contributions for the sample i; $\bar{z}$ and $\bar{\hat{z}}$ the measured and predicted mean contribution of all samples; and n the number of samples.

Name	Unit	Formula	Range	Ideal value
Prediction interval width (W50)	%	$\text{W50} = Q(0.75) - Q(0.25)$	(0, 100)	0
Mean error (ME)	%	$\text{ME} = \frac{1}{n}\sum_{i=1}^{n}(z_i - \hat{z}_i)$	$(-\infty, +\infty)$	0
Root mean square error (RMSE)	%	$\text{RMSE} = \sqrt{\frac{1}{n}\sum_{i=1}^{n}(z_i - \hat{z}_i)^2}$	$(0, +\infty)$	0
Squared Pearson's correlation coefficient (r^2)		$r^2 = \left(\frac{\sum_{i=1}^{n}(z_i-\bar{z})-(\hat{z}_i-\bar{\hat{z}})}{\sqrt{\sum_{i=1}^{n}(z_i-\bar{z})^2}\sqrt{\sum_{i=1}^{n}(\hat{z}_i-\bar{\hat{z}})^2}}\right)^2$	(0, 1)	1
Nash-Sutcliffe modelling efficiency coefficient (NSE)		$\text{NSE} = 1 - \frac{\sum(z_i-\hat{z}_i)^2}{\sum(z_i-\bar{z}_i)^2}$	$(-\infty, 1)$	1
Continuous ranked probability score (CRPS)		$(F_i, z_i) = \int_{-\infty}^{+\infty}\left(F_i(z_i) - H\{z_i \leq \hat{z}_i\}\right)^2$	$(0, +\infty)$	0

Higher values of W50 indicate a wider distribution, which is related to a higher uncertainty. The sign of the ME indicates the direction of the bias, i.e. an overestimation or underestimation (positive or negative value, respectively). As ME is affected by cancellation, a ME of zero can also reflect a balanced distribution of predictions around the 1:1 line. Although this is not a bias, it does not mean that the model outputs are devoid of errors. The RMSE is a measure of the accuracy and allows us to calculate prediction errors of different models for a particular dataset. RMSE is always positive, and its ideal value is zero, which indicates a perfect fit to the data. As RMSE depends on the squared error, it is sensitive to outliers. The r^2 describes how linear the prediction is. The NSE indicates the magnitude of variance explained by the model, i.e. how well the predictions match with the observations. A negative RMSE indicates that the mean of the measured values provides a better predictor than the model. The joint use of r^2 and NSE allows for a better appreciation of the distribution shape of predictions and thus facilitates the understanding of the nature of model prediction errors. The CRPS evaluates both the accuracy and sharpness (i.e. precision) of a distribution of predicted continuous values from a probabilistic model for each sample (Matheson and Winkler, 1976). The CRPS is minimised when the observed value corresponds to a high probability value in the distribution of model outputs. The formulae and the full description of this score are available in Jordan et al. (2019) and Laio and Tamea (2007). The calculation of the CRPS was performed using the 'crps_sample' function from the 'scoringRules' package (Jordan et al., 2019). Model global CRPS* and W50* value are calculated as the mean of individual CRPS and W50 values, respectively. In addition to the metric values, a graphical evaluation of model predictions was performed through plotting observed versus predicted CRPS sample values and W50 sample values for each source group.

All data analyses were performed using R (R Core Team, 2022, ver. 4.2.2) within RStudio (Team, 2022). An R package (fingR) implementing the approach followed in this study was developed and is freely available (Chalaux-Clergue and Bizeul, 2023).

I.3 - Results

According to the measurement uncertainty criterion (Sect.I.2.3), the following properties were removed from subsequent analysis: the elemental concentrations in Co, Cr, Cu, Ni and Rb; the visible colorimetric index A3, and the goethite peak at 445 nm (G_{445}), as their measurement uncertainties were too high.

I.3.1 - Tracer selection

I.3.1.1 - Selection of tracers

Three-step method.

The different range tests resulted in unique sets of conservative properties, with only TN and Q7/4 passing all tests (Fig. I.2). Nevertheless, the majority of tests identified TOC, G_{525}, b*, Al, Ti, L* and C* (Table I.III) as being conservative. The minimum-maximum $\pm$ 10 % is the range test criterion that identified the highest number of properties (n = 19), followed by the minimum-maximum (n = 16) and whiskers (n = 12). The minimum-maximum $\pm$ 10 % range test criterion was the only one that identified Fe, Pb, h, A1 and GT. As the minimum-maximum criterion, this test identified Ca, K, Mg and Sr as conservative. The mean and median criteria identified only three (TN, b*, Q7/4) and four properties (TOC, TN, Q7/4, G_{525}), respectively.

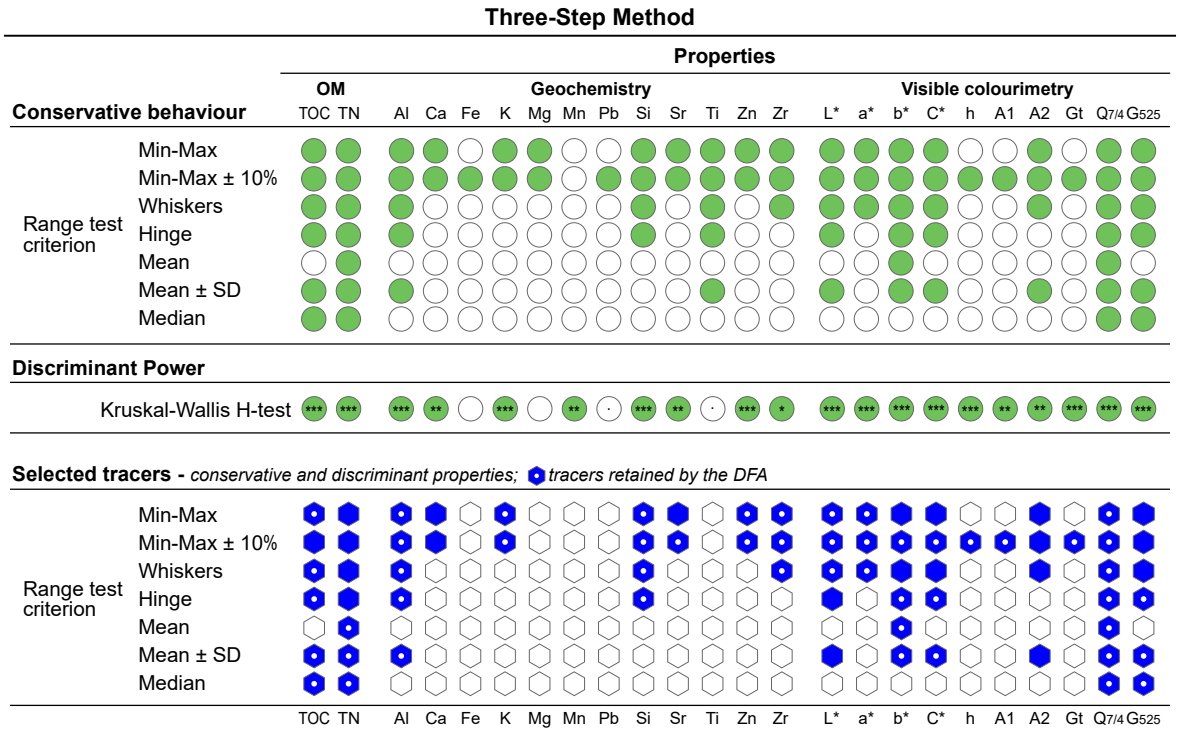


Figure I.2: Tracer selection using the three-step method (TSM) according to different range test criteria. Green filled circles indicate a property that passed the conservative behaviour (i.e. range test) or the discriminant power (Kruskal-Wallis H test) tests. Blue filled diamonds indicate selected tracers (i.e. properties that passed both conservative behaviour and discriminant power tests) and blue diamonds with white points indicate tracers retained by the discriminant function analysis (DFA) forward stepwise selection based on Wilk's lambda criterion. Kruskal-Wallis H test's p value significance: "***" p value < 0.001; "**" p value < 0.01; "*" p value < 0.05; "." p value < 0.1; " " p-value < 1. OM: organic matter; Min-Max: minimum to maximum; SD: standard deviation.

Among the properties identified as conservative, Fe, Mg, Pb and Ti were not identified as discriminant by the Kruskal-Wallis H test (p value = 0.08) and were therefore removed from the list of potential tracers. Although a majority of tests identified Ti as conservative, only the minimum-maximum $\pm$ 10 % criterion identified Fe, Mg and Pb as conservative. The DFA procedure mostly resulted in the systematic exclusion of A2 and in the frequent exclusion of TN and G_{525}, while TOC, Al, Si, L* and Q7/4 were retained by most of the range test criteria. Among the 16 tracers selected by the minimum-maximum criterion, the DFA discarded seven of them (TN, Ca, Sr, b*, C*, A2 and G_{525}). In contrast, for the minimum-maximum $\pm$ 10 % criterion that selected 19 tracers, only five tracers (i.e. TOC, TN, Ca, A2 and G_{525}) were discarded by the DFA. The outputs of the mean and median criteria were not modified by the DFA.

Consensus method.

The CI values indicate that TOC, TN, b* and C* were identified as conservative properties (CI strictly equal to 0, Fig. I.3) However, Al, Si, Ti, Q7/4 and G_{525} obtained a CI very close to zero (i.e. -0.1), whereas it was equal to -0.2 for Zn, L* and A2. For these four properties, all sediment samples (n = 32) obtained a CR score above the threshold (i.e. 70) for all sediment samples (i.e. 32 out of 32) and were therefore considered relevant and kept in the list of tracers for further analysis. In addition, properties which obtained CI values close to zero (i.e. Al, Si, Ti, Q7/4, G_{525}, Zn, L* and A2) also reached a high CR score (i.e. respectively 25, 22, 30, 25, 32, 24, 16 and 20).

Table I.III summarises the list of tracers selected by each approach.

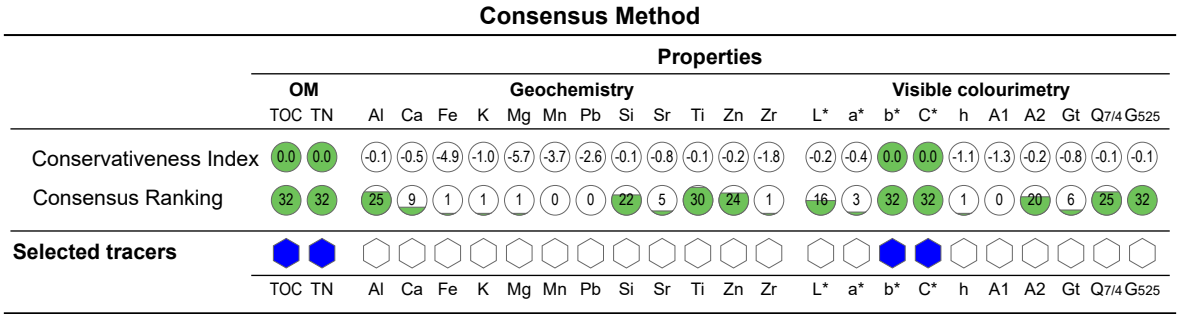


Figure I.3: Tracer selection using the consensus method (CM). Green filled circles indicate properties selected by the conservativeness index (i.e. CI = 0.0). The value in the circle refers to the number of sediment samples (out of 32) that obtained a Consensus Raking score above the threshold (i.e. CR $\geq$ 70). Blue filled diamonds indicate selected tracers. OM: organic matter.

Table I.III: Tracers selected by the three-step method (TSM) according to the range test criteria and the consensus method (CM). Tracers underlined and written in bold were retained by the discriminant function analysis (DFA) forward stepwise selection based on Wilk's lambda criterion. Min-Max = minimum to maximum.

Tracer selection method	range test	Selected tracers
Three-step method	Min-Max	**TOC**, TN, **Al**, Ca, **K**, **Si**, Sr, **Zn**, **Zr**, **L***, **a***, b*, C*, A2, **Q7/4**, G_{525}
	Min-Max $\pm$ 10 %	TOC, TN, **Al**, Ca, **K**, **Si**, **Sr**, **Zn**, **Zr**, **L***, **a***, **b***, **C***, **h**, **A1**, A2, **Gt**, **Q7/4**, G_{525}
	Whiskers	**TOC**, TN, **Al**, **Si**, **Zr**, **L***, **a***, b*, C*, A2, **Q7/4**, G_{525}
	Hinge	**TOC**, TN, **Al**, **Si**, **L***, **b***, **C***, **Q7/4**, **G_{525}**
	Mean	**TN**, **b***, **Q7/4**
	Mean $\pm$ SD	**TOC**, **TN**, **Al**, **L***, **b***, **C***, A2, **Q7/4**, G_{525}
	Median	**TOC**, **TN**, **Q7/4**, **G_{525}**
Consensus method		TOC, TN, b*, C*

I.3.2 - Prediction accuracy and tracer selection methods

The sediment source apportionment prediction accuracies obtained when using the mean range test criterion and CM for tracer selection were lower compared to that obtained when using the other TSM range test criteria (Fig. I.4 and Supplementary Materials Tables I.SM-I, I.SM-II, I.SM-III and I.SM-IV). However, the difference in prediction accuracy was greater between sources within each tracer selection method than between methods (i.e. TSM and CM). The effect of the DFA stepwise selection was to mainly modify the prediction accuracy of cropland and forest. On average, W50* values (+20 %), r^2 (+0.01) and NSE (+0.04) increased, while ME (-37 %), RMSE (-8 %) and CRPS (-1) decreased. In short, uncertainty increased (W50*), bias decreased (ME) and performance slightly increased (r^2, NSE, CRPS*) when the DFA was applied.

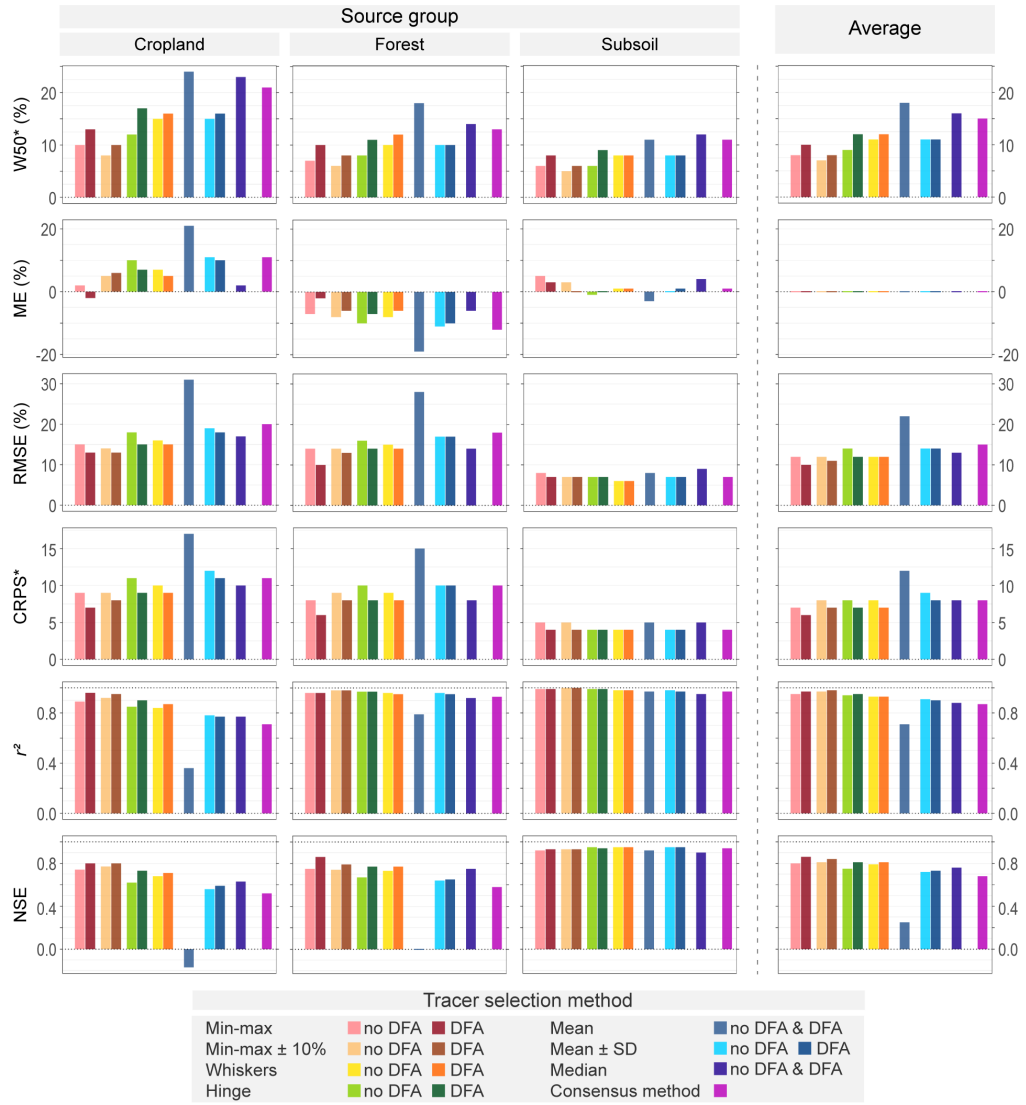


Figure I.4: Summary of MixSIAR accuracy statistics calculated on virtual mixtures (n = 138) for each tracer selection method: three-step method (TSM) range test criteria and consensus method (CM) for each individual soil source and average of all three sources for each method. Tracers selected by each method are listed in Table I.III. Model accuracy statistics were shown by darker bar plots for each selection approach. W50*: prediction interval width; ME: mean error; RMSE: root mean square error; r^2: squared Pearson's correlation coefficient; NSE: Nash-Sutcliffe modelling efficiency coefficient; CRPS: continuous ranked probability score. Note that symbol $*$ indicates mean values per source

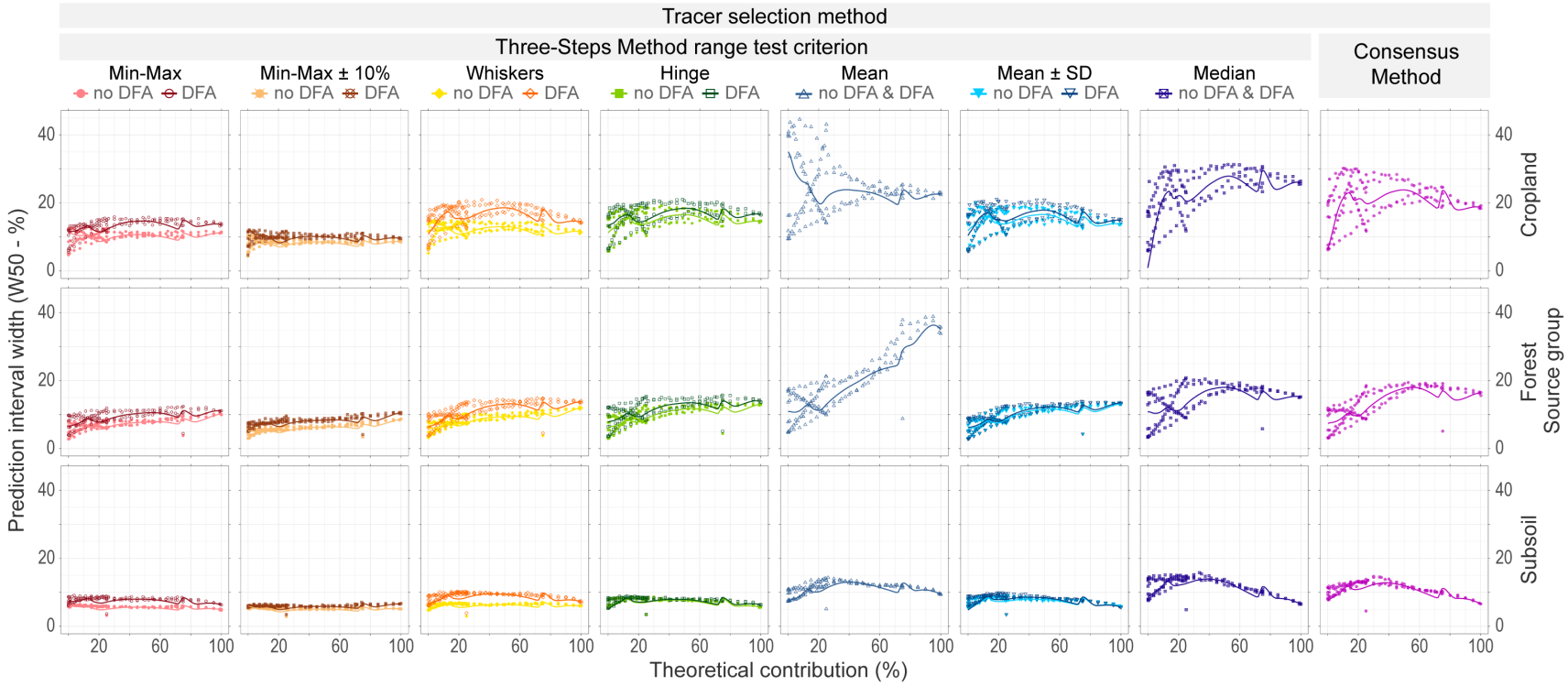


Figure I.5: Relationship between theoretical virtual mixture source contributions and prediction interval width (W50) across sources (cropland, forest and subsoil) according to each tracer selection approach: three-step method (TSM) range test criteria, which are minimum-maximum (red circle), minimum-maximum ± 10 % (brown crossed circle), whiskers (yellow/orange diamond), hinge (green square), and mean ± SD (blue triangle point down) - filled and empty symbols correspond to the selection before DFA (no DFA) and after DFA respectively, except for mean (blue triangle) and median (blue crossed square) criteria for which empty symbols correspond to the same selection of tracers before and after DFA - and consensus method (CM; purple circle plus).

Regardless of the tracer selection method, the W50* values indicate a higher uncertainty for cropland, followed by forest and subsoil (Fig. I.4). The CM, mean and median range test criteria showed higher W50* for each source (21-25, 13-18 and 11-12 % for cropland, forest and subsoil, respectively) among the tracer selection methods. The lowest W50* values were obtained by minimum-maximum $\pm$ 10 % and minimum-maximum with and without DFA stepwise selection. Overall, minimum-maximum and minimum-maximum $\pm$ 10 % showed homogeneous values over the 0-100 % contribution range for all sources (Fig. I.5). The subsoil W50 curves showed no trend over the contribution range for most of the range test criteria, while there was a slight reduction in W50 values for the median criterion and the CM. However, the W50 value for cropland and forest tended to increase for most of the range test criteria (i.e. whiskers, hinge, mean, mean $\pm$ SD, median) and the CM. This increase was more pronounced for the forest and also for the CM, the mean and median criteria. In addition, the W50 values were more scattered for these three tracer selections, especially for the contributions below 60-70 %. As observed for the W50* (Fig. I.4), the DFA stepwise selection was associated with an increase in W50 values for all range test criteria.

Regarding the model residuals for all tracer selections except that obtained with the mean criteria, the error for subsoil was low (RMSE = 6-8 %) with a small bias (ME = -3 - 5 %). In contrast, forest and cropland errors were about twice higher (RMSE = 10-20 %), with a negative bias for forest (ME = -19 - -2 %) and a positive bias for cropland (ME = 2-11 %). Accordingly, forest and cropland contributions were underestimation and overpredicted, respectively.

In terms of model performance, the subsoil predictions were highly linear (r^2 = 0.97-0.99) and well predicted (NSE = 0.92-0.95). For the TSM criteria, linearity and prediction quality were slightly improved in most cases. Nevertheless, a slight decrease in precision and accuracy was observed for contributions below 10 % and above 80 % (Fig. I.6). Forest predictions were highly linear for most tracer selections (r^2 = 0.92-0.98), although their prediction quality was lower (NSE = 0.58-0.86) due to an underestimation (i.e. ME values, Fig I.6). This underestimation was also confirmed by the CRPS values, which increased strongly and linearly above 20 % of forest contribution (Fig. I.6). Cropland predictions were relatively linear (r^2 = 0.71-0.89) but not well predicted (NSE = 0.52-0.80), representing the lowest performance among the sources. The CRPS curves were U-shaped, with a decrease in accuracy and precision for contributions below 60 % and above 70 % (Fig. I.7). This pattern was also observed on the observed versus predicted plots in Fig. I.6, with a tipping point at around 40 to 60 % of the contribution. In addition, for a contribution below 60 %, two types of behaviour were observed regardless of the tracer selection method considered (Fig. I.6). One group of virtual mixtures was well predicted with a small bias and low CRPS values ($\leq$ 0.05), while another group was significantly less well predicted with a strong positive bias and higher CRPS values (Fig. I.7). These two groups correspond to virtual mixtures with a dominant proportion of subsoil and forest, respectively. For contributions above 60 %, these two groups converge, and no difference can be observed. This suggests that selected tracers were able to successfully discriminate between subsoil and forest sources, while cropland was confused with one of the other two sources.

Among the selection of tracers, the mean range test criterion was the one that resulted in the lowest prediction quality (Fig. I.4). Despite the fact that subsoil had a prediction quality close to that of the other methods, cropland and forest were poorly predicted (NSE = -0.17 and 0.00 respectively), with modelled contributions being quite far from the theoretical values (Fig. I.6 and I.7).



Figure I.6: Relationship between theoretical and predicted virtual mixture source contributions (cropland, forest, subsoil), according to each tracer selection approach: three-step method (TSM) range test criteria, which are minimum-maximum (red circle), minimum-maximum ± 10 % (brown crossed circle), whiskers (yellow/orange diamond), hinge (green square), and mean ± SD (blue triangle point down) - filled and empty symbols correspond to the selection before DFA (no DFA) and after DFA respectively, except for mean (blue triangle) and median (blue crossed square) criteria for which empty symbols correspond to the same selection of tracers before and after DFA - and consensus method (CM; purple circle plus).

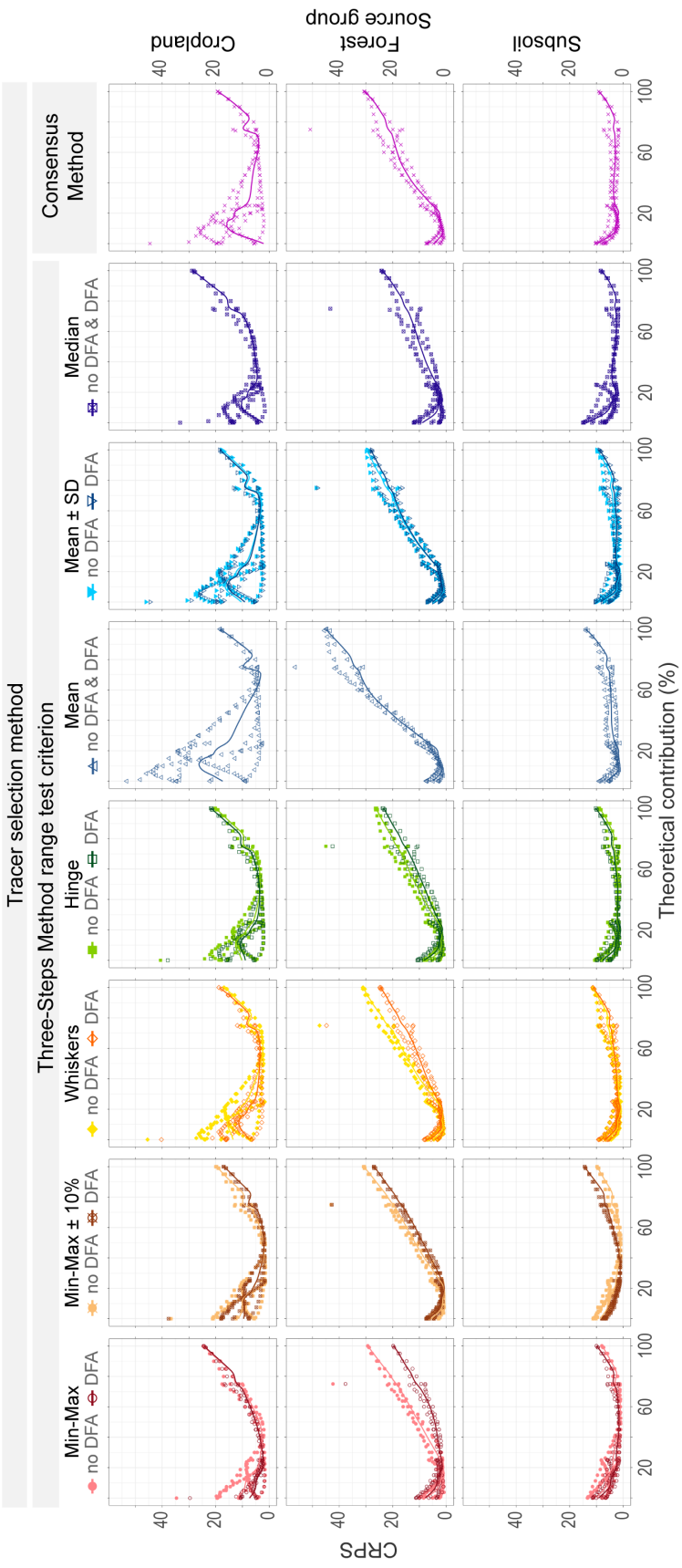


Figure I.7: Relationship between theoretical virtual mixture source contributions and continuous ranked probability score (CRPS) across sources: three-step method (TSM) range test criteria which are minimum-maximum (red circle), minimum-maximum ± 10 % (brown crossed circle), whiskers (yellow/orange diamond), hinge (green square) and mean ± SD (blue triangle point down) - filled and empty symbols correspond to the selection before DFA (no DFA) and after DFA respectively, except for mean (blue triangle) and median (blue crossed square) criteria for which empty symbols correspond to the same selection of tracers before and after DFA - and consensus method (CM; purple circle plus).

I.3.3 - Source contribution predictions

The tracer selection methods resulted in three types of source contribution trends: strong dominance of forest, strong dominance of cropland, and equivalent contribution of forest and cropland (Fig. I.8).

For all approaches, subsoil contributions were low and stable, for most methods from 0 ± 1 to 8 ± 3 %. The mean and mean ± SD criteria without DFA led to higher and more variable subsoil contributions than other methods, 12 ± 5 % versus about 4 ± 2 %. The relationship between cropland and forest was different depending on the tracer selection method. For the CM, the mean and median criteria led to model outputs showing that cropland was dominant compared to forest along the sediment core. In contrast, according to the mean ± SD and hinge criteria, the contributions of cropland and forest were modelled to be similar or with only a slight dominance of forest. Finally, for the minimum-maximum, minimum-maximum ± 10 % and whiskers criteria, the model calculated a strong dominance of forest over cropland. The DFA had limited impact on the

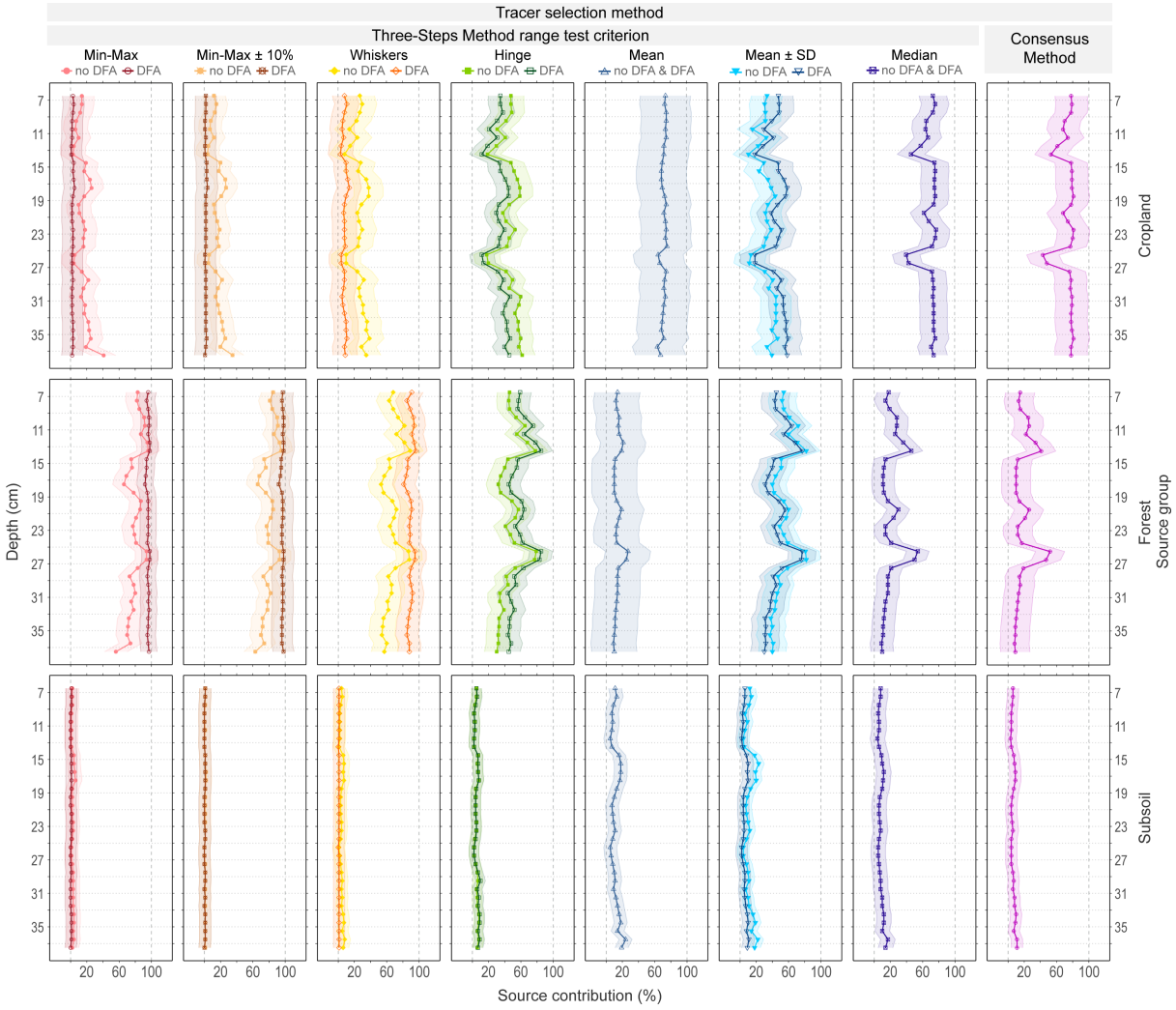


Figure I.8: Predicted source contributions for the sediment core samples according to each tracer selection approach. The different range test criteria of the three-step method (TSM) are the following: minimum-maximum (red circle), minimum-maximum ± 10 % (brown crossed circle), whiskers (yellow/orange diamond), hinge (green square), mean (blue triangle), mean ± SD (light blue triangle point down), and median (purple crossed square); the consensus method (CM; light purple circle plus) is also shown. Empty and filled symbols correspond to the use of DFA or not. The error buffer ribbons around the plotted values correspond to the respective RMSE values calculated on virtual mixtures.

trends in the contributions of cropland and forest for the mean ± SD and hinge criteria, although it resulted in a significant smoothing of the contribution values for the minimum-maximum, minimum-maximum ± 10 % and whiskers criteria. The contribution of cropland was greatly reduced from 16-27 % to 2-8 %, and the dominance of forest increased from 67-80 % to 89-97 %, resulting in an almost unique and stable contribution from forests along the entire core. However, the contributions of cropland and forest showed similar variations and tendencies along the sediment core for all tracer selection methods, although their values were significantly different. Samples taken at 9/10-10/11, 11/12-13/14, 19/20-20/21 and 24/25-07/28 cm depths were associated with higher contributions from forest and lower contributions from cropland compared to upper/lower samples.

The selected tracers did not provide the same information and therefore did not provide the same ability to discriminate between the sources (Fig. I.9). For most of the tracers, the following relationship between source group signatures (i.e. mean and SD of log-transformed values) was observed: cropland showed intermediate values, with either forest (TOC, TN) or subsoil (Al, Si, L*, a*, b*, C*, A2, Q7/4, G_{525}) being the highest values.

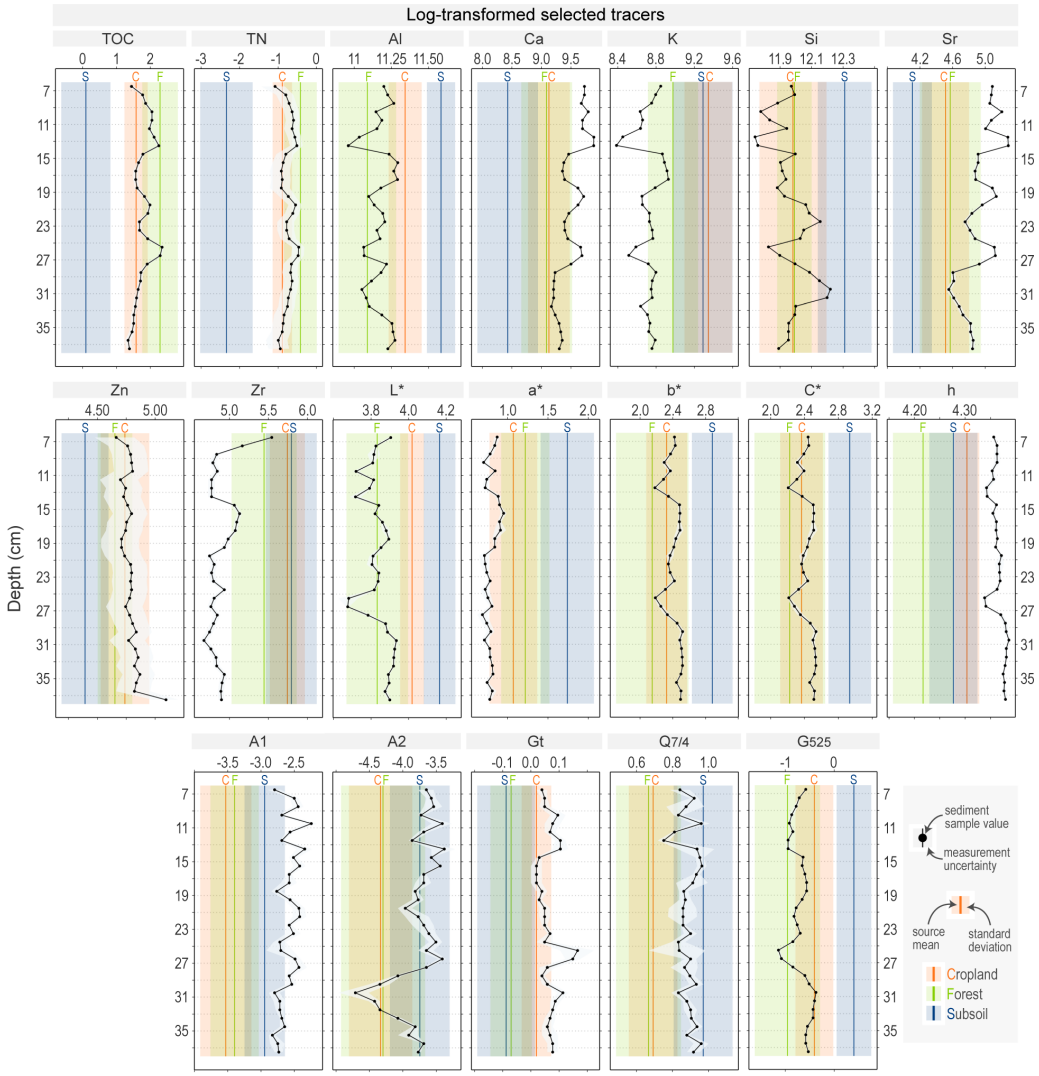


Figure I.9: Log-transformed values of selected tracers along the sediment core (black dot; measurement uncertainty is represented with a grey buffer) and in the potential source signatures (vertical line represents mean value, and the buffer zone along each line represents the standard deviation).

For most of these tracers, cropland had similar values as those of forest (TOC, TN, Si, a*, b*, C*, A2, Q7/4) or subsoil (G_{525}). For a few tracers, cropland had the higher values with either subsoil (Zn, Gt) or forest (h) corresponding to the lower values. However, for h, the signatures of cropland and subsoil were similar, and this similarity was also observed for Zn in cropland and forest, and for Gt in forest and subsoil sources. In addition, for some selected tracers (Ca, K, Sr, Zr, A1), all source signatures were all very close and hardly distinguishable, making the information derived from the relationships between sources less clear.

Depending on the tracer, sediment sample values did not show the same position in relation to the source signatures (Fig. I.9). For some tracers, sample values were close to those of cropland (i.e. Zn, b*, A1, Q7/4), forest (Al, K, Zr, L*) or subsoil (a*, C*, h). However, for most of the tracers (i.e. TOC, TN, Ca, Si, Sr, A2, Gt, G_{525}) sample values were intermediate between those of cropland and forest.

I.4 - Discussion

I.4.1 - Conservative behaviour assessment

The different tests used to assess conservative behaviour, i.e. the TSM range test using different criteria and the CM CI, resulted in the selection of properties with different restriction levels. These tests can be divided into three groups according to the number of properties selected, from the least restrictive (minimum-maximum, minimum-maximum $\pm$ 10 %, whiskers), via moderately restrictive (hinge, mean $\pm$ SD) to the more restrictive (CI, mean, median). Overall, the conservative behaviour tests tended to mainly identify the same properties as being conservative: TOC, TN, b*, C* and Q7/4.

In this study, all the tests identified organic matter properties as conservative (i.e. TOC and TN), except for the mean criterion, which did not select TOC. To assess the composition of organic matter, either from terrestrial and/or freshwater origin, the distribution of δ^{13}C versus C/N ratio can be compared to thresholds (Lamb et al., 2006). In a previous study conducted on a sediment core sampled from the same site in Hayama Lake in 2014, Huon et al. (2018) concluded that there was no autochthonous input of freshwater-originating organic matter, which was confirmed in our data (see Supplementary Materials Fig. I.SM-1). Organic matter and carbon may be expected to provide a conservative property (García-Comendador et al., 2023), and this is supported by their widespread selection.

Among the geochemical properties, Al, Ti and Si were frequently selected by range tests. This can be explained by their well-known low solubility (Meybeck and Helmer, 1989; Phillips and Greenway, 1998; Koiter et al., 2013) and more specifically for Al and Si, which are constituents of clay sheets given the granitic geological context of the study area (see Fig. B2, in Supplementary Materials). However, these geochemical properties are sensitive to grain size sorting that is occurring along the transport pathway as they are clay sheet constituents. Other geochemical properties that were rarely selected (i.e. Fe, Pb, Ca, K) or systematically rejected, such as Mn, are associated with higher solubility or higher desorption susceptibility (Koiter et al., 2013; García-Comendador et al., 2023; Meybeck and Helmer, 1989; Phillips and Greenway, 1998).

Among the visible colour indices, all conservative behaviour tests selected Q7/4, and other indices such as G_{525}, b*, C* and L* were widely selected. The colour indices L*, b* and C* were highly correlated with organic matter properties (i.e. TOC and TN) that were also identified as conservative (Pearson r^2 from -0.61 to -0.77; see Supplementary Materials Table I.SM-V). This is consistent with the fact that organic matter and iron oxides are the main soil-colouring elements. The existence of different visible-colour spaces provides

several tools for sediment fingerprinting studies and for selecting the most appropriate space and indices according to the local context (Viscarra Rossel et al., 2006). These colour spaces are interconnected, and the transformation of indices can be achieved with simple mathematical formula. However, care must be taken to avoid multi-colinearity when using multiple indices from different colour spaces together, as redundancy of information tends to degrade modelling accuracy (Cox et al., 2023). However, the visible-colour parameters are quite sensitive to spatial and temporal variations (García-Comendador et al., 2023). The acquisition of other spectral regions such as Vis-NIR, NIR (near-infrared) and MIR (mid-infrared) appears to be more robust (Chen et al., 2023), especially as these regions are a powerful and reliable way to obtain the extensive range of properties and information on the sample with the advantages of being rapid, cost-effective and non-destructive measurements (Soriano-Disla et al., 2014). Of note is that in order to ensure the exchange of spectra within the community, the adoption of a common protocol and/or the provision of calibration spectra using inter-calibration samples should be discussed, as spectra tend to be instrument-dependent (Pimstein et al., 2011).

The CI was a restrictive method compared to most range test criteria. It selected four properties, which is similar to the number of properties selected by the mean and median range test criteria. Nevertheless, some properties selected by other range test criteria, which were a priori conservative properties, showed a score close to the threshold of 0.00 defined by Lizaga et al. (2020). Thus, Al, Si, Ti, Q7/4 and G_{525} obtained a CI equal to -0.1, while it was equal to -0.2 for Zn, L* and A2. This could indicate that properties that yielded a CI score close to the threshold (i.e. 0.00) were not strictly conservative (e.g. size sorting for Al, Si and Ti). We suggest that either the CI can be used to identify less conservative properties in a selection resulting from different tests or from the modification of the CI threshold (i.e. not strictly equal to 0.00) to select properties currently considered not conservative.

As this study shows, a priori and field knowledge are essential to assess the relevance of conservative behaviour assessments (Laceby et al., 2015; Koiter et al., 2018; Batista et al., 2019). However, this knowledge is not sufficient and not usable for all measured properties, especially for relatively new properties as colour parameters, due to their complex relationship with environmental processes. Other studies developed particle size and organic matter corrections, which were shown to be effective (Koiter et al., 2018). However, they require additional measurements and are site-specific (Koiter et al., 2018). Therefore, it is essential to develop cost-effective, time-effective and generalised methods (Koiter et al., 2018).

I.4.2 - Tracer selection and contribution modelling

The CR index was designed to select properties based on their relevance to prediction, as they maximise convergence. Of the 24 properties considered in the current research, only the TOC, TN, b*, L* and G_{525} reached a CR score above 70 (Fig. I.3). These properties were redundant, as they showed very similar trends along the sediment core (Fig. I.9). By removing tracers that prevent consensus, CR favours redundant properties and discards dissenting properties that could nevertheless be relevant, and this may lead to an information gap. Dissenting properties can provide complementary information, as properties do not discriminate between sources in the same way.

Indeed, the selection of consistent properties can result in the prediction of a dominant source while ignoring another. For example, in this study, the CR selected properties for which sediment values were close to the cropland signature or were intermediate between cropland and forest values (Fig. I.9). This selection of tracers with consistent cropland signature resulted in the prediction of dominant cropland contributions (Fig. I.8).

Conversely, the DFA stepwise procedure of the TSM aims to maximise the difference between properties by simultaneously minimising redundant information, which could increase the prediction quality of MixSIAR (Cox et al., 2023). In this study, the use of the DFA improved model accuracy for all the range test criteria compared to the selection prior DFA (Fig. I.4). However, DFA application tended to reduce source contribution variations - especially for minimum-maximum, minimum-maximum ± 10 % and whiskers criteria - (Fig. I.8). Overall, the impact of the DFA on tracer selection modelling outputs needs more research to be clarified.

From the different tracer selections, which were all distinct, three main tendencies were observed in terms of modelled contributions (Fig. I.8). On the one hand, extensive tracer selections, such as minimum-maximum, minimum-maximum ± 10 % and whiskers criteria, resulted in a modelled dominance of the forest contribution over cropland and subsoil. On the other hand, restrictive selections of tracers, such as the CM, mean and median criteria, resulted in a modelled dominance of cropland contribution. Finally, methods that selected an intermediate number of tracers, i.e. mean ± SD and median criteria, led to the prediction of a balanced contribution between forest and cropland. This major impact of the tracer selection methods on the source contribution modelling was demonstrated by multiple studies (Laceby et al., 2015; Palazón et al., 2015; Smith et al., 2018; Gaspar et al., 2019).

However, in the current research, all methods agreed on a low subsoil contribution associated with high modelling accuracy statistics (Fig. I.4). It can be assumed that since all tracer selection methods selected TN, b* and C*, they allowed us to predict the general trend of the subsoil contribution behaviour. Thus, methods that selected additional tracers, such as mean ± SD and median criteria, did not result in significant modifications of the trend. However, the methods that selected a large number of tracers (i.e. minimum-maximum, minimum-maximum ± 10 %, and whiskers) resulted in a strong reduction or even disappearance of the subsoil contribution, on average about 2 % versus 8 %. The need for few tracers to predict subsoil with a good prediction accuracy can be explained by its significantly different signature compared to forest and cropland (Fig. I.9). Most of the modelling limitations were related to the prediction quality for cropland and forest, as their respective signatures were very close to each other for many tracers (Fig. I.9). However, the same variations, i.e. higher forest and lower cropland contributions, were observed for most methods. These variations could be explained by the information provided through the incorporation of TN and TOC contents, which were the most frequently selected tracers. That is consistent with the results of Huon et al. (2018), which associated a higher TOC content with a high forest contribution. Furthermore, for the methods that selected Al, these contribution variations were sharper and more detailed, especially for samples collected from the upper part of the sediment core (i.e. depth from 7 to 17 cm).

Of note, additional metrics, such as sensitivity analysis or variable importance approach, could provide a more detailed understanding of the role of each tracer in contribution predictions (Russi et al., 2008; Bennett et al., 2013; Wei et al., 2015).

I.4.3 - Assessing modelling prediction accuracy

The generation of virtual mixtures allowed for the evaluation of model prediction accuracy for a wide range of source contributions. The use of several metrics allowed us to describe different aspects of the modelling (i.e. residuals, accuracy and precision) and to better interpret the prediction on real sediment samples (Latorre et al., 2021; Batista et al., 2022). The graphical representation of the metrics (Figs. I.5, I.6, and I.7) allowed us to identify ranges of source contributions with different prediction accuracies. This understanding of the model supports a better appreciation and interpretation of predictions on sediment samples.

Virtual mixtures were generated to cover the full range of potential combinations of source contributions, varying from 0 to 100 % with 5-% increments. The range of predicted contributions for virtual mixtures (i.e. minimum and maximum) defines the space of possible model predictions obtained with a given set of tracers. However, for the majority of the tracer selections investigated here, part or totality of the sediment sample predicted contributions fell outside of the space of the virtual mixture predicted contributions (Supplementary Materials Table I.SM-VI). This result may be explained by the fact that the assumptions made when generating virtual mixtures were not respected. For instance, tracers may not behave fully conservatively during erosion processes (Koiter et al., 2013) or a source may not have been correctly identified or classified (Palazón et al., 2015; Smith et al., 2018; Batista et al., 2022). Novel techniques should be developed to quantify the extent to which a property is modified during transport (i.e. depletion or enrichment) (García-Comendador et al., 2023) to support the generation of virtual mixtures with tracer values that better represent the reality. Here, virtual mixtures were generated as simple proportional mixtures of mean properties of each source tracer, which implies that all properties are considered strictly conservative properties. This has likely not been fully achieved with the commonly implemented tests (i.e. range tests and CI). Indeed, the use of not fully conservative tracers may result in the generation of virtual mixture property values that differ from those observed in actual sediment samples. This may raise concerns regarding the validity of modelling prediction accuracy statistics calculated with virtual mixtures and their direct transferability to actual sediment samples. Accordingly, we may hypothesise that the farther the sediment sample predicted contributions are from the space of virtual mixture predicted contributions, the less transferable the accuracy statistics of the model will be to actual sediment samples. In our opinion this comparison may help with appreciating the level of confidence in the metrics calculated using virtual mixtures and their direct transferability to the model predictions obtained for actual sediment samples. This may lead to over-interpretation or misinterpretation. Future research could usefully develop novel metrics to quantify this level of confidence and better support model evaluation.

I.5 - Conclusion

In this study, we compared two source sediment fingerprinting tracer selection methods, the TSM and the CM, for their selection of tracers and their resulting predictions of source contributions for a single dataset. Conservative behaviour tests of both methods were compared, including a total of seven different TSM range test criteria and the CM CI. The different tests resulted in different selections of properties that had different sensitivity levels. On the one hand, the minimum-maximum, minimum-maximum $\pm$ 10 % and whiskers range test criteria selected a large number of properties, from 12 to 23 out of 24 potential properties, including non-conservative properties. On the other hand, the mean and median criteria and the CI selected a low number of properties, from 3 to 4 tracers, which can lead to limitations when modelling source contributions in target samples. The mean $\pm$ SD and hinge criteria resulted in an intermediate selection of tracers, selecting from 7 to 9 properties. Although differences were observed among methods, some tracers were selected by most of the methods (i.e. TOC, TN, b*, C* and Q7/4), showing some consistency among them. Although the different methods resulted in different selections of tracers, three main contribution tendencies were observed in relation with the number of tracers selected. Indeed, methods that selected a large number of tracers resulted in a strong dominance of forest. In contrast, a limited selection of tracers resulted in a dominant contribution of cropland. Finally, balanced contributions of forest and cropland were obtained for the methods selecting an intermediate number of tracers. Based on this high variability of selected tracers among methods, future research should develop novel metrics to quantify and qualify the conservative behaviour of tracer

properties during erosion and transport processes.

To assess modelling accuracy, 138 virtual mixtures were generated as a simple proportional mixtures of sources individual properties. Several modelling accuracy metrics were computed for each tracer selection using virtual mixture predicted contributions. These metrics and their associated representations provided a useful support to better evaluate the impact of each tracer selection method on model predictions. However, for most of the tracer selections, a strong divergence in the range of predicted contributions was observed for virtual mixtures and those values obtained for actual sediment samples. These divergences highlight the fact that evaluation metrics obtained for virtual mixtures are likely not directly transferable to prediction obtained for actual sediment samples. Metrics should be used with caution, to avoid over-interpretation or misinterpretation of modelling results. These divergences may likely be attributed to the selection of tracer properties with a non (fully) conservative behaviour during erosion, transport and deposition processes, which could not be quantified and reproduced when generating the virtual mixtures with currently available methods. New methods should be designed to generate virtual mixtures closer to reality to better evaluate modelling accuracy.

Among the compared methods, the high variability of selected tracers among the TSM and the CM, and within the TSM according to the range test criteria, was associated with strong divergences on modelling output results. This may raise concerns regarding the use of quantitative outputs as it may not meet the ultimate goal sought for by fingerprinting approaches as they are currently implemented by the scientific community. Consequently, to avoid a potential loss of confidence of stakeholders regarding the validity of the outputs of this method in the future, it is essential to take as much care as possible to conduct an accurate and reliable identification of conservative behaviour, as the whole methodology and the results rely on this initial step. This is fundamental both for improving our understanding of erosion and sedimentation processes and for guiding the implementation of effective landscape management measures. Accordingly, we encourage our colleagues from the scientific community to share their tracing datasets obtained in contrasted environmental conditions around the world in order to contribute to the further improvement, development and evaluation of sediment source fingerprinting techniques.

Code and data availability

The dataset is available online at Chalaux-Clergue et al. (2022) [Zenodo].

The code to run models, summarise results and plot results is available in the supplementary Materials .Rmd file. In order to facilitate the implementation of the presented framework, an R package, fingR (Chalaux-Clergue and Bizeul, 2023, ver. 1.1.0), with all the functions used in the current study has been developed and is freely accessible.

Acknowledgements & financial support

The collection and the analysis of the soil and sediment samples were funded by the TOFU (ANR-11-JAPN-001) and the AMORAD (ANR-11-RSNR-0002) projects, under the supervision of the French National Research Agency (ANR, Agence Nationale de la Recherche). The support of CEA (Commissariat à l' Energie Atomique et aux Energies Alternatives, France), CNRS (Centre National de la Recherche Scientifique, France) and JSPS (Japan Society for the Promotion of Science) through the funding of PhD fellowships (Hugo Lepage, Hugo Jaegler, Thomas Chalaux-Clergue) and collaboration projects (grant no. PRC CNRS JSPS 2019-2020, no.10; CNRS International Research Project - IRP - MITATE Lab) is also recognised. Thomas Chalaux-Clergue obtained a JSPS grant to spend the second year of his PhD at Kyoto Prefectural University (Oct. 2022 - Sept. 2023) (Grant number PE22708). This work was also supported by ERAN (Environmental Radioactivity Research Network Center) (grants I-21-22 and I-22-24) and a mini-project from the FIRE (Fédération Ile-de-France de Recherche en Environnement - CNRS FR3020 FIRE, France) entitled RICOR ('Reconstructing the Impact of Changing land Occupation on the fate of Radionuclides').

CRediT author statement

Thomas Chalaux-Clergue: Conceptualization, Methodology, Investigation, Software, Formal analysis, Laboratory analyses, Data Curation, Writing – Original Draft, Visualisation.

Rémi Bizeul: Conceptualization, Methodology, Investigation, Formal analysis, Writing – Original Draft.

Pedro V. G. Batista: Conceptualization, Investigation, Writing – review & Editing.

Núria Martínez-Carreras: Investigation, Writing – Review & Editing.

J. Patrick Laceby: Investigation, Resources, Data Curation, Writing - Review & Editing.

Olivier Evrard: Conceptualization, Investigation, Resources, Data Curation, Writing - Review & Editing, Supervision, Project administration, Funding acquisition.

Competing interests: Olivier Evrard is a member of the editorial board of the SOIL journal.

I.6 - Supplementary materials

I.6.1 - Laboratory analysis

I.6.1.1 - Organic matter

In the Hayama Lake catchment, sediment and soils were found to not contain carbonate minerals, and all the carbon associated with particulate matter is organic in nature (Huon et al., 2018). Total organic carbon (TOC) and total nitrogen (TN) elemental concentrations and isotopes (δ^{13}C and δ^{15}N) were determined by combustion using a continuous-flow elementary analyser (Elementar Vario PYRO cube) coupled with an isotope ratio mass spectrometer (EA-IRMS) (Micromass Isoprime) at the Institute of Ecology and Environmental Sciences (iEES, Paris) in France. A first analysis was conducted to measure TOC concentrations together with a set of tyrosine standards (Coplen et al., 1983). The second analysis was dedicated to measure TN concentrations after sample weight optimisation from TOC results. For combustion, oxygen was injected during 70 s (30 mL min^{-1}) at 850 °C for reduction and the combustion furnace was at 1120 °C (Agnihotri et al., 2014). The analytical precision was assessed with repeated analyses of a tyrosine internal standard (n = 51), calibrated against international reference standards (Girardin and Mariotti, 1991). The analysis of these properties in source material is described in detail in the study by Laceby et al. (2016b). To evaluate whether the samples are composed of terrestrial or freshwater-originating material, the distribution of sample values was plotted in a δ^{13}C versus TOC/TN diagram and compared to the thresholds reported in Lamb et al. (2006) (Supplementary Materials Fig.. I.SM-1).

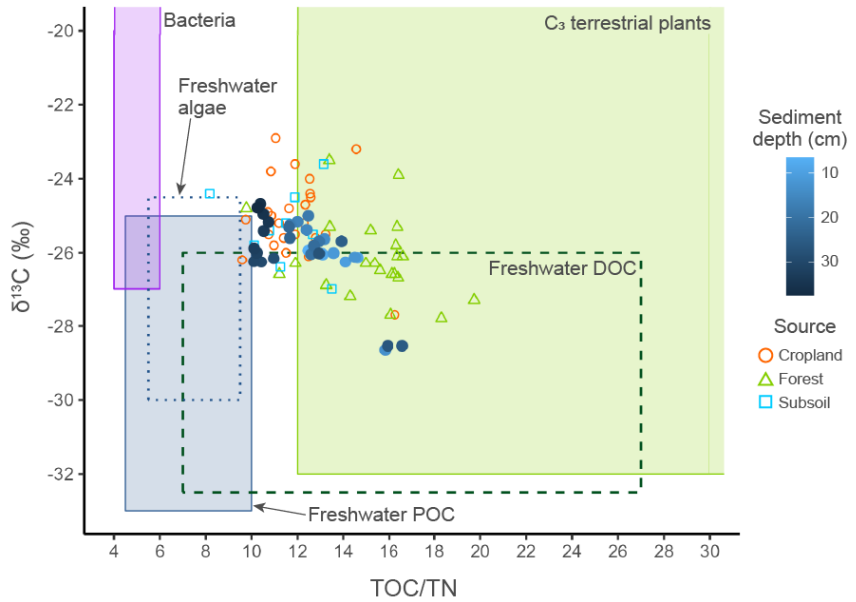


Figure I.SM-1: Sediment core and source samples δ^{13}C and TOC/N and typical ranges for organic inputs to lacustrine environments (thresholds from Lamb et al. (2006)).

I.6.1.2 - Geochemistry

Elemental geochemistry was determined using X-ray fluorescence (XRF) (Malvern Panalytical, ED-XRF Epsilon 4). A total of 17 elemental concentrations were measured (Al, Ca, Co, Cr, Cu, Fe, K, Mg, Mn, Ni, Pb,

Rb, Si, Sr, Ti, Zn, and Zr). Measurements were conducted in containers covered with a 3.6 ţm thin Mylar film (Chemplex, Mylar thin-film cat. no. 157) with a 10 mm exposure surface. A minimum of 0.1 g of material was analysed. To consider the potential heterogeneity within a sample, three replicate measurements were made, and the mean value of these replicates was calculated. To assess the accuracy of the measurements, a standard (JMS-1, sediment from the Tokyo Bay (Terashima et al., 2002)) was measured every seven samples (n = 38) and the accuracy of the measured batch was determined based on the calculation of the root mean square errors (RMSE).

I.6.1.3 - Visible colorimetry

Visible colorimetry was measured using a portable diffuse reflectance spectrophotometer, Konica Minolta CM-700d, set on a 3 mm target radius. Samples were measured in a plastic zip bag. In order to account for potential heterogeneities within a sample, three measurements were made at different locations on the bag. The spectrophotometer was calibrated at the start of each set of measurements with a zero (black) and white standards. Measurements were conducted according to the D65 illuminance standard, 10° angle observer and excluding the specular component. The spectral reflectance (in %) was measured from 360 nm to 740 nm with a 10 nm resolution (30 wavelength classes). Raw data were processed using the colour data software CM-S100w SpectraMagic NX (Minolta, 2022). Colour parameters within the Cartesian coordinate systems CIE Lab (1976) (i.e. L*, a* and b*) (CIE, 2008) and CIE LCh (i.e. C* and h) were exported. The CIE LCh is a vector representation of the CIE Lab (1976). C and h are derived from a* and b* parameters. Within the CIE Lab system: L* is the lightness of the colour, from black (0) to white (100), a* is the position between green to red (negative values are associated with green and positives with red); and b* is the position between blue and yellow (negative values are associated with blue and positive values with yellow). Within the CIE LCh system, C* is the chroma (positive values are associated to brighter colours and negative values to duller colours), and h is the hue angle (in °) in the CIE Lab colour wheel.

The Q7/4 ratio as defined by Debret et al. (2011) was calculated as the ratio between 700 nm and 400 nm reflectance values. This ratio provides a numerical description of the reflectance spectrum general slope.

The oxy-hydroxide geothite ($\alpha - \text{FeOOH}$) soil richness can be determined using visible diffuse reflectance spectra (Kosmas et al., 1984; Balsam et al., 2004; Hao et al., 2009; Torrent et al., 2007) and its peak values at 445 nm and 525 nm were calculated from the first derivative reflectance spectrum (Debret et al., 2011). In our case, the geothite concentration was not aimed for, only the relative abundance among our samples in order to differentiate between them. For each replicate of the measurements and for each sample, the first derivative reflectance spectrum was calculated and smoothed with a Savitzky-Golay filter using the 'savitzky-Golay' function (differentiation order = 1, polynomial order = 3, window size = 5 (equivalent to 50 nm)) from R package 'prospectr' (Stevens and Ramirez-Lopez, 2022) (Wadoux et al., 2021). Then the mean per sample and the standard deviation were calculated. From the first derivative of reflectance, two geothite peaks were calculated: first, the 445 nm peak value was calculated as the mean of values at 440 and 450 nm, and second, the 525 nm peak was calculated as the mean of those at 520 and 530 nm (Debret et al., 2011).

The remission function was calculated from the reflectance spectrum: $f(R) = (1 - R)^2$ according to the Kubelka-Munk relationship (Scheinost et al., 1998). Then, the second derivative was calculated and the spectrum was smoothed with a Savitzky-Golay filter using the 'savitzkyGolay' function (differentiation order = 2, polynomial order = 3, window size = 5). From the second derivative of the remission function spectrum, the iron oxide-associated parameters (A1, A2, A3) and the goethite proportion within iron oxides (Gt) were obtained (Tiecher et al., 2015). The A1 and A2 peaks are associated with goethite, and the A3 peak is

associated with hematite; all peaks were calculated as the amplitude between each maximum and minimum band. Thus, A1 is the difference between 450 and 420 nm, A2 is the difference between 510 and 480 nm, A3 is the difference between 575 (as the mean of 570 and 580 nm) and 535 nm (as the mean of 530 and 540 nm), and Gt is calculated as the ratio of A1/(A1+A3).

I.6.2 - Figures

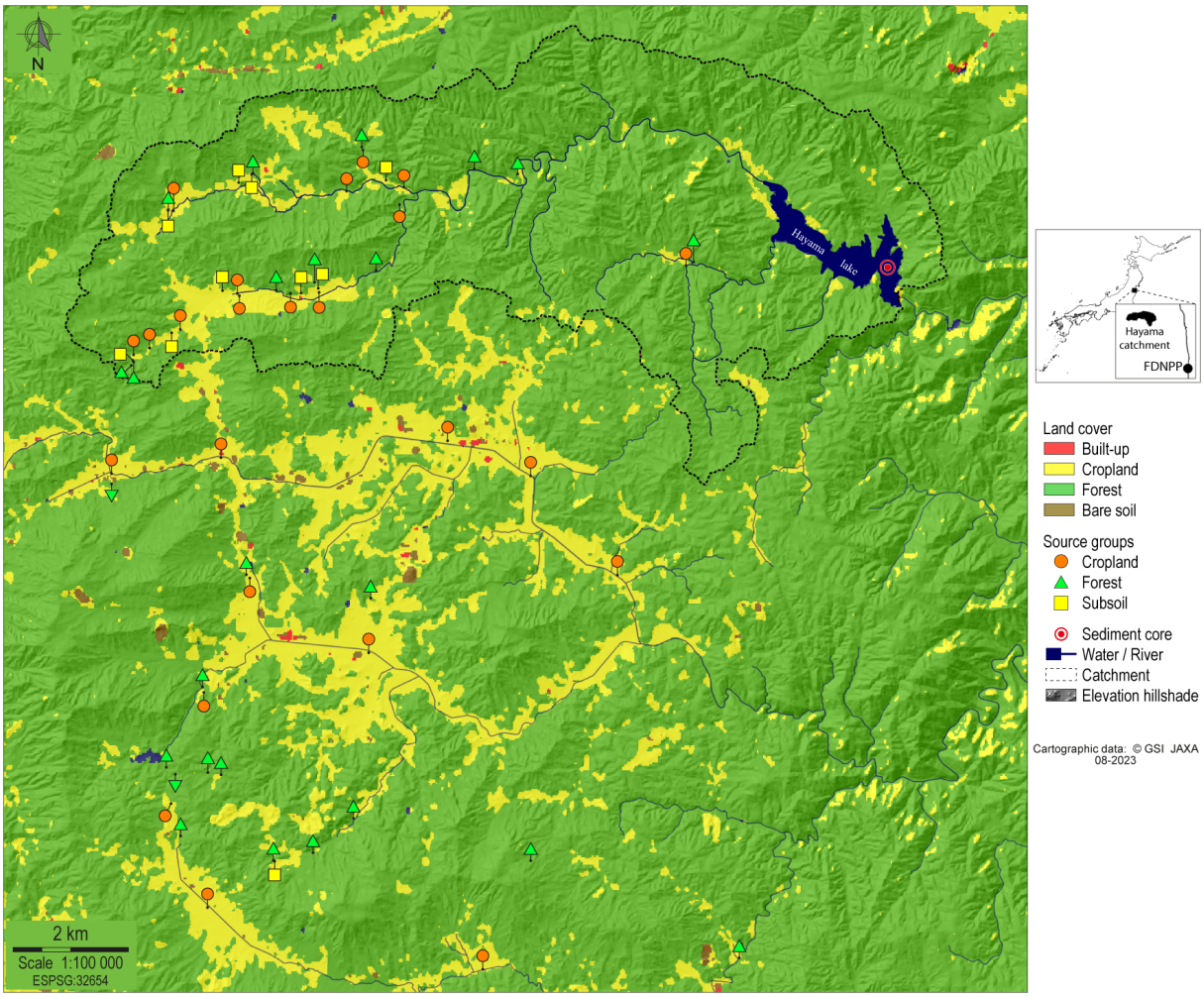


Figure I.SM-2: Map of the main land uses in the study area over the 2014-2016 period with location of the source samples and the sediment core (cartographic data: GSI and JAXA). FDNPP: Fukushima Dai-ichi Nuclear power plant.

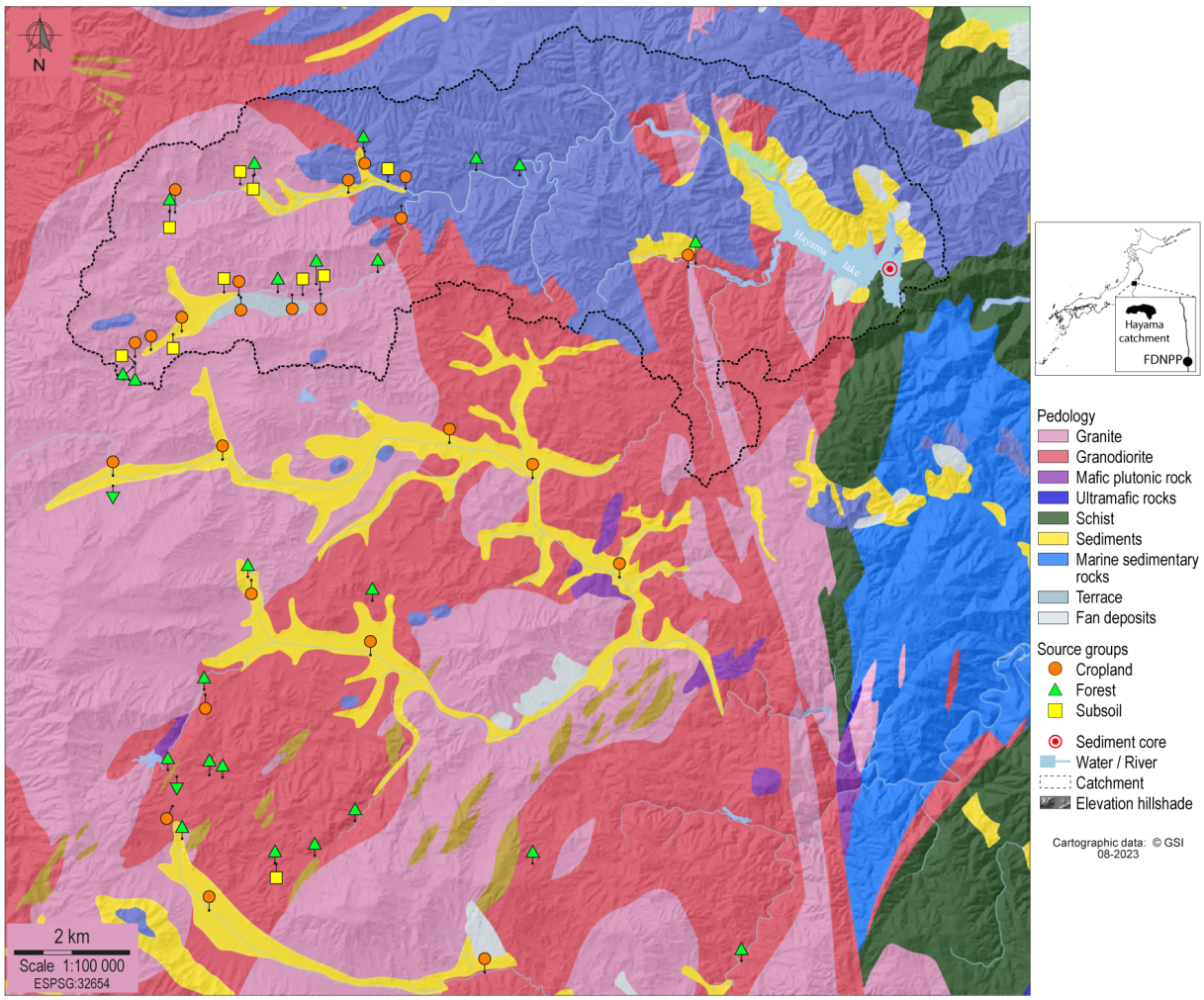


Figure I.SM-3: Map of the main geology types in the study area with location of the source samples and the sediment core (cartographic data: GSI). FDNPP: Fukushima Dai-ichi Nuclear power plant.

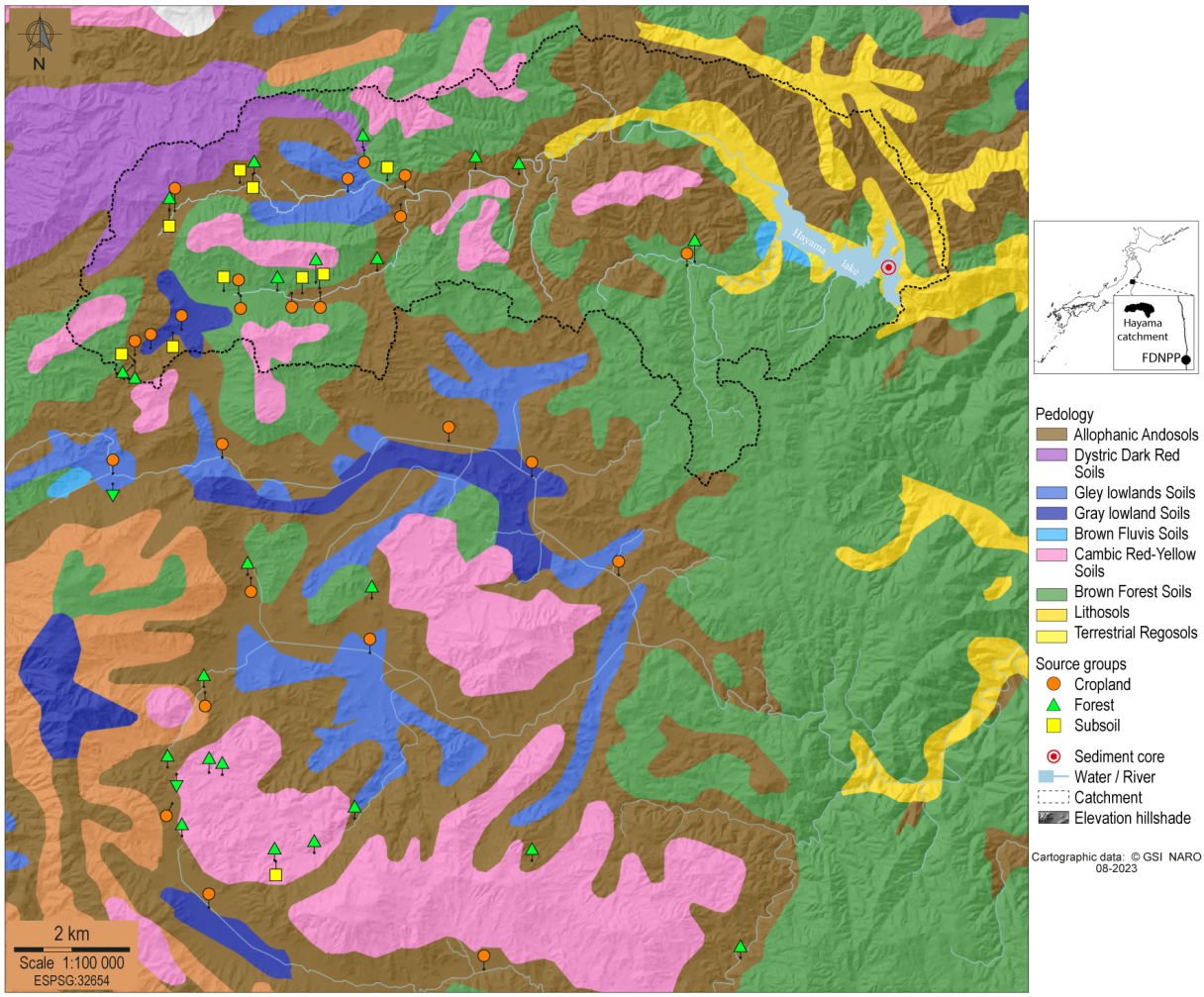


Figure I.SM-4: Map of the main soil types in the study area with location of the source samples and the sediment core (cartographic data: GSI and NARO). FDNPP: Fukushima Dai-ichi Nuclear power plant.

I.6.3 - Tables

Table I.SM-I: Summary of MixSIAR accuracy statistics calculated on virtual mixtures (n = 138) for each tracer selection method: three-step method (TSM) range test criteria and consensus method (CM) for cropland course. W50*: prediction interval width; ME: mean error; RMSE: root mean square error; r^2: squared Pearson's correlation coefficient; NSE: Nash-Sutcliffe modelling efficiency coefficient; CRPS*: continuous ranked probability score. Note that * indicates mean values per source.

Cropland

Tracer selection method			W50* (%)	ME (%)	RMSE (%)	CRPS	r^2	NSE
Method	**Range test criterion**	**DFA**						
Three-step method	Minimum-maximum	No	10	2	15	9	0.89	0.74
		Yes	13	-2	13	7	0.96	0.80
	Minimum-maximum ± 10 %	No	9	5	14	9	0.92	0.77
		Yes	10	6	13	7	0.95	0.80
	Whiskers	No	15	7	16	10	0.84	0.63
		Yes	17	5	15	9	0.87	0.71
	Hinge	No	12	10	18	11	0.85	0.62
		Yes	17	7	15	9	0.90	0.73
	Mean	No & Yes	24	21	31	17	0.36	-0.17
	Mean ± SD	No	15	11	19	12	0.78	0.56
		Yes	16	10	18	11	0.77	0.59
	Median	No & Yes	25	2	17	10	0.77	0.63
Consensus method			21	11	20	11	0.71	0.52

Table I.SM-II: Summary of MixSIAR accuracy statistics calculated on virtual mixtures (n = 138) for each tracer selection method: three-step Method (TSM) range test criteria and consensus method (CM) for forest course. W50*: prediction interval width; ME: mean error; RMSE: root mean square error; r^2: squared Pearson's correlation coefficient; NSE: Nash-Sutcliffe modelling efficiency coefficient; CRPS*: continuous ranked probability score. Note that * indicates mean values per source.

Forest

Tracer selection method			W50* (%)	ME (%)	RMSE (%)	CRPS*	r^2	NSE
Method	**Range test criterion**	**DFA**						
Three-step method	Minimum-maximum	No	7	-7	14	8	0.96	0.75
		Yes	10	-2	10	6	0.96	0.86
	Minimum-maximum ± 10 %	No	6	-8	14	9	0.98	0.74
		Yes	8	-6	13	6	0.98	0.79
	Whiskers	No	10	-8	15	9	0.96	0.73
		Yes	12	-6	14	8	0.95	0.77
	Hinge	No	8	-10	16	10	0.97	0.67
		Yes	11	-7	14	8	0.97	0.77
	Mean	No & Yes	18	-19	28	15	0.79	0.00
	Mean ± SD	No	10	-11	17	10	0.96	0.65
		Yes	10	-10	17	10	0.96	0.65
	Median	No & Yes	14	-6	14	8	0.92	0.75
Consensus method			13	-12	18	10	0.93	0.58

Table I.SM-III: Summary of MixSIAR accuracy statistics calculated on virtual mixtures (n = 138) for each tracer selection method: three-step method (TSM) range test criteria and consensus method (CM) for subsoil course. W50*: prediction interval width; ME: mean error; RMSE: root mean square error; r^2: squared Pearson's correlation coefficient; NSE: Nash-Sutcliffe modelling efficiency coefficient; CRPS*: continuous ranked probability score. Note that * indicates mean values per source.

Subsoil								
Tracer selection method			**W50***	**ME**	**RMSE**	**CRPS***	r^2	**NSE**
Method	**Range test criterion**	**DFA**	**(%)**	**(%)**	**(%)**			
Three-step method	Minimum-maximum	No	8	5	8	5	0.99	0.92
		Yes	8	3	7	4	0.99	0.93
	Minimum-maximum $\pm$ 10 %	No	5	3	7	4	1.00	0.93
		Yes	6	0	7	4	1.00	0.93
	Whiskers	No	8	1	6	4	0.98	0.95
		Yes	8	1	6	4	0.98	0.95
	Hinge	No	6	-1	7	4	0.99	0.95
		Yes	9	0	7	4	0.99	0.94
	Mean	No & Yes	11	-3	8	5	0.97	0.92
	Mean $\pm$ SD	No	8	0	7	4	0.98	0.95
		Yes	8	1	7	4	0.97	0.95
	Median	No & Yes	12	4	9	5	0.95	0.90
Consensus method			11	1	7	4	0.97	0.94

Table I.SM-IV: Summary of MixSIAR accuracy statistics calculated on virtual mixtures (n = 138) for each tracer selection method: three-step method (TSM) range test criteria and consensus method (CM) averaged on the three sources (i.e. cropland, forest and subsoil). W50*: prediction interval width; ME: mean error; RMSE: root mean square error; r^2: squared Pearson's correlation coefficient; NSE: Nash-Sutcliffe modelling efficiency coefficient; CRPS*: continuous ranked probability score. Note that $*$ indicates mean values per source.

Average								
Tracer selection method			**W50***	**ME**	**RMSE**	**CRPS***	r^2	**NSE**
Method	**Range test criterion**	**DFA**	**(%)**	**(%)**	**(%)**			
Three-step method	Minimum-maximum	No	8	0	12	7	0.95	0.80
		Yes	10	0	10	6	0.97	0.86
	Minimum-maximum $\pm$ 10 %	No	7	0	12	7	0.97	0.81
		Yes	8	0	11	6	0.98	0.84
	Whiskers	No	11	0	12	8	0.93	0.77
		Yes	12	0	12	7	0.93	0.81
	Hinge	No	9	0	14	8	0.94	0.75
		Yes	12	0	12	7	0.95	0.81
	Mean	No & Yes	18	0	22	12	0.71	0.25
	Mean $\pm$ SD	No	11	0	14	9	0.91	0.72
		Yes	11	0	14	8	0.90	0.73
	Median	No & Yes	17	0	13	8	0.88	0.76
Consensus method			15	0	15	8	0.87	0.68

Table I.SM-V: Selected tracer Pearson correlation coefficients. The symbol · represents correlation with significance test *p* value lower than 0.05.

	TOC	TN	Al	Ca	K	Si	Sr	Zn	Zr	L*	a*	b*	C*	h	A1	A2	Gt	Q7/4
TN	0.97																	
Al	-0.76	-0.83																
Ca	0.13	0.21	-0.52															
K	-0.33	-0.37	0.56	-0.50														
Si	-0.47	-0.53	0.51	-0.41	0.47													
Sr	0.05	0.12	-0.49	0.87	-0.53	-0.37												
Zn	0.06	0.20	-0.28	0.47	-0.39	-0.53	0.23											
Zr	·	-0.27	0.47	-0.43	0.71	0.24	-0.48	-0.19										
L*	-0.71	-0.77	0.83	-0.56	0.65	0.53	-0.50	-0.37	0.53									
a*	-0.29	-0.43	0.66	-0.63	0.29	0.39	-0.53	-0.43	0.37	0.61								
b*	-0.63	-0.72	0.75	-0.49	0.20	0.45	-0.38	-0.32	·	0.68	0.79							
C*	-0.61	-0.71	0.75	-0.52	0.21	0.45	-0.40	-0.34	0.17	0.69	0.83	1.00						
h	·	·	·	·	·	·	0.30	·	-0.35	·	·	·	·					
A1	·	·	·	·	-0.56	·	0.36	·	-0.55	·	·	·	·	0.55				
A2	-0.27	-0.27	·	·	·	·	·	·	·	·	0.41	0.58	0.58	·	0.77			
Gt	·	·	-0.32	0.55	-0.23	-0.21	0.52	0.33	-0.37	-0.30	-0.68	-0.28	-0.33	0.64	·	·		
Q7/4	-0.49	-0.54	0.47	·	·	0.17	·	·	·	0.35	0.52	0.83	0.81	·	0.76	0.82	·	
G_{525}	-0.59	-0.68	0.80	-0.57	0.44	0.53	-0.50	-0.42	0.33	0.83	0.78	0.89	0.89	·	·	0.44	-0.35	0.64

Table I.SM-VI: Number of sediment samples that fell inside of the space of the virtual mixture predicted contributions for each tracer selection method out of 32.

Tracer selection method			Source group		
Method	**Range test criterion**	**DFA**	**Cropland**	**Forest**	**Subsoil**
Three-step method	Minimum-maximum	No	33	2	0
		Yes	0	0	0
	Minimum-maximum ± 10 %	No	31	1	0
		Yes	0	0	0
	Whiskers	No	36	15	9
		Yes	13	0	0
	Hinge	No	37	34	6
		Yes	37	31	16
	Mean	No and Yes	37	37	30
	Mean ± SD	No	37	31	30
		Yes	37	33	10
	Median	No and Yes	6	37	13
Consensus method			10	37	7

References

Agnihotri, R., Kumar, R., Prasad, M.V.S.N., Sharma, C., Bhatia, S.K., Arya, B.C., 2014. Experimental Setup and Standardization of a Continuous Flow Stable Isotope Mass Spectrometer for Measuring Stable Isotopes of Carbon, Nitrogen and Sulfur in Environmental Samples. MAPAN 29, 195–205. URL: http://link.springer.com/10.1007/s12647-014-0099-8, doi:10.1007/s12647-014-0099-8.

Balsam, W., Ji, J., Chen, J., 2004. Climatic interpretation of the Luochuan and Lingtai loess sections, China, based on changing iron oxide mineralogy and magnetic susceptibility. Earth and Planetary Science Letters 223, 335–348. URL: https://linkinghub.elsevier.com/retrieve/pii/S0012821X04002717, doi:10.1016/j.epsl.2004.04.023.

Batista, P.V.G., Laceby, J.P., Evrard, O., 2022. How to evaluate sediment fingerprinting source apportionments. Journal of Soils and Sediments 22, 1315–1328. URL: https://link.springer.com/10.1007/s11368-022-03157-4, doi:10.1007/s11368-022-03157-4.

Batista, P.V.G., Laceby, J.P., Silva, M.L.N., Tassinari, D., Bispo, D.F.A., Curi, N., Davies, J., Quinton, J.N., 2019. Using pedological knowledge to improve sediment source apportionment in tropical environments. Journal of Soils and Sediments 19, 3274–3289. URL: http://link.springer.com/10.1007/s11368-018-2199-5, doi:10.1007/s11368-018-2199-5.

Beck, H.E., Zimmermann, N.E., McVicar, T.R., Vergopolan, N., Berg, A., Wood, E.F., 2018. Present and future Köppen-Geiger climate classification maps at 1-km resolution. Scientific Data 5, 180214. URL: http://www.nature.com/articles/sdata2018214, doi:10.1038/sdata.2018.214.

Bennett, N.D., Croke, B.F., Guariso, G., Guillaume, J.H., Hamilton, S.H., Jakeman, A.J., Marsili-Libelli, S., Newham, L.T., Norton, J.P., Perrin, C., Pierce, S.A., Robson, B., Seppelt, R., Voinov, A.A., Fath, B.D., Andreassian, V., 2013. Characterising performance of environmental models. Environmental Modelling & Software 40, 1–20. URL: https://linkinghub.elsevier.com/retrieve/pii/S1364815212002435, doi:10.1016/j.envsoft.2012.09.011.

Bing, H., Wu, Y., Liu, E., Yang, X., 2013. Assessment of heavy metal enrichment and its human impact in lacustrine sediments from four lakes in the mid-low reaches of the Yangtze River, China. Journal of Environmental Sciences 25, 1300–1309. URL: https://linkinghub.elsevier.com/retrieve/pii/S1001074212601958, doi:10.1016/S1001-0742(12)60195-8.

Blake, W.H., Walsh, R.P.D., Sayer, A.M., Bidin, K., 2006. Quantifying Fine-Sediment Sources in Primary and Selectively Logged Rainforest Catchments Using Geochemical Tracers. Water, Air, & Soil Pollution: Focus 6, 615–623. URL: https://link.springer.com/10.1007/s11267-006-9046-1, doi:10.1007/s11267-006-9046-1.

Brosinsky, A., Foerster, S., Segl, K., López-Tarazón, J.A., Piqué, G., Bronstert, A., 2014. Spectral fingerprinting: Characterizing suspended sediment sources by the use of VNIR-SWIR spectral information. Journal of Soils and Sediments 14, 1965–1981. URL: http://link.springer.com/10.1007/s11368-014-0927-z, doi:10.1007/s11368-014-0927-z.

Chalaux-Clergue, T., Bizeul, R., 2023. fingR: A support for sediment source fingerprinting studies. URL: https://github.com/tchalauxclergue/fingR, doi:10.5281/zenodo.10044404.

Chalaux-Clergue, T., Bizeul, R., Foucher, A., Evrard, O., 2024a. A unified template for sediment source fingerprinting databases. URL: https://zenodo.org/doi/10.5281/zenodo.10725788, doi:10.5281/ZENODO.10725788.

Chalaux-Clergue, T., Evrard, O., Durand, R., Caumon, A., Hayashi, S., Tsuji, H., Huon, S., Vaury, V., Wakiyama, Y., Nakao, A., Laceby, J.P., Onda, Y., 2022. Organic matter, geochemical and colorimetric properties of potential source material, target sediment and laboratory mixtures for conducting sediment fingerprinting approaches in the Mano Dam Reservoir (Hayama Lake) catchment, Fukushima Prefecture, Japan. URL: https://zenodo.org/record/7081094, doi:10.5281/ZENODO.7081094.

Chalaux-Clergue, T., Foucher, A., Chaboche, P.A., Hayashi, S., Tsuji, H., Wakiyama, Y., Huon, S., Vandromme, R., Cerdan, O., Nakao, A., Evrard, O., 2024b. Impacts of farmland decontamination on 137Cs

transfers in rivers after Fukushima nuclear accident: Evidence from a retrospective sediment core study. Science of The Total Environment 947, 174546. URL: https://linkinghub.elsevier.com/retrieve/pii/S0048969724046941, doi:10.1016/j.scitotenv.2024.174546.

Chartin, C., Evrard, O., Laceby, J.P., Onda, Y., Ottlé, C., Lefèvre, I., Cerdan, O., 2017. The impact of typhoons on sediment connectivity: Lessons learnt from contaminated coastal catchments of the Fukushima Prefecture (Japan): Typhoon Impact on Sediment Connectivity - Fukushima, Japan. Earth Surface Processes and Landforms 42, 306–317. URL: https://onlinelibrary.wiley.com/doi/10.1002/esp.4056, doi:10.1002/esp.4056.

Chartin, C., Evrard, O., Onda, Y., Patin, J., Lefèvre, I., Ottlé, C., Ayrault, S., Lepage, H., Bonté, P., 2013. Tracking the early dispersion of contaminated sediment along rivers draining the Fukushima radioactive pollution plume. Anthropocene 1, 23–34. URL: https://linkinghub.elsevier.com/retrieve/pii/S2213305413000088, doi:10.1016/j.ancene.2013.07.001.

Chen, D., Dai, W., Li, M., Wang, B., Zeng, Y., Ni, L., Fang, N., Shi, Z., 2023. Accuracy verification of optical fingerprinting methods in sediment tracing study. Hydrological Processes 37, e14870. URL: https://onlinelibrary.wiley.com/doi/10.1002/hyp.14870, doi:10.1002/hyp.14870.

CIE, 2008. C. I. C.: Colorimetry — Part 4: CIE 1976 L*a*b* Colour space. doi:ISO/CIE11664-4:2019(E).

Collins, A., Pulley, S., Foster, I., Gellis, A., Porto, P., Horowitz, A., 2017. Sediment source fingerprinting as an aid to catchment management: A review of the current state of knowledge and a methodological decision-tree for end-users. Journal of Environmental Management 194, 86–108. URL: https://linkinghub.elsevier.com/retrieve/pii/S0301479716307460, doi:10.1016/j.jenvman.2016.09.075.

Collins, A., Walling, D., 2002. Selecting fingerprint properties for discriminating potential suspended sediment sources in river basins. Journal of Hydrology 261, 218–244. URL: https://linkinghub.elsevier.com/retrieve/pii/S0022169402000112, doi:10.1016/S0022-1694(02)00011-2.

Collins, A., Walling, D., Leeks, G., 1997a. Source type ascription for fluvial suspended sediment based on a quantitative composite fingerprinting technique. CATENA 29, 1–27. URL: https://linkinghub.elsevier.com/retrieve/pii/S0341816296000641, doi:10.1016/S0341-8162(96)00064-1.

Collins, A., Walling, D., Webb, L., King, P., 2010. Apportioning catchment scale sediment sources using a modified composite fingerprinting technique incorporating property weightings and prior information. Geoderma 155, 249–261. URL: https://linkinghub.elsevier.com/retrieve/pii/S0016706109004066, doi:10.1016/j.geoderma.2009.12.008.

Collins, A., Williams, L., Zhang, Y., Marius, M., Dungait, J., Smallman, D., Dixon, E., Stringfellow, A., Sear, D., Jones, J., Naden, P., 2013. Catchment source contributions to the sediment-bound organic matter degrading salmonid spawning gravels in a lowland river, southern England. Science of The Total Environment 456–457, 181–195. URL: https://linkinghub.elsevier.com/retrieve/pii/S0048969713003987, doi:10.1016/j.scitotenv.2013.03.093.

Collins, A.L., Blackwell, M., Boeckx, P., Chivers, C.A., Emelko, M., Evrard, O., Foster, I., Gellis, A., Gholami, H., Granger, S., Harris, P., Horowitz, A.J., Laceby, J.P., Martinez-Carreras, N., Minella, J., Mol, L., Nosrati, K., Pulley, S., Silins, U., da Silva, Y.J., Stone, M., Tiecher, T., Upadhayay, H.R., Zhang, Y., 2020. Sediment source fingerprinting: Benchmarking recent outputs, remaining challenges and emerging themes. Journal of Soils and Sediments 20, 4160–4193. URL: https://link.springer.com/10.1007/s11368-020-02755-4, doi:10.1007/s11368-020-02755-4.

Collins, A.L., Walling, D.E., 2004. Documenting catchment suspended sediment sources: Problems, approaches and prospects. Progress in Physical Geography: Earth and Environment 28, 159–196. URL: http://journals.sagepub.com/doi/10.1191/0309133304pp409ra, doi:10.1191/0309133304pp409ra.

Collins, A.L., Walling, D.E., Leeks, G.J., 1997b. Fingerprinting the origin of fluvial suspended sediment in larger river basins: Combining assessment of spatial provenance and source type. Geografiska Annaler: Series A, Physical Geography 79, 239–254. URL: https://www.tandfonline.com/doi/full/10.1111/j.0435-3676.1997.00020.x, doi:10.1111/j.0435-3676.1997.00020.x.

Coplen, T.B., Kendall, C., Hopple, J., 1983. Comparison of stable isotope reference samples. Nature 302, 236–238. URL: https://www.nature.com/articles/302236a0, doi:10.1038/302236a0.

Cox, T., Laceby, J.P., Roth, T., Alewell, C., 2023. Less is more? A novel method for identifying and evaluating non-informative tracers in sediment source mixing models. Journal of Soils and Sediments 23, 3241–3261. URL: https://link.springer.com/10.1007/s11368-023-03573-0, doi:10.1007/s11368-023-03573-0.

Dabrin, A., Bégorre, C., Bretier, M., Dugué, V., Masson, M., Le Bescond, C., Le Coz, J., Coquery, M., 2021. Reactivity of particulate element concentrations: Apportionment assessment of suspended particulate matter sources in the Upper Rhône River, France. Journal of Soils and Sediments 21, 1256–1274. URL: http://link.springer.com/10.1007/s11368-020-02856-0, doi:10.1007/s11368-020-02856-0.

Debnath, A., Singh, P.K., Chandra Sharma, Y., 2021. Metallic contamination of global river sediments and latest developments for their remediation. Journal of Environmental Management 298, 113378. URL: https://linkinghub.elsevier.com/retrieve/pii/S0301479721014407, doi:10.1016/j.jenvman.2021.113378.

Debret, M., Sebag, D., Desmet, M., Balsam, W., Copard, Y., Mourier, B., Susperrigui, A.S., Arnaud, F., Bentaleb, I., Chapron, E., Lallier-Vergès, E., Winiarski, T., 2011. Spectrocolorimetric interpretation of sedimentary dynamics: The new "Q7/4 diagram". Earth-Science Reviews 109, 1–19. URL: https://linkinghub.elsevier.com/retrieve/pii/S0012825211000985, doi:10.1016/j.earscirev.2011.07.002.

Evrard, O., Batista, P.V.G., Company, J., Dabrin, A., Foucher, A., Frankl, A., García-Comendador, J., Huguet, A., Lake, N., Lizaga, I., Martínez-Carreras, N., Navratil, O., Pignol, C., Sellier, V., 2022. Improving the design and implementation of sediment fingerprinting studies: Summary and outcomes of the TRACING 2021 Scientific School. Journal of Soils and Sediments 22, 1648–1661. URL: https://link.springer.com/10.1007/s11368-022-03203-1, doi:10.1007/s11368-022-03203-1.

Evrard, O., Chaboche, P.A., Ramon, R., Foucher, A., Laceby, J.P., 2020a. A global review of sediment source fingerprinting research incorporating fallout radiocesium (137Cs). Geomorphology 362, 107103. URL: https://linkinghub.elsevier.com/retrieve/pii/S0169555X20300751, doi:10.1016/j.geomorph.2020.107103.

Evrard, O., Durand, R., Nakao, A., Laceby, P.J., Lefèvre, I., Wakiyama, Y., Hayashi, S., Asanuma-Brice, C., Cerdan, O., 2020b. Impact of the 2019 typhoons on sediment source contributions and radiocesium concentrations in rivers draining the Fukushima radioactive plume, Japan. Comptes Rendus. Géoscience 352, 199–211. URL: https://comptes-rendus.academie-sciences.fr/geoscience/item/CRGEOS_2020__352_3_199_0, doi:10.5802/crgeos.42.

Evrard, O., Laceby, J.P., Ficetola, G.F., Gielly, L., Huon, S., Lefèvre, I., Onda, Y., Poulenard, J., 2019. Environmental DNA provides information on sediment sources: A study in catchments affected by Fukushima radioactive fallout. Science of The Total Environment 665, 873–881. URL: https://linkinghub.elsevier.com/retrieve/pii/S0048969719306795, doi:10.1016/j.scitotenv.2019.02.191.

Farias Amorim, F., Jacques Agra Bezerra da Silva, Y., Cabral Nascimento, R., Jacques Agra Bezerra da Silva, Y., Tiecher, T., Williams Araújo do Nascimento, C., Paolo Gomes Minella, J., Zhang, Y., Ram Upadhayay, H., Pulley, S., Collins, A.L., 2021. Sediment source apportionment using optical property composite signatures in a rural catchment, Brazil. CATENA 202, 105208. URL: https://linkinghub.elsevier.com/retrieve/pii/S0341816221000679, doi:10.1016/j.catena.2021.105208.

García-Comendador, J., Martínez-Carreras, N., Fortesa, J., Company, J., Borràs, A., Palacio, E., Estrany, J., 2023. In-channel alterations of soil properties used as tracers in sediment fingerprinting studies. CATENA 225, 107036. URL: https://linkinghub.elsevier.com/retrieve/pii/S0341816223001273, doi:10.1016/j.catena.2023.107036.

Gaspar, L., Blake, W.H., Smith, H.G., Lizaga, I., Navas, A., 2019. Testing the sensitivity of a multivariate mixing model using geochemical fingerprints with artificial mixtures. Geoderma 337, 498–510. URL: https://linkinghub.elsevier.com/retrieve/pii/S0016706118300570, doi:10.1016/j.geoderma.2018.10.005.

Gateuille, D., Owens, P.N., Petticrew, E.L., Booth, B.P., French, T.D., Déry, S.J., 2019. Determining contemporary and historical sediment sources in a large drainage basin impacted by cumulative effects: The regulated Nechako River, British Columbia, Canada. Journal of Soils and Sediments 19, 3357–3373. URL: http://link.springer.com/10.1007/s11368-019-02299-2, doi:10.1007/s11368-019-02299-2.

Gellis, A., Gorman Sanisaca, L., 2018. Sediment Fingerprinting to Delineate Sources of Sediment in the Agricultural and Forested Smith Creek Watershed, Virginia, USA. JAWRA Journal of the American Water Resources Association 54, 1197–1221. URL: https://onlinelibrary.wiley.com/doi/10.1111/1752-1688.12680, doi:10.1111/1752-1688.12680.

Gellis, A.C., Noe, G.B., 2013. Sediment source analysis in the Linganore Creek watershed, Maryland, USA, using the sediment fingerprinting approach: 2008 to 2010. Journal of Soils and Sediments 13, 1735–1753. URL: http://link.springer.com/10.1007/s11368-013-0771-6, doi:10.1007/s11368-013-0771-6.

Gellis, A.C., Walling, D.E., 2013. Sediment Source Fingerprinting (Tracing) and Sediment Budgets as Tools in Targeting River and Watershed Restoration Programs, in: Simon, A., Bennett, S.J., Castro, J.M. (Eds.), Geophysical Monograph Series. American Geophysical Union, Washington, D. C., pp. 263–291. URL: http://doi.wiley.com/10.1029/2010GM000960, doi:10.1029/2010GM000960.

Gibbs, M.M., 2008. Identifying Source Soils in Contemporary Estuarine Sediments: A New Compound-Specific Isotope Method. Estuaries and Coasts 31, 344–359. URL: http://link.springer.com/10.1007/s12237-007-9012-9, doi:10.1007/s12237-007-9012-9.

Girardin, C., Mariotti, A., 1991. Analyse isotopique du 13C en abondance naturelle dans le carbone organique: un système automatique avec robot préparateur. Cahiers ORSTOM, Serie Pedologie 26, 371–380. URL: https://www.documentation.ird.fr/hor/fdi:39457.

Haddadchi, A., Olley, J., Laceby, P., 2014. Accuracy of mixing models in predicting sediment source contributions. Science of The Total Environment 497–498, 139–152. URL: https://linkinghub.elsevier.com/retrieve/pii/S0048969714011425, doi:10.1016/j.scitotenv.2014.07.105.

Hao, Q., Oldfield, F., Bloemendal, J., Torrent, J., Guo, Z., 2009. The record of changing hematite and goethite accumulation over the past 22 Myr on the Chinese Loess Plateau from magnetic measurements and diffuse reflectance spectroscopy. Journal of Geophysical Research 114, B12101. URL: http://doi.wiley.com/10.1029/2009JB006604, doi:10.1029/2009JB006604.

He, Q., Walling, D., 1996. Interpreting particle size effects in the adsorption of 137Cs and unsupported 210Pb by mineral soils and sediments. Journal of Environmental Radioactivity 30, 117–137. URL: https://linkinghub.elsevier.com/retrieve/pii/0265931X96892757, doi:10.1016/0265-931X(96)89275-7.

Hollander, M., A. Wolfe, D., Chicken, E., 2013. Nonparametric Statistical Methods. Wiley Series in Probability and Statistics. 1 ed., Wiley. URL: https://onlinelibrary.wiley.com/doi/book/10.1002/9781119196037, doi:10.1002/9781119196037.

Horowitze, A.J., 1991. A Primer on Sediment-Trace Element Chemistry. volume 2 of *Open-File Report*. 1 ed., Lewis Publishers Chelsea. URL: http://dx.doi.org/10.3133/ofr9176, doi:10.3133/ofr9176.

Huangfu, Y., Essington, M.E., Hawkins, S.A., Walker, F.R., Schwartz, J.S., Layton, A.C., 2020. Testing the sediment fingerprinting technique using the SIAR model with artificial sediment mixtures. Journal of Soils and Sediments 20, 1771–1781. URL: http://link.springer.com/10.1007/s11368-019-02545-7, doi:10.1007/s11368-019-02545-7.

Huon, S., Hayashi, S., Laceby, J.P., Tsuji, H., Onda, Y., Evrard, O., 2018. Source dynamics of radiocesium-contaminated particulate matter deposited in an agricultural water reservoir after the Fukushima nuclear accident. Science of The Total Environment 612, 1079–1090. URL: https://linkinghub.elsevier.com/retrieve/pii/S0048969717319083, doi:10.1016/j.scitotenv.2017.07.205.

Issaka, S., Ashraf, M.A., 2017. Impact of soil erosion and degradation on water quality: A review. Geology, Ecology, and Landscapes 1, 1–11. URL: https://www.tandfonline.com/doi/full/10.1080/24749508.2017.1301053, doi:10.1080/24749508.2017.1301053.

JAXA, 2016. High-Resolution Land-Use and Land-Cover Map of Japan [2006 ~ 2011] (ver. 16.09; 10-m resolution; 12 categories). URL: https://www.eorc.jaxa.jp/ALOS/en/dataset/lulc/lulc_jpn_e.htm.

JAXA, 2018. High-Resolution Land-Use and Land-Cover Map of Japan [2014 ~ 2016] (ver. 18.03; 30-m resolution; 12 categories). URL: https://www.eorc.jaxa.jp/ALOS/en/dataset/lulc/lulc_v1803_e.htm.

JAXA, 2022. High-Resolution Land-Use and Land-Cover Map of Japan [2018 ∼ 2020] (ver. 21.11; 10-m resolution; 12 categories). URL: https://www.eorc.jaxa.jp/ALOS/en/dataset/lulc/lulc_v2111_e.htm.

Jordan, A., Krüger, F., Lerch, S., 2019. Evaluating Probabilistic Forecasts with scoringRules. Journal of Statistical Software 90. URL: http://www.jstatsoft.org/v90/i12/, doi:10.18637/jss.v090.i12.

Kato, H., Onda, Y., Gao, X., Sanada, Y., Saito, K., 2019. Reconstruction of a Fukushima accident-derived radiocesium fallout map for environmental transfer studies. Journal of Environmental Radioactivity 210, 105996. URL: https://linkinghub.elsevier.com/retrieve/pii/S0265931X18303308, doi:10.1016/j.jenvrad.2019.105996.

Kemp, P., Sear, D., Collins, A., Naden, P., Jones, I., 2011. The impacts of fine sediment on riverine fish. Hydrological Processes 25, 1800–1821. URL: https://onlinelibrary.wiley.com/doi/10.1002/hyp.7940, doi:10.1002/hyp.7940.

Koiter, A., Owens, P., Petticrew, E., Lobb, D., 2013. The behavioural characteristics of sediment properties and their implications for sediment fingerprinting as an approach for identifying sediment sources in river basins. Earth-Science Reviews 125, 24–42. URL: https://linkinghub.elsevier.com/retrieve/pii/S0012825213001074, doi:10.1016/j.earscirev.2013.05.009.

Koiter, A.J., Owens, P.N., Petticrew, E.L., Lobb, D.A., 2018. Assessment of particle size and organic matter correction factors in sediment source fingerprinting investigations: An example of two contrasting watersheds in Canada. Geoderma 325, 195–207. URL: https://linkinghub.elsevier.com/retrieve/pii/S0016706117317652, doi:10.1016/j.geoderma.2018.02.044.

Kosmas, C.S., Curi, N., Bryant, R.B., Franzmeier, D.P., 1984. Characterization of Iron Oxide Minerals by Second-Derivative Visible Spectroscopy. Soil Science Society of America Journal 48, 401–405. URL: http://doi.wiley.com/10.2136/sssaj1984.03615995004800020036x, doi:10.2136/sssaj1984.03615995004800020036x.

Laceby, J., Batista, P., Taube, N., Kruk, M., Chung, C., Evrard, O., Orwin, J., Kerr, J., 2021. Tracing total and dissolved material in a western Canadian basin using quality control samples to guide the selection of fingerprinting parameters for modelling. CATENA 200, 105095. URL: https://linkinghub.elsevier.com/retrieve/pii/S0341816220306457, doi:10.1016/j.catena.2020.105095.

Laceby, J.P., Chartin, C., Evrard, O., Onda, Y., Garcia-Sanchez, L., Cerdan, O., 2016a. Rainfall erosivity in catchments contaminated with fallout from the Fukushima Daiichi nuclear power plant accident. Hydrology and Earth System Sciences 20, 2467–2482. URL: https://hess.copernicus.org/articles/20/2467/2016/, doi:10.5194/hess-20-2467-2016.

Laceby, J.P., Evrard, O., Smith, H.G., Blake, W.H., Olley, J.M., Minella, J.P., Owens, P.N., 2017. The challenges and opportunities of addressing particle size effects in sediment source fingerprinting: A review. Earth-Science Reviews 169, 85–103. URL: https://linkinghub.elsevier.com/retrieve/pii/S0012825216304548, doi:10.1016/j.earscirev.2017.04.009.

Laceby, J.P., Huon, S., Onda, Y., Vaury, V., Evrard, O., 2016b. Do forests represent a long-term source of contaminated particulate matter in the Fukushima Prefecture? Journal of Environmental Management 183, 742–753. URL: https://linkinghub.elsevier.com/retrieve/pii/S0301479716306661, doi:10.1016/j.jenvman.2016.09.020.

Laceby, J.P., McMahon, J., Evrard, O., Olley, J., 2015. A comparison of geological and statistical approaches to element selection for sediment fingerprinting. Journal of Soils and Sediments 15, 2117–2131. URL: http://link.springer.com/10.1007/s11368-015-1111-9, doi:10.1007/s11368-015-1111-9.

Laceby, J.P., Olley, J., 2015. An examination of geochemical modelling approaches to tracing sediment sources incorporating distribution mixing and elemental correlations. Hydrological Processes 29, 1669–1685. URL: https://onlinelibrary.wiley.com/doi/10.1002/hyp.10287, doi:10.1002/hyp.10287.

Laio, F., Tamea, S., 2007. Verification tools for probabilistic forecasts of continuous hydrological variables. Hydrology and Earth System Sciences 11, 1267–1277. URL: https://hess.copernicus.org/articles/11/1267/2007/, doi:10.5194/hess-11-1267-2007.

Lal, R., 1998. Soil Erosion Impact on Agronomic Productivity and Environment Quality. Critical Reviews in Plant Sciences 17, 319–464. URL: https://www.tandfonline.com/doi/full/10.1080/07352689891304249, doi:10.1080/07352689891304249.

Lal, R., 2001. Soil degradation by erosion. Land Degradation & Development 12, 519–539. URL: https://onlinelibrary.wiley.com/doi/10.1002/ldr.472, doi:10.1002/ldr.472.

Lal, R., 2019. Accelerated Soil erosion as a source of atmospheric CO2. Soil and Tillage Research 188, 35–40. URL: https://linkinghub.elsevier.com/retrieve/pii/S0167198718300345, doi:10.1016/j.still.2018.02.001.

Lamb, A.L., Wilson, G.P., Leng, M.J., 2006. A review of coastal palaeoclimate and relative sea-level reconstructions using δ13C and C/N ratios in organic material. Earth-Science Reviews 75, 29–57. URL: https://linkinghub.elsevier.com/retrieve/pii/S0012825205001376, doi:10.1016/j.earscirev.2005.10.003.

Latorre, B., Lizaga, I., Gaspar, L., Navas, A., 2021. A novel method for analysing consistency and unravelling multiple solutions in sediment fingerprinting. Science of The Total Environment 789, 147804. URL: https://linkinghub.elsevier.com/retrieve/pii/S0048969721028758, doi:10.1016/j.scitotenv.2021.147804.

Li, Z., Fang, H., 2016. Impacts of climate change on water erosion: A review. Earth-Science Reviews 163, 94–117. URL: https://linkinghub.elsevier.com/retrieve/pii/S0012825216303555, doi:10.1016/j.earscirev.2016.10.004.

Lizaga, I., Gaspar, L., Blake, W.H., Latorre, B., Navas, A., 2019. Fingerprinting changes of source apportionments from mixed land uses in stream sediments before and after an exceptional rainstorm event. Geomorphology 341, 216–229. URL: https://linkinghub.elsevier.com/retrieve/pii/S0169555X19302302, doi:10.1016/j.geomorph.2019.05.015.

Lizaga, I., Latorre, B., Gaspar, L., Navas, A., 2020. Consensus ranking as a method to identify non-conservative and dissenting tracers in fingerprinting studies. Science of The Total Environment 720, 137537. URL: https://linkinghub.elsevier.com/retrieve/pii/S0048969720310482, doi:10.1016/j.scitotenv.2020.137537.

Lizaga, I., Latorre, B., Gaspar, L., Navas, A., 2022. fingerPro: Sediment Source Fingerprinting. URL: https://github.com/eead-csic-eesa/fingerPro, doi:10.5281/zenodo.3355427.

Loughran, R., Campbell, B., Walling, D., 1987. Soil erosion and sedimentation indicated by caesium 137: Jackmoor Brook catchment, Devon, England. CATENA 14, 201–212. URL: https://linkinghub.elsevier.com/retrieve/pii/S0341816287800188, doi:10.1016/S0341-8162(87)80018-8.

Martínez-Carreras, N., Gallart, F., Iffly, J.F., Pfister, L., Walling, D.E., Krein, A., 2008. Uncertainty assessment in suspended sediment fingerprinting based on tracer mixing models: A case study from Luxembourg. IAHS publication 325, 94. URL: https://iahs.info/uploads/dms/14500.16-94-105-11-325-Martinez.pdf.

Martínez-Carreras, N., Krein, A., Udelhoven, T., Gallart, F., Iffly, J.F., Hoffmann, L., Pfister, L., Walling, D.E., 2010. A rapid spectral-reflectance-based fingerprinting approach for documenting suspended sediment sources during storm runoff events. Journal of Soils and Sediments 10, 400–413. URL: http://link.springer.com/10.1007/s11368-009-0162-1, doi:10.1007/s11368-009-0162-1.

Matheson, J.E., Winkler, R.L., 1976. Scoring Rules for Continuous Probability Distributions. Management

Science 22, 1087–1096. URL: http://pubsonline.informs.org/doi/10.1287/mnsc.22.10.1087, doi:10.1287/mnsc.22.10.1087.

Meybeck, M., Helmer, R., 1989. The quality of rivers: From pristine stage to global pollution. Palaeogeography, Palaeoclimatology, Palaeoecology 75, 283–309. URL: https://linkinghub.elsevier.com/retrieve/pii/0031018289901910, doi:10.1016/0031-0182(89)90191-0.

Minella, J.P., Walling, D.E., Merten, G.H., 2008. Combining sediment source tracing techniques with traditional monitoring to assess the impact of improved land management on catchment sediment yields. Journal of Hydrology 348, 546–563. URL: https://linkinghub.elsevier.com/retrieve/pii/S0022169407006208, doi:10.1016/j.jhydrol.2007.10.026.

Mingus, K.A., Liang, X., Massoudieh, A., Jaisi, D.P., 2019. Stable Isotopes and Bayesian Modeling Methods of Tracking Sources and Differentiating Bioavailable and Recalcitrant Phosphorus Pools in Suspended Particulate Matter. Environmental Science & Technology 53, 69–76. URL: https://pubs.acs.org/doi/10.1021/acs.est.8b05057, doi:10.1021/acs.est.8b05057.

Minolta, K., 2022. QCM-S100w SpectraMagic NX. Konica Minolta. URL: https://www.konicaminolta.com/instruments/download/software/color/smnx/index.html.

Montgomery, D.R., 2007. Soil erosion and agricultural sustainability. Proceedings of the National Academy of Sciences 104, 13268–13272. URL: https://pnas.org/doi/full/10.1073/pnas.0611508104, doi:10.1073/pnas.0611508104.

Mukundan, R., Radcliffe, D.E., Ritchie, J.C., Risse, L.M., McKinley, R.A., 2010. Sediment Fingerprinting to Determine the Source of Suspended Sediment in a Southern Piedmont Stream. Journal of Environmental Quality 39, 1328–1337. URL: https://onlinelibrary.wiley.com/doi/10.2134/jeq2009.0405, doi:10.2134/jeq2009.0405.

Mukundan, R., Walling, D.E., Gellis, A.C., Slattery, M.C., Radcliffe, D.E., 2012. Sediment Source Fingerprinting: Transforming From a Research Tool to a Management Tool. JAWRA Journal of the American Water Resources Association 48, 1241–1257. URL: https://onlinelibrary.wiley.com/doi/10.1111/j.1752-1688.2012.00685.x, doi:10.1111/j.1752-1688.2012.00685.x.

Nakao, A., Ogasawara, S., Sano, O., Ito, T., Yanai, J., 2014. Radiocesium sorption in relation to clay mineralogy of paddy soils in Fukushima, Japan. Science of The Total Environment 468–469, 523–529. URL: https://linkinghub.elsevier.com/retrieve/pii/S0048969713009893, doi:10.1016/j.scitotenv.2013.08.062.

NARO, 2011. Comprehensive soil map of agricultural land at 1:50,000 scale (Prefecture and National). URL: https://soil-inventory.rad.naro.go.jp/download5.html.

Nosrati, K., Govers, G., Semmens, B.X., Ward, E.J., 2014. A mixing model to incorporate uncertainty in sediment fingerprinting. Geoderma 217–218, 173–180. URL: https://linkinghub.elsevier.com/retrieve/pii/S0016706113004308, doi:10.1016/j.geoderma.2013.12.002.

Nosrati, K., Mohammadi-Raigani, Z., Haddadchi, A., Collins, A.L., 2021. Elucidating intra-storm variations in suspended sediment sources using a Bayesian fingerprinting approach. Journal of Hydrology 596, 126115. URL: https://linkinghub.elsevier.com/retrieve/pii/S0022169421001621, doi:10.1016/j.jhydrol.2021.126115.

Obara, H., Maejima, Y., Kohyama, K., Ohkura, T., Takata, Y., 2015. Outline of the Comprehensive Soil Classification System of Japan – First Approximation. Japan Agricultural Research Quarterly: JARQ 49, 217–226. URL: https://www.jstage.jst.go.jp/article/jarq/49/3/49_217/_article, doi:10.6090/jarq.49.217.

Obara, H., Ohkura, T., Takata, Y., Kohyama, K., Maejima, Y., Hamazaki, T., 2011. Comprehensive soil classification system of Japan first approximation. Nogyo Kankyo Gijutsu Kenkyusho Hokoku = Bulletin of National Institute for Agro-Environmental Sciences , 1–73URL: http://www.niaes.affrc.go.jp/sinfo/publish/public_e.html.

OCC, 2015. Soil Is a Non-Renewable Resource. Technical Report. Food and Agriculture Organization of the United Nations. URL: https://www.fao.org/documents/card/en/c/ec28fc04-3d38-4e35-8d9b-e4427e20a4f7/.

Olson, K.R., Al-Kaisi, M., Lal, R., Cihacek, L., 2016. Impact of soil erosion on soil organic carbon stocks. Journal of Soil and Water Conservation 71, 61A–67A. URL: http://www.jswconline.org/cgi/doi/10.2489/jswc.71.3.61A, doi:10.2489/jswc.71.3.61A.

Owens, P., Blake, W., Gaspar, L., Gateuille, D., Koiter, A., Lobb, D., Petticrew, E., Reiffarth, D., Smith, H., Woodward, J., 2016. Fingerprinting and tracing the sources of soils and sediments: Earth and ocean science, geoarchaeological, forensic, and human health applications. Earth-Science Reviews 162, 1–23. URL: https://linkinghub.elsevier.com/retrieve/pii/S0012825216302653, doi:10.1016/j.earscirev.2016.08.012.

Palazón, L., Latorre, B., Gaspar, L., Blake, W.H., Smith, H.G., Navas, A., 2015. Comparing catchment sediment fingerprinting procedures using an auto-evaluation approach with virtual sample mixtures. Science of The Total Environment 532, 456–466. URL: https://linkinghub.elsevier.com/retrieve/pii/S0048969715300619, doi:10.1016/j.scitotenv.2015.05.003.

Peart, M., Walling, D., 1986. Fingerprinting sediment source: The example of a drainage basin in Devon, UK. Drainage basin sediment delivery 159, 41–55. URL: http://hdl.handle.net/10722/157753.

Pennock, D., 2019. Soil Erosion: The Greatest Challenge for Sustainable Soil Management. Food and Agriculture Organization of the United Nations. URL: http://www.fao.org/3/ca4395en/ca4395en.pdf.

Phillips, I.R., Greenway, M., 1998. Changes in water-soluble and exchangeable ions, cation exchange capacity, and phosphorus $_{max}$ in soils under alternating waterlogged and drying conditions. Communications in Soil Science and Plant Analysis 29, 51–65. URL: https://www.tandfonline.com/doi/full/10.1080/00103629809369928, doi:10.1080/00103629809369928.

Pimentel, D., 2006. Soil Erosion: A Food and Environmental Threat. Environment, Development and Sustainability 8, 119–137. URL: http://link.springer.com/10.1007/s10668-005-1262-8, doi:10.1007/s10668-005-1262-8.

Pimstein, A., Notesco, G., Ben-Dor, E., 2011. Performance of Three Identical Spectrometers in Retrieving Soil Reflectance under Laboratory Conditions. Soil Science Society of America Journal 75, 746–759. URL: http://doi.wiley.com/10.2136/sssaj2010.0174, doi:10.2136/sssaj2010.0174.

Poesen, J., 2018. Soil erosion in the Anthropocene: Research needs: Soil erosion in the Anthropocene. Earth Surface Processes and Landforms 43, 64–84. URL: https://onlinelibrary.wiley.com/doi/10.1002/esp.4250, doi:10.1002/esp.4250.

QGIS Development Team, 2022. QGIS Geographic Information System. Open Source Geospatial Foundation. URL: https://www.qgis.org/fr/site/.

R Core Team, 2021. A Language and Environment for Statistical Computing. R Foundation for Statistical Computing. URL: https://www.R-project.org/.

R Core Team, 2022. A Language and Environment for Statistical Computing. R Foundation for Statistical Computing. URL: https://www.R-project.org/.

Russi, T., Packard, A., Feeley, R., Frenklach, M., 2008. Sensitivity Analysis of Uncertainty in Model Prediction. The Journal of Physical Chemistry A 112, 2579–2588. URL: https://pubs.acs.org/doi/10.1021/jp076861c, doi:10.1021/jp076861c.

Saito, T., Makino, H., Tanaka, S., 2014. Geochemical and grain-size distribution of radioactive and stable cesium in Fukushima soils: Implications for their long-term behavior. Journal of Environmental Radioactivity 138, 11–18. URL: https://linkinghub.elsevier.com/retrieve/pii/S0265931X14002306, doi:10.1016/j.jenvrad.2014.07.025.

Sawhney, B.L., 1972. Selective Sorption and Fixation of Cations by Clay Minerals: A Review. Clays and Clay Minerals 20, 93–100. URL: https://doi.org/10.1346/CCMN.1972.0200208, doi:10.1346/CCMN.1972.0200208.

Scheinost, A.C., Chavernas, A., Barrón, V., Torrent, J., 1998. Use and Limitations of Second-Derivative Diffuse Reflectance Spectroscopy in the Visible to Near-Infrared Range to Identify and Quantify Fe Oxide Minerals in Soils. Clays and Clay Minerals 46, 528–536. URL: http://link.springer.com/10.1346/CCMN.1998.0460506, doi:10.1346/CCMN.1998.0460506.

Sellier, V., Navratil, O., Laceby, J.P., Allenbach, M., Lefèvre, I., Evrard, O., 2020. Investigating the use of fallout and geogenic radionuclides as potential tracing properties to quantify the sources of suspended sediment in a mining catchment in New Caledonia, South Pacific. Journal of Soils and Sediments 20, 1112–1128. URL: http://link.springer.com/10.1007/s11368-019-02447-8, doi:10.1007/s11368-019-02447-8.

Sellier, V., Navratil, O., Laceby, J.P., Legout, C., Foucher, A., Allenbach, M., Lefèvre, I., Evrard, O., 2021. Combining colour parameters and geochemical tracers to improve sediment source discrimination in a mining catchment (New Caledonia, South Pacific Islands). SOIL 7, 743–766. URL: https://soil.copernicus.org/articles/7/743/2021/, doi:10.5194/soil-7-743-2021.

Sherriff, S.C., Franks, S.W., Rowan, J.S., Fenton, O., Ó'hUallacháin, D., 2015. Uncertainty-based assessment of tracer selection, tracer non-conservativeness and multiple solutions in sediment fingerprinting using synthetic and field data. Journal of Soils and Sediments 15, 2101–2116. URL: http://link.springer.com/10.1007/s11368-015-1123-5, doi:10.1007/s11368-015-1123-5.

Small, I.F., Rowan, J.S., Franks, S.W., 2002. Quantitative sediment fingerprinting using a Bayesian uncertainty estimation framework. International Association of Hydrological Sciences 276, 443–450.

Small, I.F., Rowan, J.S., Franks, S.W., Wyatt, A., Duck, R.W., 2004. Bayesian sediment fingerprinting provides a robust tool for environmental forensic geoscience applications. Geological Society, London, Special Publications 232, 207–213. URL: https://www.lyellcollection.org/doi/10.1144/GSL.SP.2004.232.01.19, doi:10.1144/GSL.SP.2004.232.01.19.

Smith, H.G., Blake, W.H., 2014. Sediment fingerprinting in agricultural catchments: A critical re-examination of source discrimination and data corrections. Geomorphology 204, 177–191. URL: https://linkinghub.elsevier.com/retrieve/pii/S0169555X13004017, doi:10.1016/j.geomorph.2013.08.003.

Smith, H.G., Karam, D.S., Lennard, A.T., 2018. Evaluating tracer selection for catchment sediment fingerprinting. Journal of Soils and Sediments 18, 3005–3019. URL: http://link.springer.com/10.1007/s11368-018-1990-7, doi:10.1007/s11368-018-1990-7.

Soriano-Disla, J.M., Janik, L.J., Viscarra Rossel, R.A., Macdonald, L.M., McLaughlin, M.J., 2014. The Performance of Visible, Near-, and Mid-Infrared Reflectance Spectroscopy for Prediction of Soil Physical, Chemical, and Biological Properties. Applied Spectroscopy Reviews 49, 139–186. URL: http://www.tandfonline.com/doi/abs/10.1080/05704928.2013.811081, doi:10.1080/05704928.2013.811081.

Stevens, A., Ramirez-Lopez, L., 2022. An introduction to the prospectr package. URL: https://cran.r-project.org/web/packages/prospectr/vignettes/prospectr.html.

Stock, B.C., Semmens, B.X., Ward, E.J., Parnell, A.C., Phillips, D.L., 2020. MixSIAR: Bayesian Mixing Models in R. URL: https://doi.org/10.5281/zenodo.1209993.

Stock, B.C., Semmens, B.X., Ward, E.J., Parnell, A.C., Phillips, D.L., 2022. JAGS: Bayesian Mixing Models in R. URL: https://doi.org/10.5281/zenodo.1209993.

Summers, D., Lewis, M., Ostendorf, B., Chittleborough, D., 2011. Visible near-infrared reflectance spectroscopy as a predictive indicator of soil properties. Ecological Indicators 11, 123–131. URL: https://linkinghub.elsevier.com/retrieve/pii/S1470160X09000806, doi:10.1016/j.ecolind.2009.05.001.

Team, R., 2022. RStudio: Integrated Development Environment for R. RStudio. URL: http://www.rstudio.com/.

Terashima, S., Imai, N., Taniguchi, M., Okai, T., Nishimura, A., 2002. The Preparation and Preliminary Characterisation of Four New Geological Survey of Japan Geochemical Reference Materials: Soils, JSO-1 and JSO-2; and Marine Sediments, JMS-1 and JMS-2. Geostandards Newsletter 26, 85–94. URL: https://onlinelibrary.wiley.com/doi/10.1111/j.1751-908X.2002.tb00626.x, doi:10.1111/j.1751-908X.2002.tb00626.x.

Tiecher, T., Caner, L., Minella, J.P.G., dos Santos, D.R., 2015. Combining visible-based-color parameters and geochemical tracers to improve sediment source discrimination and apportionment. Science of The Total Environment 527–528, 135–149. URL: https://linkinghub.elsevier.com/retrieve/pii/S0048969715300401, doi:10.1016/j.scitotenv.2015.04.103.

Tiecher, T., Moura-Bueno, J.M., Caner, L., Minella, J.P., Evrard, O., Ramon, R., Naibo, G., Barros, C.A., Silva, Y.J., Amorim, F.F., Rheinheimer, D.S., 2021. Improving the quantification of sediment source contributions using different mathematical models and spectral preprocessing techniques for individual or combined spectra of ultraviolet–visible, near- and middle-infrared spectroscopy. Geoderma 384, 114815. URL: https://linkinghub.elsevier.com/retrieve/pii/S0016706120325702, doi:10.1016/j.geoderma.2020.114815.

Torrent, J., Liu, Q., Bloemendal, J., Barrón, V., 2007. Magnetic Enhancement and Iron Oxides in the Upper Luochuan Loess-Paleosol Sequence, Chinese Loess Plateau. Soil Science Society of America Journal 71, 1570–1578. URL: http://doi.wiley.com/10.2136/sssaj2006.0328, doi:10.2136/sssaj2006.0328.

Vale, S., Swales, A., Smith, H.G., Olsen, G., Woodward, B., 2022. Impacts of tracer type, tracer selection, and source dominance on source apportionment with sediment fingerprinting. Science of The Total Environment 831, 154832. URL: https://linkinghub.elsevier.com/retrieve/pii/S0048969722019258, doi:10.1016/j.scitotenv.2022.154832.

Viparelli, E., Wesley Lauer, J., Belmont, P., Parker, G., 2013. A numerical model to develop long-term sediment budgets using isotopic sediment fingerprints. Computers & Geosciences 53, 114–122. URL: https://linkinghub.elsevier.com/retrieve/pii/S0098300411003347, doi:10.1016/j.cageo.2011.10.003.

Viscarra Rossel, R., Minasny, B., Roudier, P., McBratney, A., 2006. Colour space models for soil science. Geoderma 133, 320–337. URL: https://linkinghub.elsevier.com/retrieve/pii/S0016706105002314, doi:10.1016/j.geoderma.2005.07.017.

Wadoux, A.M.C., Malone, B., Minasny, B., Fajardo, M., McBratney, A.B., 2021. Soil Spectral Inference with R: Analysing Digital Soil Spectra Using the R Programming Environment. Progress in Soil Science, Springer International Publishing, Cham. URL: https://link.springer.com/10.1007/978-3-030-64896-1, doi:10.1007/978-3-030-64896-1.

Walden, J., Slattery, M., Burt, T., 1997. Use of mineral magnetic measurements to fingerprint suspended sediment sources: Approaches and techniques for data analysis. Journal of Hydrology 202, 353–372. URL: https://linkinghub.elsevier.com/retrieve/pii/S0022169497000784, doi:10.1016/S0022-1694(97)00078-4.

Wall, G.J., Wilding, L.P., 1976. Mineralogy and Related Parameters of Fluvial Suspended Sediments in Northwestern Ohio. Journal of Environmental Quality 5, 168–173. URL: http://doi.wiley.com/10.2134/jeq1976.00472425000500020012x, doi:10.2134/jeq1976.00472425000500020012x.

Walling, D.E., Owens, P.N., Waterfall, B.D., Leeks, G.J., Wass, P.D., 2000. The particle size characteristics of fluvial suspended sediment in the Humber and Tweed catchments, UK. Science of The Total Environment 251–252, 205–222. URL: https://linkinghub.elsevier.com/retrieve/pii/S0048969700003843, doi:10.1016/S0048-9697(00)00384-3.

Walling, D.E., Woodward, J., 1992. Use of radiometric fingerprints to derive information on suspended sediment sources. Erosion and Sediment Transport Monitoring Programmes in River Basins (Proceedings of the Oslo Symposium, August 1992) 210, 153–164.

Wei, P., Lu, Z., Song, J., 2015. Variable importance analysis: A comprehensive review. Reliability Engineering & System Safety 142, 399–432. URL: https://linkinghub.elsevier.com/retrieve/pii/S0951832015001672, doi:10.1016/j.ress.2015.05.018.

Weihs, C., Ligges, U., Luebke, K., Raabe, N., Szepannek, G., Zentgraf, M., Meyer, D., 2023. klaR Analyzing German Business Cycles. URL: https://statistik.tu-dortmund.de/.

Whitaker, A.C., Chapasa, S.N., Sagras, C., Theogene, U., Veremu, R., Sugiyama, H., 2022. Estimation of baseflow recession constant and regression of low flow indices in eastern Japan. Hydrological

Sciences Journal 67, 191–204. URL: https://www.tandfonline.com/doi/full/10.1080/02626667.2021.2003368, doi:10.1080/02626667.2021.2003368.

Wilkinson, S.N., Hancock, G.J., Bartley, R., Hawdon, A.A., Keen, R.J., 2013. Using sediment tracing to assess processes and spatial patterns of erosion in grazed rangelands, Burdekin River basin, Australia. Agriculture, Ecosystems & Environment 180, 90–102. URL: https://linkinghub.elsevier.com/retrieve/pii/S0167880912000564, doi:10.1016/j.agee.2012.02.002.

Williamson, T.N., Fitzpatrick, F.A., Kreiling, R.M., 2023. Building a library of source samples for sediment fingerprinting – Potential and proof of concept. Journal of Environmental Management 333, 117254. URL: https://linkinghub.elsevier.com/retrieve/pii/S0301479723000427, doi:10.1016/j.jenvman.2023.117254.

Xu, Z., Belmont, P., Brahney, J., Gellis, A.C., 2022. Sediment source fingerprinting as an aid to large-scale landscape conservation and restoration: A review for the Mississippi River Basin. Journal of Environmental Management 324, 116260. URL: https://linkinghub.elsevier.com/retrieve/pii/S0301479722018333, doi:10.1016/j.jenvman.2022.116260.

Chapter II

Decontamination and Radiocesium Transfer: Sediment Core Insights

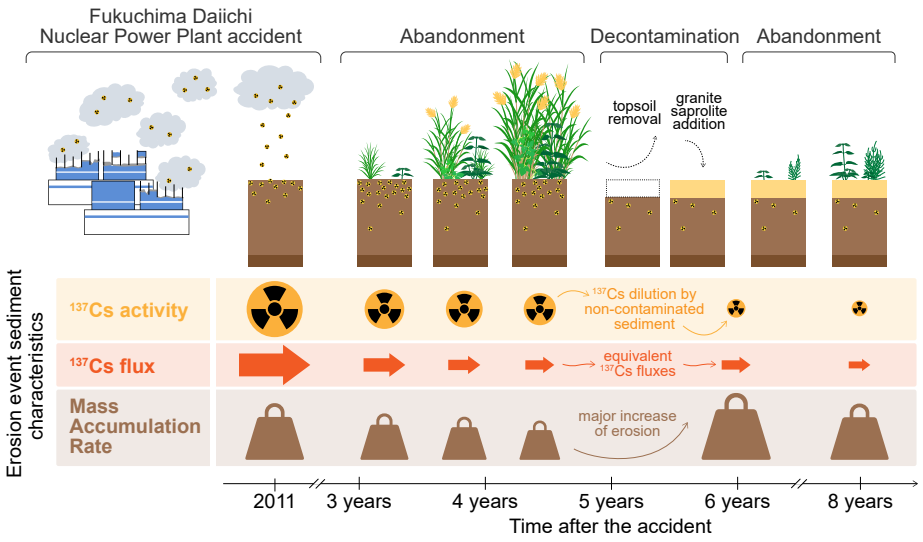
Chapter II

Decontamination and Radiocesium Transfer: Sediment Core Insights

The accident at the Fukushima Daiichi Nuclear Power Plant (FDNPP) in March 2011 resulted in widespread soil contamination with ^{137}Cs. To allow for a rapid return of the population the Japanese government initiated an unprecedented decontamination programme to reduce soil contamination. This decontamination programme focused on areas of human and economical activity, such as agricultural and residential areas, and a border of forest close to human settlements or roads. In agricultural and residential areas, decontamination involved the removal of the uppermost layer of soil and its replacement with "fresh soil" derived from local granitic saprolite. Over the years, a decrease in particle-bound ^{137}Cs transfers in the river system and was attributed to physical decay, previous erosion and the progress of decontamination, as agricultural and residential areas were identified as the main source of particle-bound ^{137}Cs. However, forested areas, which were not targeted by this programme, cover about 70-80 % of the Fukushima region and account for 74 % of the initial deposition of^{137}Cs. In this context, the impact of decontamination on the transfer of particle-bound ^{137}Cs by rivers, remains a critical area of investigation, particularly at the catchment scale.

In this chapter, a sediment core collected from the Mano Dam reservoir in June 2021 was investigated to assess the impacts of decontamination on sediment and ^{137}Cs transfers driven by extreme precipitation events. By reconstructing the sequence of sediment deposition over time and analysing changes in sediment source contributions, the study provides insights into how decontamination has affected ^{137}Cs transfers and fluxes.

During the abandonment phase (2011-2016), the contribution of farmland to sediment transfer decreased significantly, along with a reduction in ^{137}Cs activity in the sediment and depositional flux. However, after decontamination, sediment transfer from cropland and fresh soil increased significantly, although forested areas remained a consistent source of ^{137}Cs-contaminated sediment. In light of these findings, this chapter highlights the complex interplay between land-cover changes, decontamination, and sediment and particle-bound ^{137}Cs transfer processes in these post-accidental conditions.



Impacts of farmland decontamination on ^{137}Cs transfers in rivers after Fukushima nuclear accident: Evidence from a retrospective sediment core study



Thomas Chalaux-Clergue [a,*], Anthony Foucher [a], Pierre-Alexis Chaboche [b, c], Seiji Hayashi [d], Hideki Tsuji [d], Yoshifumi Wakiyama [c], Sylvain Huon [e], Rosalie Vandromme [f], Olivier Cerdan [f], Atsushi Nakao [g], and Olivier Evrard [a,*]

[a] *Laboratoire des Sciences du Climat et de l'Environnement (LSCE-IPSL), Université Paris-Saclay, UMR 8212 (CEA-CNRS-UVSQ), Gif-sur-Yvette 91190, France*

[b] *International Research Fellow of Japan Society for the Promotion of Science, Postdoctoral Fellowships for Research in Japan (Standard), Japan*

[c] *Institute of Environmental Radioactivity (IER), University of Fukushima, Fukushima, Japan*

[d] *National Institute for Environmental Science (NIES), Fukushima Branch 10-2 Fukasaku, Miharu, Tamura, Fukushima 963-7700, Japan*

[e] *Sorbonne Universités UPMC Université Paris 06, Institut d' Ecologie et des Sciences de l' Environnement de Paris (iEES), case 120, 4 place Jussieu, Paris cedex 05, 75252, France*

[f] *Risk and Prevention Division, Bureau de Recherches Géologiques et Minières (BRGM), Orléans F-45060, France*

[g] *Graduate School of Life and Environmental Sciences, Kyoto Prefectural University, Shimogamo, Hangi, Sakyo-ku, Kyoto 606-8522, Japan*

HIGHLIGHTS

- A sediment core draining a Fukushima fallout-affected catchment was analysed.
- Farmland decontamination impact on particle-bound ^{137}Cs transfer was reconstructed.
- Sediment origin was determined using sediment source fingerprinting techniques.
- Forests act as a stable and long-term source of ^{137}Cs-contaminated sediment.
- Farmland decontamination and 5-years abandonment resulted in equivalent ^{137}Cs fluxes.

ABSTRACT

Following the Fukushima Daiichi Nuclear Power Plant disaster in March 2011, the Japanese government initiated an unprecedented decontamination programme to remediate ^{137}Cs-contaminated soils and allow population return. This programme involved the removal of topsoil under farmland and residential land, and its replacement with "fresh soil" composed of granitic saprolite. However, decontamination was limited to these two land uses, without remediating forests, which cover 70 % of the surface area in the affected region. In this unprecedented context, the specific impact of this unique decontamination programme on ^{137}Cs transfers in river systems remains to be quantified at the catchment scale. In this study, based on the analysis of a sediment core collected in June 2021 in the Mano Dam reservoir draining a decontaminated catchment, the effects of soil decontamination on particle-bound ^{137}Cs dynamics and sediment source contributions in response to a succession of extreme precipitation events were retrospectively assessed. The sequence of sediment layer deposition and its chronology were reconstructed through the analysis of several diagnostic properties (organic matter, elemental geochemistry, visible colourimetry, granulometry) and contextual information. During abandonment (2011-2016), cropland contribution decreased (31 %). Concurrently, ^{137}Cs activity and deposition flux decreased (19 and 29 % year^{-1}, respectively). Following decontamination (2017), sediment transfer increased (270 %) in response to increased contributions from decontaminated cropland and "fresh soil" (625 % and 180 %, respectively). Meanwhile, forest contributions remained stable. In contrast, ^{137}Cs activity dropped (65 %), although ^{137}Cs deposition flux remained constant. Forests acted as a stable source of ^{137}Cs. Accordingly, ^{137}Cs deposition flux after decontamination (2016-2021) was similar to that observed during the 5-years period of land abandonment (2011-2016), as a result of the regrowth of

spontaneous vegetation over farmland, protecting soil against erosion. Future research should further investigate the impact of longer land abandonment that prevailed in some regions decontaminated lately on the ^{137}Cs fluxes in the rivers.

Keywords: Soil erosion; Environmental pollution; Radiocesium transfer; Source-to-sink; Sediment source fingerprinting; Soil remediation

Received 19 March 2024 - Revised 3 July 2024 - Accepted 4 July 2024 - Available online 9 July 2024 - Version of Record 13 July 2024
Published in Science of The Total Environment (STOTEN) Elsevier B.V. Volume 947, 15 October 2024, 174546.
* indicates corresponding authors - DOI: https://doi.org/10.1016/j.scitotenv.2024.174546

II.1 - Introduction

The nuclear accident at the Fukushima Daiichi Nuclear Power Plant (FDNPP) that occurred in March 2011 released a substantial amount of radionuclides into the environment (Morino et al., 2013), of which about 20 % deposited over continental land (Onda et al., 2020). Of all the radionuclides released, ^{137}Cs is particularly problematic in terms of short and long term environmental and human health impacts due to its relatively long half-life ($T_{1/2}$) of 30 years and the large amounts of this substance that were released, with about 13 PBq (Chino et al., 2011; Kobayashi et al., 2013; Steinhauser, 2014). Most of the ^{137}Cs that deposited onto terrestrial environments (2.7 PBq) has accumulated in the Fukushima Prefecture (2.0 PBq) (Kato et al., 2019; Taniguchi et al., 2019). About 83 % of the surface area in this Prefecture (i.e. 11,430 km^2) has received at least 5 kBq m^{-2}, and 26 % (i.e. 3,520 km^2) has received at least 100 kBq m^{-2} (Kato et al., 2019). The inhabitants living within a 20-km radius around FDNPP (Evacuation Zone) and those who were exposed to a radioactive dose rate exceeding 20 mSv yr^{-1} in 2011 (Planned Evacuation Zone) were evacuated in priority. A total of eleven municipalities, with a population of about 80,000 people and covering an area of 1,150 km^2, were under an evacuation order and classified as Residence Restriction Area. According to the decontamination programme, these municipalities were then classified as Special Decontamination Zone (SDZ) or Difficult-to-Return Zone (DTRZ) depending on local ambient dose rates (MoE, 2018; Taniguchi et al., 2019; Evrard et al., 2019b).

Once deposited onto the ground, ^{137}Cs is strongly and quasi-permanently bound to fine soil particles such as silt and clay (Sawhney, 1972; He and Walling, 1996), which has been confirmed in Fukushima Prefecture soils (Saito et al., 2014; Nakao et al., 2014, 2015). Consequently, 90-99 % of fallout radiocesium was found to be accumulated in the uppermost 5 cm of undisturbed soils (Kato et al., 2012; Lepage et al., 2015). In addition, in relation to ^{137}Cs behaviour in soil, the transfer from soil to plant was found to be limited in annual or perennial herbs and trees (Yamashita et al., 2014; Tamaoki et al., 2016; Onda et al., 2020), so that the nearly all of ^{137}Cs deposited onto the ground remained in the soil. Within the Fukushima Prefecture, 74 % of the ^{137}Cs deposition occurred over forests and 19 % over farmland (paddy fields and other farmland) (Kato et al., 2019). To enable a rapid return of the population and the resumption of agricultural activities, the Japanese government carried out extensive decontamination in farmland, urban areas and within a 20-m buffer zone in forests around residential areas and along roads (MoE, 2015; Evrard et al., 2020). In the SDZ, by March 2017, decontamination was conducted on 180 km^2 (16 % of the SDZ area), of which 48 % was under farmland (about 87 km^2) (MoE, 2023a, in Japanese).

In farmland, the decontamination procedure depended on the initial ^{137}Cs activity in soils (MoE, 2013, 2015, 2018). On the one hand, in soils with ^{137}Cs activities below 5 kBq kg^{-1}, inversion tillage of a layer of about

30 to 45 cm depth was carried out. On the other hand, in soils with activities exceeding 5 kBq kg^{-1}, decontamination consisted of four steps: (1) the removal of the upper 5 cm layer of soil, (2) the addition of a granite saprolite extracted from local quarries opened for this purpose to replace the removed soil (55.5 m^3 per 1.000 m^2). The Japanese authorities refer to this material as "fresh soil". Then, to prepare the return of farmers, (3) soil fertility was restored with two types of amendments applied: (a) carbonate (as needed) and phosphorus silicate (about 0.8 t ha^{-1}) or (b) zeolite amendment (about 0.5 t ha^{-1}). Finally, the soil was (4) prepared for recultivation by mixing the saprolite layer and soil productivity recovery materials with the underlying residual soil layer through a double ploughing down to a depth of about 25 to 30 cm. Accordingly, decontamination comprised three main phrases: decontamination (step 1), remediation (step 2) and preparation for recultivation (steps 3 and 4).

Soil decontamination proved to be effective in reducing radioactive ambient air dose rates, from 20 to 70 % compared to the initial situation in 2011 (MoE, 2018; Onda et al., 2020), along with a decrease of individual exposure levels (Tsubokura et al., 2019). Soil decontamination in the Fukushima Prefecture (including residential areas, farmland, forest and roads) by March 2020 generated 6.7 million m^3 of removed soil (MoE, 2023b). In parallel to decontamination, a decrease of particle-bound ^{137}Cs transported by rivers was observed year after year and was attributed to physical decay, previous erosion and the progress of decontamination (Evrard et al., 2016; Osawa et al., 2018; Konoplev et al., 2018; Vandromme et al., 2023). Indeed, particulate-bound ^{137}Cs accounted for a large portion (82 to 99 %) of ^{137}Cs transfer by water erosion during rainfall events (Yamashiki et al., 2014; Sakaguchi et al., 2015; Iwagami et al., 2017; Osawa et al., 2018). The maximum of particulate-bound ^{137}Cs contribution was found in the fine material such as the silt-sized fraction (3-63 μm) (Sakaguchi et al., 2015). The primary sources of particle-bound ^{137}Cs were shown to be paddy fields, other farmland types and urban areas despite their low relative landscape cover (Chartin et al., 2013; Lepage et al., 2016; Taniguchi et al., 2019). This disproportionate contribution was related to their very strong hydro-sedimentary connectivity, especially for paddy fields and their irrigation/drainage systems that connect them directly to the river networks (Chartin et al., 2013). In addition, as decontamination left the soil uncovered by vegetation and included the spreading of non-aggregated fresh soil, decontamination exacerbated soil erodibility (Wakahara et al., 2014; Evrard et al., 2019a; Feng et al., 2022). Accordingly, an increase in soil erosion was observed in 2015 in the Niida and Mano River catchments, and contribution of sediment originating from subsoil or fresh soil sources strongly increased compared to what was observed in previous years. Evrard et al. (2019b) found that an increase in the relative sediment contribution from subsoil from about 20 to 50 % after decontamination. However, spontaneous vegetation regrowth following abandonment or after decontamination led to a rapid recovery of the soil protection against erosion (Lal, 2001; Zuazo and Pleguezuelo, 2009), thereby reducing the contribution of farmland to sediment and particle bound-^{137}Cs transfers (Feng et al., 2022).

This soil protection by vegetation is particularly important, as tropical cyclones and typhoons were shown to generate heavy rainfall and extensive erosion each year all across Japan. Despite its location in Northern Japan less exposed to typhoons than southern regions, Fukushima Prefecture has been hit by at least one typhoon or tropical storm each year since the FDNPP accident (Laceby et al., 2016a; Evrard et al., 2020). These extreme events, which generate about 60 % of the annual rainfall and 86 % of the annual rainfall erosivity in the steep geomorphological context of the mountainous catchment of the Fukushima region (Laceby et al., 2016a) have been identified as the main driver of sediment and hence particle-bound ^{137}Cs transfer across basins (Kitamura et al., 2016; Chartin et al., 2017; Evrard et al., 2020). The timing of decontamination is therefore crucial, as typhoons may occur when soils are left bare for remediation and are therefore particularly exposed to erosion, which can lead to significant transfers of soil and particle-bound radiocesium.

However, the overall pluriannual impact of decontamination on the transfers of radiocesium in river systems remains uncertain, as nearly 70 % of the area of Fukushima Prefecture is covered by forests (Hashimoto et al., 2012) and have not been decontaminated, although they account for 74 % of ^{137}Cs deposition (Kato et al., 2019). They have also been shown to contribute a significant proportion of contaminated material to the river systems (Laceby et al., 2016b; Huon et al., 2018; Evrard et al., 2019a). In addition, these results showed that forests may provide a potential long-term source of particulate contaminated matter (Evrard et al., 2019b).

To reconstruct the long-term impact of major landscape changes on sediment transfer in catchments, sediment core collection and analysis provide an effective approach (Foucher et al., 2023). In reservoir dams located at the outlet of catchments and under steady-state conditions, when incoming and outgoing water volumes are monitored and managed to maintain a constant lake water level, grain size sorting and sediment deposition occur along the former river course (Wetzel, 2001). As the reservoir widens, downstream at the transition from a riverine to a lacustrine environment, the velocity of the water decreases, allowing suspended particles to settle down. In this lacustrine zone upstream of the dam, sediment deposition is similar to that of natural lakes. Away from the reservoir inlet, mainly fine particles settle down, resulting in homogeneous, continuous, and well-organised sediment deposits. In the area affected by the Fukushima accident, such a typical deposition pattern could be identified by the observation of a single well-defined radiocesium peak (Huon et al., 2018; Konoplev et al., 2022). However, during extreme precipitation events, dam operators proceed to water releases to prevent, to maintain or to restore water level in the reservoir. These changes in water discharge volumes could increase the velocity of the water flow within the reservoir, which affects the sediment deposition pattern. Resulting in further downstream transport and deposition of coarser particles further in the lacustrine zone and even limiting the efficiency of sediment trapping by the reservoir. Huon et al. (2018) identified this pattern within the Mano Dam reservoir by studying four sediment cores collected at up-, mid- and downstream locations. During extreme precipitation events, coarser particles that usually deposit in the upper part of the reservoir were observed in the midstream sediment core. Further downstream, slighter changes were observed compared to those observed midstream with slightly coarser particle size distribution (higher D50), likely due to the long extension of the reservoir. Furthermore, changes in the respective contributions from cropland, forest and subsoil as sources of sediment were estimated along the sediment cores. However, sampling of these sediment cores took place in November 2014, on the onset of decontamination activities in the area, initiated on June 2014.

In this study, a new sediment core sampled in the downstream part of the Mano Dam reservoir was examined. This reservoir drains an early decontaminated agricultural catchment in the Fukushima Prefecture. This sediment core was investigated to reconstruct for the first time the impact of decontamination on sediment and radiocesium transfers through the river system. A combination of analyses of Mano Dam reservoir sediment core properties and ancillary data were used to (i) identify and date the sequence of sedimentary deposits associated with the occurrence of extreme precipitation events during the 2011-2021 period. Based on this reconstruction, (ii) the temporal evolution of ^{137}Cs activity, ^{137}Cs deposition flux, and sedimentary sources among three potential sources were determined to quantify the impact of these unprecedented landscape changes. Results of the lessons learnt in Fukushima are then discussed to guide the implementation of land management in the event of a major widespread pollution event that may occur in the future.

II.2 - Materials and methods

II.2.1 - Study site

Mano Dam reservoir (1.4 km^2; 37.68887-37.76166°N, 140.66671-140.84290°E), also known as Hayama Lake, is located in Fukushima Prefecture in Northeastern Japan (Tōhoku Region). The catchment of Mano Dam reservoir (67 km^2) corresponds to the mountainous upper part of the Mano River drainage area, and its elevation ranges from 170 m to 694 m above sea level. It is a typical mountainous agricultural catchment of the eastern part of Fukushima Prefecture, mainly dominated by forests (90 %). Due to its steep topography, farmland (i.e. cropland, grassland and paddy fields - 7 %) is concentrated in the valley bottoms (Fig. II.1.a). Farmland in general and paddy fields in particular are strongly connected to river networks through irrigation systems, which results in their high hydro-sedimentary connectivity with river networks Chartin et al. (2017). Built-up areas cover less than 1 % of the catchment surface area.

The catchment is located in a Dfa cold climate with no dry season and hot summer according to Köppen's climatic classification (Beck et al., 2018). The regional hydrological year runs from November to October (Laceby et al., 2016a; Whitaker et al., 2022). Over the last 30-years period (1991−2021), the mean annual temperature was 13.4 $\pm$ 0.5 °C y^{-1} (standard deviation = SD), ranging on average from -1.5 $\pm$ 0.9 °C to 30.5 $\pm$ 2.1 °C in January and August, respectively. Annual precipitation amounted to 1207 $\pm$ 216 mm y^{-1} (SD). Most of the precipitation occurs between June and October, corresponding to 60 % of the annual precipitation and 86 % of the rainfall erosivity (Laceby et al., 2016a). This period corresponds to the Japanese typhoon season, with a peak of intensity from July to September in Fukushima Prefecture. Daily precipitation and maximum hourly precipitation records from four stations (Fukushima City, Hippo, Iitate, and Soma) of the Automated Meteorological Data Acquisition System (AMeDAS) network located within less than 20 km from the catchment boundaries (Fig. II.1), were downloaded from the Japan Meteorological Agency website (JMA, 2023, in Japanese). The downloaded records covered the period from 1 January 2006 to the date of the sediment core sampling (8 June 2021). To identify typhoons and tropical storms, tracks of all tropical cyclones from the Regional Specialized Meteorological Center (RSMC) Tokyo - Typhoon Center (RSMC, 2023, 2024) were compared with local precipitation data, to identify those events that generated more than 60 and 100 mm of daily precipitation (Evrard et al., 2014). In addition, suspended sediment concentrations recorded at two hydrological stations located upstream of the Mano Dam reservoir were used (Tsuji et al., 2023). Sediment concentrations were measured at the first station (37.738391°N, 140.803943°E; Fig. II.1) at 5-min intervals from June 2014 to September 2016, and at the second station (37.733191°N, 140.807709°E; Fig. II.1) at 10-min intervals from January 2017 to December 2019. Daily suspended sediment fluxes were calculated from the instantaneous suspended sediment concentrations recorded by the hydrological stations.

In addition, the daily water level and discharge of the Mano Dam reservoir were downloaded from the Fukushima Prefecture website (Prefecture, 2021, in Japanese). According to the hydroelectric plant operators, the water level of the dam was generally maintained below 176 m, which results in more water discharge during extreme precipitation events. These massive releases of water increase the flow of water within the reservoir, which limits the potential for suspended sediment to settle and therefore reduces the amount of sediment deposited within the reservoir.

The catchment is mainly underlied by plutonic rocks (48 % in total, with 31 % granite and 17 % granodiorite), non-alkaline mafic volcanic rocks (42 %) and some sedimentary rocks (9 % in total, with 7 % marine and non-marine sediments, $<$ 1 % terrace and $<$ 1 % fan deposits) and few schists (about 1 %) (Fig. II.1.b).

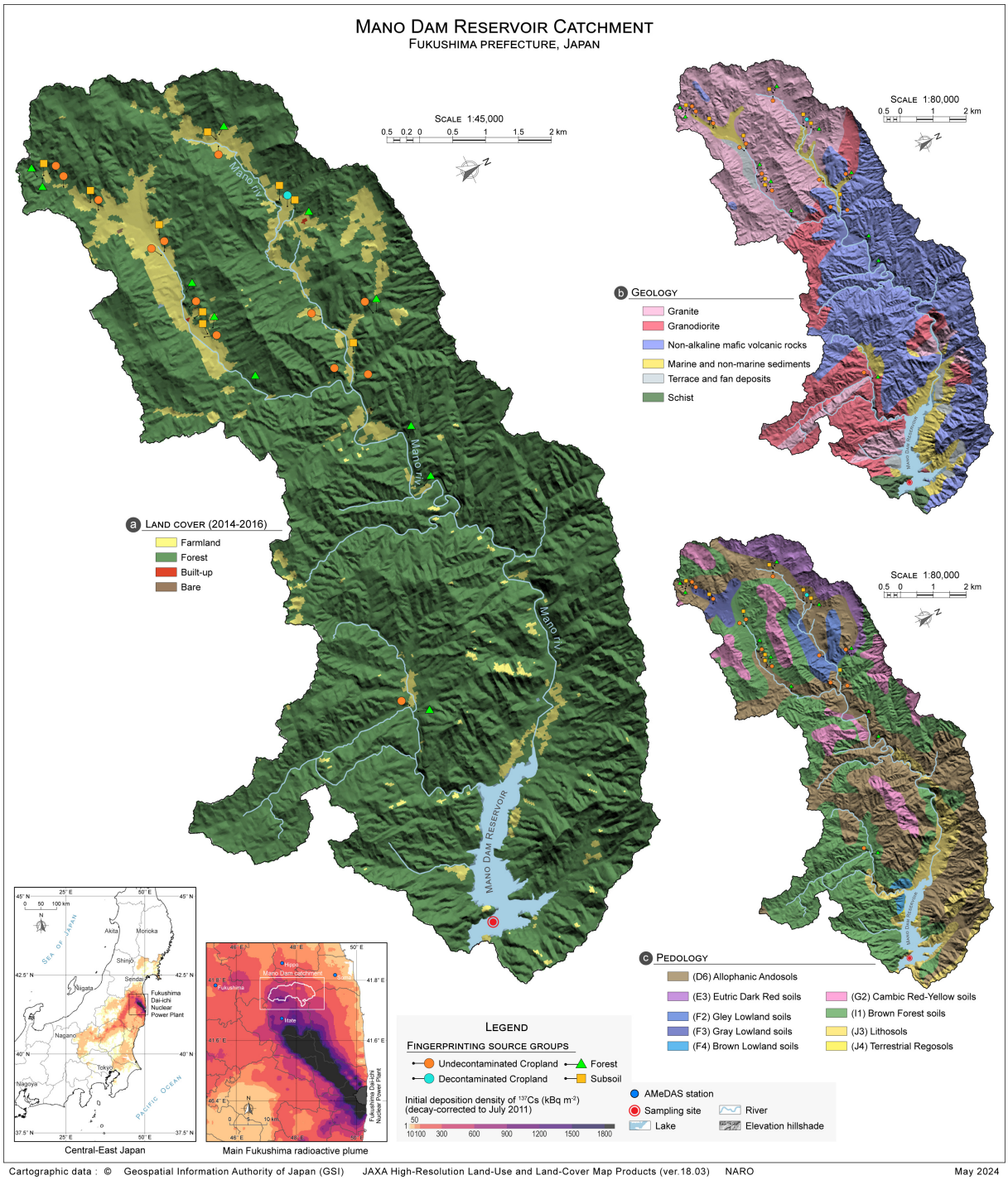


Figure II.1: Mano Dam reservoir catchment map of the main (a) land uses over the 2014-2016 period, (b) geological, and (c) pedological types with the location of source samples and sediment core sampling. Cartographic data from the Geospatial Information Authority of Japan (GSI), JAXA High-Resolution Land-Use and Lad-Cover Map Products 2014-2016 (ver. 18.03), and NARO).

According to the Comprehensive Soil classification System of Japan (Obara et al. (2011, 2015), with the equivalence of soil types given according to the World Reference Base for Soil Resources (WRB)), the main soil types in the catchment are Brown Forest Soils (37 % - WRB: Cambisols/Stagnosols) and Allophanic Andosols (36 % - WRB: Silandic Andosols) and then Cambic Red-Yellow Soils (9 % - WRB: Cambisols) and Lithosols (9 % - WRB: Leptosols) (Fig. II.1.c).

All maps and geographical processing were performed using the QGIS software (QGIS Development Team, 2022).

II.2.2 - Catchment management after FDNPP accident

The Mano Dam reservoir catchment is located in the northern part of the Iitate village, which was evacuated in 2011 due to high exposure dose rates exceeding 20 mSv per year at that time, in relation with high ^{137}Cs activities in soils ranging from 80 to 1,200 kBq m^{-2} (Kato et al., 2019). This part of the village of Iitate was submitted to a residential ban from 17 July 2012 to 31 March 2017 (MoE, 2023c, in Japanese). Decontamination were carried out in the area from June 2014 to December 2016 (MoE, 2018). The daily progress of decontamination during this period was reconstructed using records of plot decontamination dates provided by the Japanese Ministry of the Environment (MoE). However, despite this evacuation order, the main land use proportions classified by satellite remained relatively stable during this period extended from 2006 to 2020 (JAXA, 2016, 2018, 2022), as the catchment is dominated by forest, and cropland was maintained during the evacuation to prevent the development of trees prior to decontamination.

II.2.3 - Sediment core and soil sampling and processing

The sediment core was sampled using a gravity corer on 8 June 2021 in the downstream part of Mano Dam reservoir (37.72167°N, 140.83056°E) (Fig. II.1) 142 m below water level by the National Institute of Environmental Studies (Japan). The Mano Dam downstream core (IGSN: 10.58052/IETGC00WU) was 38 cm in length with a diameter of 11 cm and was sectioned into 38 layers with depth increments of 1 cm. Sediment core samples were dried at 40 °C for 96 h. Soil samples (n = 68) were collected in areas representative of the main potential sediment sources according to multiple previous fieldwork campaigns, literature review and stakeholder consultations (Evrard et al., 2015). They were collected as part of Laceby et al. (2016b) study and included 24 undecontaminated cropland, 10 remediated cropland, 24 forest and 10 subsoil (i.e. channel bank or landslide) samples. Soils were sampled with a plastic trowel and consisted of a composite of 10 sub-samples of topsoil (1-2 cm). All soil samples were dried at 40 °C for about 48 h and then successively sieved to 2000 μm to remove coarse material, and then to 63 μm to isolate the fraction bearing most of the ^{137}Cs (i.e. silt and clay; Sakaguchi et al. (2015)) and to minimise the effect of grain size sorting along the transport pathway (Walling et al., 2000).

II.2.4 - Laboratory analysis

A set of properties was measured on soil and sediment samples: radiocesium activity by gamma spectrometry (^{134}Cs and ^{137}Cs), organic matter composition determined by the combustion method coupled with an isotope ratio mass spectrometer (i.e. total organic carbon (TOC), total nitrogen (TN), δ^{13}C stable isotope ratio), elemental geochemistry analysed by X-ray fluorescence (ED-XRF) for 17 elements (i.e. Al, Ca, Co, Cr, Cu, Fe, K, Mg, Mn, Ni, Pb, Rb, Si, Sr, Ti, Zn and Zr), visible colourimetry indices by diffuse reflectance (i.e.

CIE Lab, CIE LCh), goethite peaks intensity at 445 and 525 nm (Debret et al., 2011), the 700 nm and 400 nm diffuse reflectance ratio (Q7/4; Debret et al. (2011)) and iron oxide-associated parameters derived from the remission function (A1, A2, A3 and Gt; Tiecher et al. (2015)). In addition, bulk density and particle size (grain size frequency, D10, D50, D90) by laser diffraction were measured in all sediment core samples. All analytical methods and calculations are described in the Supplementary Materials.

II.2.5 - Sediment source fingerprinting

The sediment source fingerprinting technique was conducted considering three potential sources: cropland, forest and subsoil. Subsoil refers to underlying materials exposed along riverbanks or by deep rill or gully erosion, especially under forests (Vandromme et al., 2023). As the main underlying rock is plutonic (48 %, Fig. II.1.b), most subsoil and fresh soil originate from the same material (i.e. granite saprolite). In addition, cropland underwent significant changes of properties during decontamination. However, when comparing the source signatures of subsoil and remediated cropland, virtually all properties showed the absence of significant differences (i.e. 25 out of 26 with a p value > 0.01; Supplementary Materials Tables II.SM-I and II.SM-II). Consequently, both sources were merged as subsoil. Care was taken to adjust the interpretation of the source contributions at the light of the progress of decontamination during the different stages of remediation.

II.2.5.1 - Tracer selection

The selection of tracers was performed according to the conventional three-step method (Mukundan et al., 2010; Sellier et al., 2020; Chalaux-Clergue et al., 2024a). The first two steps correspond to the identification of (1) conservative and (2) discriminant properties, subsequently referred to as tracers. Conservative properties were identified with a range test based on the hinge criterion - also referred to as interquartile range (IQR) - (Batista et al., 2022)). To consider a property as conservative, all sediment samples property values should lie within the range defined by source criteria values. The range tests were run using the 'range.tests' function from the fingR package (Chalaux-Clergue and Bizeul, 2023, ver. 1.1.1). Discriminant properties were identified with the Kolmogorov-Smirnov two-samples test using the 'fingR::discriminant.test' function. As Kolmogorov-Smirnov is a sensitive test, two sources were considered statistically different when the p value was below $\alpha = 0.01$. At least two sources must be statistically different to consider the property as discriminant. Finally, (3) a discriminant function analysis (DFA) forward stepwise selection based on Wilk's Lambda criterion was carried out on previously selected tracers (i.e. conservative and discriminant properties) using the function 'fingR::stepwise.selection'.

II.2.5.2 - Virtual mixtures

Virtual mixtures were generated to assess modeling accuracy (Palazón et al., 2015; Batista et al., 2022; Chalaux-Clergue et al., 2024a). A total of 138 virtual mixtures were generated using 'fingR::VM.builder' (contribution step = 0.05). Within the 'fingR::VM.builder' function, the virtual mixture contributions were first designed on a scale from 0 to 100 %, with 5 % increments corresponding to one source group contribution. Then, the two other source groups contributions were determined as fractions of the remaining contribution (i.e. 3/4 for source 2 and 1/4 for source 3). Afterwards, permutations of this contribution scale were determined, which generated a total of 138 unique combinations. Virtual mixture properties were determined as simple proportional mixtures of source property signatures (i.e. mean value). For each property, virtual

mixture contributions were multiplied with the source signature and then summed, which provided the virtual mixture property value.

II.2.5.3 - Un-mixing modeling

A multiple-modeling approach was followed to predict source contributions. Multiple-modeling consists of predicting the same property with independent models and then averaging their results. This approach is common in other similar fields of research (Duan et al., 2019; Bruni et al., 2022) and has shown an increase of the prediction quality (Guo et al., 2007). Source contributions were predicted using two common fingerprinting models: MixSIAR and the Bayesian Mean Model (BMM). The MixSIAR model is a Bayesian mixing model, and it was run with the MixSIAR package (Stock et al., 2020, ver. 3.1.12) with JAGS (Stock et al., 2022, ver. 4.3.1). The MixSIAR model was set with the "long" Markov Chain Monte Carlo chain length option (i.e. chain length = 300,000, burn-in = 200,000, thin = 100 and chain = 3) with a process error structure. The BMM (Batista et al., 2019) is a bootstrapping approach. It minimises the sum of square residuals of the mixing equation for each iteration of a Monte Carlo simulation (n = 7500). The model was constrained to ensure that source contributions were non-negative (lower bound = 0.001) and that their sum equaled 1. Predicted contributions were then re-scaled to 100 % to be expressed as a percentage. Each model convergence was determined by the Gelmand-Rubin diagnosis using the 'stable.GR' function from stableGR package (Knudson and Vats, 2022, ver. 1.2). None of the approaches had a value greater than 1.06.

II.2.5.4 - Accuracy assessment

Model prediction accuracy was assessed using the contributions predicted for virtual mixtures. The prediction accuracy of each model was evaluated based on different criteria (Chalaux-Clergue et al., 2024a): uncertainty (prediction interval width (W50)), residual error/bias (Mean error (ME)), performance (Squared Pearson correlation coefficient (r^2)), root-mean-square error (RMSE), Nash-Sutcliffe modeling efficiency coefficient (NSE) and continuous ranked probability score (CRPS)). Statistics were calculated using fingR functions: 'eval.groups' (ME, r^2, RMSE, NSE), 'interval.width' (W50) and 'CRPS'.

As shown in Chalaux-Clergue et al. (2024a), the comparison of the range of predicted contributions obtained for virtual mixtures and those contributions obtained for actual sediment samples appears to be relevant to assess the transferability of model accuracy metrics calculated with virtual mixtures to actual sediment samples. Indeed, virtual mixtures were generated as simple proportional mixtures of the mean properties of each source tracer. This implies that these tracers showed a strictly conservative behaviour. Therefore, as virtual mixtures were generated to represent a wide range of potential combinations of source contributions, varying from 0 to 100 % with 5 % increments, the range of their predicted contributions was expected to define the minimum and maximum of the possible predicted contributions. The occurrence of predicted contributions of actual sediment samples outside of this range implies the non-respect of some assumptions, such as the potential use of non fully-conservative tracers. To assess the transferability of the statistics calculated on virtual mixtures to actual sediment samples, the Encompassed Sample Predictions (ESP) was calculated. This value was calculated as the percentage of actual samples for which the predicted contributions remained within the lowest and the highest predicted contributions obtained for the virtual mixtures. When expressed as a percentage, ESP ranges from 0 to 100 %, the latter providing an optimal value. Values close to 100 % indicate a higher transferability of modeling evaluation statistics calculated on virtual mixture to actual sediment samples. ESP values were calculated using 'fingR::ESP' function.

All processing, analyses and modeling were performed using the R programming environment (R Core Team, 2022, ver. 4.2.2) within RStudio (RStudio Team, 2023).

II.2.6 - Identifying and dating sedimentation associated to extreme precipitation events

In the Fukushima region, extreme events (i.e. typhoon, tropical storm) that generate daily precipitation exceeding 60 to 100 mm (Evrard et al., 2014), have been shown to generate significant ^{137}Cs transfers (Chartin et al., 2013; Laceby et al., 2016a). Therefore, extreme precipitation events have been used as elementary time unit as they are responsible of the majority of sediment transfers, and they took place over short and precise periods of time. According to the study of Huon et al. (2018) in which four sediment were sampled at up-, mid- and downstream locations of the Mano Dam reservoir in November 2014, extreme precipitation events were characterised by the initial deposition of coarser organic-rich material followed by the gradual deposition of finer mineral particles at the downstream location of the Mano reservoir. According to the analysed properties (i.e. organic matter content, element geochemistry, visible colourimetry and grain size), the initiation of sediment deposition following an extreme event should be indicated by higher D10, D50, D90, TOC values, and lower SSA, L*, b*, Al, Si, Ti values, followed by a gradual shift towards the deposition of finer mineral particles. Based on the tipping point of properties between successive events, events can be identified.

The context of the Mano Dam reservoir catchment makes dating of sedimentation events a challenging task. Over the past two decades, the catchment has experienced extreme precipitation events with variable total rainfall depths (from 110 to 396 mm; Evrard et al. (2019a)) and different occurrence times during the year (from August to October) as shown in other studies (Laceby et al., 2016a; Evrard et al., 2019a; Vandromme et al., 2023). These differences likely significantly impact sediment transfers across the catchment and associated sediment records in the lake (Evrard et al., 2016). Furthermore, rapid changes in anthropogenic activities associated with decontamination have modified soil sensitivity to erosion and its composition (Feng et al., 2022; Evrard et al., 2019b). Following the evacuation of the area in July 2011 and its reopening to the population in March 2017 (MoE, 2018), the region remained devoid of human activity for 6 years and 9 months until decontamination was carried out. Most of this remediation took place between mid-October and December 2016, with 80 % of the remediated area being decontaminated during this period (Vandromme et al., 2023). Despite the reopening, the return of population and agricultural activities remain limited (Asanuma-Brice et al., 2023), allowing for natural vegetation to develop again after decontamination.

Accordingly, the identified events were dated by combining their ^{137}Cs activity distribution along the sediment core, and their comparison with that found in previously studied sediment cores (Huon et al., 2018), daily precipitation records and information on the progress of decontamination. The identification and dating of successive events was done within the Results section of the manuscript (sec. II.3.1.6 and II.3.2.5) to further calculate and understand calculation of the properties of the events (^{137}Cs activity and deposition flux per event, sediment transfer, and source contribution per event) without discussing it. However, the identification and dating were discussed within the Discussion section (sec. II.4.1).

II.2.7 - Extreme events averaged properties

After identification of successive sedimentation events in the sediment core, the average ^{137}Cs activity and source contributions of the entire extreme event were calculated. To do this, each sediment layer and the total event density were taken into account using the following formula:

$$X_{\text{event}} = \sum_{i=1}^{n} \frac{\rho_i}{\rho_{\text{event}}} X_i \ \text{; with} \ \rho_{\text{event}} = \frac{\sum_{i=1}^{n} \frac{\rho_i}{t_i}}{t_{\text{event}}} \tag{II.1}$$

With ρ the density (g cm^{-3}), t the layer thickness (cm), and X the property value of, respectively, the sediment layer i or the event, with n the number of sampling layers within the extreme event.

In addition, the Mass Accumulation Rate (MAR) for the core was calculated for each identified extreme event (expressed in g cm^{-2} event^{-1}). The MAR was calculated as the product of each event sedimentation accumulation rate (SAR, in cm^{-2} event^{-1}), corresponding to the quantity of sediment transported per extreme event or in other terms the event thickness in the core in cm, and the event bulk density (ρ_{event}, in g cm^{-3}).

$$\text{MAR}_{\text{event}} = SAR_{\text{event}} \cdot \rho_{\text{event}} \tag{II.2}$$

Using the predicted contributions of the potential sources, the quantitative contribution of each source was calculated as the product of relative contributions and MAR values. Finally, the ^{137}Cs deposition flux per extreme event (in Bq m^{-2} event^{-1}) was calculated, as the product of the extreme event MAR and ^{137}Cs activity.

$$\text{Flux}_X = \text{MAR}_{\text{event}} \cdot X_{\text{event}} \tag{II.3}$$

II.3 - Results

II.3.1 - Identifying sedimentation events

II.3.1.1 - Sediment core description

The sediment core displayed a pattern of fine sediment deposition (in average D50 = 23.4 $\pm$ 12.8 μm (SD)), with alternating darker and lighter brown layers. About six darker layers were identified from 5.4 to 28.7 cm depths, averaging 1.9 $\pm$ 0.9 cm (SD) of thickness (Figure II.2.a). Notably, two layers exhibited coarse plant debris from leaves or litter, just below a darker brown layer (i.e. at 10.1 and 13.8 cm). The unit between 19.6$-$22.1 cm, which contains two dark layers, 19.6$-$20.3 cm and 21.1$-$22.1 cm, appeared to be slightly disturbed as the layer was locally diffuse and lightly irregular. This was likely the result of the following extreme precipitation event. The most recent sediment, from the top to 6/7 cm, was lighter brown and more yellow than the nearby underlying sediments and closer to that of older sediments found below 28 cm. This was confirmed by their higher b* and L* values, about 16 % and 9 %, than the mean values for sediment between 7 to 28 cm (i.e. 12.4 $\pm$ 0.8 versus 10.7 $\pm$ 0.9, and 49.7 $\pm$ 0.9 versus 45.5 $\pm$ 2.6, respectively) (Fig. II.2.b and c).

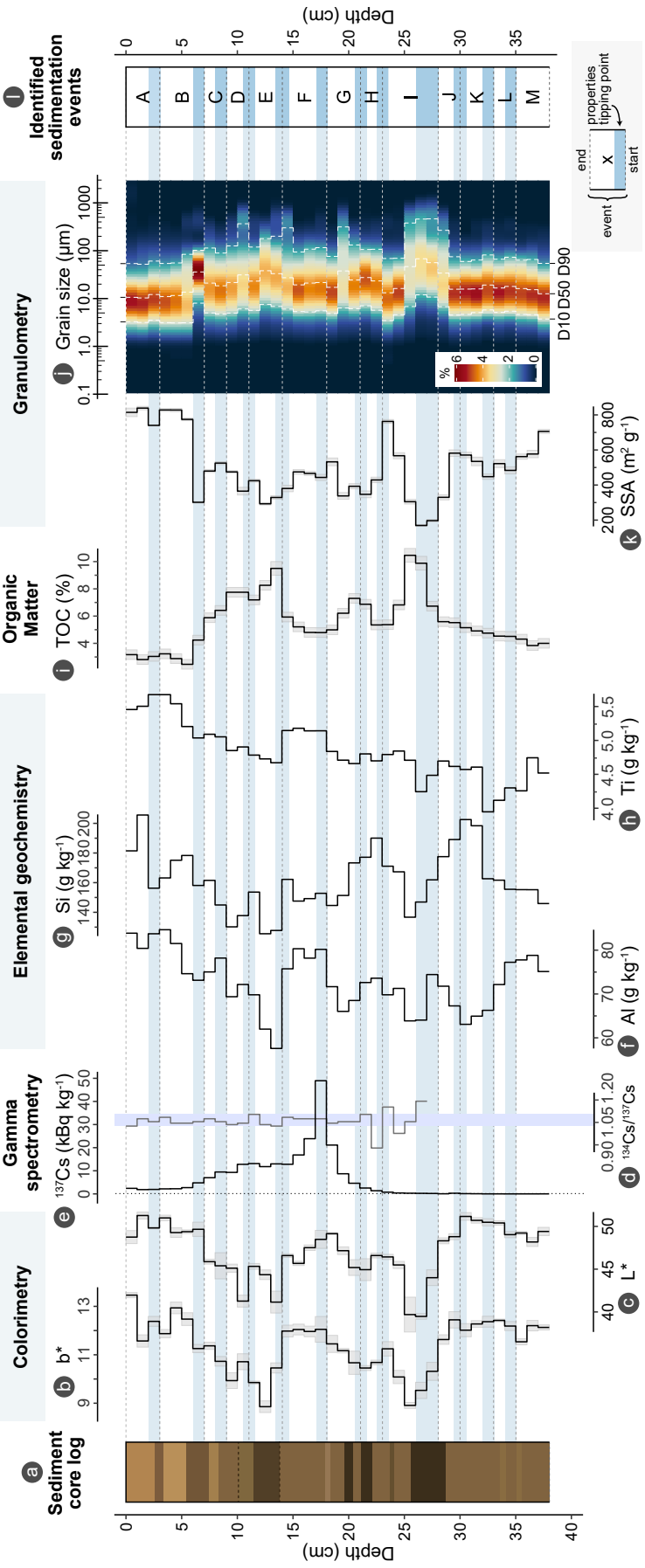


Figure II.2: Mano Dam reservoir (a) sediment core log and analysed properties, from left to right: colour indices: (b) L* and (c) b*, (d) $^{134}Cs/^{137}Cs$ ratio decay-corrected to 11 March 2011 along with the 1.06 $\pm$ 0.04 (standard deviation) range attributed to material exposed to Fukushima fallout (blue area) (Kobayashi et al., 2013), (e)^{137}Cs activity, elemental geochemistry of: (f) Al, (g) Si, (h) Ti, (i) total organic carbon (TOC) content, and granulometry: (j) frequency of grain size from 0.1 to 2500 μm along with the D10, D50 and D90 (white dashed lines) and (k) specific surface area (SSA), and (l) identified extreme precipitation events. Measurement uncertainties are displayed as a grey ribbon.

II.3.1.2 - Radiocesium activities

The $^{134}Cs/^{137}Cs$ ratio from 22 cm to the top of the sediment core remained within the range of 1.06 $\pm$ 0.04 (SD) attributed to material exposed to Fukushima fallout (Kobayashi et al., 2013) (Fig. II.2.d). Consequently, sediment layers above 22 cm were inferred to have deposited after the FDNPP accident.

The depth distribution profile of ^{137}Cs was characterised by a distinct peak of about 50 kBq kg^{-1} at 17$-$18 cm depth (Fig. II.2.e). Below this peak, the ^{137}Cs activity exponentially decreased until reaching a stable level of about ten Bq kg^{-1} (i.e. from 7 to 19 Bq kg^{-1}) for layers deeper than 32 cm, consistent with expected pre-accidental levels (Fukuyama et al., 2010). Conversely, above this peak, from 14 to 11 cm, activities rapidly decreased down to a plateau of about 13 $\pm$ 0.5 kBq kg^{-1} (SD). Following this, a gradual decrease of activity was observed from 8 to 5 cm, with the ^{137}Cs activity decreasing from 9.7 to 2.3 kBq kg^{-1}, then reaching a lower plateau of about 2.2 $\pm$ 0.2 kBq kg^{-1} (SD) from 5 cm depth to the top of the sediment core.

II.3.1.3 - Elemental geochemistry

Among the geochemical elements analysed, Al, Si, and Ti showed similar variations along the sediment core, with Ti showing lower variations (Fig. II.2.f, g, and h). Along the sediment core, four zones (i.e. 9$-$10, 12$-$14, 19$-$21, 25$-$27 cm) were characterised by a decrease of concentrations in these elements, with reductions of 11 %, 13 %, and 5 %, respectively, compared to the surrounding layers. Furthermore, the most recently deposited sediments, from 5 cm depth to the top of the core, showed marked increases in Al and Ti concentrations, by 15 % and 17 %, respectively, compared to previously deposited sediments (Fig. II.2.g and h).

II.3.1.4 - Organic matter

The TOC content varied along the sediment, and was characterised by four distinct peaks (i.e. 9$-$11 cm, 12$-$15 cm, 20$-$22 cm, and 25$-$27 cm) of higher TOC contents, with an increase from about 39 % to 100 % (ranging from 7.1 to 10.2 $\pm$ 0.4 % (SD)) compared to the surrounding sediments (i.e. 5.1 $\pm$ 0.8 % (SD)) (Fig. II.2.i). In addition, the sediment from 6 cm to the top of the sediment core exhibited significantly lower TOC contents averaging 2.9 $\pm$ 0.3 %, which was 59 % lower than for previously deposited sediment.

II.3.1.5 - Grain size and specific surface area

Along the sediment core, distinct peaks of coarser grain size and lower SSA were identified (i.e. 10$-$11 cm, 14$-$15 cm, 19$-$20 cm and 25$-$29 cm) (Fig. II.2.j and k). These peaks were characterised by a sharp increase of D50 and D90 values, in average, by about 130 % and 280 %, respectively, a moderate increase of D10 (by about 47 %), and a decreased SSA by about 36 %, compared to surrounding sediment layers (D10 = 5 $\pm$ 1 μm, D50 = 20 $\pm$ 6 μm, D90 = 96 $\pm$ 37 μm, SSA = 516 $\pm$ 101 $m^2\ g^{-1}$). These peaks, for which mainly D50, D90 and SSA varied, were likely to reflect a greater amount of coarse particles.

In addition, sediment from 7 to 15 cm showed less uniform grain size distribution compared to underlying sediments ($<$ 30 cm), despite a less marked variation of SSA. This suggests a greater frequency of recorded events than deeper in the sediment core (i.e. more events over a shorter depth) as well as the supply of more similar material (Fig. II.2.j).

Conversely, the most recently deposited sediments, from 5/6 cm to the top of the sediment core, showed

a high homogeneity with fine sediment, comparable to that of sediment below 29 cm. However, their grain sizes were found to be the lowest along the sediment core (D10 = 3 $\pm$ 0 μm, D50 = 11 $\pm$ 1 μm, and D90 = 59 $\pm$ 11 μm), and they showed the highest SSA (816 $\pm$ 24 $m^2\ g^{-1}$).

II.3.1.6 - Identifying sedimentation events along the sediment core

According to the comparison of the properties, including elemental geochemistry, organic matter, visible colourimetry and grain size, and criteria defined in sec II.2.6 a total of 13 sedimentary events were identified along the sediment core, systematically labelled alphabetically from the top to the bottom (Fig. II.2.l).

II.3.2 - Dating of events

II.3.2.1 - Identification of extreme precipitation events

From the FDNPP accident in March 2011 to the sediment core sampling in June 2021, 27 and 6 extreme precipitation events that generated more than 60 or 100 mm d^{-1} of daily precipitation, respectively, were identified (Fig. II.3.a). Of these, 17 were major tropical storms and typhoons (Fig. II.3.a; Supplementary Materials Table II.SM-III). Whilst some years were devoid of extreme precipitation events (i.e. 2012 and 2018), most years recorded one such event (i.e. 2017 and 2020), other years recorded two (i.e. 2013 and 2015) or even three events (i.e. 2014, 2016 and 2019).

Among the 27 extreme precipitation events, 16 events led to exceptionally high cumulative precipitation exceeding 100 mm. Among those 16 events only six events yielded cumulative precipitation exceeding 150 mm: typhoon Roke in September 2011 (ID: 1105 - 259 mm), extra-tropical cyclone Etau in September 2015 (ID: 1518 - 396 mm), tropical storm Chanthu (ID: 1607 - 197 mm) and severe tropical storm Lionrock (ID: 1610 - 157 mm) in August 2016, extra-tropical cyclone Lan in October 2017 (ID: 1721 - 264 mm) and typhoon Hagibis in October 2019 (ID: 1919 - 372 mm). Moreover, some events occurred successively within a 10-days period, such as typhoon Phanfone (ID: 1418 - 130 mm) and extra-tropical storm Vongfong (ID: 1419 - 94 mm) in October 2014, Chanthu and Lionrock in August 2016, and Hagibis and extra-tropical cyclone Bualoi (ID: 1921 - 129 mm) in October 2019.

II.3.2.2 - Extreme precipitation events and reservoir management

Extreme precipitation events that generated more than 60 mm of daily precipitation consistently led to daily water discharges exceeding the usual discharges (i.e. 87×10^3 $m^3\ d^{-1}$; Fig. II.3.a, b and c). The extreme precipitation events of 2014, 2017 and 2020, which had equivalent precipitation levels, led to similar water discharges by dam operators (about 20-30 $m^3\ s^{-1}$; Fig. II.3.a and c; Supplementary Materials Fig. II.SM-2 and Table II.SM-IV). However, the 2016 event, characterised by a series of moderate extreme precipitation events (daily precipitation between 60 and 100 mm; Fig. II.3.a), resulted in higher water discharges and a prolonged discharge period (35.8 versus about 19.5 $m^3\ s^{-1}$ on average; Fig. II.3.c; Supplementary Materials Fig. II.SM-2 and Table II.SM-IV) despite relatively low dam water levels (Fig. II.3.b). The exceptionally high cumulative precipitation events of 2015 and 2019 led to maximum daily water discharges that were two to ten times higher than those associated with the 2014, 2016, 2017 and 2020 events (203.3 and 364.8 $m^3\ s^{-1}$, respectively; Supplementary Materials Fig. II.SM-2 and Table II.SM-IV).

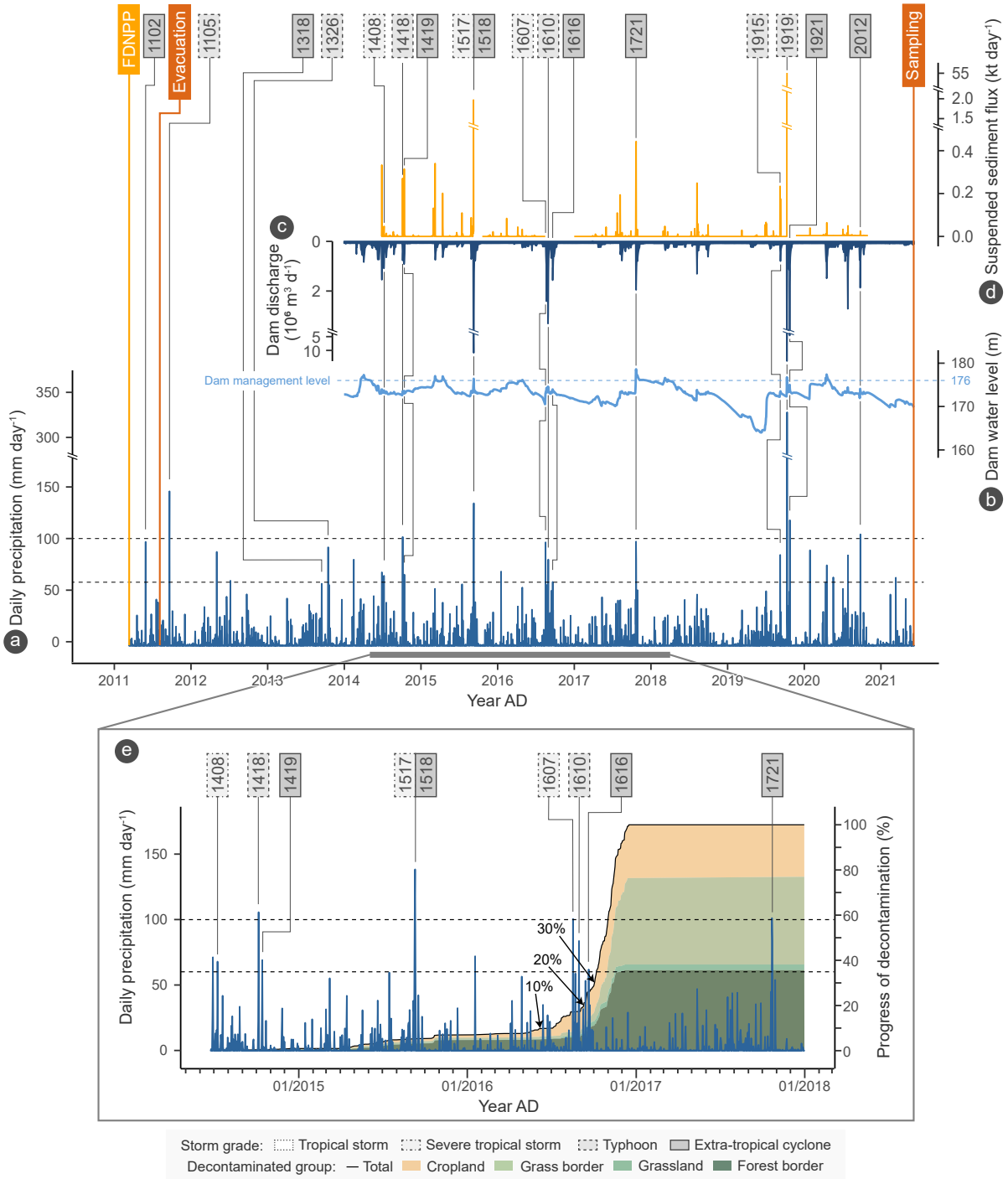


Figure II.3: (a) Mean daily precipitation at the four precipitation monitoring AMeDAS stations surrounding the Mano Dam reservoir catchment between March 2011 and June 2021, reservoir dam (b) water level and (c) water discharge between January 2014 and June 2021, (d) suspended sediment flux at the hydrological station upstream the reservoir, and (e) the progress of decontamination as of cumulative proportion of the total decontaminated area under contrasted land uses (cropland, grass border, grassland, forest border). Extreme precipitation events ranked as extra-tropical cyclone (solid), typhoon (dash), severe tropical storm (dot-dash) and tropical storm (dot) that generated more than 60 or 100 mm of daily precipitation (horizontal dotted lines, Evrard et al. (2014)) are identified by their international number ID. The progress of the total decontaminated surface area with the successive levels of 10 %, 20 % and 30 % are indicated. The grey bar in sub-figure (a) represents the time frame displayed in sub-figure (b).

Water level management procedures differ significantly depending on the amount of precipitation during an extreme event (Supplementary Material Fig. II.SM-2 and Table II.SM-IV). In 2015 and 2019, during higher-magnitude precipitation events, water level of the dam systematically exceeded the water level management threshold (i.e. 176 m). Dam operators responded rapidly to this increased water inflow (max. 349.3 and 695.0 m^3 s^{-1} versus from 40 to 200 m^3 s^{-1} for lower-magnitude events; Supplementary Materials Fig. II.SM-2 and Table II.SM-IV), leading to large variations in water levels over a short period, about 4.9 and 7.3 m (max. water level 177.6 and 179.5 m), respectively. During the 2015 events, it took about 12 h to return below the water level management threshold and 15 h for the 2019 event. Conversely, lower-magnitude events, such as those that occurred in 2014, 2017, and 2020, which showed lower inflows, only the 2017 event exceeded the water level management threshold (max. 178.9 m). This pattern allowed for a smoother dam management and more gradual water level changes, about 1.4 to 4.1 m managed from two to more than four days. However, despite the fact that the 2017 event was associated with a large water level change of 5.9 m (max. water level 178.9 m), dam management was not associated with large water discharge, and it took 16 days to return to the management level.

II.3.2.3 - Deposited sediment flux to the reservoir

Over the recorded period, significant suspended sediment fluxes at the reservoir inlet were highly associated with extreme precipitation events and occurred over a short period of time (Fig. II.3.d). Some isolated precipitation events, with daily precipitation below 60 mm, resulted in some sediment transfer. These events were always associated with higher than usual water discharges (Fig. II.3.c and d). The lower-magnitude events of 2014, 2017 and 2020, which had similar precipitation levels, led to different maximum suspended sediment fluxes: about 12 to 20.4 kg s^{-1} and 20.5 kg s^{-1} in 2014 and 2017, respectively, and 0.5 kg s^{-1} in 2020 (Fig. II.3.d; Supplementary Materials Fig. II.SM-2 and Table II.SM-IV). The higher-magnitude events of 2015 and 2019, resulted in maximum suspended sediment fluxes of 169.7 and 7495.1 kg s^{-1}, until the monitoring stations were damaged, which was about 10 and 430 times higher than those observed on average during lower-magnitude events.

II.3.2.4 - Decontamination progress and extreme rainfall events

From June 2014 to December 2016 (i.e. 31 months), a total of 8.2 km^2 underwent decontamination, representing 12 % of the total catchment area of the Mano Dam reservoir (Fig. II.3.e). Within the decontaminated area, the majority (66 %) of the operations did not involve the addition of fresh soil, as it concentrated in the remediation of grass borders (i.e. grass strips adjacent to cultivated plots, nearby roads, and houses) (3.2 km^2, 39 %), forest borders (2.9 km^2, 35 %) and grassland (0.2 km^2, 2 %). Remediated cropland accounted for 1.8 km^2, representing only 22 % of the total decontaminated area and 3 % of the total catchment area. Most of the decontamination (80 %) occurred in the last four months of 2016, from 10 September to 31 December. In contrast, only 10 % of the total area underwent decontamination during the 25 months that occurred between the initiation of decontamination in June 2014 and 7 July 2016.

Until mid-2016, the progress of decontamination remained limited, and affected a marginal area which was unlikely to be reflected in sediment records associated to extreme precipitation events that occurred since 2014 (Fig. II.3.e). However, in the six weeks preceding the occurrence of Chanthu and Lionrock events in August 2016, significant progress was made in decontamination, mainly under cropland. Within this period, an additional 0.44 km^2 of cropland was decontaminated, representing 24 % of the total area of decontaminated cropland and 5 % of the catchment area. Conversely, over the 26 months since the initiation of decontamina-

tion, only 0.29 km^2 (16 %) had been decontaminated. However, the majority of decontamination (83 %) was carried out after the two extreme events that occurred in August 2016 (Chanthu and Lionrock). Following the completion of decontamination in December 2016, the subsequent extreme precipitation event, Lan, occurred in October 2017.

II.3.2.5 - Dating of identified sedimentation events

The sediment core analysis revealed a single peak of ^{137}Cs activity at 17-18 cm layer, indicating the occurrence of the FDNPP accident (Fig. II.2.d). The exponential decrease of ^{137}Cs activity below the 17-18 cm layer suggest downward diffusion over time as observed in other lacustrine sediment cores (Cao et al., 2017; Funaki et al., 2022). This peak aligned with sedimentation event F (from 14 to 18 cm, Fig. II.2.k), suggesting that all the sedimentation events below it occurred prior to March 2011. In relation to the objectives of the study, among all the sedimentation events identified in section II.3.1.6, events G through M were not assigned to specific extreme precipitation events.

In September 2011, typhoon Roke generated exceptionally high cumulative precipitation (Fig. II.3.a and Supplementary Materials Table II.SM-III). This event, resulted in significant sediment transfers in response to a high hydro-sedimentary connectivity (Chartin et al., 2017) and high erositivity (Laceby et al., 2016a). Consequently, the event F was associated with the occurrence of Roke in September 2011 (Fig. II.4).

In addition, in November 2014, Huon et al. (2018) collected two sediment cores (referred to as DD1 and DD2) at the same location as the core analysed in the current study. When comparing the distribution of ^{137}Cs activity and TOC content between these sediment cores revealed high similarities between the DD1 $0-30$ cm and DD2 $0-15$ cm sections and the 11-24 cm section of our sediment core (Supplementary Materials Fig. II.SM-1). This suggests that the sediment deposition below 10 cm occurred before November 2014. Thereafter, between event F and 10 cm depth, only one event was identified, event E (Fig. II.4). While no extreme event occurred in 2012, two events took place in 2013 and two more in 2014. Although 2013 and 2014 were affected by events of similar intensity, the events in 2014 occurred within a 10 days period and later in the year (October) than in 2013 (September and October). Events occurring close together were more likely to generate erosion due to soil saturation. In addition, as the events in 2014 occurred later in the year, the vegetation cover was less developed and therefore less prone to protect the soil from erosion. Accordingly, event E was associated with the occurrence of typhoons Phanfone & Vongfong in October 2014 (Fig. II.4).

In the Mano Dam reservoir catchment, after 2014, the next significant change in terms of land use was the implementation of decontamination. As most of the decontamination took place at the end of 2016 and after the extreme precipitation events of the year, the effects of decontamination could only be visible from the subsequent year events (i.e. from 2017) (Fig. II.3). Notably, within the sediment core, an abrupt change of properties was observed for sediment from 0 to 7 cm depth, contrasting with previously deposited sediment layers (Fig. II.2). Moreover, their properties tended towards those characteristics of subsoil or fresh soil (Fig. II.2; Supplementary Materials Table II.SM-III), which suggests that decontamination had occurred before their deposition (Evrard et al., 2019a; Feng et al., 2022). Within this interval, two sedimentation events were identified: events A and B (Fig. II.2). Subsequently, between 2017 and the sediment core sampling in June 2021, only two major precipitation events occurred: Lan in 2017 and Hagibis & Bualoi in 2019 (Fig. II.3). In 2017, although Lan was a moderate event in terms of cumulative precipitation, it generated a higher sus-

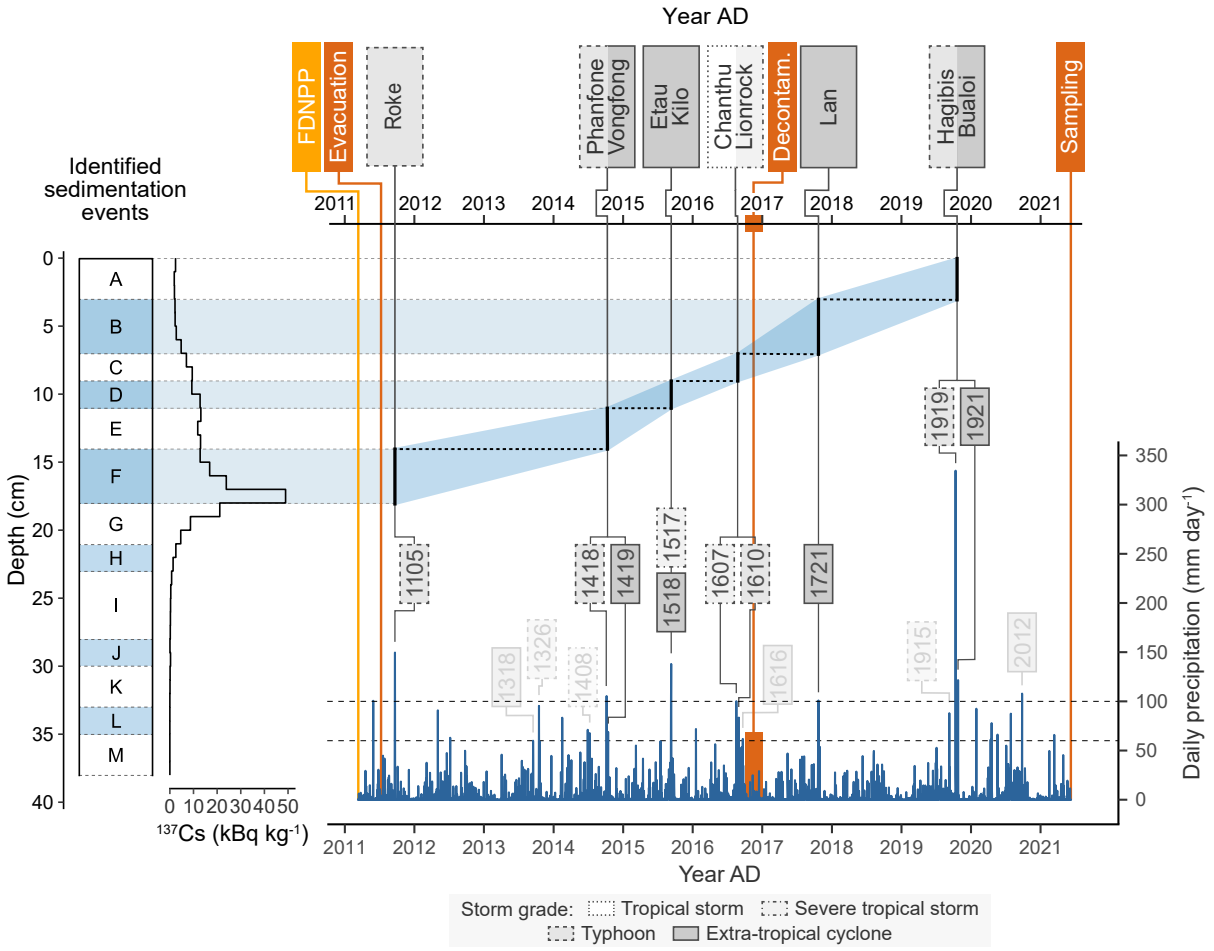


Figure II.4: (a) Identification of extreme precipitation events-associated deposits and (b) dating of these identified deposits by comparing ^{137}Cs distribution along the sediment core, progress of decontamination, and the extreme precipitation events that occurred since the Fukushima Daiichi Nuclear Power Plant (FDNPP) accident in March 2011. Decontam. stands for decontamination. Extreme precipitation events ranked as extra-tropical cyclone (solid), typhoon (dash), severe tropical storm (dot-dash) and tropical storm (dot) that generated more than 60 mm of daily precipitation (horizontal dotted line, Evrard et al. (2014)) are identified by their international number ID and named when associated with a deposit.

pended sediment flux than previous equivalent events (i.e., versus 2014 events; Fig. II.3.a and c). In addition, the dam operators operated a moderate water discharges and kept the water level at the management level for the next six months (i.e. about 175-176 m until April 2018; Fig. II.3.b and c), which likely allowed the deposition of a large proportion of the eroded sediment. In contrast, in 2019, Hagibis & Bualoi generated large cumulative precipitation and large suspended sediment fluxes at the reservoir inlet (Fig. II.3.a and d). The dam operators therefore operated large water releases and managed the water level to rapidly return to about 173 m (Fig. II.3.b and c). This water level management likely accelerated water flow within the reservoir and thus limited sediment deposition. Hagibis & Bualoi was likely under-represented in the sediment record. In summary, both events, Lan and Hagibis & Bualoi, were likely recorded in the sediment. Despite the moderate intensity of Lan, dam management likely allowed better sedimentation during this event than during Hagibis & Bualoi. Therefore, Lan and Hagibis & Bualoi events were associated with sedimentation events B and A, respectively (Fig. II.4).

Lastly, two sedimentation events were identified between 7 and 14 cm: event C and D. Corresponding to the dating of events discussed earlier, these events occurred between early 2015 and mid-2016. In October 2015, the simultaneous occurrence of Etau and Kilo generated high precipitation and erosivity (Laceby et al.

(2016a); Fig. II.3.a), which resulted in large suspended sediment fluxes at the reservoir inlet (Fig. II.3.d). The dam operators therefore operated large water releases and managed the water level to rapidly return to about 173 m (Fig. II.3.b and c), which likely limited sediment deposition. In contrast, August 2016, Chanthu & Lionrock were two moderate events that occurred within a 10 days period. The dam operators operated moderate water discharge and remained well below management level (Fig. II.3.c), which likely affected to a limited extent sediment deposition. In addition, Chanthu & Lionrock occurred just before the acceleration of decontamination. Consequently, the sedimentation events C and D were associated to Etau-Kilo in October 2015 and Chanthu & Lionrock in August 2016, respectively (Fig. II.4).

II.3.3 - Source sediment fingerprinting

II.3.3.1 - Origin of organic matter

Undecontaminated cropland, remediated cropland, and subsoil had similar δ^{13}C mean values, respectively, with -25.0 $\pm$ 1.1 ‰ (SD) (range: -27.7 ‰ to -22.9 $\pm$ 0.1 ‰), -24.4 $\pm$ 1.5 ‰ (-26.2 ‰ to -22.0 $\pm$ 0.1 ‰) and -25.4 $\pm$ 1.0 ‰ (-27.0‰ to -23.6 $\pm$ 0.1 ‰) (Fig. II.5; Supplementary Materials Table II.SM-I and II.SM-II). However, the δ^{13}C values of the forest were significantly lower than those of undecontaminated and remediated cropland, -26.3 $\pm$ 1.1‰ (-27.8 ‰ to -23.5 $\pm$ 0.1 ‰) (Supplementary Materials Table II.SM-I and II.SM-II).

Conversely, with the exception of subsoil and remediated cropland, all sources differed significantly in TOC/TN values (Supplementary Materials Table II.SM-I and II.SM-II). Forest had the highest TOC/TN values with a mean of 15.4 $\pm$ 2.3 (SD) (range: 9.8 to 19.7 $\pm$ 2.1), followed by undecontaminated cropland (11.9 $\pm$ 1.4 $-$ 9.6 to 16.3 $\pm$ 2.1), subsoil (11.6 $\pm$ 1.6 $-$ 8.2 to 13.5 $\pm$ 2.1) and remediated cropland (10.3 $\pm$ 2.0 $-$ 6.3 to 13.0 $\pm$ 2.1) in decreasing order (Fig. II.5). Remediated cropland and subsoil and cropland signals were closer to the soil organic matter signature, while that of forest was closer to plant debris signature. The δ^{13}C and

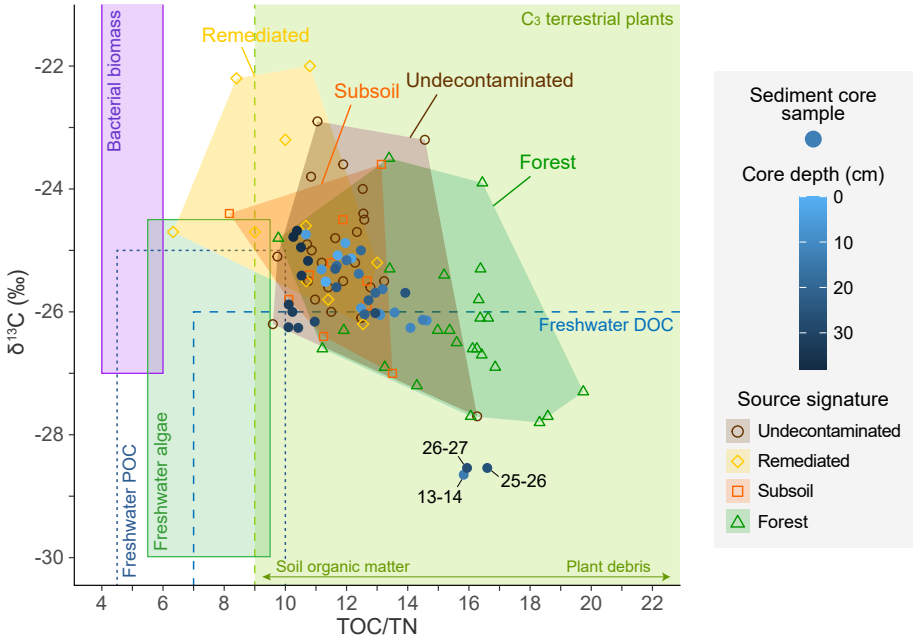


Figure II.5: Signatures of δ^{13}C and TOC/TN in potential sources and in sediment core samples along with typical ranges for organic inputs to clay-sized dominant terrestrial environments (according to Lamb et al. (2006) and Amorim et al. (2022)). Sediment core samples showing values lying outside of the range found in potential sources are indicated by their depth intervals (cm). TOC stands for total organic carbon; TN for total nitrogen; POC for particulate organic matter; DOC for dissolved organic matter.

TOC/TN values of the sediment samples were included within the range of values found in potential sources, with the exception of three samples (Fig. II.5). The δ^{13}C values of the sediment samples varied from -28.65 ‰ to -24.68 $\pm$ 0.04 ‰, and their TOC/TN values changed from 10.1 % to 16.6 $\pm$ 2.1 %. However, three sediment samples lied outside of the space defined by potential sources (i.e. 13−14, 25−26 and 26−27 cm). These three sediment samples were similar and characterised by very low δ^{13}C values (respectively -28.65 ‰, -28.54 ‰ and -28.54 $\pm$ 0.04 ‰) and high TOC/TN values (respectively 15.8 %, 16.6 % and 15.9 $\pm$ 2.1 %). However, all the sediment samples had signatures plotting within the range of typical C_3 terrestrial plants organic inputs (Fig. II.5) (Lamb et al., 2006; Amorim et al., 2022).

II.3.3.2 - Tracer selection

Of the 24 properties measured and analysed on potential source soil samples and sediment core layers (Supplementary Materials Table II.SM-III), only ten were found to show a conservative behaviour when tested according to the hinge criterion range test (TOC, TN, Al, Si, Ti, L*, b*, C*, Q7/4, G_{525}) (Fig. II.6). Among these ten conservative properties, only Ti did not significantly (*p* value $<$ 0.01) discriminate between potential sources (i.e. cropland, forest, subsoil). This resulted in the selection of eight tracers. These tracers consist of two organic matter parameters (TOC, TN), two geochemical elements (Al, Si) and five colour parameters (L*, b*, C*) and indices (Q7/4, G_{525}). Among the eight potential tracers, a suite of four tracers was selected by the DFA stepwise selection (Al, Si, b*, C*).

Different levels of source discrimination were observed among the eight tracers. Half of the tracers provided strong and equivalent discrimination capacity of the potential sources (TOC, TN, Al, L*, G_{525}). Conversely, the other half did not significantly discriminate between forest and undecontaminated cropland sources (Si, b*, C*). Therefore, sediment source fingerprinting modeling was run using the tracer selection obtained prior to DFA stepwise selection (TOC, TN, Al, Si, Ti, L*, b*, C*, Q7/4, G_{525}).

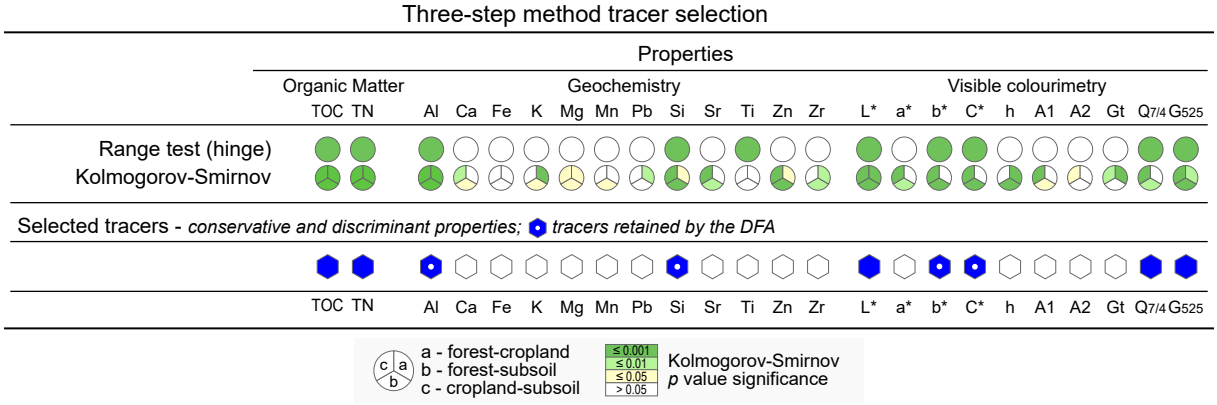


Figure II.6: Tracer selection according to the Three-Step Method using range test hinge criteria. Green filled circles and portions indicate a property that passed the conservativity (i.e. range test) and the discriminant power (i.e. Kolmogorov-Smirnov two-samples test *p* value $<$ 0.01) tests, respectively. Blue filled diamonds indicate selected tracers (i.e. properties that passed both conservativity and discriminant power tests) and blue diamonds with white dots indicate tracers retained by the discriminant function analysis (DFA) forward stepwise selection based on Wilk's lambda criterion. TOC stands for total organic carbon.

II.3.3.3 - Sediment source fingerprinting modeling

Modeling accuracy metrics obtained with MixSIAR and BMM were strongly similar among sources (Supplementary Materials Table II.SM-V). The largest differences were found in terms of model performance for undecontaminated cropland and forest. In any case, results were better for the multiple model approach than those obtained with each model run independently. On average, the multiple model bias (ME) and linearity (r^2) were intermediate, whereas accuracy (RMSE) and modeling efficiency (NSE) were slightly higher than for the individual model approach.

Regarding the relationship between the theoretical and the predicted contributions for the virtual mixtures, different tendencies were observed (Fig. II.7.a, b and c). The subsoil and forest contributions were well predicted, despite that forest tended to be under-predicted above 30 % of theoretical contributions (Fig. b and c). The undecontaminated cropland contributions prediction quality was lower although being rather linear,

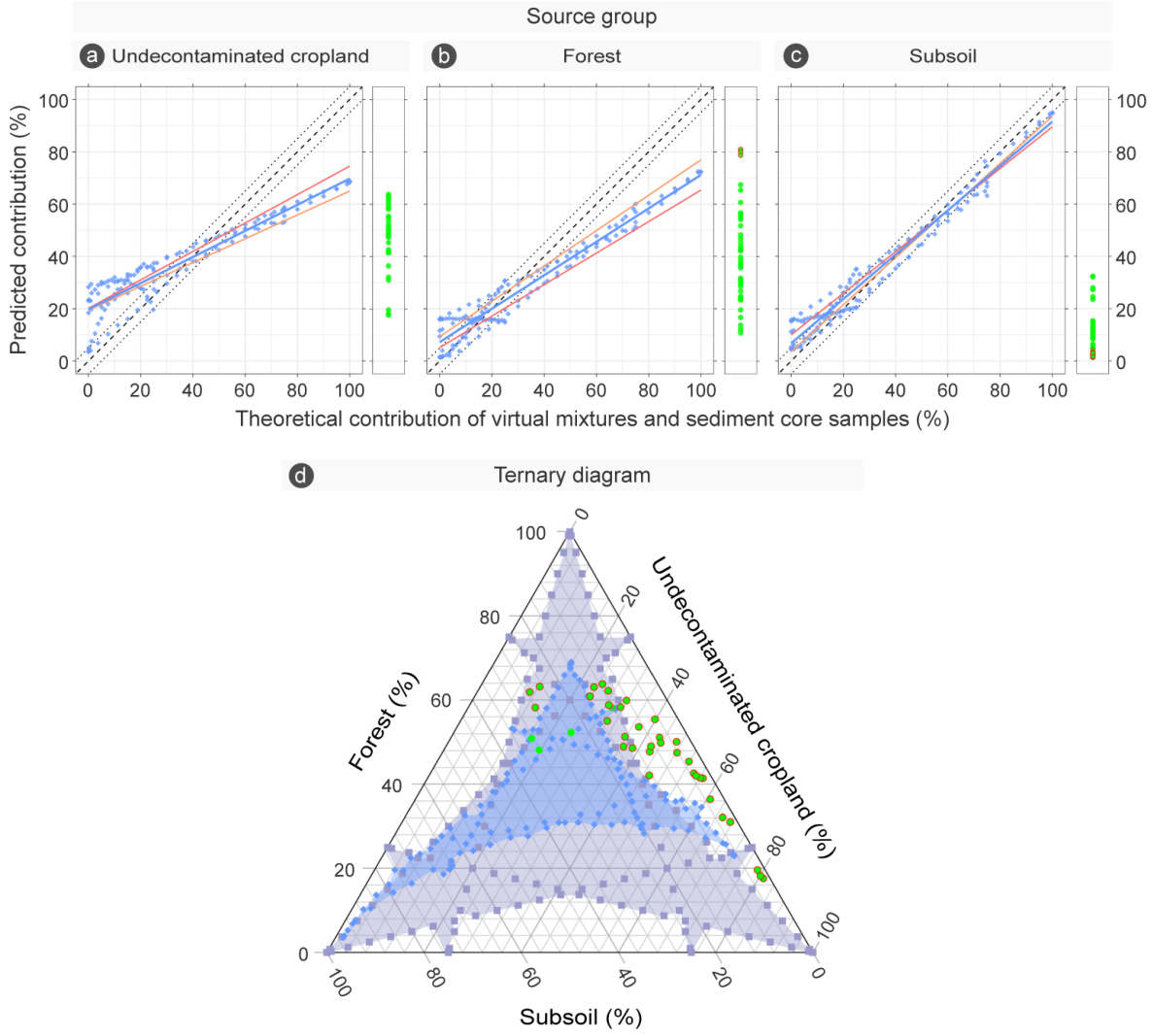


Figure II.7: Relationship between theoretical and predicted contributions of the virtual mixtures (blue diamond) for each source: (a) undecontaminated cropland, (b) forest, (c) subsoil, of the multiple model (blue line) as the average of MixSIAR (red line) and Bayesian Mean Model (orange line) predictions along with actual Mano Dam sediment core samples predicted contributions (green circle). (d) Ternary plot of the theoretical (light blue diamond) and predicted (blue diamond) contributions of the virtual mixtures and predicted contributions of the Mano Dam sediment core samples (green dot). Mano Dam sediment core samples with predicted contributions outside of the range/space defined by the predicted contributions of the virtual mixtures are circled in red.

and were over-predicted below 40 % of theoretical contributions and under-predicted above it (Fig. II.7.a).

When evaluating the transferability of the model accuracy metrics derived from virtual mixture predictions to those of actual sediment samples, notable differences were found across sources (Fig. II.7.a, b and c). The actual sediment samples predictions for undecontaminated cropland and forest contributions closely aligned with those from virtual mixtures, with ESP of 100 % and 92 %, while subsoil predictions exhibited lower consistency, with ESP of 66 % (Supplementary Materials Table II.SM-V). However, when considering theoretical and predicted contributions of virtual mixtures simultaneously for all three sources (Fig. II.7.d), the predicted contribution space appeared contracted compared to the initial theoretical space. This contraction was mainly related to the narrower range of predicted contributions for uncontaminated cropland (from 4 % to 69 %), and the lower maximum for forest contributions (73 %). Only three out of 38 sediment samples had predicted contributions within the virtual mixtures space, about 15 samples were close to this space. Sediment samples located the furthest from this space were characterised by low predicted subsoil contributions ($<$ 10 %) and balanced contributions from forest and uncontaminated cropland. Modeling accuracy metrics are therefore likely not fully transferable to model outputs obtained for actual sediment samples.

II.3.4 - Evolution of sediment transfers and sources throughout time

Following the accident, there were notable changes in both the quantitative (MAR) and qualitative (sources) sediment transfer pattern associated to extreme precipitation events (Fig. II.8.a). The first typhoon following the accident, Roke in September 2011, likely reflected the pre-accidental sources contributions, characterised by a cropland dominance (about 54 %), followed by forest (about 35 %) and subsoil (about 10 %) (Fig. II.8.a; Supplementary Materials Table II.SM-VI). However, this event resulted in sediment accumulation about twice-fold compared to pre-accidental levels (MAR = 1.87 versus 0.96 $\pm$ 0.25 g cm^{-2} event^{-1}). This significant increased sediment deposition was likely a consequence of the intensity of the event and the landscape disturbances after the Great Tōhoku Earthquake, including landslides and bank collapses, which have not been immediately dealt with given the subsequent evacuation order (July 2011).

During the abandonment period, the three sedimentation events that occurred (2014, 2015 and 2016) were characterised by MAR values closer to pre-accidental levels although they showed significant changes in source contributions. In 2014 and 2015, there was a significant decrease of quantitative contributions of undecontaminated cropland (24 % and 39 %), while those of forest increased (41 % and 11 %) compared to pre-accidental levels. Conversely, in 2016, the MAR slightly increased compared to 2015 (6 %), along with an increase of the quantitative contribution of undecontaminated cropland (43 %). This trend likely resulted from the occurrence of some decontamination shortly before the occurrence of 2016 precipitation events, which left the soil bare and vulnerable to rainfall and runoff.

After the completion of decontamination, the events of 2017 and 2019 were characterised by a significant increase in sediment transfers, with their MAR values reaching 270 % and 190 % of the pre-accidental levels despite the intensity of the 2017 event that was similar to that of 2016 events (Fig. II.3; Supplementary Materials Table II.SM-VII). This massive increase of sediment transfer was associated with a drastic increase in the quantitative contribution from subsoil (+180 % and +108 %) and undecontaminated cropland (625 % and 419 %), while contribution of forest remained similar to pre-accidental levels.

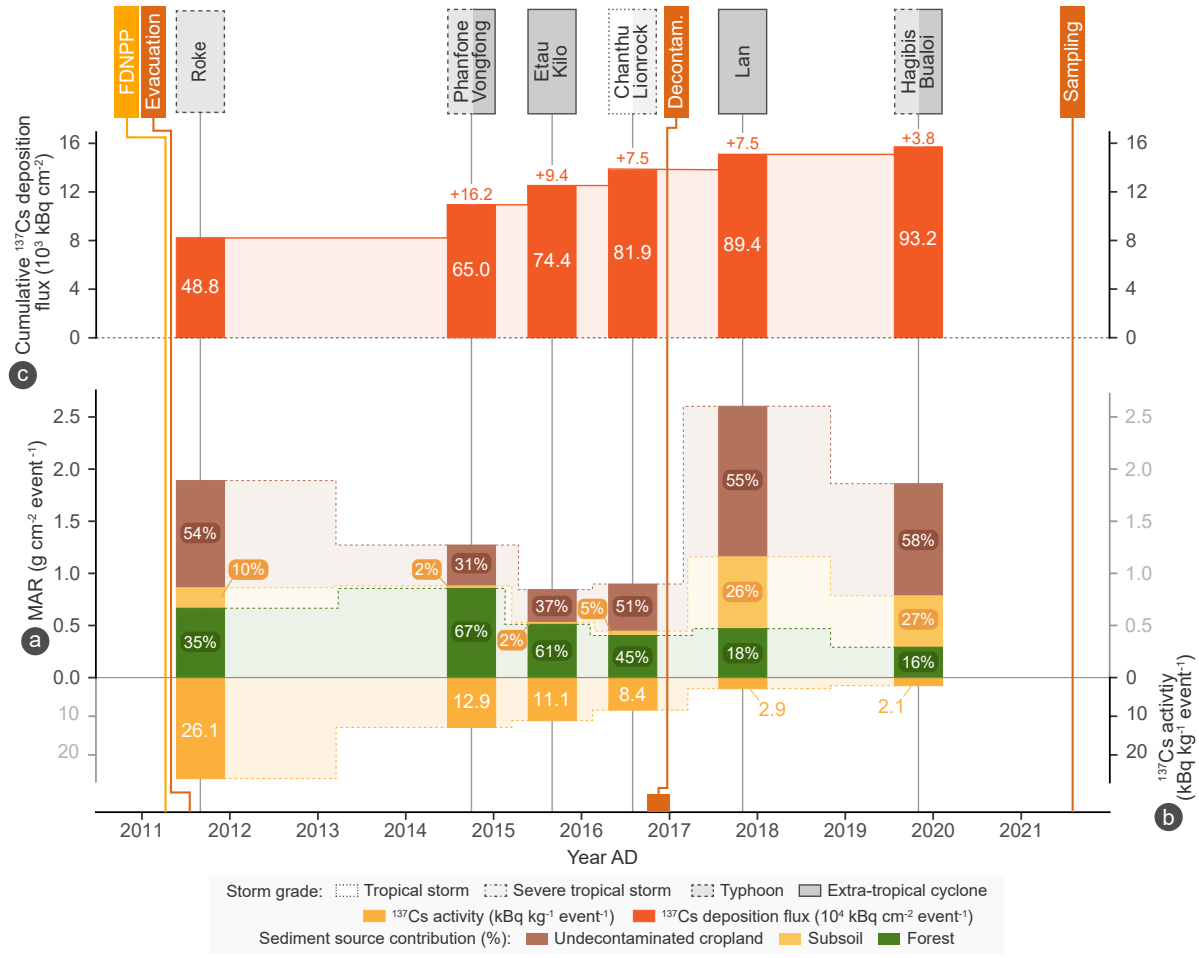


Figure II.8: Evolution of the (a) mass accumulation rate (MAR) as a function of the contribution of each sedimentary source (%), ^{137}Cs (b) activity and (c) cumulative deposition flux per extreme precipitation event identified along the sediment core sampled in the downstream part of the Mano Dam reservoir.

II.3.5 - Evolution of ^{137}Cs transfers through time

Throughout each event, the ^{137}Cs activity in the sediment has consistently decreased (Fig. II.8.b; Supplementary Materials Table II.SM-VII). From 2011 to 2016, the activity gradually decreased over time, almost following an exponential decay, with reductions of about 20 %, 15 %, and 27 % per year between 2011−2014, 2014−2015 and 2015−2016, respectively, averaging 21 % per year between 2011 and 2016 events. Following the completion of decontamination, there was a notable drop of 65 % in ^{137}Cs activities between 2016−2017 events, equivalent to a decrease of 56 % per year. Subsequently, there was again a gradual decrease of 28 % between 2017-2019, equivalent to a decrease of about 14 % per year. Over the period from the initial extreme precipitation event post-accident in 2011 to the most recent events in 2017 and 2019, ^{137}Cs activities decreased significantly by about 89 % to 92 % (26.1 versus 2.9 and 2.1 kBq kg^{-1} event^{-1} respectively), which was equivalent to a decrease of about 30 % and 26 % per year, respectively.

Conversely, the evolution of total ^{137}Cs deposition flux per event did not fully reflect the same trends as that of ^{137}Cs activities (Fig. II.8.c; Supplementary Materials Table II.SM-VII). From 2011 to 2016, the decrease trend

was similar, with reductions of about 30 %, 45 % and 22 % per year between 2011−2014, 2014−2015 and 2015−2016, respectively, averaging 32 % per year between 2011 and 2016 events. Conversely, following the completion of decontamination, the ^{137}Cs deposition flux in 2017 remained unchanged from that of 2016 (i.e. 7.5 10^3 kBq m^{-2} $event^{-1}$). Subsequently, there was again a decrease of 49 % between 2017−2019, equivalent to a decrease of about 26 % per year. Over the period from 2011 to 2017 and 2019, ^{137}Cs deposition flux was reduced by 85 to 92 %, which was equivalent to a decrease of about 26 % per year.

Furthermore, Roke, the first extreme precipitation event that took place after FDNPP accident in 2011, accounted for 52 % of the total ^{137}Cs transferred between 2011 and 2021. The next three events, in 2014, 2015, and 2016, accounted for 18 %, 10 %, 8 % of the total ^{137}Cs transferred. Accordingly, these four events supplied 88 % of the total ^{137}Cs deposition flux exported during the monitored period. In contrast, the last two events, in 2017 and 2019, transferred a limited deposition flux of ^{137}Cs with only 8 % and 4 %, respectively.

II.4 - Discussion

II.4.1 - Identifying and dating sedimentation events along the sediment core

In this study, insights from Huon et al. (2018) research were used to identify sediment deposition associated with extreme precipitation events based on specific changes in the sediment properties. In addition, as most of the sediment transfer in river occurred during extreme precipitation events (Laceby et al., 2016a; Osawa et al., 2018; Taniguchi et al., 2019; Evrard et al., 2020), deposits were assumed to correspond to a succession of distinct events. However, despite the fine sampling resolution at a thickness of 1-cm, some of the changes occurred within this 1 cm interval and were smoothed out. For example, in layers at 9−11, 16−18, 19−21 and 26−27 cm depths, the decrease in SSA coincided with an increase in TOC and particle size (i.e. D90) and occurred slightly before the decrease in Al content, although all these changes should have occurred simultaneously (Fig. II.4.a). Such smoothing could be reduced by increasing the resolution of the analysis, such as what can be obtained using XRF core scanner (Rapuc et al., 2020) or high-resolution hyperspectral imagery (Jacq et al., 2019).

In addition, challenges were faced in the dating of the sedimentation events due to the inability to use conventional dating methods based on $^{210}Pb_{ex}$ and ^{137}Cs. To overcome this, several types of contextual information were used, including previously published data (Huon et al., 2018), the identification of the ^{137}Cs peak related to FDNPP fallout, management of the reservoir, the progress of decontamination, in particular the addition of fresh soil, and finally the date of sampling of the current sediment core. Consequently, our dating approach relied on establishing a relative chronology based on these contextual factors. This led to inherent uncertainties in the dating process. Notably, the strong similarities in the distribution of the properties between the sediment core studied in this study and the two downstream sediment cores studied by Huon et al. (2018) (i.e., DD1 and DD2; Supplementary Materials Fig. II.SM-1), which were sampled at the same location in the reservoir, supports a high repeatability and representativeness of sediment core sampling at this location in the reservoir. However, investigation of additional sediment cores would provide confirmation of the results.

Moreover, water level management at the Mano Dam likely impacted sedimentation in the reservoir. Adjustments of water outflow to maintain usual water levels changed the water velocity along the reservoir. Increased water release elevates water velocity, reducing the residence time of sediment-laden water, which reduces the sediment trapping potential within the reservoir. During higher-magnitude events, such as Etau-Kilo (2015) and Hagibis & Bualoi (2019), water discharges were significantly higher during a shorter period of time com-

pared to what was observed during lower-magnitude events (e.g. Roke (2011), Phanfone & Vongfong (2014), Chanthu & Lionrock (2016) and Lan (2017)) (Fig. II.3). This fast and abrupt management pattern during higher-magnitude events was less favourable for sediment trapping than the gradual and smoother management observed for lower-magnitude events. Despite the fact that these events generated massive erosion, as observed in the suspended sediment flux records at the reservoir inlet monitoring station (Fig. II.3.d) and in other studies (Thothong et al., 2011; Chartin et al., 2017; Evrard et al., 2019b; Vandromme et al., 2023), the management of the water reservoir likely resulted in a lower representation of this type of event in the lake sediment records. Conversely, the 2017 event, Lan, which occurred after decontamination and was equivalent to the Phanfone & Vongfong events (2014) in terms of precipitation, was associated with significantly higher suspended sediment flux although not with higher dam water discharge. Accordingly, this management was likely to trap more sediments in the water reservoir. The Chanthu & Lionrock events events (2016), both lower-magnitude events that occurred over a short period of time, resulted in a slightly higher water discharge than Lan (2017) or Phanfone & Vongfong (2014) events. Unexpectedly, the extreme precipitation event of September 2020 (Dolphin - 2012) did not generate significant sediment transfer (Fig. II.3.d), despite having similar maximum daily precipitation as events such as Chanthu & Lionrock (2014), Phanfone & Vongfong (2016), or Lan (2017) (Supplementary Materials Table II.SM-III). The Dolphin event (2020) was not identified in the sediment core, which could be due to the resolution of the sediment core analyses (i.e. 1 cm) and a low amount of sediment deposition. Understanding the complex influence of these types of short-term management of water discharge and reservoir water level on sediment dynamics across the reservoir, would require the development and use of 3D water-sediment dynamics models, which could be developed in further studies. In addition, it may be possible to quantify the sediment trapping efficiency of the reservoir by comparing suspended sediment fluxes at the inlet and outlet of the reservoir (Verstraeten and Poesen, 2000).

Dam water level management types likely control the potential trapping of sediment particles in the lacustrine zone of the reservoir, in particular for the coarse particles that usually settle down first (i.e. coarse organic matter). Therefore, the occurrence of large water discharges over a short period of time may lead to a lower trapping of sediments and therefore to a lower representation of the contribution sources. However, according to Vandromme et al. (2023), the most intense events can generate rill (or gully) erosion that mobilises subsoils, depleted in organic matter. The signature of these higher-magnitude events was therefore likely to be depleted in coarser organic matter particles, resulting in a higher contribution of sediment originating from subsoil compartments. Unlike natural lakes, managed water reservoirs do not show homogeneous sedimentation conditions throughout time, in particular in areas subject to heavy precipitation events, such as typhoons, which require rapid and major dam water releases to prevent damages to the dam structure and any flooding downstream, thereby modify the sedimentation conditions and sedimentation events signature across the reservoir.

II.4.2 - Evolution of sediment source contributions and ^{137}Cs transfers through time

Although the contrasted extreme precipitation events, all land use changes in the Mano Dam reservoir catchment have occurred over a relatively short period of ten years have been responsible for significant changes in terms of trends in the sediment source contribution. Soon after the abandonment of agricultural activities, between 2011 and 2016, the spontaneous regrowth of vegetation has progressively protected the soil from erosion and reduced the contribution of agricultural land to sediment and particle-bound ^{137}Cs transfer, as deposition flux decreased over time. Conversely, the decontamination, which mainly took place over a three-

month period at the end of 2016 has drastically increased erosion of the cultivated land by leaving the soil uncovered by vegetation and/or covered with a fresh soil making it highly susceptible to erosion (Evrard et al., 2019a). As also shown by Feng et al. (2022), this effect appears to be pluriannual, as it was still visible in Mano Dam reservoir during Hagibis in 2019. However, even if these fresh soils were more sensitive to erosion, they did not provide ^{137}Cs contaminated sediments. In fact, they acted as diluents for contaminated ^{137}Cs sediment originating from undecontaminated forests, as shown by Vandromme et al. (2023). This may raise concerns about soil conservation in the decontaminated farmland. Nevertheless, due to the impact of dam water level management on sediment storage, it was likely that some intense events were not fully recorded in the sedimentation sequence. Therefore, not all the sediment and ^{137}Cs transfer episodes that occurred in the catchment were likely to be fully represented in this study. In addition, according to Funaki et al. (2022), under anoxic conditions ^{137}Cs elutes in the pore water, which may cause migration within the sediment column over time, as observed between layers F and G (Fig. II.2.e and i). Although this phenomenon appears to be limited according to Funaki et al. (2022), the ^{137}Cs stock of a sedimentation event could be slightly modified after a prolonged period.

The initial intention of the sediment fingerprinting approach was to adjust the potential cropland sources as decontamination progressed (uncontaminated, decontaminated, remediated). However, it was not possible to distinguish certain sources, such as subsoil and the fresh soil added to remediated cropland, which did not allow to trace each source individually. In addition, in contrast with decontamination records no detailed spatial and/or temporal information was found on the progress of the preparation for recultivation. Moreover, due to the limitations in the Bayesian models (i.e. MixSIAR and BMM) that appear not to handle missing sources correctly Stock et al. (2018) and recommendations to limit the number of potential sources considered (≤ 4, Lees (1997)), it was decided to use three well-defined sources (undecontaminated cropland, forest, subsoil).

The use of a multiple-modeling approach allowed to slightly improve the values of the evaluation metrics compared to those obtained with independent models (MixSIAR and BMM). Although multiple-modeling metrics generally exceeded those of individual models, they remained higher on average. In addition, comparing the trends obtained with individual models, which show some consistency, increased our confidence in the modeling outputs. Future studies could incorporate additional unmixing models to further improve the multi-modeling approach. Investigation of the transferability of modeling metrics from virtual mixtures to actual sediment samples, using ESP values, did not support a high confidence in the transferability of the metrics in the current context. This was probably attributed to the selection of tracers with non-(fully) conservative behaviour, which was reproduced in the generation of the virtual mixtures (Chalaux-Clergue et al., 2024a).

II.4.3 - Perspectives and management implications

Previous studies showed a strong decrease in the ^{137}Cs activities in sediment over time (Osawa et al., 2018; Taniguchi et al., 2019; Evrard et al., 2020). Prior to the decontamination, this reduction in ^{137}Cs activity was associated to both physical decay and prior lateral transfer in rivers. After decontamination, previous studies associated the significant decrease in ^{137}Cs activity with the removal of contaminated soils or the physical decay that reduced ^{137}Cs fluxes. However, the current results suggest that it was more likely to be related to the dilution of contaminated sediment with fresh soil spread over decontaminated farmland, rather than a decrease in ^{137}Cs deposition fluxes. The natural regrowth of spontaneous vegetation over farmland since 2011 until decontamination has gradually reduced soil erosion, decreasing the contribution of this source to sediment and particle-bound ^{137}Cs transfer in rivers (Feng et al., 2022). Here, decontamination appeared to have achieved a similar or slightly better reduction than natural regrowth, by removing contaminated erodible

soil.

Nevertheless, as observed along the sediment core, the forest has consistently contributed sediment and particle-bound ^{137}Cs and while remaining the main source of ^{137}Cs in the catchment (Laceby et al., 2016b). The resumption of agricultural activities on decontaminated soil, associated with a denser vegetation cover, may further reduce erosion from cropland. Therefore, this will likely reduce the supply of sediment depleted in radiocesium, which may reduce the dilution of that of forest - enriched in radiocesium -, leading to a potential future increase of sediment ^{137}Cs activity. However, over time, ^{137}Cs tends to migrate into forest soils and becomes increasingly immobilised by clay minerals (Kurikami et al., 2019; Onda et al., 2020). Moreover, Taira et al. (2020) showed that ^{137}Cs activity in forest soils was not modified by the occurrence of extreme precipitation events, as they mainly induce rill erosion mainly transferring material depleted in radiocesium (Vandromme et al., 2023). This could potentially lead to a reduction in radiocesium-rich sediment originating from forests.

This being said, the primary objective of the decontamination was to reduce the ambient air dose rate, which proved to be successful (Evrard et al., 2019b). In farmland, the ambient air dose rate was reduced by an average of about 59 %, reaching 0.59 $\mu Sv\ h^{-1}$ (MoE, 2018, 2023b). This level remains above the long term target ambient air dose rate of 0.23 μSv h^{-1} (equivalent to an exposure dose rate of 1 mSv yr^{-1}), although it allows the resumption of agricultural activities. However, in contrast with conclusions of previous studies, our current research emphasises that decontamination may not have reduced the deposition flux of particle-bound ^{137}Cs in the reservoir transferred by erosion in rivers as much as it was often previously assumed. This finding is supported by a modelling approach conducted by Vandromme et al. (2023), demonstrating a 17 % reduction in ^{137}Cs flux in rivers compared to scenarios without decontamination. Decontamination resulted in a similar ^{137}Cs deposition flux as that observed in landscapes characterised by a dense vegetation regrowth, such as that which developed during the early post-accidental period when farmlands were abandoned. This raises the question of the worthiness of decontamination in terms of reduction in particulate transfers in rivers, considering the workload, cost and quantity of waste generated by the remediation (Evrard et al., 2023). However, decontamination - through reducing the ambient air dose rate in residential and agricultural areas - theoretically allows the population to return. Nevertheless, according to Asanuma-Brice et al. (2023), very few people have returned or moved to these areas. This is related to the deterioration and modification of living conditions in comparison with pre-accidental conditions (e.g. dislocation of families and neighbourhood relations, lack of facilities, public services and economic activities, transformation of the landscape, restricted access to forest by-products such as gathering wild vegetables or mushrooms).

Nevertheless, if the objective is to allow a rapid return of the population and to limit riverine transfers of radioactive contamination, as intended by the Japanese government, our current results suggest that further reducing the delay between the accident and the decontamination could have reduced ^{137}Cs transfers in rivers more effectively. Therefore, an earlier implementation of farmland decontamination within 4-5 years after an accident could have led to a more effective reduction of transfers. This recommendation is consistent with similar findings obtained in forests, where it was shown that decontamination within 1 to 5-years after the accident would be more effective (Thiry et al., 2018; Koarashi et al., 2020). The validity of this recommendation could be further tested by studying catchments decontaminated over different timescales (relatively early or later after the accident).

II.5 - Conclusions

Through a combination of analyses of the Mano Dam reservoir sediment core properties (organic matter, elemental geochemistry, visible colourimetry, and granulometry) coupled with contextual information (previous study of Huon et al. (2018), daily precipitation records, dam water level management, progress of decontamination), sedimentation events of the last decade were identified and dated despite the impossibility of using a more conventional dating approach. In total, six major events were identified between the FDNPP accident in March 2011 and the core sampling campaign in June 2021. Among these events, four occurred before the completion of decontamination at the end of 2016 and two thereafter.

The study revealed significant modifications in sediment source contributions over the last decade following FDNPP accident, mainly driven by rapid and drastic changes in land uses. During the period of abandonment of agricultural activities in response to the evacuation order, the quantitative contribution of cropland gradually decreased (by about 27 % of the pre-accidental level). Furthermore, a decrease in both ^{137}Cs activity in the sediment (by about 67 % equivalent to 19 % yr^{-1}) and ^{137}Cs deposition flux per extreme precipitation event (by about 84 %) was observed during these five years, between 2011 and 2016. In contrast, after decontamination, cropland and added fresh soil excessively contributed to sediment transfer. Meanwhile, forests that have not been decontaminated, appeared to supply a stable and perennial source of ^{137}Cs-contaminated sediment. Therefore, by providing non-contaminated sediment, decontaminated cropland and fresh soil contributed to the dilution of ^{137}Cs borne by contaminated sediment, resulting in an overall drop of ^{137}Cs activity in the sediment (by 65 % between 2016 and 2017). However, this was not associated with a reduction in the ^{137}Cs deposition flux, as forested areas act a stable source of ^{137}Cs-contaminated sediment. Accordingly, the resulting ^{137}Cs deposition flux after decontamination (2016-2021) was similar to that observed during the 5-year period of land abandonment (2011-2016), as a result of the natural regrowth of spontaneous vegetation over farmland, which protected soils and limited ^{137}Cs transfer by rivers.

Future studies should investigate other catchments of the Fukushima region that have been decontaminated later than the Mano Dam reservoir catchment, or that have not been decontaminated yet, to assess the effect of longer land abandonment periods on ^{137}Cs fluxes in rivers.

Code and data availability

The dataset is available online at https://zenodo.org/records/10836974 (Chalaux-Clergue et al., 2024b). The code to run models, summarise results and plot results is available in the Supplement (.Rmd file).

Acknowledgements

The assistance provided by Dr. Hironoi Funaki and Dr. Kazuya Yoshimura from the Japan Atomic Energy Agency (JAEA) in conducting the sediment core sampling in the Mano Dam reservoir is gratefully acknowledged.

Financial support

The collection and the analysis of the soil and sediment samples were funded by the TOFU (ANR-11-JAPN-001) and the AMORAD (ANR-11-RSNR-0002) projects, under the supervision of the French National Research Agency (ANR, Agence Nationale de la Recherche). The support of CEA (Commissariat à l' Energie Atomique et aux Energies Alternatives, France), CNRS (Centre National de la Recherche Scientifique, France) and JSPS (Japan Society for the Promotion of Science) through the funding of PhD fellowships (Hugo Lepage, Hugo Jaegler, Thomas Chalaux-Clergue) and collaboration projects (grant no. PRC CNRS JSPS 2019-2020, no.10; CNRS International Research Project - IRP -MITATE Lab) is recognised. Thomas Chalaux-Clergue obtained a JSPS grant to spend the second year of his PhD at Kyoto Prefectural University (Oct. 2022 - Sept. 2023) (Grant number PE22708). This work was also supported by ERAN (Environmental Radioactivity Research Network Center) (Grants I-21-22 and I-22-24) and a mini-project from the FIRE (Fédération Ile-de-France de Recherche en Environnement - CNRS FR3020 FIRE, France) entitled RICOR ('Reconstructing the Impact of Changing land Occupation on the fate of Radionuclides').

CRediT author statement

Thomas Chalaux-Clergue: Conceptualization, Methodology, Software, Formal analysis, Investigation, Data Curation, Writing - Original Draft, Visualisation.

Anthony Foucher: Conceptualization, Methodology, Writing - Review & Editing.

Pierre-Alexis Chaboche: Writing - Review & Editing.

Seiji Hayashi: Investigation, Resources, Data Curation, Writing - Review & Editing.

Hideki Tsuji: Investigation, Resources, Data Curation, Writing - Review & Editing.

Yoshifumi Wakiyama: Investigation, Resources, Writing - Review & Editing.

Sylvain Huon: Investigation, Writing - Review & Editing.

Rosalie Vandromme: Writing - Review & Editing.

Olivier Cerdan: Writing - Review & Editing.

Atsushi Nakao: Writing - Review & Editing, Supervision.

Olivier Evrard: Conceptualization, Investigation, Data Curation, Writing - Review & Editing, Supervision, Project administration, Funding acquisition.

II.6 - Supplementary materials

II.6.1 - Laboratory analysis methodology

II.6.1.1 - Radiocesium analysis

Gamma spectrometry with a low-background coaxial HPGe detector was used to determined the ^{134}Cs and ^{137}Cs activities in the sediment samples. The counting times ranged from 3×10^4 to 8×10^4 s. The ^{137}Cs and ^{134}Cs activities were measured at the 605 keV and 662 keV emission peaks, respectively, errors reached about 5 % at 95 % confidence level. All measured counts were corrected for background levels which were, as detector and geometry efficiency, estimated at least every two months. Counting efficiency and quality assurance were implemented using certified International Atomic Energy Agency reference materials prepared in the same containers as the sample. Radiocesium activities were decay-corrected to the sampling date.

The ^{134}Cs and ^{137}Cs were also decay-corrected to 11 March 2011 and ^{134}Cs/^{137}Cs ratio were compared to the ratio 1.06 $\pm$ 0.04 (Kobayashi et al., 2013) to further confirm the FDNPP origin.

II.6.1.2 - Organic Matter

In the Mano Dam reservoir catchment, sediment and soils were found not to contain carbonate minerals, and all the carbon associated with particulate matter is organic in nature (Huon et al., 2018). Total organic carbon (TOC) and total nitrogen (TN) elemental concentrations and isotopes (δ^{13}C and δ^{15}N) were determined by a combustion method using a continuous flow elementary analyser (Elementar VarioPyro cube) coupled with an Isotope Ratio Mass Spectrometer (EA-IRMS) (Micromass Isoprime) at the Institute of Ecology and Environmental Sciences (iEES Paris) in France. A first analysis run was conducted to measure TOC concentration together with a set of tyrosine standards (Coplen et al., 1983). The second analysis run was dedicated to measure TN concentration after sample weight optimisation from TOC results. For combustion, oxygen was injected during 70 s (30 mL min^{-1}) at 850 °C for reduction and the combustion furnace at 1120 °C (Agnihotri et al., 2014). The analytical precision was assessed with repeated analyses of a tyrosine intern standard (n = 51), calibrated against international reference standards (Girardin and Mariotti, 1991). The analysis of these properties in source material is described in details in the study of Laceby et al. (2016b). To evaluate whether the samples are composed of terrestrial or freshwater-originating material, the distribution of sample values was plotted in a δ^{13}C versus TOC/TN diagram and compared to the thresholds reported in Lamb et al. (2006) and Amorim et al. (2022).

II.6.1.3 - Elemental geochemistry

Elemental geochemistry was determined using Energy Dispersive X-ray fluorescence (XRF) (Malvern Panalytical, ED-XRF Epsilon 4). A total of 17 elemental concentrations were measured (Al, Ca, Co, Cr, Cu, Fe, K, Mg, Mn, Ni, Pb, Rb, Si, Sr, Ti, Zn, and Zr). Measurements were conducted in containers covered with a 3.6 μm thin Mylar film (Chemplex, Mylar Thin-Film cat. no. 157) with a 10 mm exposure surface. A minimum of 0.1 g of material was analysed. To consider the potential heterogeneity within a sample, three replicate measurements were made, and the mean value of these replicates was calculated. To assess the accuracy of the measurements, a standard (JMS-1, sediment from the Tokyo Bay (Terashima et al., 2002)) was measured every seven samples (n = 38) and the accuracy of the measured batch was determined based on the calculation of the Root Mean Square Errors (RMSE).

II.6.1.4 - Visible colorimetry

Visible colorimetry was measured using a portable diffuse reflectance spectrophotometer, Kanonica Minolta CM-700d, set on a 3 mm target radius. Samples were measured in a plastic zip bag. To account for potential heterogeneities within a sample, three measurements were made at different locations on the bag. The spectrophotometer was calibrated at the start of each set of measurements with zero (black) and white standards. Measurements were conducted according to the D65 illuminance standard, 10° angle observer and excluding the specular component. The spectral reflectance (R in %) was measured from 360 nm to 740 nm with a 10 nm resolution (30 wavelength classes). Raw data was processed using the colour data software CM-S100w SpectraMagic NX (Minolta, 2022). Colour parameters within the Cartesian coordinate systems CIE Lab (1976) (i.e. L*, a* and b*) (CIE, 2008) and CIE LCh (i.e. C* and h) were exported. The CIE LCh is a vector representation of the CIE Lab (1976). C and h are derived from a* and b* parameters. Within the CIE Lab system: L* is the lightness of the colour, from black (0) to white (100), a* is the position between green to red (negative values are associated with green and positives with red), b* is the position between blue and yellow (negative values are associated with blue and positive values with yellow). Within the CIE LCh system: C* is the chroma (positive values are associated to brighter colors and negative values to duller colors) and h is the hue angle (in °) in the CIE Lab color wheel.

The Q7/4 ratio as defined by Debret et al. (2011) was calculated as the ratio between 700 nm and 400 nm reflectance values. This ratio provides a numerical description of the reflectance spectrum general slope.

The oxy-hydroxide geothite (α-FeOOH) soil richness can be determined using visible diffuse reflectance spectra (Kosmas et al., 1984; Balsam et al., 2004; Hao et al., 2009; Torrent et al., 2007) and its peak values at 445 nm and 525 nm were calculated from the first derivative reflectance spectrum Debret et al. (2011). In our case, the geothite concentration was not target, only the relative abundance within our samples was used to differentiate them. For each replicate of the measurements and for each sample, the first derivative reflectance spectrum was calculated and smoothed with a Savitzky-Golay filter using the 'savitzkyGolay' function (differentiation order = 1, polynomial order = 3, window size = 5 (eq. 50 nm)) from the R package 'prospectr' (Stevens and Ramirez-Lopez, 2022) (Wadoux et al., 2021). Then, the mean per sample and the standard deviation were calculated. From the first derivative of reflectance, two geothite peaks were calculated: first, the 445 nm peak value was calculated as the mean of values at 440 and 450 nm, and the 525 nm peak as the mean of those at 520 and 530 nm (Debret et al., 2011).

The remission function was calculated from the reflectance spectrum: $f(R) = (1 - R)^2$ according to the Kubelka-Munk relationship (Scheinost et al., 1998). Then, the second derivative was calculated and the spectrum was smoothed with a Savitzky-Golay filter using the 'savitzkyGolay' function (differentiation order = 2, polynomial order = 3, window size = 5). From the second derivative of remission function spectrum, the iron oxide-associated parameters A1, A2, A3 and the goethite proportion within iron oxides (Gt) were determined (Tiecher et al., 2015). The A1 and A2 peaks are associated with goethite and the A3 peak is associated with hematite, and all peaks were calculated as the amplitude between each maximum and minimum bands. Thus, A1 is the difference between 450 and 420 nm, A2 is the difference between 510 and 480 nm and A3 is the difference between 575 (as the mean of 570 and 580 nm) and 535 nm (as the mean of 530 and 540 nm) and Gt is calculated as the ratio of A1/(A1+A3).

II.6.1.5 - Particle sizes

Particle size analyses were performed with a laser diffraction particle size analyser (Mastersizer 3000 with Hydro LV, Malvern Panalytical) in osmotic water on fresh sediment without sonic dispersion. Each sediment sample was measured 5 times. The grain size distribution was measured from 0.01 μm to 3500 μm. It was used to determine the portion of particles which are smaller than 10 % (D10), 50 % (D50) and 90 % (D90) of the whole measured particles. The specific surface area (SSA) was measured under the assumption of spherical shape. It is defined as the total surface area of a solid material divided by its mass. The SSA depends on particle size and also on its structure and porosity.

II.6.1.6 - Bulk density

Bulk density (ρ_b) was determined on fresh sediment using a 1.7 cm^3 (V) acrylic cube. Before filling the cube, the empty weight (g) was reported. Cubes were filled with fresh sediment using a metallic spatula, the humid weight (m_{humid} in g) was reported, then oven-dried at 110 °C for 96 hours (Heraeus T12, Thermo Electron Corporation) and the dry weight (m_{dry} in g) was measured. The bulk density (ρ_b in g cm^{-3}) in calculated as follows:

$$\rho_b = \frac{m_{dry}}{V} \tag{II.4}$$

II.6.2 - Figures

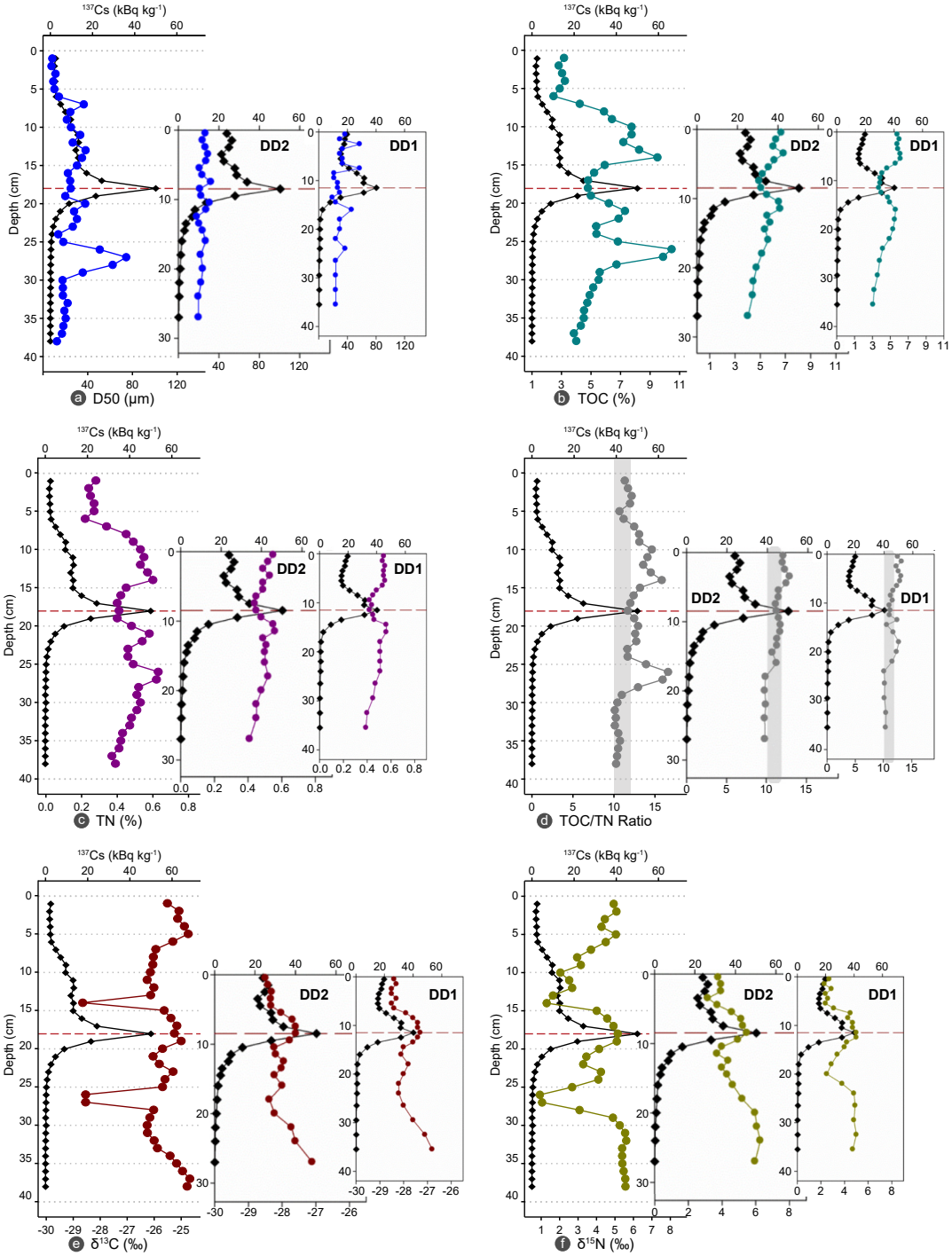


Figure II.SM-1: Comparison of sediment cores collected at the downstream location of the Mano Dam reservoir in June 2021 and in November 2014 (DD1 and DD2) in Huon et al. (2018) study.

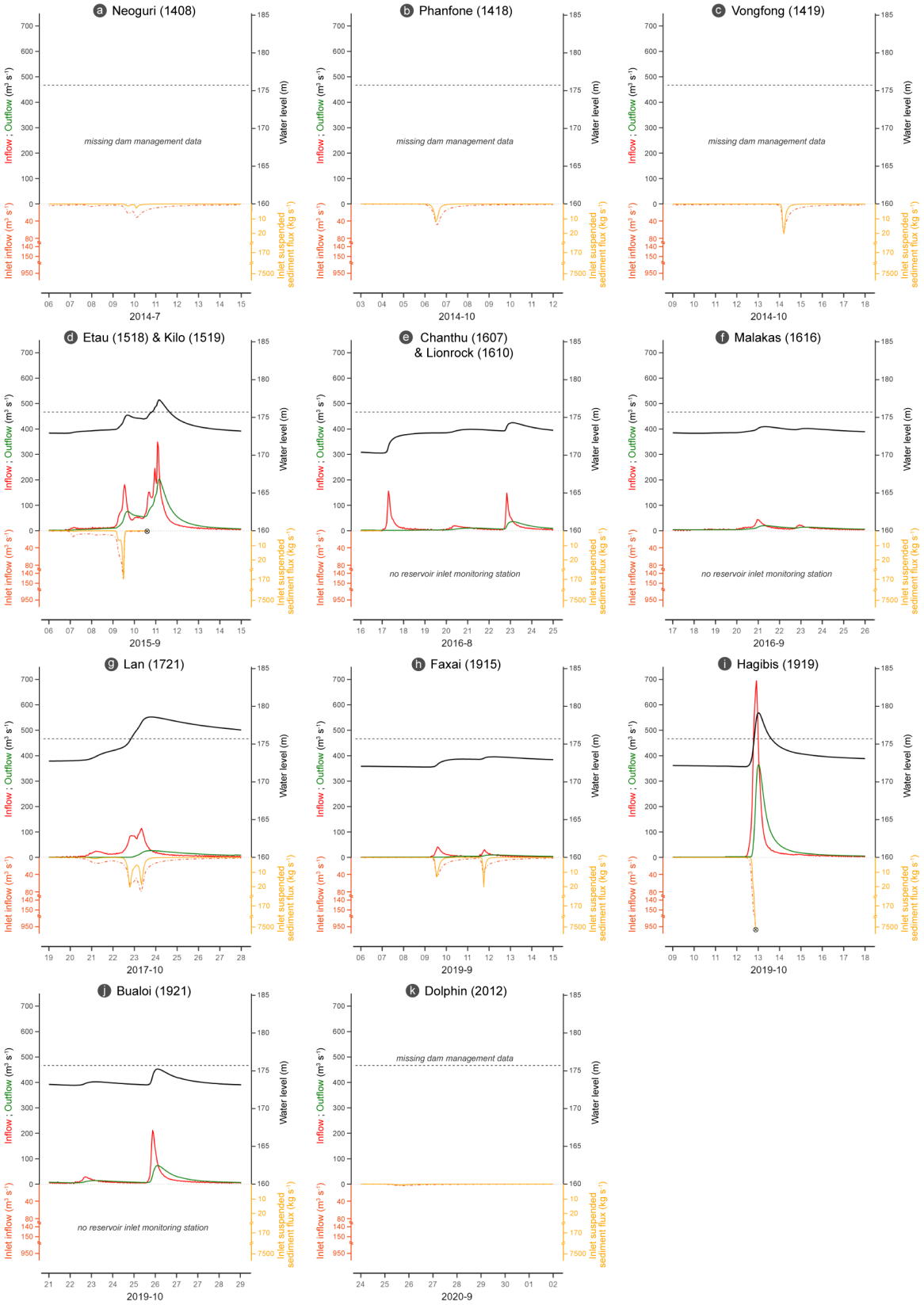


Figure II.SM-2: Mano Dam Reservoir management and metrics during extreme precipitation events, as hourly observations over nine-days of water inflow (red) and outflow (green) and dam water level (dark) along with water flow (red dot-dashed) and suspended sediment flux (orange) at the reservoir inlet river monitoring station. The black dashed line marks the dam management water level threshold at 176 *m*. Crossed circles denote damaged monitoring stations during (d) Etau & Kilo and (i) Hagibis.

Table II.SM-I: Kolmogorov-Smirnov two-samples tests for source groups significance of the *p* value. "***" *p* value $\leq$ 0.001; "**" *p* value $\leq$ 0.01; "*" *p* value $\leq$ 0.05; "." *p* value $\leq$ 0.1; " " *p* value $>$ 0.1.

	TOC	TN	δ^{13}C	δ^{15}N	Al	Ca	Fe	K	Mg	Mn	Pb	Si	Sr	Ti	Zn	Zr	L*	a*	b*	C*	h	A1	A2	Gt	Q7/4	G_{525}
Forest - Undecontaminated	***	***	***	***	***	.		***	*		**	*		.	*	**	***				***			***		**
Forest - Remediated	***	***	**	**	***			***	***		*	***		**	*	*	***	*	***	***	***			**	**	***
Forest - Subsoil	***	***	*	*	***	*		*	*	*		***	**		***	**	***	**	***	***	***	*	.		**	***
Subsoil - Undecontaminated	***	***			***	**			*		*	***	***		***		***	***	***	***		***	*	**	***	***
Subsoil - Remediated									*	**			.								.			*		

Table II.SM-II: Summary mean and standard deviation values of analysed properties for each potential source group: forest (n = 24), undecontaminated cropland (n = 24), remediated cropland (n = 10) and subsoil (i.e. channel bank or landslide, n = 10).

	TOC (%)	TN (%)	TOC/TN	δ^{13}C (‰)	δ^{15}N (‰)	Al (g kg^{-1})	Ca (g kg^{-1})	Fe (g kg^{-1})	K (g kg^{-1})	Mg (g kg^{-1})	Mn (g kg^{-1})	Pb (g kg^{-1})	Si (g kg^{-1})	Sr (g kg^{-1})
Forest	10.92 $\pm$ 4.25	0.70 $\pm$ 0.25	15.4 $\pm$ 2.3	-26.2 $\pm$ 1.1	3.6 $\pm$ 0.25	67.5 $\pm$ 12.2	9.2 $\pm$ 4.5	51.7 $\pm$ 12.3	8.1 $\pm$ 2.0	6.7 $\pm$ 3.6	887 $\pm$ 449	39 $\pm$ 11	163.0 $\pm$ 17.8	100 $\pm$ 45
Undecontaminated	5.16 $\pm$ 2.05	0.42 $\pm$ 0.11	11.9 $\pm$ 1.4	-25.0 $\pm$ 1.1	5.1 $\pm$ 0.25	84.9 $\pm$ 9.3	9.8 $\pm$ 3.6	49.5 $\pm$ 13.2	11.8 $\pm$ 2.4	6.4 $\pm$ 2.2	657 $\pm$ 229	31 $\pm$ 10	163.1 $\pm$ 32.2	95 $\pm$ 30
Remediated	0.95 $\pm$ 0.88	0.09 $\pm$ 0.07	10.3 $\pm$ 2.0	-24.4 $\pm$ 1.5	5.5 $\pm$ 0.25	105.8 $\pm$ 13.4	8.5 $\pm$ 4.7	50.5 $\pm$ 5.5	14.1 $\pm$ 2.7	6.8 $\pm$ 0.9	935 $\pm$ 204	28 $\pm$ 6	227.0 $\pm$ 19.5	86 $\pm$ 36
Subsoil	1.41 $\pm$ 1.10	0.12 $\pm$ 0.10	11.6 $\pm$ 1.6	-25.4 $\pm$ 1.0	5.4 $\pm$ 0.25	107.8 $\pm$ 9.7	5.1 $\pm$ 2.7	48.9 $\pm$ 15.6	11.3 $\pm$ 3.3	5.4 $\pm$ 2.6	504 $\pm$ 181	32 $\pm$ 14	225.0 $\pm$ 41.8	62 $\pm$ 15

	Ti (g kg^{-1})	Zn (g kg^{-1})	Zr	L*	a*	b*	C*	h	A1	A2	Gt	Q7/4	G_{525}
Forest	4.4 $\pm$ 0.7	105 $\pm$ 16	246 $\pm$ 102	47.2 $\pm$ 7.7	3.6 $\pm$ 1.1	9.5 $\pm$ 3.8	10.2 $\pm$ 3.9	68.0 $\pm$ 3.8	3.7 $\pm$ 1.3 $\cdot$ 10^{-2}	1.7 $\pm$ 0.8 $\cdot$ 10^{-2}	0.93 $\pm$ 0.07	2.01 $\pm$ 0.36	0.49 $\pm$ 0.32
Undecontaminated	4.9 $\pm$ 0.9	117 $\pm$ 28	319 $\pm$ 69	55.7 $\pm$ 3.5	3.1 $\pm$ 1.0	10.6 $\pm$ 2.8	11.0 $\pm$ 2.9	74.0 $\pm$ 1.8	3.2 $\pm$ 1.3 $\cdot$ 10^{-2}	1.5 $\pm$ 0.7 $\cdot$ 10^{-2}	1.02 $\pm$ 0.05	2.02 $\pm$ 0.30	0.73 $\pm$ 0.38
Remediated	5.0 $\pm$ 0.5	93 $\pm$ 19	342 $\pm$ 158	62.7 $\pm$ 3.0	4.9 $\pm$ 1.4	17.6 $\pm$ 3.7	18.3 $\pm$ 3.9	74.7 $\pm$ 2.4	4.3 $\pm$ 1.0 $\cdot$ 10^{-2}	1.7 $\pm$ 0.4 $\cdot$ 10^{-2}	1.03 $\pm$ 0.06	2.40 $\pm$ 0.29	1.43 $\pm$ 0.35
Subsoil	4.1 $\pm$ 1.7	82 $\pm$ 17	344 $\pm$ 120	64.6 $\pm$ 5.5	6.0 $\pm$ 1.8	18.3 $\pm$ 4.2	19.3 $\pm$ 4.4	72.1 $\pm$ 3.3	5.5 $\pm$ 1.8 $\cdot$ 10^{-2}	2.6 $\pm$ 1.4 $\cdot$ 10^{-2}	0.92 $\pm$ 0.09	2.67 $\pm$ 0.45	1.57 $\pm$ 0.46

Table II.SM-III: Summary of the 27 extreme precipitation events that occurred between March 2011 and June 2021 and were recorded by the four precipitation monitoring AMeDAS stations surrounding the Mano Dam reservoir catchment located in Fukushima City, Hippo, Iitate and Soma. The dash indicates missing data.

Year	Name	International number ID	Date (year − month)	Storm grade	Cumulative precipitation (mm)	Duration (day)
2011	Songda	1102	2011-05	Extra-tropical cyclone	130	2
	Roke	1105	2011-09	Typhoon	259	4
2012	-	-	2012-05	-	102	3
	-	-	2012-07	-	105	4
2013	Man-Yi	1318	2013-09	Extra-tropical cyclone	97	2
	Wipha	1326	2013-10	Typhoon	122	2
2014	-	-	2014-02	-	95	3
	-	-	2014-06	-	117	3
	Neoguri	1408	2014-07	Tropical storm	76	2
	Phanfone	1418	2014-10	Typhoon	130	3
	Vongfong	1419	2014-10	Extra-tropical cyclone	94	2
2015	Etau-Kilo	1518 & 1519	2015-09	Extra-tropical cyclone	396	6
2016	-	-	2016-01	-	72	1
	Chanthu	1607	2016-08	Tropical storm	197	8
	Lionrock	1610	2016-08	Severe tropical storm	157	5
	Malakas	1616	2016-09	Extra-tropical cyclone	139	7
2017	Lan	1721	2017-10	Extra-tropical cyclone	264	5
2019	Faxai	1915	2019-09	Typhoon	121	3
	Hagibis	1919	2019-10	Typhoon	372	4
	Bualoi	1921	2019-10	Extra-tropical cyclone	129	2
2020	-	-	2020-01	-	111	2
	-	-	2020-04	-	63	3
	-	-	2020-04	-	96	3
	-	-	2020-05	-	87	5
	-	-	2020-07	-	139	4
	Dolphin	2012	2020-09	Extra-tropical cyclone	136	5
2021	-	-	2021-03	-	72	2

Table II.SM-IV: Summary of management and metrics during extreme precipitation events between 2014 and 2019, of the maximum water flow and suspended sediment flux at the reservoir inlet river monitoring station, maximum dam water flow metrics (inflow and outflow) and dam water level (maximum and level range). The KO indicates damaged river monitoring station during the event; max. stands for maximum; n.a. stands for not applicable; dash indicates missing data.

Name	**International number ID**	**Date** (year − month)	**Inlet river (max.)**		**Dam water flow (max.)**		**Dam water level**		
			Water flow ($m^3\ s^{-1}$)	**Suspended sediment flux** ($kg\ s^{-1}$)	**Inlet** ($m^3\ s^{-1}$)	**Outlet** ($m^3\ s^{-1}$)	**Max.** (m)	**Level change** (m)	**Delay to return to threshold**
Songda	1102	2011-05	-	-	-	-	-	-	-
Roke	1105	2011-09	-	-	-	-	-	-	-
Man-Yi	1318	2013-09	-	-	-	-	-	-	-
Wipha	1326	2013-10	-	-	-	-	-	-	-
Neoguri	1408	2014-07	31.7	2.9	-	-	-	-	-
Phanfone	1418	2014-10	48.0	12.0	-	-	-	-	-
Vonfong	1419	2014-10	62.1	20.4	-	-	-	-	-
Etau-Kilo	1518-1519	2015-09	143.7 (KO)	169.7 (KO)	349.3	203.3	177.6	4.5	$\sim$ 12 h
Chanthu-Lionrock	1607-1610	2016-08	-	-	156.5	35.8	174.6	4.1	n.a.
Malakas	1616	2016-09	-	-	44.2	20.1	174.0	0.9	n.a.
Lan	1721	2017-10	80.5	20.5	44.2	26.7	178.9	5.9	+ 16 days
Faxai	1915	2019-09	43.7	20.3	41.4	11.7	173.6	1.4	n.a.
Hagibis	1919	2019-10	941.4 (KO)	7495.1 (KO)	695.0	364.8	179.5	7.3	$\sim$ 15 h
Bualoi	1921	2019-10	-	-	211.8	73.5	175.5	2.2	n.a.
Dolphin	2012	2020-09	3.7	0.5	-	-	-	-	-

Table II.SM-V: Summary of sediment source fingerprinting modeling prediction accuracy statistics calculated on virtual mixtures predictions (n = 138) for each model (i.e. MixSIAR, BMM, and Multiple-model). ME: mean error; RMSE: root mean square error; r^2: squared Pearson's correlation coefficient; NSE: Nash-Sutcliffe modeling efficiency coefficient; W50: prediction interval width; CRPS: continuous ranked probability score; ESP: encompassed sample predictions expressed as number of sample within the range out of 38 (n) and as percentage (%). BMM stands for bayesian mean model. Note: * indicates the mean values per source.

Model	**Source group**	**W50*** **(%)**	**ME (%)**	**RMSE (%)**	r^2	**NSE**	**CRPS***	**ESP**	
								(n)	(%)
MixSIAR	Undecontaminated cropland	15	5	15	0.88	0.72	9	38	100
	Forest	10	-8	14	0.96	0.75	8	33	87
	Subsoil	8	3	8	0.98	0.93	4	22	58
	Average	*11*	*0*	*12*	*0.94*	*0.80*	*7*	-	-
BMM	Undecontaminated cropland	43	1	17	0.85	0.66	11	27	71
	Forest	29	-1	11	0.91	0.85	8	36	95
	Subsoil	26	0	6	0.96	0.95	5	38	100
	Average	*0*	*11*	*0.91*	*0.82*	*33*	*8*	-	-
Multiple-modeling	Undecontaminated cropland	-	3	16	0.87	0.70	-	38	100
	Forest	-	-5	12	0.94	0.82	-	35	92
	Subsoil	-	2	6	0.97	0.95	-	25	66
	Average	-	*0*	*11*	*0.93*	*0.82*	-	-	-

Table II.SM-VI: Summary of predicted source contributions by each model for each potential source (in %). MM: Multiple-model.

Depth (cm)	Predicted contribution (%)								
	Undecontaminated cropland			Forest			Subsoil		
	MixSIAR	BMM	MM	MixSIAR	BMM	MM	MixSIAR	BMM	MM
00-01	42	63	52	48	1	24	10	37	24
01-02	60	63	62	22	0	11	18	37	28
02-03	51	65	58	28	0	14	21	35	28
03-04	58	69	63	24	0	12	18	31	25
04-05	39	63	51	33	0	17	27	37	32
05-06	40	56	48	39	0	20	21	44	32
06-07	53	74	64	37	12	25	10	13	11
07-08	42	61	51	50	36	43	9	3	6
08-09	44	56	50	50	44	47	6	0	3
09-10	37	46	41	59	54	57	4	0	2
10-11	26	39	32	70	61	65	5	0	3
11-12	37	46	42	59	54	56	5	0	2
12-13	24	38	31	74	62	67	3	0	2
13-14	15	25	19	82	75	79	3	0	2
14-15	41	54	48	47	38	42	12	8	10
15-16	43	64	54	45	30	37	12	6	9
16-17	49	68	58	40	23	31	12	9	11
17-18	51	66	58	37	23	30	13	12	12
18-19	53	67	60	39	25	32	8	9	8
19-20	41	54	48	53	43	48	6	2	4
20-21	33	39	36	61	61	61	6	0	3
21-22	37	48	43	57	52	54	6	0	3
22-23	46	65	55	46	34	40	8	2	5
23-24	40	60	50	52	36	44	8	4	6
24-25	39	52	45	56	48	52	6	0	3
25-26	15	20	18	82	80	81	3	0	1
26-27	16	20	18	80	80	80	3	0	2
27-28	37	47	42	57	53	55	6	0	3
28-29	43	55	49	47	38	42	10	8	9
29-30	37	47	42	50	41	45	13	12	13
30-31	49	48	48	42	36	39	9	17	13
31-32	47	51	49	42	31	37	12	18	14
32-33	46	57	51	44	27	36	10	16	13
33-34	48	62	55	38	23	30	14	16	15
34-35	49	68	59	37	20	29	13	12	12
35-36	52	72	62	37	17	27	11	11	11
36-37	48	74	61	37	10	24	15	16	15
37-38	54	72	63	35	12	23	12	16	14

Table II.SM-VII: Characteristics of each extreme events identified along the Mano Dam reservoir sediment core with the sediment source contributions, ^{137}Cs activity and flux. MAR = mass accumulation rate, FDNPP = Fukushima Daiichi Nuclear Power Plant. Average per event apart from 23−28 event are indicated as mean ± standard deviation.

Depth (cm)	Extreme event	Date (yr-m)	Delay since FDNPP (yr)	Thickness (cm)	Density (g cm^{-3})	MAR (g cm^{-2} event^{-1})	**Sediment source contribution** (%)			**MAR per source** (g cm^{-2} event^{-1})			^{137}Cs activity (kBq kg^{-1} event^{-1})	^{137}Cs deposition flux (10^3 kBq cm^{-2} event^{-1})	Cumulative ^{137}Cs flux	
							Undecontaminated cropland	Forest	Subsoil	Undecontaminated cropland	Forest	Subsoil			(10^3 kBq cm^{-2})	(%)
0-3	Hagibis & Bualoi	2019-11	8.8	3	0.61	1.83	58	16	27	1.06	0.29	0.48	2.1	3.8	93.2	100
3-7	Lan	2017-11	6.7	4	0.65	2.61	55	18	26	1.43	0.46	0.69	2.9	7.5	89.4	96
7-9	Chanthu & Lionrock	2016-08	5.4	2	0.44	0.89	51	45	5	0.45	0.40	0.04	8.4	7.5	81.9	88
9-11	Etau-Kilo	2015-09	4.5	2	0.42	0.84	37	61	2	0.31	0.51	0.02	11.1	9.4	74.4	80
11-14	Phanfone & Vongfong	2014-10	3.6	3	0.42	1.26	31	67	2	0.39	0.85	0.02	12.9	16.2	65.0	70
14-18	Roke	2011-09	0.5	4	0.47	1.87	54	35	10	1.03	0.67	0.19	26.1	48.8	48.8	52
18-21	-	-	-	3	0.38	1.15	50	45	6	0.57 .	0.52	0.06	-	-	-	-
21-23	-	-	-	2	0.44	0.88	49	47	4	0.43	0.41	0.04	-	-	-	-
23-28	-	-	-	5	0.42	2.11	35	61	3	0.74	1.28	0.07	-	-	-	-
28-30	-	-	-	2	0.38	0.77	46	44	11	0.35	0.34	0.08	-	-	-	-
30-33	-	-	-	3	0.30	0.89	50	37	13	0.44	0.33	0.12	-	-	-	-
33-35	-	-	-	2	0.36	0.71	57	20	14	0.41	0.21	0.10	-	-	-	-
35-38	-	-	-	3	0.46	1.37	62	25	13	0.85	0.34	0.18	-	-	-	-
Average per event before FDNPP accident:				2.5 ± 0.6	0.39 ± 0.06	0.96 ± 0.25	52 ± 6	38 ± 9	10 ± 4	0.51 ± 0.18	0.36 ± 0.10	0.10 ± 0.05	-	-	-	-

References

Agnihotri, R., Kumar, R., Prasad, M.V.S.N., Sharma, C., Bhatia, S.K., Arya, B.C., 2014. Experimental Setup and Standardization of a Continuous Flow Stable Isotope Mass Spectrometer for Measuring Stable Isotopes of Carbon, Nitrogen and Sulfur in Environmental Samples. MAPAN 29, 195–205. URL: http://link.springer.com/10.1007/s12647-014-0099-8, doi:10.1007/s12647-014-0099-8.

Amorim, H.C., Hurtarte, L.C., Souza, I.F., Zinn, Y.L., 2022. C:N ratios of bulk soils and particle-size fractions: Global trends and major drivers. Geoderma 425, 116026. URL: https://linkinghub.elsevier.com/retrieve/pii/S0016706122003330, doi:10.1016/j.geoderma.2022.116026.

Asanuma-Brice, C., Evrard, O., Chalaux, T., 2023. Why did so few refugees return to the Fukushima fallout-impacted region after remediation? An interdisciplinary case study from Iitate village, Japan. International Journal of Disaster Risk Reduction 85, 103498. URL: https://linkinghub.elsevier.com/retrieve/pii/S2212420922007178, doi:10.1016/j.ijdrr.2022.103498.

Balsam, W., Ji, J., Chen, J., 2004. Climatic interpretation of the Luochuan and Lingtai loess sections, China, based on changing iron oxide mineralogy and magnetic susceptibility. Earth and Planetary Science Letters 223, 335–348. URL: https://linkinghub.elsevier.com/retrieve/pii/S0012821X04002717, doi:10.1016/j.epsl.2004.04.023.

Batista, P.V.G., Laceby, J.P., Evrard, O., 2022. How to evaluate sediment fingerprinting source apportionments. Journal of Soils and Sediments 22, 1315–1328. URL: https://link.springer.com/10.1007/s11368-022-03157-4, doi:10.1007/s11368-022-03157-4.

Batista, P.V.G., Laceby, J.P., Silva, M.L.N., Tassinari, D., Bispo, D.F.A., Curi, N., Davies, J., Quinton, J.N., 2019. Using pedological knowledge to improve sediment source apportionment in tropical environments. Journal of Soils and Sediments 19, 3274–3289. URL: http://link.springer.com/10.1007/s11368-018-2199-5, doi:10.1007/s11368-018-2199-5.

Beck, H.E., Zimmermann, N.E., McVicar, T.R., Vergopolan, N., Berg, A., Wood, E.F., 2018. Present and future Köppen-Geiger climate classification maps at 1-km resolution. Scientific Data 5, 180214. URL: http://www.nature.com/articles/sdata2018214, doi:10.1038/sdata.2018.214.

Bruni, E., Chenu, C., Abramoff, R.Z., Baldoni, G., Barkusky, D., Clivot, H., Huang, Y., Kätterer, T., Pikuła, D., Spiegel, H., Virto, I., Guenet, B., 2022. Multi-modelling predictions show high uncertainty of required carbon input changes to reach a 4 ‰ target. European Journal of Soil Science 73, e13330. URL: https://bsssjournals.onlinelibrary.wiley.com/doi/10.1111/ejss.13330, doi:10.1111/ejss.13330.

Cao, L., Ishii, N., Zheng, J., Kagami, M., Pan, S., Tagami, K., Uchida, S., 2017. Vertical distributions of Pu and radiocesium isotopes in sediments from Lake Inba after the Fukushima Daiichi Nuclear Power Plant accident: Source identification and accumulation. Applied Geochemistry 78, 287–294. URL: https://linkinghub.elsevier.com/retrieve/pii/S0883292716303651, doi:10.1016/j.apgeochem.2017.01.012.

Chalaux-Clergue, T., Bizeul, R., 2023. fingR: A support for sediment source fingerprinting studies. URL: https://github.com/tchalauxclergue/fingR, doi:10.5281/zenodo.10044404.

Chalaux-Clergue, T., Bizeul, R., Batista, P.V.G., Martínez-Carreras, N., Laceby, J.P., Evrard, O., 2024a. Sensitivity of source sediment fingerprinting to tracer selection methods. SOIL 10, 109–138. URL: https://soil.copernicus.org/articles/10/109/2024/, doi:10.5194/soil-10-109-2024.

Chalaux-Clergue, T., Evrard, O., Durand, R., Caumon, A., Hayashi, S., Tsuji, H., Huon, S., Vaury, V., Wakiyama, Y., Nakao, A., Laceby, J.P., Onda, Y., 2024b. Organic matter, geochemical, visible spectrocolorimetric properties, radiocesium properties, and grain size of potential source material, target sediment core layers and laboratory mixtures for conducting sediment fingerprinting approaches in the Mano Dam Reservoir (Hayama Lake) catchment, Fukushima Prefecture, Japan. URL: https://zenodo.org/records/10836974, doi:10.5281/zenodo.10836974.

Chartin, C., Evrard, O., Laceby, J.P., Onda, Y., Ottlé, C., Lefèvre, I., Cerdan, O., 2017. The impact of typhoons on sediment connectivity: Lessons learnt from contaminated coastal catchments of the Fukushima Prefec-

ture (Japan): Typhoon Impact on Sediment Connectivity - Fukushima, Japan. Earth Surface Processes and Landforms 42, 306–317. URL: https://onlinelibrary.wiley.com/doi/10.1002/esp.4056, doi:10.1002/esp.4056.

Chartin, C., Evrard, O., Onda, Y., Patin, J., Lefèvre, I., Ottlé, C., Ayrault, S., Lepage, H., Bonté, P., 2013. Tracking the early dispersion of contaminated sediment along rivers draining the Fukushima radioactive pollution plume. Anthropocene 1, 23–34. URL: https://linkinghub.elsevier.com/retrieve/pii/S2213305413000088, doi:10.1016/j.ancene.2013.07.001.

Chino, M., Nakayama, H., Nagai, H., Terada, H., Katata, G., Yamazawa, H., 2011. Preliminary Estimation of Release Amounts of ^{131}I and ^{137}Cs Accidentally Discharged from the Fukushima Daiichi Nuclear Power Plant into the Atmosphere. Journal of Nuclear Science and Technology 48, 1129–1134. URL: http://www.tandfonline.com/doi/abs/10.1080/18811248.2011.9711799, doi:10.1080/18811248.2011.9711799.

CIE, 2008. C. I. C.: Colorimetry — Part 4: CIE 1976 L*a*b* Colour space. doi:ISO/CIE11664-4:2019(E).

Coplen, T.B., Kendall, C., Hopple, J., 1983. Comparison of stable isotope reference samples. Nature 302, 236–238. URL: https://www.nature.com/articles/302236a0, doi:10.1038/302236a0.

Debret, M., Sebag, D., Desmet, M., Balsam, W., Copard, Y., Mourier, B., Susperrigui, A.S., Arnaud, F., Bentaleb, I., Chapron, E., Lallier-Vergès, E., Winiarski, T., 2011. Spectrocolorimetric interpretation of sedimentary dynamics: The new "Q7/4 diagram". Earth-Science Reviews 109, 1–19. URL: https://linkinghub.elsevier.com/retrieve/pii/S0012825211000985, doi:10.1016/j.earscirev.2011.07.002.

Duan, H., Zhang, G., Wang, S., Fan, Y., 2019. Robust climate change research: A review on multi-model analysis. Environmental Research Letters 14, 033001. URL: https://iopscience.iop.org/article/10.1088/1748-9326/aaf8f9, doi:10.1088/1748-9326/aaf8f9.

Evrard, O., Chalaux-Clergue, T., Chaboche, P.A., Wakiyama, Y., Thiry, Y., 2023. Research and management challenges following soil and landscape decontamination at the onset of the reopening of the Difficult-To-Return Zone, Fukushima (Japan). SOIL 9, 479–497. URL: https://soil.copernicus.org/articles/9/479/2023/, doi:10.5194/soil-9-479-2023.

Evrard, O., Chartin, C., Onda, Y., Lepage, H., Cerdan, O., Lefèvre, I., Ayrault, S., 2014. Renewed soil erosion and remobilisation of radioactive sediment in Fukushima coastal rivers after the 2013 typhoons. Scientific Reports 4, 4574. URL: https://www.nature.com/articles/srep04574, doi:10.1038/srep04574.

Evrard, O., Durand, R., Foucher, A., Tiecher, T., Sellier, V., Onda, Y., Lefèvre, I., Cerdan, O., Laceby, J.P., 2019a. Using spectrocolourimetry to trace sediment source dynamics in coastal catchments draining the main Fukushima radioactive pollution plume (2011–2017). Journal of Soils and Sediments 19, 3290–3301. URL: http://link.springer.com/10.1007/s11368-019-02302-w, doi:10.1007/s11368-019-02302-w.

Evrard, O., Durand, R., Nakao, A., Laceby, P.J., Lefèvre, I., Wakiyama, Y., Hayashi, S., Asanuma-Brice, C., Cerdan, O., 2020. Impact of the 2019 typhoons on sediment source contributions and radiocesium concentrations in rivers draining the Fukushima radioactive plume, Japan. Comptes Rendus. Géoscience 352, 199–211. URL: https://comptes-rendus.academie-sciences.fr/geoscience/item/CRGEOS_2020__352_3_199_0, doi:10.5802/crgeos.42.

Evrard, O., Laceby, J.P., Lepage, H., Onda, Y., Cerdan, O., Ayrault, S., 2015. Radiocesium transfer from hillslopes to the Pacific Ocean after the Fukushima Nuclear Power Plant accident: A review. Journal of Environmental Radioactivity 148, 92–110. URL: https://linkinghub.elsevier.com/retrieve/pii/S0265931X1530031X, doi:10.1016/j.jenvrad.2015.06.018.

Evrard, O., Laceby, J.P., Nakao, A., 2019b. Effectiveness of landscape decontamination following the Fukushima nuclear accident: A review. SOIL 5, 333–350. URL: https://soil.copernicus.org/articles/5/333/2019/, doi:10.5194/soil-5-333-2019.

Evrard, O., Laceby, J.P., Onda, Y., Wakiyama, Y., Jaegler, H., Lefèvre, I., 2016. Quantifying the dilution of the radiocesium contamination in Fukushima coastal river sediment (2011–2015). Scientific Reports 6, 34828. URL: https://www.nature.com/articles/srep34828, doi:10.1038/srep34828.

Feng, B., Onda, Y., Wakiyama, Y., Taniguchi, K., Hashimoto, A., Zhang, Y., 2022. Persistent impact of Fukushima decontamination on soil erosion and suspended sediment. Nature Sustainability URL: https://www.nature.com/articles/s41893-022-00924-6, doi:10.1038/s41893-022-00924-6.

Foucher, A., Tassano, M., Chaboche, P.A., Chalar, G., Cabrera, M., Gonzalez, J., Cabral, P., Simon, A.C., Agelou, M., Ramon, R., Tiecher, T., Evrard, O., 2023. Inexorable land degradation due to agriculture expansion in South American Pampa. Nature Sustainability 6, 662–670. URL: https://www.nature.com/articles/s41893-023-01074-z, doi:10.1038/s41893-023-01074-z.

Fukuyama, T., Onda, Y., Gomi, T., Yamamoto, K., Kondo, N., Miyata, S., Kosugi, K., Mizugaki, S., Tsubonuma, N., 2010. Quantifying the impact of forest management practice on the runoff of the surface-derived suspended sediment using fallout radionuclides. Hydrological Processes 24, 596–607. URL: https://onlinelibrary.wiley.com/doi/10.1002/hyp.7554, doi:10.1002/hyp.7554.

Funaki, H., Tsuji, H., Nakanishi, T., Yoshimura, K., Sakuma, K., Hayashi, S., 2022. Remobilisation of radiocaesium from bottom sediments to water column in reservoirs in Fukushima, Japan. Science of The Total Environment 812, 152534. URL: https://linkinghub.elsevier.com/retrieve/pii/S0048969721076129, doi:10.1016/j.scitotenv.2021.152534.

Girardin, C., Mariotti, A., 1991. Analyse isotopique du 13C en abondance naturelle dans le carbone organique: un système automatique avec robot préparateur. Cahiers ORSTOM, Serie Pedologie 26, 371–380. URL: https://www.documentation.ird.fr/hor/fdi:39457.

Guo, Z., Dirmeyer, P.A., Gao, X., Zhao, M., 2007. Improving the quality of simulated soil moisture with a multi-model ensemble approach. Quarterly Journal of the Royal Meteorological Society 133, 731–747. URL: https://onlinelibrary.wiley.com/doi/10.1002/qj.48, doi:10.1002/qj.48.

Hao, Q., Oldfield, F., Bloemendal, J., Torrent, J., Guo, Z., 2009. The record of changing hematite and goethite accumulation over the past 22 Myr on the Chinese Loess Plateau from magnetic measurements and diffuse reflectance spectroscopy. Journal of Geophysical Research 114, B12101. URL: http://doi.wiley.com/10.1029/2009JB006604, doi:10.1029/2009JB006604.

Hashimoto, S., Ugawa, S., Nanko, K., Shichi, K., 2012. The total amounts of radioactively contaminated materials in forests in Fukushima, Japan. Scientific Reports 2, 416. URL: https://www.nature.com/articles/srep00416, doi:10.1038/srep00416.

He, Q., Walling, D., 1996. Interpreting particle size effects in the adsorption of 137Cs and unsupported 210Pb by mineral soils and sediments. Journal of Environmental Radioactivity 30, 117–137. URL: https://linkinghub.elsevier.com/retrieve/pii/0265931X96892757, doi:10.1016/0265-931X(96)89275-7.

Huon, S., Hayashi, S., Laceby, J.P., Tsuji, H., Onda, Y., Evrard, O., 2018. Source dynamics of radiocesium-contaminated particulate matter deposited in an agricultural water reservoir after the Fukushima nuclear accident. Science of The Total Environment 612, 1079–1090. URL: https://linkinghub.elsevier.com/retrieve/pii/S0048969717319083, doi:10.1016/j.scitotenv.2017.07.205.

Iwagami, S., Onda, Y., Tsujimura, M., Abe, Y., 2017. Contribution of radioactive 137Cs discharge by suspended sediment, coarse organic matter, and dissolved fraction from a headwater catchment in Fukushima after the Fukushima Dai-ichi Nuclear Power Plant accident. Journal of Environmental Radioactivity 166, 466–474. URL: https://linkinghub.elsevier.com/retrieve/pii/S0265931X16302557, doi:10.1016/j.jenvrad.2016.07.025.

Jacq, K., Perrette, Y., Fanget, B., Sabatier, P., Coquin, D., Martinez-Lamas, R., Debret, M., Arnaud, F., 2019. High-resolution prediction of organic matter concentration with hyperspectral imaging on a sediment core. Science of The Total Environment 663, 236–244. URL: https://linkinghub.elsevier.com/retrieve/pii/S0048969719303699, doi:10.1016/j.scitotenv.2019.01.320.

JAXA, 2016. High-Resolution Land-Use and Land-Cover Map of Japan [2006 ~ 2011] (ver. 16.09; 10-m resolution; 12 categories). URL: https://www.eorc.jaxa.jp/ALOS/en/dataset/lulc/lulc_jpn_e.htm.

JAXA, 2018. High-Resolution Land-Use and Land-Cover Map of Japan [2014 ~ 2016] (ver. 18.03; 30-m resolution; 12 categories). URL: https://www.eorc.jaxa.jp/ALOS/en/dataset/lulc/lulc_v1803_e.htm.

JAXA, 2022. High-Resolution Land-Use and Land-Cover Map of Japan [2018 ∼ 2020] (ver. 21.11; 10-m resolution; 12 categories). URL: https://www.eorc.jaxa.jp/ALOS/en/dataset/lulc/lulc_v2111_e.htm.

JMA, 2023. Historical weather data and download from all over Japan. URL: https://www.jma.go.jp/jma/jma-eng/jma-center/rsmc-hp-pub-eg/RSMC_HP.htm.

Kato, H., Onda, Y., Gao, X., Sanada, Y., Saito, K., 2019. Reconstruction of a Fukushima accident-derived radiocesium fallout map for environmental transfer studies. Journal of Environmental Radioactivity 210, 105996. URL: https://linkinghub.elsevier.com/retrieve/pii/S0265931X18303308, doi:10.1016/j.jenvrad.2019.105996.

Kato, H., Onda, Y., Teramage, M., 2012. Depth distribution of 137Cs, 134Cs, and 131I in soil profile after Fukushima Dai-ichi Nuclear Power Plant Accident. Journal of Environmental Radioactivity 111, 59–64. URL: https://linkinghub.elsevier.com/retrieve/pii/S0265931X11002426, doi:10.1016/j.jenvrad.2011.10.003.

Kitamura, A., Kurikami, H., Sakuma, K., Malins, A., Okumura, M., Machida, M., Mori, K., Tada, K., Tawara, Y., Kobayashi, T., Yoshida, T., Tosaka, H., 2016. Redistribution and export of contaminated sediment within eastern Fukushima Prefecture due to typhoon flooding: Redistribution and export of contaminated sediment. Earth Surface Processes and Landforms 41, 1708–1726. URL: https://onlinelibrary.wiley.com/doi/10.1002/esp.3944, doi:10.1002/esp.3944.

Knudson, C., Vats, D., 2022. StaleGR: A Stable Gelman-Rubin Diagnostic for Markov Chain Monte Carlo. URL: https://cran.r-project.org/web/packages/stableGR/index.html.

Koarashi, J., Atarashi-Andoh, M., Nishimura, S., Muto, K., 2020. Effectiveness of decontamination by litter removal in Japanese forest ecosystems affected by the Fukushima nuclear accident. Scientific Reports 10, 6614. URL: https://www.nature.com/articles/s41598-020-63520-8, doi:10.1038/s41598-020-63520-8.

Kobayashi, T., Nagai, H., Chino, M., Kawamura, H., 2013. Source term estimation of atmospheric release due to the Fukushima Dai-ichi Nuclear Power Plant accident by atmospheric and oceanic dispersion simulations: Fukushima NPP Accident Related. Journal of Nuclear Science and Technology 50, 255–264. URL: http://www.tandfonline.com/doi/abs/10.1080/00223131.2013.772449, doi:10.1080/00223131.2013.772449.

Konoplev, A., Golosov, V., Wakiyama, Y., Takase, T., Yoschenko, V., Yoshihara, T., Parenyuk, O., Cresswell, A., Ivanov, M., Carradine, M., Nanba, K., Onda, Y., 2018. Natural attenuation of Fukushima-derived radiocesium in soils due to its vertical and lateral migration. Journal of Environmental Radioactivity 186, 23–33. URL: https://linkinghub.elsevier.com/retrieve/pii/S0265931X17303296, doi:10.1016/j.jenvrad.2017.06.019.

Konoplev, A., Wakiyama, Y., Wada, T., Ivanov, M., Komissarov, M., Nanba, K., 2022. Reconstruction of time changes in radiocesium concentrations in the river of the Fukushima Dai-ichi NPP contaminated area based on its depth distribution in dam reservoir's bottom sediments. Environmental Research 206, 112307. URL: https://linkinghub.elsevier.com/retrieve/pii/S001393512101608X, doi:10.1016/j.envres.2021.112307.

Kosmas, C.S., Curi, N., Bryant, R.B., Franzmeier, D.P., 1984. Characterization of Iron Oxide Minerals by Second-Derivative Visible Spectroscopy. Soil Science Society of America Journal 48, 401–405. URL: http://doi.wiley.com/10.2136/sssaj1984.03615995004800020036x, doi:10.2136/sssaj1984.03615995004800020036x.

Kurikami, H., Sakuma, K., Malins, A., Sasaki, Y., Niizato, T., 2019. Numerical study of transport pathways of 137Cs from forests to freshwater fish living in mountain streams in Fukushima, Japan. Journal of Environmental Radioactivity 208–209, 106005. URL: https://linkinghub.elsevier.com/retrieve/pii/S0265931X18308853, doi:10.1016/j.jenvrad.2019.106005.

Laceby, J.P., Chartin, C., Evrard, O., Onda, Y., Garcia-Sanchez, L., Cerdan, O., 2016a. Rainfall erosivity in catchments contaminated with fallout from the Fukushima Daiichi nuclear power plant accident. Hydrology and Earth System Sciences 20, 2467–2482. URL: https://hess.copernicus.org/articles/20/2467/2016/, doi:10.5194/hess-20-2467-2016.

Laceby, J.P., Huon, S., Onda, Y., Vaury, V., Evrard, O., 2016b. Do forests represent a long-term source of contaminated particulate matter in the Fukushima Prefecture? Journal of Environmental Management 183, 742–753. URL: https://linkinghub.elsevier.com/retrieve/pii/S0301479716306661, doi:10.1016/j.jenvman.2016.09.020.

Lal, R., 2001. Soil degradation by erosion. Land Degradation & Development 12, 519–539. URL: https://onlinelibrary.wiley.com/doi/10.1002/ldr.472, doi:10.1002/ldr.472.

Lamb, A.L., Wilson, G.P., Leng, M.J., 2006. A review of coastal palaeoclimate and relative sea-level reconstructions using δ13C and C/N ratios in organic material. Earth-Science Reviews 75, 29–57. URL: https://linkinghub.elsevier.com/retrieve/pii/S0012825205001376, doi:10.1016/j.earscirev.2005.10.003.

Lees, J.A., 1997. Mineral magnetic properties of mixtures of environmental and synthetic materials: Linear additivity and interaction effects. Geophysical Journal International 131, 335–346. URL: https://academic.oup.com/gji/article-lookup/doi/10.1111/j.1365-246X.1997.tb01226.x, doi:10.1111/j.1365-246X.1997.tb01226.x.

Lepage, H., Evrard, O., Onda, Y., Lefèvre, I., Laceby, J.P., Ayrault, S., 2015. Depth distribution of cesium-137 in paddy fields across the Fukushima pollution plume in 2013. Journal of Environmental Radioactivity 147, 157–164. URL: https://linkinghub.elsevier.com/retrieve/pii/S0265931X15001484, doi:10.1016/j.jenvrad.2015.05.003.

Lepage, H., Laceby, J.P., Bonté, P., Joron, J.L., Onda, Y., Lefèvre, I., Ayrault, S., Evrard, O., 2016. Investigating the source of radiocesium contaminated sediment in two Fukushima coastal catchments with sediment tracing techniques. Anthropocene 13, 57–68. URL: https://linkinghub.elsevier.com/retrieve/pii/S2213305416300042, doi:10.1016/j.ancene.2016.01.004.

Minolta, K., 2022. QCM-S100w SpectraMagic NX. Konica Minolta. URL: https://www.konicaminolta.com/instruments/download/software/color/smnx/index.html.

MoE, 2013. Decontamination Guidelines. Technical Report 2. Japanese Ministry of Environment. Japan.

MoE, 2015. Decontamination Report - A Compilation of Experiences to Date on Decontamination for the Living Environment Conducted by the Ministry of the Environment. Technical Report. Japanese Ministry of Environment. Japan. URL: http://josen.env.go.jp/en/policy_document/.

MoE, 2018. Decontamination Projects for Radioactive Contamination Discharged by Tokyo Electric Power Company Fukushima Daiichi Nuclear Power Station Accident. Technical Report. Japanese Ministry of Environment.

MoE, 2023a. Decontamination status. URL: http://josen.env.go.jp/area/.

MoE, 2023b. Environmental Remediation. URL: http://josen.env.go.jp/en/decontamination/.

MoE, 2023c. Information on decontamination – Fukushima revitalisation in data. Technical Report. Japanese Ministry of Environment. URL: http://josen.env.go.jp/plaza/info/data/pdf/data_2303_01.pdf.

Morino, Y., Ohara, T., Watanabe, M., Hayashi, S., Nishizawa, M., 2013. Episode Analysis of Deposition of Radiocesium from the Fukushima Daiichi Nuclear Power Plant Accident. Environmental Science & Technology 47, 2314–2322. URL: https://pubs.acs.org/doi/10.1021/es304620x, doi:10.1021/es304620x.

Mukundan, R., Radcliffe, D.E., Ritchie, J.C., Risse, L.M., McKinley, R.A., 2010. Sediment Fingerprinting to Determine the Source of Suspended Sediment in a Southern Piedmont Stream. Journal of Environmental Quality 39, 1328–1337. URL: https://onlinelibrary.wiley.com/doi/10.2134/jeq2009.0405, doi:10.2134/jeq2009.0405.

Nakao, A., Ogasawara, S., Sano, O., Ito, T., Yanai, J., 2014. Radiocesium sorption in relation to clay mineralogy of paddy soils in Fukushima, Japan. Science of The Total Environment 468–469,

523–529. URL: https://linkinghub.elsevier.com/retrieve/pii/S0048969713009893, doi:10.1016/j.scitotenv.2013.08.062.

Nakao, A., Takeda, A., Ogasawara, S., Yanai, J., Sano, O., Ito, T., 2015. Relationships between Paddy Soil Radiocesium Interception Potentials and Physicochemical Properties in Fukushima, Japan. Journal of Environmental Quality 44, 780–788. URL: http://doi.wiley.com/10.2134/jeq2014.10.0423, doi:10.2134/jeq2014.10.0423.

Obara, H., Maejima, Y., Kohyama, K., Ohkura, T., Takata, Y., 2015. Outline of the Comprehensive Soil Classification System of Japan – First Approximation. Japan Agricultural Research Quarterly: JARQ 49, 217–226. URL: https://www.jstage.jst.go.jp/article/jarq/49/3/49_217/_article, doi:10.6090/jarq.49.217.

Obara, H., Ohkura, T., Takata, Y., Kohyama, K., Maejima, Y., Hamazaki, T., 2011. Comprehensive soil classification system of Japan first approximation. Nogyo Kankyo Gijutsu Kenkyusho Hokoku = Bulletin of National Institute for Agro-Environmental Sciences , 1–73URL: http://www.niaes.affrc.go.jp/sinfo/publish/public_e.html.

Onda, Y., Taniguchi, K., Yoshimura, K., Kato, H., Takahashi, J., Wakiyama, Y., Coppin, F., Smith, H., 2020. Radionuclides from the Fukushima Daiichi Nuclear Power Plant in terrestrial systems. Nature Reviews Earth & Environment 1, 644–660. URL: https://www.nature.com/articles/s43017-020-0099-x, doi:10.1038/s43017-020-0099-x.

Osawa, K., Nonaka, Y., Nishimura, T., Tanoi, K., Matsui, H., Mizogichi, M., Tatsuno, T., 2018. Quantification of dissolved and particulate radiocesium fluxes in two rivers draining the main radioactive pollution plume in Fukushima, Japan (2013–2016). Anthropocene 22, 40–50. URL: https://linkinghub.elsevier.com/retrieve/pii/S2213305418300262, doi:10.1016/j.ancene.2018.04.003.

Palazón, L., Latorre, B., Gaspar, L., Blake, W.H., Smith, H.G., Navas, A., 2015. Comparing catchment sediment fingerprinting procedures using an auto-evaluation approach with virtual sample mixtures. Science of The Total Environment 532, 456–466. URL: https://linkinghub.elsevier.com/retrieve/pii/S0048969715300619, doi:10.1016/j.scitotenv.2015.05.003.

Prefecture, F., 2021. Management of the Mano Dam reservoir water level. URL: https://kaseninf.pref.fukushima.jp/.

QGIS Development Team, 2022. QGIS Geographic Information System. Open Source Geospatial Foundation. URL: https://www.qgis.org/fr/site/.

R Core Team, 2022. A Language and Environment for Statistical Computing. R Foundation for Statistical Computing. URL: https://www.R-project.org/.

Rapuc, W., Jacq, K., Develle, A.L., Sabatier, P., Fanget, B., Perrette, Y., Coquin, D., Debret, M., Wilhelm, B., Arnaud, F., 2020. XRF and hyperspectral analyses as an automatic way to detect flood events in sediment cores. Sedimentary Geology 409, 105776. URL: https://linkinghub.elsevier.com/retrieve/pii/S0037073820301913, doi:10.1016/j.sedgeo.2020.105776.

RSMC, 2023. RSMC Typhoon Best Track Data and Graphics [2006 ~ 2021]. URL: https://www.jma.go.jp/jma/jma-eng/jma-center/rsmc-hp-pub-eg/trackarchives.html.

RSMC, 2024. Tropical Cyclone Information. URL: https://www.jma.go.jp/jma/jma-eng/jma-center/rsmc-hp-pub-eg/RSMC_HP.htm.

RStudio Team, 2023. RStudio: Integrated Development Environment for R. RStudio. URL: http://www.rstudio.com/.

Saito, T., Makino, H., Tanaka, S., 2014. Geochemical and grain-size distribution of radioactive and stable cesium in Fukushima soils: Implications for their long-term behavior. Journal of Environmental Radioactivity 138, 11–18. URL: https://linkinghub.elsevier.com/retrieve/pii/S0265931X14002306, doi:10.1016/j.jenvrad.2014.07.025.

Sakaguchi, A., Tanaka, K., Iwatani, H., Chiga, H., Fan, Q., Onda, Y., Takahashi, Y., 2015. Size distribution studies of 137Cs in river water in the Abukuma Riverine system following the Fukushima Dai-ichi Nuclear

Power Plant accident. Journal of Environmental Radioactivity 139, 379–389. URL: https://linkinghub.elsevier.com/retrieve/pii/S0265931X14001519, doi:10.1016/j.jenvrad.2014.05.011.

Sawhney, B.L., 1972. Selective Sorption and Fixation of Cations by Clay Minerals: A Review. Clays and Clay Minerals 20, 93–100. URL: https://doi.org/10.1346/CCMN.1972.0200208, doi:10.1346/CCMN.1972.0200208.

Scheinost, A.C., Chavernas, A., Barrón, V., Torrent, J., 1998. Use and Limitations of Second-Derivative Diffuse Reflectance Spectroscopy in the Visible to Near-Infrared Range to Identify and Quantify Fe Oxide Minerals in Soils. Clays and Clay Minerals 46, 528–536. URL: http://link.springer.com/10.1346/CCMN.1998.0460506, doi:10.1346/CCMN.1998.0460506.

Sellier, V., Navratil, O., Laceby, J.P., Allenbach, M., Lefèvre, I., Evrard, O., 2020. Investigating the use of fallout and geogenic radionuclides as potential tracing properties to quantify the sources of suspended sediment in a mining catchment in New Caledonia, South Pacific. Journal of Soils and Sediments 20, 1112–1128. URL: http://link.springer.com/10.1007/s11368-019-02447-8, doi:10.1007/s11368-019-02447-8.

Steinhauser, G., 2014. Fukushima's Forgotten Radionuclides: A Review of the Understudied Radioactive Emissions. Environmental Science & Technology 48, 4649–4663. URL: https://pubs.acs.org/doi/10.1021/es405654c, doi:10.1021/es405654c.

Stevens, A., Ramirez-Lopez, L., 2022. An introduction to the prospectr package. URL: https://cran.r-project.org/web/packages/prospectr/vignettes/prospectr.html.

Stock, B.C., Jackson, A.L., Ward, E.J., Parnell, A.C., Phillips, D.L., Semmens, B.X., 2018. Analyzing mixing systems using a new generation of Bayesian tracer mixing models. PeerJ 6, e5096. URL: https://peerj.com/articles/5096, doi:10.7717/peerj.5096.

Stock, B.C., Semmens, B.X., Ward, E.J., Parnell, A.C., Phillips, D.L., 2020. MixSIAR: Bayesian Mixing Models in R. URL: https://doi.org/10.5281/zenodo.1209993.

Stock, B.C., Semmens, B.X., Ward, E.J., Parnell, A.C., Phillips, D.L., 2022. JAGS: Bayesian Mixing Models in R. URL: https://doi.org/10.5281/zenodo.1209993.

Taira, Y., Matsuo, M., Yamaguchi, T., Yamada, Y., Orita, M., Takamura, N., 2020. Radiocesium levels in contaminated forests has remained stable, even after heavy rains due to typhoons and localized downpours. Scientific Reports 10, 19215. URL: https://www.nature.com/articles/s41598-020-75857-1, doi:10.1038/s41598-020-75857-1.

Tamaoki, M., Yabe, T., Furukawa, J., Watanabe, M., Ikeda, K., Yasutani, I., Nishizawa, T., 2016. Comparison of Potentials of Higher Plants for Phytoremediation of Radioactive Cesium from Contaminated Soil. Environment Control in Biology 54, 65–69. URL: https://www.jstage.jst.go.jp/article/ecb/54/1/54_65/_article, doi:10.2525/ecb.54.65.

Taniguchi, K., Onda, Y., Smith, H.G., Blake, W., Yoshimura, K., Yamashiki, Y., Kuramoto, T., Saito, K., 2019. Transport and Redistribution of Radiocesium in Fukushima Fallout through Rivers. Environmental Science & Technology 53, 12339–12347. URL: https://pubs.acs.org/doi/10.1021/acs.est.9b02890, doi:10.1021/acs.est.9b02890.

Terashima, S., Imai, N., Taniguchi, M., Okai, T., Nishimura, A., 2002. The Preparation and Preliminary Characterisation of Four New Geological Survey of Japan Geochemical Reference Materials: Soils, JSO-1 and JSO-2; and Marine Sediments, JMS-1 and JMS-2. Geostandards Newsletter 26, 85–94. URL: https://onlinelibrary.wiley.com/doi/10.1111/j.1751-908X.2002.tb00626.x, doi:10.1111/j.1751-908X.2002.tb00626.x.

Thiry, Y., Albrecht, A., Tanaka, T., 2018. Development and assessment of a simple ecological model (TRIPS) for forests contaminated by radiocesium fallout. Journal of Environmental Radioactivity 190–191, 149–159. URL: https://linkinghub.elsevier.com/retrieve/pii/S0265931X17309499, doi:10.1016/j.jenvrad.2018.05.009.

Thothong, W., Huon, S., Janeau, J.L., Boonsaner, A., De Rouw, A., Planchon, O., Bardoux, G., Parkpian, P., 2011. Impact of land use change and rainfall on sediment and carbon accumulation in a water reservoir

of North Thailand. Agriculture, Ecosystems & Environment 140, 521–533. URL: https://linkinghub.elsevier.com/retrieve/pii/S0167880911000442, doi:10.1016/j.agee.2011.02.006.

Tiecher, T., Caner, L., Minella, J.P.G., dos Santos, D.R., 2015. Combining visible-based-color parameters and geochemical tracers to improve sediment source discrimination and apportionment. Science of The Total Environment 527–528, 135–149. URL: https://linkinghub.elsevier.com/retrieve/pii/S0048969715300401, doi:10.1016/j.scitotenv.2015.04.103.

Torrent, J., Liu, Q., Bloemendal, J., Barrón, V., 2007. Magnetic Enhancement and Iron Oxides in the Upper Luochuan Loess-Paleosol Sequence, Chinese Loess Plateau. Soil Science Society of America Journal 71, 1570–1578. URL: http://doi.wiley.com/10.2136/sssaj2006.0328, doi:10.2136/sssaj2006.0328.

Tsubokura, M., Murakami, M., Takebayashi, Y., Nomura, S., Ono, K., Ozaki, A., Sawano, T., Kobashi, Y., Oikawa, T., 2019. Impact of decontamination on individual radiation doses from external exposure among residents of Minamisoma City after the 2011 Fukushima Daiichi nuclear power plant incident in Japan: A retrospective observational study. Journal of Radiological Protection 39, 854–871. URL: https://iopscience.iop.org/article/10.1088/1361-6498/ab280e, doi:10.1088/1361-6498/ab280e.

Tsuji, H., Nishikiori, T., Ito, S., Ozaki, H., Watanabe, M., Sakai, M., Ishii, Y., Hayashi, S., 2023. Monthly particulate/dissolved 137Cs and main cation/anion concentrations in Hama-dori region river water in 2014-2021 under baseflow condition. URL: https://doi.org/10.34355/Fukushima.NIES.00025, doi:10.34355/Fukushima.NIES.00025.

Vandromme, R., Hayashi, S., Tsuji, H., Evrard, O., Grangeon, T., Landemaine, V., Laceby, J.P., Wakiyama, Y., Cerdan, O., 2023. Lessons learnt on the impact of an unprecedented soil decontamination program in Fukushima on contaminant fluxes. Proceedings of the National Academy of Sciences 120, e2301811120. URL: https://pnas.org/doi/10.1073/pnas.2301811120, doi:10.1073/pnas.2301811120.

Verstraeten, G., Poesen, J., 2000. Estimating trap efficiency of small reservoirs and ponds: Methods and implications for the assessment of sediment yield. Progress in Physical Geography: Earth and Environment 24, 219–251. URL: http://journals.sagepub.com/doi/10.1177/030913330002400204, doi:10.1177/030913330002400204.

Wadoux, A.M.C., Malone, B., Minasny, B., Fajardo, M., McBratney, A.B., 2021. Soil Spectral Inference with R: Analysing Digital Soil Spectra Using the R Programming Environment. Progress in Soil Science, Springer International Publishing, Cham. URL: https://link.springer.com/10.1007/978-3-030-64896-1, doi:10.1007/978-3-030-64896-1.

Wakahara, T., Onda, Y., Kato, H., Sakaguchi, A., Yoshimura, K., 2014. Radiocesium discharge from paddy fields with different initial scrapings for decontamination after the Fukushima Dai-ichi Nuclear Power Plant accident. Environ. Sci.: Processes Impacts 16, 2580–2591. URL: http://xlink.rsc.org/?DOI=C4EM00262H, doi:10.1039/C4EM00262H.

Walling, D.E., Owens, P.N., Waterfall, B.D., Leeks, G.J., Wass, P.D., 2000. The particle size characteristics of fluvial suspended sediment in the Humber and Tweed catchments, UK. Science of The Total Environment 251–252, 205–222. URL: https://linkinghub.elsevier.com/retrieve/pii/S0048969700003843, doi:10.1016/S0048-9697(00)00384-3.

Wetzel, R.G., 2001. Rivers and lakes — Their distribution, origins, and forms, in: Limnology. Lake and River Ecosystems.. third edition ed.. Elsevier, pp. 15–42. URL: https://linkinghub.elsevier.com/retrieve/pii/B9780080574394500071, doi:10.1016/B978-0-08-057439-4.50007-1.

Whitaker, A.C., Chapasa, S.N., Sagras, C., Theogene, U., Veremu, R., Sugiyama, H., 2022. Estimation of baseflow recession constant and regression of low flow indices in eastern Japan. Hydrological Sciences Journal 67, 191–204. URL: https://www.tandfonline.com/doi/full/10.1080/02626667.2021.2003368, doi:10.1080/02626667.2021.2003368.

Yamashiki, Y., Onda, Y., Smith, H.G., Blake, W.H., Wakahara, T., Igarashi, Y., Matsuura, Y., Yoshimura, K., 2014. Initial flux of sediment-associated radiocesium to the ocean from the largest river impacted by Fukushima Daiichi Nuclear Power Plant. Scientific Reports 4, 3714. URL: https://www.nature.com/articles/srep03714, doi:10.1038/srep03714.

Yamashita, J., Enomoto, T., Yamada, M., Ono, T., Hanafusa, T., Nagamatsu, T., Sonoda, S., Yamamoto, Y., 2014. Estimation of soil-to-plant transfer factors of radiocesium in 99 wild plant species grown in arable lands 1 year after the Fukushima 1 Nuclear Power Plant accident. Journal of Plant Research 127, 11–22. URL: http://link.springer.com/10.1007/s10265-013-0605-z, doi:10.1007/s10265-013-0605-z.

Zuazo, V.H.D., Pleguezuelo, C.R.R., 2009. Soil-Erosion and Runoff Prevention by Plant Covers: A Review, in: Lichtfouse, E., Navarrete, M., Debaeke, P., Véronique, S., Alberola, C. (Eds.), Sustainable Agriculture. Springer Netherlands, Dordrecht, pp. 785–811. URL: http://link.springer.com/10.1007/978-90-481-2666-8_48, doi:10.1007/978-90-481-2666-8_48.

Chapter III

Decontamination and Radiocesium Transfer: Flood Deposits Insights

Chapter III

Decontamination and Radiocesium Transfer: Flood Deposits Insights

In the previous chapter, the impact of decontamination on sediment and radiocesium transfers was reconstructed by analysing a sediment core sampled in the downstream part of the Mano Dam reservoir. The results confirmed the main role played by extreme precipitation events on sediment transfers in the catchment. In addition, the protective role of the vegetation cover that regrew spontaneously after the abandonment of the catchment allowed to temporarily protect soil from erosion, resulting in equivalent radiocesium transfers as those observed after decontamination. Results also highlighted the role of forests as a potential long-term source of contaminated sediment to the river system.

In this chapter, the impact of decontamination on the transfer of sediment and radiocesium was investigated over a similar period, from 2011 to 2023, using instead sediment samples referred to as "flood deposits" collected each year in November-October at ten sites distributed across the Mano Dam reservoir catchment. This sampling pattern allows to compare different spatial contexts across the catchment. In order to better understand the provenance of the sediment, an index of connectivity was calculated by combining topographical and land use information. This allows to take into account explicitly the progress of the decontamination across the catchment and its impact on the sensitivity of soils to erosion. In addition, to investigate the impact of extreme erosive events, the erosive intensity of each major event prior to the sampling campaigns was spatialised and used to weight the index of connectivity derived from topographical and land use information. The spatial and temporal evolution of the sediment sources and their radiocesium activity were also discussed at light of the progress of decontamination and the occurrence of erosive events reflected in the values of the index of connectivity.

The calculation of the annual index of connectivity showed that the connectivity of the agricultural areas with the river system, which gradually and significantly decreased during the abandonment period (from 2011 to 2015) as a result of the spontaneous regrowth of vegetation, was restored by the decontamination of farmland. The explicit consideration of the erosive events highlighted their strong influence on sediment connectivity. The decontamination programme (2014-2016), by targeting farmland areas in priority, which are areas showing a high sediment connectivity with river systems (contributing on average 73 $\pm$ 14 of sediment), appeared to effectively reduce radiocesium transfers to and within the river systems, from 18.5 $\pm$ 1.9 in 2011 to 1.5 $\pm$ 1.0 kBq kg^{-1} in 2016. However, forested areas, which were not targeted by the decontamination programme and which contain most of the remaining ^{137}Cs, could likely act as a long-term source of contaminated sediment. Nevertheless, these areas were only significantly connected to the river system when extremely erosive events occurred, such as those in 2015 (Etau & Kilo) and 2019 (Hagibis & Bualoi). However, these severe events were shown to cause extensive rill and gully erosion and localised mass movements that were found not to be associated with contaminated sediment transfers, which may limit their contribution to radiocesium transfers over the long term.

Reconstructing particle-bound radiocesium transfers using river lag deposits: A chronology through abandonment, decontamination and agricultural resumption

III.1 - Introduction

The Fukushima Daiichi Nuclear Power Plant (FDNPP) accident in March 2011 resulted in the widespread release of a considerable amount of radionuclides, of which 20 % were deposited over Japan (Morino et al., 2013; Onda et al., 2020). Among the emitted radionuclides, 2.7 PBq of ^{137}Cs were deposited over Japan, of which 2.0 PBq (74 %) were deposited within Fukushima Prefecture (Kato et al., 2019; Taniguchi et al., 2019). In addition to the large quantity of ^{137}Cs emitted, ^{137}Cs is problematic because of its relatively long half-life of 30 year and its potential long-term environmental and human health impacts. Approximately 83 % of the Prefecture area (11,430 km^2) received more than 5 kBq m^{-2} of ^{137}Cs, with 26 % of the surface area that received activities exceeding 100 kBq m^{-2} (Kato et al., 2019). The areas where inhabitants could be exposed to radioactive dose rates exceeding 20 mSv yr^{-1} in 2011 were evacuated. However, in order to allow a rapid return of the population, the Japanese government initiated an unprecedented large-scale decontamination programme to remediate ^{137}Cs-contaminated soils.

As a consequence of the rapid and quasi-permanent binding of ^{137}Cs to fine soil particles (i.e. silt and clay; Saito et al. (2014); Nakao et al. (2014, 2015)), 90 to 99 % of the deposited radiocesium accumulated in the upper 5 cm of undisturbed soils (Kato et al., 2012; Lepage et al., 2015; Konoplev et al., 2016). In relation to this strong binding to fine particles, ^{137}Cs transfer from soil to plant was found to be limited in annual or perennial herbs and trees (Yamashita et al., 2014; Tamaoki et al., 2016; Onda et al., 2020), so that almost all of the ^{137}Cs deposited on the soil remained in the upper organo-mineral layer of the soil. This specific behaviour allowed the implementation of a decontamination programme of ^{137}Cs contaminated soils consisting in the removal of this upper soil layer. The Japanese government initiated extensive decontamination in agricultural areas, urban areas, within a 20-m buffer zone in forests around residential areas and along roads, and grass strips near residential and farmland areas (MoE, 2015, 2018, 2023a; Evrard et al., 2020). By March 2017, decontamination had been carried out on 180 km^2 within the Special Decontamination Zone (SDZ) (16 % of the area), where 48 % was farmland (about 87 km^2) (MoE (2023a), in Japanese; Evrard et al. (2023)).

The decontamination procedure of farmland depended on the initial ^{137}Cs activity in the soil. In soils with activities below 5 kBq kg^{-1}, inversion tillage was carried out to a depth of 30-45 cm. In soils with a higher activity, the following four steps were carried out: (1) removal of the upper 5 cm of soil, (2) addition of granite saprolite from local quarries (55.5 m^3 per 1,000 m^2), referred to as "fresh soil", (3) restoration of soil fertility with amendments, either carbonate (as needed) and phosphorus silicate (about 0.8 t ha^{-1}) or zeolite amendment (about 0.5 t ha^{-1}), and (4) the mixing of the saprolite layer with the underlying soil layer with a double deep-ploughing (25-30 cm) (MoE, 2015, 2018, 2023a). It therefore consisted of three main phases: decontamination (step 1), remediation (step 2) and preparation for recultivation (steps 3 and 4). Depending on the date when the plot was decontaminated and the date when the restriction was lifted, the time between the decontamination/remediation phases (1 and 2) and the preparation for recultivation (3 and 4) may have varied considerably across a catchment with respect to the overall progress of decontamination. The decontamination of farmland soil has resulted in a reduction of 20 to 70 % in ambient air dose rates compared to the 2011 levels (MoE, 2018; Onda et al., 2020), which also led to a reduction in individual radiation exposure (Tsubokura et al., 2019). Then, the decontamination of forest and grass strips differed from that of farmland in

that it did not involve soil removal (MoE, 2015, 2018, 2023a). The decontamination of grass strips consisted of cutting down and removing weeds and shrubs. The 20-m forest buffer zone was decontaminated by removing litter and fallen organic material (leaves, branches) - referred to as "sediment" by the Japanese authorities - to a depth of about 5 cm, without reaching the "mineral soil" layer. The forest was also cleared of underbrush and shrubs. In addition, conifers were pruned to a height of about 4 m from the ground if they were within about 5 m of the forest edge, and the pruned branches were collected. Of note, care was taken to ensure that the pruning did not affect the survival of the trees, so that more than half of their original canopy shall be left. All organic material collected from the grass strips and forest decontamination was transported to special facilities for processing. By March 2020, a total of 6.7 million m^3 of contaminated soil and materials had been removed from all the above-mentioned decontaminated areas in Fukushima Prefecture (MoE, 2023b; Evrard et al., 2023). In parallel to the progress of decontamination, a decrease in particle-bound ^{137}Cs in river sediments has been observed (Osawa et al., 2018; Konoplev et al., 2018). Several factors have been proposed to explain this decrease, such as radioactive decay, the reduction of stocks due to successive erosion events, the progress of decontamination and/or the reduction of erosion through the protection of the soil by spontaneous vegetation cover (Evrard et al., 2016; Vandromme et al., 2023; Chalaux-Clergue et al., 2024b). Nevertheless, Feng et al. (2022) highlighted that decontamination and remediation of farmland, increased the sediment discharge by about a two-fold over a 2 to 3 year time lag.

Consequently, soil sensitivity to erosion varied considerably during the transition from abandonment, decontamination, and resumption of agricultural activities, influencing the impact of erosive events of sediment and contaminant transfer (Evrard et al., 2016; Konoplev et al., 2018; Wakiyama et al., 2019; Taniguchi et al., 2019; Vandromme et al., 2023; Chalaux-Clergue et al., 2024b). In fact, despite its location in northern Japan, Fukushima Prefecture has been hit annually by at least one extreme precipitation event (typhoon or tropical storm), since the FDNPP accident (Laceby et al., 2016a; Evrard et al., 2020). In the context of steep topographic of the mountainous catchments of Fukushima region, these extreme precipitation events were shown to induce significant soil erosion and sediment transfer, which leads to the transfer of contaminated sediment to the Pacific Ocean (Chartin et al., 2013; Evrard et al., 2014, 2015; Osawa et al., 2018; Diacre et al., 2023). Indeed, these extreme events have been identified as the main driver of sediment and particle-bound ^{137}Cs, since they account for 86 % of the annual rainfall erosivity in the region (Laceby et al., 2016a). Indeed, these events accounted for 82 to 99 % of the particulate-bound ^{137}Cs transfer (Yamashiki et al., 2014; Sakaguchi et al., 2015; Iwagami et al., 2017; Osawa et al., 2018). In addition, Sakaguchi et al. (2015) highlighted that the maximum of the particle-bound ^{137}Cs contribution was found in the fine material, such as the silt and clay-sized fraction (3-63 μm). The timing of decontamination is therefore crucial, as extreme events may occur during a period of high soil sensitivity to water erosion, exacerbating the transfer of contaminated sediment.

However, an erosion sensitive area must be potentially or actually connected to the river network for an erosive event to induce sediment transfer. Understanding the spatial variation of parameters controlling erosion within a region is fundamental to better discuss the provenance of sediment and the impact of anthropogenic activities on these transfers (Delmas et al., 2019; Evrard et al., 2022). In order to identify the main potential areas contributing to sediment supply across the landscape, geomorphometric indices have been developed to assess the degree of connectivity of an area to the river network (Borselli et al., 2008; Cavalli et al., 2013). The assessment of the index of connectivity (IC) is mainly based on topographic criteria (i.e. elevation, slope, surface roughness) and state of the soil (i.e. land use or land cover), which provides information on the connectivity under a given land usages. However, this initial approach did not account for the actual rainfall pattern of the studied region. Indeed, the areas subject to erosion can vary greatly depending on the type and pattern of precipitation. As such, the provenance of the resulting sediment can strongly vary between

flood events (Navratil et al., 2012b,a; Evrard et al., 2022). Since extreme rainfall events were shown to drive the sediment transfers in the Fukushima Prefecture, Chartin et al. (2017) proposed to further consider the intensity of erosive events to account of their influence on sediment connectivity. This enables to spatially assess how the interaction of the erosive events and land usages influence connectivity within the catchment.

In addition, decontamination did not progress uniformly across the Fukushima Prefecture (Evrard et al., 2019). Nevertheless, the scale of the Mano Dam reservoir catchment, although the decontamination was initiated in June 2014, most of it took place during the last four months of 2016 (80 %; Chalaux-Clergue et al. (2024b)). Moreover, only 12 % of the catchment area was decontaminated, which represents about 8.2 km^2 out of 67 km^2 (Vandromme et al., 2023). However, within Fukushima Prefecture, only 19 % of the ^{137}Cs deposition occurred over farmland (paddy fields and other types of agricultural land), while 74 % occurred over forest (Hashimoto et al., 2012; Kato et al., 2019). Throughout the period from the accident in March 2011 to 2023, the transfer of particle-bound radiocesium associated with sediment has been influenced by the evolution of land cover during abandonment, decontamination and the progressive resumption of agricultural activities. It is therefore crucial to reconstruct the potential changes in the sources of sediment in order to better understand the transfer of this particle-bound pollution over a catchment (Owens et al., 2005; Collins et al., 2020).

To reconstruct the effects of landscape change on sediment and pollutant transfers within catchments, sediment samples collected along the river system or in water bodies can be used (Owens et al., 2005; Collins et al., 2020). Sediment core collection in lakes has been shown to be effective in reconstructing sediment transfers, and could allow to study several decades with one sample collection (Owens, 2020; Foucher et al., 2023a,b). In Chalaux-Clergue et al. (2024b), sediment and particle-bound radiocesium transfers were reconstructed from 2011 to 2021 through the analysis of a sediment core sampled downstream of the Mano Dam reservoir. It was highlighted that the development of spontaneous vegetation cover during abandonment and decontamination limited sediment and radiocesium transfers similarly. However, to study spatial heterogeneities of the erosion phenomena that occur across catchments, sediment deposits that occurs after flood events, also called flood deposits, can be used as a surrogate investigation material (Collins and Walling, 2004; Olley et al., 2013). Using several sampling sites distributed along the river system allows to investigate different local contexts, in terms of landscape, anthropogenic activities, and local erosion processes (Chartin et al., 2013; Evrard et al., 2014, 2020). In addition, iterative sampling through collecting sediment material systematically at the same location on multiple occasions allows to investigate and compare local evolutions over time. For example, in previous work Evrard et al. (2020) investigated the spatial heterogeneity of the sediment source contributions among several catchments during the 2019 event (Hagibis), or Evrard et al. (2016), Laceby et al. (2016b) and Chartin et al. (2017) that studied the temporal and spatial evolution of particle-bound radiocesium transfer over several years, 2011-2015 in Evrard et al. (2016) and Chartin et al. (2017) and 2012-2014 in Laceby et al. (2016b).

In this study, 101 flood deposits collected annually from 2011 to 2023 at ten sites across the Mano Dam reservoir catchment were investigated. This catchment is an early decontaminated agricultural catchment located in the eastern part of Fukushima Prefecture. This sampling period covers the critical phases of land usages changes following the Fukushima accident, including the abandonment of agricultural activities after evacuation, soil decontamination and the subsequent resumption of agricultural activities. To account for the evolution of these changes, (i) a topography and land-use based sediment connectivity was assessed prior to each sediment sampling campaign, and was then (ii) refined by integrating the impact of the erosive energy of the last major erosive event(s) identified prior to each sampling campaign. A combination of analyses of the sediment samples was used to (iii) reconstruct the spatial and temporal evolution of ^{137}Cs activity across the catchment, and (iv) to determine the relative contributions of potential sources of these sediment lags.

The evolution of the source of sediment and their radiocesium activity were be discussed at light of the spatial distribution of local and upstream sediment connectivity, taking into account the influence of decontamination progress and the relative intensity of erosive events. Results of this research demonstrate that the incorporation of sediment connectivity is crucial for assessing the potential of transfer of contaminants, and therefore, their management.

III.2 - Materials and Methods

III.2.1 - Study site

Mano Dam reservoir (1.4 km^2; 37.68887-37.76166°N, 140.66671-140.84290°E), also known as Hayama Lake, is located in Fukushima Prefecture, in Northeastern Japan (Tōhoku Region). The catchment of Mano Dam reservoir (67 km^2) corresponds to the mountainous upper part of the Mano River drainage area, and its elevation ranges from 170 to 694 m above sea level. It is a typical mountainous agricultural catchment of the eastern part of Fukushima Prefecture, mainly dominated by forests (92 %). Due to its steep topography, farmland (i.e. cropland and paddy fields - 4 %; 2.3 km^2) and grassland (3 %; 1.8 km^2) are concentrated in the valley bottoms (Fig. III.1.a) (2018-2020 period; JAXA (2022)). Farmland areas in general, and paddy fields in particular, are strongly connected to river networks through irrigation systems, which results in their high hydro-sedimentary connectivity with river networks Chartin et al. (2017). Built-up areas cover less than 1 % of the catchment surface area.

The catchment is located under a Dfa cold climate with no dry season and hot summers according to Köppen's climatic classification (Beck et al., 2018). The regional hydrological year runs from November to October (Laceby et al., 2016b; Whitaker et al., 2022). Over the last 30-years period (1991−2021), the mean annual temperature was 13.4 $\pm$ 0.5 °C yr^{-1} (standard deviation = SD), ranging on average from -1.5 $\pm$ 0.9 °C to 30.5 $\pm$ 2.1 °C in January and August, respectively. Annual precipitation amounted to 1207 $\pm$ 216 mm yr^{-1} (SD). Most of the precipitation occurs between June and October, corresponding to 60 % of the annual precipitation and 86 % of the rainfall erosivity (Laceby et al., 2016a). This period corresponds to the Japanese typhoon season, with a peak of intensity taking place from July to September in Fukushima Prefecture.

The catchment is mainly underlied by plutonic rocks (48 % in total, with 31 % granite and 17 % granodiorite), non-alkaline mafic volcanic rocks (42 %) and some sedimentary rocks (9 % in total, with 7 % marine and non-marine sediments, $<$ 1 % terrace and $<$ 1 % fan deposits) and few schists (about 1 %) (Fig. III.1.b). However, 44 % of farmland are located over the main plutonic rocks, due to the steep topography, 46 % of farmland is located on sedimentary rocks (31 % marine and non-marine sediments, 15 % terrace and about 1 % fan deposits) and volcanic rocks are under-represented (10 %). On the contrary, forest are mainly located on plutonic (total 48 % - 31 % granite and 18 % granodiorite) and volcanic rocks (44 %), and only marginally on sedimentary bedrocks (7 %). This unbalanced representation between plutonic/volcanic rocks and sedimentary bedrocks and between forest and farmland is mainly due to the topography, as sedimentary bedrocks and farmland are both located in the valley bottoms.

According to the Comprehensive Soil classification System of Japan (Obara et al. (2011, 2015), with the equivalence of soil types given according to the World Reference Base for Soil Resources (WRB)), the main soil types in the catchment are Brown Forest Soils (37 % - WRB: Cambisols/Stagnosols) and Allophanic

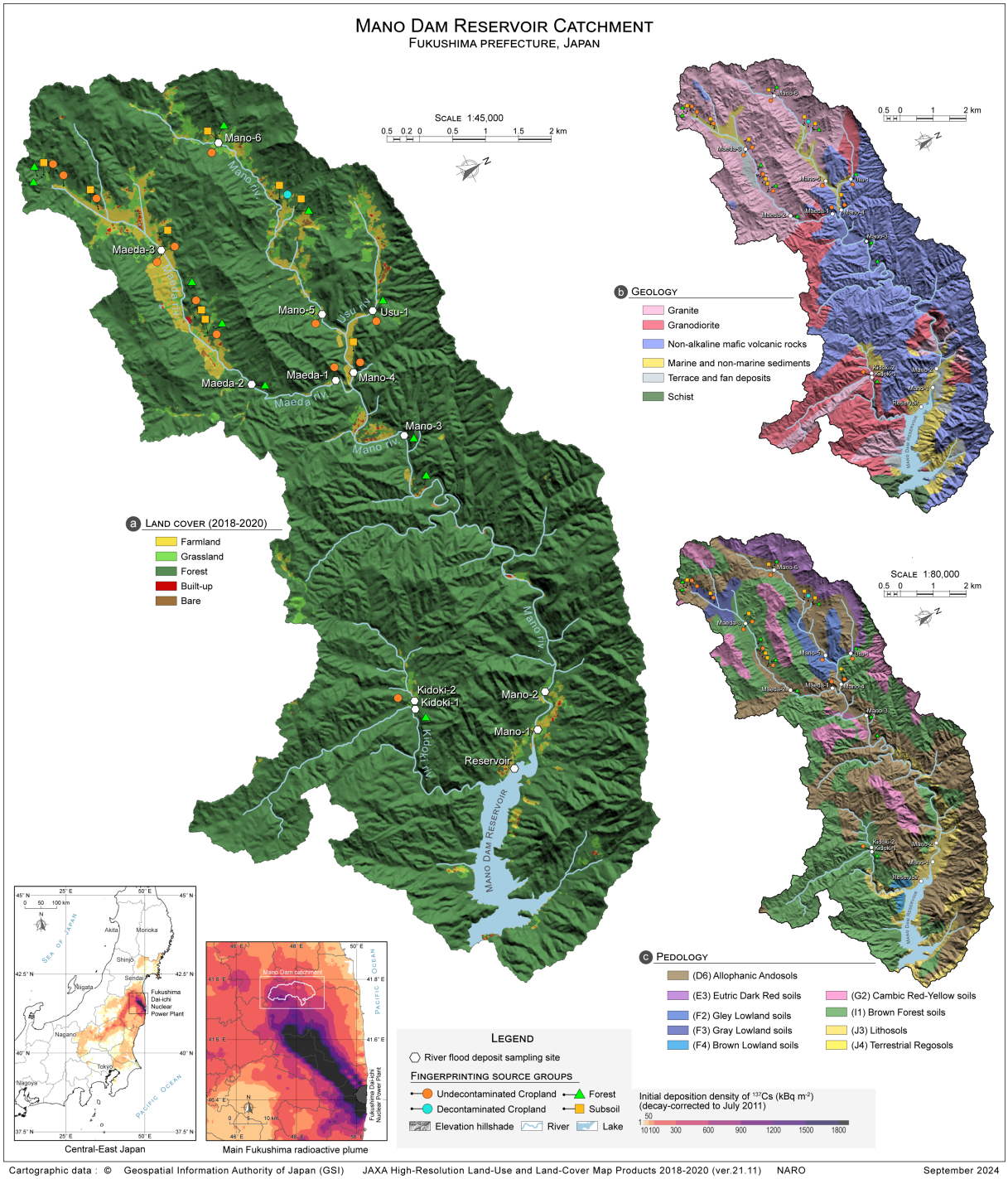


Figure III.1: Mano Dam reservoir catchment map of the main (a) land uses over the 2018-2020 period, (b) geological substrates, and (c) soil types, with the location of the ten lag deposit sampling sites (pink octagon) and potential source samples. Cartographic data from the Geospatial Information Authority of Japan (GSI), JAXA High-Resolution Land-Use and Lad-Cover Map Products 2018-2020 (ver. 21.11), and NARO).

Andosols (36 % - WRB: Silandic Andosols) and then Cambic Red-Yellow Soils (9 % - WRB: Cambisols) and Lithosols (9 % - WRB: Leptosols) (Fig. III.1.c). Most of the farmland is located on Allophanic Andosols (46 %), while 25 % is located on Brown Forest soils and 10 % on Gray Lowland soils. Gray Lowland Soils mainly correspond to paddy fields. Under forest, most of the soils are Brow Forest Soils (39 %) or Allophanic Andosols (36 %), with a low representation of Cambic Red-Yellow Soils (9 %) and Lithosols (7 %).

All maps and geographical processing were performed using the QGIS software (ver. 3.34.8 - Prizren; QGIS Development Team (2024)).

III.2.2 - Catchment management after FDNPP accident

The Mano Dam reservoir catchment is located in the northern part of Iitate village, which was evacuated in 2011 due to the exposure of population to high radiation dose rates exceeding 20 mSv per year at that time, as a consequence of high ^{137}Cs activities in soils ranging from 80 to 1,200 kBq m^{-2} (Kato et al., 2019). The catchment was submitted to a residential ban from 17 July 2012 to 31 March 2017 (MoE, 2023c, in Japanese). Decontamination were carried out in the area from June 2014 to December 2016 (MoE, 2018). Vandromme et al. (2023) reconstructed the daily progress of decontamination during this period using records of plot decontamination dates provided by the Japanese Ministry of the Environment (MoE). However, about 80 % of the decontamination took place during the last three months of 2016 (Vandromme et al., 2023; Chalaux-Clergue et al., 2024b). Based on filed observations, farmland were prepared for the resumption of agricultural activity in 2019, by ploughing the fresh soil layer with underlying residual soil. Despite, only few plots were re-cultivated in 2019, agricultural activity was close to that prevailing before the accident by 2020. Nevertheless, despite the evacuation order, the main land use proportions classified by satellite remained relatively stable during this period extended from 2006 to 2023 (JAXA, 2016, 2018, 2022, 2023), as the catchment is dominated by forest, and farmland was maintained during the evacuation to prevent the development of trees prior to decontamination. However, the land cover of farmland changed during this period, as a consequence of agriculture abandonment, the decontamination and then resumption of agricultural activity.

III.2.3 - Sediment and soil sampling and processing

Flood deposit samples were collected from 10 sampling sites across the Mano Dam catchment (Fig. III.1 and Supplementary Materials Table III.SM-I). Each year from 2011 to 2023, between 5 and 11 flood deposit sediment samples were collected within one day between late October and early November, following the typhoon season and associated flooding (Laceby et al., 2016b). In total, 102 flood deposit samples were collected (Supplementary Materials Table III.SM-I). The absence of deposit or the occurrence of flooding during the field campaign at a sampling site were also reported. In recent years, some sampling sites have no longer been visited: Kidoki-1 and Kidoki-2 since 2019, Usu-1 since 2020 since 2022 because of a simplification of the field expeditions in this post-accidental context (Supplementary Materials Table III.SM-I) following the observed decrease in radiocesium concentrations in river sediment (Evrard et al., 2020).

Based on a literature review, and stakeholder consultations (Evrard et al., 2014), 68 soil samples were collected during previous fieldwork from areas identified as representative of potential sediment sources. These soil samples were described in the Laceby et al. (2016b) study, and included 24 samples from farmland, 24 samples from forested areas, 10 samples from subsoil sources and 10 samples from "fresh soil" material. Subsoil refers to the underlying materials exposed along riverbanks or through deep rill or gully erosion, particularly under forest (Vandromme et al., 2023). Given that the main underlying rock type is plutonic (48 %;

Fig. III.1.b), both subsoil and fresh soil added during the remediation step of decontamination originated from granite saprolite.

Sediment and soil samples consisted of composites of 10 sub-samples collected with a plastic trowel from the 1-2 cm upper layer of material. All samples were dried at 40 °C for 24 to 48 h. They were then successively sieved to 2000 μm and 63 μm to isolate the fraction bearing most of the ^{137}Cs (i.e. silt and clay; Iwagami et al. (2017)) and to minimise the effect of grain size sorting along the transport pathway (Walling et al., 2000).

III.2.4 - Laboratory analyses

Various properties were analysed on soil and sediment samples: radiocesium activity (^{137}Cs) by gamma spectrometry, organic matter composition using combustion and isotope ratio mass spectrometer (total organic carbon (TOC), total nitrogen (TN), and δ^{13}C stable isotope ratio), and visible spectrocolourimetry indices by diffuse reflectance (CIE Lab space). From the visible spectra, several indices were calculated: geothite peak intensities at 445 and 525 nm (Debret et al., 2011), the 700/400 nm diffuse reflectance ratio related to organic matter enrichment (Q7/4; Debret et al. (2011)), and iron oxide-associated parameters derived from the remission function (A1, A2, A3 and Gt; Tiecher et al. (2015)). Elemental geochemistry was primarily analysed by X-ray fluorescence (ED-XRF) for 19 elements (Al, As, Ba, Ca, Co, Cr, Cu, Fe, K, Mg, Mn, Ni, Pb, Rb, Si, Sr, Ti, Zn, and Zr). Due to the failure of the ED-XRF analyser, ICP-MS was used to analyse elemental geochemistry in eight sediment samples. Only the concentrations of the elements that were found to be consistent between the two methods were kept for analysis in the current research (i.e. Al, K, Ca and Mn; see Supplementary Materials section III.6.1.3). All analytical methods and calculations are described in the Supplementary Materials section III.6.1.

III.2.5 - Sediment connectivity

To map the potential sediment connectivity across the landscape, Borselli et al. (2008) introduced an index of connectivity (IC), which links sediment and water runoff from sources to sinks. Initially, this landscape-based approach focused on topographic features to assess sediment connectivity. The IC is calculated as the ratio between upslope (D_{up}) and downslope (D_{dn}) components:

$$IC_k = \log_{10}\left(\frac{D_{up,k}}{D_{dn,k}}\right) \tag{III.1}$$

where k is the cell for which the IC is calculated. The IC value ranges from $-\infty$ to $+\infty$, with higher IC values indicating higher connectivity and lower probability of sediment deposition, the range of values being case-dependent. The upslope component, D_{up}, corresponds to the potential for sediment produced in the upslope contributing area to be transported to the considered downstream k cell area, and it is estimated as follows:

$$D_{up,k} = \sqrt{A_k}\,\overline{S_k}\,\overline{W_k} \tag{III.2}$$

where A is the upslope contributing area (m^2), $\overline{S}$ is the average slope gradient of the upslope contributing area (m m^{-1}), and $\overline{W}$ is the average weighting factor of the contributing area (dimensionless) initially estimated by the C-factor from the Universal Soil Loss Equation (USLE) (Renard and Freimund, 1994).

The downslope component, D_{dn}, corresponds to the potential for sediment transported through the considered k cell to be transported further downstream to the nearest sink. It is estimated as follows:

$$D_{dn,k} = \sum_{i=1}^{n_k} \frac{d_i}{S_i \, W_i} \tag{III.3}$$

where d_i is the distance at the i^{th} cell along the downslope path (m), S_i (m m^{-1}) and W_i (dimensionless) are the slope gradient and weight of the i^{th} cell, respectively.

Subsequent improvements were proposed to better account for catchment and erosive event characteristics. Cavalli et al. (2013) proposed to adapt the slope factor for mountainous catchments by setting a maximum threshold for the slope gradient in addition to the minimum threshold defined by Borselli et al. (2008). Furthermore, several developments of the weighting factor (W) were proposed: (i) through an explicit use of the C-factor from the Universal Soil Loss Equation (USLE) (Renard and Freimund, 1994), (ii) a topographic surface roughness index weighting factor (Ru), and (iii) a precipitation erosivity weighting factor (P) to reflect the characteristics of erosive events.

To describe the the catchment, the weighting factor (i.e. W) was first composed of catchment characteristics, using a topographic index and land cover. The formula was then:

$$IC_k = \log_{10}\left(\frac{\sqrt{A_k}\,\overline{S_k}\,\overline{W_k}}{\sum_{i=1}^{n_k}\frac{d_i}{S_i\,W_i}}\right) = \log_{10}\left(\frac{\sqrt{A_k}\,\overline{S_k}\,\left(\overline{C_k}\,\overline{Ru_k}\right)}{\sum_{i=1}^{n_k}\frac{d_i}{S_i\,\left(C_i\,Ru_i\right)}}\right) \tag{III.4}$$

where C is the USLE C-factor (dimensionless), and Ru the surface roughness index weighting factor (dimensionless).

Then, the effect of the last erosive event before the November flood sediment sampling campaign on the IC was assessed by adding the event precipitation erosivity weighting factor (P; dimensionless):

$$IC_k = \log_{10}\left(\frac{\sqrt{A_k}\,\overline{S_k}\,\left(\overline{C_k}\,\overline{Ru_k}\,\overline{P_k}\right)}{\sum_{i=1}^{n_k}\frac{d_i}{S_i\,\left(C_i\,Ru_i\,E_i\right)}}\right) \tag{III.5}$$

To determine the landscape-based parameters A, S, Ru and d of the Mano Dam reservoir catchment, the 30-metre resolution Digital Surface Model (DSM) of the Advanced Land Observing Satellite (ALOS) project was downloaded from the Japan Aerospace Exploration Agency (JAXA) website (ALOS, 2020).

III.2.5.1 - Contributing area

To estimate the upslope contributing area, A factor, Cavalli et al. (2013) proposed using a multiple flow deterministic infinity approach (Tarboton, 1997, D-infinity). In the D-infinity approach, the algorithm distributes flow proportionally among downslope neighbouring cells. The drainage area of the channel is not limited to the resolution of the cell, which differs from the Deterministic 8 algorithm originally used by (Borrelli et al., 2021, D8). In addition, the D-infinity algorithm is adapted for mountainous catchments with steep slopes and rapid changes of elevation. Prior to computing the upslope contributing area, the DSM was pre-processed to ensure that it did not contain any depression (Planchon and Darboux, 2002).

III.2.5.2 - Distance in downslope direction

The distance along the downslope path at the i^{th} cell was calculated as the distance from the downstream part. The further the cell is from the downstream drainage location, such as the outlet, the higher is the cell distance value.

III.2.5.3 - Slope gradient

The slope gradient, S factor, was calculated from the DSM. The lower limit was set to 0.005 m m^{-1} to avoid infinite values (Borselli et al., 2008), and the upper limit was set to 1 m m^{-1} to avoid bias from very high values on steep slopes (Cavalli et al., 2013).

III.2.5.4 - Cover factor

The USLE cover factor, C-factor, accounts for the effects of vegetation, soil cover, soil biomass, and soil disturbing activities on soil erosion (Wischmeier and Smith, 1978; Renard and Freimund, 1994). The C-factor ranges from 0 to 1, with higher values indicating a higher risk of erosion. According to the C-factor used in the previous work of Chartin et al. (2017) and based on other data found in the literature (Shiono et al., 2002; Yoshikawa et al., 2004), the following values were applied: 0.01 for forested areas, 0.02 for grassland, and 1.0 for bare soils and built-up areas. For farmland, the C-factor was adjusted according to the vegetation development following the abandonment of agricultural activities. The C-factor was set at 0.38 in 2011, 0.17 in 2012, and 0.04 in 2013 for all farmland areas until decontamination started (Yoshikawa et al., 2004). According to Feng et al. (2022), the decontamination of farmland and the addition of "fresh soil" increased the sediment discharged from farmland by about two fold. Natural restoration then reduced sediment transfer close to pre-abandonment levels. Therefore, the farmland post-decontamination C-factor was defined to decrease annually as following the decontamination: 0.76, 0.57, 0.38, 0.17, and 0.04. Progress in farmland decontamination was recorded before each year's October flood deposit sampling, and the corresponding C-factor was applied (Vandromme et al., 2023; Chalaux-Clergue et al., 2024b). In terms of grassland and farmland grass strip decontamination, as it consisted of activities that should not significantly modify their sensitivity to erosion, they were considered as stable over the studied period and a C-factor of 0.02 was applied (similar to "mowing grass"; Yoshikawa et al. (2004)). The decontamination of forest outer strips and roadsides was not considered, as it affected areas smaller than the resolution of the DSM (30 m). From 2019, most of the farmland plots were prepared for recultivation, which consisted of a double deep ploughing without a systematic immediate recultivation, and from 2020 onwards most of the farmland was cultivated. Therefore, the farmland C-factor was set at 0.57 in 2019, and at 0.38 in 2020 and afterwards. Depending on the years studied, JAXA high-resolution land use and land core maps (HRLULC) acquired over different time periods were used. For the study period 2011-2013, the HRLULC acquired over the period 2006-2011 (ver. 16.09; (JAXA, 2016)), for the study period 2014-2017, the HRLULC acquired over the period 2014-2016 (ver. 18.03; (JAXA, 2018)), for the period 2018-2021 the HRLULC acquired over the period 2018-2020 (ver. 21.11; (JAXA, 2022)) and finally for the period 2022-2023 the HRLULC acquired in 2022 (ver. 23.12; (JAXA, 2023)).

III.2.5.5 - Surface roughness index

Cavalli et al. (2013) proposed to use a local measure of topographic surface roughness as a weighting factor. The surface roughness index, RI, was calculated by averaging the weighted absolute elevation differences between the central cell k and its 5×5 surrounding cells. The neighbouring cells were weighed according to their distance from the central cell, using an exponential decay function to reduce the influence of the more distant cells, which was formulated as follows:

$$RI_k = \sqrt{\frac{1}{n}\sum_{i=1}^{n}\left(w_i \left|z_k - z_i\right|\right)} \tag{III.6}$$

where z_k is the elevation of the k cell (m), z_i the elevation of the i^{th} neighbouring cell (m), n the number of neighbouring cells (in this case, 24 for a 5×5 square window), and w_i the distance weighting of the i^{th} neighbouring cell following an exponential exponential function based on the distance d_i from the central k cell, as follows:

$$w_i = e^{-k\ d_i} \tag{III.7}$$

where k is the decay constant power fixed to 2, and d_i the distance from the central k cell.

The surface roughness index weighting factor at the cell k, Ru_k, is expressed as follows:

$$Ru_k = 1 - \left(\frac{RI_k}{RI_{\text{max}}}\right) \tag{III.8}$$

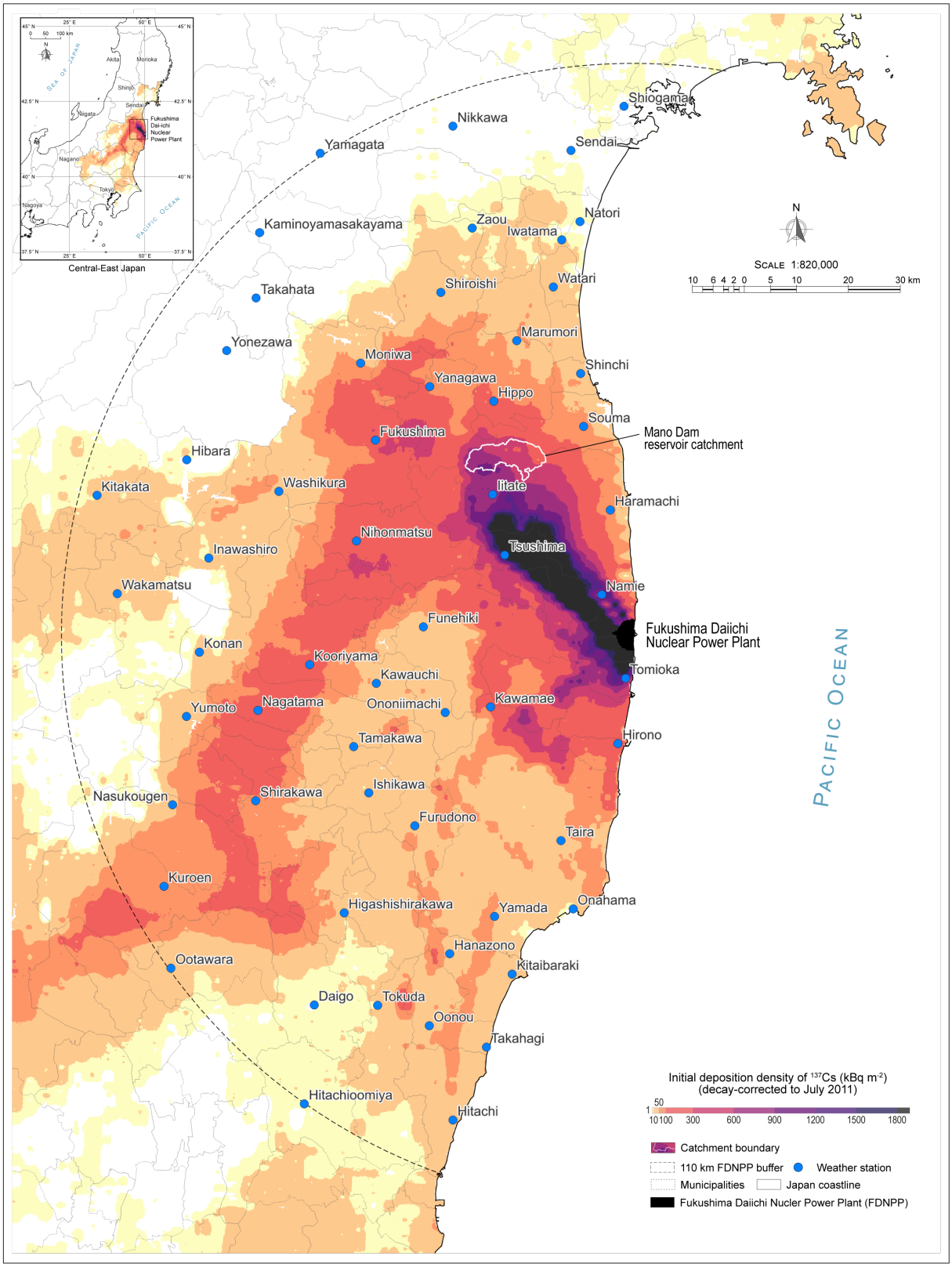
where RI_{max} is the maximum RI in the study area (i.e. the catchment).

III.2.5.6 - Precipitation intensity and erosivity factors

Precipitation and temperature records were downloaded from 58 Automated Meteorological Data Acquisition System stations (AMeDAS) operated by the Japanese Meteorological Agency (JMA) within a 110 km radius around the FDNPP (JMA, 2024, in Japanese) (Fig. III.2). The dataset includes measurements collected every 10 min from 11 March 2011 to 6 November 2023. Previous research has shown the reliability of the 10 min rainfall dataset from JMA, indicating that further correction was not required (Shiono et al., 2013; Duan et al., 2015; Laceby et al., 2016a; Chartin et al., 2017).

Two criteria were used to separate erosive events in the data: (1) cumulative precipitation of the event was greater than 12.7 mm (Panagos et al., 2015) and (2) cumulative precipitation of less than 1.27 mm over a period of 6 h separated events. (Renard and Freimund, 1994; Yin et al., 2017). To account for the occurrence of snowfall, precipitation records were removed when the temperature was below 0 °C (Meusburger et al., 2012), if temperature records were available.

The rainfall erosivity index was calculated for the last main erosive event that occurred before the sampling campaign between the accident and the last sampling campaign, from 11 March 2011 to 6 November 2023. In order to identify the last main erosive event, tracks of all tropical cyclones (typhoons and tropical storms) from the Regional Specialized Meteorological Center (RSMC) Tokyo - Typhoon Center (RSMC, 2023, 2024)



Cartographic data : © Geospatial Information Authority of Japan (GSI) Initial deposition density of ^{137}Cs (Kato et al., 2019) September 2024

Figure III.2: Location of the 58 weather stations within a 110 km buffer zone around the Fukushima Daiichi Nuclear Power Plant (FDNPP) over the ^{137}Cs deposition on soils across north-eastern Japan after Kato et al. (2019), and location of the Mano Dam reservoir catchment (white line). Cartographic data available from the Geospatial Information Authority of Japan (GSI).

were compared with local precipitation data that generated cumulative precipitation higher than the threshold considered to generate overflow and significant erosion in the region according to previous studies (i.e. 60-100 mm; (Evrard et al., 2014)). For each erosive event, the rainfall erosivity index, EI_{30} in MJ mm ha^{-1} h^{-1}, was calculated as the product of the energy of the precipitation event (E, in MJ ha^{-1}) and its maximum 30-mm intensity (I_{30}, in mm h^{-1}) (Brown and Foster, 1987; Renard and Freimund, 1994; Yin et al., 2017) at each precipitation station:

$$EI_{30} = \left(\sum_{r=1}^{l} e_r \, v_r \right) \cdot I_{30} \tag{III.9}$$

where e_r represents the surface precipitation energy per unit of precipitation (MJ ha^{-1} mm^{-1}), and v_r is the volume of precipitation (mm) during a given time interval (here 10 min) for the r^{th} time interval of the event from 1, the first precipitation record during the event, to *l*, the last record of the event. For each time interval, e_t was calculated as:

$$e_r = 0.29 \left(1 - 0.72 \, e^{-0.08 \, i_r}\right) \tag{III.10}$$

where i_r is the precipitation intensity (mm h^{-1}, i.e. 6$\times v_i$).

To describe annual and monthly statistics, the annual or monthly R factor was calculated as the average cumulative EI_{30} value of erosive events identified over the period 2011-2023 as follows:

$$R = \frac{1}{n} \sum_{i=1}^{n} \sum_{j=1}^{m_j} (EI_{30\,j}) \tag{III.11}$$

where R is the annual or monthly average rainfall erosivity in MJ mm ha^{-1} h^{-1} yr^{-1} and MJ mm ha^{-1} h^{-1} mo^{-1}, respectively, n is the number of years or months of data, j the number of erosive events during the year$_i$ or the month$_i$.

The calculations of EI_{30} were done in R language and the functions have been compiled into a package: RainErosivity (Chalaux-Clergue, 2025, version 1.0.0).

Following the approach of Laceby et al. (2016a) and Chartin et al. (2017), EI_{30} was mapped over the Mano Dam reservoir catchment for the most recent erosive event(s) prior to each annual flood sediment sampling campaign between 2011 and 2023. Where multiple extreme precipitation events were identified, their respective EI_{30} were summed for each station and considered as a single event. A regression approach was used to spatialise the EI_{30} values of each station with spatially-distributed covariates. The covariates included morphometric attributes (elevation, slope, slope aspect index), distance to the coast, geographical coordinates and average climatic data over the observed typhoon season (i.e. August to October, Laceby et al. (2016a)) (average cumulative precipitation and mean temperature). Average cumulative precipitation and mean temperature were downloaded from WorldClim ($\sim$1 km^2 resolution; Fick and Hijmans (2017)).

The morphometric attributes were calculated from the 30 m resolution DSM (ALOS, 2020). The aspect refers to the degree to which the slope is oriented towards the east and north. It was composed up of two main components, the wind effect (windward and leeward indices) and the orientation (Easting and Northing). The combined use of slope and aspect allows the local slope orientation to be captured. The distance to the coast

was calculated based on the official delineation of Japanese borders (GSI, 2016). All the covariates were re-scaled at 30 m using a Cubist interpolation.

Each annual extreme precipitation event prior the sediment flood sampling campaign, EI_{30} values were spatialised over the Mano Dam reservoir catchment using a generalised additive models (GAMs; Hastie and Tibshirani (1987)). GAMs are an extend of conventional generalised linear model (GLM; McCullagh and Nelder (2019)), where the global response variables is defined as the sum of smooth functions of the predictor variables, refereed to as covariates. The smooth function allows to consider the potential non-linear relation between the response variables and each covariate, which provide more flexibility than GLMs. The structure of a GAM is represented as :

$$E(Y_i) = \mu_i \tag{III.12}$$

$$g(\mu_i) = \beta_0 + f_{1i}(X_{1i}) + f_{2i}(X_{2i}) + ... + f_{pi}(X_{pi}) + \epsilon_i \tag{III.13}$$

where Y_i is the response variable that follows an exponential family distribution, g a monotonic link function, X_i the covariate of the i^{th} observation, f_i the smooth function of the one or more than one X_i covariate, β_0 the intercept and ϵ_i random error that are independent for different i (Hastie and Tibshirani, 1987; Wood, 2017, 2003).

For each year, a GAM model was fitted on EI_{30} values as response variable using the maximum available stations without zero values (up to 58; Supplementary Materials Table III.SM-II). A total of thirteen GAM models were fitted, with one model for the erosive event or cumulative of erosive events that occurred during each year on the 2011-2023 period. The predictor variables were ten spatial covariates of the weather stations: elevation, slope, windward and leeward indices, Easting, Northing, distance to the coastline, typhoon season average temperature and average cumulative precipitation, latitude, and longitude. In relation to distribution of the event EI_{30} values close to a Quasi-Poisson distribution, a log-linear link function $g(\mu) = \log(\mu)$ was implemented. The models were built using the 'gam' function, from the mgcv package (Wood, 2017). The smooth function of covariates was the 's' function from mgcv. The smooth function was set as a thin plate regression splines (setting: 'bs = tp'), with an automatic selection of neighbourhood size ('k = -1'). In the case of geographical coordinates, their respective interaction was added as a two-dimensional spline using the 'te' function from mgcv. An extra penalty was added to each smoothing predictor ('gam' setting: 'select = TRUE'), so that each could potentially be set to zero during fitting process in case of multi-collinearity or multi-concurvity (Wood, 2003). The model was set to use a restricted maximum likelihood (REML) ('gam' settings: 'method = REML') for smoothing parameter estimation. The REML method considers the smooth predictors as random effects and focuses on estimating the variance components of the model, which makes the method more robust and less prone to local minima. The importance of the predictors to the model could be assessed by checking their effective degrees of freedom (EDF). The predictors for which the model had added an extra penalty would have EDF values tending towards zero. The EDF values close to 1 indicate that the predictor potentially has a linear relationship with the response variable, whereas EDF values above 1 indicate a non-linear relationship. However, an EDF value approaching zero does not always mean that the predictor was actually uninformative. It is possible that one or more other covariates with which that predictor was correlated were more mathematically informative for the model than the considered predictor itself.

The prediction accuracy of the final models was estimated using the REML procedure realised when building model with the 'gam' function. The predicted and observed EI_{30} values were compared to calculate the

mean error (ME), the root mean square error (RMSE), the coefficient of determination (R^2)), and adjusted coefficient of determination (R^2_{adj}). The R^2_{adj} is calculated using the following formula:

$$R^2_{\text{adj}} = 1 - \left(\frac{(1 - R^2)(n - 1)}{n - p - 1} \right) \tag{III.14}$$

where n is the number of observations (i.e. weather stations) and p is the number of covariates. The R^2_{adj} indicates the proportion of variance explained by the independent variable, taking into account the number of predictors in the model, which limits the inflation that could occur with a larger selection of predictors. It also allows a better comparison between GAM models. A value of 1 indicates a perfect fit, while a value of 0 or a negative value indicate a limited predictive ability.

Finally, the event precipitation erosivity weighting factor for an erosive event, P, was determined by normalising the EI_{30} values across the study area (initially marked as R_t in Chartin et al. (2017)), as follows:

$$P = \frac{EI_{30}}{EI_{30\,\text{max}}} \tag{III.15}$$

where $EI_{30\ max}$ is the maximum EI_{30} predicted in the Mano Dam reservoir catchment area.

The procedure followed in QGIS Development Team (2024) and R Core Team (2024) is described in the Supplementary Materials.

III.2.6 - Sediment source fingerprinting

A sediment source fingerprinting approach was developed to assess the evolution of sediment sources across the catchment and over time. Three potential sources were considered: farmland (n = 24), forest (n = 24), subsoil (n = 10), and "fresh soil" (n = 10) (Supplementary Materials Table III.SM-IV). Farmland refers to agricultural land (i.e. cropland, paddy field, grassland) prior to decontamination. Subsoil refers to the underlying materials exposed along riverbanks or by deep gully or gully erosion under forests (Vandromme et al., 2023). As shown in Chalaux-Clergue et al. (2024b), since the main underlying rock is plutonic, most of the subsoil and fresh soil are derived from the same material and were not statistically distinguishable using the potential tracing properties (Supplementary Materials Table III.SM-III). Therefore the subsoil and "fresh soil" samples were merged into a single source group labelled "subsoil and fresh soil" (n = 20) (Supplementary Materials Table III.SM-IV and III.SM-III). Care has been taken to adjust the interpretation of the subsoil and fresh soil contribution at the light of the progress of decontamination.

III.2.6.1 - Tracer selection

Tracer selection followed the widely employed three-step method (Collins et al., 2020; Chalaux-Clergue et al., 2024a): conservative behaviour was assessed with a range test, and source class discrimination was verified using a two-sample Kolmogov-Smirnov test (α = 0.01). The discriminant function analysis was omitted because of the covariance structure of MixSIAR (Owens et al., 2016), which may deal with potential tracer redundancy (Blake et al., 2018). Among the potential range tests, the mean plus or minus one standard deviation (SD) of the log-transformed values was used as a criterion, later referred to as "mean $\pm$ SD". Since

MixSIAR assumes a normal distribution of properties, applying a log transformation of the property values during the range test, which enforces normality, ensures that the assessment of conservative behaviour was consistent with the model's prerequisites and requirements. The source class property range was based on the highest and lowest mean plus or minus one standard deviation of the log-transformed values. Conservativity was assumed if all log-transformed values of the sediment samples were within the source range. In addition, it was reported whether the sample value lied above or below the source range. For the sediment samples where elemental geochemistry was analysed by TQ-ICP-MS, only their elemental concentrations of comparable elements were added to the rang test of the geochemical elements (i.e. Al, K, Ca, and Mn; sec. III.2.4). If a geochemical element other than those that were comparable was selected, those sediment samples would not be included in the following study. The range test and the discriminant test were performed using the functions 'range.tests' and 'discriminant.test', respectively, from the package (Chalaux-Clergue and Bizeul, 2024, version 2.1.0).

III.2.6.2 - Source contribution modeling

The Bayesian mixing model MixSIAR was used to predict source contributions (Stock and Semmens, 2016). The model was run using the MixSIAR package (Stock et al., 2020, version 3.1.12) and JAGS (Stock et al., 2022, version 4.3.1), using the process error formulation (Batista et al., 2022) and a long Markov Chain Monte Carlo chain length with default burn-in and thinning values (i.e. chain length = 300,000, burn-in = 200,000, thin = 100, chain = 3).

III.2.6.3 - Modeling accuracy assessment

To assess the modeling prediction accuracy, a total of 231 virtual mixtures were generated (Palazón et al., 2015; Batista et al., 2022; Chalaux-Clergue et al., 2024a). The virtual mixture contributions were generated as a combination of the three potential sources, each varying from 0 to 100 % with 5 % increments and summing to 100 %, using the fingR::VM.builder function. The properties of the virtual mixtures were calculated as simple proportional mixtures of the potential source property signatures (i.e. mean and SD values) and the respective virtual source contributions.

Modeling prediction accuracy was assessed using several criteria: uncertainty (prediction interval width (W50)), residual bias (mean error (ME)) and model performance (root mean square error RMSE, squared Pearson correlation coefficient (r^2), Nash-Sutcliffe modeling efficiency coefficient (NSE) and continuous ranked probability score (CRPS)) (Batista et al., 2022; Chalaux-Clergue et al., 2024a). These statistics were calculated using fingR functions: 'eval.groups' (ME, RMSE, r^2, NSE), 'interval.width' (W50) and 'CRPS' (CRPS). To evaluate the transferability of the statistics from virtual mixtures to actual mixtures, the predicted contributions of both types of mixtures were compared using ternary diagrams and Encompassed Sample Predictions values (ESP; Chalaux-Clergue et al. (2024b)). ESP ranges, expressed as percentages, represent the proportion of actual mixture predictions within the virtual mixture predictions range. Values near to 100 % indicate a higher transferability of the modeling prediction accuracy.

All processing, analyses and modeling were performed using the R programming environment (R Core Team, 2024, version 4.3.3) in RStudio (RStudio Team, 2023, version 2023.06.1.524).

III.3 - Results

III.3.1 - Rainfall erosivity throughout time

Within a radius of 110 km around FDNPP and across the 58 weather stations considered, the average annual R factor ranged from 1627 $\pm$ 725 MJ mm ha^{-1} h^{-1} yr^{-1} at the Yanagawa station (Fukushima Prefecture) to 7506 $\pm$ 3319 MJ mm ha^{-1} h^{-1} yr^{-1} at the Hanazono station (Ibaraki Prefecture) (Table III.I). The annual average R factor for the 58 stations was 3427 $\pm$ 912 MJ mm ha^{-1} h^{-1} yr^{-1} for the period 2011-2023 (Table III.II). The annual R-factor showed a positive gradient from the north-northwest to the south-southeast (Table III.I). The highest annual R factor were observed in 2019, 2014 and 2013, with 5896 $\pm$ 3429, 4089 $\pm$ 1837 and 3971 $\pm$ 1670 MJ mm ha^{-1} h^{-1} yr^{-1}, respectively (Table III.II). On the contrary, the lowest annual R factor were observed in 2018, 2017, and 2022, with 2136 $\pm$ 1221, 2661 $\pm$ 1151 and 2757 $\pm$ 17190 MJ mm ha^{-1} h^{-1} yr^{-1}, respectively. The difference in the R factor between the most erosive and the least erosive years was of the order of a factor of 1.8.

In addition, rainfall erosivity was not uniformly distributed within the year. The highest monthly R factor occurred in summer and early in autumn, between July and October, which accounted for 73 % of the annual R factor (Table III.II). Among these months, September was the most erosive month with an average R factor of 826 $\pm$ 376 MJ mm ha^{-1} h^{-1} mo^{-1}, followed by July, August and October with month R factor of 691 $\pm$ 274, 622 $\pm$ 273 and 568 $\pm$ 343 MJ mm ha^{-1} h^{-1} mo^{-1}, respectively.

However, although that an average of 27 $\pm$ 3 erosive events occurred each year, most of the events were low-energy events. The average erosive event had an EI_{30} value of 125 $\pm$ 36 MJ mm ha^{-1} h^{-1} (Table III.I), with about 80 % of the events showing EI_{30} values below this average. The average erosive event EI_{30} value across the weather stations ranged from 68 $\pm$ 48 MJ mm ha^{-1} h^{-1} at the Kitakata station (Fukushima Prefecture) to 207 $\pm$ 88 MJ mm ha^{-1} h^{-1} at the Hanazono station (Ibaraki Prefecture). The event EI_{30} showed a positive gradient from the north-northwest to the south-southeast.

The erosive energy of the large extreme precipitation events that occurred prior the sampling campaign varied widely between years (Table III.III). The mean EI_{30} values per event ranged from 51 $\pm$ 103 MJ mm ha^{-1} h^{-1} (number of stations = 49) for the extra-tropical cyclone Malou in 2021 to 2682 $\pm$ 2216 MJ mm ha^{-1} h^{-1} (n = 57) for the typhoon Hagibis in 2019. During the four years 2014, 2016, 2019 and 2022, several events separated by a short period devoid of heavy rainfall (around 10 days) occurred before the sampling campaign. Whilst two events were observed in 2014, 2016 and 2019, a total of five events were observed in 2016. Although in 2016, the first event, Chanthu, had a high average erosivity (913 $\pm$ 709 MJ mm ha^{-1} h^{-1}; n = 58), the subsequent events were of decreasing intensity, up to Malakas that showed an average EI_{30} value of 175 $\pm$ 163 MJ mm ha^{-1} h^{-1} (n = 58). Nonetheless, the cumulative total of erosivity of these five events made 2016 the second most erosive year after 2019, with a mean EI_{30} of 2236 $\pm$ 1225 MJ mm ha^{-1} h^{-1} (n = 58) against 3380 $\pm$ 2566 MJ mm ha^{-1} h^{-1} (n = 57), respectively. In terms of event intensity, these two years were followed by the extra-tropical cyclone Yun-yeung in 2023 with an EI_{30} of 1715 $\pm$ 2150 MJ mm ha^{-1} h^{-1} (n = 52) and the typhoon Roke in 2011 with 1685 $\pm$ 1144 MJ mm ha^{-1} h^{-1} (n = 54). On the contrary, the years 2012, 2018, 2022 and 2021 were those with the least erosive events, with average EI_{30} values of 243 $\pm$ 201 MJ mm ha^{-1} h^{-1} (n = 54), 281 $\pm$ 267 MJ mm ha^{-1} h^{-1} (n = 56), 440 $\pm$ 449 MJ mm ha^{-1} h^{-1} (n = 54) and 51 $\pm$ 103 MJ mm ha^{-1} h^{-1} (n = 49). These events had on average an erosive energy 9 times

Table III.I: Annual statistics of erosive events, erosive energy (EI_{30}) and associated precipitation and annual R factor, at each 58 weather stations within a radius of 110 km around the Fukushima Daiichi Nuclear Power Plant (FDNPP) for the period 2011-2023. Prefecture and stations are ordered from North-West to South-East. SD stands for standard deviation, * indicates that 2012 was missing, ** indicates that 2022 and 2023 were missing, *** indicates that the period 2019-2023 was missing.

		Annual erosive events statistics											
Weather stations information		Number of years	Number of events		Cumulative precipitation (mm)			Event EI_{30} (MJ mm ha^{-1} h^{-1})			R factor (MJ mm ha^{-1} h^{-1} yr^{-1})		
Prefecture	Name		Mean	SD	Median	Mean	SD	Median	Mean	SD	Median	Mean	SD
Yamagata	Yamagata	13	22.3	3.4	686	676	150	82	86	41	1580	1943	1046
	Kaminoyamasakayama	13	25.1	3.5	771	725	140	68	85	53	1914	2054	1166
	Takahata	13	22.8	5.0	664	678	191	75	79	33	1761	1854	1087
	Yonezawa	13	25.2	3.8	796	746	171	72	74	44	1904	1878	1165
Miyagi	Shiogama	13	22.5	2.6	774	766	106	83	106	53	1768	2353	1187
	Nikkawa	13	29.2	3.7	991	1044	138	96	104	38	2688	2992	1004
	Sendai	13	24.9	3.8	921	919	139	119	136	72	2933	3334	1689
	Natori	13	21.5	4.2	820	766	143	104	141	124	2545	2770	1681
	Zaou	13	25.2	4.2	893	916	120	96	103	42	2698	2514	864
	Iwatama**	11	22.5	5.2	868	866	162	145	171	156	3120	3233	1653
	Watari	13	23.6	2.8	863	855	171	97	107	56	2727	2522	1289
	Shiroishi	13	25.5	3.8	856	928	174	104	103	37	2432	2649	1198
	Marumori	13	24.7	3.6	985	925	196	96	121	96	2518	2951	2352
	Hippo	13	26.2	2.7	1076	1114	261	100	165	155	2550	4374	4121
Fukushima	Moniwa	13	24.6	3.3	745	777	147	67	93	44	1951	2287	1114
	Shinchi**	11	24.3	7.8	1006	951	336	114	144	102	2761	3571	2407
	Yanagawa	13	21.3	2.4	681	650	130	74	75	29	1482	1627	725
	Souma	13	26.9	5.6	1052	1061	256	158	146	60	3762	3795	1394
	Fukushima	13	24.1	4.0	861	813	163	102	108	47	2285	2560	1185
	Hibara	13	30.5	4.8	895	930	186	61	81	63	1449	2443	1822
	Washikura	13	34.7	4.3	1590	1576	262	147	142	63	4873	4978	2475
	Iitate	13	24.4	4.0	859	896	181	94	122	67	2323	2937	1676
	Kitakata	13	29.9	5.7	897	867	158	56	68	48	1916	1945	1264
	Haramachi	13	25.8	3.8	1028	1041	188	141	158	74	3959	4026	1703
	Nihonmatsu	13	25.4	5.2	828	796	158	87	114	87	2218	2811	2098
	Tsushima	13	27.5	4.6	1020	1004	208	113	118	46	3249	3239	1268
	Inawashiro	13	21.2	2.1	622	618	110	74	86	42	1622	1820	900
	Namie	13	26.0	4.2	1047	1102	197	138	163	78	4014	4122	1728
	Wakamatsu	13	22.5	3.4	593	631	154	69	74	31	1631	1660	776
	Funehiki	13	24.9	5.7	795	773	201	95	103	37	2656	2596	1212
	Konan	13	23.2	2.8	727	715	142	74	84	44	1600	1944	1119
	Kooriyama	13	24.8	4.4	693	732	139	90	95	38	2252	2302	848
	Tomioka*	12	26.2	8.0	1051	1029	360	125	125	44	3073	3352	1551
	Kawauchi	13	27.0	4.1	996	1081	239	130	158	114	3220	4261	3046
	Nagatama	13	27.8	3.8	857	866	173	97	96	32	2369	2676	995
	Ononiimachi	13	25.5	3.6	772	786	118	93	99	37	2168	2524	973
	Yumoto	13	27.8	4.8	1054	1031	183	107	125	36	3255	3399	857
	Kawamae	13	27.2	4.5	956	952	203	116	123	40	2928	3365	1354
	Hirono	13	27.2	4.5	956	952	203	116	123	40	2928	3365	1354
	Tamakawa	13	24.8	3.7	723	743	142	87	101	32	2638	2480	744
	Ishikawa	13	26.5	3.0	805	858	152	113	128	61	2853	3390	1699
	Shirakawa	13	30.9	2.5	945	1021	204	106	131	84	3288	4088	2810
	Furudono**	11	26.1	8.9	947	915	330	112	126	68	2941	3401	1810
	Taira	13	27.8	4.7	972	1077	253	150	160	76	3789	4444	2124
	Onahama	13	29.3	4.1	1056	1124	202	125	160	62	3522	4666	1847
	Higashishirakawa	13	29.3	5.0	972	974	177	125	139	43	3596	4007	1099
	Yamada	13	31.8	3.5	1166	1243	230	165	170	67	4901	5390	2172
Tochigi	Nasukougen	13	35.8	3.8	1445	1505	249	165	178	66	5957	6351	2416
	Kuroen	13	32.6	3.8	1008	1106	213	137	153	68	4716	4893	2059
	Ootawara	13	32.7	5.6	1218	1134	249	152	165	66	5327	5425	2248
Ibaraki	Hanazono	13	36.4	4.6	1510	1638	292	188	207	88	6961	7506	3319
	Kitaikaraki	13	29.5	3.7	1074	1122	196	140	161	75	4216	4684	2171
	Daigo	13	31.2	5.8	1068	1050	221	131	150	71	4039	4574	1957
	Tokuda	13	31.8	6.4	1076	1103	247	127	147	72	4333	4477	1879
	Oonou	13	36.3	5.5	1409	1488	253	154	167	63	5404	6008	2252
	Takahagi***	8	28.6	11.2	1060	1024	380	107	122	49	2964	3340	2023
	Hitachioomiya	13	31.8	5.4	1041	1027	191	134	135	51	4364	4183	1396
	Hitachi	13	30.1	4.3	1072	1080	197	121	151	98	3878	4429	2509

Table III.II: Annual Erosive events mean R factor and standard deviation (SD) for 58 weather stations within a radius of 110 km around the Fukushima Daiichi Nuclear Power Plant (FDNPP) for the period 2011-2023.

Year	R factor (MJ mm ha^{-1} h^{-1} yr^{-1})	
	Mean	**SD**
2011	3602	2068
2012	3192	1685
2013	3971	1970
2014	4089	1837
2015	3241	1882
2016	3258	1787
2017	2661	1151
2018	2136	1221
2019	5897	3429
2020	3164	1449
2021	2977	1868
2022	2757	1719
2023	3609	2604
Average	*3427*	*912*

Table III.II: Monthly Erosive events mean R factor and standard deviation (SD) for 58 weather stations within a radius of 110 km around the Fukushima Daiichi Nuclear Power Plant (FDNPP) for the period 2011-2023.

Month	R factor (MJ mm ha^{-1} h^{-1} mo^{-1})	
	Mean	**SD**
January	48	43
February	60	61
March	92	56
April	146	123
May	183	110
June	328	165
July	691	274
August	622	273
September	826	376
October	568	343
November	72	74
December	49	35
Average	*307*	*290*

lower than the most erosive years. In addition, there was an increase in the intensity classification associated with the event, as from 2011 to 2016 most of the events were classified as severe tropical storms (Grade = 4) or typhoons (5), while from 2017 to 2023 most of them were referred to as typhoons (5) or extra-tropical cyclones (6) (Table III.III).

Furthermore, the location of the weather station that recorded the highest EI_{30} value varied from event to event (Table III.III and Fig. III.2). Some events were associated with higher EI_{30} in the northern part of the study area, such as in 2011, 2014, 2015, 2019, 2020 and 2021, or conversely, in the southern part in 2013, 2018, 2022 and 2023. Moreover, in 2011, 2014, 2015, 2017, 2019, 2020, the highest EI_{30} were recorded at weather stations located close to the the Mano Dam reservoir catchment, such as at Hippo (Miyagi Pref.) in 2015, at Souma (Fukushima Pref.) in 2017, and at Hippo and Namie (Fukushima Pref.) in 2019. In 2016, despite four out of the five events that had the highest EI_{30} at station located in the southern part, the highest cumulative EI_{30} was recorded at Washikura (Fukushima Pref.), located in the central part of the study area. However, in other years with cumulative events (i.e. 2014, 2019 and 2022), the weather stations with the highest EI_{30} at event scale and at the cumulation of these events were located in the same area.

Although some interannual variability, reflecting differences in the spatial distribution and variable intensity, the GAM models were devoid a bias (ME of 0) and, in most cases, an high accuracy. Indeed, the RMSE values ranged from 4 MJ mm ha^{-1} h^{-1} in 2021 (mean EI_{30} = 494 MJ mm ha^{-1} h^{-1}) to a maximum of 1,253 MJ mm ha^{-1} h^{-1} in 2019 (mean EI_{30} = 3440 MJ mm ha^{-1} h^{-1}) (Table III.IV). In addition, apart from 2015, 2016 and 2019, models showed high linearity, with r^2 values ranging from 0.90 to 1.00, and high modelling efficiency, with R^2 ranging 0.89 to 1.00 and R^2_{adj} ranging from 0.83 to 0.99. Although the lowest accuracy metrics were observed in 2015, 2016 and 2019, accuracy metrics were intermediate. The models were associated with relatively high linearity (r^2 of 0.72, 0.73 and 0.77 respectively) and high modelling efficiency (R^2 of 0.68, 0.72, and 0.76; R^2_{adj} of 0.58, 0.63 and 0.70).

Table III.III: Observed cumulative precipitation and rainfall erosivity (EI_{30}) of the erosive events that occurred before the annual November sampling campaign from 2011 to 2023 within a 110 km radius area around the Fukushima Daiichi Nuclear Power Plant (FDNPP), along with maximum EI_{30} observed at a weather station. 'Cumulative' line in bold corresponds to the event statistics for the year summed by station. Extreme precipitation event intensity classification grades stand for: 2 = tropical depression, 3 = tropical storm, 4 = severe tropical storm, 5 = typhoon, 6 = extra-tropical cyclone.

Year	Event information				Number of stations	Cumulative precipitation (mm)			EI_{30} (MJ mm ha^{-1} h^{-1})			Local maximum EI_{30} (MJ mm ha^{-1} h^{-1})		
	Name	International ID	Date (mo/d)	Grade		Median	Mean	SD	Median	Mean	SD	Prefecture	Station	
2011	Roke	1105	09/19-09/22	5	54	231	232	57	1405	1685	1144	Miyagi	Natori	5085
2012	Jelawat	1217	09/30-10/04	5	54	44	52	31	196	243	201	Fukushima	Washikura	1370
2013	Man-Yi	1322	09/14-09/16	4	58	100	104	46	723	940	758	Ibaraki	Daigo	3764
2014	Phanfone	1418	10/05-10/07	4	58	115	119	41	283	466	462	Fukushima	Onahama	2493
	Vonfong	1419	10/13-10/14	4	58	85	93	40	454	654	681	Fukushima	Shinchi	3354
	Cumulative	**-**	**10/05-10/14**	**-**	**58**	**214**	**212**	**67**	**931**	**1120**	**929**	**Fukushima**	**Shinchi**	**4438**
2015	Etau & Kilo	1518-1517	09/05-09/11	6-4	58	181	218	118	907	1366	1408	Miyagi	Hippo	7879
2016	Chanthu	1607	08/15-08/18	4	58	112	112	50	804	913	709	Ibaraki	Hanazono	2987
	Mindulle & Kompasu	1609-1611	08/21-08/24	4-3	58	68	74	34	378	550	454	Ibaraki	Hitachi	1814
	Lionrock	1610	08/26-08/30	5	58	74	84	52	244	330	348	Miyagi	Hippo	1829
	Namtheun	1618	09/05-09/09	2	58	42	55	38	146	268	385	Tochigi	Nasukougen	2404
	Malakas	1616	09/17-09/21	6	58	88	89	35	117	175	163	Ibaraki	Tokuda	817
	Cumulative	**-**	**08/15-09/21**	**-**	**58**	**391**	**414**	**126**	**2052**	**2236**	**1225**	**Fukushima**	**Washikura**	**6540**
2017	Lan	1721	10/17-10/23	6	58	182	201	67	535	718	578	Fukushima	Souma	2996
2018	Trami	1824	09/29-10/02	5	56	41	46	24	214	281	267	Tochigi	Nasukougen	1247
2019	Hagibis	1919	10/09-10/13	5	57	257	265	101	2131	2682	2216	Miyagi	Hippo	12843
	Bualoi	1921	10/24-10/27	6	57	73	94	59	211	698	924	Fukushima	Namie	3769
	Cumulative	**-**	**10/09-10/27**	**-**	**57**	**348**	**358**	**136**	**3148**	**3380**	**2566**	**Miyagi**	**Hippo**	**13817**
2020	Dolphin	2012	09/07-09/14	6	44	46	62	54	158	512	985	Fukushima	Shinchi	5672
2021	Malou	2120	10/25-10/26	6	49	27	30	13	27	51	103	Fukushima	Tomioka	732
2022	Nanmadol	2214	09/16-09/20	6	31	54	59	42	84	220	303	Ibaraki	Kitaibaraki	1105
	Talas	2215	09/22-09/24	6	54	55	62	27	232	314	331	Tochigi	Nasukougen	1711
	Cumulative	**-**	**09/16-09/24**	**-**	**54**	**74**	**96**	**60**	**299**	**440**	**449**	**Ibaraki**	**Kitaibaraki**	**2239**
2023	Yun-yeung	2313	09/03-09/11	6	52	134	172	114	771	1715	2150	Ibaraki	Hatachi	8664

Table III.IV: Observed and predicted rainfall erosivity mean and standard deviation (SD) (EI_{30} in MJ mm ha^{-1} h^{-1}) for the last(s) erosive events that occurred before the November sampling campaign from 2011 to 2023 over 58 weather stations located within a 100 km radius around the Fukushima Daiichi Nuclear Power Plant (FDNPP), along with the generalised additive models (GAMs) accuracy metrics. ME stands for mean error, RMSE for root mean square error, r^2 for squared Pearson's linear correlation, R^2 for coefficient of determination, R^2_{adj} for adjusted coefficient of determination. The covariates used to fit each model are listed in Supplementary Materials Table III.SM-V.

Year	Number of stations	Observed EI_{30}		Predicted EI_{30}		Accuracy metrics				
		Mean	SD	Mean	SD	ME	RMSE	r^2	R^2	R^2_{adj}
2011	54	1766	1171	1766	1067	0	290	0.94	0.94	0.88
2012	54	254	239	254	230	0	33	0.98	0.98	0.95
2013	58	1082	857	1082	750	0	231	0.93	0.93	0.85
2014	58	1124	928	1124	814	0	300	0.90	0.89	0.83
2015	58	1619	1475	1619	1089	0	774	0.73	0.72	0.63
2016	58	2074	1216	2074	781	0	683	0.72	0.68	0.58
2017	58	801	652	801	609	0	133	0.96	0.96	0.93
2018	56	295	276	295	267	0	24	0.99	0.99	0.97
2019	57	3440	2594	3440	2046	0	1253	0.77	0.76	0.70
2020	44	494	978	494	918	0	132	0.98	0.98	0.96
2021	49	50	102	50	100	0	4	1.00	1.00	0.99
2022	54	460	474	460	453	0	60	0.99	0.98	0.97
2023	52	1830	2220	1830	2166	0	156	1.00	0.99	0.98

Among the covariates, coordinates (i.e., latitude and longitude) had the highest EDF values (mean 21.9 $\pm$ 9.9) for most years (Supplementary Materials Table III.SM-V). The highest EDF values for coordinates were observed for the 2021 and 2018 models with values of 35.36 and 36.74, respectively, indicating the importance of spatial information in predicting the erosive spatial distribution of events. Conversely, the lowest EDF values for coordinates were observed for the 2019 and 2015 models with values of 4.92 and 8.13, respectively, which may indicate a lower spatial variability of these intense erosive events. Furthermore, despite having lower EDF values than coordinates, other covariates such as slope, windward and leeward indices, and distance to the coastline varied in importance between years. For example, slope had a significantly higher EDF value of 2.35 in 2015 and 2.20 in 2023, supporting a non-linear effect of topographic steepness on erosivity in these two years. In contrast, in most years, the slope EDF value was lower than one, as in 2014 with an EDF value of 0.44, indicating a more linear and less important effect of slope, and was considered non-informative in 2012, 2017, 2018, 2020 and 2022. Conversely, covariates such as altitude and mean temperature were removed from most of the models, 9 and 10 out of 13 respectively, which could be related to convergence issues, indicating that their inclusion either did not improve model performance or did not lead to to better prediction accuracy. Overall, no specific pattern was observed in the selection of covariates.

Overall, the predicted EI_{30} values at the scale of the Mano Dam reservoir catchment were similar to the observed EI_{30} at the scale of the 110 km radius around the FDNPP, although some local differences and occasional extreme erosive events (Table III.V). Indeed, for the events of 2015, 2023 and 2019, the predicted maximum EI_{30} largely exceeded the observed values, reaching 30,272,234, 148,560 and 11,269,263 MJ mm ha^{-1} h^{-1}, respectively. As these values exceeded the maximum EI_{30} observed at the weather stations during these events, it was decided to set a threshold to the upper rounding of the maximum EI_{30} observed. Therefore, the maximum EI_{30} observed during 2015 event was 7879 MJ mm ha^{-1} h^{-1} at Hippo (Miyagi Pref.) for a prediction threshold of 8000, for 2019 events, it was 13,817 MJ mm ha^{-1} h^{-1} in Hippo (Miyagi Pref.) for a threshold of 14,000, and for 2023 event it was 8664 MJ mm ha^{-1} h^{-1} in Hatachi (Ibaraki Pref.) for a threshold of 9,000. After adjusting the predictions, the average EI_{30} for 2015 and 2023 events decreased

Table III.V: Summary of predicted rainfall erosivity (EI_{30} in MJ mm ha^{-1} h^{-1}) across the Mano Dam reservoir catchment areas for the last erosive events that occurred before the sampling campaign from 2011 to 2023. SD stands for standard deviation. '*' indicates years with cumulative of events.

Year	Erosive event date (mo/d)	Predicted EI_{30} (MJ mm ha^{-1} h^{-1})				
		Minimum	Maximum	Median	Mean	SD
2011	09/19-09/22	997	4203	2094	2146	479
2012	09-30/10-04	228	759	455	452	118
2013	09/14-09/16	719	4937	427	1519	427
2014	10/05-10/14 *	266	1392	572	626	215
2015	*10/13-10/14 **	*2119*	*30272234*	*4193*	*11619*	*126009*
	Threshold to 8,000	2119	8000	4193	4863	1948
2016	08/15-09/21*	1789	2670	2241	2226	147
2017	10/17-10/23	637	2279	1087	1087	290
2018	09/29-10/02	114	684	205	213	49
2019	*10/09-10/27 **	*2241*	*148560*	*9505*	*10928*	6711
	Threshold to 14,000	2241	14000	9505	9467	3687
2020	09/07-09/14	119	473	202	218	74
2021	10/25-10/26	33	1279	138	148	64
2022	09/16-09/24 *	126	227	154	159	20
2023	*09/03-09/11*	*567*	*11269263*	*2166*	*5772*	*50423*
	Threshold to 9,000	567	9000	2166	2105	2381

significantly and tended towards the median, indicating that the extreme values affected a significant area of the catchment. No such significant change was observed for 2019 events, indicating that a small area was affected by extreme EI_{30} predictions.

For several events, such as those in 2011, 2016, 2018 and 2023, the average predicted and observed EI_{30} were close, differing from -24 % to 27 % in 2018. In addition, almost no difference were found for the 2016 events, with an average predicted EI_{30} lower of 10 MJ mm ha^{-1} h^{-1} than the average observed EI_{30} at regional scale. Although, the 2016 events showed large heterogeneity in terms of rainfall intensity within the 110 km radius around FDNPP (observed EI_{30} SD of 1225 MJ mm ha^{-1} h^{-1}), this heterogeneity remained limited at the scale of the Mano Dam reservoir catchment (predicted EI_{30} SD of 147 MJ mm ha^{-1} h^{-1}). In contrast, 2015 and 2019 events predictions were significantly higher EI_{30} values that the observed EI_{30}, with a mean excess of about 750 % and 2780 %, respectively. However, these events showed wide variations at regional scale, with observed EI_{30} SD of 1408 and 2566 MJ mm ha^{-1} h^{-1}, which could support such local divergence observed in the Mano Dam reservoir catchment. Overall, at the catchment scale, the predicted EI_{30} was lower than the regional average, such as 2014, 2018, 2020 and 2022 events, while it was higher during all the other years events, except 2016.

At the scale of the Mano Dam reservoir catchment, EI_{30} showed an overall similar spatial pattern during most events, with an increasing intensity from inland Japan (west) to the Pacific coast (east), although there were interannual variations in intensity (Fig. III.3). Conversely, the erosive events of 2012, 2016, 2018, 2021, and 2022, showed no significant spatial pattern. The interannual variation in event intensity varied with intensities being classified as low (2018, 2020, 2021, 2022), moderately low (2012, 2014), intermediate (2013, 2017, 2016), moderately high (2011, 2016) or high (2015, 2019 and 2023). In addition, the erosive events in 2019 and 2023 showed a clear east-to-west decrease in intensity, which was not as pronounced during the 2015 event.

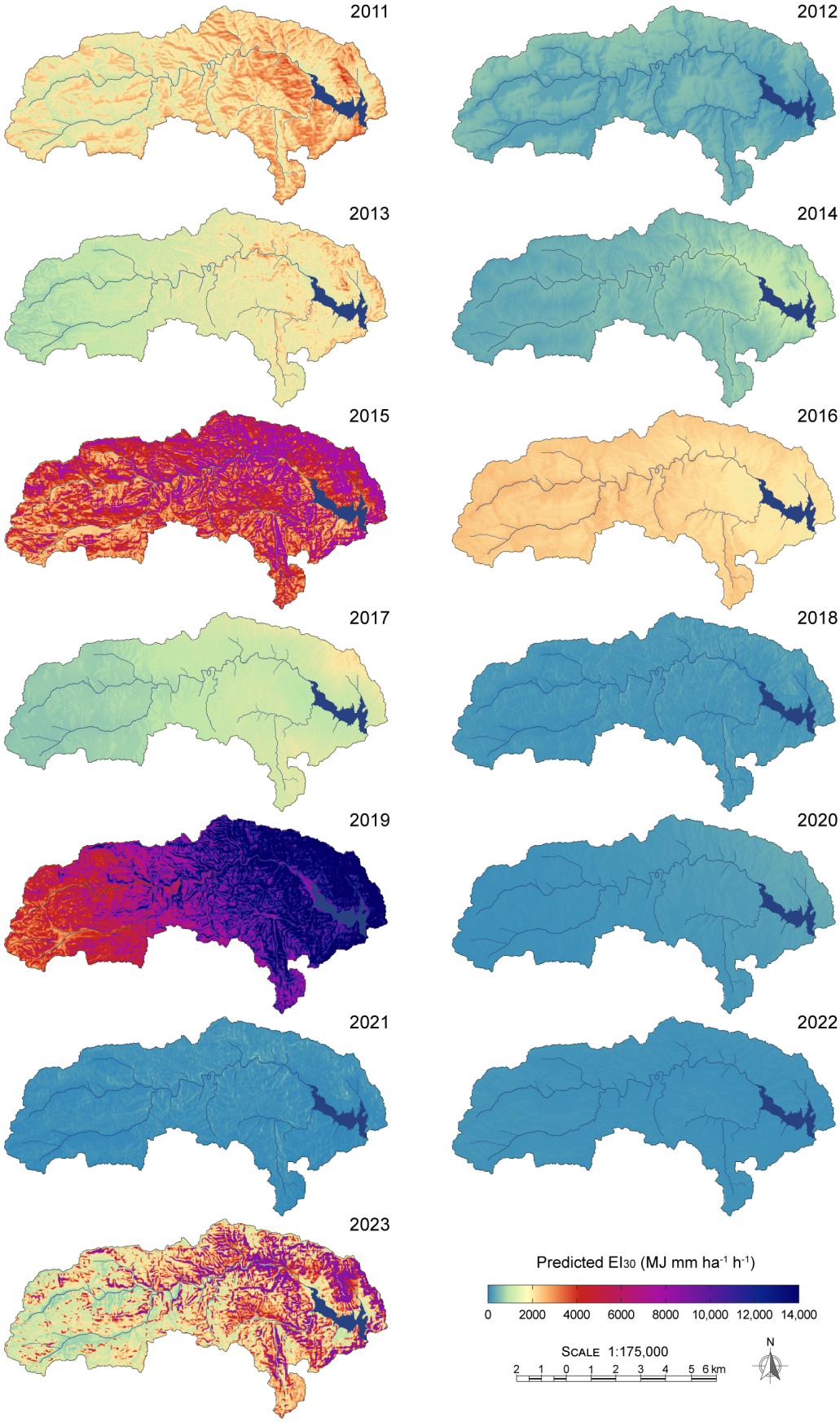


Figure III.3: Predicted rainfall erosivity (EI_{30} in MJ mm ha^{-1} h^{-1}) for the last erosive events that occurred prior to each November sediment sampling campaign from 2011 to 2023 across the Mano Dam reservoir catchment.

III.3.2 - Evolution of sediment connectivity through time

In 2011, IC values varied widely across the catchment (Fig. III.4). Most of the areas across the catchment, and particularly the forested areas, showed consistently low and stable IC values, largely reflecting topographical features. In contrast, higher IC values were concentrated in the valley bottoms close to the river system and more specifically in the western and southern upstream agricultural areas in the upstream Mano, Usu and Maeda tributaries, as well as near the reservoir inlet.

Between 2011 and 2023, IC values showed changed significantly in agricultural areas, while remaining stable in other parts of the catchment (Table III.VI and Fig. III.4). From 2012, IC values in agricultural areas started to decrease and stabilised by 2014 and 2015, with the mean and maximum IC values decreasing from -8.21 $\pm$ 1.04 to -8.33 $\pm$ 1.01 and from -0.57 to -0.60, respectively (Table III.VI). From 2016, IC values increased and reached their maximum in 2018 and 2019 with an average IC value of -8.13 $\pm$ 1.13 and -8.12 $\pm$ 1.14, which was mainly associated with IC modification in the western part of the catchment (Fig. III.4). Following 2019, IC values stabilised and gradually decreased until 2022-2023, with IC values lower than to those observed in 2011, with an average IC value of -8.15 $\pm$ 1.09.

Table III.VI: Annual statistics of the index of connectivity in the Mano Dam reservoir catchment at the time of the annual November flood deposit sampling campaign, from 2011 to 2023. SD stands for standard deviation. Years annotated with * and ** were generated with identical C-factor and JAXA Land Use layers respectively. Note: These statistics were computed using the 'zonal statistics' tool in QGIS [ver. 3.34.8] on the maps presented in figure III.4.

Year	Minimum	Maximum	Median	Mean	SD
2011	-18.21	-0.57	-8.32	-8.21	1.04
2012	-18.22	-0.57	-8.33	-8.23	1.02
2013	-18.22	-0.57	-8.36	-8.28	1.01
2014	-18.24	-0.60	-8.40	-8.33	1.01
2015	-18.24	-0.60	-8.40	-8.33	1.01
2016	-18.24	-0.60	-8.33	-8.21	1.04
2017	-18.24	-0.57	-8.30	-8.18	1.06
2018	-18.77	-0.54	-8.29	-8.13	1.13
2019	-18.77	-0.54	-8.29	-8.12	1.14
2020*	-18.77	-0.54	-8.29	-8.14	1.11
2021*	-18.77	-0.54	-8.29	-8.14	1.11
2022**	-18.72	-0.64	-8.29	-8.15	1.09
2023**	-18.72	-0.64	-8.29	-8.15	1.09
Average ($\pm$ SD)	*-18.47 $\pm$ 0.27*	*-0.58 $\pm$ 0.04*	*-8.32 $\pm$ 0.04*	*-8.20 $\pm$ 0.07*	

III.3.3 - Impact of erosive events on sediment connectivity

When considering the relative impact of erosive events on local sediment connectivity, the IC values showed a significant variation between events (Fig. III.5 and Table III.III). The highest IC values were observed during the major erosive events in 2015 (Etau & Kilo) and 2019 (Hagibis & Bualoi), with mean IC values of -9.84 $\pm$ 1.33 and -8.79 $\pm$ 1.43, respectively (Table III.III). Conversely, the events in 2021 (Malou) and 2022 (Manmadol & Talas), had the lowest IC values over the studied period, with mean IC values of -14.24 $\pm$ 1.40 and -13.95 $\pm$ 1.32, respectively. In addition, the events in 2020 (Dolphin) and 2018 (Trami) were close to those of 2021 and 2022, with mean IC values of -13.58 $\pm$ 1.37 and -13.63 $\pm$ 1.37. In the other years, the events showed intermediate IC values, ranging from -12.75 $\pm$ 1.27 for 2012 (Jelawat) to -10.53 $\pm$ 1.44 in 2023 (Yun-

yeung). In contrast, despite that high EI_{30} values were predicted in 2023 (Table III.V), this did not reflect in the IC values, resulting in an average connectivity similar to that observed for 2016 and 2011 events. Indeed, when comparing the values of the P factor, strong differences were found among events (Supplementary Materials Table III.SM-VI). In 2019, when the highest EI_{30} values were predicted, the mean P factor was 0.68 $\pm$ 0.26 (SD). Whilst, 2015 event, the second largest one, had a mean P factor of 0.35 $\pm$ 0.14, which represents only 51 % of 2019 event. Consequently, other erosive events observed from 2011 to 2023, such as 2011, 2016, and 2023, had mean P factors ranging from 0.22 $\pm$ 0.17 in 2023 to 0.15 $\pm$ 0.03 in 2011 (Roke). Furthermore, least erosive events were associated with very low P-factor, such as in 2012, 2021, 2022, and 2023, with mean P factor ranging from 0.01 $\pm$ 0.00 to 0.03 $\pm$ 0.01.

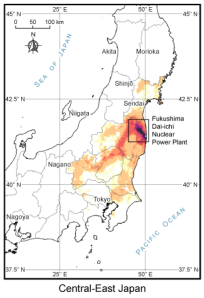
The IC values showed significant annual and spatial variations at the scale of the Mano Dam reservoir, which mainly reflected the underlying topographic features and dominant land use (i.e. forest) instead of emphasising the progression of decontamination (Fig. III.5). The events in 2015 and 2019, were associated with an overall increase of IC across the catchment. Nevertheless, only the 2019 event showed a pronounced increase in IC values in areas located in the vicinity of the river system, near the reservoir inlet and in agricultural areas located the western part of the catchment. This increase was particularly marked in the middle part of the upstream Mano, Maeda, and Usu tributaries. In contrast, the events from 2011 to 2014 were characterised by an overall moderate IC and decreasing IC values near the river system over the period. Then, the 2016 events were associated with an increase of the IC value along the river system. After 2017, although the change of overall IC values under different erosive events, the agricultural areas had IC values similar to that of observed for 2016 events. This pattern remained stable after 2019 events, and for 2020 and 2021 events, although the overall catchment connectivity appeared very low, the agricultural areas showed IC values similar to that observed from 2016/2017 events. Finally, the sediment connectivity at the 2023 event appeared similar to that observed in 2011 event.

Table III.VII: Annual statistics of the index of connectivity in the Mano Dam reservoir catchment at the time of the annual November sampling campaign considering the impact of the last erosive event before each campaign, from 2011 to 2023. SD stands for standard deviation. Note: These statistics were computed using the 'zonal statistics' tool in QGIS [ver. 3.34.8] on the maps presented in figure III.5.

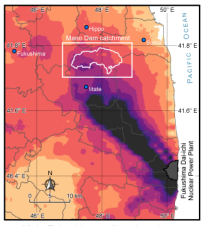
Year	Minimum	Maximum	Median	Mean	SD
2011	-23.86	-1.75	-10.77	-10.69	1.28
2012	-26.32	-4.43	-12.80	-12.75	1.27
2013	-24.07	-2.06	-11.26	-11.22	1.32
2014	-25.21	-2.56	-12.45	-12.37	1.36
2015	-22.76	-1.03	-9.86	-9.84	1.33
2016	-23.60	-1.84	-10.65	-10.55	1.29
2017	-24.50	-2.43	-11.60	-11.51	1.31
2018	-27.92	-4.75	-13.75	-13.63	1.37
2019	-22.35	0.32	-8.86	-8.79	1.43
2020	-26.76	-4.10	-13.71	-13.58	1.37
2021	-28.68	-5.75	-14.31	-14.24	1.40
2022	-27.47	-5.34	-14.07	-13.95	1.32
2023	-24.46	-1.79	-10.59	-10.53	1.44
Average ($\pm$ SD)	*-25.23 $\pm$ 2.02*	*-2.89 $\pm$ 1.82*	*-11.90 $\pm$ 1.75*	*-11.82 $\pm$ 1.73*	

Mano Dam Reservoir Catchment

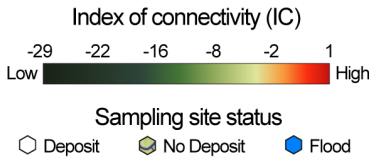
Fukushima Prefecture, Japan



Central-East Japan



Main Fukushima radioactive plume





Part 1 of 2

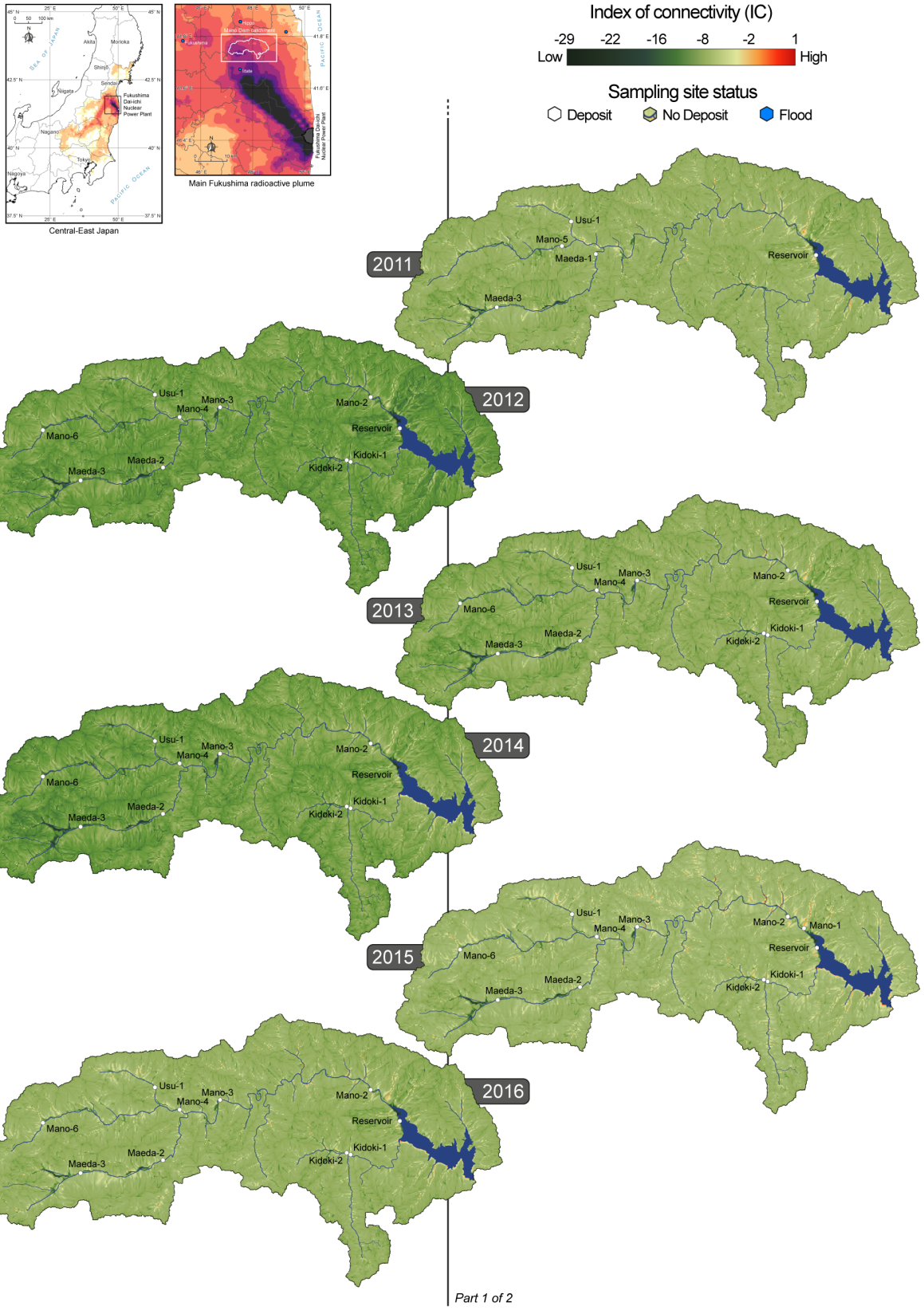


Cartographic data : © Geographical Information Authority of Japan (GSI)
JAXA High-Resolution LULC Map Products (ver. 16.09, 18.03, 21.11, 23.12) JAXA - ALOS Global Digital Surface Model - World 3D-30m (ver. 3.1)

Figure III.4: Evolution of the index of connectivity (IC) in the Mano Dam reservoir catchment based on topographical and contextual information at the time of the annual November flood deposit sampling campaign from 2011 to 2023. White and empty octagons indicate the occurrence or the absence of sediment when conducting sampling, respectively, and blue octagons indicate those sites where water level was too high during the campaign. *This graph is composed of two sub-figures.*

Mano Dam Reservoir Catchment

Fukushima Prefecture, Japan



Part 1 of 2



Cartographic data : © Geographical Information Authority of Japan (GSI)
JAXA High-Resolution LULC Map Products (ver. 16.09, 18.03, 21.11, 23.12) JAXA - ALOS Global Digital Surface Model - World 3D-30m (ver. 3.1)

Figure III.5: Evolution of the index of connectivity (IC) in the Mano Dam reservoir catchment based on topographical and contextual information and the intensity of the last erosive event at the time of the annual November sampling campaign from 2011 to 2023. White and empty octagons indicate the occurrence or the absence of sediment when conducting sampling, respectively, and blue octagon indicates those sites where water level was too high during the campaign. *This graph is composed of two sub-figures.*

III.3.4 - Evolution of ^{137}Cs transfers in space and time

The ^{137}Cs activity in the river flood sediments remained high from 2011 to 2013, then it decreased rapidly from 2013 to 2016, reaching a plateau when decontamination was completed (Fig. III.6). From 2011 to 2016, the mean ^{137}Cs activity in the sediment decreased by 8 times, from 18.5 $\pm$ 1.9 kBq kg^{-1} (SD; n = 5) to 1.5 $\pm$ 1.0 kBq kg^{-1} (n = 10), respectively (Supplementary material Table III.SM-VII). In addition, between 2011 and 2015, some samples showed a significantly higher ^{137}Cs activity, up to 50.9 kBq kg^{-1} in 2011, 23.8 kBq kg^{-1} in 2012, 19.2 kBq kg^{-1} in 2013, 31.5 kBq kg^{-1} in 2014 and 19.4 kBq kg^{-1} in 2015 (Fig. III.6 and Supplementary material Table III.SM-VII). However, after 2015, similar outliers were no longer observed. From 2016 to 2023, the ^{137}Cs activity remained at relatively low levels, fluctuating around an average activity of 1.4 $\pm$ 0.3 kBq kg^{-1} (Supplementary material Table III.SM-VII). However, 2019 showed a slight increase in ^{137}Cs activity, with an average activity of 1.9 $\pm$ 1.8 kBq kg^{-1} (n = 7) and one outlying sample reaching 5.8 kBq kg^{-1} (Supplementary Materials Table III.SM-VII).

While an overall decrease in ^{137}Cs activity was observed at all sampling sites, the annual dynamics varied depending on the location of the individual sites along the river system (Fig. III.7). The upstream sites (Mano-6, Maeda-3, Usu-1 and Kidoki-2) gradually reached a high ^{137}Cs activity peak of 20 to 30 kBq kg^{-1} a few years after the accident, while the downstream sites (Mano-2, Mano-3, Mano-4, Maeda-2 and Kidoki-1) followed the general decreasing trend. In particular, activities at Maeda-3 site peaked in 2012 (23.8 kBq kg^{-1}), they peaked at Mano-6 site in 2013 (19.2 kBq kg^{-1}), at Kidoki-2 site in 2014 (31.5 kBq kg^{-1}) and at Usu-1 site in 2012 and 2015 (8.1 and 19.4 kBq kg^{-1}). In addition, the maximum ^{137}Cs activities at individual sites decreased in downstream direction, with the exception of the Maeda-1 site where the highest ^{137}Cs activity was recorded in 2011. Finally, most sites reached a stable, comparatively low level of ^{137}Cs activity from 2016 onwards. It must be underlined that some sites reached this plateau earlier, such as Mano-6 in 2014, Mano-4 and at Reservoir in 2015, while Mano-2 and Usu-1 reached it later, in 2017. Thereafter, although moderate variations of ^{137}Cs activity were visible between 2016 and 2023, only the Mano-6 site showed a significant peak in 2019 (i.e. 5.8 kBq kg^{-1}).

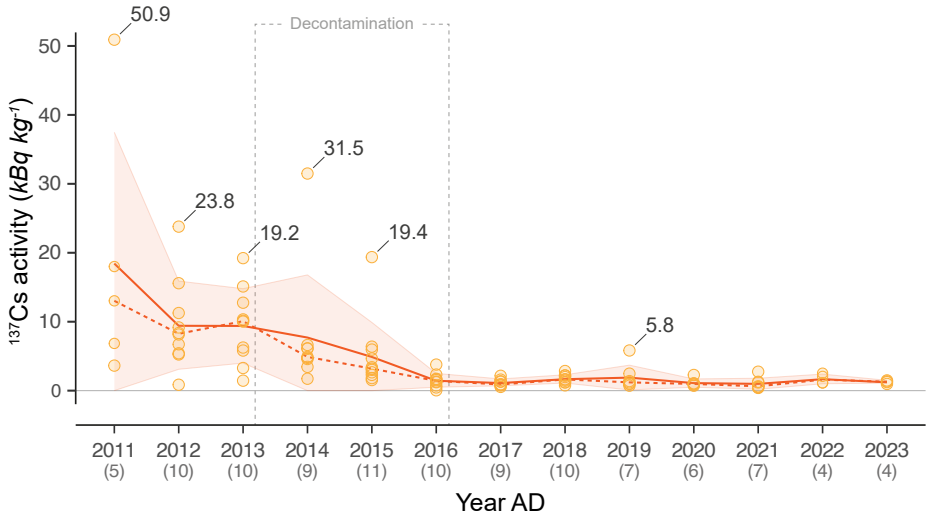


Figure III.6: Annual evolution of ^{137}Cs activities in flood deposits collected in November across the Mano Dam reservoir catchment from 2011 to 2023. Orange solid and dotted lines indicate annual mean and median values, respectively, with the standard deviation around the mean indicated by the light orange ribbon. Number in brackets indicates the number of samples collected during each campaign. Dotted line indicates the occurrence of the decontamination period that took place from June 2014 to December 2016.

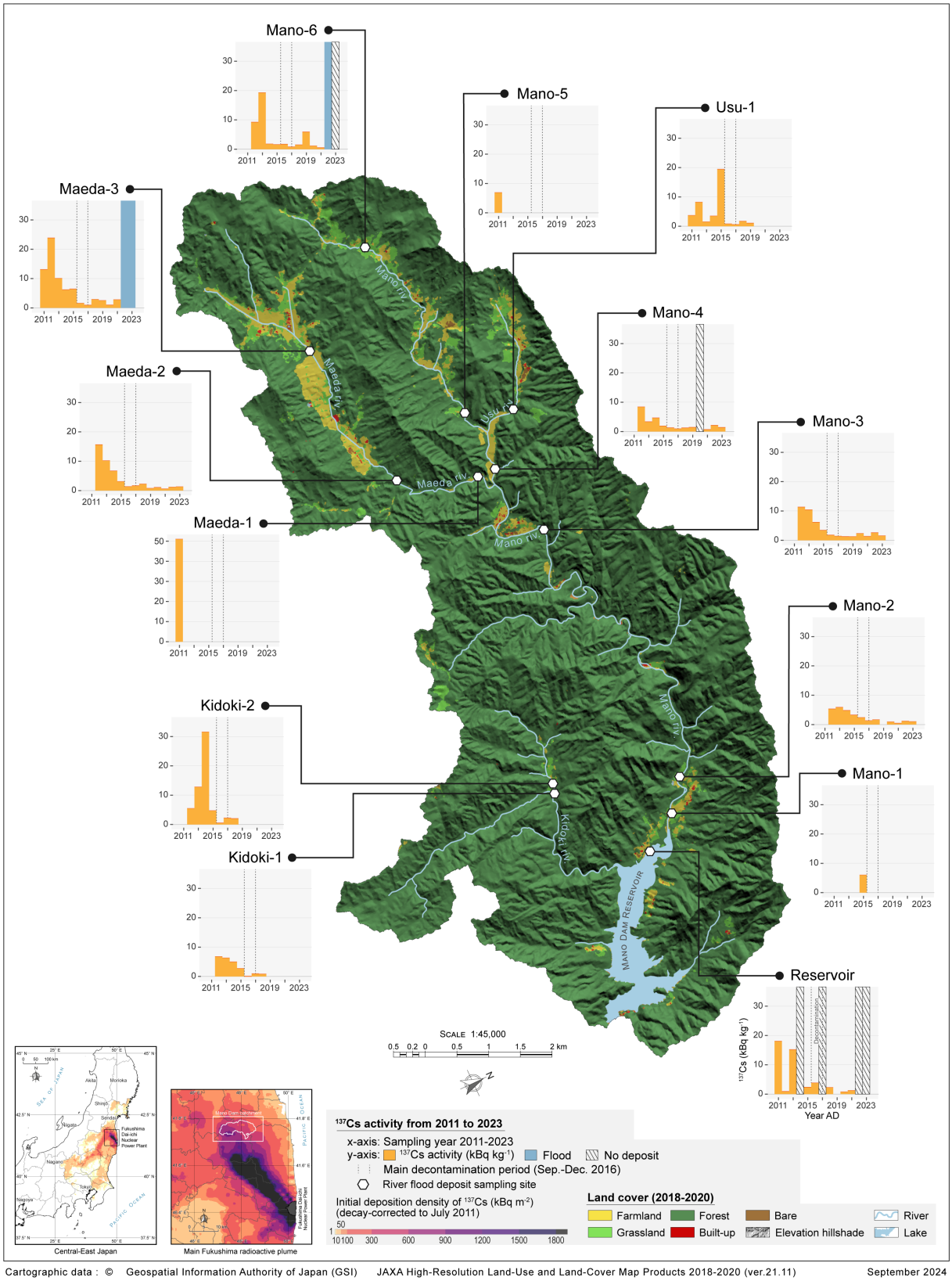


Figure III.7: Annual evolution of ^{137}Cs activity in flood deposits collected annually from 2011 to 2023 during the November sampling campaign at ten sampling sites across the Mano Dam reservoir catchment. Cartographic data available from the Geospatial Information Authority of Japan (GSI) and JAXA High-Resolution Land-Use and Lad-Cover Map Products 2018-2020 (ver. 21.11).

III.3.5 - Sediment source fingerprinting

III.3.5.1 - Tracer selection

Out of the 19 geochemical elements analysed by ED-XRF, eight elements were removed from the subsequent analysis as their measurement uncertainties were too high (i.e. As, Ba, Co, Cr, Cu, Ni, Pb, Rb).

Among the remaining 23 properties analysed or calculated for potential source soil and flood deposit samples (summarised in Supplementary Materials Table III.SM-IV), only nine properties were identified as showing a conservative behaviour in all 96 flood deposit samples, according to the range test using the mean $\pm$ SD criterion (Fig. III.8). These eight conservative properties were: TOC, TN, Al, Ti, L*, a*, b*, G_{445} and G_{545}. However, for properties where not all target samples passed the range tests, when considering the number of target samples that passed the range tests, for some properties a significant number of target samples were within the range of those found in sources. This was observed for Si, Zn, Q7/4, A1, A2, and K for which between 96 and 93 % of the target samples had properties values remaining within the range of those found in the sources (Fig. III.8). In addition, for Ca, Fe, Mg, Mn, Sr, Zn, Zr, A1, A2, Q7/4, all or the majority of the samples that did not pass the test were above the range of values found in the sources, while for the TOC/TN ratio and K they were below the range, and they were equally distributed for Si.

Among the eight conservative properties, only Ti was not significantly discriminant between potential sources (p values < 0.01) (Fig. III.8). The conservativeness and discriminant capacity tests resulted in the selection of seven tracers. These tracers consist of two organic matter properties (TOC and TN), one geochemical element (Al) and three colour parameters (L*, a* and b*) and the intensity of two diffuse reflectance peaks of geothite (G_{445} and G_{545}).

The resulting selection of tracers showed a majority of tracers that provide a high level of source discrimination (Fig. III.8 and Supplementary Materials Fig. III.SM-2). More than half of the tracers provided a strong discrimination between the three potential sources (p value ≤ 0.001; TOC, TN, Al, L*, G_{445}) although G_{525} did not provide a very strong discrimination between forest and farmland (p value = 0.0014). Only, a*

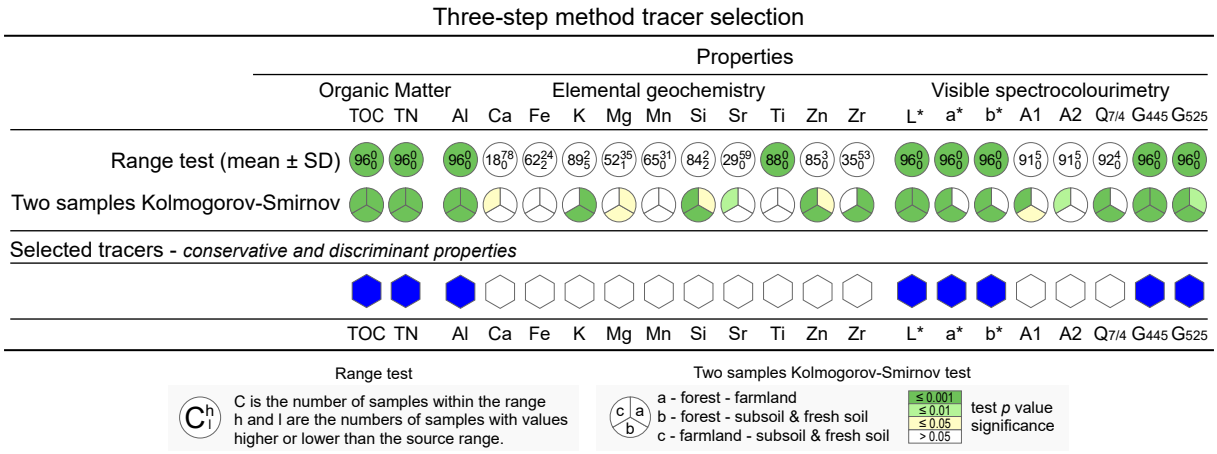


Figure III.8: Tracer selection according to the three-step method. Green filled circles and sections indicate a property considered conservative according to the range test based on the mean $\pm$ one standard deviation of the log-transformed values and the discriminant power test (two-sample Kolmogorov-Smirnov test p value < 0.01), respectively. Blue filled diamonds indicate selected tracers (i.e. properties that passed both the conservative behaviour and discriminant capacity tests). TOC stands for total organic carbon, TN stands for total nitrogen, CN stands for TOC/TN ratio.

and b* did not significantly discriminate between forest and farmland (p value > 0.05), and a* did not strongly discriminate between forest and subsoil ($0.001 \leq p$ value ≤ 0.01).

The sediment source fingerprinting modelling was run using the eight following tracer selection: TOC, TN, Al, L*, a*, b*, G_{445} and G_{525}.

III.3.5.2 - Sediment source fingerprinting modelling accuracy

The accuracy metrics obtained for the MixSIAR model using virtual mixtures demonstrated generally a good predictive capacity and reliability, although the performance varied significantly between the sources (Table III.VIII and Fig. III.9). On average, the model was unbiased (ME = 0 %) and displayed a high degree of linearity between theoretical and predicted contributions (r^2 = 0.87). This was further supported by an intermediate NSE of 0.66 and a low CRPS of 8, indicating a relatively good predictive capacity, with a satisfactory accuracy as indicated by a RMSE of 14 % and a W50* of 12 %.

Regarding the relationship between the theoretical and the predicted contributions for the virtual mixtures, different behaviours were observed among the sources (Fig. III.9.a, III.9.b and III.9.c). The subsoil source predictive accuracy was very good (NSE = 0.90 and RMSE = 8 %) and was associated with a highly linear relationship between theoretical and predicted contributions (r^2 = 0.94) and a very low positive bias (ME = 3 %) (Table III.VIII). For forest and farmland, the prediction accuracies were moderate, with NSE of 0.56 and 0.53, respectively, although they resulted in different types of prediction errors (Table III.VIII). The forest was under-predicted for contributions above 10 % (Fig. III.9.b) which was confirmed with a ME of -13 % and which was associated with a moderate accuracy (W50* = 16 %, RMSE = 17 %). In contrast, farmland was slightly over-predicted (ME = 9 %) but showed a large dispersion in predictions that decreased for higher contributions (W50* = 16, RMSE = 17 %) (Fig. III.9.a and Table III.VIII). Farmland tended to be over-predicted below 60 % of contributions and under-predicted above this value (Fig. III.9.a).

When considering the transferability of model accuracy metrics calculated using virtual mixture predictions to those of actual sediment samples simultaneously for all three sources, there were significant disparities among the sources (Table III.VIII; Fig. III.9.a, b and c) and an overall limited overlap (Fig. III.9.d). The totality of the forest contributions to sediment were within the range of those of virtual mixtures (ESP = 100 %), while about half of the samples were within the range for farmland and subsoil-fresh soil sources, with ESP values of 47 % and 45 %, respectively (Table III.VIII; Fig. III.9.a, b and c). The predicted contribution space of the virtual mixtures appeared moderately contracted compared to the initial theoretical space (Fig. III.9.d). This contraction was mainly observed for farmland with a high contribution from subsoil and

Table III.VIII: Summary of sediment source fingerprinting MixSIAR modeling prediction accuracy statistics calculated on virtual mixtures (n = 231). W50 stands from prediction interval width; ME stands for mean error; RMSE stands for root mean square error, r^2 stands for squared Pearson's correlation coefficient, NSE stands for Nash-Sutcliffe modeling efficiency coefficient; CRPS stands for continuous ranked probability score; ESP stands from encompassed sample predictions expression as the number of samples within the range of source out of 101 (n) and as a percentage (%). The * indicates mean value per source.

Source	W50* (%)	ME (%)	RMSE (%)	r^2	NSE	CRPS*	ESP	
							(n)	(%)
Farmland	16	9	17	0.73	0.53	10	45	47
Forest	10	-13	17	0.95	0.56	11	96	100
Subsoil	9	3	8	0.94	0.90	4	43	45
Average	*12*	*0*	*14*	*0.87*	*0.66*	*8*	-	-

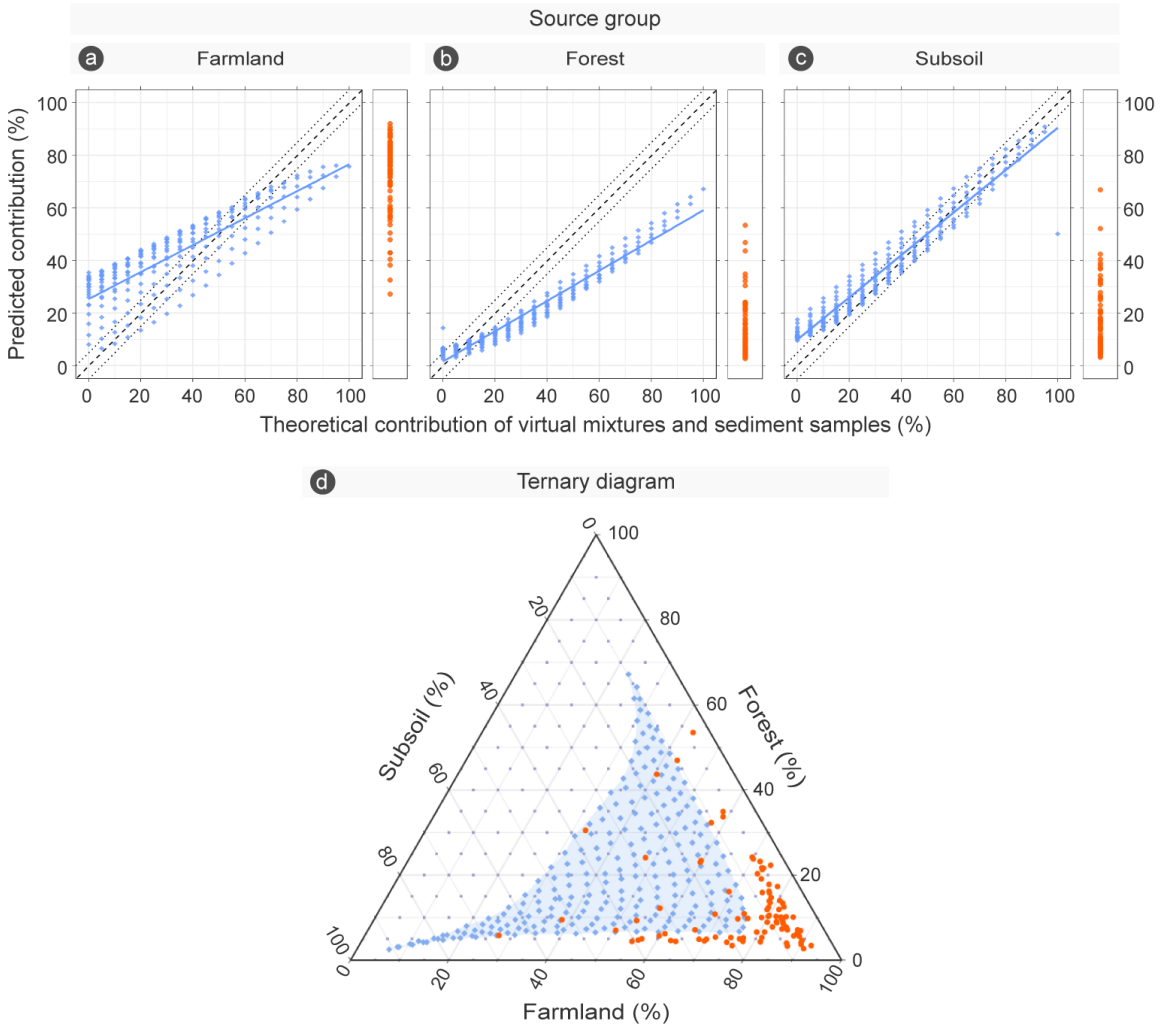
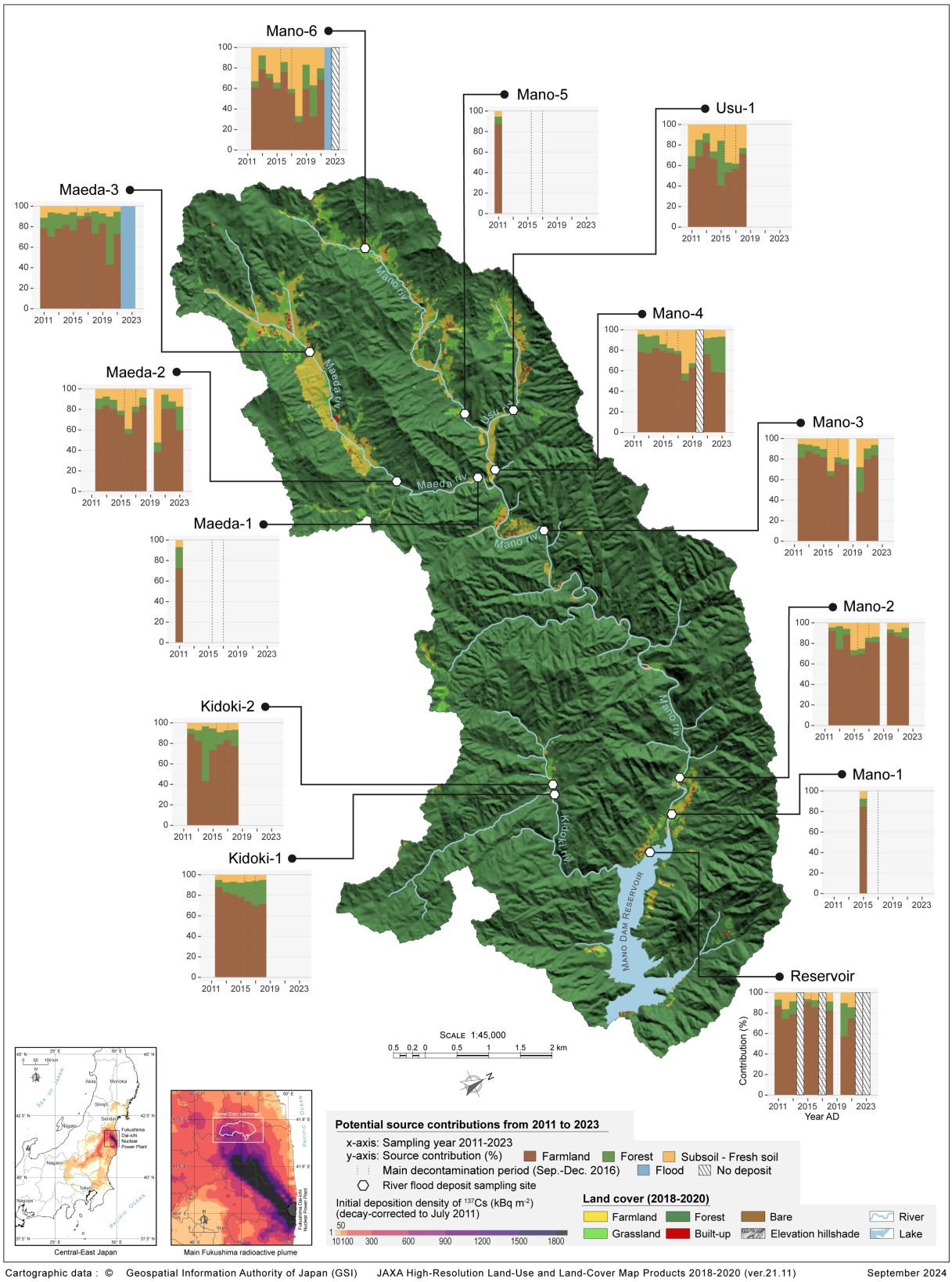


Figure III.9: Relationship between theoretical and predicted contributions of the 231 virtual mixtures (blue diamond) for each source: (a) farmland, (b) forest, (c) subsoil, of the MixSIAR model (blue line) predictions along with the 101 lag deposit samples predicted contributions (orange dot). (d) Ternary plot of the theoretical (light blue diamond) and predicted (blue diamond) contributions of the virtual mixtures and predicted contribution of the lag deposit samples (orange dot).

a low contribution from forest. In addition, few sediment samples had predicted contributions coinciding with the predicted virtual mixtures space (n = 15; 16 %). Most sediment samples were grouped and located in the space of high contributions of farmland (80-100 %) with low contributions of forest (0-30%) and subsoil-fresh soil (0-20 %), which was outside of the space covered by the virtual mixtures (Fig. III.9.d). The transferability of modelling accuracy metrics calculated using virtual mixtures was therefore unlikely to be fully transferable to model outputs obtained for sediment samples.

III.3.5.3 - Sediment source contribution through space and time

At the catchment scale, farmland soils were the dominant source of sediment for all ten sites over the period 2011-2023, with an average of 73 $\pm$ 14 % across the catchment (Fig. III.10 and Supplementary materials Table III.SM-VIII). Furthermore, this dominance tended to increase in downstream direction, although the source contributions varied locally from year to year. However, the second source of sediment differed depending on the tributary of the Mano Dam catchment under consideration. For the upper Mano (Mano-6) and Usu (Usu-1)



Cartographic data : © Geospatial Information Authority of Japan (GSI) JAXA High-Resolution Land-Use and Land-Cover Map Products 2018-2020 (ver.21.11) September 2024

Figure III.10: Annual evolution of sediment source contribution from three potential sources, among farmland (brown), forest (green), subsoil-"fresh soil" (yellow), in flood deposits collected annually from 2011 to 2023 during the November sampling campaign at ten sampling sites across the Mano Dam reservoir catchment. Cartographic data available from the Geospatial Information Authority of Japan (GSI) and JAXA High-Resolution Land-Use and Lad-Cover Map Products 2018-2020 (ver. 21.11).

tributaries, subsoil was the second main contributing source. Meanwhile, for the upstream Maeda (Maeda-3) and Kidoki (Kidoki-2 and Kidoki-1) tributaries, forest was the second main sediment supply. Subsequently, the Mano-4 and Mano-3 sites, located downstream of the confluence of the upper Mano and Usu tributaries, and downstream of the junction with the Maeda tributary, respectively, showed comparable dynamics with subsoil supplying the second sediment source. A similar behaviour was observed at the Maeda-2 site. The trends at the Mano-2 and Mano-1 sites were rather similar to those found at the upstream sites. The reservoir site showed limited source variations over the whole period, except for 2020, which recorded an exceptionally high forest contribution, with 32 % versus an average of 11 % for the whole investigated period.

For the upper Mano River site (Mano-6), contributions fluctuated from 2012 to 2017 between a higher contribution from subsoil and a higher contribution from farmland. On average, in 2012, 2014, 2015 and 2017, although farmland was the main source of sediment (62 $\pm$ 6 %), subsoil contributed a large proportion (34 $\pm$ 6 %), while forest contribution was limited (5 $\pm$ 1 %). In 2013 and 2016, the contribution of farmland increased significantly (79 and 76 %, respectively), along with a higher contribution of forest (14 and 10 %, respectively), while the contribution of subsoil decreased (8 and 14 %). On the contrary, in 2018, the contribution of subsoil increased significantly and became the first source of sediment (67 %), which was associated with a lower contribution of farmland (27 %), while the contribution of forest remained similar as previously observed in 2012, 2014, 2015 and 2017 (6 %). In 2019 and 2020, the contribution of forests increased significantly to 23 and 31 %, respectively, which was associated with lower contributions of subsoil (17 %) in 2019 and farmland (33 %) in 2020. In 2021, the contribution pattern returned to the situation that prevailed in 2012 with a slightly higher contribution of forest (11 %) and a lower contribution of subsoil (20 %).

In the Maeda tributary (Maeda-3, Maeda-2, Maeda-1), the second contributing source differed between Maeda-3 (forest) and Maeda-2 (subsoil). At the Maeda-3 site, although no general tendency was observed, some years were associated with higher contributions of forest. Indeed, in 2012, 2015, 2018, and 2021 forest contribution was higher than during other years (i.e. 2011, 2013, 2014 and 2019), with 22 $\pm$ 3 % versus 11 $\pm$ 3 %, along with a lower farmland contribution, 73 $\pm$ 2 % versus 81 $\pm$ 2 %, and a similar subsoil contribution (6 $\pm$ 1 % versus 8 $\pm$ 2 %). The 2020 year was associated with a significantly higher contribution of forest (47 %) and a lower contribution of farmland (43 %), while subsoil supply remained stable (10 %). In contrast, in 2016 and 2017, farmland contribution increased (87 and 90 %, respectively) along with a decrease of forest contribution (3 and 4 %) and a stable contribution of subsoil (6 and 5%). On the opposite, at Maeda-2 site, after 2014, the second main contributing source was subsoil. Indeed, from 2012 to 2014, contributions were stable and similar to those found at the Maeda-3 site at the same period, with 81 $\pm$ 2 % of farmland, 10 $\pm$ 1 % of forest and 9 $\pm$ 1 % of subsoil. From 2015 to 2016, subsoil contributions increased (21 to 39 %) along with the decrease of farmland contribution (75 to 56 %). Then, in 2017-2018 and 2021-2022, contributions returned to similar levels as those observed in 2012-2014, and 2020 showed a significantly high contribution of subsoil (52 %), along with a lower farmland contribution (38 %), while forest contribution remained stable (10 %). Finally, 2023 was associated with a lower contribution of farmland (60 %) and comparatively higher contributions of forest (23 %) and subsoil (17 %).

Conversely, in the Usu River, from 2011 to 2013, the contributions of farmland increased (57 to 82 %), together with a decrease in the contribution from subsoil (31 to 9 %) while that of forest remained stable (12 $\pm$ 2 %). In 2015, the contribution of forest increased significantly, being equivalent to that of farmland (44 % and 41 % respectively), while the contribution of subsoil was comparatively low and similar to that of 2012 (16 % and 15 % respectively). Afterwards, the contribution patterns of 2016 and 2017 were similar, with dominant contribution of farmland (54 and 57 % respectively) and a significant increase in subsoil contribution (37 and 38 %). In 2018, the contribution was similar to that observed in 2012-2013.

Downstream of the confluence between the upper Mano (Mano-6 and Mano-5) and the Usu River (Usu-1), the Mano-4 sampling site showed a stable contribution pattern from 2012 to 2014, with a dominant contribution of farmland (79 $\pm$ 3 %), followed by forest (15 $\pm$ 2 %) and subsoil (6 $\pm$ 2 %). Afterwards, from 2015 to 2017, the contribution of subsoil increased (14 to 21 %), along with a decreasing contribution of forest (from 7 to 4 %). In 2018 and 2019, a high contribution of subsoil (43 and 33 %) along with a lower contribution of farmland were observed (51 and 63 %). In 2021, the contribution pattern was similar to that of 2012-2014. However, in 2022 and 2023, contribution from forest increased significantly (34 and 35 %) along with a decrease of farmland contribution (59 % during both years) while subsoil contribution was low and similar to that of 2012-2014 (7 % during both years). At Mano-3 site from 2012 to 2015, similarly to what was found at Mano-4 in 2015-2017, the contribution of subsoil increased (from 5 to 10 %), along with a decreased contribution of forest (13 to 8 %), while farmland remained stable (84 $\pm$ 3 %). However, in 2016, the contribution of subsoil increased significantly (32 %), together with a decrease of farmland contribution (64 %), similarly to what was observed on the same year at Maeda-2. In 2017-2018, the contribution of subsoil decreased slightly (18 and 20 %) along with an increase of the contribution from farmland (77 and 75 %). In 2020, while the contribution from subsoil remained similar to that of 2016 (28 %), the contribution from forest increased significantly (24 %) along with a decrease of farmland contribution (48 %). In 2021 and 2023, the contribution pattern was similar to that of the 2012-2015 period.

At Mano-2 site, from 2012 and 2014, the contribution of farmland was high (92 and 89 %) along with a low contribution of subsoil (5 and 6 %) and forest (3 and 5 %). However, in 2013, forest contribution increased significantly (55 %) along with a decrease of farmland contribution (75 %). In 2015-2016, subsoil contribution increased significantly (27 and 25 %) together with a decreased contribution of farmland (68 and 70 %). The 2017-2018 period show an intermediate situation compared to those observed between the 2012-2014 and 2015-2016 periods,with 81 % of farmland and 14 % subsoil for both years. After, from 2020 to 2022, contributions were similar to those of 2012 and 2014, with slight variations between forest and subsoil contributions.

For Kidoki River, at both sampling sites (Kidoki-1 and Kidoki-2) the contribution of farmland decreased from 2012 to 2015, from 88 and 89 % to 78 and 73 %, respectively, while the contribution of forest increased, from 7 and 5 % to 14 and 21 %, respectively. Moreover, this trend continued until 2017 at Kidoki-1 site, and it stabilised in 2018, with about 71 % of farmland, 24 % of forest and 6 % of subsoil. At the Kidoki-2 site, a peak of 53 % forest contribution was observed in 2014 together with a decrease of farmland contribution (43 %). Apart from this peak, at Kidoki-2, contribution pattern tended to stabilise from 2015 and afterwards. However, an increase of farmland contribution was observed from 2015 to 2017, raising from 73 to 83 %, along with a decrease of forest contribution, from 21 to 9 %. In 2018, contribution patterns were similar between Kidoki-1 and Kidoki-2, with a higher contribution of farmland at Kidoki-2 than at Kidoki-1.

III.4 - Discussion

III.4.1 - Rainfall erosivity and mapping

The rainfall erosivity showed both spatial and temporal variations across the study area, which extended within a radius of 110 km around the FDNPP and covered the entire eastern Fukushima Prefecture, the southern Yamagata and Miyagi Prefectures, along with the northern Tochigi and Ibaraki Prefectures. Across a similar area, Laceby et al. (2016a) and Yamaguchi et al. (2014) estimated average R factors of 3696 $\pm$ 1327 MJ mm ha^{-1} h^{-1} yr^{-1} (1995-2015; 42 stations) and 3366 MJ mm ha^{-1} h^{-1} yr^{-1} (2011-2011; 10 years; 23 stations), respectively. These values were, respectively, 7 % higher and 2 % lower than the R factor of 3427 $\pm$ 912 MJ mm ha^{-1} h^{-1}yr^{-1} (58 stations) calculated for the period 2011-2023. These differences may likely be attributed to distinct study durations and extents. In fact, the annual R factor determined over the period 2011-2023, which ranged from 2136 to 5896 MJ mm ha^{-1} h^{-1} yr^{-1} (2018 and 2019, respectively), matched with the ranges found by Laceby et al. (2016b) and Shiono et al. (2013), who reported values from 1866 to 7159 MJ mm ha^{-1} h^{-1} yr^{-1} (1996 and 1998, respectively) and 2500 to 7500 MJ mm ha^{-1} h^{-1} yr^{-1}, respectively. However, the 2019 annual R factor exceeded the maximum of 4217 MJ mm ha^{-1} h^{-1} yr^{-1} reported by Yamaguchi et al. (2014) by 40 %. Although some heterogeneity was observed between events, the annual R factor tended to increase from north to south, ranging from 1580 $\pm$ 1046 MJ mm ha^{-1} h^{-1} yr^{-1} at Yanagawa (Yanagawa Prefecture, northern study area) to 7506 $\pm$ 3319 MJ mm ha^{-1} h^{-1} yr^{-1} at Hanazono station (Ibaraki Prefecture, southernmost part of the study area). This north-to-south increase in annual R factor was consistent with the trends identified by Laceby et al. (2016a) and Shiono et al. (2013). In addition, there was a decreasing rainfall intensity from east-to-west, from the Pacific Ocean coast towards inner Japan (Shiono et al., 2013; Laceby et al., 2016a). This was observed by Loa and Kawagoe (2021), who estimated a lower annual R factor in 2019 within the Abukuma River catchment (3639 MJ mm ha^{-1} h^{-1} yr^{-1}), which is located in the western part of the study area. However, although 27 $\pm$ 3 erosive events occurred each year on average in the region, most of them were characterised by a low energy, with 80 % of events having an erosive energy below average (EI_{30} = 125 $\pm$ 36 MJ mm ha^{-1} h^{-1}). Similarly, Laceby et al. (2016a) observed that 60 % of the annual erosivity was generated by extreme erosive events, occurring mainly between July and September, with 82 % of the annual erosivity taking place during these months. However, during the period examined between 2011 and 2023, the most erosive period extended slightly until October, and these four months (i.e., September to October) accounted for 73 % of the annual erosivity. With the exception of 2019, these changes were likely mainly attributed to the events that occurred after 2015 that were on average less erosive, with fewer extreme events.

On average, the GAM models were associated with good modelling accuracy metrics, with mean predicted values close to those observed at the weather stations, apart from those obtained for 2015, 2016 and 2019 events, with R^2 ranging from 0.89 to 0.99. Indeed, the lowest prediction accuracies were observed in 2015 and 2019, which were associated with the most extreme erosive events, and in 2016, with the succession of five events, with R^2 of 0.72, 0.68, 0.76 respectively. Nevertheless, modelling accuracy remained high for these three years as well. Overall, these modelling accuracy statistics were better than those observed by Laceby et al. (2016a) and Chartin et al. (2017), with R^2 ranging from 0.56 to 0.83 and 0.83 to 0.95, respectively. This was likely related to the lower number of stations examined in the previous studies (44-58 in the current research against 42 and 36-40 in previous articles, respectively), and/or to the procedure used to fit the models. Indeed, the leave-one-out procedure used in Laceby et al. (2016a) and Chartin et al. (2017) tends to require a larger dataset than the REML procedure. In terms of covariate selection, spatial coordinates

(latitude and longitude) consistently emerged as the most influential covariates, particularly for events with complex spatial distributions. Other environmental factors, such as slope and windward or leeward indices, showed a variable importance between events, while elevation and temperature were often excluded from the models. A similar absence of pattern in the selection of covariates was observed by Laceby et al. (2016a) and Chartin et al. (2017). However, since GAMs were set in all three publications with an extra-penalty to the smoothing term, the non-inclusion of a covariate likely reflected the fact that other covariates had a similar or stronger relationship with the target variable.

Consistently with what was observed at the regional scale, the rainfall erosivity of the events that took place within the Mano Dam catchment followed the same overall pattern across years. However, for most events, the mean predicted rainfall erosivity within the catchment was higher, with the exception of that calculated in 2014 and 2022, which was lower. At the catchment scale, the most erosive events were those that occurred in 2015 and 2019, with the latter being about twice as erosive as the 2015 event. These two events were followed by those of 2011, 2016 and 2023, which were of equivalent intensity. Conversely, the events of 2012, 2014, 2018, 2020, 2021 and 2022 showed a low erosive energy. The mean EI_{30} values from Chartin et al. (2017) calculated for the entire Mano River catchment were similar to those calculated for the 2011, 2012 and 2023 events in the current research. However, significant differences were found for 2013 and 2014. In fact, in 2013 Chartin et al. (2017) studied two erosive events, Wipha and Francisco (9-26 October), while in the current study only the Man-Yi event (14-16 September) was considered. Although the Wipha and Francisco events were identified as erosive events during the selection of the last major erosive event that took place prior to the sampling campaign, they were not retained for further analysis in the current research as they were associated with a much lower intensity than Man-Yi (Supplementary Materials Table III.SM-IX). In 2014, although Chartin et al. (2017) considered a longer period from 28 September to 14 October (17 days) for Phanfone and Vongfong events than the one that what was considered in the current work, two separated periods on 5-7 and 13-14 October (5 days) and these two cumulated erosive events resulted in similar EI_{30} at the regional scale although they diverged at the scale of the Mano Dam catchment (Supplementary Materials Table III.SM-X). The difference observed at the catchment scale was likely the result of the fitting of the GAMs, which may differ depending on the number of weather stations considered, 58 in the current research vs. 40 in Chartin et al. (2017), and the selected covariates.

III.4.2 - Evolution of the index of connectivity under land use changes and the occurrence of erosive events

The IC estimated on the basis of topographic information and land use allowed to identify the main areas that were the most connected to the river system and to highlight their evolution during the main changing phases that affected the catchment including abandonment, decontamination and resumption of agricultural activities. The upstream area in the western part of the catchment, where most of the farmland is located, was the area with the highest IC values in the vicinity of the river system. Conversely, the IC of the Kidoki tributary, which mainly drains forested areas, was comparatively low. Forested areas were associated with low IC values, resulting in moderate variations according to topographic features. Consequently, the area between Mano-3 and Mano-2 stations appeared to be less connected to the river system.

Over the abandonment period, the IC of the agricultural zones of the catchment decreased rapidly and stabilised in 2014-2015. However, according to Chartin et al. (2017), the agricultural areas, especially those located along the Maeda, Usu and upstream Mano tributaries, appeared more connected over the same period. This result was most likely related to the fact that grassland was considered as cropland in Chartin et al.

(2017), which possibly artificially expanded the erosion-sensitive areas close to the river system. Moreover, for the period 2011-2014, the HRLULC map used for the spatialisation of the C-factor was processed with satellite imagery acquired during the period 2006-2011 (JAXA, 2016). Since the satellite imagery acquired in 2011 was used, farmland abandoned in March 2011 was likely identified as grassland, resulting in a lower C-factor (i.e. 0.02) compared to the attribution of a C-factor following an annual decrease from 0.38, 0.17 to 0.04 as proposed in the current research. Subsequently, the completion of decontamination at the end of 2016 was associated with an increase in IC values from 2016 to 2017. Afterwards, in 2018, the IC values increased again, which was more likely related to a more precise identification of farmland areas as in the HRLULC maps, since the resolution changed from 30 m to 10 m between the 2014-2016 and the 2018-2020 versions, respectively (JAXA, 2018, 2022). Finally, after the preparation of farmland for recultivation from 2019 to 2023, the connectivity in the western part of the Mano Dam reservoir catchment and near the reservoir inlet appeared to remain high and stable in the farmland areas. This spatial distribution was similar to that observed in 2011 by Chartin et al. (2017).

The IC values varied significantly between erosive events, in relation with the relative intensity of the events. Between 2011 and 2014, when moderate erosive events occurred, the overall IC declined even further across the catchment. In 2015, the intense Etau & Kilo events led to a significant increase in the overall IC, with the increase in connectivity being more related to topography than to land use. Indeed, the development of spontaneous vegetation in farmland limited their sensitivity to water erosion (Feng et al., 2022). A comparable pattern in IC values was observed by Chartin et al. (2017), with a significant increase in IC values during Etau & Kilo. Following the completion of decontamination in late 2016, the IC values of farmland increased, thereby reflecting the higher erosion sensitivity of the decontaminated farmland and/or the addition of fresh soil. However, in 2017, Lan was a medium-intensity erosive event, it resulted in overall low IC values, and farmland appeared to display a moderate connectivity with the river systems. The impact of farmland decontamination was further visible in 2018, when agricultural areas were associated with increased intermediate IC values, although the event that occurred in 2018 was of very low intensity (five times lower than the 2017 event). In 2019, the combination of high soil sensitivity following soil preparation for the resumption of agricultural activities and the occurrence of the strongest erosive event since 2011 (Hagibis & Bualoi) resulted in exceptionally high connectivity levels, particularly in agricultural areas. Subsequently, in the following years (2020-2022), despite the occurrence of lower intensity events, farmland remained clearly associated with moderate to high IC values, in contrast to what was observed during the abandonment period (2011-2015) when stronger events occurred. The 2023 event, Yun-yeung, similar to Roke (2011) in terms of intensity, produced a connectivity pattern across the catchment that was comparable to that observed prior to the FDNPP accident, which indicated a return to the conditions that prevailed prior to 2011. This corroborates the significant impact of rainfall erosivity on the assessment of sediment connectivity and the investigation of local erosion processes, which are dynamic phenomena subject to multiple forcing factors that interact in both time and space, as highlighted previously by (Chartin et al., 2017).

The use of the P factor allowed to weight the sediment connectivity estimated based on topographical and land uses information with event specific information. However, since the P factor is a weighting factor, it varies between 0 and 1 with the highest EI_{30} observed being equal to 1. Accordingly, in the context of the occasional occurrence of exceptionally intense events, the upper limit of observed EI_{30} significantly moves upward. This weights conventional events close to zero. For example, as the strongest events were Hagibis & Bualoi in 2019, with a maximum EI_{30} value of 14,000 MJ mm ha^{-1} h^{-1} yr^{-1}, the resulting average P factor of the events was 0.68 $\pm$ 0.26. The following two strongest events, Etau & Kilo in 2015 and Roke in 2011, had average P factors of 0.35 $\pm$ 0.14 and 0.15 $\pm$ 0.03, respectively, which was about 2 to 5 times lower.

Furthermore, low-intensity events, such as those that occurred between 2020 and 2022, had mean P factors of about 0.01 to 0.02. Therefore, the P factor was found to be sensitive to occasional extremely intense events, which could tend to an underestimation of more average events. However, the P factor offers an opportunity to compare erosivity of different events using simplified information.

III.4.3 - Dynamic of ^{137}Cs transfer and sediment sources

Across most sites, ^{137}Cs activities in sediment gradually declined from 2011 to 2015, then they sharply decreased in 2016, which was followed by a stabilisation of the activities afterwards at relatively low levels compared to initial activities. This general trend with an abrupt change of ^{137}Cs activities in sediment was observed all across the Fukushima Prefecture (Evrard et al., 2016; Chartin et al., 2017; Osawa et al., 2018). During this period, farmland provided consistently the dominant source of sediment across the entire catchment, contributing an average of about 70 %, similarly to what was found at the regional scale in previous work (Laceby et al., 2016b). The contributions from forest and subsoil also remained stable, with forest contributing a minor proportion of sediment (5-15 %) compared to subsoil (8-35 %). Nevertheless, delayed peaks of ^{137}Cs activities were recorded at upstream sites, such as at Maeda-3 and Usu-1 in 2012, at Mano-6 in 2013 and in 2014 at Kidoki-2. These peaks of ^{137}Cs activity were associated with a significantly higher contribution of forest at Kidoki-2, and a moderate one at Maeda-3 and Usu-1, while it was associated with higher farmland contribution at Mano-6. This delay likely suggests that, depending on the local context, the transport of topsoil fine soil particles may vary with local condition, with a longer delay in forested sub-catchments (Iwagami et al., 2017; Niida et al., 2022; Oda et al., 2022). In addition, the simultaneous increase in ^{137}Cs activities and contribution from forest (Kidoki-2 in 2014, Usu-1 in 2015, Mano-6 in 2019), could be related to organically bound radiocesium as found by Naulier et al. (2017). Conversely, sites where ^{137}Cs activities decreased from year to year likely illustrated the reduction of contaminated material available for erosion and the progressive dilution of upstream contaminated sediments (Sakaguchi et al., 2015; Eyrolle-Boyer et al., 2016; Vandromme et al., 2023).

During intense events, such as Etau & Kilo in 2015 and Hagibis & Bualoi in 2019, no significant change of contributions was observed across the catchment after their occurrence, although a slight increase of forest contribution was observed at upstream sites or in forested areas (i.e. Kidoki tributary). In 2015 at Usu-1 and in 2019 at Mano-6, an increase in ^{137}Cs activity was observed along with higher forest contributions. However, during the year following the major event (i.e. in 2016 and 2020, respectively), sediment source contributions changed significantly across the catchment, with an increase of forest contribution at upstream sites and increased contributions of subsoil and farmland further downstream. The increase of subsoil contribution was likely related to the large transfer of subsoil materials reported for Etau & Kilo in 2015 and Hagibis & Bualoi in 2019 (Evrard et al., 2016, 2020). Indeed, such extreme erosive events tend to erode deeper soil layers when triggering rill and gully erosion, exposing and transferring non-contaminated subsoil material to river systems (Vandromme et al., 2023). They may also lead to the remobilisation of deposited material during subsequent years, such as in 2016 and 2020 (Laceby et al., 2016a). Following these two extreme events, the ^{137}Cs activity in the sediment was observed to decrease significantly (Evrard et al., 2016; Tsuji et al., 2023).

During decontamination, in 2016 and 2017, the sediment source contribution was mainly affected by the occurrence of the Etau & Kilo events in 2015. After 2016-2017, and apart from the occurrence of Hagibis & Bualoi in 2019, the sediment source contributions tended to return to the typical erosion dynamics that were observed during the 2011-2014 period, with farmland supplying the dominant sediment source, and with the exception of the Mano-4 site where forest contribution was twice higher than previously. Nevertheless,

from 2016 onwards, across the catchment ^{137}Cs activities were significantly lower and remained stable until 2023. This significant decrease in ^{137}Cs activity along with major contributions from farmland similar to what was observed just after the accident and during the abandonment phase likely demonstrates in itself the result of farmland decontamination. Indeed, the decontamination, through removing the contaminated topsoil layer which is the most susceptible to be eroded (Kato et al., 2012; Lepage et al., 2015), was effective in limiting the subsequent transfer of radiocesium in the river systems (Wakiyama et al., 2019; Ikenoue et al., 2020; Feng et al., 2022; Vandromme et al., 2023). This impact was further increased since farmland areas were highly connected to the river system, as shown in this work and in Chartin et al. (2017). However, through decontaminating only a small proportion of the catchment surface area, the reduction of the overall ^{137}Cs inventory in soils of the Fukushima region remains limited (Hashimoto et al., 2012; Onda et al., 2020; Vandromme et al., 2023). Nevertheless, these areas with the highest residual ^{137}Cs inventories and mainly forested areas, appeared to be effectively connected to the river system only during exceptional erosive events (Chartin et al., 2017). However, such events were shown to mainly generate rill and gully erosion erosion associated with the transport of uncontaminated subsoil material (Vandromme et al., 2023). This could limit the role of potential long term source of these forested areas (Laceby et al., 2016b; Naulier et al., 2017; Huon et al., 2018; Chalaux-Clergue et al., 2024b), although they will remain sensitive to forest management and the occurrence of environmental hazards (e.g. fire) (Fukuyama et al., 2010; Ikenoue et al., 2020; Hashimoto et al., 2022; Evrard et al., 2023).

III.5 - Conclusions

Under the context of major changes of land uses that occurred throughout the successive phases of abandonment, decontamination and resumption of agricultural activities, the dynamics of sediment sources and particle-bound radiocesium transfers were investigated in one of the main Fukushima-impacted regions. A total of 101 flood deposits collected annually from 2011 to 2023 at ten sites distributed across the Mano Dam reservoir catchment were analysed. During these thirteen years, decontamination was shown to restore sediment connectivity between farmland and the river system, which had decreased significantly during land abandonment as a consequence of the spontaneous regrowth of vegetation protecting the soils against erosion. The computation and spatialization of rainfall erosivity associated with the last erosive event(s) that occurred prior to each annual sampling campaign reflected the major impact of these rainfall events on sediment connectivity, which results from multiple forcing factors. Therefore, by targeting farmland areas, which are zones showing a high sediment connectivity with river systems in this catchment (and supplying on average73 $\pm$ 14 % of sediment contribution), the decontamination programme organised by the Japanese authorities (2014-2016) appeared to effectively reduce radiocesium transfers to and within the river systems, from 18.5 $\pm$ 1.9 in 2011 to 1.5 $\pm$ 1.0 kBq kg^{-1} in 2016. Interestingly, the increase of sediment contribution from farmland following the resumption of agricultural activities, reaching values comparable to those observed prior to the FDNPP accident (Chapter 2 - Chalaux-Clergue et al. (2024b)), was not associated with an increased transfer of particle-bound radiocesium. However, forested areas, which covers about 70 % of the Fukushima Prefecture and where 74 % of the ^{137}Cs deposited, contain most of the residual ^{137}Cs stock, and could theoretically behave as a long term source of contaminated sediment in the future. Nonetheless, these forested areas were found to be only significantly connected to the river system when extreme erosive events, such as those of 2015 and 2019, occur. These heavy events were shown to generate extensive rill and gully erosion along with localised mass movements, that were not associated with significant contamination transfers, which may limit their contribution to radiocesium transfers over the long term. Future research

should investigate contexts in which the timing of decontamination was different, to assess whether this may have affected in a distinct way the dynamics of particle-bound radiocesium transfers.

Data availability

The dataset is available online at https://doi.org/10.5281/zenodo.11609434 (Chalaux-Clergue et al., 2024c).

Acknowledgements

The collaboration and support of Nicolas Tenaud, student at the Laboratoire des Sciences du Climat et de l'Environnement (LSCE; Gif-sur-Yvette, France), in carrying out several analyses on the lag samples and discussions of results are sincerely and greatly appreciated.

The assistance of Dr Mercedes Mendez-Millan, research engineer at the Institut de Recherche pour le Développement (IRD), in carrying out the organic matter analyses at the Alyses platform (Bondy, France), and of Amélie Ogier, laboratory technician at the Centre National de la Recherche Scientifique (CNRS), in carrying out the TQ-ICP-MS at the LSCE, is gratefully acknowledged.

III.6 - Supplementary materials

III.6.1 - Laboratory analysis methodology

III.6.1.1 - Radiocesium analysis

Gamma spectrometry with a low-background coaxial HPGe detector was used to determined the ^{134}Cs and ^{137}Cs activities in the sediment samples. The counting times ranged from 3×10^4 to 8×10^4 s. The ^{137}Cs and ^{134}Cs activities were measured at the 605 keV and 662 keV emission peaks, respectively, errors reached about 5 % at 95 % confidence level. All measured counts were corrected for background levels which were, as detector and geometry efficiency, estimated at least every two months. Counting efficiency and quality assurance were implemented using certified International Atomic Energy Agency reference materials prepared in the same containers as the samples. radiocesium activities were decay-corrected to the sampling date.

III.6.1.2 - Organic Matter

In the Mano Dam reservoir catchment, sediment and soils were found not to contain carbonate minerals, and all the carbon associated with particulate matter is organic in nature (Huon et al., 2018). Total organic carbon (TOC, in %) and total nitrogen (TN, in %) elemental content and δ^{13}C isotope ratio (δ^{13}C expressed in ‰ against PDB) were determined for a part of the samples by a combustion method using a continuous flow elementary analyser (Elementar VarioPyro cube) coupled with an Isotope Ratio Mass Spectrometer (EA-IRMS) (Micromass Isoprime) at the Institute of Ecology and Environmental Sciences (iEES Paris) in France. A first analysis run was conducted to measure TOC concentration together with a set of tyrosine standards (Coplen et al., 1983). The second analysis run was dedicated to measure TN concentration after sample weight optimisation from TOC results. For combustion, oxygen was injected during 70 s (30 mL min^{-1}) at 850 °C for reduction and the combustion furnace at 1120 °C (Agnihotri et al., 2014). The analytical precision was assessed with repeated analyses of a tyrosine intern standard (n = 51), calibrated against international reference standards (Girardin and Mariotti, 1991). The analysis of these properties in source material is described in details in the study of Laceby et al. (2016b). The other part of the samples were analysed at the Alyses Platform (Bondy) in France, by a combustion method with an elemental analyser (Flash HT 2000) coupled to an isotope ratio mass spectrometer (Advantage Delta V) via a Conflow IV interface from Thermo Scientific. The EA-IRMS was calibrated against two standards : EMAP2 (TOC = 68.35 $\pm$ 0.28 %, TN = 7.46 $\pm$ 0.10 %, δ^{13}C = -28.19 ‰) and IAEA-CH3 (δ^{13}C = -24.72 ‰). Analytical precision and repeatability were assessed using the reference material HOS (TOC = 7.45 $\pm$ 0.14 %, TN = 0.52$\pm$ 0.02 %, δ^{13}C = -28.85 ‰). To evaluate whether the samples are composed of terrestrial or freshwater-originating material, the distribution of sample values was plotted in a δ^{13}C versus TOC/TN diagram and compared to the thresholds reported in Lamb et al. (2006) and Amorim et al. (2022).

III.6.1.3 - Elemental geochemistry

Energy Dispersive X-ray fluorescence

Elemental geochemistry was determined using Energy Dispersive X-ray fluorescence (ED-XRF) (Malvern Panalytical, ED-XRF Epsilon 4). A total of 17 elemental concentrations were measured (Al, Ca, Co, Cr, Cu, Fe, K, Mg, Mn, Ni, Pb, Rb, Si, Sr, Ti, Zn, and Zr). Measurements were conducted in containers covered with a 3.6 μm thin Mylar film (Chemplex, Mylar Thin-Film cat. no. 157) with a 10 mm exposure surface. A

minimum of 0.1 g of material was analysed. To consider the potential heterogeneity within a sample, three replicate measurements were made, and the mean value of these replicates was calculated. To assess the accuracy of the measurements, a standard (JMS-1, sediment from the Tokyo Bay (Terashima et al., 2002)) was measured every seven samples (n = 38) and the accuracy of the measured batch was determined based on the calculation of the Root Mean Square Errors (RMSE).

Triple quadrupole Inductively coupled plasma mass spectrometry

Elemental geochemistry was measured using triple quadrupole inductively coupled plasma mass spectrometry (TQ-ICP-MS from Thermo Scientific iCAP) for 48 elemental concentrations (Na, Mg, Al, K, Ca, Sc, Ti, V, Cr, Mn, Fe, Co, Ni, Cu, Zn, As, Se, Rb, Sr, Y, Mo, Ag, Cd, Sb, Cs, Ba, REEs, Tl, Pb, Th, and U). About 100 mg of sample was digested by successively adding 4 mL of HF (47-51 %) and 2 mL of $HClO_4$ (65-71 %), then 3.75 mL of HCl (34-37 %) and 1.25 mL of HNO_3 (67 %) (TraceMetal grade, Fisher Scientific) in closed Teflon vessel on hot plates (Digiprep, SCP Science) (Briard et al., 2023). A certified reference material (IAEA lake sediment SL1) and a chemical blank were digested in the same way as the sediment samples to control the mineralisation efficiency and evaluate the potential contamination during digestion and analysis. The median recovery rate of Al, Ca, K and Mn are 120 %, 104 %, 85 % and 94 % based on 23 geostandards analysed and treated in the same way than our samples (6 MAG-1 samples; 16 SL-1 samples and 1 BCR 723 sample).

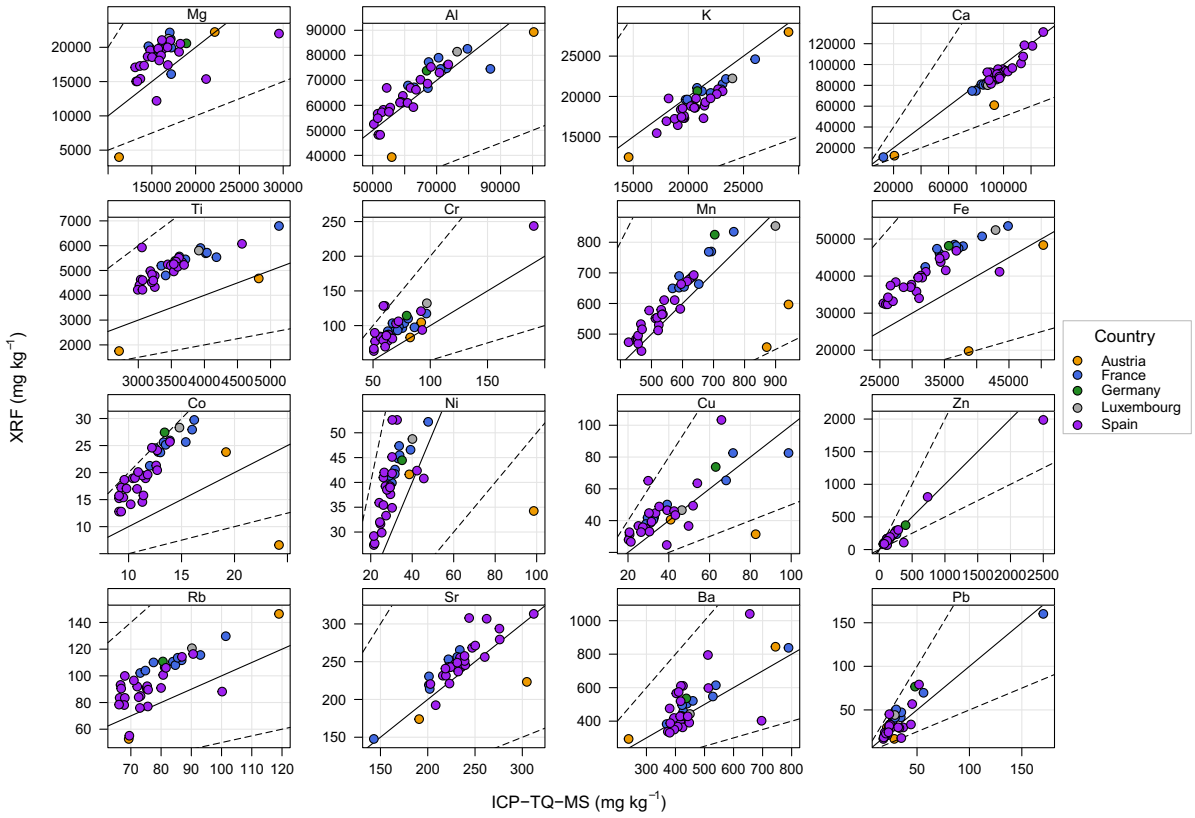


Figure III.SM-1: Comparison of the element concentrations of Mg, Al, K, Ca, Ti, Cr, Mn, Fe, Co, Ni, Cu, Zn, Rb, Sr, Ba, and Pb measured using quadrupole inductively coupled plasma mass spectrometry (TQ-ICP-MS) and X-ray florescence (XRF) on 34 Saharan dust samples collected throughout Europe.

To ensure comparability between geochemical elemental concentrations measured by ED-XRF and TQ-ICP-MS, 17 elemental concentrations measured by both methods were compared on a set of 34 samples (Mg, Al, K, Ca, Ti, Cr, Mn, Fe, Co, Ni, Cu, Zn, Rb, Sr, Ba, and Pb) (Fig III.SM-1). These samples were Saharan dust deposits collected across Europe after a Saharan dust event investigated in the work of **?**. Prior to analysis, the samples were sieved to 63 μm and then digested following the same digestion protocol as described above. The elemental concentrations of Al, K, Ca, and Mn were found to be consistent between the two methods.

III.6.1.4 - Visible colorimetry

Visible colorimetry was measured using a portable diffuse reflectance spectrophotometer, Kanonica Minolta CM-700d, set on a 3 mm target radius. Samples were measured in a plastic zip bag. To account for potential heterogeneities within a sample, three measurements were made at different locations on the bag. The spectrophotometer was calibrated at the start of each set of measurements with zero (black) and white standards. Measurements were conducted according to the D65 illuminance standard, 10° angle observer and excluding the specular component. The spectral reflectance (R in %) was measured from 360 nm to 740 nm with a 10 nm resolution (30 wavelength classes). Raw data was processed using the colour data software CM-S100w SpectraMagic NX (Minolta, 2022). Colour parameters within the Cartesian coordinate systems CIE Lab (1976) (i.e. L*, a* and b*) (CIE, 2008) and CIE LCh (i.e. C* and h) were exported. The CIE LCh is a vector representation of the CIE Lab (1976). C and h are derived from a* and b* parameters. Within the CIE Lab system: L* is the lightness of the colour, from black (0) to white (100), a* is the position between green to red (negative values are associated with green and positives with red), b* is the position between blue and yellow (negative values are associated with blue and positive values with yellow). Within the CIE LCh system: C* is the chroma (positive values are associated to brighter colors and negative values to duller colors) and h is the hue angle (in °) in the CIE Lab color wheel.

The Q7/4 ratio as defined by Debret et al. (2011) was calculated as the ratio between 700 nm and 400 nm reflectance values. This ratio provides a numerical description of the reflectance spectrum general slope.

The oxy-hydroxide geothite (α-FeOOH) soil richness can be determined using visible diffuse reflectance spectra (Kosmas et al., 1984; Balsam et al., 2004; Hao et al., 2009; Torrent et al., 2007) and its peak values at 445 nm and 525 nm were calculated from the first derivative reflectance spectrum Debret et al. (2011). In our case, the geothite concentration was not target, only the relative abundance within our samples was used to differentiate them. For each replicate of the measurements and for each sample, the first derivative reflectance spectrum was calculated and smoothed with a Savitzky-Golay filter using the savitzkyGolay function (differentiation order = 1, polynomial order = 3, window size = 5 (eq. 50 nm)) from the R package prospectr (Stevens and Ramirez-Lopez, 2022) (Wadoux et al., 2021). Then, the mean per sample and the standard deviation were calculated. From the first derivative of reflectance, two geothite peaks were calculated: first, the 445 nm peak value was calculated as the mean of values at 440 and 450 nm, and the 525 nm peak as the mean of those at 520 and 530 nm (Debret et al., 2011).

The remission function was calculated from the reflectance spectrum: $f(R) = (1 - R)^2/(2R)$ according to the Kubelka-Munk relationship (Scheinost et al., 1998). Then, the second derivative was calculated and the spectrum was smoothed with a Savitzky-Golay filter using the savitzkyGolay function (differentiation order = 2, polynomial order = 3, window size = 5). From the second derivative of remission function spectrum, the iron oxide-associated parameters A1, A2, A3 and the goethite proportion within iron oxides (Gt) were determined (Tiecher et al., 2015). The A1 and A2 peaks are associated with goethite and the A3 peak is associated

with hematite, and all peaks were calculated as the amplitude between each maximum and minimum bands. Thus, A1 is the difference between 450 and 420 nm, A2 is the difference between 510 and 480 nm and A3 is the difference between 575 (as the mean of 570 and 580 nm) and 535 nm (as the mean of 530 and 540 nm) and Gt is calculated as the ratio of A1/(A1+A3).

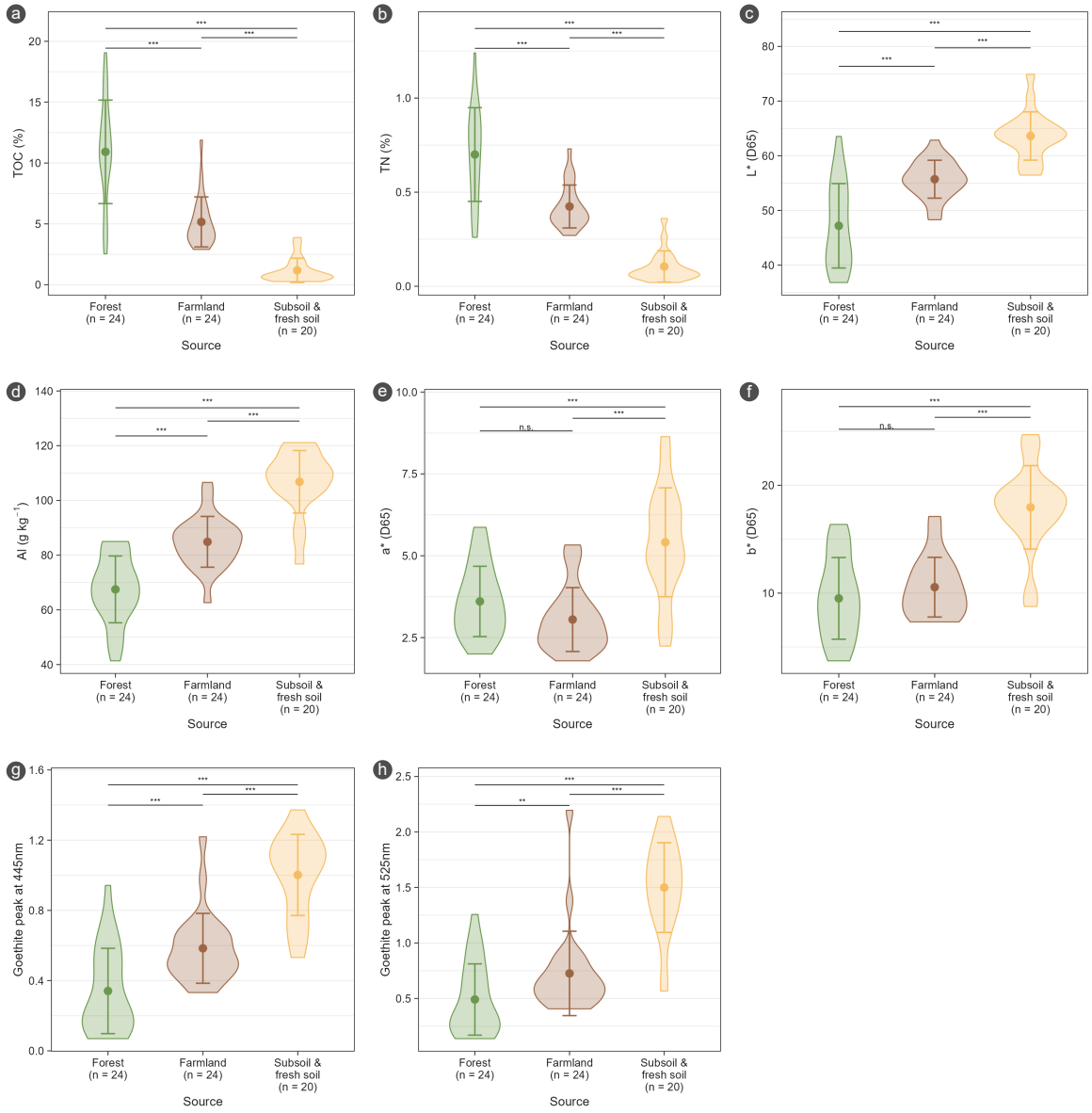


Figure III.SM-2: Distribution of potential sources among forest (green), Farmland (brown), and Subsoil - Fresh soil (yellow), and lag sediment samples (blue dots) values for the tracers retained for sediment source fingerprinting. Kolmogorov-Smirnov two-samples tests for source groups significance of the *p* value. "***" *p* value $\leq$ 0.001; "**" *p* value $\leq$ 0.01; "*" *p* value $\leq$ 0.05; "." *p* value $\leq$ 0.1; " " *p* value $>$ 0.1.

Table III.SM-I: Location of flood deposit sampling sites and annual sampling during the annual sampling campaign after typhoon season from 2011 to 2023. The collected sediment samples are indicated with their label, "n.d." stands for no deposit, "flood" for site under a flood event at the time of the sampling campaign, and "-" for sites that have not been visited.

Sampling site information				Sampling campaign (year month-day)												
River	Site	Coordinates (WGS 84)		2011	2012	2013	2014	2015	2016	2017	2018	2019	2020	2021	2022	2023
		Latitude (X)	Longitude (Y)	11-20	10-05	10-30	11-01	11-09	11-01	10-24	10-29	10-29	10-31	10-31	10-08	11-06
Mano	Reservoir	140.807709	37.733191	FML_0068-A	FML_0234	FML_0453	n.d.	FML_0887	FML_1023	n.d.	FML_1378	FML_1538	FML_1538	FML_1582	n.d.	n.d.
	Mano-1	140.803943	37.738391	-	-	-	-	FML_0889	-	-	-	-	-	-	-	-
	Mano-2	140.798481	37.741413	-	FML_0233	FML_0452	FML_0637	FML_0888	FML_1024	FML_1306	FML_1379	-	FML_1539	FML_1583	FML_1811	FML_1847
	Mano-3	140.747869	37.738704	-	FML_0241	FML_0459	FML_0631	FML_0882	FML_1018	FML_1300	FML_1373	FML_1540	FML_1584	FML_1584	FML_1812	FML_1846
	Mano-4	140.734274	37.736047	-	FML_0242	FML_0460	FML_0632	FML_0881	FML_1017	FML_1299	FML_1372	FML_1446-A	n.d.	FML_1585	FML_1813	FML_1844
	Mano-5	140.722874	37.735462	FML_0061	-	-	-	-	-	-	-	-	-	-	-	-
	Mano-6	140.688333	37.732447	-	FML_0244	FML_0458	FML_0628	FML_0879	FML_1015	FML_1297	FML_1370	FML_1444	FML_1544	FML_1588	flood	n.d.
Maeda	Maeda-1	140.734274	37.733341	FML_0060	-	-	-	-	-	-	-	-	-	-	-	-
	Maeda-2	140.728725	37.722582	-	FML_0239	FML_0456	FML_0630	FML_0883	FML_1019	FML_1301	FML_1374	FML_1448	FML_1542	FML_1586	FML_1814	FML_1845
	Maeda-3	140.701056	37.719053	FML_0059	FML_0240	FML_0457	FML_0629	FML_0884	FML_1020	FML_1302	FML_1375	FML_1449	FML_1543	FML_1587	flood	flood
Usu	Usu-1	140.725950	37.742007	FML_0062	FML_0243	FML_0461	FML_0633	FML_0880	FML_1016	FML_1298	FML_1371	FML_1445	-	-	-	-
Kidoki	Kidoki-1	140.791787	37.724208	-	FML_0236	FML_0455	FML_0635	FML_0886	FML_1022	FML_1304	FML_1377	-	-	-	-	-
	Kidoki-2	140.790469	37.724665	-	FML_0235	FML_0454	FML_0634	FML_0885	FML_1021	FML_1303	FML_1376	-	-	-	-	-

Table III.SM-II: Weather stations information (prefecture, name, number, coordinates) along with the morphometric attributes (elevation,

Weather station information			Coordinates			
			ESPG:4326 WGS 84		ESPG:32654 WGS 84 / UTM 54N	
Prefecture	Name	Number	Latitude (Y)	Longitude (X)	Latitude (Y)	Longitude (X)
Yamagata	Yamagata	47588	38.255000	140.345000	4234301.00	442707.16
	Kaminoyamasakayama	1562	38.116667	140.213333	4219055.00	431064.88
	Takahata	1132	38.003333	140.206667	4206498.00	430371.88
	Yonezawa	279	37.911667	140.143333	4196354.00	424689.06
Miyagi	Shiogama	1030	38.338333	141.013333	4243365.00	501150.38
	Nikkawa	251	38.303333	140.636667	4239540.00	468237.06
	Sendai	47590	38.261667	140.896667	4234883.00	490967.25
	Natori	1464	38.138333	140.916667	4221189.50	492685.88
	Zaou	1564	38.126667	140.680000	4219914.50	471951.50
	Iwatama	1632	38.106667	140.876667	4217669.00	489193.19
	Watari	257	38.025000	140.858333	4208604.50	487557.72
	Shiroishi	256	38.015000	140.611667	4207579.00	465936.31
	Marumori	1220	37.931667	140.778333	4198248.50	480497.03
	Hippo	1298	37.826667	140.728333	4186602.25	476094.81
Fukushima	Moniwa	1293	37.891667	140.436667	4193957.75	450461.59
	Shinchi	1633	37.875000	140.918333	4191951.75	492812.13
	Yanagawa	281	37.851667	140.588333	4189444.00	463779.72
	Souma	285	37.783333	140.925000	4181782.00	493397.22
	Fukushima	47595	37.758333	140.470000	4179135.00	453331.41
	Hibara	1282	37.721667	140.058333	4175345.75	417026.97
	Washikura	1116	37.668333	140.260000	4169271.75	434747.31
	Iitate	1130	37.665000	140.726667	4168686.75	475899.78
	Kitakata	286	37.658333	139.863333	4168506.75	399746.41
	Haramachi	288	37.638333	140.983333	4165677.75	498523.88
	Nihonmatsu	291	37.583333	140.430000	4159743.00	449681.47
	Tsushima	1150	37.560000	140.753333	4157040.25	478212.34
	Inawashiro	290	37.551667	140.108333	4156455.25	421262.03
	Namie	295	37.491667	140.965000	4149406.00	496880.00
	Wakamatsu	47570	37.488333	139.910000	4149612.50	403620.00
	Funehiki	294	37.435000	140.576667	4143220.75	462553.78
	Konan	1386	37.388333	140.090000	4138344.75	419478.84
	Kooriyama	299	37.368333	140.330000	4135948.75	440681.97
	Tomioka	300	37.346667	141.016667	4133329.50	501462.78
	Kawauchi	1129	37.336667	140.475000	4132354.50	453498.56
	Kawamae	1274	37.296667	140.723333	4127813.00	475481.84
	Nagatama	1268	37.288333	140.218333	4127144.25	430735.16
	Ononiimachi	304	37.286667	140.625000	4126726.25	466760.97
	Yumoto	1294	37.276667	140.063333	4125974.00	416971.25
	Hirono	1034	37.233333	141.000000	4120763.75	500013.94
	Tamakawa	1466	37.226667	140.426667	4120178.75	449152.06
	Ishikawa	307	37.146667	140.460000	4111262.75	452049.75
	Shirakawa	47597	37.131667	140.215000	4109758.25	430261.50
	Furudono	1634	37.090000	140.560000	4104938.00	460909.91
	Taira	310	37.065000	140.876667	4102068.25	489022.84
	Onahama	47598	36.946667	140.903333	4088969.00	491372.34
	Higashishirakawa	312	36.938333	140.408333	4088185.00	447324.34
	Yamada	1607	36.933333	140.733333	4087513.00	476250.97
Tochigi	Nasukougen	326	37.123333	140.035000	4109006.00	414296.47
	Kuroen	329	36.981667	140.018333	4093281.50	412629.19
	Ootawara	331	36.840000	140.035000	4077544.00	413973.31
Ibaraki	Hanazono	314	36.868333	140.636667	4080316.25	467626.19
	Kitaibaraki	315	36.833333	140.771667	4076396.00	479639.28
	Tokuda	1173	36.778333	140.481667	4070403.50	453736.94
	Daigo	316	36.778333	140.345000	4070487.50	441555.84
	Oonou	1421	36.743333	140.593333	4066483.00	463705.84
	Takahagi	1635	36.706667	140.716667	4062366.75	474682.84
	Hitachioomiya	1331	36.606667	140.325000	4051445.75	439623.66
	Hitachi	1011	36.580000	140.645000	4048337.50	468242.25

slope, slope indices) and average climatic data during the August to October period.

Morphometric attributes					Distance to Pacific Ocean coast (m)	Average climatic data	
Elevation (m)	Slope (% of rise)	Windward & Leeward indices	Easting	Northing		Average temperature (°C)	Cumulative precipitation (mm)
154	1.7	0.89753	-0.12548	0.99210	53480	20.0	386
263	11.8	0.96329	0.04071	0.99917	60314	18.8	395
231	2.5	0.90632	-0.62298	-0.78224	60411	19.3	394
249	1.5	0.89875	-0.11594	-0.99326	67394	19.4	402
100	10.6	1.20145	-0.72944	-0.68404	2400	19.2	443
258	2.4	1.02479	0.61324	0.78989	30812	18.3	440
41	1.2	1.12549	-0.82539	-0.56456	9020	20.2	473
3	0.4	1.00631	-0.38268	0.92388	2404	20.4	461
109	15.1	1.15257	-0.46014	-0.88785	20974	19.4	459
3	5.7	0.99643	0.98149	-0.19153	5016	20.4	470
5	1.1	1.03222	0.80329	0.59558	3454	20.3	468
87	3.1	1.11893	-0.08434	-0.99644	24935	19.9	472
17	0.3	0.96714	0.28731	0.95784	12433	20.1	468
306	15.1	0.96529	-0.98959	-0.14393	19051	18.3	471
196	5.0	0.88122	0.33185	0.94333	42325	18.7	422
13	3.1	1.03924	0.44231	0.89686	1600	20.2	468
45	1.0	0.89903	-0.96476	0.26313	30377	20.1	444
10	2.3	0.92730	-0.07701	-0.99703	3733	20.3	475
72	4.3	0.86781	0.27488	-0.96148	43045	20.4	408
828	16.3	0.90276	0.97255	-0.23269	73365	16.2	525
1225	41.7	1.05815	0.97580	0.21865	63428	14.4	619
460	1.9	1.10401	-0.99970	0.02441	24639	17.6	487
217	0.9	0.90964	-0.78008	-0.62568	64633	19.6	384
21	0.5	1.04888	-0.95028	-0.31141	3600	20.1	491
237	4.8	1.06182	-0.88700	-0.46177	51832	19.3	422
418	12.3	1.06651	-0.66791	-0.74424	24301	17.6	495
524	0.0	1.08486	-0.51380	-0.85791	80067	17.9	447
46	1.6	1.10738	0.78493	-0.61958	6379	20.0	489
213	0.2	0.87071	0.91453	-0.40452	80639	19.8	364
439	34.8	0.95147	0.93199	-0.36248	40648	18.0	487
534	0.2	0.95424	-0.73466	0.67843	82672	17.5	470
252	1.4	1.01431	0.54883	0.83593	61790	19.7	436
51	7.8	1.09506	-0.69114	-0.72272	1300	20.2	477
364	51.9	1.08303	0.00817	0.99997	48578	18.4	470
674	29.2	1.24257	-0.26797	0.96343	26148	16.8	543
317	4.0	1.05637	-0.99667	0.08150	66826	18.6	445
460	19.4	1.13613	0.01439	0.99990	34642	17.9	505
650	9.1	1.08651	-0.45229	-0.89187	77303	16.8	532
44	4.3	1.12265	-0.99093	0.13439	1200	20.1	476
371	2.5	1.02374	0.92312	0.38450	48519	18.6	484
293	10.5	0.91744	0.67861	0.73449	40282	18.5	486
359	1.6	1.09810	-0.77019	-0.63781	57837	18.8	490
359	19.7	1.15312	0.17515	0.98454	29442	18.4	495
18	3.2	0.96555	-0.14208	0.98986	8956	20.5	478
3	1.5	0.97804	-0.38909	-0.92120	510	20.5	481
184	2.5	0.91381	0.98465	0.17457	34829	19.1	477
13	4.4	0.98293	-0.52889	-0.84869	6741	19.9	475
746	12.8	1.27963	-0.14665	0.98919	72358	16.9	573
338	4.9	1.12660	0.04919	0.99879	68746	19.2	489
187	3.0	1.06959	-0.86010	-0.51012	62893	19.9	468
387	24.1	1.16665	0.26317	0.96475	13259	17.9	535
5	1.3	1.00639	-0.66352	-0.74816	1166	20.3	472
294	40.6	1.06989	0.15859	0.98734	23092	18.5	521
114	15.6	0.89292	-0.46862	-0.88340	34687	19.6	481
404	1.7	1.18394	0.17888	-0.98387	12448	18.1	547
6	0.2	1.01225	0.93834	-0.34572	806	20.5	486
77	3.3	0.96139	0.81788	0.57539	29577	19.9	489
28	14.5	1.12164	-0.79519	0.60636	1562	20.3	504

Table III.SM-III: Kolmogorov-Smirnov two-samples tests for source groups significance of the *p* value. "***" *p* value $\leq$ 0.001; "**" *p* value $\leq$ 0.01; "*" *p* value $\leq$ 0.05; "." *p* value $\leq$ 0.1; " " *p* value $>$ 0.1.

	TOC	TN	TOC/TN	$\delta^{13}C$	Al	Ca	Fe	K	Mg	Mn	Si	Sr	Ti	Zn	Zr	L*	a*	b*	A1	A2	Q7/4	G_{445}	G_{525}
Forest - Farmland	***	***	***	***	***	.		***	*		*		.	*	**	***				.		***	**
Forest - Subsoil	***	***	***	*	***	*		*	*	*	***	**		***	**	***	**	***	**		**	***	***
Forest - Fresh soil	***	***	***	**	***			***	***		***		**	*	*	***	*	***			**	***	***
Farmland - Subsoil	***	***			***	**			*		***	***		***		***	***	***	***	*	***	***	***
Farmland - Fresh soil	***	***	*		***			*	.	**	***			**		***	**	***	**	.	***	***	***
Subsoil - Fresh soil									*	**		.											
Forest - Subsoil & fresh soil	***	***	***	***	***	.		***	*		***	.	.	***	**	***	***	***	*		***	***	***
Farmland - Subsoil & fresh soil	***	***			***	*		.			***	**		***		***	***	***	***	**	***	***	***

Table III.SM-IV: Summary mean and standard deviation values of analysed properties for each potential source group: forest (n = 24),farmland (n = 24), "fresh soil" (n = 10), subsoil (i.e. channel bank or landslide, n = 10), and merged subsoil - fresh soil (n = 20).

	TOC (%)	TN (%)	TOC/TN	$\delta^{13}C$ (‰)	Al (g kg^{-1})	Ca (g kg^{-1})	Fe (g kg^{-1})	K (g kg^{-1})	Mg (g kg^{-1})	Mn (mg kg^{-1})	Si (g kg^{-1})	Sr (mg kg^{-1})
Forest	10.92 $\pm$ 4.25	0.7 $\pm$ 0.25	15.37 $\pm$ 2.31	-26.23 $\pm$ 1.10	67.5 $\pm$ 12.2	9.2 $\pm$ 4.5	51.7 $\pm$ 12.3	8.2 $\pm$ 2.0	6.4 $\pm$ 3.6	884 $\pm$ 449	163 $\pm$ 18	100 $\pm$ 45
Farmland	5.16 $\pm$ 2.05	0.42 $\pm$ 0.11	11.90 $\pm$ 1.45	-25.03 $\pm$ 1.06	84.9 $\pm$ 9.3	9.8 $\pm$ 3.6	49.5 $\pm$ 13.2	11.8 $\pm$ 2.4	6.4 $\pm$ 2.2	657 $\pm$ 229	163 $\pm$ 32	95 $\pm$ 30
Fresh soil	0.95 $\pm$ 0.88	0.09 $\pm$ 0.07	10.28 $\pm$ 1.98	-24.41 $\pm$ 1.46	105.8 $\pm$ 13.4	8.5 $\pm$ 4.7	50.5 $\pm$ 5.5	14.1 $\pm$ 2.7	6.8 $\pm$ 0.9	935 $\pm$ 204	227 $\pm$ 20	86 $\pm$ 36
Subsoil	1.41 $\pm$ 1.10	0.12 $\pm$ 0.1	11.57 $\pm$ 1.60	-25.37 $\pm$ 1.00	107.8 $\pm$ 9.7	5.1 $\pm$ 2.7	48.9 $\pm$ 15.6	11.3 $\pm$ 3.3	5.4 $\pm$ 2.6	504 $\pm$ 181	225 $\pm$ 42	62 $\pm$ 15
Subsoil - Fresh soil	1.18 $\pm$ 1.00	0.10 $\pm$ 0.08	10.93 $\pm$ 1.87	-24.89 $\pm$ 1.32	106.8 $\pm$ 11.4	6.8 $\pm$ 4.1	49.7 $\pm$ 11.4	12.7 $\pm$ 3.3	6.1 $\pm$ 2.0	719 $\pm$ 290	226 $\pm$ 32	74 $\pm$ 30

	Ti (g kg^{-1})	Zn (mg kg^{-1})	Zr (mg kg^{-1})	L*	a*	b*	A1	A2	Q7/4	G_{445}	G_{525}
Forest	4.4 $\pm$ 6.6	105 $\pm$ 16	246 $\pm$ 102	47.19 $\pm$ 7.72	3.60 $\pm$ 1.07	9.51 $\pm$ 3.79	3.7 $\pm$ 1.3 $\cdot 10^{-2}$	1.7 $\pm$ 0.8 $\cdot 10^{-2}$	2.00 $\pm$ 0.36	0.34 $\pm$ 0.24	0.49 $\pm$ 0.32
Farmland	4.9 $\pm$ 0.9	117 $\pm$ 28	319 $\pm$ 69	55.72 $\pm$ 3.47	3.05 $\pm$ 0.98	10.55 $\pm$ 2.77	3.2 $\pm$ 1.3 $\cdot 10^{-2}$	1.5 $\pm$ 0.7 $\cdot 10^{-2}$	2.02 $\pm$ 0.30	0.58 $\pm$ 0.20	0.73 $\pm$ 0.38
Fresh soil	5.0 $\pm$ 0.5	93 $\pm$ 19	342 $\pm$ 159	62.66 $\pm$ 2.96	4.86 $\pm$ 1.43	17.59 $\pm$ 3.74	4.3 $\pm$ 1.0 $\cdot 10^{-2}$	1.7 $\pm$ 0.4 $\cdot 10^{-2}$	2.40 $\pm$ 0.29	1.00 $\pm$ 0.21	1.43 $\pm$ 0.35
Subsoil	4.1 $\pm$ 1.8	82 $\pm$ 17	344 $\pm$ 120	64.58 $\pm$ 5.51	5.96 $\pm$ 1.77	18.32 $\pm$ 4.16	5.5 $\pm$ 1.8 $\cdot 10^{-2}$	2.6 $\pm$ 1.3 $\cdot 10^{-2}$	2.67 $\pm$ 0.45	1.00 $\pm$ 0.26	1.57 $\pm$ 0.46
Subsoil - Fresh soil	4.5 $\pm$ 1.3	88 $\pm$ 18	343 $\pm$ 137	63.62 $\pm$ 4.42	5.41 $\pm$ 1.66	17.95 $\pm$ 3.87	4.9 $\pm$ 1.5 $\cdot 10^{-2}$	2.1 $\pm$ 1.1 $\cdot 10^{-2}$	2.54 $\pm$ 0.39	1.00 $\pm$ 0.23	1.50 $\pm$ 0.40

Table III.SM-V: Effective degree of freedom (EDF) values of the covariates of the generalised additive models (GAM) fitted on the last erosive events before sampling campaign measured intensity (EI_{30}) from 2011 to 2023. '-' indicates covariates that prevented model convergence and that were removed.

Year	Covariate effective degree of freedom (EDF) values								
	Elevation	**Slope**	**Windward & Leeward indices**	**Easting**	**Northing**	**Distance to coastline**	**Cumulative precipitation**	**Average temperature**	**Coordinates**
2011	0.85	0.44	0.85	1.43	$4.95 \cdot 10^{-5}$	$4.50 \cdot 10^{-5}$	0.65	$1.08 \cdot 10^{-3}$	22.12
2012	$1.64 \cdot 10^{-5}$	$1.69 \cdot 10^{-5}$	1.91	$5.71 \cdot 10^{-5}$	$7.13 \cdot 10^{-6}$	0.23	$2.95 \cdot 10^{-6}$	0.96	29.50
2013	$1.30 \cdot 10^{-5}$	0.74	0.34	$1.16 \cdot 10^{-5}$	$1.89 \cdot 10^{-5}$	$2.19 \cdot 10^{-5}$	0.44	$8.62 \cdot 10^{-6}$	26.99
2014	0.95	0.04	$3.19 \cdot 10^{-5}$	$1.56 \cdot 10^{-4}$	0.70	$3.11 \cdot 10^{-5}$	0.97	$2.79 \cdot 10^{-5}$	18.00
2015	$2.90 \cdot 10^{-5}$	2.35	$6.48 \cdot 10^{-5}$	0.86	$6.27 \cdot 10^{-5}$	1.49	0.90	$8.42 \cdot 10^{-5}$	8.13
2016	$1.39 \cdot 10^{-3}$	$5.62 \cdot 10^{-5}$	0.39	0.25	$2.76 \cdot 10^{-3}$	$9.31 \cdot 10^{-5}$	0.96	$7.30 \cdot 10^{-5}$	12.18
2017	$2.94 \cdot 10^{-4}$	$2.75 \cdot 10^{-5}$	$3.33 \cdot 10^{-5}$	$1.90 \cdot 10^{-5}$	1.14	5.17	$2.17 \cdot 10^{-5}$	3.19	14.04
2018	$8.80 \cdot 10^{-6}$	0.77	1.26	0.35	1.73	$3.51 \cdot 10^{-5}$	0.91	$1.34 \cdot 10^{-5}$	36.74
2019	$8.11 \cdot 10^{-5}$	0.93	$5.33 \cdot 10^{-5}$	0.58	$2.91 \cdot 10^{-4}$	5.47	0.34	$6.14 \cdot 10^{-5}$	4.92
2020	$6.04 \cdot 10^{-5}$	$8.04 \cdot 10^{-6}$	$1.79 \cdot 10^{-5}$	$1.98 \cdot 10^{-5}$	0.61	$9.72 \cdot 10^{-6}$	$4.76 \cdot 10^{-5}$	$3.85 \cdot 10^{-5}$	25.71
2021	$1.45 \cdot 10^{-4}$	0.90	$1.14 \cdot 10^{-5}$	2.20	$1.16 \cdot 10^{-5}$	0.84	0.45	$2.20 \cdot 10^{-5}$	35.36
2022	1.45	$6.55 \cdot 10^{-5}$	$1.75 \cdot 10^{-4}$	1.42	$1.92 \cdot 10^{-5}$	1.83	$2.05 \cdot 10^{-5}$	$3.50 \cdot 10^{-4}$	23.91
2023	0.92	2.20	0.90	$7.35 \cdot 10^{-5}$	0.81	$1.78 \cdot 10^{-4}$	$9.39 \cdot 10^{-5}$	3.34	27.23

Table III.SM-VI: Annual statistics of the P factor in the Mano Dam reservoir catchment at the time of the last erosive events before each sampling campaigns, from 2011 to 2023. SD stands for standard deviation.

Year	Minimum	Maximum	Median	Mean	SD
2011	0.07	0.30	0.15	0.15	0.03
2012	0.02	0.05	0.03	0.03	0.01
2013	0.05	0.35	0.11	0.11	0.03
2014	0.02	0.10	0.04	0.04	0.02
2015	0.15	0.57	0.30	0.35	0.14
2016	0.13	0.19	0.16	0.16	0.01
2017	0.05	0.16	0.08	0.08	0.02
2018	0.01	0.05	0.01	0.02	0.00
2019	0.16	1.00	0.68	0.68	0.26
2020	0.01	0.03	0.01	0.02	0.01
2021	0.00	0.09	0.01	0.01	0.00
2022	0.01	0.02	0.01	0.01	0.00
2023	0.04	0.64	0.15	0.22	0.17
Average ($\pm$ SD)	*0.05 $\pm$ 0.06*	*0.27 $\pm$ 0.30*	*0.13 $\pm$ 0.18*	*0.14 $\pm$ 0.19*	

Table III.SM-VII: The annual statistics of the ^{137}Cs activity of the flood deposits in flood deposit sediments sampled in November across the catchment of the Mano Dam reservoir.

Sampling year	Reference date	Number of samples	^{137}Cs activity (kBq kg^{-1})				
			Minimum	Maximum	Median	Mean	SD
2011	2011-11-20	5	3.6	50.9	13.0	18.5	19.0
2012	2012-11-05	10	8.6	23.8	8.3	9.5	6.4
2013	2013-10-30	10	1.5	19.2	10.1	9.4	5.4
2014	2014-11-01	9	1.7	31.5	4.9	7.8	9.0
2015	2015-11-09	11	1.6	19.3	3.2	4.9	5.0
2016	2016-11-01	10	0.1	3.8	1.4	1.5	1.0
2017	2017-10-24	9	0.5	2.2	0.9	1.2	0.5
2018	2018-10-29	10	0.8	2.8	1.6	1.7	0.6
2019	2019-10-30	7	0.7	5.8	1.2	1.9	1.8
2020	2020-10-31	6	0.7	2.3	1.0	1.1	0.6
2021	2021-10-31	7	0.4	2.6	0.6	1.0	0.8
2022	2022-10-08	4	1.1	2.5	1.6	1.7	0.7
2023	2023-11-06	4	1.0	1.5	1.3	1.3	0.2

Table III.SM-VIII: Median of the predicted source contributions predicted by MixSIAR of the flood deposits sampled from 2011 to 2023 at ten sampling sites within the Mano Dam reservoir catchment. "n.d." stands for no deposit, "-" for sites that have not been visited.

River	Site	Sediment source	Sediment source contribution per year (%)												
			2011	2012	2013	2014	2015	2016	2017	2018	2019	2020	2021	2022	2023
Mano	Reservoir	Farmland	87	74	79		91	85		82		57	75		
		Forest	6	10	12	n.d.	3	7	n.d.	9	-	32	11	n.d.	n.d.
		Subsoil	7	16	9		6	8		9		10	14		
Mano	Mano-1	Farmland					85								
		Forest	-	-	-	-	8	-	-	-	-	-	-	-	-
		Subsoil					7								
	Mano-2	Farmland		92	75	89	68	70	81	81		90	87	85	
		Forest	-	3	22	5	5	5	4	5	-	4	4	10	-
		Subsoil		5	3	6	27	25	14	14		6	9	5	
	Mano-3	Farmland		81	88	85	82	64	77	75		48	80	84	
		Forest	-	13	6	8	8	4	5	5	-	24	10	10	-
		Subsoil		5	6	7	10	32	18	20		28	10	6	
	Mano-4	Farmland		78	77	82	80	78	76	51	63		76	59	59
		Forest	-	17	16	13	7	4	3	7	5	n.d.	16	34	35
		Subsoil		4	7	6	14	18	21	43	33		8	7	7
	Mano-5	Farmland	88												
		Forest	7	-	-	-	-	-	-	-	-	-	-	-	-
		Subsoil	5												
	Mano-6	Farmland		61	79	70	60	76	55	27	60	33	69		
		Forest	-	6	13	4	6	10	4	6	23	31	11	flood	n.d.
		Subsoil		33	8	26	34	14	41	67	17	37	20		
Maeda	Maeda-1	Farmland	73												
		Forest	20	-	-	-	-	-	-	-	-	-	-	-	-
		Subsoil	7												
	Maeda-2	Farmland		80	84	80	75	56	77	84		38	80	81	60
		Forest	-	11	9	9	4	5	5	7	-	10	14	7	23
		Subsoil		9	8	11	21	39	17	9		52	6	12	17
	Maeda-3	Farmland	79	70	78	82	76	87	90	73	83	43	73		
		Forest	10	24	15	10	18	3	4	22	10	47	22	flood	flood
		Subsoil	11	6	7	8	6	10	6	5	7	10	5		
Usu	Usu-1	Farmland	57	69	82	67	41	54	57	72					
		Forest	12	16	9	7	44	9	5	5	-	-	-	-	-
		Subsoil	31	15	9	26	16	37	38	23					
Kidoki	Kidoki-1	Farmland		88	83	81	78	74	70	72					
		Forest	-	7	10	12	14	19	24	23	-	-	-	-	-
		Subsoil		5	7	7	8	7	6	5					
	Kidoki-2	Farmland		89	83	43	73	79	83	77					
		Forest	-	5	10	53	21	12	9	16	-	-	-	-	-
		Subsoil		6	7	4	6	9	7	7					

Table III.SM-IX: Observed cumulative precipitation and rainfall erosivity (EI_{30}) of the erosive events that occurred before the annual November 2013 sampling campaign within a 110 km radius area around the Fukushima Daiichi Nuclear Power Plant (FDNPP), along with maximum EI_{30} observed at a weather station. 'Cumulative' line in bold corresponds to the event statistics for the year summed by station. Extreme precipitation event intensity classification grades stand for: 2 = tropical depression, 3 = tropical storm, 4 = severe tropical storm, 5 = typhoon, 6 = extra-tropical cyclone.

Year	Event information				Number of stations	Cumulative precipitation (mm)			EI_{30} (MJ mm ha^{-1} h^{-1})			Local maximum EI_{30} (MJ mm ha^{-1} h^{-1})		
	Name	International ID	Date (mo/d)	Grade		Median	Mean	SD	Median	Mean	SD	Prefecture	Station	
2013	Man-Yi	1322	09/14-09/16	4	58	100	104	46	723	940	758	Ibaraki	Daigo	3764
2013	Wipha	1326	10/14-10/16	5	58	107	109	21	325	329	142	Ibaraki	Kitaibaraki	708
	Francisco	1327	10/24-10-26	6	57	40	41	19	39	50	29	Tochigi	Nasukougen	122
	Cumulative	-	**10/14-10/26**	**-**	**58**	**145**	**149**	**34**	**349**	**378**	**152**	**Ibaraki**	**Kitaibaraki**	**790**

Table III.SM-X: Observed cumulative precipitation and rainfall erosivity (EI_{30}) during the Phanfone and Vonfong events within a 110 km radius area around the Fukushima Daiichi Nuclear Power Plant (FDNPP), along with maximum EI_{30} observed at a weather station, and compared Chartin et al. (2017). 'Cumulative' line in bold corresponds to the event statistics for the year summed by station. Extreme precipitation event intensity classification grades stand for: 2 = tropical depression, 3 = tropical storm, 4 = severe tropical storm, 5 = typhoon, 6 = extra-tropical cyclone.

Year	Event information				Number of stations	Cumulative precipitation (mm)			EI_{30} (MJ mm ha^{-1} h^{-1})			Local maximum EI_{30} (MJ mm ha^{-1} h^{-1})		
	Name	International ID	Date (mo/d)	Grade		Median	Mean	SD	Median	Mean	SD	Prefecture	Station	
2014	Phanfone	1418	10-05-10/07	4	58	115	119	41	283	466	462	Fukushima	Onahama	2493
	Vonfong	1419	10/13-10/14	4	58	85	93	40	454	654	681	Fukushima	Shinchi	3354
	Cumulative	**-**	**10/05-10/14**	**-**	**58**	**214**	**212**	**67**	**931**	**1120**	**929**	**Fukushima**	**Shinchi**	**4438**
2014	Phanfone & Vongong	1418-1419	09/28-10/14	4	58	214	213	67	930	1120	928	Fukushima	Shinchi	4436
Chartin et al. (2017)	Phanfone & Vongong	-	09/28-10/14	-	40	-	-	-	-	1034	759	-	-	-

References

Agnihotri, R., Kumar, R., Prasad, M.V.S.N., Sharma, C., Bhatia, S.K., Arya, B.C., 2014. Experimental Setup and Standardization of a Continuous Flow Stable Isotope Mass Spectrometer for Measuring Stable Isotopes of Carbon, Nitrogen and Sulfur in Environmental Samples. MAPAN 29, 195–205. URL: http://link.springer.com/10.1007/s12647-014-0099-8, doi:10.1007/s12647-014-0099-8.

ALOS, 2020. Global Digital Surface Model "ALOS World 3D - 30m (AW3D30)" version 3.2/3.1. URL: https://www.eorc.jaxa.jp/ALOS/en/dataset/aw3d30/aw3d30_e.htm.

Amorim, H.C., Hurtarte, L.C., Souza, I.F., Zinn, Y.L., 2022. C:N ratios of bulk soils and particle-size fractions: Global trends and major drivers. Geoderma 425, 116026. URL: https://linkinghub.elsevier.com/retrieve/pii/S0016706122003330, doi:10.1016/j.geoderma.2022.116026.

Balsam, W., Ji, J., Chen, J., 2004. Climatic interpretation of the Luochuan and Lingtai loess sections, China, based on changing iron oxide mineralogy and magnetic susceptibility. Earth and Planetary Science Letters 223, 335–348. URL: https://linkinghub.elsevier.com/retrieve/pii/S0012821X04002717, doi:10.1016/j.epsl.2004.04.023.

Batista, P.V.G., Laceby, J.P., Evrard, O., 2022. How to evaluate sediment fingerprinting source apportionments. Journal of Soils and Sediments 22, 1315–1328. URL: https://link.springer.com/10.1007/s11368-022-03157-4, doi:10.1007/s11368-022-03157-4.

Beck, H.E., Zimmermann, N.E., McVicar, T.R., Vergopolan, N., Berg, A., Wood, E.F., 2018. Present and future Köppen-Geiger climate classification maps at 1-km resolution. Scientific Data 5, 180214. URL: http://www.nature.com/articles/sdata2018214, doi:10.1038/sdata.2018.214.

Blake, W.H., Boeckx, P., Stock, B.C., Smith, H.G., Bodé, S., Upadhayay, H.R., Gaspar, L., Goddard, R., Lennard, A.T., Lizaga, I., Lobb, D.A., Owens, P.N., Petticrew, E.L., Kuzyk, Z.Z.A., Gari, B.D., Munishi, L., Mtei, K., Nebiyu, A., Mabit, L., Navas, A., Semmens, B.X., 2018. A deconvolutional Bayesian mixing model approach for river basin sediment source apportionment. Scientific Reports 8, 13073. URL: https://www.nature.com/articles/s41598-018-30905-9, doi:10.1038/s41598-018-30905-9.

Borrelli, P., Alewell, C., Alvarez, P., Anache, J.A.A., Baartman, J., Ballabio, C., Bezak, N., Biddoccu, M., Cerdà, A., Chalise, D., Chen, S., Chen, W., De Girolamo, A.M., Gessesse, G.D., Deumlich, D., Diodato, N., Efthimiou, N., Erpul, G., Fiener, P., Freppaz, M., Gentile, F., Gericke, A., Haregeweyn, N., Hu, B., Jeanneau, A., Kaffas, K., Kiani-Harchegani, M., Villuendas, I.L., Li, C., Lombardo, L., López-Vicente, M., Lucas-Borja, M.E., Märker, M., Matthews, F., Miao, C., Mikoš, M., Modugno, S., Möller, M., Naipal, V., Nearing, M., Owusu, S., Panday, D., Patault, E., Patriche, C.V., Poggio, L., Portes, R., Quijano, L., Rahdari, M.R., Renima, M., Ricci, G.F., Rodrigo-Comino, J., Saia, S., Samani, A.N., Schillaci, C., Syrris, V., Kim, H.S., Spinola, D.N., Oliveira, P.T., Teng, H., Thapa, R., Vantas, K., Vieira, D., Yang, J.E., Yin, S., Zema, D.A., Zhao, G., Panagos, P., 2021. Soil erosion modelling: A global review and statistical analysis. Science of The Total Environment 780, 146494. URL: https://linkinghub.elsevier.com/retrieve/pii/S004896972101562X, doi:10.1016/j.scitotenv.2021.146494.

Borselli, L., Cassi, P., Torri, D., 2008. Prolegomena to sediment and flow connectivity in the landscape: A GIS and field numerical assessment. CATENA 75, 268–277. URL: https://linkinghub.elsevier.com/retrieve/pii/S0341816208000982, doi:10.1016/j.catena.2008.07.006.

Briard, J., Ayrault, S., Roy-Barman, M., Bordier, L., L'Héritier, M., Azéma, A., Syvilay, D., Baron, S., 2023. Determining the geochemical fingerprint of the lead fallout from the Notre-Dame de Paris fire: Lessons for a better discrimination of chemical signatures. Science of The Total Environment 864, 160676. URL: https://linkinghub.elsevier.com/retrieve/pii/S0048969722077798, doi:10.1016/j.scitotenv.2022.160676.

Brown, L., Foster, G.R., 1987. Storm Erosivity Using Idealized Intensity Distributions. Transactions of the ASAE 30, 0379–0386. URL: http://elibrary.asabe.org/abstract.asp??JID=3&AID=31957&CID=t1987&v=30&i=2&T=1, doi:10.13031/2013.31957.

Cavalli, M., Trevisani, S., Comiti, F., Marchi, L., 2013. Geomorphometric assessment of spatial sediment con-

nectivity in small Alpine catchments. Geomorphology 188, 31–41. URL: https://linkinghub.elsevier.com/retrieve/pii/S0169555X12002267, doi:10.1016/j.geomorph.2012.05.007.

Chalaux-Clergue, T., 2025. RainErosivity: Customisable tools to calculate precipitation event rainfall erosivity index. URL: https://github.com/tchalauxclergue/RainErosivity, doi:10.5281/zenodo.14745961.

Chalaux-Clergue, T., Bizeul, R., 2024. fingR: A support for sediment source fingerprinting studies. URL: https://github.com/tchalauxclergue/fingR, doi:10.5281/zenodo.12187654.

Chalaux-Clergue, T., Bizeul, R., Batista, P.V.G., Martínez-Carreras, N., Laceby, J.P., Evrard, O., 2024a. Sensitivity of source sediment fingerprinting to tracer selection methods. SOIL 10, 109–138. URL: https://soil.copernicus.org/articles/10/109/2024/, doi:10.5194/soil-10-109-2024.

Chalaux-Clergue, T., Foucher, A., Chaboche, P.A., Hayashi, S., Tsuji, H., Wakiyama, Y., Huon, S., Vandromme, R., Cerdan, O., Nakao, A., Evrard, O., 2024b. Impacts of farmland decontamination on 137Cs transfers in rivers after Fukushima nuclear accident: Evidence from a retrospective sediment core study. Science of The Total Environment 947, 174546. URL: https://linkinghub.elsevier.com/retrieve/pii/S0048969724046941, doi:10.1016/j.scitotenv.2024.174546.

Chalaux-Clergue, T., Tenaud, N., Durand, R., Caumon, A., Wakiyama, Y., Laceby, J.P., Lefèvre, I., Huon, S., Vaury, V., Mendes-Millan, M., Ogier, A., Onda, Y., Nakao, A., Evrard, O., 2024c. Diagnostic properties of river flood deposit sediment collected annually from 2011 to 2023 at ten sites across a water reservoir catchment contaminated after the fukushima daiichi nuclear accident radiocesium fallout (mano dam). URL: https://doi.org/10.5281/zenodo.11609434, doi:10.5281/zenodo.11609434.

Chartin, C., Evrard, O., Laceby, J.P., Onda, Y., Ottlé, C., Lefèvre, I., Cerdan, O., 2017. The impact of typhoons on sediment connectivity: Lessons learnt from contaminated coastal catchments of the Fukushima Prefecture (Japan): Typhoon Impact on Sediment Connectivity - Fukushima, Japan. Earth Surface Processes and Landforms 42, 306–317. URL: https://onlinelibrary.wiley.com/doi/10.1002/esp.4056, doi:10.1002/esp.4056.

Chartin, C., Evrard, O., Onda, Y., Patin, J., Lefèvre, I., Ottlé, C., Ayrault, S., Lepage, H., Bonté, P., 2013. Tracking the early dispersion of contaminated sediment along rivers draining the Fukushima radioactive pollution plume. Anthropocene 1, 23–34. URL: https://linkinghub.elsevier.com/retrieve/pii/S2213305413000088, doi:10.1016/j.ancene.2013.07.001.

CIE, 2008. C. I. C.: Colorimetry — Part 4: CIE 1976 L*a*b* Colour space. doi:ISO/CIE11664-4:2019(E).

Collins, A.L., Blackwell, M., Boeckx, P., Chivers, C.A., Emelko, M., Evrard, O., Foster, I., Gellis, A., Gholami, H., Granger, S., Harris, P., Horowitz, A.J., Laceby, J.P., Martinez-Carreras, N., Minella, J., Mol, L., Nosrati, K., Pulley, S., Silins, U., da Silva, Y.J., Stone, M., Tiecher, T., Upadhayay, H.R., Zhang, Y., 2020. Sediment source fingerprinting: Benchmarking recent outputs, remaining challenges and emerging themes. Journal of Soils and Sediments 20, 4160–4193. URL: https://link.springer.com/10.1007/s11368-020-02755-4, doi:10.1007/s11368-020-02755-4.

Collins, A.L., Walling, D.E., 2004. Documenting catchment suspended sediment sources: Problems, approaches and prospects. Progress in Physical Geography: Earth and Environment 28, 159–196. URL: http://journals.sagepub.com/doi/10.1191/0309133304pp409ra, doi:10.1191/0309133304pp409ra.

Coplen, T.B., Kendall, C., Hopple, J., 1983. Comparison of stable isotope reference samples. Nature 302, 236–238. URL: https://www.nature.com/articles/302236a0, doi:10.1038/302236a0.

Debret, M., Sebag, D., Desmet, M., Balsam, W., Copard, Y., Mourier, B., Susperrigui, A.S., Arnaud, F., Bentaleb, I., Chapron, E., Lallier-Vergès, E., Winiarski, T., 2011. Spectrocolorimetric interpretation of sedimentary dynamics: The new "Q7/4 diagram". Earth-Science Reviews 109, 1–19. URL: https://linkinghub.elsevier.com/retrieve/pii/S0012825211000985, doi:10.1016/j.earscirev.2011.07.002.

Delmas, M., Garcia-Sanchez, L., Onda, Y., 2019. Factors controlling the variability of 137Cs concentrations in 5 coastal rivers around Fukushima Dai-ichi power plant. Journal of Environmental Radioactivity 204,

1–11. URL: https://linkinghub.elsevier.com/retrieve/pii/S0265931X18307252, doi:10.1016/j.jenvrad.2019.03.013.

Diacre, A., Chalaux-Clergue, T., Burban, S., Gauthier, C., Hubert, A., Humbert, A.C., Lefevre, I., Fauré, A.L., Pointurier, F., Evrard, O., 2023. Temporal evolution of plutonium concentrations and isotopic ratios in the Ukedo - Takase Rivers draining the Difficult-To-Return zone in Fukushima, Japan (2013–2020). Environmental Pollution 319, 120963. URL: https://linkinghub.elsevier.com/retrieve/pii/S0269749122021789, doi:10.1016/j.envpol.2022.120963.

Duan, W., He, B., Takara, K., Luo, P., Hu, M., Alias, N.E., Nover, D., 2015. Changes of precipitation amounts and extremes over Japan between 1901 and 2012 and their connection to climate indices. Climate Dynamics 45, 2273–2292. URL: http://link.springer.com/10.1007/s00382-015-2778-8, doi:10.1007/s00382-015-2778-8.

Evrard, O., Batista, P.V.G., Company, J., Dabrin, A., Foucher, A., Frankl, A., García-Comendador, J., Huguet, A., Lake, N., Lizaga, I., Martínez-Carreras, N., Navratil, O., Pignol, C., Sellier, V., 2022. Improving the design and implementation of sediment fingerprinting studies: Summary and outcomes of the TRACING 2021 Scientific School. Journal of Soils and Sediments 22, 1648–1661. URL: https://link.springer.com/10.1007/s11368-022-03203-1, doi:10.1007/s11368-022-03203-1.

Evrard, O., Chalaux-Clergue, T., Chaboche, P.A., Wakiyama, Y., Thiry, Y., 2023. Research and management challenges following soil and landscape decontamination at the onset of the reopening of the Difficult-To-Return Zone, Fukushima (Japan). SOIL 9, 479–497. URL: https://soil.copernicus.org/articles/9/479/2023/, doi:10.5194/soil-9-479-2023.

Evrard, O., Chartin, C., Onda, Y., Lepage, H., Cerdan, O., Lefèvre, I., Ayrault, S., 2014. Renewed soil erosion and remobilisation of radioactive sediment in Fukushima coastal rivers after the 2013 typhoons. Scientific Reports 4, 4574. URL: https://www.nature.com/articles/srep04574, doi:10.1038/srep04574.

Evrard, O., Durand, R., Nakao, A., Laceby, P.J., Lefèvre, I., Wakiyama, Y., Hayashi, S., Asanuma-Brice, C., Cerdan, O., 2020. Impact of the 2019 typhoons on sediment source contributions and radiocesium concentrations in rivers draining the Fukushima radioactive plume, Japan. Comptes Rendus. Géoscience 352, 199–211. URL: https://comptes-rendus.academie-sciences.fr/geoscience/item/CRGEOS_2020__352_3_199_0, doi:10.5802/crgeos.42.

Evrard, O., Laceby, J.P., Lepage, H., Onda, Y., Cerdan, O., Ayrault, S., 2015. Radiocesium transfer from hillslopes to the Pacific Ocean after the Fukushima Nuclear Power Plant accident: A review. Journal of Environmental Radioactivity 148, 92–110. URL: https://linkinghub.elsevier.com/retrieve/pii/S0265931X1530031X, doi:10.1016/j.jenvrad.2015.06.018.

Evrard, O., Laceby, J.P., Nakao, A., 2019. Effectiveness of landscape decontamination following the Fukushima nuclear accident: A review. SOIL 5, 333–350. URL: https://soil.copernicus.org/articles/5/333/2019/, doi:10.5194/soil-5-333-2019.

Evrard, O., Laceby, J.P., Onda, Y., Wakiyama, Y., Jaegler, H., Lefèvre, I., 2016. Quantifying the dilution of the radiocesium contamination in Fukushima coastal river sediment (2011–2015). Scientific Reports 6, 34828. URL: https://www.nature.com/articles/srep34828, doi:10.1038/srep34828.

Eyrolle-Boyer, F., Boyer, P., Garcia-Sanchez, L., Métivier, J.M., Onda, Y., De Vismes, A., Cagnat, X., Boulet, B., Cossonnet, C., 2016. Behaviour of radiocaesium in coastal rivers of the Fukushima Prefecture (Japan) during conditions of low flow and low turbidity – Insight on the possible role of small particles and detrital organic compounds. Journal of Environmental Radioactivity 151, 328–340. URL: https://linkinghub.elsevier.com/retrieve/pii/S0265931X15301442, doi:10.1016/j.jenvrad.2015.10.028.

Feng, B., Onda, Y., Wakiyama, Y., Taniguchi, K., Hashimoto, A., Zhang, Y., 2022. Persistent impact of Fukushima decontamination on soil erosion and suspended sediment. Nature Sustainability URL: https://www.nature.com/articles/s41893-022-00924-6, doi:10.1038/s41893-022-00924-6.

Fick, S.E., Hijmans, R.J., 2017. WorldClim 2: New 1-km spatial resolution climate surfaces for global land areas. International Journal of Climatology 37, 4302–4315. URL: https://rmets.onlinelibrary.wiley.com/doi/10.1002/joc.5086, doi:10.1002/joc.5086.

Foucher, A., Morera, S., Sanchez, M., Orrillo, J., Evrard, O., 2023a. El Niño–Southern Oscillation (ENSO)-driven hypersedimentation in the Poechos Reservoir, northern Peru. Hydrology and Earth System Sciences 27, 3191–3204. URL: https://hess.copernicus.org/articles/27/3191/2023/, doi:10.5194/hess-27-3191-2023.

Foucher, A., Tassano, M., Chaboche, P.A., Chalar, G., Cabrera, M., Gonzalez, J., Cabral, P., Simon, A.C., Agelou, M., Ramon, R., Tiecher, T., Evrard, O., 2023b. Inexorable land degradation due to agriculture expansion in South American Pampa. Nature Sustainability 6, 662–670. URL: https://www.nature.com/articles/s41893-023-01074-z, doi:10.1038/s41893-023-01074-z.

Fukuyama, T., Onda, Y., Gomi, T., Yamamoto, K., Kondo, N., Miyata, S., Kosugi, K., Mizugaki, S., Tsubonuma, N., 2010. Quantifying the impact of forest management practice on the runoff of the surface-derived suspended sediment using fallout radionuclides. Hydrological Processes 24, 596–607. URL: https://onlinelibrary.wiley.com/doi/10.1002/hyp.7554, doi:10.1002/hyp.7554.

Girardin, C., Mariotti, A., 1991. Analyse isotopique du 13C en abondance naturelle dans le carbone organique: un système automatique avec robot préparateur. Cahiers ORSTOM, Serie Pedologie 26, 371–380. URL: https://www.documentation.ird.fr/hor/fdi:39457.

GSI, 2016. Global Map Japan version 2.2 Vector data. URL: https://www.gsi.go.jp/kankyochiri/gm_japan_e.html.

Hao, Q., Oldfield, F., Bloemendal, J., Torrent, J., Guo, Z., 2009. The record of changing hematite and goethite accumulation over the past 22 Myr on the Chinese Loess Plateau from magnetic measurements and diffuse reflectance spectroscopy. Journal of Geophysical Research 114, B12101. URL: http://doi.wiley.com/10.1029/2009JB006604, doi:10.1029/2009JB006604.

Hashimoto, S., Komatsu, M., Miura, S., 2022. Forest Radioecology in Fukushima: Radiocesium Dynamics, Impact, and Future. Springer Nature Singapore, Singapore. URL: https://link.springer.com/10.1007/978-981-16-9404-2, doi:10.1007/978-981-16-9404-2.

Hashimoto, S., Ugawa, S., Nanko, K., Shichi, K., 2012. The total amounts of radioactively contaminated materials in forests in Fukushima, Japan. Scientific Reports 2, 416. URL: https://www.nature.com/articles/srep00416, doi:10.1038/srep00416.

Hastie, T., Tibshirani, R., 1987. Generalized Additive Models: Some Applications. Journal of the American Statistical Association 82, 371–386. URL: http://www.tandfonline.com/doi/abs/10.1080/01621459.1987.10478440, doi:10.1080/01621459.1987.10478440.

Huon, S., Hayashi, S., Laceby, J.P., Tsuji, H., Onda, Y., Evrard, O., 2018. Source dynamics of radiocesium-contaminated particulate matter deposited in an agricultural water reservoir after the Fukushima nuclear accident. Science of The Total Environment 612, 1079–1090. URL: https://linkinghub.elsevier.com/retrieve/pii/S0048969717319083, doi:10.1016/j.scitotenv.2017.07.205.

Ikenoue, T., Shimadera, H., Kondo, A., 2020. Impact of soil erosion potential uncertainties on numerical simulations of the environmental fate of radiocesium in the Abukuma River basin. Journal of Environmental Radioactivity 225, 106452. URL: https://www.sciencedirect.com/science/article/pii/S0265931X20306986, doi:10.1016/j.jenvrad.2020.106452.

Iwagami, S., Onda, Y., Tsujimura, M., Abe, Y., 2017. Contribution of radioactive 137Cs discharge by suspended sediment, coarse organic matter, and dissolved fraction from a headwater catchment in Fukushima after the Fukushima Dai-ichi Nuclear Power Plant accident. Journal of Environmental Radioactivity 166, 466–474. URL: https://linkinghub.elsevier.com/retrieve/pii/S0265931X16302557, doi:10.1016/j.jenvrad.2016.07.025.

JAXA, 2016. High-Resolution Land-Use and Land-Cover Map of Japan [2006 ~ 2011] (ver. 16.09; 10-m resolution; 12 categories). URL: https://www.eorc.jaxa.jp/ALOS/en/dataset/lulc/lulc_jpn_e.htm.

JAXA, 2018. High-Resolution Land-Use and Land-Cover Map of Japan [2014 ~ 2016] (ver. 18.03; 30-m resolution; 12 categories). URL: https://www.eorc.jaxa.jp/ALOS/en/dataset/lulc/lulc_v1803_e.htm.

JAXA, 2022. High-Resolution Land-Use and Land-Cover Map of Japan [2018 ∼ 2020] (ver. 21.11; 10-m resolution; 12 categories). URL: https://www.eorc.jaxa.jp/ALOS/en/dataset/lulc/lulc_v2111_e.htm.

JAXA, 2023. High-Resolution Land-Use and Land-Cover Map of Japan [2022] (ver.23.12; 10-m resolution; 12 categories). URL: https://www.eorc.jaxa.jp/ALOS/en/lulc/data/index.htm#japan_v23.12.

JMA, 2024. Historical weather data of Japan. URL: https://www.data.jma.go.jp/stats/etrn/index.php.

Kato, H., Onda, Y., Gao, X., Sanada, Y., Saito, K., 2019. Reconstruction of a Fukushima accident-derived radiocesium fallout map for environmental transfer studies. Journal of Environmental Radioactivity 210, 105996. URL: https://linkinghub.elsevier.com/retrieve/pii/S0265931X18303308, doi:10.1016/j.jenvrad.2019.105996.

Kato, H., Onda, Y., Teramage, M., 2012. Depth distribution of 137Cs, 134Cs, and 131I in soil profile after Fukushima Dai-ichi Nuclear Power Plant Accident. Journal of Environmental Radioactivity 111, 59–64. URL: https://linkinghub.elsevier.com/retrieve/pii/S0265931X11002426, doi:10.1016/j.jenvrad.2011.10.003.

Konoplev, A., Golosov, V., Wakiyama, Y., Takase, T., Yoschenko, V., Yoshihara, T., Parenyuk, O., Cresswell, A., Ivanov, M., Carradine, M., Nanba, K., Onda, Y., 2018. Natural attenuation of Fukushima-derived radiocesium in soils due to its vertical and lateral migration. Journal of Environmental Radioactivity 186, 23–33. URL: https://linkinghub.elsevier.com/retrieve/pii/S0265931X17303296, doi:10.1016/j.jenvrad.2017.06.019.

Konoplev, A.V., Golosov, V.N., Yoschenko, V.I., Nanba, K., Onda, Y., Takase, T., Wakiyama, Y., 2016. Vertical distribution of radiocesium in soils of the area affected by the Fukushima Dai-ichi nuclear power plant accident. Eurasian Soil Science 49, 570–580. URL: http://link.springer.com/10.1134/S1064229316050082, doi:10.1134/S1064229316050082.

Kosmas, C.S., Curi, N., Bryant, R.B., Franzmeier, D.P., 1984. Characterization of Iron Oxide Minerals by Second-Derivative Visible Spectroscopy. Soil Science Society of America Journal 48, 401–405. URL: http://doi.wiley.com/10.2136/sssaj1984.03615995004800020036x, doi:10.2136/sssaj1984.03615995004800020036x.

Laceby, J.P., Chartin, C., Evrard, O., Onda, Y., Garcia-Sanchez, L., Cerdan, O., 2016a. Rainfall erosivity in catchments contaminated with fallout from the Fukushima Daiichi nuclear power plant accident. Hydrology and Earth System Sciences 20, 2467–2482. URL: https://hess.copernicus.org/articles/20/2467/2016/, doi:10.5194/hess-20-2467-2016.

Laceby, J.P., Huon, S., Onda, Y., Vaury, V., Evrard, O., 2016b. Do forests represent a long-term source of contaminated particulate matter in the Fukushima Prefecture? Journal of Environmental Management 183, 742–753. URL: https://linkinghub.elsevier.com/retrieve/pii/S0301479716306661, doi:10.1016/j.jenvman.2016.09.020.

Lamb, A.L., Wilson, G.P., Leng, M.J., 2006. A review of coastal palaeoclimate and relative sea-level reconstructions using δ13C and C/N ratios in organic material. Earth-Science Reviews 75, 29–57. URL: https://linkinghub.elsevier.com/retrieve/pii/S0012825205001376, doi:10.1016/j.earscirev.2005.10.003.

Lepage, H., Evrard, O., Onda, Y., Lefèvre, I., Laceby, J.P., Ayrault, S., 2015. Depth distribution of cesium-137 in paddy fields across the Fukushima pollution plume in 2013. Journal of Environmental Radioactivity 147, 157–164. URL: https://linkinghub.elsevier.com/retrieve/pii/S0265931X15001484, doi:10.1016/j.jenvrad.2015.05.003.

Loa, E., Kawagoe, S., 2021. Prediction of sediment production in the Abukuma River basin due to rainfall sensitivity. Tohoku journal of natural disaster science 57, 41–45. URL: http://nds-tohoku.in.arena.ne.jp/ndsjournal/volume57/57-8.pdf.

McCullagh, P., Nelder, J., 2019. Generalized Linear Models. 2 ed., Routledge. URL: https://www.taylorfrancis.com/books/9781351445856, doi:10.1201/9780203753736.

Meusburger, K., Steel, A., Panagos, P., Montanarella, L., Alewell, C., 2012. Spatial and temporal variability of rainfall erosivity factor for Switzerland. Hydrology and Earth System Sciences 16, 167–177. URL: https://hess.copernicus.org/articles/16/167/2012/, doi:10.5194/hess-16-167-2012.

Minolta, K., 2022. QCM-S100w SpectraMagic NX. Konica Minolta. URL: https://www.konicaminolta.com/instruments/download/software/color/smnx/index.html.

MoE, 2015. Decontamination Report - A Compilation of Experiences to Date on Decontamination for the Living Environment Conducted by the Ministry of the Environment. Technical Report. Japanese Ministry of Environment. Japan. URL: http://josen.env.go.jp/en/policy_document/.

MoE, 2018. Decontamination Projects for Radioactive Contamination Discharged by Tokyo Electric Power Company Fukushima Daiichi Nuclear Power Station Accident. Technical Report. Japanese Ministry of Environment.

MoE, 2023a. Decontamination status. URL: http://josen.env.go.jp/area/.

MoE, 2023b. Environmental Remediation. URL: http://josen.env.go.jp/en/decontamination/.

MoE, 2023c. Information on decontamination – Fukushima revitalisation in data. Technical Report. Japanese Ministry of Environment. URL: http://josen.env.go.jp/plaza/info/data/pdf/data_2303_01.pdf.

Morino, Y., Ohara, T., Watanabe, M., Hayashi, S., Nishizawa, M., 2013. Episode Analysis of Deposition of Radiocesium from the Fukushima Daiichi Nuclear Power Plant Accident. Environmental Science & Technology 47, 2314–2322. URL: https://pubs.acs.org/doi/10.1021/es304620x, doi:10.1021/es304620x.

Nakao, A., Ogasawara, S., Sano, O., Ito, T., Yanai, J., 2014. Radiocesium sorption in relation to clay mineralogy of paddy soils in Fukushima, Japan. Science of The Total Environment 468–469, 523–529. URL: https://linkinghub.elsevier.com/retrieve/pii/S0048969713009893, doi:10.1016/j.scitotenv.2013.08.062.

Nakao, A., Takeda, A., Ogasawara, S., Yanai, J., Sano, O., Ito, T., 2015. Relationships between Paddy Soil Radiocesium Interception Potentials and Physicochemical Properties in Fukushima, Japan. Journal of Environmental Quality 44, 780–788. URL: http://doi.wiley.com/10.2134/jeq2014.10.0423, doi:10.2134/jeq2014.10.0423.

Naulier, M., Eyrolle-Boyer, F., Boyer, P., Métivier, J.M., Onda, Y., 2017. Particulate organic matter in rivers of Fukushima: An unexpected carrier phase for radiocesiums. Science of The Total Environment 579, 1560–1571. URL: https://linkinghub.elsevier.com/retrieve/pii/S0048969716326304, doi:10.1016/j.scitotenv.2016.11.165.

Navratil, O., Evrard, O., Esteves, M., Ayrault, S., Lefèvre, I., Legout, C., Reyss, J.L., Gratiot, N., Nemery, J., Mathys, N., Poirel, A., Bonté, P., 2012a. Core-derived historical records of suspended sediment origin in a mesoscale mountainous catchment: The River Bléone, French Alps. Journal of Soils and Sediments 12, 1463–1478. URL: http://link.springer.com/10.1007/s11368-012-0565-2, doi:10.1007/s11368-012-0565-2.

Navratil, O., Evrard, O., Esteves, M., Legout, C., Ayrault, S., Némery, J., Mate-Marin, A., Ahmadi, M., Lefèvre, I., Poirel, A., Bonté, P., 2012b. Temporal variability of suspended sediment sources in an alpine catchment combining river/rainfall monitoring and sediment fingerprinting. Earth Surface Processes and Landforms 37, 828–846. URL: https://onlinelibrary.wiley.com/doi/10.1002/esp.3201, doi:10.1002/esp.3201.

Niida, T., Wakiyama, Y., Takata, H., Taniguchi, K., Kurosawa, H., Fujita, K., Konoplev, A., 2022. A comparative study of riverine 137Cs dynamics during high-flow events at three contaminated river catchments in Fukushima. Science of The Total Environment 821, 153408. URL: https://linkinghub.elsevier.com/retrieve/pii/S0048969722005009, doi:10.1016/j.scitotenv.2022.153408.

Obara, H., Maejima, Y., Kohyama, K., Ohkura, T., Takata, Y., 2015. Outline of the Comprehensive Soil Classification System of Japan – First Approximation. Japan Agricultural Research Quarterly: JARQ 49, 217–226. URL: https://www.jstage.jst.go.jp/article/jarq/49/3/49_217/_article, doi:10.6090/jarq.49.217.

Obara, H., Ohkura, T., Takata, Y., Kohyama, K., Maejima, Y., Hamazaki, T., 2011. Comprehensive soil classification system of Japan first approximation. Nogyo Kankyo Gijutsu Kenkyusho Hokoku = Bulletin of National Institute for Agro-Environmental Sciences , 1–73URL: http://www.niaes.affrc.go.jp/sinfo/publish/public_e.html.

Oda, T., Hotta, N., Miura, S., Endo, I., Tanoi, K., Renschler, C.S., Ohte, N., 2022. Redistribution of the soil ^{137}Cs inventory through litter and sediment transport on a hillslope covered by deciduous forest in Fukushima, Japan. Earth Surface Processes and Landforms 47, 2531–2543. URL: https://onlinelibrary.wiley.com/doi/10.1002/esp.5393, doi:10.1002/esp.5393.

Olley, J., Burton, J., Smolders, K., Pantus, F., Pietsch, T., 2013. The application of fallout radionuclides to determine the dominant erosion process in water supply catchments of subtropical South-east Queensland, Australia: DOMINANT EROSION PROCESS IN SUBTROPICAL SE QUEENSLAND, AUSTRALIA. Hydrological Processes 27, 885–895. URL: https://onlinelibrary.wiley.com/doi/10.1002/hyp.9422, doi:10.1002/hyp.9422.

Onda, Y., Taniguchi, K., Yoshimura, K., Kato, H., Takahashi, J., Wakiyama, Y., Coppin, F., Smith, H., 2020. Radionuclides from the Fukushima Daiichi Nuclear Power Plant in terrestrial systems. Nature Reviews Earth & Environment 1, 644–660. URL: https://www.nature.com/articles/s43017-020-0099-x, doi:10.1038/s43017-020-0099-x.

Osawa, K., Nonaka, Y., Nishimura, T., Tanoi, K., Matsui, H., Mizogichi, M., Tatsuno, T., 2018. Quantification of dissolved and particulate radiocesium fluxes in two rivers draining the main radioactive pollution plume in Fukushima, Japan (2013–2016). Anthropocene 22, 40–50. URL: https://linkinghub.elsevier.com/retrieve/pii/S2213305418300262, doi:10.1016/j.ancene.2018.04.003.

Owens, P., Blake, W., Gaspar, L., Gateuille, D., Koiter, A., Lobb, D., Petticrew, E., Reiffarth, D., Smith, H., Woodward, J., 2016. Fingerprinting and tracing the sources of soils and sediments: Earth and ocean science, geoarchaeological, forensic, and human health applications. Earth-Science Reviews 162, 1–23. URL: https://linkinghub.elsevier.com/retrieve/pii/S0012825216302653, doi:10.1016/j.earscirev.2016.08.012.

Owens, P.N., 2020. Soil erosion and sediment dynamics in the Anthropocene: A review of human impacts during a period of rapid global environmental change. Journal of Soils and Sediments 20, 4115–4143. URL: http://link.springer.com/10.1007/s11368-020-02815-9, doi:10.1007/s11368-020-02815-9.

Owens, P.N., Batalla, R.J., Collins, A.J., Gomez, B., Hicks, D.M., Horowitz, A.J., Kondolf, G.M., Marden, M., Page, M.J., Peacock, D.H., Petticrew, E.L., Salomons, W., Trustrum, N.A., 2005. Fine-grained sediment in river systems: Environmental significance and management issues. River Research and Applications 21, 693–717. URL: https://onlinelibrary.wiley.com/doi/10.1002/rra.878, doi:10.1002/rra.878.

Palazón, L., Latorre, B., Gaspar, L., Blake, W.H., Smith, H.G., Navas, A., 2015. Comparing catchment sediment fingerprinting procedures using an auto-evaluation approach with virtual sample mixtures. Science of The Total Environment 532, 456–466. URL: https://linkinghub.elsevier.com/retrieve/pii/S0048969715300619, doi:10.1016/j.scitotenv.2015.05.003.

Panagos, P., Ballabio, C., Borrelli, P., Meusburger, K., Klik, A., Rousseva, S., Tadić, M.P., Michaelides, S., Hrabalíková, M., Olsen, P., Aalto, J., Lakatos, M., Rymszewicz, A., Dumitrescu, A., Beguería, S., Alewell, C., 2015. Rainfall erosivity in Europe. Science of The Total Environment 511, 801–814. URL: https://linkinghub.elsevier.com/retrieve/pii/S004896971500011X, doi:10.1016/j.scitotenv.2015.01.008.

Planchon, O., Darboux, F., 2002. A fast, simple and versatile algorithm to fill the depressions of digital elevation models. CATENA 46, 159–176. URL: https://linkinghub.elsevier.com/retrieve/pii/S0341816201001643, doi:10.1016/S0341-8162(01)00164-3.

QGIS Development Team, 2024. QGIS Geographic Information System. Open Source Geospatial Foundation. URL: https://www.qgis.org/fr/site/.

R Core Team, 2024. A Language and Environment for Statistical Computing. R Foundation for Statistical Computing. URL: https://www.R-project.org/.

Renard, K.G., Freimund, J.R., 1994. Using monthly precipitation data to estimate the R-factor in the revised USLE. Journal of Hydrology 157, 287–306. URL: https://linkinghub.elsevier.com/retrieve/pii/0022169494901104, doi:10.1016/0022-1694(94)90110-4.

RSMC, 2023. RSMC Typhoon Best Track Data and Graphics [2006 ~ 2021]. URL: https://www.jma.go.jp/jma/jma-eng/jma-center/rsmc-hp-pub-eg/trackarchives.html.

RSMC, 2024. Tropical Cyclone Information. URL: https://www.jma.go.jp/jma/jma-eng/jma-center/rsmc-hp-pub-eg/RSMC_HP.htm.

RStudio Team, 2023. RStudio: Integrated Development Environment for R. RStudio. URL: http://www.rstudio.com/.

Saito, T., Makino, H., Tanaka, S., 2014. Geochemical and grain-size distribution of radioactive and stable cesium in Fukushima soils: Implications for their long-term behavior. Journal of Environmental Radioactivity 138, 11–18. URL: https://linkinghub.elsevier.com/retrieve/pii/S0265931X14002306, doi:10.1016/j.jenvrad.2014.07.025.

Sakaguchi, A., Tanaka, K., Iwatani, H., Chiga, H., Fan, Q., Onda, Y., Takahashi, Y., 2015. Size distribution studies of 137Cs in river water in the Abukuma Riverine system following the Fukushima Dai-ichi Nuclear Power Plant accident. Journal of Environmental Radioactivity 139, 379–389. URL: https://linkinghub.elsevier.com/retrieve/pii/S0265931X14001519, doi:10.1016/j.jenvrad.2014.05.011.

Scheinost, A.C., Chavernas, A., Barrón, V., Torrent, J., 1998. Use and Limitations of Second-Derivative Diffuse Reflectance Spectroscopy in the Visible to Near-Infrared Range to Identify and Quantify Fe Oxide Minerals in Soils. Clays and Clay Minerals 46, 528–536. URL: http://link.springer.com/10.1346/CCMN.1998.0460506, doi:10.1346/CCMN.1998.0460506.

Shiono, T., Kamimura, K.i., Okushima, S., Fukumoto, M., 2002. Soil Loss Estimation on a Local Scale for Soil Conservation Planning. Japan Agricultural Research Quarterly: JARQ 36, 157–161. URL: https://www.jstage.jst.go.jp/article/jarq/36/3/36_157/_article, doi:10.6090/jarq.36.157.

Shiono, T., Ogawa, S., Miyamoto, T., Kameyama, K., 2013. Expected impacts of climate change on rainfall erosivity of farmlands in Japan. Ecological Engineering 61, 678–689. URL: https://linkinghub.elsevier.com/retrieve/pii/S0925857413000955, doi:10.1016/j.ecoleng.2013.03.002.

Stevens, A., Ramirez-Lopez, L., 2022. An introduction to the prospectr package. URL: https://cran.r-project.org/web/packages/prospectr/vignettes/prospectr.html.

Stock, B.C., Semmens, B.X., 2016. Unifying error structures in commonly used biotracer mixing models. Ecology 97, 2562–2569. URL: https://onlinelibrary.wiley.com/doi/10.1002/ecy.1517, doi:10.1002/ecy.1517.

Stock, B.C., Semmens, B.X., Ward, E.J., Parnell, A.C., Phillips, D.L., 2020. MixSIAR: Bayesian Mixing Models in R. URL: https://doi.org/10.5281/zenodo.1209993.

Stock, B.C., Semmens, B.X., Ward, E.J., Parnell, A.C., Phillips, D.L., 2022. JAGS: Bayesian Mixing Models in R. URL: https://doi.org/10.5281/zenodo.1209993.

Tamaoki, M., Yabe, T., Furukawa, J., Watanabe, M., Ikeda, K., Yasutani, I., Nishizawa, T., 2016. Comparison of Potentials of Higher Plants for Phytoremediation of Radioactive Cesium from Contaminated Soil. Environment Control in Biology 54, 65–69. URL: https://www.jstage.jst.go.jp/article/ecb/54/1/54_65/_article, doi:10.2525/ecb.54.65.

Taniguchi, K., Onda, Y., Smith, H.G., Blake, W., Yoshimura, K., Yamashiki, Y., Kuramoto, T., Saito, K., 2019. Transport and Redistribution of Radiocesium in Fukushima Fallout through Rivers. Environmental Science & Technology 53, 12339–12347. URL: https://pubs.acs.org/doi/10.1021/acs.est.9b02890, doi:10.1021/acs.est.9b02890.

Tarboton, D.G., 1997. A new method for the determination of flow directions and upslope areas in grid digital elevation models. Water Resources Research 33, 309–319. URL: https://agupubs.onlinelibrary.wiley.com/doi/10.1029/96WR03137, doi:10.1029/96WR03137.

Terashima, S., Imai, N., Taniguchi, M., Okai, T., Nishimura, A., 2002. The Preparation and Preliminary Characterisation of Four New Geological Survey of Japan Geochemical Reference Materials: Soils, JSO-1 and JSO-2; and Marine Sediments, JMS-1 and JMS-2. Geostandards Newsletter 26, 85–94. URL: https://onlinelibrary.wiley.com/doi/10.1111/j.1751-908X.2002.tb00626.x, doi:10.1111/j.1751-908X.2002.tb00626.x.

Tiecher, T., Caner, L., Minella, J.P.G., dos Santos, D.R., 2015. Combining visible-based-color parameters and geochemical tracers to improve sediment source discrimination and apportionment. Science of The Total Environment 527–528, 135–149. URL: https://linkinghub.elsevier.com/retrieve/pii/S0048969715300401, doi:10.1016/j.scitotenv.2015.04.103.

Torrent, J., Liu, Q., Bloemendal, J., Barrón, V., 2007. Magnetic Enhancement and Iron Oxides in the Upper Luochuan Loess-Paleosol Sequence, Chinese Loess Plateau. Soil Science Society of America Journal 71, 1570–1578. URL: http://doi.wiley.com/10.2136/sssaj2006.0328, doi:10.2136/sssaj2006.0328.

Tsubokura, M., Murakami, M., Takebayashi, Y., Nomura, S., Ono, K., Ozaki, A., Sawano, T., Kobashi, Y., Oikawa, T., 2019. Impact of decontamination on individual radiation doses from external exposure among residents of Minamisoma City after the 2011 Fukushima Daiichi nuclear power plant incident in Japan: A retrospective observational study. Journal of Radiological Protection 39, 854–871. URL: https://iopscience.iop.org/article/10.1088/1361-6498/ab280e, doi:10.1088/1361-6498/ab280e.

Tsuji, H., Nishikiori, T., Ito, S., Ozaki, H., Watanabe, M., Sakai, M., Ishii, Y., Hayashi, S., 2023. Influential factors of long-term and seasonal 137Cs change in agricultural and forested rivers: Temperature, water quality and an intense Typhoon Event. Environmental Pollution 338, 122617. URL: https://linkinghub.elsevier.com/retrieve/pii/S0269749123016196, doi:10.1016/j.envpol.2023.122617.

Vandromme, R., Hayashi, S., Tsuji, H., Evrard, O., Grangeon, T., Landemaine, V., Laceby, J.P., Wakiyama, Y., Cerdan, O., 2023. Lessons learnt on the impact of an unprecedented soil decontamination program in Fukushima on contaminant fluxes. Proceedings of the National Academy of Sciences 120, e2301811120. URL: https://pnas.org/doi/10.1073/pnas.2301811120, doi:10.1073/pnas.2301811120.

Wadoux, A.M.C., Malone, B., Minasny, B., Fajardo, M., McBratney, A.B., 2021. Soil Spectral Inference with R: Analysing Digital Soil Spectra Using the R Programming Environment. Progress in Soil Science, Springer International Publishing, Cham. URL: https://link.springer.com/10.1007/978-3-030-64896-1, doi:10.1007/978-3-030-64896-1.

Wakiyama, Y., Onda, Y., Yoshimura, K., Igarashi, Y., Kato, H., 2019. Land use types control solid wash-off rate and entrainment coefficient of Fukushima-derived 137Cs, and their time dependence. Journal of Environmental Radioactivity 210, 105990. URL: https://linkinghub.elsevier.com/retrieve/pii/S0265931X1730886X, doi:10.1016/j.jenvrad.2019.105990.

Walling, D.E., Owens, P.N., Waterfall, B.D., Leeks, G.J., Wass, P.D., 2000. The particle size characteristics of fluvial suspended sediment in the Humber and Tweed catchments, UK. Science of The Total Environment 251–252, 205–222. URL: https://linkinghub.elsevier.com/retrieve/pii/S0048969700003843, doi:10.1016/S0048-9697(00)00384-3.

Whitaker, A.C., Chapasa, S.N., Sagras, C., Theogene, U., Veremu, R., Sugiyama, H., 2022. Estimation of baseflow recession constant and regression of low flow indices in eastern Japan. Hydrological Sciences Journal 67, 191–204. URL: https://www.tandfonline.com/doi/full/10.1080/02626667.2021.2003368, doi:10.1080/02626667.2021.2003368.

Wischmeier, Wh., Smith, DD., 1978. Predicting rainfall erosion losses-A guide to conservation planning. Predicting rainfall erosion losses-A guide to conservation planning. US Department of Agriculture .

Wood, S.N., 2003. Thin Plate Regression Splines. Journal of the Royal Statistical Society Series B: Statistical Methodology 65, 95–114. URL: https://academic.oup.com/jrsssb/article/65/1/95/7110632, doi:10.1111/1467-9868.00374.

Wood, S.N., 2017. Generalized Additive Models: An Introduction with R. 2 ed., Chapman and Hall/CRC. URL: https://www.taylorfrancis.com/books/9781498728348, doi:10.1201/9781315370279.

Yamaguchi, M., Kitamura, A., Oda, Y., Onishi, Y., 2014. Predicting the long-term 137Cs distribution in Fukushima after the Fukushima Dai-ichi nuclear power plant accident: A parameter sensitivity analysis. Journal of Environmental Radioactivity 135, 135–146. URL: https://linkinghub.elsevier.com/retrieve/pii/S0265931X14001179, doi:10.1016/j.jenvrad.2014.04.011.

Yamashiki, Y., Onda, Y., Smith, H.G., Blake, W.H., Wakahara, T., Igarashi, Y., Matsuura, Y., Yoshimura, K., 2014. Initial flux of sediment-associated radiocesium to the ocean from the largest river impacted by Fukushima Daiichi Nuclear Power Plant. Scientific Reports 4, 3714. URL: https://www.nature.com/articles/srep03714, doi:10.1038/srep03714.

Yamashita, J., Enomoto, T., Yamada, M., Ono, T., Hanafusa, T., Nagamatsu, T., Sonoda, S., Yamamoto, Y., 2014. Estimation of soil-to-plant transfer factors of radiocesium in 99 wild plant species grown in arable lands 1 year after the Fukushima 1 Nuclear Power Plant accident. Journal of Plant Research 127, 11–22. URL: http://link.springer.com/10.1007/s10265-013-0605-z, doi:10.1007/s10265-013-0605-z.

Yin, S., Nearing, M.A., Borrelli, P., Xue, X., 2017. Rainfall Erosivity: An Overview of Methodologies and Applications. Vadose Zone Journal 16, 1–16. URL: https://acsess.onlinelibrary.wiley.com/doi/10.2136/vzj2017.06.0131, doi:10.2136/vzj2017.06.0131.

Yoshikawa, S., Yamamoto, H., Hanano, Y., Ishihara, A., 2004. Hilly-Land Soil Loss Equation (HSLE) for Evaluation of Soil Erosion Caused by the Abandonment of Agricultural Practices. Japan Agricultural Research Quarterly: JARQ 38, 21–29. URL: https://www.jstage.jst.go.jp/article/jarq/38/1/38_21/_article, doi:10.6090/jarq.38.21.

Chapter IV

Radiocesium and Sediment Transfers: Perspectives on Decontamination Timing

Chapter IV

Radiocesium and Sediment Transfers: Perspectives on Decontamination Timing

In the previous chapter, sediment and radiocesium transfer dynamics and fluxes were reconstructed by analysing sediment samples collected within a single catchment, including one sediment core collected in the downstream part of the Mano Dam reservoir and 101 lag deposits collected annually at ten sites across the upstream catchment. The investigation of this early decontaminated catchment allowed to investigate how the land uses changed following the Fukushima accident, including the abandonment of agricultural activities after evacuation, soil decontamination and the subsequent resumption of agricultural activities, to investigate how they impacted sediment and radiocesium transfers across river systems. The results highlighted the complex interplay between land-cover changes including decontamination, and sediment and particle-bound ^{137}Cs transfer processes in these post-accidental conditions. Nevertheless, these results emphasised the role of the spontaneous regrowth of vegetation after the abandonment of agricultural areas in reducing their connectivity to the river system and thereby limiting the particle-bound ^{137}Cs transfers.

In this chapter, the influence of decontamination timing on sediment and radiocesium transfer fluxes will be investigated by examining three sediment cores collected from the reservoir of three comparable mountainous catchments in the eastern part of Fukushima Prefecture, in terms of their environmental conditions. The Mano Dam and Ogaki Dam reservoirs were similar mixed agricultural/forested catchment until the FDNPP accident. The Yokokawa Dam reservoir catchment, in contrast, is a forested catchment that may be considered as representative of the 'pristine' conditions in this region. After the accident, the Mano Dam catchment was decontaminated between 2014 and 2016, while the Ogaki Dam catchment was not initially included in the decontamination programme. The decontamination of the Ogaki Dam catchment area was initiated in Spring in 2022, when the Japanese authorities started to reopen the Difficult-to-Return Zone in which it is located. A panel of physico-chemical analyses was conducted on a succession of 1-cm sediment layers collected from these cores, in addition to running high-resolution Energy-Dispersive X-ray Fluorescence (ED-XRF) core scanner analyses following 1 mm increments, as proposed in Chapter II.

The reconstruction of particle-bound ^{137}Cs transfers, together with the evolution of sediment source contributions demonstrated how the timing of decontamination, if any, affected ^{137}Cs and sediment transfers. The high-resolution ED-XRF core scanner analyses of the sediment cores allowed a finer identification of the sediment deposition sequences, and the comparison of the results with those obtained in Chapter II for the Mano Dam sediment core using a panel of analyses on discrete samples along the core. Overall, these results were confirmed by those obtained in the current chapter. However, attempts to calibrate the high-resolution ED-XRF measurements were not successful, and the implementation of an appropriate protocol to meet this goal was therefore discussed. Despite the contrasting management modes and distinct dominant land uses in the three catchments, the patterns of radiocesium transfers and source contributions were found to stabilise relatively quickly in the three catchments, mainly about 60 % of the sediment originating from topsoil sources and 40 % from subsoil sources, suggesting that stable sources contribute to the transfer of contaminated materials and have been fully addressed by the decontamination programme.

Radiocesium and sediment transfers after Fukushima accident: Perspective on decontamination timing based on lessons learnt from contrasted catchments

IV.1 - Introduction

The nuclear accident that occurred in March 2011 at the Fukushima Daiichi Nuclear Power Plant (FDNPP) resulted in the widespread release of a considerable amount of radionuclides into the environment, estimated to 520 PBq without considering noble gases (Steinhauser, 2014; Yamamoto, 2015), of which about 20 % deposited over the northeastern part of Honshū island, the main island of Japan (Morino et al., 2013; Onda et al., 2020). Among the emitted radionuclides, about 10 PBq of ^{137}Cs were emitted, of which about 2.7 PBq were deposited over inland Japan, mostly within the Fukushima Prefecture (74 %) (Kato et al., 2019; Taniguchi et al., 2019). About 83 % of the Prefecture area (i.e. 11,430 km^2) received at least 5 kBq m^{-2}, and 26 % (i.e. 3,520 km^2) received at least 100 kBq m^{-2} (Kato et al., 2019). The inhabitants living within a radius of 20-km around FDNPP (the so-called Evacuation Zone) and those who could be exposed to radioactive dose rates exceeding 20 mSv yr^{-1} in 2011 were evacuated. A total of 11 municipalities, with a population of about 80,000 people, covering an area of 1,150 km^2, were evacuated from a zone classified as Residence Restriction Area. In order to enable a rapid return of the population and the resumption of economic activities, the Japanese government initiated an unprecedented large-scale decontamination programme to remediate ^{137}Cs-contaminated soils (MoE, 2013; Evrard et al., 2019c). According to the decontamination programme published in December 2011 and based on locally measured ambient dose rates, these 11 evacuated municipalities were classified as Special Decontamination Zone (SDZ) or Difficult-to-Return Zone (DTRZ).

Once deposited onto the soil, ^{137}Cs binds strongly and quasi-permanently to fine soil particles (Sawhney, 1972; He and Walling, 1996) resulting in an accumulation of 90-99 % of ^{137}Cs concentrated in the uppermost 5 cm of undisturbed soils (Kato et al., 2012; Lepage et al., 2015), which justified the implementation of such a decontamination programme. In relation to the initial deposition levels, decontamination was implemented from 2012 in the SDZ. In the SDZ, the decontamination programme concentrated on farmland areas, urban areas and in forested zones located within a 20-m buffer area in residential settlements and along roads (MoE, 2015, 2018a, 2023). In farmland, the decontamination procedure depended on the initial ^{137}Cs activities in the soil. In soils with activities below 5 kBq kg^{-1}, inversion tillage was carried out down to a depth of 30-45 cm. In contrast, in farmland with higher activities, the following procedure was followed: (1) removal of the upper 5 cm of soil, (2) addition of granite saprolite from local quarries (55.5 m^3 per 1,000 m^2), referred to as "fresh soil", (3) restoration of soil fertility with amendments, either carbonate (as needed) and phosphorus silicate (about 0.8 t ha^{-1}) or zeolite amendments (about 0.5 t ha^{-1}), and (4) the mixing of the saprolite layer with the underlying soil layer with a double deep-ploughing (25-30 cm) . The 20-m forest buffer zone was decontaminated by removing litter and fallen organic material (leaves, branches) - referred to as "sediment" by the Japanese authorities - down to a depth of about 5 cm, without reaching the "mineral soil" layer. The forest was also cleared of underbrush and shrubs. In addition, conifers were pruned to a height of about 4 m from the ground when they were located within about 5 m of the forest edge, and the pruned branches were collected.

By March 2017, the decontamination of the SDZ area had been completed across a total surface of 180 km^2, representing 16 % of the SDZ area (1,150 km^2), of which 48 % of the decontaminated area were under farmland (about 87 km^2; MoE (2023, in Japanese)). Throughout the period from April 2014 to March 2020,

the evacuation order was gradually lifted in the 11 municipalities of the SDZ, as radioactive air dose rates decreased as a result of the progress of decontamination and physical decay (MoE, 2023). Indeed, the soil decontamination proved to be effective in reducing the radioactive air dose rates from 20 to 70 % compared to the initial situation in 2011 (MoE, 2018a; Onda et al., 2020). Conversely, the evacuation order was maintained after 2020 in the DTRZ, which was exposed to the highest radiocesium fallout and which was not initially targeted by decontamination. However, after a partial reopening of the DTRZ in Spring in 2022, the DTRZ was gradually reopened from 2023 without mandatory decontamination, except in "special reconstruction and revitalisation zones", which are mainly areas with residential settlements. Nevertheless, decontamination generated a large amount of waste by 2020, with 13.43 million m^3 of waste transported to interim storage facilities. This decontamination also resulted in significant costs: during the period from 2011 to 2020, 16 % of the total cost of recovery and reconstruction following the Great Tohoku Earthquake and FDNPP accident, amounting to JPY 6,122.3 billion, was spent on the "Nuclear Recovery Policy", including decontamination (Board of Audit of Japan, 2023).

Along with the progress of decontamination, a decrease in particle-bound ^{137}Cs activity in river sediments has been observed (Osawa et al., 2018; Konoplev et al., 2018). Various factors have been proposed to explain this reduction, including radioactive decay, reduced ^{137}Cs stocks due to repeated erosion events, progress of decontamination, and decreased erosion as a result of soil protection by the spontaneous vegetation regrowth (Evrard et al., 2016; Vandromme et al., 2023; Chalaux-Clergue et al., 2024c). The Fukushima region is annually affected by extreme erosive events, such as typhoons or tropical storms, which lead to intense rainfall and significant erosion (Laceby et al., 2016a). These events were identified as the main driver of sediment and particle-bound ^{137}Cs transfers across the region's river systems (Kitamura et al., 2016; Evrard et al., 2020). In addition, farmland was identified as the main source of contaminated sediment, which may be explained by its high connectivity to the river network due to its location in the valley bottoms and to the widespread occurrence of irrigation/drainage systems. However, these extreme erosive events mainly occur in summer and early in autumn - the period from July to October accounting for 73 % of the annual rainfall erosivity (Chapter III) - when vegetation cover is well established, which mitigates erosion intensity (Chartin et al. (2017); Chapter III). Accordingly, the contrasted decontamination approaches implemented between the SDZ and DTRZ likely impacted the transfer of particle-bound ^{137}Cs within the catchments (Chartin et al., 2017; Feng et al., 2022). For instance, in the Mano Dam reservoir catchment, the completion of decontamination led to a shift in sediment connectivity patterns as well as to significant sediment and particle-bound ^{137}Cs transfers between the abandonment and the post-decontamination periods (Chalaux-Clergue et al. (2024c); Chapter III).

In this study, three sediments core sampled in the downstream part of the Mano Dam, Ogaki Dam and Yokokawa Dam reservoirs were investigated. Both Mano Dam and Ogaki Dam reservoirs drain partly agricultural catchments while the Yokokawa Dam reservoir drains a fully forested catchment. Whilst the Mano Dam reservoir catchment, located in the SDZ, was decontaminated between 2014 and 2016, the Ogaki Dam reservoir catchment is located in the DTRZ and only started to be decontaminated from Spring 2022 onwards. These sediment cores were investigated to assess the timing of decontamination on the sediment and radiocesium transfers across the river systems. A combination of sediment core property analyses was used to (i) explore the potential of high-resolution ED-XRF core scanner data to reconstruct sediment deposition sequences and conduct sediment source fingerprinting, (ii) to compare the magnitude of the ^{137}Cs transfers between the catchments, (iii) to infer the temporal evolution of the sediment source contributions (i.e., topsoil and subsoil sources) in order to quantify and compare the origin of contaminated materials. The lessons learnt from the comparison of distinct timings of soil decontamination are then discussed to promote best

practices in landscape management, should other widespread pollution events similar to the FDNPP accident occur in the future.

IV.2 - Materials and Methods

IV.2.1 - Study sites

The Mano Dam (1.4 km^2), Ogaki Dam (0.5 km^2) and Yokokawa Dam (0.5 km^2) reservoirs are located in North-eastern Japan, in the Fukushima Prefecture (Tōhoku Region) (Fig. IV.1). The catchment areas drained by these three reservoirs correspond to the mountainous upper parts of the Mano River, the Ukedo River and the Ota River, respectively, covering surface areas of 67 km^2 (37.68887-37.76166 °N, 140.66671-140.84290 °E), 110 km^2 (37.49387-37.60376 °N, 140.68435-140.89478 °E), and 44 km^2 (37.54153-37.61876 °N, 140.80179-140.90556 °E). Their respective altitude ranges vary from 170-694 m, 167-1036 m and 147-721 m. These three catchments are typical of the eastern part of the Fukushima Prefecture mainly dominated by forested areas, covering 92, 86, and 99 % of the surface areas of Mano Dam, Ogaki Dam, and Yokokawa Dam reservoir catchments, respectively. In addition, farmland (i.e. cropland and paddy fields) and grassland represent 7 % of the Mano Dam (about 4 % farmland and 3 % grassland) and 11 % of Ogaki Dam (1 % farmland and 10 % grassland) catchment areas (2018-2020 period; JAXA (2022)). Conversely, the Yokokawa Dam catchment farmland and grassland cover a negligible proportion, both occupying about 0.2 % of the catchment area (0.08 and 0.09 km^2, respectively). These farmland areas, which are concentrated in the valley bottoms due to the overall steep topography, are highly connected to the river network due to their location and to the creation of irrigation systems. Built-up areas consist mainly of isolated houses or hamlets and cover a very small part of the catchment areas of about 1 % in all three catchments.

The region is located under a Dfa cold climate with no dry season and hot summers according to Köppen's climatic classification (Beck et al., 2018). The regional hydrological year runs from November to October (Laceby et al., 2016b; Whitaker et al., 2022). Over the last 30-years period (1991-2021), the mean annual temperature was 13.4 $\pm$ 0.5 °C yr^{-1} (standard deviation = SD), ranging on average from -1.5 $\pm$ 0.9 °C to 30.5 $\pm$ 2.1 °C in January and August, respectively. Annual precipitation amounted to 1207 $\pm$ 216 mm yr^{-1} (SD). Most of the precipitation occurs between June and October, corresponding to 60 % of the annual precipitation and 86 % of the rainfall erosivity (Laceby et al. (2016a); Chapter V). This period corresponds to the Japanese typhoon season, with a peak of intensity taking place from July to September in Fukushima Prefecture.

The two catchments of Yokokawa and Ogaki dams are almost entirely underlied by plutonic rocks, 95 % for Yokokawa (49 % granite, 28 % granodiorite 6 % diorite, 9 % felsic plutonic rocks and 2 % non-alkaline felsic volcanic rocks) and 93 % for Ogaki (19 % granite, 38 % granodiorite and 37 % felsic plutonic rocks) (Supplementary Materials Fig. IV.SM-2). The remaining part of these catchments is underlied by sedimentary rocks (in total $<$ 1 % and 3 % (2 % marine and non-marine sediments and 1 % fan sediments)) and, respectively, by schists (about 4 %) or mafic plutonic rocks (3 %). The lithology of the Mano Dam reservoir catchment is more diverse, with two main underlying rock types: plutonic (48 % in total, with 31 % granite and 17 % granodiorite) and non-alkaline mafic volcanic rocks (42 %), with some sedimentary rocks (9 % in total, with 7 % marine and non-marine sediments, $<$ 1 % terrace and $<$ 1 % fan deposits) and few schists (about 1 %). However, in the two agricultural catchments (i.e., Mano Dam and Ogaki Dam), most of the farmland is located

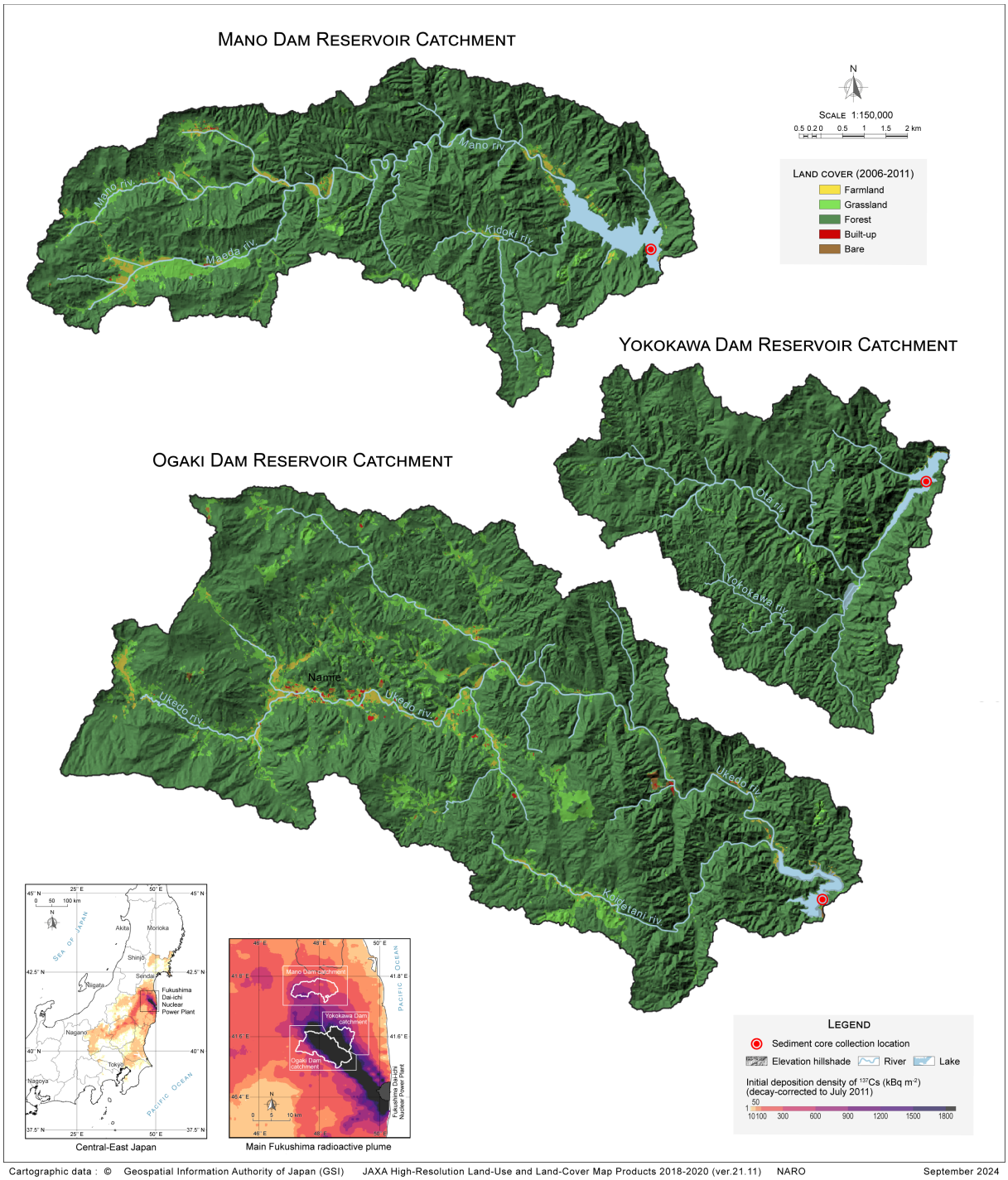


Figure IV.1: Main land uses over the 2006-2011 period in the (a) Mano Dam, (b) Ogaki Dam, and (c) Yokokawa Dam reservoir catchments. Cartographic data from the Geospatial Information Authority of Japan (GSI), and JAXA High-Resolution Land-Use and Lad-Cover Map Products 2006-2011 (ver. 16.09).

on plutonic rocks (44 % and 84 % respectively) or sedimentary rocks (39 % and 12 % respectively). This high proportion of farmland on sedimentary substrates comparatively to the proportion of sedimentary rocks found in the catchment (i.e. 9 % and 3 %, respectively) is mainly related to the topography, as both sedimentary rocks and farmland are located in the valley bottoms. In addition, in relation to its more diverse lithology, within the Mano Dam catchment, 47 % of the forest is located on plutonic rocks, 44 % on volcanic rocks and, to a lesser extent, 7 % on sedimentary rocks.

According to the Comprehensive Soil classification System of Japan (Obara et al. (2011, 2015), with the equivalence of soil types given according to the World Reference Base for Soil Resources (WRB)), in all three catchments, the main two soil types are Brown Forest Soils (WRB: Cambisols/Stagnosols; Mano Dam 38 %, Ogaki Dam 60 %, Yokokawa 95 %), and Allophanic Andosols (WRB: Silandic Andosols; Mano Dam 36 %, Ogaki Dam 19 %, Yokokawa 5 %) (Supplementary Materials Fig. IV.SM-1). In the Mano Dam reservoir catchment, the third and following main soil types are Cambic Red-Yellow Soils (WRB: Cambisols; 9 %), Lithosols (WRB: Leptosols; 9 %), Dystric Dark Red Soils (WRB: Alisols, Acrisols, or Cambisols ; 5 %), Gley Lowland Soils (WRB: Gleyic Fluvisols; 3 %) and Gray Lowland Soils (WRB: Gleuic Fluvisols; 1 %). In the Ogaki Dam reservoir, the third and following main soil types are Wet Andosols (WRB: Gleyic Silandic or Aluandic Andosols; 12 %), Cambic Red-Yellow Soils (6 %), while Brown Low Land Soils (WRB: Haplic Fluvisols), Terrestrial Regosols (WRB: Regosols, Leptosols, or Phaeozems) and Lithosols each represent about 1 % of the catchment area. In addition, the farmland of the Mano Dam and Ogaki Dam reservoir catchments are mainly located on the same soil types: Allophanic Andosols (46 and 35 %, respectively) and Brown Forest soils (25 % and 33 %, respectively), with some additional Gray Lowland soils in the Mano Dam catchment (10 %) and by Wet Andosols in the Ogaki Dam catchment (22 %).

All maps and geographical processing were performed using the QGIS software (ver. 3.34.8 - Prizren; QGIS Development Team (2024)).

IV.2.2 - Sampling and processing of sediment cores and potential sources

The sediment cores were sampled using a gravity corer in the downstream part of each reservoir, on 8 June 2021 in the Mano Dam reservoir (37.72167°N, 140.83056°E), on 22 August 2022 in the Yokokawa Dam reservoir (37.594222°N, 140.899528°E) and on 15 September 2022 in the Ogaki Dam reservoir (37.517564°N, 140.884347°E) (Fig. IV.1). The Mano Dam and Yokokawa Dam reservoirs were sampled by the National Institute of Environmental Studies (NIES, Japan) and the Ogaki Dam reservoir by the Japan Atomic Energy Agency (JAEA, Japan). The Mano Dam (IGSN: 10.58052/IETGC00WU), Ogaki Dam (IGSN: 10.58052/IEPAC009T), and Yokokawa Dam (IGSN: 10.58052/IEPAC009U) sediment cores were 38 cm, 16 cm, and 35 cm long, respectively, all with a diameter of 11 cm. The Mano Dam core was opened on 11 October 2021 at LSCE, and the Ogaki and Yokokawa cores were opened at the Institute of Environmental Radioactivity (IER, Fukushima University, Japan) on 23 January 2023. The cores were opened using a circular saw, and then carefully cut into two halves by inserting two thin PVC plates into them. All three sediment cores were sliced into 1 cm layers and dried at 40 °C for 48 to 96 h to ensure high-resolution data and sample collection, while the second half was stored at a temperature of 5 °C in a cold room to preserve its integrity for the subsequent non-destructive core scanner analyses presented in section IV.2.4.

A total of 85 soil samples were collected in areas representative of the main potential sediment sources across the landscapes draining into the three reservoirs during multiple previous field campaigns since 2011,

literature reviews, and stakeholder consultations (Evrard et al., 2015). A first part of the soil samples was collected in the upper part of the Mano and Niida Rivers catchments in the framework of the study conducted by Laceby et al. (2016b) in 2015 and included: 23 farmland, 21 forest and 10 subsoil (i.e. channel bank or landslide) samples, along with 10 "fresh soil" samples sampled in 2019. To complement this sample set with soil samples from the upper part of the Ukedo River catchment, 10 additional farmland, 5 forest, 1 subsoil and 5 "fresh soil" samples were also collected in this catchment in 2022. Soils were sampled with a plastic trowel and consisted of a composite of 10 sub-samples of topsoil (1-2 cm). All soil samples were dried at 40 °C for about 48 h and then sieved to 63 μm to isolate the fraction bearing most of the ^{137}Cs (i.e. silt and clay; Sakaguchi et al. (2015)) and to minimise the effect of grain size sorting during erosion, transport and deposition of particles during their transit across the catchments (Walling et al., 2000).

IV.2.3 - Laboratory analyses

A set of multiple properties was measured on soil and sediment samples: radiocesium activity by gamma spectrometry (^{134}Cs and ^{137}Cs), organic matter composition determined by the combustion method coupled with an isotope ratio mass spectrometer (i.e. total organic carbon (TOC), total nitrogen (TN), δ^{13}C stable isotope ratio), elemental geochemistry analysed by X-ray fluorescence (ED-XRF) for a set of 17 elements (i.e. Al, Ca, Co, Cr, Cu, Fe, K, Mg, Mn, Ni, Pb, Rb, Si, Sr, Ti, Zn and Zr). The bulk density of each sediment core layers was measured. All analytical methods and calculations are described in the Supplementary Materials sec. IV.6.1.

IV.2.4 - Energy Dispersive X-ray Fluorescence (ED-XRF) core scanner

Energy Dispersive X-ray fluorescence (ED-XRF) core scanning is a non-destructive technique used to obtain high-resolution elemental data from sediment cores. The sediment cores collected in all three investigated catchments were analysed with a high-resolution (0.1 cm) using two different ED-XRF core scanners, to obtain semi-quantitative values (counts per second, cps) of the elemental geochemistry contents along the sediment cores.

The Mano Dam core elemental geochemistry profiles were measured using the Avaatech XRF core scanner (Avaatech XRF Technology, 4th generation, Alkmaar, The Netherlands) with a rhodium anode available at the LSCE. Profiles were obtained at different tube voltage values. A first run was conducted at 10 kV for the measurement of Al, Si, S, Cl, K, Ca, Ti, Mn, and Fe. A second run at 30 kV was performed to measure Zn, Br, Sr, Rb, Zr and the Compton/Rayleigh scattering ratios (Mo inc:coh) (Richter et al., 2006). The Ogaki and Yokokawa cores were analysed with an ITRAX-XRF (COX analytical systems) core scanner available at the Center for Advanced Marine Core Research, Kōchi University (Japan). The ITRAX measurements were conducted using a molybdenum tube with acquisition parameters of 30 kV, 55 mA and an exposure time of 10 s.

The ED-XRF core scanner data from Mano dam were used to investigate whether the previously identified pattern of extreme events (Chapter II) can be observed at higher resolution. Here, we used two proxies: a terrigenous proxy represented by the Fe elemental profile from the core scanner XRF, and the Mo inc:coh, which serve as a reliable proxy for TOC. Following the rationale of the previous study, it is anticipated that this pattern will be present in the high-resolution XRF data from Mano Dam. Accordingly, this approach aims to determine whether the succession of event patterns observed in the Mano core can be identified at this finer resolution. If such patterns were confirmed, the methodology will be directly applied to the other sediment

cores from Yokokawa and Ogaki to identify the successions of events along those cores.

The raw ED-XRF data obtained on the Ogaki and Yokokawa cores from the ITRAX core scanner were processed using the 'itraxR' package (Bishop, 2024). This package offers a comprehensive suite of functions for managing and analysing ITRAX data, including tools to identify measurement errors. Several quality control procedures were applied to ensure the reliability of the elemental geochemistry data. First, data flagged as invalid by the ITRAX software were identified using the validity flags embedded in the dataset. These flags were consolidated into a single quality control variable to facilitate subsequent filtering (denoted "qc"). Second, the dataset was analysed for irregular patterns indicative of measurement artifacts. This included evaluating measurements where the optical configuration is out of position (validity), the mean square error (MSE) of the model fit for each element, correcting for surface slope effects (Croudace and Rothwell, 2015), and addressing anomalously high argon (Ar) counts, which can indicate the presence of air bubbles or other inconsistencies during the measurement process. To further refine data quality, low count rates were identified by calculating the mean and standard deviation of the counts per second (cps) for each element. Data points falling outside of a three-standard deviation threshold from the mean were flagged as potentially invalid. Anomalously high or low argon (Ar) counts were identified using a two-standard deviation threshold from the mean Ar count. Data points failing these quality checks were removed before further analysis.

Elemental concentrations were quantified from ED-XRF core scanner data using bivariate linear models to establish the relationship between core scanner peak areas and independently derived element concentrations obtained at a 1 cm resolution (as described in sec. IV.2.3). For Ogaki and Yokokawa cores, the 'itrax_reduce' function was employed to resample the core scanner data (0.1 cm) to match the resolution of the ED-XRF data (1 cm). The same methodology was applied to the Mano Dam data, although the calibration was performed manually. Linear models were then applied to evaluate the robustness of calibrating the ED-XRF core scanner data with the ED-XRF data. We specifically focused on calibrating aluminium (Al) and the Mo inc:coh ratios (used in this study as a proxy for total organic carbon (Chawchai et al., 2016)) to explore the potential of using high-resolution data for sediment tracing.

IV.2.5 - Initial deposition density of ^{137}Cs

To assess the amount of initially deposited ^{137}Cs within all three catchments, the initial deposition density of ^{137}Cs following the FDNPP accident was estimated from the reconstruction map of the accident-derived radiocesium fallout map proposed by Kato et al. (2019). In this work, Kato et al. (2019) reconstructed the radiocesium deposition densities (Bq m^{-2}) decay-corrected to July 2012 from the third and fifth airborne monitoring surveys conducted by the Japanese Ministry of Education, Culture, Sports, Science and Technology (MEXT). This reconstructed initial fallout point grid map was made public via the database website of the Center for Research in Isotopes of Environmental Dynamics (CRIED; University of Tsukuba, Japan) (www.ied.tsukuba.ac.jp/~ fukushimafallout/). From this point grid map, a ^{137}Cs fallout raster was generated. A total of 126 tiles (0.25×0.25 degree) were generated by inverse distance weighted (IDW) interpolation using the 'IDW interpolation tool' (distance coefficient P = 1.0; pixel size (x and y) = 0.0015 degree) from QGIS (ver. 3.34.8 - Prizren; QGIS Development Team (2024)). Tiles were then merged into a single tile using the 'merge raster' tool. The initial point grid footprint was manually delineated to define the spatial applicability zone of the airborne survey. A buffer zone corresponding to half plus 10% of the longest distance between two airborne points (x = 0.002, y = 0.003), i.e. 0.0017 degree (eq. about 53.2 m), was generated using the buffer tool. Finally, a single raster tile was cut according to the delineated footprint of the buffer zone using the 'clip a raster by mask layer' tool (CRS: EPSG:4326 - WGS 84). The final raster tile was reprojected

to the WGS 84 / UTM zone 54N (ESPG:32654) to better match with the investigated area using the 'Warp (Reproject)' tool, and forcing the output resolution cell size to 53.2 m by the q cubic (4×4 Kernel) resampling method. The initial deposition density of ^{137}Cs within all three catchments was determined using the 'zonal statistics' tool. The amount of initially deposited ^{137}Cs was determined by multiplying the 'Sum' with the cell surface (i.e. 2830.2 m^2).

IV.2.6 - Sediment source fingerprinting

A sediment source fingerprinting approach was developed to assess the evolution of sediment sources along all three sediment cores. Two potential sources were considered: topsoil, regrouping farmland (n = 33) and forest (n = 26) samples, and subsoil, corresponding to the so-called subsoil (n = 11) and "fresh soil" (n = 15) samples (Supplementary Materials Table IV.SM-II).Topsoil refers to the uppermost layer of the organo-mineral layer of soil that was sampled in forested areas and in farmland (i.e. cropland, paddy field, grassland) prior to decontamination. Subsoil refers to the underlying materials exposed along riverbanks or by deep gully or gully erosion under forested areas (Vandromme et al., 2023).

As shown in Chalaux-Clergue et al. (2024c), since the main underlying rock is plutonic, most of the subsoil and fresh soil are derived from the same parent material and both types of material were therefore not statistically distinguishable using the potential tracing properties investigated here (Supplementary Materials Table IV.SM-I). Therefore, care has been taken to adjust the interpretation of the subsoil contribution at the light of the progress of decontamination in the Mano Dam reservoir catchment.

IV.2.6.1 - Tracer selection

According to previous sediment source fingerprinting approaches that were conducted in these catchments, the organic matter content parameters TOC and TN and the elemental concentration of aluminium (Al) were identified as potential tracer properties (Laceby et al. (2016b); Huon et al. (2018); Chalaux-Clergue et al. (2024c); Chapter III). To ensure that these three properties could indeed be used as tracers, the three-step method tracer selection was followed (Collins et al., 2020; Chalaux-Clergue et al., 2024a). The conservative behaviour was evaluated with a range test, and source class discrimination was verified using a two-sample Kolmogov-Smirnov test (α = 0.01). The mean plus or minus one standard deviation (SD) of the log-transformed values was used as the range test criterion, later referred to as "mean $\pm$ SD". The property range of source classes was based on the highest and lowest mean plus or minus one standard deviation of the log-transformed values. Conservativity was assumed if all log-transformed values of the sediment samples were within the source range. The range test and the discriminant test were performed using the functions 'range.tests' and 'discriminant.test', respectively, from the package (Chalaux-Clergue and Bizeul, 2024, version 2.1.0).

IV.2.6.2 - Source contribution modeling

The Bayesian mixing model MixSIAR was used to predict relative source contributions (Stock and Semmens, 2016). The model was run using the MixSIAR package (Stock et al., 2020, version 3.1.12) and JAGS (Stock et al., 2022, version 4.3.1), using the process error formulation (Batista et al., 2022) and a long Markov Chain Monte Carlo chain length with default burn-in and thinning values (i.e. chain length = 300,000, burn-in = 200,000, thin = 100, chain = 3).

IV.2.6.3 - Modelling accuracy assessment

To assess the modelling prediction accuracy (Palazón et al., 2015; Batista et al., 2022; Chalaux-Clergue et al., 2024a), a total of 41 virtual mixtures were generated. The virtual mixture contributions were generated as a combination of the two potential sources (i.e. topsoil and subsoil), each varying from 0 to 100 % with 2.5 % increments and summing to 100 %, using the fingR::VM.builder function. The properties of the virtual mixtures were calculated as simple proportional mixtures of the potential source property signatures (i.e. mean and SD values) and the respective virtual source contributions.

Modelling prediction accuracy was assessed using several criteria: uncertainty (prediction interval width (W50)), residual bias (mean error (ME)) and model performance (root mean square error RMSE, squared Pearson correlation coefficient (r^2), Nash-Sutcliffe modeling efficiency coefficient (NSE) and continuous ranked probability score (CRPS)) (Batista et al., 2022; Chalaux-Clergue et al., 2024a). These statistics were calculated using fingR functions: 'eval.groups' (ME, RMSE, r^2, NSE), 'interval.width' (W50) and 'CRPS' (CRPS). To evaluate the transferability of the statistics from virtual mixtures to actual sediment mixtures, the predicted contributions of both types of mixtures were compared using ternary diagrams and Encompassed Sample Predictions values (ESP; Chalaux-Clergue et al. (2024c)). ESP ranges, expressed as percentages, represent the proportion of actual mixture predictions within the virtual mixture predictions range. Values near to 100 % indicate a higher transferability of the modelling prediction accuracy.

All processing, analyses and modelling were performed using the R programming environment (R Core Team, 2024, version 4.3.3) in RStudio (RStudio Team, 2023, version 2023.06.1.524).

IV.3 - Results

IV.3.1 - Initial deposition density and transfers of ^{137}Cs

From the reconstruction map of the FDNPP accident derived ^{137}Cs initial fallout map of Kato et al. (2019), the figure IV.2 was generated. On this map, the initial deposition densities and stocks of ^{137}Cs in all three catchments were calculated.

The initial deposition of ^{137}Cs after the FDNPP accident differed greatly between the three catchments of interest here (Table IV.I). The Mano Dam catchment had the lowest deposition density (median of $445 \cdot 10^3$ Bq m^{-2}), whereas the Ogaki and Yokokawa Dam catchments had higher but comparable deposition levels (median of 2557 and $2021 \cdot 10^3$ Bq m^{-2}, respectively). The larger catchment area of the Ogaki Dam reservoir (110 km^2) coupled with the higher deposition density in the vicinity of FDNPP resulted in a ^{137}Cs stock of $2.91 \cdot 10^{14}$ Bq, representing 10.8 % of the total initial deposition over inland Japan. In comparison, the smaller Yokokawa Dam catchment (44 km^2) had an initial ^{137}Cs stock of $8.69 \cdot 10^{13}$ Bq, or 3.2 % of the national total. Meanwhile, the Mano Dam catchment, although larger than the Yokokawa Dam catchment (67 km^2), accumulated a ^{137}Cs total stock of $3.32 \cdot 10^{13}$ Bq, which was about 8.8 times lower than that of the Ogaki Dam catchment and 2.9 times lower than that of the Yokokawa Dam catchment, accounting for 1.2 % of the total inland initial deposition.

In the previous study of the Mano Dam sediment core, in Chapter II, the 14−18 cm layer was associated with sediment transfers following Typhoon Roke in September 2011, the first major erosive event that took place

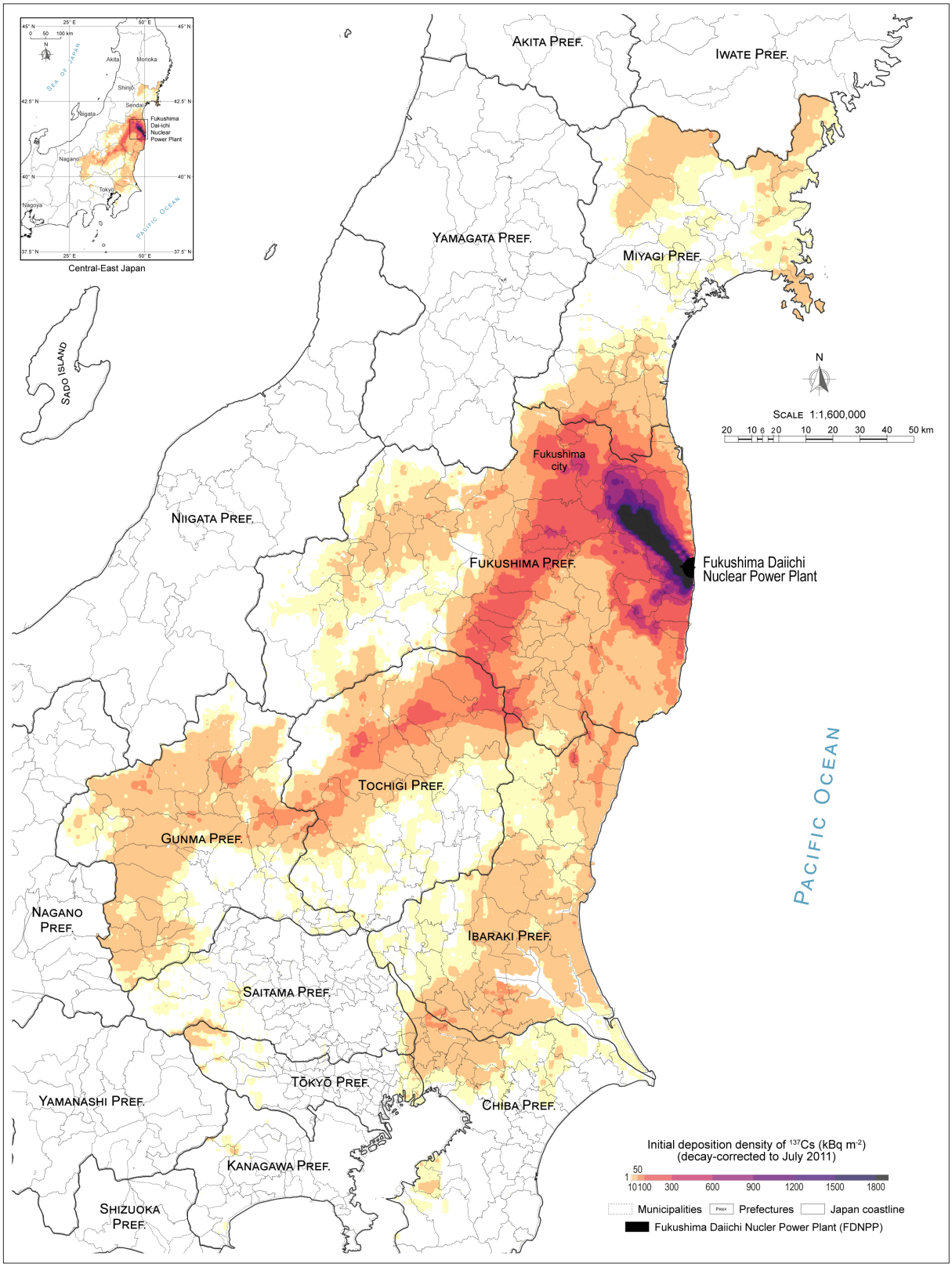


Figure IV.2: Rasterized map of the reconstructed initial ^{137}Cs fallout map (decay corrected to July 2011) after the Fukushima Daiichi Nuclear Power Plan (FDNPP) from Kato et al. (2019), with a minimum threshold of 1 kBq m^{-2}.
The map raster is available online at `https://zenodo.org/records/7827616` (Evrard et al., 2023)

Table IV.I: Summary of the initial deposition density and stock of ^{137}Cs following the Fukushima Daiichi Nuclear Power Plant (FDNPP) accident in March 2011 (decay-corrected to July 2011) within the Mano Dam, Ogaki Dam and Yokokawa Dam reservoir catchments. In addition, the catchment stock is compared to the initial deposition of $2.7 \cdot 10^{15}$ Bq on the terrestrial surface of Japan (in %). Note: These statistics were computed using the "zonal statistics" tool in QGIS [ver. 3.34.8] on the map presented in Supplementary Materials Fig. IV.2 and available online at (Evrard et al., 2023).

Catchment	River	Area (km^2)	Initial ^{137}Cs deposition						
			Density (10^3 Bq m^{-2})					Stock	
			Minimum	Maximum	Median	Mean	SD	(Bq)	(%)
Mano Dam	Mano	67	79	1184	445	501	225	$3.32 \cdot 10^{13}$	1.2
Ogaki Dam	Ukedo	110	244	6156	2577	2635	1463	$2.91 \cdot 10^{14}$	10.8
Yokokawa Dam	Ota	44	511	4467	2021	1987	766	$8.69 \cdot 10^{13}$	3.2

after FDNPP, with ^{137}Cs activity concentrations reaching about 50 kBq kg^{-1}. Comparable peaks of ^{137}Cs were found in sediment cores from the Ogaki Dam (11−15 cm; about 167 kBq kg^{-1}) and Yokokawa Dam reservoirs (24−27 cm; about 20 kBq kg^{-1}) (Fig. IV.3). While both Mano and Ogaki dam cores showed decreasing ^{137}Cs activities above these peaks, a second, more pronounced peak of ^{137}Cs activity was also found in the Yokokawa dam core between 14 and 21 cm depths. In this core, two additional distinct peaks were identified at 17−21 cm (about 36 kBq kg^{-1}) and at 14−17 cm (about 31 kBq kg^{-1}) depths.

Above these peaks, all three sediment cores showed a gradual decrease in ^{137}Cs activities until a stable level was reached. In the Mano Dam core, ^{137}Cs activities stabilised at around 9 kBq kg^{-1} before decontamination (below 7 cm depth), and they then further decreased down to about 2 kBq kg^{-1} after decontamination (above 7 cm depth), representing 18 % and 2 % of the maximum ^{137}Cs activity concentration peak, respectively. The plateau values found in the Ogaki and Yokokawa cores were comparatively higher, accounting for 26 % (43 kBq kg^{-1}) and 33 % (12 kBq kg^{-1}) of their maximum ^{137}Cs peak, respectively (Fig. IV.3).

Moreover, the ^{137}Cs accumulation from the peak activity concentration layer to the top of the sediment cores showed differences between the sediment cores in terms of total accumulation and deposition rates. The Ogaki Dam core showed the highest ^{137}Cs cumulative deposition, amounting to 4150 kBq m^{-2} for 15 cm of deposited sediment. The Yokokawa Dam core accumulated about 1760 kBq m^{-2} over 27 cm, about 2.4 times less than the Ogaki Dam core, while the Mano Dam core accumulated 930 kBq m^{-2} over 18 cm, which was bout 4.5 times less. This was associated with higher deposition rates in the Ogaki Dam core (277 kBq cm^{-1}) compared to the similar rates observed in the Mano and Yokokawa sediment cores, with 65 kBq cm^{-1} and 52 kBq cm^{-1}, respectively. However, when the uppermost sediment layer associated with decontamination in the Mano Dam core (above 7 cm; Chalaux-Clergue et al. (2024c)) is no longer taken into account, the resulting deposition rate increased to 763 kBq cm^{-1} (840 kBq m^{-2} over 11 cm). Nevertheless, when assessing the efficiency of ^{137}Cs transfer relative to the initial catchment deposition, the Mano Dam catchment showed a higher transfer rate ($2.9 \cdot 10^{-8}$), which is about two-fold higher than that of the Ogaki Dam catchment ($1.4 \cdot 10^{-8}$) and 1.4 times greater than that of the Yokokawa Dam catchment ($2.0 \cdot 10^{-8}$).

IV.3.2 - Evolution of properties along the sediment cores

IV.3.2.1 - Validity and comparison of ED-XRF core scanner data with ED-XRF concentration data

The approach used to identify invalid values during core scanner measurements revealed several depth intervals in which the data was flagged as invalid (Supplementary Materials Fig. IV.SM-3). For the Ogaki Dam core, these intervals include isolated measurements at 0.0, 1.5, 2.2, 3.6, 3.8, 4.3, 4.8, 7.8, 8.4, 9.1, 10.7, 11.6, and 12.3 cm depths, as well as a larger interval between 14.8 cm and 15.2 cm, which corresponds to the bottom of the sediment core. For the Yokokawa sediment core, the flagged intervals include isolated depths at 0.0, 4.0, 7.0, 9.0, 5.2, 6.4, 19.0, 19.8, 25.3, 26.0, 31.5, 32.2 and 32.8 cm depths, along with larger intervals from 20.5 to 20.9 cm, 21.3 to 21.4 cm and 32.5 to 32.6 cm. Data from these intervals was excluded from further analysis as a consequence of the failure to meet validity thresholds across one or more criteria.

Insufficient correlation coefficients were found between the ED-XRF core scanner count numbers and ED-XRF concentration data for most of the elements analysed, including those of particular interest in this study (Al, TOC) (Supplementary Materials Fig. IV.SM-4). Consequently, calibration of the ED-XRF core scanner data could not be performed, preventing the evaluation of the potential of high-resolution sediment fingerprinting approaches.

IV.3.2.2 - High-resolution proxy-based event identification

A comparative analysis of the stratigraphic succession of events within the Mano Dam core, using both the event identification methodology described in Chapter II, and that presented in this chapter using Fe and Mo inc : Mo coh proxies showed a strong concordance. As illustrated in (Fig. IV.3), several events were identified using these two proxies, which generally show an inverse relationship along the sediment core. Millimetre-scale fluctuations were observed within the same event (i.e., slight peaks of one proxy or the other). However, these variations did not prevent both approaches from providing similar information. For example, the pattern described in Chapter II for Typhoon Lan (3–7 cm depth) shows increasing values of the Mo inc : Mo coh ratios at the base of the event, gradually decreasing, while the Fe proxy conversely increases, reflecting the granulometric sorting occurring during sedimentation processes. This pattern is also clearly observed for Typhoon Etau-Kilo (9–11 cm), Typhoons Phanfone & Vongfong (11–14 cm), and between 18–21 cm. In contrast, no significant variations in the two proxies were observed in the sediment layer associated with the ^{137}Cs peak (18–14 cm). Interestingly, both Mo inc : Mo coh ratios and TOC measurements followed the same pattern. Consequently, these two proxies were used to identify the successions of events to investigate the sedimentary dynamics and ^{137}Cs transfers in the three investigated catchments.

For the Ogaki Dam core, Fe peak area increased from the base of the sequence (14.8 cm) to reach a first peak at 14.5 cm, which coincides with the depth where the ^{137}Cs peak was observed (Fig. IV.3). Interestingly, an increase of the Mo inc : Mo coh ratio was also observed over this interval, with a first peak observed around 13.0 cm. The Fe peak area slightly fluctuated up to 13.5 cm before reaching a second, more pronounced peak at 12.5 cm depth, where the highest Fe peak area in the sequence was measured. From this depth to the top of the sediment core, at least six events were characterized based on the previously established pattern from Mano Dam data (Chapter II). These events were observed at depths of approximately 11.0–12.5, 9.5–11.0, 8.0–8.0,

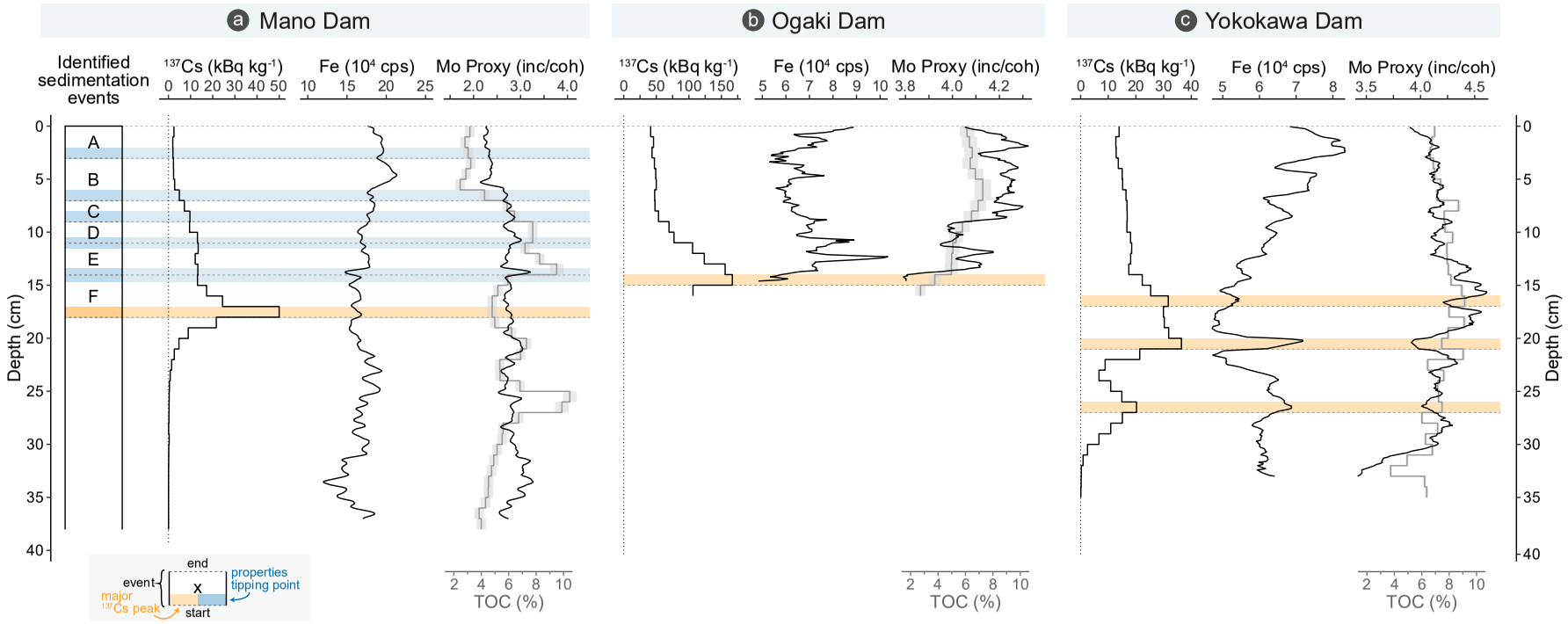


Figure IV.3: Evolution of analysed properties along the (a) Mano Dam, (b) Ogaki Dam, and (c) Yokokawa Dam sediment cores, from left to right: previously identified extreme precipitation events in the Mano Dam sediment core in Chalaux-Clergue et al. (2024c), ^{137}Cs activity and ED-XRF terrigenous proxy represented by the Al and Fe elemental profile, the Compton/Rayleigh scattering ratios (Mo inc:coh), the Al elemental geochemistry measured by quantitative ED-XRF, total organic carbon (TOC) content analysed by EA-IRMS (light grey) (measurement uncertainties are displayed as a grey ribbon). 'cps' stands for count-per-second.

7.0–8.0, 4.5–7.0, and 2.5–4.5 cm. A final event was recorded before sampling in July 2022, extending from 2.5 cm to the surface of the Ogaki sediment core. Furthermore, the TOC profile exhibited a similar trend as the Mo inc:coh ratio along the profile, despite higher fluctuations in the latter.

For Yokokawa Dam, the Fe cps profile (Fig. IV.3) displayed distinct variations in peak area with depth. A first peak was observed at approximately 26.0−27.0 cm, corresponding to the depth where the first ^{137}Cs peak activity was observed in the core. The peak area showed an overall downward trend toward approximately 21 cm, with a slight increase observed between 23.0 and 24.0 cm. Then, a significant increase in Fe peak area is found between 20.0 and 21.0 cm depth, followed by a similarly pronounced decrease in the signal towards 19.0 cm. Importantly, this second Fe peak area corresponds to the depth where the maximum ^{137}Cs peak activity was observed. From 19.0 cm depth onward, the Fe peak area fluctuates, with an overall increasing trend toward 2.5 cm, where a series of peaks are observed at 17.0−18.0, 12.0, 10.0, 8.5, 5.0, and 2.5 cm depths. As observed in the Mano and Ogaki sediment cores, the Fe and Mo inc:coh proxies showed an inverse relationship along the sediment core. On the opposite, the TOC profile and the Mo inc:coh ratio showed distinct trends with depth.

IV.3.3 - Sediment source fingerprinting

IV.3.3.1 - Origin of organic matter

Topsoil and subsoil δ^{13}C mean values were similar (*p* value $>$ 0.1; Supplementary Materials Table IV.SM-I), with -25.7 $\pm$ 1.6 ‰ (SD) and -25.2 $\pm$ 1.5 ‰, respectively (Fig. IV.4 and Supplementary Materials Table IV.SM-II). Nevertheless, topsoil showed a slightly greater variability than subsoil for this property, ranging from -29.9 ‰ to -20.3 $\pm$ 0.1 ‰ against a range varying from -27.5 ‰ to -22.0 $\pm$ 0.1 ‰ for subsoil (Fig. IV.4). Conversely, the TOC/TN values differed significantly between both sources (*p* value $<$ 0.001), with the TOC/TN values of topsoil being significantly higher than those of subsoil (13.4 $\pm$ 2.5 and 9.9 $\pm$ 3.0, respectively).

The δ^{13}C and TOC/TN values of the sediment cores differed between the reservoirs (Fig. IV.4). The Ogaki and Yokokawa Dam reservoir sediment core samples had similar δ^{13}C values, -27.3 $\pm$ 0.4 ‰ and -27.9 $\pm$ 0.3 ‰, respectively, while Yokokawa samples had higher TOC/TN values (13.0 $\pm$ 0.9 and 11.0 $\pm$ 1.1, respectively) (Supplementary Materials Table IV.SM-II). Regarding the Mano Dam sediment core, although its TOC/TN values covered the range observed in the other two sediment cores, its δ^{13}C values were significantly lower (-25.8 $\pm$ 0.9 ‰). Nonetheless, apart from the 15-16 cm layer of the Ogaki Dam sediment core which showed a very low TOC/TN value of 8.5, all the sediment core samples displayed δ^{13}C and TOC/TN signatures plotting within the range of typical organic inputs from C_3 terrestrial plants (Lamb et al., 2006; Amorim et al., 2022).

IV.3.3.2 - Tracer selection

The three properties, TOC, TN, and Al, were identified as showing a conservative behaviour for all three sediment core samples (n = 89) according to the range test using the mean $\pm$ SD criterion. Furthermore, they were shown to provide a very strong discrimination between topsoil and subsoil (*p* value $<$ 0.001) (Supplementary Materials Table IV.SM-I). The sediment source fingerprinting modelling was therefore run using these three tracers.

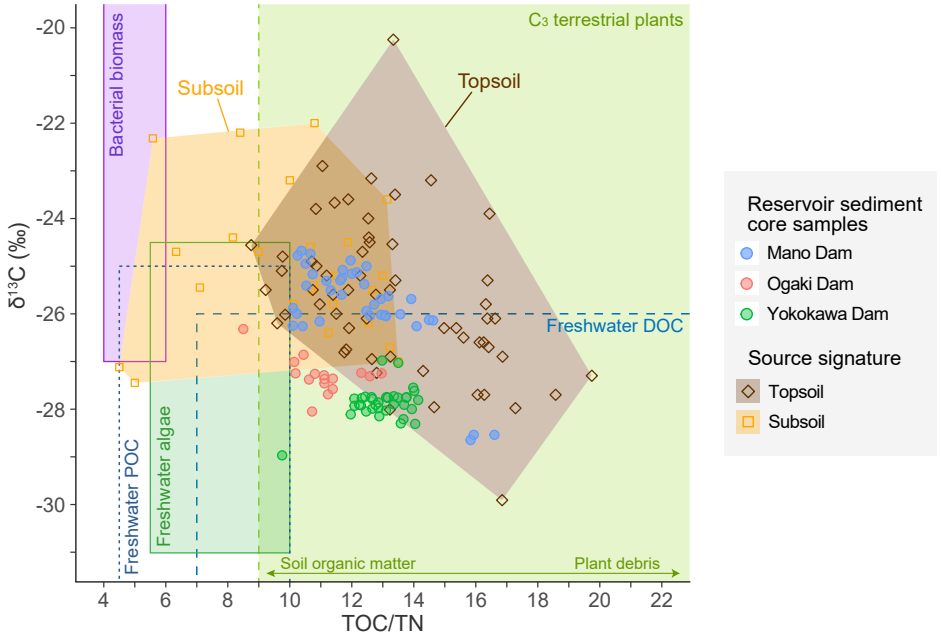


Figure IV.4: Signatures of δ^{13}C and TOC/TN in potential sources and in Mano (blue dot), Ogaki (pink dot) and Yokokawa (Green dot) Dam reservoir sediment core samples along with typical ranges for organic inputs to clay-sized dominant terrestrial environments (according to Lamb et al. (2006) and Amorim et al. (2022)). TOC stands for total organic carbon; TN for total nitrogen; POC for particulate organic matter; DOC for dissolved organic matter.

IV.3.3.3 - Sediment source fingerprinting modelling accuracy

The modelling accuracy metrics calculated for the MixSIAR model using 41 virtual mixtures demonstrated a high predictive capacity (Supplementary Materials Table IV.SM-III). For both sources, MixSIAR displayed a very high linearity between theoretical and modelled contributions (r^2 = 0.94). Although the predictive capacity and accuracy of the model outputs were intermediate (NSE = 0.71, CRPS* = 9), the prediction accuracy was lower with a RMSE and W50 of both 16 %. In addition, while the topsoil was underpredicted (ME = -11 %) especially for contributions exceeding about 30 %, subsoils were, symmetrically, overpredicted (ME = 11 %) for those contributions below 70 % (Fig. IV.5.a and b).

However, when comparing the overlapping of the space of the virtual mixtures with that occupied by the actual sediment core samples, although 80 % of the actual sediment core samples remained within the range of virtual mixture predicted contributions, and slightly different results were obtained for the three sediment cores (Supplementary Materials Table IV.SM-III; Fig. IV.5). Indeed, most of the Ogaki Dam sediment core samples were found within this space (15 out of 16), while less samples from Mano Dam and Yokokawa Dam were found in this space (30 out of 38 and 26 out of 35, respectively) (Supplementary Materials Table IV.SM-III). Most of the sediment samples falling outside of the range were samples with high contributions of topsoil (70-85 %) and low contributions of subsoil (16-30 %) (Fig. IV.5 and Supplementary Materials Table IV.SM-IV). Despite these differences between the sediment cores, the transferability of the modelling accuracy metrics calculated using virtual mixtures model outputs to actual sediment samples was considered to be acceptable.

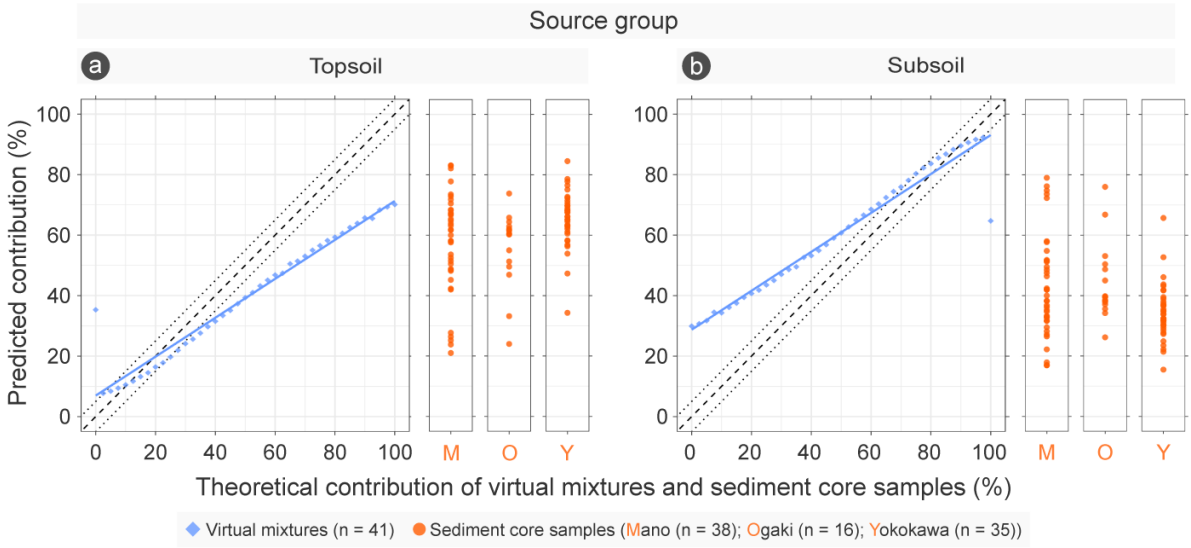


Figure IV.5: Relationship between theoretical and predicted contributions of the 41 virtual mixtures (blue diamond) for each source: (a) topsoil, and (b) subsoil, for the MixSIAR model (blue line) predictions obtained for each individual sediment core 1-cm layer samples predicted contributions (orange dot) collected in Mano Dam (n = 38), Ogaki Dam (n = 16) and Yokokawa Dam reservoirs (n = 35).

IV.3.3.4 - Evolution of sediment source contribution

While both reservoirs draining partly agricultural catchments (Mano and Ogaki Dam) showed variations in the relative contributions of topsoil and subsoil sources from the FDNPP peak layer to the top of the sediment core, the sediment core from the forested Yokokawa Dam reservoir showed more stable contributions all throughout these layers (Supplementary Materials Table IV.SM-IV). In the Mano and Ogaki Dam catchments, the sediment layers associated with the first peak of ^{137}Cs, i.e. the 14-18 cm and 11-15 cm layers, respectively, showed balanced relative contributions between topsoil and subsoil sources, with contributions of 52-48 $\pm$ 4% and 51-49 $\pm$ 17%, respectively. In contrast, in the Yokokawa Dam sediment core, the first ^{137}Cs peak (24-27 cm layer) corresponded to a predominance of topsoil, with 65 $\pm$ 1 % of topsoil sources and 36 $\pm$1 % of subsoil. In addition, although the topsoil quantitative contributions were similar in all three sediments cores (Mano: 24 $\pm$ 2 g cm^{-3}; Ogaki: 19 $\pm$ 6 g cm^{-3}; Yokokawa: 22 $\pm$ 2 g cm^{-3}), the quantitative contribution of subsoil was lower in the Yokokawa sediment core (12 $\pm$ 0 g cm^{-3}) compared to those found in the Mano and Ogaki sediment cores, which were similar, 23 $\pm$ 2 g cm^{-3} and 18 $\pm$ 8 g cm^{-3}, respectively. Above the FDNPP peak layers, apart from the 0-7 cm layer in the Mano Dam core, topsoil relative contributions became dominant in both the Mano and Ogaki Dam sediment cores (64 and 61 %, respectively), although remaining rather similar to the quantitative levels observed previously (28 $\pm$ 4 and 15 $\pm$ 3 g cm^{-3}, respectively). However, in the Mano and Ogaki Dam sediment cores, the relative decrease of subsoil contributions (39 $\pm$ 4 % and 31 $\pm$ 6 %, respectively) was associated with a decrease in quantitative contributions (16 $\pm$ 6 and 10 $\pm$ 3 g cm^{-3}). Conversely, in the Yokokawa Dam sediment core, the topsoil and subsoil contributions remained stable (69-31 % - 22 $\pm$ 3-10 $\pm$ 3 g cm^{-3}). In the Mano Dam sediment core, the 0-7 cm layer was marked by a significant increase in both the relative and quantitative contributions of subsoil (67 $\pm$ 15 % and 44 $\pm$ 16 g cm^{-3}), although it was not associated with a decrease in the quantitative contribution of topsoil (20 $\pm$ 6 g cm^{-3}).

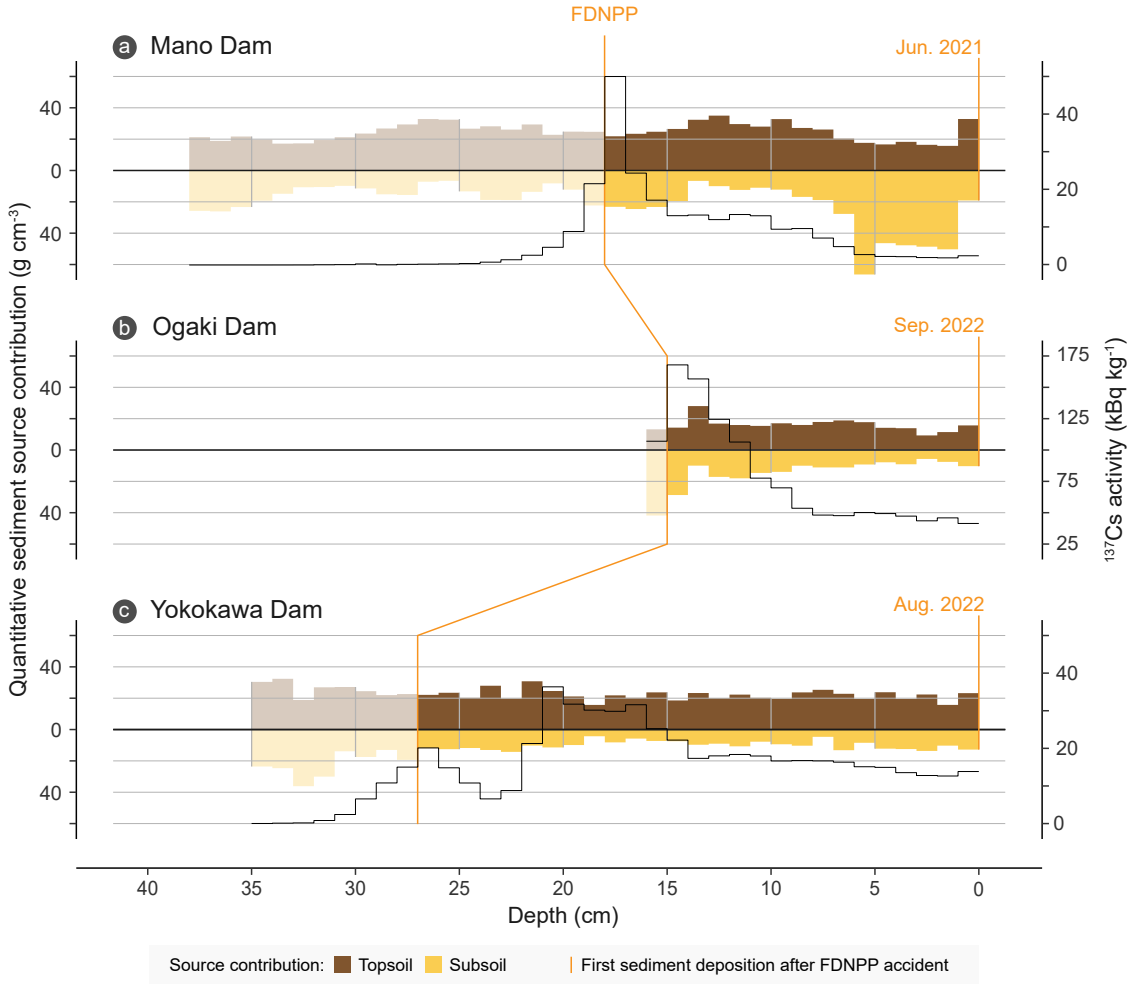


Figure IV.6: Evolution of the quantitative source contributions between topsoil and subsoil sedimentary sources (in g cm^{-3}) and radiocesium activity (in Bq kg^{-1}) along the sediment core collected in the downstream part of reservoir of the (a) Mano Dam (June 2021), (b) Ogaki Dam (September 2022) and (c) Yokokawa Dam (August 2022). FDNPP stands for Fukushima Daiichi Nuclear Power Plant accident

IV.4 - Discussion

IV.4.1 - Challenges in combining ED-XRF core scanner analyses with sediment source fingerprinting techniques

One of the main objectives of this chapter was to explore the potential of high-resolution ED-XRF core scanner data for both sediment fingerprinting studies and for reconstructing the chronology of extreme erosion/sedimentation events since the FDNPP accident in Yokokawa and Ogaki sediment cores. As discussed in Chapter II, sediment core analyses conducted at a 1 cm resolution in depth may mask property fluctuations occurring at finer scales, potentially resulting in the overlapping of two distinct events within a single sediment layer. This overlap can smoothen the geochemical and physical properties measured in successive sediment layers, thereby affecting the accuracy of sediment fingerprinting results and the interpretations derived.

Nevertheless, calibrating high-resolution ED-XRF core scanner data for sediment source fingerprinting is associated with several challenges. Reducing the resolution of the core scanner data to match that of the 1 cm resolution "conventional" ED-XRF data was necessary to create linear models before calibration. However, a coarser property resolution was shown to mask finer-scale fluctuations in the peak area signals observed for the three sediment cores. As a consequence, the accurate calibration of the linear models was impossible, particularly for elemental concentrations in aluminium (Al), which was identified as one of the optimal tracing properties. The approach of analysing 1 cm bulk sediment layers failed to capture the full complexity of the geochemical variations with depth.

To overcome these calibration issues and fully exploit the capabilities of the ED-XRF core scanner data, an unconstrained cluster analysis can be employed. This approach identifies similar layers within the sediment cores by grouping measurements based on their similarity, allowing for determining an arbitrary number of clusters (Weltje et al., 2015; Bishop, 2024). This method effectively identifies recurring compositional units and may help in the selection of representative samples for conducting further analyses using techniques such as conventional ED-XRF, EA-IRMS, infrared spectroscopy (IR), or inductively coupled plasma mass spectrometry (ICP-MS). Such a targeted sampling strategy enables a more accurate selection of sediment layers, accounting for previously identified potential tracers, thereby enhancing calibration and potentially enabling the use of high-resolution ED-XRF core scanner data for sediment fingerprinting.

The application of proxies, including Fe and Mo inc./coh ratios, which were previously validated on the Mano Dam core, is readily applicable to the Yokokawa and Ogaki sediment core. This methodology establishes a robust framework for identifying sedimentary events recorded since the FDNPP accident, contributing to a more comprehensive understanding of sediment deposition dynamics in this area. Another approach to identify sedimentary events would be to apply constrained cluster analysis on this high-resolution data. This method would help to identify depositional units within the sedimentary sequence while ensuring that each sample remains in sequential order, thereby preventing the recurrence of units along the stratigraphy.

Despite the calibration challenges associated with this high-resolution data for sediment source fingerprinting, this data offers valuable insights into sedimentary processes. The finer resolution reveals millimetre-scale fluctuations that were previously undetected at the 1 cm resolution. Such fluctuations enhance the characterisation of sedimentation event sequence, particularly for those intra-annual and annual low-intensity events, along with extreme erosive events marked by increases in the peak area of the Mo incoherent/coherent and Fe ratios. Notably, while calibration challenges persist, the results and primary conclusions articulated in Chapter II for the Mano Dam core were fully confirmed by those of the current chapter. Furthermore, this approach

further improves our detailed understanding of processes and allows underlining the limitations associated with a 1 cm resolution analysis.

IV.4.2 - Evolution of sediment source contribution and ^{137}Cs transfers

The comparison of sediment cores collected from the Mano, Ogaki and Yokokawa Dam reservoirs revealed marked differences in ^{137}Cs accumulation patterns, transfer rates, and sediment source contributions. The initial ^{137}Cs deposition from the FDNPP accident varied significantly between the catchments, resulting in different levels of ^{137}Cs accumulation in the sediment cores. The Ogaki Dam catchment, which was located in the main part of the initial ^{137}Cs plume, showed the highest initial deposition ($2.91 \cdot 10^{14}$ Bq), representing a significant proportion of the total ^{137}Cs deposition over inland Japan (10.8 %). In contrast, the Mano Dam catchment showed the lowest deposition ($3.32 \cdot 10^{13}$ Bq; 1.2 %) most likely because it is located further away from FDNPP site and on the border of the main radioactivity plume. Interestingly, despite a high initial deposition density similar to that found in the Ogaki Dam catchment, the Yokokawa Dam catchment displayed a lower deposition stock ($8.69 \cdot 10^{13}$ Bq; 3.2 %), closer to that of Mano Dam catchment, which is likely explained by the smaller catchment area of 44 km^2.

In both sediment cores from the Mano and Ogaki dam reservoirs draining partly agricultural catchments, the ^{137}Cs profiles were similar, although the ^{137}Cs activity levels were about three times higher at the Ogaki site, which may be attributed to the initial radiocesium deposition pattern (Wakahara et al., 2014; Yoshimura et al., 2015). In both sediment cores, after a single radiocesium peak following the FDNPP accident, the ^{137}Cs activity gradually decreased, until rapidly reaching a stable level of about 9 kBq kg^{-1} and 43 kBq kg^{-1}, respectively. This gradual decrease in ^{137}Cs activities was associated with an overall decrease in the topsoil contribution. This likely results from the initial significant export of contaminated sediment from farmland, which gradually decreased in response to the spontaneous regrowth of vegetation (Yoshimura et al., 2015; Chartin et al., 2017). Indeed, in cultivated farmland, during the first 3 years following FDNPP accident from 2011 to 2014, 15 % of the ^{137}Cs initially deposited over farmland was exported by run-off (Wakiyama et al., 2019). Furthermore, in the Mano Dam sediment core, the stable ^{137}Cs activity level was further reduced to about 2 kBq kg^{-1} after completion of decontamination (i.e. 2016; MoE (2023)). In the Mano Dam catchment, decontamination resulted in a significant increase in the subsoil contribution, related to the addition of 'fresh soil' having a subsoil signature (Chalaux-Clergue et al., 2024c), in decontaminated farmland, while the topsoil contribution remained stable (Evrard et al., 2019a; Feng et al., 2022). As suggested in Chalaux-Clergue et al. (2024c) (Chapter II), this decrease in the ^{137}Cs activity of sediment was likely related to the dilution effect of the high 'fresh soil' contributions rather than to a reduction of the available stock of contaminated sediment, since the ^{137}Cs depositional flux did not significantly change after decontamination. Concomitantly, forest contributions appeared to act as a stable source of contaminated sediment (Laceby et al., 2016b; Huon et al., 2018). In addition, in the Ogaki Dam sediment core, although a stable level of ^{137}Cs was rapidly reached, the total sediment deposition flux and ^{137}Cs level tended to gradually decrease in the most recently deposited layers.

The ^{137}Cs profile of the sediment core from the Yokokawa Dam reservoir differed from the other two sediment cores, displaying three ^{137}Cs peaks, at 26−27, 20−21 and 16−17 cm depths. The stable contribution patterns observed along the Yokokawa Dam sediment core suggest that these peaks were not associated with changes in sediment sources, but with other factors instead that may have impacted ^{137}Cs distribution in the catchment. In evergreen coniferous forests of the Fukushima Region, the initial deposition of ^{137}Cs occurred over the canopy, while it occurred directly onto the soil in deciduous forests (Hashimoto et al., 2012). In evergreen

coniferous forests, about 1.5 to 3 years after the initial fallout, the litterfall led to an increase of the ^{137}Cs inventory in the litter, which later moved to the uppermost mineral soil layer after the decomposition of the litter organic matter (Fujii et al., 2014; Kurihara et al., 2018; Takahashi et al., 2018). Between 2011 and 2015, the relative inventory of ^{137}Cs in the 0-2 cm of forest soil increased from 18 % to 48 % (Takahashi et al., 2018). Moreover, most of the ^{137}Cs remained in the upper soil given the very low migration rate in forest soils (Takahashi et al., 2018). While in deciduous forests most of the ^{137}Cs was deposited over the litter, it took about 5 years for the ^{137}Cs deposited over coniferous forest canopy to be gradually transferred to the soil surface by litterfall (Onda et al., 2020). In addition, due to the steep topography of the region, a part of the litter-associated ^{137}Cs was transported and accumulated in large amounts at the bottom of the hillslopes (Koarashi et al., 2014; Sakai et al., 2016). This gradual transfer and accumulation of the uppermost organic layer of soil, combined with the relatively low export of particulate ^{137}Cs from the forested catchments (Naulier et al., 2017), which was confirmed by the lower transfer efficiency in this environment ($2.0 \cdot 10^{-8}$) compared to the situation observed in decontaminated agricultural catchments ($2.9 \cdot 10^{-8}$), supports the fact that ^{137}Cs transfers in the Yokokawa catchment were mainly related to the occurrence of erosion events that transported contaminated organic matter rather than to a significant continuous erosion process. The absence of changes in source contributions in the layers associated with the peak of ^{137}Cs, and the higher ^{137}Cs activity of the second and third peaks (i.e. at 20−21 and 16−17 cm depths) compared to the first one, likely resulted from the gradual transfer of the canopy deposited ^{137}Cs to the soil layer. Chartin et al. (2013) observed a similar delay of about 2 to 3 years in the increase of ^{137}Cs activities in river sediment deposits collected across the Yokokawa Dam catchment, while high activities were directly observed in sediment deposits collected across the Mano Dam catchment. In Chalaux-Clergue et al. (2024c) (Chapter II), the next sedimentation events identified after Roke in 2011, were Phanfone & Vongfong in 2014, Etau-Kilo in 2015, and Chanthu & Lionrock in 2016. Therefore, the second and third peaks of ^{137}Cs, were likely associated with two of these intense erosive events that occurred between 2014 and 2016.

Furthermore, in 2019, typhoon Hagibis, followed by the extra tropical cyclone Bualoi, was the strongest erosive events recorded since the FDNPP accident, with a cumulative precipitation of 372 mm (Chalaux-Clergue et al., 2024c) (Chapter II) and a mean erosive energy of 2682 $\pm$ 2216 MJ mm ha^{-1} h^{-1} as recorded within a 110 km^2 radius around FDNPP (Chapter III). For events of this magnitude, Vandromme et al. (2023) modelled a significant sediment load resulting from rill and gully erosion processes in forests (i.e. subsoil material), and from topsoil in farmland or urban areas. This likely results in a decrease of the ^{137}Cs activity induced by the dilution of contaminated topsoil material with non-contaminated subsoil material. However, in none of the three sediment cores, Hagibis was associated with an increase in ^{137}Cs activities, in the sediment deposition nor in changes of source contributions patterns, whereas Etau was associated with such changes. This absence of a marked typhoon signature in the sediment cores - i.e., initial deposition of coarser organic-rich material followed by the gradual deposition of finer mineral particles (Huon et al., 2018; Chalaux-Clergue et al., 2024c) - despite the intensity of the event, may likely be attributed to other factors. In the Mano Dam catchment, according to Vandromme et al. (2023), during Hagibis, decontamination decreased the sediment ^{137}Cs activity from a theoretical value of 7500 Bq kg^{-1} without decontamination, to 2500-5000 Bq kg^{-1} after this process (modelled and measured activities, respectively). This was close to what has been observed in the Mano Dam sediment core, with about 9000 Bq kg^{-1} before decontamination and about 3000 Bq kg^{-1} after decontamination and during Hagibis. Conversely, in the not-decontaminated Ogaki Dam catchment and in the forested catchment of Yokokawa Dam, no decrease of ^{137}Cs activity was observed, which was consistent with the modelling of Vandromme et al. (2023) in the absence of decontamination. However, the management of the reservoir water levels to preserve the integrity of the dam during such intense rainfall

events also likely played a role in the potential trapping of sediment within the reservoirs and may therefore have modified the signature of Hagibis deposits, which limits the reconstruction potential of the transfers that took place during the event (Evrard et al., 2019b; Chalaux-Clergue et al., 2024c).

IV.4.3 - Perspectives on decontamination timing and management implications

Nonetheless, although the management of these three catchments after the FDNPP accident differed, with a decontaminated agricultural catchment (Mano Dam), a long abandoned agricultural catchment (Ogaki Dam), and an abandoned forested catchment (Yokokawa Dam), the ^{137}Cs activity of sediment deposits stabilised rather rapidly in all three sediment cores. However, the different ^{137}Cs activity levels observed in the three dams can be attributed to the initial radiocesium deposition pattern, which was particularly heterogeneous (Wakahara et al., 2014; Yoshimura et al., 2015).

In both agricultural catchments, the gradual increase in soil protection by the spontaneous vegetation regrowth after their abandonment effectively reduced sediment and ^{137}Cs transfers to the river systems (Evrard et al., 2016; Chartin et al., 2017; Vandromme et al., 2023). In the Mano Dam catchment, however, the decontamination was associated with a decrease in sediment ^{137}Cs activity without a reduction in ^{137}Cs deposition fluxes, suggesting a dilution effect caused by the addition of 'fresh soil' in farmland (Evrard et al., 2019a; Feng et al., 2022; Chalaux-Clergue et al., 2024c). In contrast, in the Ogaki Dam catchment, which remained abandoned for a longer period, the protective role of the vegetation cover persisted and even slightly increased over time, with decreasing sediment deposition fluxes. Despite different decontamination management modes, both catchments reached a stable pattern of ^{137}Cs levels and stable source contributions within a few years, suggesting that a stable contaminated source contributions regime of ^{137}Cs-contaminated sediment continued to supply material to the river systems, a process that soil decontamination did not fully modify.

In the forested catchment of the Yokokawa Dam reservoir, the initial ^{137}Cs deposition over the litter of broadleaf trees and over the canopy of the evergreen coniferous trees was associated with a delayed and larger secondary transfer of ^{137}Cs through erosion several years after the FDNPP accident, in relation to the litterfall dynamics of these forests. Similarly, in Chapter III, we showed that one to three years after the FDNPP accident, a delayed increase of ^{137}Cs activity in river lag deposits along an increase of forest contribution were observed at several upstream sites, draining mainly forested areas, across the Mano Dam catchment. This delayed transfer pattern leads to significant challenges for the effective contamination management in forested areas. As suggested by Thiry et al. (2018) and Koarashi et al. (2020), decontamination of forests should be initiated within 1 to 5 years after the accident to align with the foliar cycle, thereby maximising its effectiveness, which corroborates the observations made from the Yokokawa Dam sediment core analysis. The gradual release of radiocesium through litterfall suggests that immediate and repeated litter removal could reduce the transfer of radiocesium from the litter to the mineral soil layer (Ayabe et al., 2017; Koarashi et al., 2020). However, the removal of the litter could increase soil vulnerability to erosion and, subsequently, it could lead to an increase in radiocesium runoff (López-Vicente et al., 2018). In addition, the decontamination of the 20-m buffer zone around forests could reduce the role of litter in trapping contaminated sediment before it is exported from the forest, potentially increasing the risk of secondary contamination in nearby rivers (Gomi et al., 2002; Sakai et al., 2021). Moreover, the ecological consequences of litter removal, such as habitat disruption and altered soil carbon cycling, should be carefully considered before implementing such a measure (Sakai et al., 2021). Overall, effectiveness of forest decontamination will depend on its timing, on site-specific conditions, and on the continuous removal of new litterfall (Taira et al., 2020).

However, the decontamination programme primarily aimed at reducing ambient air dose rates to allow a rapid return of population and the resumption of agricultural activities. The decontamination programme has proven to be effective in reducing air dose rates by approximately 58 % in farmland, 56 % in urban areas, and 23 % in forests (MoE, 2018a), thereby allowing the theoretical resumption of agricultural activities. Nevertheless, by January 2018, the decontamination process was carried out over 16 % of the SDZ (180 km^2 of 1,150 km^2), involving large number of workers and producing 9 million m^3 of soil waste, at a cost of approximately JPY 1500 billion (about EUR 11 billion, with a 2017 conversion rate of EUR 1 = JPY 130) (MoE, 2018b). Although the decontamination allowed for the gradual lifting of all evacuation orders in the SDZ by April 2017, only about 30 % of the evacuated residents had returned by 2020 (Taira et al., 2020; Asanuma-Brice et al., 2023). Several factors contributed to this low return rate, including changes in living conditions (such as family separations and loss of community life), the lack of infrastructure, limited public services, diminished economic opportunities, transformed natural and urban landscapes, anxiety about radiation exposure, and restrictions on outdoor activities like hiking, freshwater fishing, and traditional plucking of wild vegetables (山菜 - 'sansai') and mushrooms in forests. In addition, for instance, in the Mano Dam catchment, decontaminating 16 % of the area resulted in just a 17 % reduction in ^{137}Cs fluxes, leaving 67 % of the original radiocesium stock beneath forested areas (Vandromme et al., 2023). These issues may raise questions regarding the appropriate character of conducting such a large-scale decontamination programme, through mobilizing significant investment, and generating a considerable quantity of waste for restoring a limited portion of the landscape in which only a minor percentage of the initial population decided to return. Nonetheless, the lessons learned from the ecological understanding of the transfers mechanisms of radiocesium across the landscape and ecosystems could form the basis of a more sustainable pollution management strategy based on natural processes.

IV.5 - Conclusions

The application of high-resolution ED-XRF core scanner analyses (1 mm) was found to provide a suitable technique to identify sedimentation events and reconstruct in more details the sedimentation sequence along lacustrine cores. In addition, it confirmed that the use of lower resolution sampling (1 cm) enabled to identify well the main erosive events, although not all events could systematically be identified. In addition, calibration challenges, however, limited the broader use of this method for conducting detailed quantitative sediment source fingerprinting. The relative and quantitative sediment source contributions could nevertheless be successfully reconstructed every 1 cm along the sediment cores.

Significant differences in the initial ^{137}Cs deposition fluxes were observed across the three reservoir catchments (Mano, Ogaki, and Yokokawa Dams), likely resulting from their geographical position relative to the FDNPP site and their exposition to initial radioactive fallout. The Ogaki Dam catchment, located within the main radiocesium plume, showed the highest initial ^{137}Cs deposition stock ($2.91 \cdot 10^{14}$ Bq), while the Mano Dam catchment, located the furthest away from the accident site, displayed the lowest deposition stock ($3.32 \cdot 10^{13}$ Bq). In both agricultural catchments (Mano and Ogaki Dams), ^{137}Cs activity levels in sediment cores stabilised rapidly after reaching an initial peak (about 9 kBq kg^{-1} and 43 kBq kg^{-1}, respectively), which is assumed to be linked to the spontaneous vegetation regrowth in abandoned farmland, which gradually and increasingly reduced soil erosion and radiocesium transfers to river systems. The decontamination of the Mano Dam catchment was associated with a significant increase in 'fresh soil' contribution (from 48 $\pm$ 4 % to 67 $\pm$ 15 %), along with a decrease in ^{137}Cs activity to about 2 kBq kg^{-1}, which may be attributed to the dilution of contamination due to high contributions of 'fresh soil' showing a subsoil signature. The core collected in the reservoir draining the Yokokawa Dam catchment, a forested catchment, exhibited multiple peaks of

^{137}Cs. These peaks were associated with the delayed transfer of radiocesium from the litter to the soil mineral layer along with the progressive transfer from the canopy of evergreen coniferous trees to the litter, leading to secondary erosion and radiocesium transfers to the river network. Despite the contrasted management and the distinct dominant land uses in the three investigated catchments, sediment and radiocesium dynamics rapidly stabilised, suggesting that stable sources contribute to the transfer of contaminated material, and they were not fully addressed by the decontamination programme. Therefore, the lessons learnt from FDNPP accident on sediment dynamics, control mechanisms and radiocesium transfers across ecosystems and landscapes could provide the basis for establishing more sustainable contamination management strategies, as a more balanced approach between intervention and natural stabilisation processes to mitigate contamination transfers over time.

Data availability

The rasterized initial deposition density of ^{137}Cs map (decay corrected to July 2011) is available online at https://zenodo.org/records/7827616 (Evrard et al., 2023). A single-band pseudo-colour scale was provided and displays radiocesium deposition densities above 1000 Bq m^{-2} (global background).

The dataset is available online at https://doi.org/10.5281/zenodo.14731789 (Chalaux-Clergue et al., 2024b).

Acknowledgements

The assistance provided by Dr. Hironoi Funaki and Dr. Kazuya Yoshimura from the Japan Atomic Energy Agency (JAEA) in conducting the sediment core sampling in the Mano Dam reservoir is gratefully acknowledged.

The collaboration and support of Nicolas Tenaud, student at the Laboratoire des Sciences du Climat et de l'Environnement (LSCE; Gif-sur-Yvette, France), in carrying out several analyses on the sediment cores and discussions of results are sincerely and greatly appreciated. The assistance of Prof. Masafumi Murayama and Takuya Matsuzaki for conducting ED-XRF Core scanner measurements at the Center for Advanced Marine Core Research, Kōchi University (Japan), and of Dr. Mercedes Mendez-Millan, research engineer at Institut de Recherche pour le Développement (IRD), in conducting the organic matter analysis at the Alyses platform (Bondy, France) is gratefully acknowledged.

IV.6 - Supplementary materials

IV.6.1 - Laboratory analysis methodology

IV.6.1.1 - Radiocesium analysis

Gamma spectrometry with a low-background coaxial HPGe detector was used to determined the ^{134}Cs and ^{137}Cs activities in the sediment samples. The counting times ranged from 3×10^4 to 8×10^4 s. The ^{137}Cs and ^{134}Cs activities were measured at the 605 keV and 662 keV emission peaks, respectively, errors reached about 5 % at 95 % confidence level. All measured counts were corrected for background levels which were, as detector and geometry efficiency, estimated at least every two months. Counting efficiency and quality assurance were implemented using certified International Atomic Energy Agency reference materials prepared in the same containers as the sample. Radiocesium activities were decay-corrected to the sampling date.

The ^{134}Cs and ^{137}Cs were also decay-corrected to 11 March 2011 and ^{134}Cs/^{137}Cs ratio were compared to the ratio 1.06 $\pm$ 0.04 (Kobayashi et al., 2013) to further confirm the FDNPP origin.

IV.6.1.2 - Organic Matter

According to Huon et al. (2018), sediments and soils in the Mano Dam reservoir catchment did not contain carbonate minerals and all carbon associated with particulate matter was organic in nature. It was assumed that this was also the case in the Ogaki and Yokokawa dam catchments, due to their highly similar geology and overall context. Total organic carbon (TOC, in %) and total nitrogen (TN, in %) elemental content and δ^{13}C isotope ratio (δ^{13}C expressed in ‰ against PDB) were determined for a part of the samples by a combustion method using a continuous flow elementary analyser (Elementar VarioPyro cube) coupled with an Isotope Ratio Mass Spectrometer (EA-IRMS) (Micromass Isoprime) at the Institute of Ecology and Environmental Sciences (iEES Paris) in France. A first analysis run was conducted to measure TOC concentration together with a set of tyrosine standards (Coplen et al., 1983). The second analysis run was dedicated to measure TN concentration after sample weight optimisation from TOC results. For combustion, oxygen was injected during 70 s (30 mL min^{-1}) at 850 °C for reduction and the combustion furnace at 1120 °C (Agnihotri et al., 2014). The analytical precision was assessed with repeated analyses of a tyrosine intern standard (n = 51), calibrated against international reference standards (Girardin and Mariotti, 1991). The analysis of these properties in source material is described in details in the study of Laceby et al. (2016b). The other part of the samples were analysed at the Alyses Platform (Bondy) in France, by a combustion method with an elemental analyser (Flash HT 2000) coupled to an isotope ratio mass spectrometer (Advantage Delta V) via a Conflow IV interface from Thermo Scientific. The EA-IRMS was calibrated against two standards : EMAP2 (TOC = 68.35 $\pm$ 0.28 %, TN = 7.46 $\pm$ 0.10 %, δ^{13}C = -28.19 ‰) and IAEA-CH3 (δ^{13}C = -24.72 ‰). Analytical precision and repeatability were assessed using the reference material HOS (TOC = 7.45 $\pm$ 0.14 %, TN = 0.52 $\pm$ 0.02 %, δ^{13}C = -28.85 ‰). To evaluate whether the samples are composed of terrestrial or freshwater-originating material, the distribution of sample values was plotted in a δ^{13}C versus TOC/TN diagram and compared to the thresholds reported in Lamb et al. (2006) and Amorim et al. (2022).

IV.6.1.3 - Elemental geochemistry

Elemental geochemistry was determined using Energy Dispersive X-ray fluorescence (ED-XRF) (Malvern Panalytical, ED-XRF Epsilon 4). A total of 17 elemental concentrations were measured (Al, Ca, Co, Cr, Cu,

Fe, K, Mg, Mn, Ni, Pb, Rb, Si, Sr, Ti, Zn, and Zr). Measurements were conducted in containers covered with a 3.6 μm thin Mylar film (Chemplex, Mylar Thin-Film cat. no. 157) with a 10 mm exposure surface. A minimum of 0.1 g of material was analysed. To consider the potential heterogeneity within a sample, two replicate measurements were made, and the mean value of these replicates was calculated. To assess the accuracy of the measurements, a standard (JMS-1, sediment from the Tokyo Bay (Terashima et al., 2002)) was measured every seven samples and the accuracy of the measured batch was determined based on the calculation of the Root Mean Square Errors (RMSE).

IV.6.1.4 - Bulk density

In the Mano Dam reservoir core, the bulk density (ρ_b) was determined on fresh sediment using a 1.7 cm^3 (V) acrylic cube. Before filling the cube, the emptyweight (g) was reported. Cubes were filled with fresh sediment using a metallic spatula, the humid weight (m_{humid} in g) was reported, then oven-dried at 110 °C for 96 h (Heraeus T12, Thermo Electron Corporation) and the dry weight (m_{dry} in g) was measured.

In the Ogaki and Yokokawa reservoir cores, bulk density was determined on fresh sediment by extracting the entire 1 cm layer (h). The extracted volume of sediment was equal to half the volume of a cylinder with a diameter of 11 cm (D), calculated as follows:

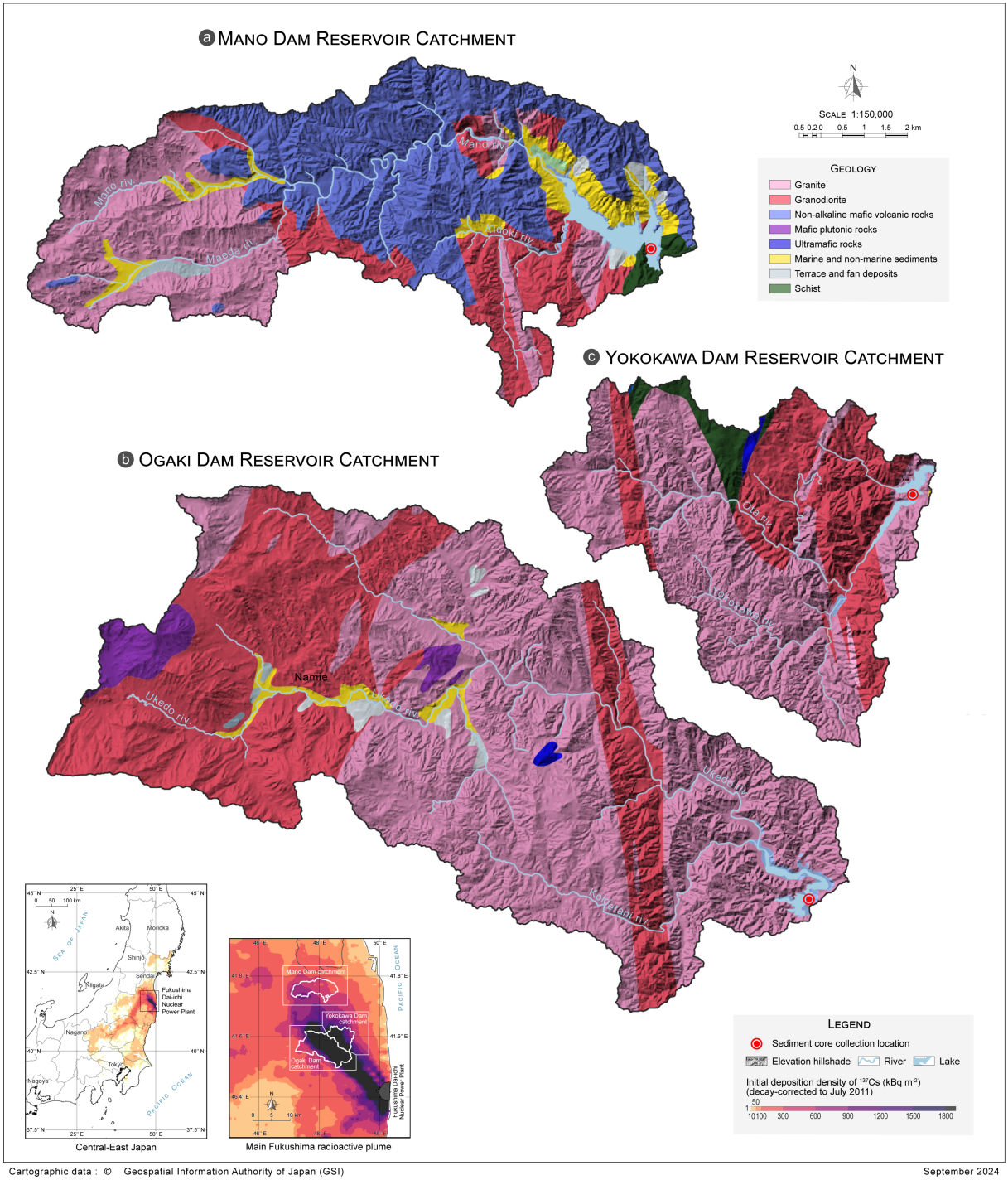
$$V = \frac{1}{2}\left(\pi \left(\frac{D}{2}\right)^2 h\right) = \frac{30.25}{2}\pi = 47.52 \text{ cm}^3 \quad \text{(IV.1)}$$

The 1 cm layer was extracted using a metal spatula and the humidweight was reported. It was then oven dried at 40 °C for 48 to 96 h and the dryweight was measured.

The bulk density (ρ_b in g cm^{-3}) is calculated as follows:

$$\rho_b = \frac{m_{dry}}{V} \quad \text{(IV.2)}$$

IV.6.2 - Figures



Cartographic data : © Geospatial Information Authority of Japan (GSI) September 2024

Figure IV.SM-1: Main geological substrate in the (a) Mano Dam, (b) Ogaki Dam, and (c) Yokokawa Dam reservoir catchments. Cartographic data from the Geospatial Information Authority of Japan (GSI).

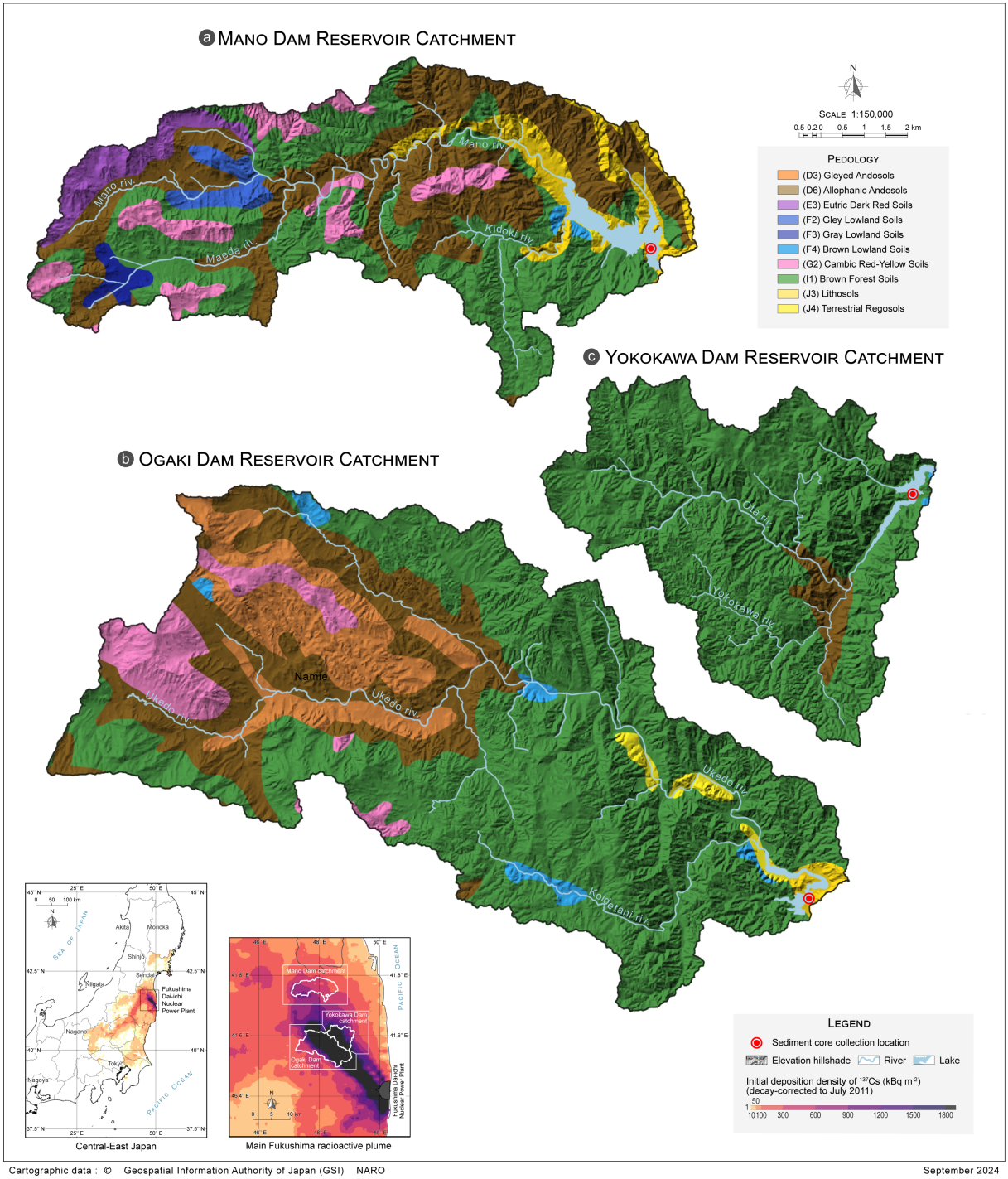


Figure IV.SM-2: Main soil types over the 2006-2011 period in the (a) Mano Dam, (b) Ogaki Dam, and (c) Yokokawa Dam reservoir catchments. Cartographic data from the Geospatial Information Authority of Japan (GSI), and NARO).

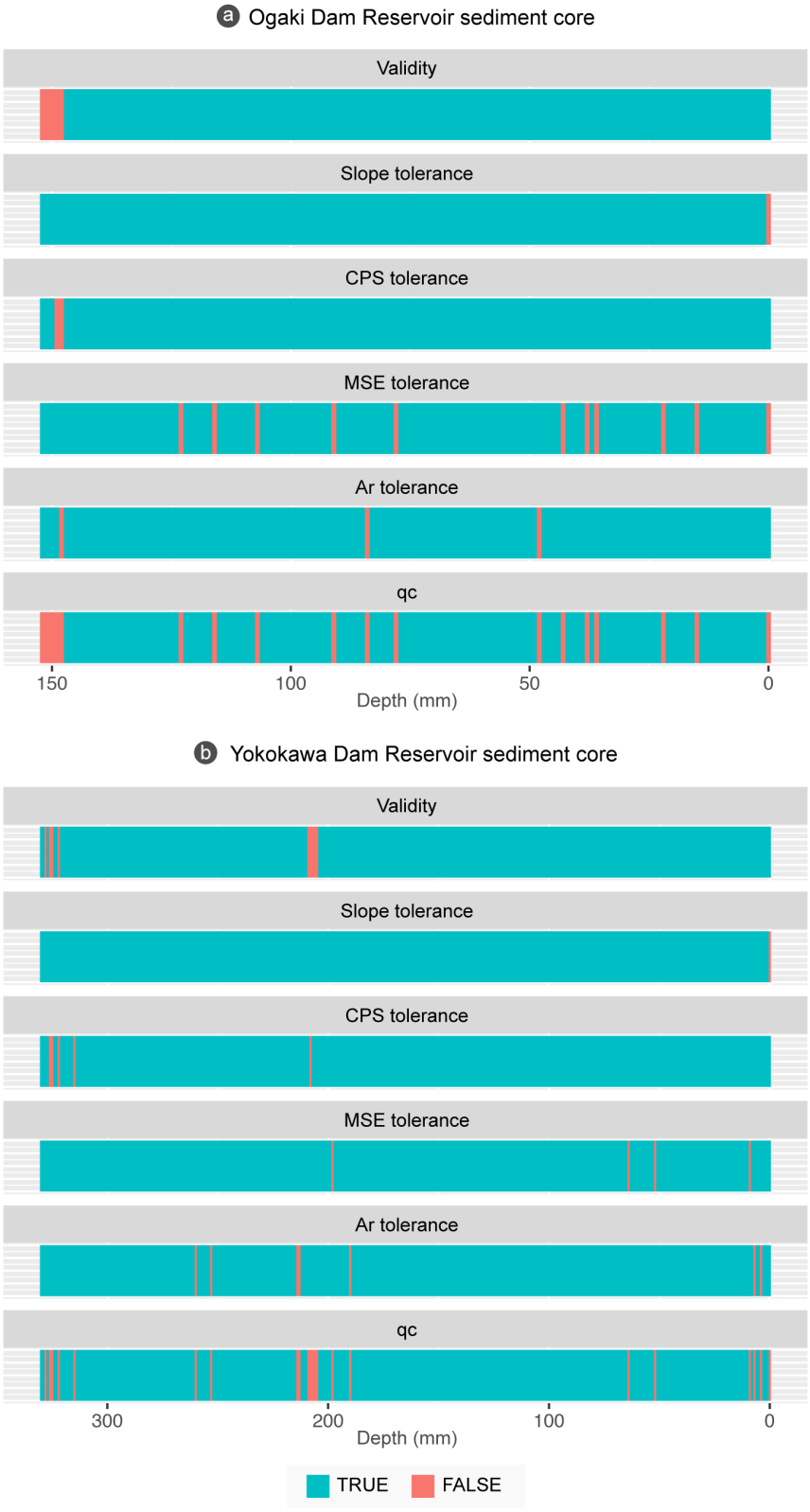


Figure IV.SM-3: Evaluation of the validity of the analyses realised by the Itrax Energy-Dispersive X-ray Fluorescence (ED-XRF) every 1 mm on the (a) Ogaki and (b) Yokokawa Dam reservoir sediment cores.

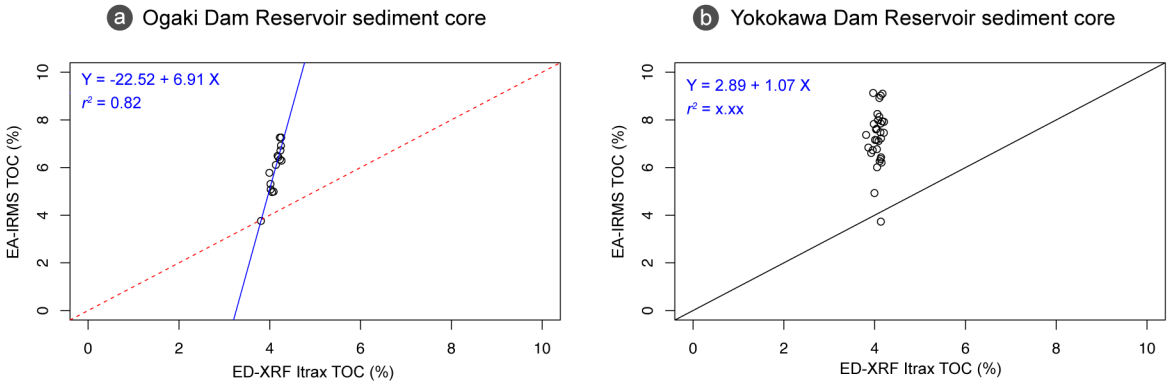


Figure IV.SM-4: Comparison of the calibrated total organic carbon (TOC) from Energy-Dispersive X-ray Fluorescence (ED-XRF) and EA-IRMS measured TOC on the sediment layer of the (a) Ogaki and (b) Yokokawa Dam reservoir sediment cores. r^2 stands for the Pearson squared correlation.

IV.6.3 - Tables

Table IV.SM-I: Kolmogorov-Smirnov two-samples tests for topsoil (n = 59) and subsoil (n = 24) groups and for reservoir sediment cores: Mano Dam (n = 38), Ogaki (n = 16), and Yokokawa Dam (n = 35), significance of the *p* value. "***" *p* value $\leq$ 0.001; "**" *p* value $\leq$ 0.01; "*" *p* value $\leq$ 0.05; "." *p* value $\leq$ 0.1; " " *p* value $>$ 0.1.

	TOC	**TN**	**TOC/TN**	δ^{13}**C**	**AI**
Topsoil - Subsoil	***	***	**	0.34	***
Mano - Ogaki	0.22	*	**	***	***
Mano - Yokokawa	***	***	***	***	***
Ogaki - Yokokawa	***	0.28	***	***	***

Table IV.SM-II: Summary mean and standard deviation values of analysed properties for each potential source group: topsoil (n = 59) and subsoil (n = 24), and reservoir sediment core layer samples: Mano Dam (n = 38), Ogaki (n = 16), and Yokokawa Dam (n = 35).

	TOC (%)	**TN** (%)	**TOC/TN**	δ^{13}C (‰)	**AI** (g kg^{-1})
Topsoil	9.10 $\pm$ 6.31	0.65 $\pm$ 0.36	13.35 $\pm$ 2.54	-25.68 $\pm$ 1.60	75.8 $\pm$ 19.4
Subsoil	1.14 $\pm$ 1.03	0.11 $\pm$ 0.08	9.89 $\pm$ 2.98	-25.16 $\pm$ 1.53	104.0 $\pm$ 16.7
Mano Dam	5.59 $\pm$ 1.96	0.45 $\pm$ 0.11	12.29 $\pm$ 1.71	-25.82 $\pm$ 0.94	72.9 $\pm$ 6.6
Ogaki Dam	5.78 $\pm$ 1.25	0.52 $\pm$ 0.08	11.04 $\pm$ 1.05	-27.29 $\pm$ 0.37	103.0 $\pm$ 13.2
Yokokawa Dam	7.30 $\pm$ 1.13	0.56 $\pm$ 0.09	12.99 $\pm$ 0.85	-27.87 $\pm$ 0.33	85.5 $\pm$ 6.0

Table IV.SM-III: Summary of sediment source fingerprinting MixSIAR modeling prediction accuracy statistics calculated on virtual mixtures (n = 41). W50 stands from prediction interval width; ME stands for mean error; RMSE stands for root mean square error, r^2 stands for squared Pearson's correlation coefficient, NSE stands for Nash-Sutcliffe modeling efficiency coefficient; CRPS stands for continuous ranked probability score; ESP stands from encompassed sample predictions expression as the number of samples within the range of source out of 89 (n) and as a percentage (%). The * indicates mean value per source.

Source	**W50***	**ME (%)**		**RMSE**	r^2	**NSE**	**CRPS***	**ESP (n - %)**		
		Topsoil	**Subsoil**					**Mano** (n = 38)	**Ogaki** (n = 16)	**Yokokawa** (n = 35)
Topsoil & Subsoil	16	-11	11	16	0.94	0.71	9	30 - 79	15 - 94	26 - 74
Average	*16*	*0*		*16*	*0.94*	*0.71*	*9*	*71 - 80*		

Table IV.SM-IV: Evolution of the relative source contributions between two potential sources (i.e. Topsoil and subsoil; in %) predicted by the MixSIAR un-mixing model along the sediment cores collected in (a) Mano Dam, (b) Ogaki Dam, and (c) Yokokawa Dam reservoirs..

(a) **Mano Dam reservoir**

Layer (cm)	Contribution (%)	
	Topsoil	Subsoil
00-01	63	37
01-02	24	76
02-03	25	75
03-04	28	72
04-05	26	74
05-06	21	79
06-07	42	58
07-08	58	42
08-09	62	38
09-10	73	27
10-11	72	28
11-12	71	30
12-13	78	22
13-14	83	17
14-15	58	42
15-16	52	49
16-17	49	51
17-18	49	52
18-19	53	48
19-20	67	33
20-21	74	27
21-22	68	32
22-23	58	42
23-24	60	40
24-25	67	33
25-26	83	17
26-27	82	18
27-28	65	35
28-29	64	36
29-30	67	33
30-31	68	32
31-32	65	35
32-33	62	38
33-34	54	46
34-35	51	50
35-36	48	52
36-37	42	58
37-38	45	55

(b) **Ogaki Dam reservoir**

Layer (cm)	Contribution (%)	
	Topsoil	Subsoil
00-01	60	40
01-02	60	40
02-03	62	38
03-04	61	40
04-05	64	36
05-06	66	34
06-07	63	37
07-08	62	38
08-09	62	39
09-10	55	45
10-11	51	49
11-12	47	53
12-13	50	50
13-14	74	26
14-15	33	67
15-16	24	76

(c) **Yokokawa Dam reservoir**

Layer (cm)	Contribution (%)	
	Topsoil	Subsoil
00-01	65	36
01-02	61	40
02-03	62	38
03-04	61	39
04-05	66	34
05-06	70	30
06-07	63	37
07-08	85	16
08-09	70	30
09-10	68	32
10-11	72	28
11-12	68	33
12-13	69	31
13-14	71	29
14-15	71	29
15-16	77	24
16-17	78	22
17-18	73	27
18-19	79	21
19-20	68	32
20-21	68	32
21-22	75	25
22-23	58	42
23-24	68	32
24-25	63	37
25-26	65	35
26-27	65	35
27-28	54	46
28-29	63	37
29-30	58	42
30-31	66	34
31-32	47	53
32-33	34	66
33-34	57	43
34-35	56	44

Table IV.SM-V: Evolution of quantitative source contributions between two potential sources (i.e. Topsoil and subsoil; in g cm^{-3}) predicted by the MixSIAR un-mixing model along the sediment cores collected in (a) Mano Dam, (b) Ogaki Dam, and (c) Yokokawa Dam reservoirs.

(a) **Mano Dam reservoir**

Layer (cm)	Contribution (g cm^{-3})	
	Topsoil	**Subsoil**
00-01	33	19
01-02	16	50
02-03	16	49
03-04	18	48
04-05	17	46
05-06	18	66
06-07	20	28
07-08	26	19
08-09	27	17
09-10	33	12
10-11	28	11
11-12	30	12
12-13	35	10
13-14	32	7
14-15	27	20
15-16	25	23
16-17	23	25
17-18	22	23
18-19	25	22
19-20	25	12
20-21	23	8
21-22	29	14
22-23	26	19
23-24	28	19
24-25	27	13
25-26	32	7
26-27	33	7
27-28	29	16
28-29	27	15
29-30	24	11
30-31	21	10
31-32	19	11
32-33	17	11
33-34	17	15
34-35	20	19
35-36	22	23
36-37	19	26
37-38	21	26

(b) **Ogaki Dam reservoir**

Layer (cm)	Contribution (g cm^{-3})	
	Topsoil	**Subsoil**
00-01	16	10
01-02	11	8
02-03	9	6
03-04	14	9
04-05	14	8
05-06	18	9
06-07	19	11
07-08	18	11
08-09	16	10
09-10	17	14
10-11	15	15
11-12	16	18
12-13	17	17
13-14	28	10
14-15	14	29
15-16	13	42

(c) **Yokokawa Dam reservoir**

Layer (cm)	Contribution (g cm^{-3})	
	Topsoil	**Subsoil**
00-01	23	13
01-02	16	10
02-03	22	14
03-04	20	12
04-05	24	12
05-06	20	8
06-07	23	13
07-08	25	5
08-09	24	10
09-10	20	9
10-11	20	8
11-12	22	11
12-13	20	9
13-14	23	10
14-15	19	7
15-16	24	7
16-17	20	6
17-18	22	8
18-19	16	4
19-20	21	10
20-21	25	11
21-22	31	10
22-23	20	14
23-24	28	13
24-25	20	12
25-26	23	13
26-27	22	12
27-28	23	19
28-29	22	13
29-30	24	18
30-31	27	14
31-32	27	30
32-33	19	36
33-34	32	25
34-35	30	24

References

Agnihotri, R., Kumar, R., Prasad, M.V.S.N., Sharma, C., Bhatia, S.K., Arya, B.C., 2014. Experimental Setup and Standardization of a Continuous Flow Stable Isotope Mass Spectrometer for Measuring Stable Isotopes of Carbon, Nitrogen and Sulfur in Environmental Samples. MAPAN 29, 195–205. URL: http://link.springer.com/10.1007/s12647-014-0099-8, doi:10.1007/s12647-014-0099-8.

Amorim, H.C., Hurtarte, L.C., Souza, I.F., Zinn, Y.L., 2022. C:N ratios of bulk soils and particle-size fractions: Global trends and major drivers. Geoderma 425, 116026. URL: https://linkinghub.elsevier.com/retrieve/pii/S0016706122003330, doi:10.1016/j.geoderma.2022.116026.

Asanuma-Brice, C., Evrard, O., Chalaux, T., 2023. Why did so few refugees return to the Fukushima fallout-impacted region after remediation? An interdisciplinary case study from Iitate village, Japan. International Journal of Disaster Risk Reduction 85, 103498. URL: https://linkinghub.elsevier.com/retrieve/pii/S2212420922007178, doi:10.1016/j.ijdrr.2022.103498.

Ayabe, Y., Hijii, N., Takenaka, C., 2017. Effects of local-scale decontamination in a secondary forest contaminated after the Fukushima nuclear power plant accident. Environmental Pollution 228, 344–353. URL: https://linkinghub.elsevier.com/retrieve/pii/S0269749116319704, doi:10.1016/j.envpol.2017.05.041.

Batista, P.V.G., Laceby, J.P., Evrard, O., 2022. How to evaluate sediment fingerprinting source apportionments. Journal of Soils and Sediments 22, 1315–1328. URL: https://link.springer.com/10.1007/s11368-022-03157-4, doi:10.1007/s11368-022-03157-4.

Beck, H.E., Zimmermann, N.E., McVicar, T.R., Vergopolan, N., Berg, A., Wood, E.F., 2018. Present and future Köppen-Geiger climate classification maps at 1-km resolution. Scientific Data 5, 180214. URL: http://www.nature.com/articles/sdata2018214, doi:10.1038/sdata.2018.214.

Bishop, T., 2024. itraxR: Itrax Data Analysis Tools. URL: https://CRAN.R-project.org/package=itraxR.

Board of Audit of Japan, 2023. Status of Implementation of Projects Related to Recovery from the Great East Japan Earthquake. Technical Report. Board of Audit of Japan. URL: https://www.jbaudit.go.jp/pr/kensa/result/5/pdf/050203_01_zenbun.pdf.

Chalaux-Clergue, T., Bizeul, R., 2024. fingR: A support for sediment source fingerprinting studies. URL: https://github.com/tchalauxclergue/fingR, doi:10.5281/zenodo.12187654.

Chalaux-Clergue, T., Bizeul, R., Batista, P.V.G., Martínez-Carreras, N., Laceby, J.P., Evrard, O., 2024a. Sensitivity of source sediment fingerprinting to tracer selection methods. SOIL 10, 109–138. URL: https://soil.copernicus.org/articles/10/109/2024/, doi:10.5194/soil-10-109-2024.

Chalaux-Clergue, T., Chaboche, P.A., Tenaud, N., Durand, R., Caumon, A., Hayashi, S., Tsuji, H., Funaki, H., Yoshimura, K., Wakiyama, Y., Laceby, J.P., Murayama, M., Matsuzaki, T., Lefèvre, I., Huon, S., Vaury, V., Mendes-Millan, M., Ogier, A., Nakao, A., Evrard, O., 2024b. Diagnostic properties of three sediment cores collected in 2021-2022 fromThree water reservoirs draining contaminated catchments after the fukushima daiichi nuclear power plant accident (mano dam, ogaki dam, and yokokawa dam). URL: https://doi.org/10.5281/zenodo.14731789, doi:10.5281/zenodo.14731789.

Chalaux-Clergue, T., Foucher, A., Chaboche, P.A., Hayashi, S., Tsuji, H., Wakiyama, Y., Huon, S., Vandromme, R., Cerdan, O., Nakao, A., Evrard, O., 2024c. Impacts of farmland decontamination on 137Cs transfers in rivers after Fukushima nuclear accident: Evidence from a retrospective sediment core study. Science of The Total Environment 947, 174546. URL: https://linkinghub.elsevier.com/retrieve/pii/S0048969724046941, doi:10.1016/j.scitotenv.2024.174546.

Chartin, C., Evrard, O., Laceby, J.P., Onda, Y., Ottlé, C., Lefèvre, I., Cerdan, O., 2017. The impact of typhoons on sediment connectivity: Lessons learnt from contaminated coastal catchments of the Fukushima Prefecture (Japan): Typhoon Impact on Sediment Connectivity - Fukushima, Japan. Earth Surface Processes and Landforms 42, 306–317. URL: https://onlinelibrary.wiley.com/doi/10.1002/esp.4056, doi:10.1002/esp.4056.

Chartin, C., Evrard, O., Onda, Y., Patin, J., Lefèvre, I., Ottlé, C., Ayrault, S., Lepage, H., Bonté, P., 2013. Tracking the early dispersion of contaminated sediment along rivers draining the Fukushima radioactive pollution plume. Anthropocene 1, 23–34. URL: https://linkinghub.elsevier.com/retrieve/pii/S2213305413000088, doi:10.1016/j.ancene.2013.07.001.

Chawchai, S., Kylander, M.E., Chabangborn, A., Löwemark, L., Wohlfarth, B., 2016. Testing commonly used X-ray fluorescence core scanning-based proxies for organic-rich lake sediments and peat. Boreas 45, 180–189. URL: https://onlinelibrary.wiley.com/doi/10.1111/bor.12145, doi:10.1111/bor.12145.

Collins, A.L., Blackwell, M., Boeckx, P., Chivers, C.A., Emelko, M., Evrard, O., Foster, I., Gellis, A., Gholami, H., Granger, S., Harris, P., Horowitz, A.J., Laceby, J.P., Martinez-Carreras, N., Minella, J., Mol, L., Nosrati, K., Pulley, S., Silins, U., da Silva, Y.J., Stone, M., Tiecher, T., Upadhayay, H.R., Zhang, Y., 2020. Sediment source fingerprinting: Benchmarking recent outputs, remaining challenges and emerging themes. Journal of Soils and Sediments 20, 4160–4193. URL: https://link.springer.com/10.1007/s11368-020-02755-4, doi:10.1007/s11368-020-02755-4.

Coplen, T.B., Kendall, C., Hopple, J., 1983. Comparison of stable isotope reference samples. Nature 302, 236–238. URL: https://www.nature.com/articles/302236a0, doi:10.1038/302236a0.

Croudace, I.W., Rothwell, R.G. (Eds.), 2015. Micro-XRF Studies of Sediment Cores: Applications of a Non-Destructive Tool for the Environmental Sciences. volume 17 of *Developments in Paleoenvironmental Research*. Springer Netherlands, Dordrecht. URL: https://link.springer.com/10.1007/978-94-017-9849-5, doi:10.1007/978-94-017-9849-5.

Evrard, O., Chalaux-Clergue, T., Chaboche, P.A., Wakiyama, Y., Thiry, Y., 2023. Spatial datasets associated with decontamination and remediation operations following the Fukushima nuclear accident, Japan (2011–2023). URL: https://zenodo.org/doi/10.5281/zenodo.7827616, doi:10.5281/ZENODO.7827616.

Evrard, O., Durand, R., Foucher, A., Tiecher, T., Sellier, V., Onda, Y., Lefèvre, I., Cerdan, O., Laceby, J.P., 2019a. Using spectrocolourimetry to trace sediment source dynamics in coastal catchments draining the main Fukushima radioactive pollution plume (2011–2017). Journal of Soils and Sediments 19, 3290–3301. URL: http://link.springer.com/10.1007/s11368-019-02302-w, doi:10.1007/s11368-019-02302-w.

Evrard, O., Durand, R., Nakao, A., Laceby, P.J., Lefèvre, I., Wakiyama, Y., Hayashi, S., Asanuma-Brice, C., Cerdan, O., 2020. Impact of the 2019 typhoons on sediment source contributions and radiocesium concentrations in rivers draining the Fukushima radioactive plume, Japan. Comptes Rendus. Géoscience 352, 199–211. URL: https://comptes-rendus.academie-sciences.fr/geoscience/item/CRGEOS_2020__352_3_199_0, doi:10.5802/crgeos.42.

Evrard, O., Laceby, J.P., Ficetola, G.F., Gielly, L., Huon, S., Lefèvre, I., Onda, Y., Poulenard, J., 2019b. Environmental DNA provides information on sediment sources: A study in catchments affected by Fukushima radioactive fallout. Science of The Total Environment 665, 873–881. URL: https://linkinghub.elsevier.com/retrieve/pii/S0048969719306795, doi:10.1016/j.scitotenv.2019.02.191.

Evrard, O., Laceby, J.P., Lepage, H., Onda, Y., Cerdan, O., Ayrault, S., 2015. Radiocesium transfer from hillslopes to the Pacific Ocean after the Fukushima Nuclear Power Plant accident: A review. Journal of Environmental Radioactivity 148, 92–110. URL: https://linkinghub.elsevier.com/retrieve/pii/S0265931X1530031X, doi:10.1016/j.jenvrad.2015.06.018.

Evrard, O., Laceby, J.P., Nakao, A., 2019c. Effectiveness of landscape decontamination following the Fukushima nuclear accident: A review. SOIL 5, 333–350. URL: https://soil.copernicus.org/articles/5/333/2019/, doi:10.5194/soil-5-333-2019.

Evrard, O., Laceby, J.P., Onda, Y., Wakiyama, Y., Jaegler, H., Lefèvre, I., 2016. Quantifying the dilution of the radiocesium contamination in Fukushima coastal river sediment (2011–2015). Scientific Reports 6, 34828. URL: https://www.nature.com/articles/srep34828, doi:10.1038/srep34828.

Feng, B., Onda, Y., Wakiyama, Y., Taniguchi, K., Hashimoto, A., Zhang, Y., 2022. Persistent impact of

Fukushima decontamination on soil erosion and suspended sediment. Nature Sustainability URL: https://www.nature.com/articles/s41893-022-00924-6, doi:10.1038/s41893-022-00924-6.

Fujii, K., Ikeda, S., Akama, A., Komatsu, M., Takahashi, M., Kaneko, S., 2014. Vertical migration of radiocesium and clay mineral composition in five forest soils contaminated by the Fukushima nuclear accident. Soil Science and Plant Nutrition 60, 751–764. URL: http://www.tandfonline.com/doi/abs/10.1080/00380768.2014.926781, doi:10.1080/00380768.2014.926781.

Girardin, C., Mariotti, A., 1991. Analyse isotopique du 13C en abondance naturelle dans le carbone organique: un système automatique avec robot préparateur. Cahiers ORSTOM, Serie Pedologie 26, 371–380. URL: https://www.documentation.ird.fr/hor/fdi:39457.

Gomi, T., Sidle, R.C., Richardson, J.S., 2002. Understanding Processes and Downstream Linkages of Headwater Systems. BioScience 52, 905. URL: https://academic.oup.com/bioscience/article/52/10/905-916/354918, doi:10.1641/0006-3568(2002)052[0905:UPADLO]2.0.CO;2.

Hashimoto, S., Ugawa, S., Nanko, K., Shichi, K., 2012. The total amounts of radioactively contaminated materials in forests in Fukushima, Japan. Scientific Reports 2, 416. URL: https://www.nature.com/articles/srep00416, doi:10.1038/srep00416.

He, Q., Walling, D., 1996. Interpreting particle size effects in the adsorption of 137Cs and unsupported 210Pb by mineral soils and sediments. Journal of Environmental Radioactivity 30, 117–137. URL: https://linkinghub.elsevier.com/retrieve/pii/0265931X96892757, doi:10.1016/0265-931X(96)89275-7.

Huon, S., Hayashi, S., Laceby, J.P., Tsuji, H., Onda, Y., Evrard, O., 2018. Source dynamics of radiocesium-contaminated particulate matter deposited in an agricultural water reservoir after the Fukushima nuclear accident. Science of The Total Environment 612, 1079–1090. URL: https://linkinghub.elsevier.com/retrieve/pii/S0048969717319083, doi:10.1016/j.scitotenv.2017.07.205.

JAXA, 2022. High-Resolution Land-Use and Land-Cover Map of Japan [2018 $\sim$ 2020] (ver. 21.11; 10-m resolution; 12 categories). URL: https://www.eorc.jaxa.jp/ALOS/en/dataset/lulc/lulc_v2111_e.htm.

Kato, H., Onda, Y., Gao, X., Sanada, Y., Saito, K., 2019. Reconstruction of a Fukushima accident-derived radiocesium fallout map for environmental transfer studies. Journal of Environmental Radioactivity 210, 105996. URL: https://linkinghub.elsevier.com/retrieve/pii/S0265931X18303308, doi:10.1016/j.jenvrad.2019.105996.

Kato, H., Onda, Y., Teramage, M., 2012. Depth distribution of 137Cs, 134Cs, and 131I in soil profile after Fukushima Dai-ichi Nuclear Power Plant Accident. Journal of Environmental Radioactivity 111, 59–64. URL: https://linkinghub.elsevier.com/retrieve/pii/S0265931X11002426, doi:10.1016/j.jenvrad.2011.10.003.

Kitamura, A., Kurikami, H., Sakuma, K., Malins, A., Okumura, M., Machida, M., Mori, K., Tada, K., Tawara, Y., Kobayashi, T., Yoshida, T., Tosaka, H., 2016. Redistribution and export of contaminated sediment within eastern Fukushima Prefecture due to typhoon flooding: Redistribution and export of contaminated sediment. Earth Surface Processes and Landforms 41, 1708–1726. URL: https://onlinelibrary.wiley.com/doi/10.1002/esp.3944, doi:10.1002/esp.3944.

Koarashi, J., Atarashi-Andoh, M., Nishimura, S., Muto, K., 2020. Effectiveness of decontamination by litter removal in Japanese forest ecosystems affected by the Fukushima nuclear accident. Scientific Reports 10, 6614. URL: https://www.nature.com/articles/s41598-020-63520-8, doi:10.1038/s41598-020-63520-8.

Koarashi, J., Atarashi-Andoh, M., Takeuchi, E., Nishimura, S., 2014. Topographic heterogeneity effect on the accumulation of Fukushima-derived radiocesium on forest floor driven by biologically mediated processes. Scientific Reports 4, 6853. URL: https://www.nature.com/articles/srep06853, doi:10.1038/srep06853.

Kobayashi, T., Nagai, H., Chino, M., Kawamura, H., 2013. Source term estimation of atmospheric release due to the Fukushima Dai-ichi Nuclear Power Plant accident by atmospheric and oceanic dis-

persion simulations: Fukushima NPP Accident Related. Journal of Nuclear Science and Technology 50, 255–264. URL: http://www.tandfonline.com/doi/abs/10.1080/00223131.2013.772449, doi:10.1080/00223131.2013.772449.

Konoplev, A., Golosov, V., Wakiyama, Y., Takase, T., Yoschenko, V., Yoshihara, T., Parenyuk, O., Cresswell, A., Ivanov, M., Carradine, M., Nanba, K., Onda, Y., 2018. Natural attenuation of Fukushima-derived radiocesium in soils due to its vertical and lateral migration. Journal of Environmental Radioactivity 186, 23–33. URL: https://linkinghub.elsevier.com/retrieve/pii/S0265931X17303296, doi:10.1016/j.jenvrad.2017.06.019.

Kurihara, M., Onda, Y., Suzuki, H., Iwasaki, Y., Yasutaka, T., 2018. Spatial and temporal variation in vertical migration of dissolved 137Cs passed through the litter layer in Fukushima forests. Journal of Environmental Radioactivity 192, 1–9. URL: https://linkinghub.elsevier.com/retrieve/pii/S0265931X17309335, doi:10.1016/j.jenvrad.2018.05.012.

Laceby, J.P., Chartin, C., Evrard, O., Onda, Y., Garcia-Sanchez, L., Cerdan, O., 2016a. Rainfall erosivity in catchments contaminated with fallout from the Fukushima Daiichi nuclear power plant accident. Hydrology and Earth System Sciences 20, 2467–2482. URL: https://hess.copernicus.org/articles/20/2467/2016/, doi:10.5194/hess-20-2467-2016.

Laceby, J.P., Huon, S., Onda, Y., Vaury, V., Evrard, O., 2016b. Do forests represent a long-term source of contaminated particulate matter in the Fukushima Prefecture? Journal of Environmental Management 183, 742–753. URL: https://linkinghub.elsevier.com/retrieve/pii/S0301479716306661, doi:10.1016/j.jenvman.2016.09.020.

Lamb, A.L., Wilson, G.P., Leng, M.J., 2006. A review of coastal palaeoclimate and relative sea-level reconstructions using δ13C and C/N ratios in organic material. Earth-Science Reviews 75, 29–57. URL: https://linkinghub.elsevier.com/retrieve/pii/S0012825205001376, doi:10.1016/j.earscirev.2005.10.003.

Lepage, H., Evrard, O., Onda, Y., Lefèvre, I., Laceby, J.P., Ayrault, S., 2015. Depth distribution of cesium-137 in paddy fields across the Fukushima pollution plume in 2013. Journal of Environmental Radioactivity 147, 157–164. URL: https://linkinghub.elsevier.com/retrieve/pii/S0265931X15001484, doi:10.1016/j.jenvrad.2015.05.003.

López-Vicente, M., Onda, Y., Takahashi, J., Kato, H., Chayama, S., Hisadome, K., 2018. Radiocesium concentrations in soil and leaf after decontamination practices in a forest plantation highly polluted by the Fukushima accident. Environmental Pollution 239, 448–456. URL: https://linkinghub.elsevier.com/retrieve/pii/S0269749117345906, doi:10.1016/j.envpol.2018.04.045.

MoE, 2013. Decontamination Guidelines. Technical Report 2. Japanese Ministry of Environment. Japan.

MoE, 2015. Decontamination Report - A Compilation of Experiences to Date on Decontamination for the Living Environment Conducted by the Ministry of the Environment. Technical Report. Japanese Ministry of Environment. Japan. URL: http://josen.env.go.jp/en/policy_document/.

MoE, 2018a. Decontamination Projects for Radioactive Contamination Discharged by Tokyo Electric Power Company Fukushima Daiichi Nuclear Power Station Accident. Technical Report. Japanese Ministry of Environment.

MoE, 2018b. Environmental Remediation Updates. URL: http://josen.env.go.jp/en/policy_document/.

MoE, 2023. Decontamination status. URL: http://josen.env.go.jp/area/.

Morino, Y., Ohara, T., Watanabe, M., Hayashi, S., Nishizawa, M., 2013. Episode Analysis of Deposition of Radiocesium from the Fukushima Daiichi Nuclear Power Plant Accident. Environmental Science & Technology 47, 2314–2322. URL: https://pubs.acs.org/doi/10.1021/es304620x, doi:10.1021/es304620x.

Naulier, M., Eyrolle-Boyer, F., Boyer, P., Métivier, J.M., Onda, Y., 2017. Particulate organic matter in rivers of Fukushima: An unexpected carrier phase for radiocesiums. Science of The Total Environment 579, 1560–1571. URL: https://linkinghub.elsevier.com/retrieve/pii/S0048969716326304, doi:10.1016/j.scitotenv.2016.11.165.

Obara, H., Maejima, Y., Kohyama, K., Ohkura, T., Takata, Y., 2015. Outline of the Comprehensive Soil Classification System of Japan – First Approximation. Japan Agricultural Research Quarterly: JARQ 49, 217–226. URL: https://www.jstage.jst.go.jp/article/jarq/49/3/49_217/_article, doi:10.6090/jarq.49.217.

Obara, H., Ohkura, T., Takata, Y., Kohyama, K., Maejima, Y., Hamazaki, T., 2011. Comprehensive soil classification system of Japan first approximation. Nogyo Kankyo Gijutsu Kenkyusho Hokoku = Bulletin of National Institute for Agro-Environmental Sciences , 1–73URL: http://www.niaes.affrc.go.jp/sinfo/publish/public_e.html.

Onda, Y., Taniguchi, K., Yoshimura, K., Kato, H., Takahashi, J., Wakiyama, Y., Coppin, F., Smith, H., 2020. Radionuclides from the Fukushima Daiichi Nuclear Power Plant in terrestrial systems. Nature Reviews Earth & Environment 1, 644–660. URL: https://www.nature.com/articles/s43017-020-0099-x, doi:10.1038/s43017-020-0099-x.

Osawa, K., Nonaka, Y., Nishimura, T., Tanoi, K., Matsui, H., Mizogichi, M., Tatsuno, T., 2018. Quantification of dissolved and particulate radiocesium fluxes in two rivers draining the main radioactive pollution plume in Fukushima, Japan (2013–2016). Anthropocene 22, 40–50. URL: https://linkinghub.elsevier.com/retrieve/pii/S2213305418300262, doi:10.1016/j.ancene.2018.04.003.

Palazón, L., Latorre, B., Gaspar, L., Blake, W.H., Smith, H.G., Navas, A., 2015. Comparing catchment sediment fingerprinting procedures using an auto-evaluation approach with virtual sample mixtures. Science of The Total Environment 532, 456–466. URL: https://linkinghub.elsevier.com/retrieve/pii/S0048969715300619, doi:10.1016/j.scitotenv.2015.05.003.

QGIS Development Team, 2024. QGIS Geographic Information System. Open Source Geospatial Foundation. URL: https://www.qgis.org/fr/site/.

R Core Team, 2024. A Language and Environment for Statistical Computing. R Foundation for Statistical Computing. URL: https://www.R-project.org/.

Richter, T.O., Van Der Gaast, S., Koster, B., Vaars, A., Gieles, R., De Stigter, H.C., De Haas, H., Van Weering, T.C.E., 2006. The Avaatech XRF Core Scanner: Technical description and applications to NE Atlantic sediments. Geological Society, London, Special Publications 267, 39–50. URL: https://www.lyellcollection.org/doi/10.1144/GSL.SP.2006.267.01.03, doi:10.1144/GSL.SP.2006.267.01.03.

RStudio Team, 2023. RStudio: Integrated Development Environment for R. RStudio. URL: http://www.rstudio.com/.

Sakaguchi, A., Tanaka, K., Iwatani, H., Chiga, H., Fan, Q., Onda, Y., Takahashi, Y., 2015. Size distribution studies of 137Cs in river water in the Abukuma Riverine system following the Fukushima Dai-ichi Nuclear Power Plant accident. Journal of Environmental Radioactivity 139, 379–389. URL: https://linkinghub.elsevier.com/retrieve/pii/S0265931X14001519, doi:10.1016/j.jenvrad.2014.05.011.

Sakai, M., Gomi, T., Negishi, J.N., Iwamoto, A., Okada, K., 2016. Different cesium-137 transfers to forest and stream ecosystems. Environmental Pollution 209, 46–52. URL: https://linkinghub.elsevier.com/retrieve/pii/S0269749115301858, doi:10.1016/j.envpol.2015.11.025.

Sakai, M., Tsuji, H., Ishii, Y., Ozaki, H., Takechi, S., Jo, J., Tamaoki, M., Hayashi, S., Gomi, T., 2021. Untangling radiocesium dynamics of forest-stream ecosystems: A review of Fukushima studies in the decade after the accident. Environmental Pollution 288, 117744. URL: https://linkinghub.elsevier.com/retrieve/pii/S0269749121013269, doi:10.1016/j.envpol.2021.117744.

Sawhney, B.L., 1972. Selective Sorption and Fixation of Cations by Clay Minerals: A Review. Clays and Clay Minerals 20, 93–100. URL: https://doi.org/10.1346/CCMN.1972.0200208, doi:10.1346/CCMN.1972.0200208.

Steinhauser, G., 2014. Fukushima's Forgotten Radionuclides: A Review of the Understudied Radioactive Emissions. Environmental Science & Technology 48, 4649–4663. URL: https://pubs.acs.org/doi/10.1021/es405654c, doi:10.1021/es405654c.

Stock, B.C., Semmens, B.X., 2016. Unifying error structures in commonly used biotracer mixing models. Ecology 97, 2562–2569. URL: https://onlinelibrary.wiley.com/doi/10.1002/ecy.1517, doi:10.1002/ecy.1517.

Stock, B.C., Semmens, B.X., Ward, E.J., Parnell, A.C., Phillips, D.L., 2020. MixSIAR: Bayesian Mixing Models in R. URL: https://doi.org/10.5281/zenodo.1209993.

Stock, B.C., Semmens, B.X., Ward, E.J., Parnell, A.C., Phillips, D.L., 2022. JAGS: Bayesian Mixing Models in R. URL: https://doi.org/10.5281/zenodo.1209993.

Taira, Y., Matsuo, M., Yamaguchi, T., Yamada, Y., Orita, M., Takamura, N., 2020. Radiocesium levels in contaminated forests has remained stable, even after heavy rains due to typhoons and localized downpours. Scientific Reports 10, 19215. URL: https://www.nature.com/articles/s41598-020-75857-1, doi:10.1038/s41598-020-75857-1.

Takahashi, J., Onda, Y., Hihara, D., Tamura, K., 2018. Six-year monitoring of the vertical distribution of radiocesium in three forest soils after the Fukushima Dai-ichi Nuclear Power Plant accident. Journal of Environmental Radioactivity 192, 172–180. URL: https://linkinghub.elsevier.com/retrieve/pii/S0265931X17309256, doi:10.1016/j.jenvrad.2018.06.015.

Taniguchi, K., Onda, Y., Smith, H.G., Blake, W., Yoshimura, K., Yamashiki, Y., Kuramoto, T., Saito, K., 2019. Transport and Redistribution of Radiocesium in Fukushima Fallout through Rivers. Environmental Science & Technology 53, 12339–12347. URL: https://pubs.acs.org/doi/10.1021/acs.est.9b02890, doi:10.1021/acs.est.9b02890.

Terashima, S., Imai, N., Taniguchi, M., Okai, T., Nishimura, A., 2002. The Preparation and Preliminary Characterisation of Four New Geological Survey of Japan Geochemical Reference Materials: Soils, JSO-1 and JSO-2; and Marine Sediments, JMS-1 and JMS-2. Geostandards Newsletter 26, 85–94. URL: https://onlinelibrary.wiley.com/doi/10.1111/j.1751-908X.2002.tb00626.x, doi:10.1111/j.1751-908X.2002.tb00626.x.

Thiry, Y., Albrecht, A., Tanaka, T., 2018. Development and assessment of a simple ecological model (TRIPS) for forests contaminated by radiocesium fallout. Journal of Environmental Radioactivity 190–191, 149–159. URL: https://linkinghub.elsevier.com/retrieve/pii/S0265931X17309499, doi:10.1016/j.jenvrad.2018.05.009.

Vandromme, R., Hayashi, S., Tsuji, H., Evrard, O., Grangeon, T., Landemaine, V., Laceby, J.P., Wakiyama, Y., Cerdan, O., 2023. Lessons learnt on the impact of an unprecedented soil decontamination program in Fukushima on contaminant fluxes. Proceedings of the National Academy of Sciences 120, e2301811120. URL: https://pnas.org/doi/10.1073/pnas.2301811120, doi:10.1073/pnas.2301811120.

Wakahara, T., Onda, Y., Kato, H., Sakaguchi, A., Yoshimura, K., 2014. Radiocesium discharge from paddy fields with different initial scrapings for decontamination after the Fukushima Dai-ichi Nuclear Power Plant accident. Environ. Sci.: Processes Impacts 16, 2580–2591. URL: http://xlink.rsc.org/?DOI=C4EM00262H, doi:10.1039/C4EM00262H.

Wakiyama, Y., Onda, Y., Yoshimura, K., Igarashi, Y., Kato, H., 2019. Land use types control solid wash-off rate and entrainment coefficient of Fukushima-derived 137Cs, and their time dependence. Journal of Environmental Radioactivity 210, 105990. URL: https://linkinghub.elsevier.com/retrieve/pii/S0265931X1730886X, doi:10.1016/j.jenvrad.2019.105990.

Walling, D.E., Owens, P.N., Waterfall, B.D., Leeks, G.J., Wass, P.D., 2000. The particle size characteristics of fluvial suspended sediment in the Humber and Tweed catchments, UK. Science of The Total Environment 251–252, 205–222. URL: https://linkinghub.elsevier.com/retrieve/pii/S0048969700003843, doi:10.1016/S0048-9697(00)00384-3.

Weltje, G.J., Bloemsma, M.R., Tjallingii, R., Heslop, D., Röhl, U., Croudace, I.W., 2015. Prediction of Geochemical Composition from XRF Core Scanner Data: A New Multivariate Approach Including Automatic Selection of Calibration Samples and Quantification of Uncertainties, in: Croudace, I.W., Rothwell, R.G. (Eds.), Micro-XRF Studies of Sediment Cores. Springer Netherlands, Dordrecht. volume 17, pp. 507–534. URL: https://link.springer.com/10.1007/978-94-017-9849-5_21, doi:10.1007/978-94-017-9849-5_21.

Whitaker, A.C., Chapasa, S.N., Sagras, C., Theogene, U., Veremu, R., Sugiyama, H., 2022. Estimation of baseflow recession constant and regression of low flow indices in eastern Japan. Hydrological Sciences Journal 67, 191–204. URL: https://www.tandfonline.com/doi/full/10.1080/02626667.2021.2003368, doi:10.1080/02626667.2021.2003368.

Yamamoto, M., 2015. Overview of the Fukushima Dai-ichi Nuclear Power Plant (FDNPP) accident, with amounts and isotopic compositions of the released radionuclides. Journal of Radioanalytical and Nuclear Chemistry 303, 1227–1231. URL: http://link.springer.com/10.1007/s10967-014-3639-3, doi:10.1007/s10967-014-3639-3.

Yoshimura, K., Onda, Y., Sakaguchi, A., Yamamoto, M., Matsuura, Y., 2015. An extensive study of the concentrations of particulate/dissolved radiocaesium derived from the Fukushima Dai-ichi Nuclear Power Plant accident in various river systems and their relationship with catchment inventory. Journal of Environmental Radioactivity 139, 370–378. URL: https://linkinghub.elsevier.com/retrieve/pii/S0265931X14002550, doi:10.1016/j.jenvrad.2014.08.021.

General Discussion, Perspectives and Conclusions

General Discussion, Perspectives and Conclusions

Main findings of the doctoral project

The nuclear accident at the FDNPP that occurred in March 2011 resulted in the widespread release of a considerable amount of radionuclides into the environment, of which about 20 % were deposited over the east-northern part of Honshū island, the main island of Japan (Morino et al., 2013; Onda et al., 2020). Among the emitted radionuclides, about 10 PBq of ^{137}Cs were emitted, of which about 2.7 PBq were deposited over inland Japan, mostly (74 %) within the Fukushima Prefecture (Kato et al., 2019; Taniguchi et al., 2019). The 80,000 inhabitants of the 11 municipalities located within a radius of 20-km around FDNPP (Evacuation Zone) and those living in areas in which radioactive dose rates exceeded 20 mSv yr^{-1} in 2011 (1,150 km^2), were evacuated. In order to enable a rapid return of the population and the resumption of economic activities, the Japanese government initiated an unprecedented large-scale decontamination programme to remediate ^{137}Cs-contaminated soils (MoE, 2011, 2013; Evrard et al., 2019b). This was allowed because of the behaviour of ^{137}Cs which, once deposited onto the soil, binds strongly and quasi-permanently to fine soil particles (Sawhney, 1972; He and Walling, 1996), resulting in an accumulation of 90-99 % of deposited ^{137}Cs in the uppermost 5 cm of undisturbed soils (Kato et al., 2012; Lepage et al., 2015). According to the decontamination programme, these 11 evacuated municipalities were classified as Special Decontamination Zone (SDZ) or Difficult-to-Return Zone (DTRZ), depending on local and initial ambient dose rates. In the SDZ, the decontamination programme focused mainly on farmland areas, urban areas and in forested zones located within a 20-m buffer area in residential settlements and along roads (MoE, 2015, 2018a), which has proved to be effective in reducing the radioactive air dose rates from 20 to 70 % compared to the initial situation in 2011 (MoE, 2018a; Onda et al., 2020). By March 2017, the decontamination of the SDZ area had been completed, with a total of 180 km^2 (16 % of the SDZ) (MoE, 2023). According to the progress of decontamination and physical decay, the evacuation orders was gradually lifted in the 11 municipalities of the SDZ throughout the period from April 2014 to March 2020 (MoE, 2023). Conversely, the evacuation order was maintained in the DTRZ, which was exposed to the highest radiocesium fallout and which was not initially targeted by decontamination. However, after a partial reopening in Spring in 2022, the DTRZ was gradually reopened from 2023 without mandatory decontamination, except in "special reconstruction and revitalisation zones", which correspond mainly to residential settlements and their vicinity.

In parallel to the progress of decontamination, a decrease in particle-bound ^{137}Cs activities in river sediments has been observed (Osawa et al., 2018; Konoplev et al., 2018). Various factors have been proposed to explain this reduction, including physical radioactive decay, reduced ^{137}Cs stocks due to repeated erosion events, progress of decontamination, and decreased erosion as a result of soil protection by the spontaneous vegetation regrowth after land abandonment (Evrard et al., 2016; Vandromme et al., 2023; Chalaux-Clergue et al., 2024). Over the last decade following the FDNPP accident, significant changes in radiocesium and sediment transfers along with changes in sediment source contributions were observed, driven by rapid shifts in land uses and covers following the evacuation of the contaminated areas and the implementation of the decontamination programme (Evrard et al., 2020, 2023). It was therefore relevant to investigate how the progressive implementation of decontamination and the subsequent resumption of agricultural activities impacted the transfers of sediment and radiocesium in the rivers draining the main Fukushima radioactive plume from

the FDNPP accident to the present days.

In agricultural catchments (Mano Dam and Ogaki Dam), the occurrence of the first major erosive events after the FDNPP accident, Typhoon Roke in September 2011, was associated with significant transfer and deposition fluxes of radiocesium and sediments (Chapter II, Chapter III and IV). This first transfer was associated with a dominant sediment contribution from farmland (Chapter II), which had recently been abandoned, and with a hydro-sedimentary connectivity remaining at high levels at that time (Chartin et al. (2017); Chapter III). This high sediment connectivity between farmland and river systems was mainly related to their location in the valley bottoms due to the steep topography, accentuated by their strong connection to the river networks through irrigation/drainage systems, and to their high sensitivity to erosion due to the absence of vegetation cover when the zone was evacuated. During the subsequent period of land abandonment, the radiocesium activity in sediment and radiocesium deposition fluxes decreased along with the sediment deposition fluxes (Chapter II and IV). A few years after the FDNPP accident, from three to five years (Chapter II and III), stable levels of radiocesium activity were reached in both sediment cores collected in reservoirs draining agricultural catchments (Chapter IV). For instance, in the Mano Dam reservoir sediment core, the sediment deposition fluxes decreased to about 27 % of pre-accidental levels (Chapter II), as a result of a decrease of the farmland or topsoil contribution. This was linked to the spontaneous vegetation regrowth in abandoned farmland, which gradually and increasingly reduced soil erosion and radiocesium transfers to river systems, mainly through reducing their sediment connectivity (Chapter III). The stable level of radiocesium activity was further decreased in the Mano Dam catchment after the completion of decontamination (in 2016), along with significant sediment contributions from 'fresh soil' (i.e., granite saprolite added on farmland) showing a subsoil signature (Chapter II and III). Nonetheless, this decrease in radiocesium activity levels was not associated with a reduction of the radiocesium deposition fluxes in the sediment core. Meanwhile, the contribution from forests, which were not decontaminated, remained stable (Laceby et al. (2016b); Huon et al. (2018); Chapter II). Therefore, this reduction in radiocesium activity levels, observed across the catchment area and in the sediment core, was attributed to the dilution of contaminated sediment originating from stable sources, such as forests, by uncontaminated sediment originating from 'fresh soil' (Chapter II). Subsequently, the progressive preparation of soil for the resumption of agricultural activities and the effective resumption of these were associated with the return of sediment contribution patterns similar to those found during the pre-accidental period or to the situation observed in 2011, although it was associated with limited radiocesium transfers (Chapter II and III).

In the forested catchment (Yokokawa Dam), similarly to what has been found in the agricultural catchments, an initial major deposition of radiocesium was associated with the occurrence of typhoon Roke in 2011. However, this initial phase was followed by two delayed and larger transfer episodes of radiocesium (Chapter IV). A similar delayed transfer of radiocesium along with increased contributions of forest were observed one to three years after the FDNPP accident, at several sites located well upstream of the Mano Dam reservoir catchment (Chapter III). This delayed radiocesium transfer pattern was likely associated with the complex dynamics of litter in forests. Indeed, at the time of the accident, the initial radiocesium deposition occurred over the litter of broadleaf trees, as no leaf was present on the trees at the time of the accident in March, and over the canopy of the evergreen coniferous trees. The gradual release of radiocesium through litter decomposition and through the gradual litterfall of evergreen coniferous trees induced a secondary provision of contaminated materials that could be transferred to river systems. In relation to the foliar cycle, immediate and repeated litter removal should be carried out within 1 to 5 years after an accident to reduce the transfer of radiocesium from the litter to the mineral soil layer (Ayabe et al., 2017; Thiry et al., 2018; Koarashi et al., 2020; Taira et al., 2020). However, the removal of the litter could also increase soil sensitivity to erosion, and subsequently, increase the potential runoff of radiocesium (López-Vicente et al., 2018). As a result, the actual

removal of the litter within the 20-m buffer area of forest around residential settlements and along roads may be counter-productive as it could reduce the role of litter in trapping eroded contaminated sediment before it is exported to the river systems (Gomi et al., 2002; Sakai et al., 2021). Moreover, the ecological consequences of litter removal, such as habitat disruption and alteration of soil carbon cycling should be carefully considered before implementing such a measure (Sakai et al., 2021). Nevertheless, 74 % of the initial radiocesium deposition occurred over forests in the Fukushima Prefecture (Hashimoto et al., 2012; Kato et al., 2019), and residual radiocesium inventories beneath forests remain high, amounting to at least 67 % of the initial deposit (Onda et al., 2020; Vandromme et al., 2023), which could represent a potential long term source of radiocesium to downstream environments (Laceby et al., 2016b; Naulier et al., 2017; Huon et al., 2018; Chalaux-Clergue et al., 2024). However, forested areas appeared to be effectively connected to the river system only during exceptional erosive events (Chartin et al. (2017), Chapter III). Furthermore, such events were shown to mainly generate rill and gully erosion erosion associated with the transport of uncontaminated subsoil material, which limits their actual potential to transfer radiocesium to downstream areas (Vandromme et al. (2023), Chapter II).

Moreover, the analysis of the erosivity of the extreme precipitation events (Chapter III), such as typhoons and tropical storms, has confirmed their importance as the main driver of erosion (Laceby et al., 2016a; Chartin et al., 2017). Indeed, the highest monthly R factor occurs in summer and early in autumn, between July and October, accounting for 73 % of the annual rainfall erosivity, a period that was slightly longer than that reported by Laceby et al. (2016a) (July to September). Nonetheless, the intensity of the erosive events greatly varies from one event to another, and also from one year to another, which strongly influences sediment connectivity (Chartin et al. (2017); Chapter III). For instance, in 2019, typhoon Hagibis, followed by the extra tropical cyclone Bualoi, was the strongest erosive event recorded since the FDNPP accident, with a cumulative precipitation of 372 mm (Chalaux-Clergue et al., 2024) (Chapter II) and a mean erosive energy of 2682 ± 2216 MJ mm ha^{-1} h^{-1} as measured within a 110 km^2 radius around FDNPP (Chapter III), which was about twice as erosive as the last major erosive event of 2015, Etau (396 mm 1366 ± 1408 MJ mm ha^{-1} h^{-1}). Such events were associated with a significant runoff and sediment load, mainly resulting in deep rill and gully erosion processes in forests (i.e. subsoil material) and from topsoil in farmland or inhabited areas (Vandromme et al., 2023). However, in none of the three sediment cores, Hagibis was associated with an increase in ^{137}Cs activities, in the sediment deposition nor in changes of source contributions patterns, whereas Etau was. This difference in the sediment deposition signature was likely related to the management of the reservoir water levels. To preserve the integrity of the dam during such intense precipitation events, dam operators operated rapid and major water discharge, which likely played a role in the potential trapping of sediment within the reservoirs and may therefore have modified the signature of Hagibis deposits, limiting the reconstruction potential of transfers and fluxes based on sediment cores only (Evrard et al., 2019a; Chalaux-Clergue et al., 2024). Unlike natural lakes, management of water reservoirs should be considered in these core-based reconstructions, as managed reservoirs do not show homogeneous sedimentation conditions throughout time, in particular in regions subject to heavy precipitation events, such as typhoons, which require rapid and major dam water releases to prevent damages to the dam structure and any flooding downstream, thereby modifying the sedimentation conditions and the signature of sedimentation events across the reservoir.

Discussion and perspectives for future research

The collection and analysis of lacustrine sediment cores and annual river sediment referred to as "lag deposits" allowed the reconstruction of sediment and particle-bound contaminant transfers using two different sediment matrices, allowing the contribution of each matrix to be discussed and compared. In the catchment area of the Mano Dam reservoir, both types of sediment allowed the investigation of sediment and particle-bound contaminant transfers in the context of major land use and cover changes that occurred during the successive phases of abandonment, decontamination and resumption of agricultural activities, over the period from 2011 to 2021 for the sediment core and from 2011 to 2023 for the lag deposits.

The analysis of the sediment cores allowed the reconstruction of the radiocesium transfer and deposition fluxes along with the relative and quantitative contributions of potential sediment sources, along the sediment sequence. For the Mano Dam sediment core, in Chapter II, the delineation of sediment layers and their chronology were determined through the analysis of multiple sediment properties (organic matter, elemental geochemistry, visible colourimetry and granulometry) coupled with contextual information (previous study of Huon et al. (2018), daily precipitation records, dam water level management, decontamination progress), following the impossibility of using a more conventional dating approach based on the measurement of natural radionuclides (i.e. excess^{210}Pb) due to the high radiocesium activity (masking the low energies at which ^{210}Pb is detected by gamma spectrometry). This alternative indirect dating method was possible in the erosive context of the Fukushima region. Indeed, most of the sediment transfer occurs during extreme rainfall events, such as typhoons or tropical storms (Laceby et al., 2016a), which allows to simplify the reconstruction of sediment dynamics through considering a succession of extreme erosive events and neglecting sediment transfers that may occur between these heavy events. However, extreme erosive events have been associated with an additional limitation when attempting to reconstruct sediment deposition within a managed reservoir. During such extreme events, as described in Chapter II, dam operators tend to release large volumes of water in a short period of time, which likely modifies the potential trapping of sediment particles and therefore the estimated contaminant transfers and the contributions of sources. Therefore, in areas exposed to heavy precipitation events, the investigation of sediment cores from managed reservoirs should take into account the potential for non-homogeneous sedimentation conditions over time, which would not be required for natural lakes. In addition, bathymetry measurements along with the development of 3D water-sediment dynamics models could support a better understanding of the complex influence of water level management on sediment dynamics and deposition across the reservoirs. In addition, information on the suspended matter flux at the inlet and at the outlet of the reservoir coupled with water discharge data could allow an estimation of the effective sediment trapping effectiveness of the reservoir. However, the collection of sediment cores in the lower section of the reservoir showed a high repeatability, considering the strong similarities in the distribution of sediment properties observed in the sediment core investigated in this thesis and in the downstream sediment cores analysed by (Huon et al., 2018). Nevertheless, the collection of several sediment cores within the lacustrine part (i.e. downstream part) of a reservoir would provide a more robust understanding of the sedimentation processes. This approach to reconstruct a contextual-based chronology of sediment deposition, although supported by several converging lines of evidence, was associated with inherent dating and reconstruction uncertainties, and may therefore be considered as a most likely sediment reconstruction scenario that we think best fits with our observations.

Furthermore, the resolution of the sampling interval at which the analyses were initially carried out (i.e., 1-cm depth increments along the sediment cores), could potentially limit our detailed understanding of sediment deposition. Indeed, some changes in properties could have occurred within these 1 cm intervals and were

therefore likely smoothed out by this sampling resolution. In Chapter II (i.e. Chalaux-Clergue et al. (2024)), it was proposed to increase the resolution of the analyses to improve these reconstructions, which could be achieved using high-resolution Energy Dispersive X-Ray Fluorescence (ED-XRF) core scanners (Rapuc et al., 2020) or high-resolution hyperspectral imagery (Jacq et al., 2019). Accordingly, in addition to the sampling of 1-cm thick sediment layers, a 1-mm step ED-XRF core scanner analysis was implemented and analysed in Chapter IV on the same Mano Dam reservoir sediment core at the *Laboratoire des Sciences du Climat et de l'Environement* (LSCE) in France and on two sediment cores from the Ogaki and Yokokawa Dam reservoirs at the *Center for Advanced Marine Core Research (Kōchi University)* in Japan. Indeed, this finer resolution allowed the identification of variations, which had been smoothed out by the 1-cm sampling method. However, high-resolution ED-XRF core scanner elemental geochemistry data is a dimensionless analysis. Therefore, to reconstruct sediment source contributions quantitatively, high-resolution ED-XRF core scanner elemental data should be calibrated to estimate the corresponding quantitative elemental concentrations. Most calibration methods rely on establishing a relationship between the high-resolution ED-XRF core scanner peak area and the analysed elemental concentration in specific layer samples identified along the sediment core (using typically quantitative ED-XRF or ICP-MS). However, for some properties or some of the sediment cores, it did not provide an effective or accurate calibration as discussed in Chapter IV. This could be associated with different potential analytical biases, such as the core water content that could affect ED-XRF measurements. Moreover, given the large quantities of data produced by the high-resolution ED-XRF core scanner as a consequence of the detailed resolution achieved here at 1 mm (up to 100-200 μm), the data should be carefully pre-treated to remove layers where analytical errors occurred during the analysis. The identification of of irregular patterns indicative of measurement artifacts could be achieved by considering several parameters: low or high counts-per-second, surface slope, high Argon measurement, in addition to parameters that are likely material- and brand-dependent, such as large dead-time or modelling errors. Moreover, since high-resolution ED-XRF is sensitive to water content, data should be corrected with other analytical methods (e.g. bulk density, loss-on-ignition). However, such analytical methods are generally performed on a sample interval larger than the scan interval, which could also induce errors. Therefore, analyses should be performed soon after the collection of the sediment core and within a short period of time. Accordingly, cold storage is essential for preserving the integrity of the sediment and maintaining a stable water content throughout the collection, analysis, and archiving process. This highlights the importance of implementing robust and repeatable protocols to ensure comparable analyses of newly collected samples and the re-analysis of archived samples. In addition, the organic matter content could not be estimated with the ED-XRF technique. The Compton/Rayleigh scattering ratios (Mo inc:Mo coh) only provided an estimation of the organic matter content, which could not be calibrated based on EA-IRMS analysis in most cases. However, organic matter provided, in most cases, a powerful tracer when implementing a sediment source fingerprinting approach, as it enables to either distinguish between topsoil and subsoil compartments, or between different topsoil land uses, such as farmland and forest.

Indeed, the calibration of the ED-XRF core scanner data with discrete ED-XRF measurements presented significant challenges. As discussed in Chapter IV, the alignment of high-resolution core scanner data (0.1 cm) with the lower resolution of the discrete measurements (1 cm) required resampling. While linear models were employed to evaluate the feasibility of this calibration approach, the coarser resolution inevitably masked finer-scale variations in the peak area signals observed across the three sediment cores. To investigate the potential of using high-resolution ED-XRF core scanner data with sediment fingerprinting techniques, the following protocol is proposed. As highlighted in the Mano Dam study in Chapter II, sediment cores should be collected from downstream reservoir areas, where fine-grained sediments deposition sequences are more likely to be

well-preserved (Croudace and Rothwell, 2015). Multiple cores should be sampled from these locations, to improve representativeness and minimise analytical bias. Prior to opening the cores, conducting computed tomography (CT) scans to visualise the internal structure could help detecting potential disturbances or irregularities as well as generating a precise 3D image of the core's internal composition. Therefore, CT scans could provide a valuable reference before any physical sampling. Following the CT scans, high-resolution elemental geochemistry profiling could be performed using a high-resolution ED-XRF core scanner, with a resolution from 100-200 μm, 0.1 cm, to 0.5 cm. Multiple scans may be required to capture the full range of geochemical variability and mitigate potential artifacts from single scans, resulting in a detailed geochemical fingerprint of the sediment cores. Subsequently, an unconstrained clustering analysis could be applied on high-resolution ED-XRF data to identify changes in properties and therefore, geochemically distinct layers within the sediment core. These distinct layers, identified by their elemental compositions, could guide the selection of targeted samples for collecting representative samples, for further analyses using complementary techniques such as EA-IRMS, samples ED-XRF or ICP-MS. These methods should provide quantitative elemental geochemistry data, enabling the calibration of ED-XRF data, and therefore a more comprehensive characterisation of sediment and its sources.

Both Itrax and Avaatech core scanners have proven their ability to efficiently determine detailed elemental records in sediment cores. Importantly, the analysis of the Itrax ED-XRF core scanner data obtained on Ogaki and Yokokawa sediment cores benefited from a well-developed R package, specifically designed for processing and interpreting such high-resolution ED-XRF datasets.(Bishop, 2024). This package offered a comprehensive suite of functions for data visualisation, calibration, and statistical analysis. In contrast, a comparable resource for the Avaatech core scanner is currently lacking. Developing an open-access Avaatech package would harmonize data analysis between both methods, facilitate broader comparative studies, and enhance research on erosion and sedimentation processes on short time scales like those investigated in this study.

The river lag deposits provided valuable insights into sediment transfers with a spatial perspective, allowing a more detailed reconstruction of the variations of the sediment source contributions across the landscape. The annual collection of lag deposits enabled the assessment of changes in land uses and land covers over the studied period. The analysis of these deposits also highlighted the spatial heterogeneity of erosive events, allowing for a better understanding of the way with which specific areas responded to intense events. However, while lag deposits can be linked to previous erosive events, it remains difficult - in the case of a succession of several heavy events - to determine which specific event led to the observed deposits, especially in regions such as that of Fukushima Prefecture where multiple erosive events of varying intensity may occur during a single year. Unlike sediment cores, which provide continuous records of deposition, lag deposits capture discrete moments of sediment accumulation from specific events. This difference is illustrated by the varying contributions of sediment sources, particularly those of forest and farmland, observed in lag deposits compared to those found in sediment cores. These variations are likely related to differences in local hydrodynamic conditions in the channel during different stages of an event, influenced by water levels and flow velocities at the collection sites. It is therefore likely that the sediment deposition occurs at the end of an event (i.e., recession limb of the hydrograph), when conditions for deposition are the most favourable. Moreover, while lag deposits are effective for understanding spatial patterns in sediment and contaminant transfers, they are likely not the most suitable for reconstructing fluxes of sediment and particle-bound contaminants.

The combination of sediment core and lag deposit sampling strategies provides a more comprehensive and spatially-distributed understanding of erosion processes across a catchment area. However, understand-

ing the temporal dynamics of sediment transfers during individual erosive events would require the use of monitoring and/or suspended matter automated sampling stations. These stations necessitate significant financial investments - potentially reaching several thousands euros -, require the acquisition of data over a long period of time, and a stable permanent structure in concrete, which limit their widespread deployment at multiple sites across the catchment. In addition, in regions that frequently experience intense erosive events such as typhoons or tropical storms as those occurring in the Fukushima Prefecture, these stations could be damaged or even destroyed. For instance, the automated sampling station managed by the NIES located upstream of the Mano Dam, was damaged during events in 2015 and 2019 (see picture GD.1). Developing more affordable monitoring stations capable of performing similar measurements (e.g. turbidity) would constitute a valuable opportunity, allowing for the wider implementation of a more comprehensive monitoring network across the catchment. In addition, as highlighted in Chapter III, estimating sediment connectivity using a connectivity index derived from topographic information could assist in determining the optimal locations of sediment monitoring stations within the catchment. To study the temporal changes in sediment source contributions to suspended matter during erosive events, it would also be interesting to integrate sensors capable of measuring sediment characteristics in addition to turbidity. Infrared technology, and particularly Near Infrared (NIR) spectroscopy, appears particularly promising in this regard. As previously discussed, organic matter is a critical tracer for differentiating between topsoil and subsoil, as well as between various land uses, and this property can be accurately predicted using NIR spectra (Soriano-Disla et al., 2014; Jacq et al., 2019). This was further investigated during the Master 2 internship of Clément Leroy (that took place at LSCE from Feb. to Aug. 2024), which assessed the predictive accuracy of high-resolution NIR spectra for estimating total organic carbon (TOC) contents in dried sediment lag samples, and confirmed this high predictive accuracy. Nevertheless, transferring the knowledge gained from high-resolution dried samples to low-resolution spectra for suspended sediment is challenging. Further experimental work will be necessary to ensure that NIR spectra measured from suspended sediments in river water at varying concentrations remain accurate for predicting tracer properties. In addition, the careful inter-calibration of infrared sensors would remain crucial. Nevertheless, NIR technology holds significant potential, as previous research has demonstrated its capacity in predicting a variety of soil properties, including complex parameters (Summers et al., 2011; Rossel and Webster, 2012; Brosinsky et al., 2014; Shi et al., 2020). Moreover, integrating Internet of Things (IoT) technology could enable real-time remote data acquisition, enhancing our ability to monitor sediment transfers during events. This would significantly improve our understanding of erosion and sediment transfer processes and guide the design of more effective, real-time landscape management measures.

The assessment of the origin of sediments using source-to-sink fingerprinting techniques, initially designed to better understand erosion processes, were increasingly used over time as a tool to guide landscape management in order to mitigate soil erosion. Therefore, in the current context of accelerating soil erosion, exacerbated by global warming (OCC, 2015), sediment source fingerprinting has gained increasing interest from the scientific community (Collins et al., 2020; Evrard et al., 2022). Nevertheless, despite attempts to simplify and homogenise the approach, sediment source fingerprinting remains likely too complex for its direct practical application by stakeholders involved in landscape management, restricting its application to the scientific community alone. The research conducted in Chapter I, demonstrated that both the variants of the conventional three-step method (TSM) (Collins et al., 2010; Wilkinson et al., 2013; Laceby et al., 2015) and the consensus method (CM) (Lizaga et al., 2020) have not yet made significant progress towards this objective.

The current fingerprinting approach is based on selecting tracer properties that meet two criteria: they must distinguish between potential sediment sources and maintain a conservative behaviour throughout the erosion process. Between both criteria, assessing the conservative behaviour is the main challenge as it was shown



Figure GD.1: Damaged concrete river bank after the occurrence of the Typhoon Etau in September 2015 at the inlet of the Mano Dam reservoir (© Olivier Evrard - 2 November 2015).

to strongly decrease the overall un-mixing model quality (Sherriff et al., 2015; Smith et al., 2018; Vale et al., 2022). The CM approach, proposed by Lizaga et al. (2020), introduced the Conservativity Index (CI), which is an estimate of the extent to which a property deviates from its theoretical undisturbed values. Conversely, the TSM relies on range tests that exclude non-conservative properties when the target sample values fall outside of the range of source values. However, range tests cannot detect property changes corresponding to source variability. This limitation became apparent when comparing the predicted contribution spaces of the virtual mixtures - generated based on strict conservativity assumptions - with actual sediment data. Indeed, when the predicted contributions of actual sediment samples were outside of the expected range defined by the predicted contributions of the virtual mixtures, it suggests the non-respect of some assumptions made when generating the virtual mixtures. This could be related to the non-respect of the strict conservative behaviour of the selected tracers and/or to a mis-identification or a mis-classification of the potential sources. While the incorrect consideration of potential contributing sources could be improved by a better understanding of the local environmental conditions and while a mis-classification could be detected by a clustering approach and potentially resolved through conducting additional analyses, the consideration of non-conservative behaviour requires new methodological advancements.

Therefore, when considering the theoretical value of a property of a target sediment that results from the mixture of n sources, the relationship is as follows:

$$p_t = c_{S1}\, p_{S1} + c_{S2}\, p_{S2} + ... + c_{Sn}\, p_{Sn} = \sum_{i=1}^{n} (c_{Si}\, p_{Si}) \tag{1}$$

where p_t is the property values of the target sample, p_{Si} the mean value of the i^{th} source class among n source class, and c_{Si} the contribution of the i^{th} source class between 0 and 1.

When considering non-conservative behaviour, the perturbation/corruption factor (w) of the property value during erosion processes can be assumed to change the relationship as follows:

$$p_t = \sum_{i=1}^{n} (c_{Si}\, p_{Si}) \cdot w \tag{2}$$

where w is the degree to which the property was modified/corrupted during erosion processes. A negative value indicates a diminution of the property value while a positive value indicates an increase of the property value.

When considering the use of several tracer properties, the relationship between the properties of the target sediment sample and the mean properties of sources could be expressed as the following matricial equations:

$$P_t = C \cdot P_S \cdot W \tag{3}$$

$$\begin{bmatrix} p_{t\,1} & \cdots & p_{t\,m} \end{bmatrix} = \begin{bmatrix} c_{S1} & \cdots & c_{Sn} \end{bmatrix} \cdot \begin{bmatrix} p_{S1\,1} & \cdots & p_{Sn\,1} \\ \vdots & \ddots & \vdots \\ p_{S1\,m} & \cdots & p_{Sn\,m} \end{bmatrix} \cdot \begin{bmatrix} w_1 \\ \vdots \\ w_m \end{bmatrix} \tag{4}$$

where P_t is the vector of the m property values of the target sample ($p_{t\,m}$; dimension 1×m), C the vector of the contribution of the source classes ($c_{Sn\,m}$; dim. 1×n), P_S is the matrix of the m property mean values of the n source classes ($p_{Sn\,m}$; dim. n×m), and W the column matrix of the m properties corruption factors (w_m; dim. m×1).

To assess the extent to which diagnostic properties are altered during erosion processes, experiments could be conducted in the field or under controlled laboratory conditions. However, the degree of alteration is influenced by a complex interplay of factors, including environmental conditions such as temperature, pH and redox potential, as well as biological processes and the composition of organic matter. Given the complexity of these interactions, results are likely to be site- and condition-specific. An alternative strategy would be to use modelling with machine learning tools. However, the effectiveness of machine learning models is highly dependent on the quality and size of the training dataset, which must include labelled data (i.e. response and observation variables). In practice, sediment source fingerprinting studies only provide information on the properties of the target (P_t) and source classes (P_S), while ignoring source contributions (C) and degradation levels (W). Nevertheless, virtual mixtures, which have been shown to provide a reliable alternative to laboratory mixtures (Batista et al., 2022), could be used to overcome this limitation by providing large datasets of labelled data.

To build a suitable machine learning dataset, the contributions of the source groups in the virtual mixtures must cover variable conditions to encompass all possible combinations (C). The properties of each virtual mixture (P_t) would then be calculated using the source property values (P_S) and their respective contribution combinations, according to the formula: $P_t = C \cdot P_S$. At this stage, the dataset could be used to train a machine learning un-mixing model to predict source contributions (C) using the virtual mixture properties (P_t) and source classes (P_S) as observation variables. To simulate the influence of erosion processes, several corruption vectors (W) should be applied to each virtual mixture property (P_t). However, since the number of possible combinations of corruption factors increases exponentially with the number of properties and the range of disturbances considered, a random generation approach would be more efficient. Multiple corruption vectors should be applied to each virtual mixture to significantly increase the number of corruption scenarios explored. Finally, by training a machine learning model to predict source contributions (C) and corruption factors (W) using the properties of the virtual mixtures (P_t) and source classes (P_S) as observation variables,

it would be possible to predict both the potential contribution of sources and the degree of corruption of each property in real sediment samples.

The validation of this type of machine learning based un-mixing model could be assessed through controlled laboratory experiments on laboratory mixtures. If the model structure is found to be reliable, such a modelling structure could be applied to a wide range of sediment source fingerprinting studies in different contexts without the need of conducting additional field sampling or analyses, as long as a representative dataset of source classes is available. In addition, because machine learning models self-adjust by weighting relevant information, uninformative variables are ignored or minimised. This would have the advantage of integrating data that is difficult to incorporate into conventional Bayesian un-mixing models (e.g. MixSIAR or BMM), such as spectral data. Furthermore, once a machine learning model has been trained, it provides rapid predictive capabilities that could support real-time analysis. For example, real-time source contributions could be estimated using remotely acquired turbidity and NIR spectra from multiple monitoring stations. The development would support a better understanding of erosion and sediment transport processes, enabling more effective landscape and pollution management, as well as providing a tool to investigate the evolution of organic and geochemical properties along erosion processes.

Conclusive remarks

This thesis has endeavoured to reconstruct sediment and radiocesium transfers in coastal rivers draining the main radioactive plume generated by the FDNPP accident, covering the periods of land abandonment, decontamination, until that of resumption of agricultural activities. To achieve this goal, various sediment matrices, including sediment cores and lag deposits collected in three contrasted catchments under different dominant land uses and management modes after the FDNPP accident, were analysed. Transfers of sediment and radiocesium, mainly driven by intense rainfall events, such as typhoons or tropical storms, revealed the occurrence of substantial changes over the last thirteen years following the accident, mainly as the result of rapid and drastic changes in land uses and covers. In the agricultural catchments, ^{137}Cs activity in the sediment gradually decrease over time during the abandonment phase, in response to the increasing protective effect of spontaneous vegetation regrowth on abandoned farmland. In the Mano Dam catchment, decontamination (late 2016) led to further decrease ^{137}Cs activity in sediment, along with a significant sediment contribution from 'fresh soil' materials. However, decontamination was not associated with a decrease in ^{137}Cs deposition flux, which remained similar to that observed during the last year of the abandonment phase (2014-2016). This was associated to the stable quantitative contribution of material originating from forests, supplying ^{137}Cs contaminated sediment that was diluted by the 'fresh soil', resulting in an overall decrease of ^{137}Cs activity levels in the sediment and similar ^{137}Cs deposition fluxes in the sediment. This highlights the protective effect of vegetation, which, as observed in the undecontaminated Ogaki Dam catchment, further reduced ^{137}Cs and sediment transfers to the river system, over time. In contrast, in forested areas that were not targeted by the decontamination programme, a delay of three to five years in radiocesium transfers was observed compared to observations made in decontaminated areas, in response to the natural cycles of leaf litter and canopy foliage renewal. Despite the differences in dominant land uses and differing management, sediment and radiocesium transfers stabilised relatively rapidly in all catchments, suggesting that similar source mixtures continued to contribute to the transfer of contaminated material, and were not fully addressed by decontamination.

Nonetheless, decontamination program successfully achieved its primary goal of reducing ambient air dose rates, allowing the gradual lifting of evacuation orders, the resumption of agricultural activities, and the re-

turn of residents if they accepted to do so. However, despite the scale of the decontamination programme — involving a large number of workers, producing significant quantities of waste, and a cost of around JPY 1,500 billion (about EUR 11 billion at the 2017 rate of EUR 1 = JPY 130) (MoE, 2018b) — only a small proportion of evacuated residents returned (Taira et al., 2020; Asanuma-Brice et al., 2023). Several factors have contributed to the low return rate, including changes in living conditions (such as family separations and loss of community life), the lack of infrastructure and public services, concerns over radiation exposure, and restrictions on outdoor activities like hiking, freshwater fishing, and traditional plant/mushroom harvesting. In addition, since the decontaminated areas cover a limited portion of the overall region, most of the initial deposition stock of radiocesium remains stored in non-decontaminated forested regions. This raises considerations about the appropriateness of conducting such a large-scale decontamination programme, investing significant manpower and financial resources, to restore a limited portion of the landscape in which only a minor percentage of the initial residents decided to return.

Nevertheless, the unique circumstances of the FDNPP accident, with its rapid and widespread release of contaminants followed by the cessation of human activity over a large area, provided a rare opportunity to deepen our understanding of environmental dynamics, such as those in plant and animal ecology, forest ecology, and hydrology. This research specifically focused on improving our understanding of the erosion-driven transfer of pollutants with a strong affinity for fine soil particles. The lessons learned from this event could pave the way for designing more sustainable pollution management strategies relying on natural-based solutions, applicable to similar or other widespread contaminants such as pesticides, herbicides, and pharmaceuticals, which can persist in the environment and impact both ecosystems and human health over time, accentuated by a context of an increasing number and acceleration of environmental hazards (e.g. fire, extreme precipitation, increasing strength of typhoon) in relation to global warming.

References

Asanuma-Brice, C., Evrard, O., Chalaux, T., 2023. Why did so few refugees return to the Fukushima fallout-impacted region after remediation? An interdisciplinary case study from Iitate village, Japan. International Journal of Disaster Risk Reduction 85, 103498. URL: https://linkinghub.elsevier.com/retrieve/pii/S2212420922007178, doi:10.1016/j.ijdrr.2022.103498.

Ayabe, Y., Hijii, N., Takenaka, C., 2017. Effects of local-scale decontamination in a secondary forest contaminated after the Fukushima nuclear power plant accident. Environmental Pollution 228, 344–353. URL: https://linkinghub.elsevier.com/retrieve/pii/S0269749116319704, doi:10.1016/j.envpol.2017.05.041.

Batista, P.V.G., Laceby, J.P., Evrard, O., 2022. How to evaluate sediment fingerprinting source apportionments. Journal of Soils and Sediments 22, 1315–1328. URL: https://link.springer.com/10.1007/s11368-022-03157-4, doi:10.1007/s11368-022-03157-4.

Bishop, T., 2024. itraxR: Itrax Data Analysis Tools. URL: https://CRAN.R-project.org/package=itraxR.

Brosinsky, A., Foerster, S., Segl, K., López-Tarazón, J.A., Piqué, G., Bronstert, A., 2014. Spectral fingerprinting: Characterizing suspended sediment sources by the use of VNIR-SWIR spectral information. Journal of Soils and Sediments 14, 1965–1981. URL: http://link.springer.com/10.1007/s11368-014-0927-z, doi:10.1007/s11368-014-0927-z.

Chalaux-Clergue, T., Foucher, A., Chaboche, P.A., Hayashi, S., Tsuji, H., Wakiyama, Y., Huon, S., Vandromme, R., Cerdan, O., Nakao, A., Evrard, O., 2024. Impacts of farmland decontamination on 137Cs transfers in rivers after Fukushima nuclear accident: Evidence from a retrospective sediment core study. Science of The Total Environment 947, 174546. URL: https://linkinghub.elsevier.com/retrieve/pii/S0048969724046941, doi:10.1016/j.scitotenv.2024.174546.

Chartin, C., Evrard, O., Laceby, J.P., Onda, Y., Ottlé, C., Lefèvre, I., Cerdan, O., 2017. The impact of typhoons on sediment connectivity: Lessons learnt from contaminated coastal catchments of the Fukushima Prefecture (Japan): Typhoon Impact on Sediment Connectivity - Fukushima, Japan. Earth Surface Processes and Landforms 42, 306–317. URL: https://onlinelibrary.wiley.com/doi/10.1002/esp.4056, doi:10.1002/esp.4056.

Collins, A., Walling, D., Webb, L., King, P., 2010. Apportioning catchment scale sediment sources using a modified composite fingerprinting technique incorporating property weightings and prior information. Geoderma 155, 249–261. URL: https://linkinghub.elsevier.com/retrieve/pii/S0016706109004066, doi:10.1016/j.geoderma.2009.12.008.

Collins, A.L., Blackwell, M., Boeckx, P., Chivers, C.A., Emelko, M., Evrard, O., Foster, I., Gellis, A., Gholami, H., Granger, S., Harris, P., Horowitz, A.J., Laceby, J.P., Martinez-Carreras, N., Minella, J., Mol, L., Nosrati, K., Pulley, S., Silins, U., da Silva, Y.J., Stone, M., Tiecher, T., Upadhayay, H.R., Zhang, Y., 2020. Sediment source fingerprinting: Benchmarking recent outputs, remaining challenges and emerging themes. Journal of Soils and Sediments 20, 4160–4193. URL: https://link.springer.com/10.1007/s11368-020-02755-4, doi:10.1007/s11368-020-02755-4.

Croudace, I.W., Rothwell, R.G. (Eds.), 2015. Micro-XRF Studies of Sediment Cores: Applications of a Non-Destructive Tool for the Environmental Sciences. volume 17 of *Developments in Paleoenvironmental Research*. Springer Netherlands, Dordrecht. URL: https://link.springer.com/10.1007/978-94-017-9849-5, doi:10.1007/978-94-017-9849-5.

Evrard, O., Batista, P.V.G., Company, J., Dabrin, A., Foucher, A., Frankl, A., García-Comendador, J., Huguet, A., Lake, N., Lizaga, I., Martínez-Carreras, N., Navratil, O., Pignol, C., Sellier, V., 2022. Improving the design and implementation of sediment fingerprinting studies: Summary and outcomes of the TRACING 2021 Scientific School. Journal of Soils and Sediments 22, 1648–1661. URL: https://link.springer.com/10.1007/s11368-022-03203-1, doi:10.1007/s11368-022-03203-1.

Evrard, O., Chalaux-Clergue, T., Chaboche, P.A., Wakiyama, Y., Thiry, Y., 2023. Research and management challenges following soil and landscape decontamination at the onset of the reopening of the Difficult-To-

Return Zone, Fukushima (Japan). SOIL 9, 479–497. URL: https://soil.copernicus.org/articles/9/479/2023/, doi:10.5194/soil-9-479-2023.

Evrard, O., Durand, R., Nakao, A., Laceby, P.J., Lefèvre, I., Wakiyama, Y., Hayashi, S., Asanuma-Brice, C., Cerdan, O., 2020. Impact of the 2019 typhoons on sediment source contributions and radiocesium concentrations in rivers draining the Fukushima radioactive plume, Japan. Comptes Rendus. Géoscience 352, 199–211. URL: https://comptes-rendus.academie-sciences.fr/geoscience/item/CRGEOS_2020__352_3_199_0, doi:10.5802/crgeos.42.

Evrard, O., Laceby, J.P., Ficetola, G.F., Gielly, L., Huon, S., Lefèvre, I., Onda, Y., Poulenard, J., 2019a. Environmental DNA provides information on sediment sources: A study in catchments affected by Fukushima radioactive fallout. Science of The Total Environment 665, 873–881. URL: https://linkinghub.elsevier.com/retrieve/pii/S0048969719306795, doi:10.1016/j.scitotenv.2019.02.191.

Evrard, O., Laceby, J.P., Nakao, A., 2019b. Effectiveness of landscape decontamination following the Fukushima nuclear accident: A review. SOIL 5, 333–350. URL: https://soil.copernicus.org/articles/5/333/2019/, doi:10.5194/soil-5-333-2019.

Evrard, O., Laceby, J.P., Onda, Y., Wakiyama, Y., Jaegler, H., Lefèvre, I., 2016. Quantifying the dilution of the radiocesium contamination in Fukushima coastal river sediment (2011–2015). Scientific Reports 6, 34828. URL: https://www.nature.com/articles/srep34828, doi:10.1038/srep34828.

Gomi, T., Sidle, R.C., Richardson, J.S., 2002. Understanding Processes and Downstream Linkages of Headwater Systems. BioScience 52, 905. URL: https://academic.oup.com/bioscience/article/52/10/905-916/354918, doi:10.1641/0006-3568(2002)052[0905:UPADLO]2.0.CO;2.

Hashimoto, S., Ugawa, S., Nanko, K., Shichi, K., 2012. The total amounts of radioactively contaminated materials in forests in Fukushima, Japan. Scientific Reports 2, 416. URL: https://www.nature.com/articles/srep00416, doi:10.1038/srep00416.

He, Q., Walling, D., 1996. Interpreting particle size effects in the adsorption of 137Cs and unsupported 210Pb by mineral soils and sediments. Journal of Environmental Radioactivity 30, 117–137. URL: https://linkinghub.elsevier.com/retrieve/pii/0265931X96892757, doi:10.1016/0265-931X(96)89275-7.

Huon, S., Hayashi, S., Laceby, J.P., Tsuji, H., Onda, Y., Evrard, O., 2018. Source dynamics of radiocesium-contaminated particulate matter deposited in an agricultural water reservoir after the Fukushima nuclear accident. Science of The Total Environment 612, 1079–1090. URL: https://linkinghub.elsevier.com/retrieve/pii/S0048969717319083, doi:10.1016/j.scitotenv.2017.07.205.

Jacq, K., Perrette, Y., Fanget, B., Sabatier, P., Coquin, D., Martinez-Lamas, R., Debret, M., Arnaud, F., 2019. High-resolution prediction of organic matter concentration with hyperspectral imaging on a sediment core. Science of The Total Environment 663, 236–244. URL: https://linkinghub.elsevier.com/retrieve/pii/S0048969719303699, doi:10.1016/j.scitotenv.2019.01.320.

Kato, H., Onda, Y., Gao, X., Sanada, Y., Saito, K., 2019. Reconstruction of a Fukushima accident-derived radiocesium fallout map for environmental transfer studies. Journal of Environmental Radioactivity 210, 105996. URL: https://linkinghub.elsevier.com/retrieve/pii/S0265931X18303308, doi:10.1016/j.jenvrad.2019.105996.

Kato, H., Onda, Y., Teramage, M., 2012. Depth distribution of 137Cs, 134Cs, and 131I in soil profile after Fukushima Dai-ichi Nuclear Power Plant Accident. Journal of Environmental Radioactivity 111, 59–64. URL: https://linkinghub.elsevier.com/retrieve/pii/S0265931X11002426, doi:10.1016/j.jenvrad.2011.10.003.

Koarashi, J., Atarashi-Andoh, M., Nishimura, S., Muto, K., 2020. Effectiveness of decontamination by litter removal in Japanese forest ecosystems affected by the Fukushima nuclear accident. Scientific Reports 10, 6614. URL: https://www.nature.com/articles/s41598-020-63520-8, doi:10.1038/s41598-020-63520-8.

Konoplev, A., Golosov, V., Wakiyama, Y., Takase, T., Yoschenko, V., Yoshihara, T., Parenyuk, O., Cresswell, A., Ivanov, M., Carradine, M., Nanba, K., Onda, Y., 2018. Natural attenuation of Fukushima-

derived radiocesium in soils due to its vertical and lateral migration. Journal of Environmental Radioactivity 186, 23–33. URL: https://linkinghub.elsevier.com/retrieve/pii/S0265931X17303296, doi:10.1016/j.jenvrad.2017.06.019.

Laceby, J.P., Chartin, C., Evrard, O., Onda, Y., Garcia-Sanchez, L., Cerdan, O., 2016a. Rainfall erosivity in catchments contaminated with fallout from the Fukushima Daiichi nuclear power plant accident. Hydrology and Earth System Sciences 20, 2467–2482. URL: https://hess.copernicus.org/articles/20/2467/2016/, doi:10.5194/hess-20-2467-2016.

Laceby, J.P., Huon, S., Onda, Y., Vaury, V., Evrard, O., 2016b. Do forests represent a long-term source of contaminated particulate matter in the Fukushima Prefecture? Journal of Environmental Management 183, 742–753. URL: https://linkinghub.elsevier.com/retrieve/pii/S0301479716306661, doi:10.1016/j.jenvman.2016.09.020.

Laceby, J.P., McMahon, J., Evrard, O., Olley, J., 2015. A comparison of geological and statistical approaches to element selection for sediment fingerprinting. Journal of Soils and Sediments 15, 2117–2131. URL: http://link.springer.com/10.1007/s11368-015-1111-9, doi:10.1007/s11368-015-1111-9.

Lepage, H., Evrard, O., Onda, Y., Lefèvre, I., Laceby, J.P., Ayrault, S., 2015. Depth distribution of cesium-137 in paddy fields across the Fukushima pollution plume in 2013. Journal of Environmental Radioactivity 147, 157–164. URL: https://linkinghub.elsevier.com/retrieve/pii/S0265931X15001484, doi:10.1016/j.jenvrad.2015.05.003.

Lizaga, I., Latorre, B., Gaspar, L., Navas, A., 2020. Consensus ranking as a method to identify non-conservative and dissenting tracers in fingerprinting studies. Science of The Total Environment 720, 137537. URL: https://linkinghub.elsevier.com/retrieve/pii/S0048969720310482, doi:10.1016/j.scitotenv.2020.137537.

López-Vicente, M., Onda, Y., Takahashi, J., Kato, H., Chayama, S., Hisadome, K., 2018. Radiocesium concentrations in soil and leaf after decontamination practices in a forest plantation highly polluted by the Fukushima accident. Environmental Pollution 239, 448–456. URL: https://linkinghub.elsevier.com/retrieve/pii/S0269749117345906, doi:10.1016/j.envpol.2018.04.045.

MoE, 2011. Basic Principles on the Act on Special Measures Concerning the Handling of Environment Pollution by Radioactive Materials Discharged by the Nuclear Power Station Accident Associated with the Tohoku District-Off the Pacific Ocean Earthquake That Occurred on March 11, 2011. Technical Report. Ministry of the Environment. Japan. URL: https://josen.env.go.jp/en/framework/pdf/basic_principles.pdf.

MoE, 2013. Decontamination Guidelines. Technical Report 2. Japanese Ministry of Environment. Japan.

MoE, 2015. Decontamination Report - A Compilation of Experiences to Date on Decontamination for the Living Environment Conducted by the Ministry of the Environment. Technical Report. Japanese Ministry of Environment. Japan. URL: http://josen.env.go.jp/en/policy_document/.

MoE, 2018a. Decontamination Projects for Radioactive Contamination Discharged by Tokyo Electric Power Company Fukushima Daiichi Nuclear Power Station Accident. Technical Report. Japanese Ministry of Environment.

MoE, 2018b. Environmental Remediation Updates. URL: http://josen.env.go.jp/en/policy_document/.

MoE, 2023. Decontamination status. URL: http://josen.env.go.jp/area/.

Morino, Y., Ohara, T., Watanabe, M., Hayashi, S., Nishizawa, M., 2013. Episode Analysis of Deposition of Radiocesium from the Fukushima Daiichi Nuclear Power Plant Accident. Environmental Science & Technology 47, 2314–2322. URL: https://pubs.acs.org/doi/10.1021/es304620x, doi:10.1021/es304620x.

Naulier, M., Eyrolle-Boyer, F., Boyer, P., Métivier, J.M., Onda, Y., 2017. Particulate organic matter in rivers of Fukushima: An unexpected carrier phase for radiocesiums. Science of The Total Environment 579, 1560–1571. URL: https://linkinghub.elsevier.com/retrieve/pii/S0048969716326304, doi:10.1016/j.scitotenv.2016.11.165.

OCC, 2015. Soil Is a Non-Renewable Resource. Technical Report. Food and Agriculture Organization of the United Nations. URL: https://www.fao.org/documents/card/en/c/ec28fc04-3d38-4e35-8d9b-e4427e20a4f7/.

Onda, Y., Taniguchi, K., Yoshimura, K., Kato, H., Takahashi, J., Wakiyama, Y., Coppin, F., Smith, H., 2020. Radionuclides from the Fukushima Daiichi Nuclear Power Plant in terrestrial systems. Nature Reviews Earth & Environment 1, 644–660. URL: https://www.nature.com/articles/s43017-020-0099-x, doi:10.1038/s43017-020-0099-x.

Osawa, K., Nonaka, Y., Nishimura, T., Tanoi, K., Matsui, H., Mizogichi, M., Tatsuno, T., 2018. Quantification of dissolved and particulate radiocesium fluxes in two rivers draining the main radioactive pollution plume in Fukushima, Japan (2013–2016). Anthropocene 22, 40–50. URL: https://linkinghub.elsevier.com/retrieve/pii/S2213305418300262, doi:10.1016/j.ancene.2018.04.003.

Rapuc, W., Jacq, K., Develle, A.L., Sabatier, P., Fanget, B., Perrette, Y., Coquin, D., Debret, M., Wilhelm, B., Arnaud, F., 2020. XRF and hyperspectral analyses as an automatic way to detect flood events in sediment cores. Sedimentary Geology 409, 105776. URL: https://linkinghub.elsevier.com/retrieve/pii/S0037073820301913, doi:10.1016/j.sedgeo.2020.105776.

Rossel, R.A., Webster, R., 2012. Predicting soil properties from the Australian soil visible-near infrared spectroscopic database. European Journal of Soil Science 63, 848–860. URL: https://onlinelibrary.wiley.com/doi/10.1111/j.1365-2389.2012.01495.x, doi:10.1111/j.1365-2389.2012.01495.x.

Sakai, M., Tsuji, H., Ishii, Y., Ozaki, H., Takechi, S., Jo, J., Tamaoki, M., Hayashi, S., Gomi, T., 2021. Untangling radiocesium dynamics of forest-stream ecosystems: A review of Fukushima studies in the decade after the accident. Environmental Pollution 288, 117744. URL: https://linkinghub.elsevier.com/retrieve/pii/S0269749121013269, doi:10.1016/j.envpol.2021.117744.

Sawhney, B.L., 1972. Selective Sorption and Fixation of Cations by Clay Minerals: A Review. Clays and Clay Minerals 20, 93–100. URL: https://doi.org/10.1346/CCMN.1972.0200208, doi:10.1346/CCMN.1972.0200208.

Sherriff, S.C., Franks, S.W., Rowan, J.S., Fenton, O., Ó'hUallacháin, D., 2015. Uncertainty-based assessment of tracer selection, tracer non-conservativeness and multiple solutions in sediment fingerprinting using synthetic and field data. Journal of Soils and Sediments 15, 2101–2116. URL: http://link.springer.com/10.1007/s11368-015-1123-5, doi:10.1007/s11368-015-1123-5.

Shi, P., Castaldi, F., Van Wesemael, B., Van Oost, K., 2020. Vis-NIR spectroscopic assessment of soil aggregate stability and aggregate size distribution in the Belgian Loam Belt. Geoderma 357, 113958. URL: https://linkinghub.elsevier.com/retrieve/pii/S0016706119310298, doi:10.1016/j.geoderma.2019.113958.

Smith, H.G., Karam, D.S., Lennard, A.T., 2018. Evaluating tracer selection for catchment sediment fingerprinting. Journal of Soils and Sediments 18, 3005–3019. URL: http://link.springer.com/10.1007/s11368-018-1990-7, doi:10.1007/s11368-018-1990-7.

Soriano-Disla, J.M., Janik, L.J., Viscarra Rossel, R.A., Macdonald, L.M., McLaughlin, M.J., 2014. The Performance of Visible, Near-, and Mid-Infrared Reflectance Spectroscopy for Prediction of Soil Physical, Chemical, and Biological Properties. Applied Spectroscopy Reviews 49, 139–186. URL: http://www.tandfonline.com/doi/abs/10.1080/05704928.2013.811081, doi:10.1080/05704928.2013.811081.

Summers, D., Lewis, M., Ostendorf, B., Chittleborough, D., 2011. Visible near-infrared reflectance spectroscopy as a predictive indicator of soil properties. Ecological Indicators 11, 123–131. URL: https://linkinghub.elsevier.com/retrieve/pii/S1470160X09000806, doi:10.1016/j.ecolind.2009.05.001.

Taira, Y., Matsuo, M., Yamaguchi, T., Yamada, Y., Orita, M., Takamura, N., 2020. Radiocesium levels in contaminated forests has remained stable, even after heavy rains due to typhoons and localized downpours. Scientific Reports 10, 19215. URL: https://www.nature.com/articles/s41598-020-75857-1, doi:10.1038/s41598-020-75857-1.

Taniguchi, K., Onda, Y., Smith, H.G., Blake, W., Yoshimura, K., Yamashiki, Y., Kuramoto, T., Saito, K., 2019. Transport and Redistribution of Radiocesium in Fukushima Fallout through Rivers. Environmental Science & Technology 53, 12339–12347. URL: https://pubs.acs.org/doi/10.1021/acs.est.9b02890, doi:10.1021/acs.est.9b02890.

Thiry, Y., Albrecht, A., Tanaka, T., 2018. Development and assessment of a simple ecological model (TRIPS) for forests contaminated by radiocesium fallout. Journal of Environmental Radioactivity 190–191, 149–159. URL: https://linkinghub.elsevier.com/retrieve/pii/S0265931X17309499, doi:10.1016/j.jenvrad.2018.05.009.

Vale, S., Swales, A., Smith, H.G., Olsen, G., Woodward, B., 2022. Impacts of tracer type, tracer selection, and source dominance on source apportionment with sediment fingerprinting. Science of The Total Environment 831, 154832. URL: https://linkinghub.elsevier.com/retrieve/pii/S0048969722019258, doi:10.1016/j.scitotenv.2022.154832.

Vandromme, R., Hayashi, S., Tsuji, H., Evrard, O., Grangeon, T., Landemaine, V., Laceby, J.P., Wakiyama, Y., Cerdan, O., 2023. Lessons learnt on the impact of an unprecedented soil decontamination program in Fukushima on contaminant fluxes. Proceedings of the National Academy of Sciences 120, e2301811120. URL: https://pnas.org/doi/10.1073/pnas.2301811120, doi:10.1073/pnas.2301811120.

Wilkinson, S.N., Hancock, G.J., Bartley, R., Hawdon, A.A., Keen, R.J., 2013. Using sediment tracing to assess processes and spatial patterns of erosion in grazed rangelands, Burdekin River basin, Australia. Agriculture, Ecosystems & Environment 180, 90–102. URL: https://linkinghub.elsevier.com/retrieve/pii/S0167880912000564, doi:10.1016/j.agee.2012.02.002.

Appendix

Appendix A

`fingR` package: A Support for Sediment Source Fingerprinting Studies



The `fingR` is a comprehensive package designed to support sediment source fingerprinting studies. It provides essential tools including: dataset characterisation, tracer selection from analysed properties using the three-step method, modelling of source contributions using the Bayesian Mixing Model (BMM), and evaluation of model predictions using virtual mixtures, and it supports BMM and MixSIAR models. The fingR package is available in a Github repository and is archived on Zenodo:

Chalaux-Clergue, T., & Bizeul, R. (2024).
fingR: A support for sediment source fingerprinting studies [R].
GitHub https://github.com/tchalauxclergue/fingR
Zenodo https://doi.org/10.5281/zenodo.8293595

The package can be cited using the DOI: https://doi.org/10.5281/zenodo.8293595. This DOI represents all versions, and will always resolve to the latest one.

In addition, data sharing is an important part of open science, making research more reliable and accessible to the community. Over the past few years, the sediment source fingerprinting community has been engaged in promoting best practices to improve the design and implementation of sediment fingerprinting techniques (Evrard et al., 2022). To move forward and improve data sharing, we propose these templates for databases and metadata (Appendix B):

Chalaux-Clergue, T., Bizeul, R., Foucher, A., & Evrard, O. (2024)
An unified template for sediment source fingerprinting databases
(Version 24.03.01) [Dataset]. https://doi.org/10.5281/ZENODO.10725788

These templates include: common metadata for samples (soil, lag deposits, sediment core, etc.) description (name, IGSN, location, sampling date, etc.), list and description of common properties (elemental geochemistry, organic matter, radionuclides, etc.) used in sediment source fingerprinting studies. These templates are intended to evolve thanks to the participation of the community, as part of a collaborative project.

To encourage the community, but also by way of example, the sediment source fingerprinting database of the study of the Mano Dam Down sediment core collected in 2021 has been published and made available on Zenodo (Chalaux-Clergue et al., 2022) (Appendix C):

Chalaux-Clergue, T., Evrard, O., Durand, R., Caumon, A., Hayashi, S., Tsuji, H., Huon, S., Vaury, V., Wakiyama, Y., Nakao, A., Laceby, J. P., & Onda, Y. (2022). **Organic matter, geochemical and colorimetric properties of potential source material, target sediment and laboratory mixtures for conducting sediment fingerprinting approaches in the Mano Dam Reservoir (Hayama Lake) catchment, Fukushima Prefecture, Japan.** (Version 1) [Dataset].
Zenodo. https://doi.org/10.5281/ZENODO.7081094

This database was used to illustrate the use of the fingR package.

A.1 - Installation

The user can instal the package from the Github repository or from the downloaded package (under tar.gr format).

```
# install.packages('devtools')
library('devtools')

# Install the 2.1.1 version from GitHub - check github page for updates
devtools::install_github("https://github.com/tchalauxclergue/fingR/releases/tag/2.1.1", ref = "master", force = TRUE)

# Alternatively, install from a downloaded '.tar.gz' file
devtools::install_local("path_to_file/fingR_2.1.1.tar.gz", repos = NULL)
# 'path_to_file' should be modified accordingly to your working environment
```

A.2 - Usage

To illustrate the usage of the `fingR` package, a database containing layers from a sediment core and potential sources samples was used. The 38 layers of a sediment core collected in the Mano Dam reservoir (Fukushima, Japan) in June 2021 were used as mixture targets. The potential source samples include four classes: undecontaminated cropland (n = 24), remediated cropland (n = 22), forest (n = 24), and subsoil (mainly granite saprolite; n = 24). All sediment and soil samples were sieved to 63 μm and analysed, the organic matter (total organic carbon (TOC), and total nitrogen (TN)) and elemental geochemistry by ED-XRF (Al, Ca, Co, Cr, Cu, Fe, K, Mg, Mn, Ni, Pb, Rb, Si, Sr, Ti, Zn, Zr) were used as potential tracer properties.

This dataset, along with detailed measurement protocols, is available for download on Zenodo at Chalaux-Clergue et al. (2022) (Version 2; https://doi.org/10.5281/zenodo.7081094).

A.2.1 - Data preparation

The first step is to load the database, in this guide it consists of a data file and a metadata file. To support database sharing and compatibility, a database template has been proposed and made available on Zenodo at Chalaux-Clergue et al. (2024b) (ver. 24.03.01; https://doi.org/10.5281/zenodo.10725788).

```
# Load the fingR package
library('fingR')

# Get the directory to data and metadata files within the fingR package
data.dr <- system.file("extdata", "TCC_MDD_20210608_data_ChalauxClergue_et_al_v240319.csv", package = "fingR")
metadata.dr <- system.file("extdata", "TCC_MDD_20210608_metadata_ChalauxClergue_et_al_v240319.csv", package = "fingR")
```

```

# Load the csv files of data and metadata - replace the dir with your file direction
db.data <- read.csv(data.dr, sep = ";", fileEncoding = "latin1", na = "")
db.metadata <- read.csv(metadata.dr, sep = ";", fileEncoding = "latin1", na = "")
```

The different classes of potential sources and sediment samples information is in the `Class_decontamination` column. In which, the `Target` class refers to sediment core layers, and other classes to potential sediment sources.

```
table(db.metadata$Class_decontamination)
```

```
>    Forest       Remediated       Subsoil       Target       Cropland
>        24               10            10           38             24
```

A.2.1.1 - Database construction

A single dataset is built by joining the metadata (general information) and the data (analyses) sub-datasets. Both metadata and data `data.frames` are joined by common variables, here using the columns `IGSN` and `Sample_name` (lines 5-7). In addition, two filters were applied. On line 8, a filter to keep the analyses performed on the fraction $\leq$ 63 μm. On line 9, a filter to remove remediated cropland from the dataset, and therefore using three potential sources.

```
library('dplyr')

# Create a single dataset with metadata and data information
database <- dplyr::left_join(x = db.metadata,
                             y = db.data,
                             by = join_by(IGSN, Sample_name)) %>%
    dplyr::filter(Sample_size == "< 63 µm") %>%
    dplyr::filter(Class_decontamination != "Remediated")
```

Therefore, the final dataset contains three potential sources (i.e. forest, subsoil, and undecontaminated cropland).

```
table(database$Class_decontamination)
```

```
>    Forest       Subsoil       Target       Cropland
>        24            10           38             24
```

A.2.1.2 - Selecting properties vectors

Among the analysed properties, a vector is created listing the column names of the values of the potential tracer properties, `prop.values` (lines 5-8).

```
1  # Display the database columns
2  # colnames(database)
3
4  # Select the column names of the properties values
5  prop.values <- database %>%
6      dplyr::select(TOC_PrC, TN_PrC,
7                    EDXRF_Al_mg.kg.1:EDXRF_Zr_mg.kg.1) %>%
8      base::names # Extract colunm names
9
10 prop.values
```

```
>  [1] "TOC_PrC"          "TN_PrC"           "EDXRF_Al_mg.kg.1"
>  [4] "EDXRF_Ca_mg.kg.1" "EDXRF_Co_mg.kg.1" "EDXRF_Cr_mg.kg.1"
>  [7] "EDXRF_Cu_mg.kg.1" "EDXRF_Fe_mg.kg.1" "EDXRF_K_mg.kg.1"
> [10] "EDXRF_Mg_mg.kg.1" "EDXRF_Mn_mg.kg.1" "EDXRF_Ni_mg.kg.1"
> [13] "EDXRF_Pb_mg.kg.1" "EDXRF_Rb_mg.kg.1" "EDXRF_Si_mg.kg.1"
> [16] "EDXRF_Sr_mg.kg.1" "EDXRF_Ti_mg.kg.1" "EDXRF_Zn_mg.kg.1"
> [19] "EDXRF_Zr_mg.kg.1"
```

A vector of property measurement uncertainty column names is also created, `prop.uncertainties` (lines 2-5). In order to maintain the relationship between the column names of the properties and the uncertainty, the column names of the properties are set as names of the vector of property names (line 8). This also simplifies the selection of the uncertainty column names, as they can be selected from the property column names.

```
1  # Select the column names of the property measurement uncertainties values
2  prop.uncertainties <- database %>%
3      dplyr::select(TOC_SD, TN_SD,
4                    EDXRF_Al_RMSE:EDXRF_Zr_RMSE) %>%
5      base::names
6
7  # Set property names to property uncertainty names for easier selection
8  base::names(prop.uncertainties) <- prop.values
9
10 unname(prop.uncertainties)
```

```
>  [1] "TOC_SD"         "TN_SD"          "EDXRF_Al_RMSE"
>  [4] "EDXRF_Ca_RMSE" "EDXRF_Co_RMSE" "EDXRF_Cr_RMSE"
>  [7] "EDXRF_Cu_RMSE" "EDXRF_Fe_RMSE" "EDXRF_K_RMSE"
> [10] "EDXRF_Mg_RMSE" "EDXRF_Mn_RMSE" "EDXRF_Ni_RMSE"
> [13] "EDXRF_Pb_RMSE" "EDXRF_Rb_RMSE" "EDXRF_Si_RMSE"
> [16] "EDXRF_Sr_RMSE" "EDXRF_Ti_RMSE" "EDXRF_Zn_RMSE"
> [19] "EDXRF_Zr_RMSE"
```

A.2.1.3 - Evaluation of measurement quality

The `data.watcher` function allows to check the format of the selected properties. The function verifies if the values of the property are all negative (e.g. $\delta^{13}C$, $\delta^{15}N$), which will require an inversion of the value prior to Bayesian modelling where the data is systematically log-transformed, and if some samples have negative values, which will require manual verification or correction of the data. If the measurement uncertainties are provided to the `prop.uncer` argument, the function will indicate if the measurement uncertainty makes some values virtually impossible, and will give the maximum relative uncertainty if it is greater than 5 %. The result of this function should encourage the user to consider the quality of his data.

```
fingR::data.watcher(data = database,
                    properties = prop.values,
                    prop.uncer = prop.uncertainties)
```

```
> Following column(s) contain(s) some negative values: EDXRF_Cr_mg.kg.1.
> Following column(s) have a measurement uncertainty that makes some values↩
     to be virtually impossible: EDXRF_Co_mg.kg.1, EDXRF_Cr_mg.kg.1, EDXRF_↩
    Cu_mg.kg.1, EDXRF_Ni_mg.kg.1.
> Following column(s) have a relative measurement uncertainty above 5% (up ↩
    to - number): EDXRF_Co_mg.kg.1 (max:753% - n:26), EDXRF_Cr_mg.kg.1 (max↩
    :211% - n:38), EDXRF_Ni_mg.kg.1 (max:105% - n:96), EDXRF_Cu_mg.kg.1 (↩
    max:103% - n:52), EDXRF_Rb_mg.kg.1 (max:89% - n:93), TN_PrC (max:45% - ↩
    n:91), EDXRF_Pb_mg.kg.1 (max:38% - n:91), EDXRF_Zn_mg.kg.1 (max:34% - n↩
    :96), EDXRF_Sr_mg.kg.1 (max:15% - n:46), TOC_PrC (max:14% - n:95), ↩
    EDXRF_Zr_mg.kg.1 (max:7% - n:2).
```

According to the `data.watcher` function, some samples have negative ED-XRF Cr values and the Co, Cr, Cu, Ni and Rb appear to be high. These properties are removed from the properties used in the following guide.

```
# Remove the properties listed from the vector of properties
prop.values <- prop.values[!prop.values %in% c("EDXRF_Co_mg.kg.1", "EDXRF_↩
    Cr_mg.kg.1", "EDXRF_Cu_mg.kg.1", "EDXRF_Ni_mg.kg.1", "EDXRF_Rb_mg.kg.1"↩
    )]

prop.values
```

```
>  [1] "TOC_PrC"          "TN_PrC"           "EDXRF_Al_mg.kg.1"
>  [4] "EDXRF_Ca_mg.kg.1" "EDXRF_Fe_mg.kg.1" "EDXRF_K_mg.kg.1"
>  [7] "EDXRF_Mg_mg.kg.1" "EDXRF_Mn_mg.kg.1" "EDXRF_Pb_mg.kg.1"
> [10] "EDXRF_Si_mg.kg.1" "EDXRF_Sr_mg.kg.1" "EDXRF_Ti_mg.kg.1"
> [13] "EDXRF_Zn_mg.kg.1" "EDXRF_Zr_mg.kg.1"
```

As well the measurement uncertainties of these properties are removed from the selection.

```
# Keep uncertainties associated to the new vector of properties
prop.uncertainties <- prop.uncertainties[prop.values]
```

```
prop.uncertainties
```

```
>  [1] "TOC_SD"         "TN_SD"          "EDXRF_Al_RMSE"
>  [4] "EDXRF_Ca_RMSE" "EDXRF_Fe_RMSE" "EDXRF_K_RMSE"
>  [7] "EDXRF_Mg_RMSE" "EDXRF_Mn_RMSE" "EDXRF_Pb_RMSE"
> [10] "EDXRF_Si_RMSE" "EDXRF_Sr_RMSE" "EDXRF_Ti_RMSE"
> [13] "EDXRF_Zn_RMSE" "EDXRF_Zr_RMSE"
```

A.3 - Tracer selection

A.3.1 - Conservative behaviour

The three-step method assesses conservative behaviour using range tests (RT), also known as bracket tests. For a property to be considered conservative, the values of each target sample must fall within the range of potential source classes. This range is defined by the highest and lowest values in a given source class for a given criterion. The **`range.test`** function allows the calculation of the range test on each property according to multiple range test criteria.

Several range test criteria have been documented, including minimum-maximum (`MM`), minimum-maximum with a 10 % margin of error (`MMe`), boxplot whiskers (outlier exclusion threshold), boxplot hinges (representing the middle 50 %), mean, mean plus/minus one standard deviation (`mean.sd`), and median. For the mean and mean.sd criteria, log-transformed values are used, assuming a normal distribution. The function applies all criteria by default (`criteria = c("all")`), or the user can freely select several tests from the following list: `MM` , `MMe` , `whiskers` , `hinge` , `mean` , `mean.sd` and/or `median` . Their effectiveness in detecting conservative properties varies. Among them, the `mean.sd` criterion is mathematically the most robust.

The **`range.test`** function outputs a list with two data frames:

- `$results.df` : A summary overview of all properties range test outcomes.
- `$results.RT` : Detailed range test results for each target sample across properties, where `TRUE` indicates that the sample value is within the range, while `high` and `low` indicate values outside the range.

Within the **`range.test`** function, the `class` argument specifies the column name containing the classifications for potential source and target mixture samples. The label for the target mixtures used in `class` should be provided in the `mixture` argument. The `sample.id` argument designates the column containing the unique identifiers or labels for each sample. When a saving directory path the results is provided to `save.dir` , the function write two CSV files: "RT_samples[_note].csv" corresponding to `results.RT` , and "Range_test[_note].csv" corresponding to `results.df` .

```
rt.results <- fingR::range.tests(data = database,
                                 class = "Class_decontamination",
                                 mixture = "Target",
                                 properties = prop.values,
                                 sample.id = "Sample_name",
                                 criteria = c("mean.sd")
                                 # MM.error = c(0.1),
                                 # save.dir = dir.example,
                                 # note = "example"
                                 )

# Results of the mean.sd range test for all properties
rt.results$results.df
```

```
>            Property n_source n_mixture NAs RT_mean.sd_single
> 1            TOC_PrC       58        38   0              TRUE
> 2             TN_PrC       58        38   0              TRUE
> 3  EDXRF_Al_mg.kg.1       58        38   0              TRUE
> 4  EDXRF_Ca_mg.kg.1       58        38   0             FALSE
> 5  EDXRF_Fe_mg.kg.1       58        38   0             FALSE
> 6   EDXRF_K_mg.kg.1       58        38   0             FALSE
> 7  EDXRF_Mg_mg.kg.1       58        38   0             FALSE
> 8  EDXRF_Mn_mg.kg.1       58        38   0             FALSE
> 9  EDXRF_Pb_mg.kg.1       58        38   0             FALSE
> 10 EDXRF_Si_mg.kg.1       58        38   0             FALSE
> 11 EDXRF_Sr_mg.kg.1       58        38   0             FALSE
> 12 EDXRF_Ti_mg.kg.1       58        38   0              TRUE
> 13 EDXRF_Zn_mg.kg.1       58        38   0             FALSE
> 14 EDXRF_Zr_mg.kg.1       58        38   0             FALSE
```

The result of the range test for some target samples and a property that did not pass the range test.

```
rt.results$results.RT$EDXRF_Pb_mg.kg.1[1:5,]
```

```
>      Sample_name Property          n_source RT_mean.sd
> 1 MDd_2106_00-01 EDXRF_Pb_mg.kg.1       58       TRUE
> 2 MDd_2106_01-02 EDXRF_Pb_mg.kg.1       58       TRUE
> 3 MDd_2106_02-03 EDXRF_Pb_mg.kg.1       58       high
> 4 MDd_2106_03-04 EDXRF_Pb_mg.kg.1       58       high
> 5 MDd_2106_04-05 EDXRF_Pb_mg.kg.1       58       TRUE
```

Based on the `$results.df` data frame from `range.tests`, the `is.conservative` function filter the properties that passed the range tests for each criterion, and returns a list of vectors. Each vector contains the names of the properties that were identified as conservative according to each criterion.

```r
prop.cons <- fingR::is.conservative(data = rt.results$results.df,
                                    # property = "Property",
                                    # test.format = "RT",
                                    # position = 2,
                                    # separator = "_",
                                    # note = "example"
                                    )

prop.cons
```

```
> $mean.sd
> [1] "TOC_PrC" "TN_PrC" "EDXRF_Al_mg.kg.1" "EDXRF_Ti_mg.kg.1"
```

A.3.2 - Discriminant power

The three-step method evaluates the ability of the traits to discriminate between source groups using a statistical test to test whether or not samples are from the same distribution. Conventionally, the non-parametric Kruskal-Wallis H test (KW) is used. The KW test is an extension of the two-sample Mann-Whitney U test. As an alternative to the KW test, the two-sample Kolmogorov-Smirnov (KS) test could be used. The KS test allows for a more detailed understanding of the discrimination between pairs of source groups. For instance, the KS tests for for three source groups will be structed as: source A vs. source B, source A vs. source C, and source B vs source C. The `discriminant.test` function allows the calculation of the discriminant power of each property. By setting the using the `test` argument to `KW` or `KS`, the Kruskal-Wallis H-test or Kolmogorov-Smirnov test is carried out.

When using the KS test (`test = "KW"`), the significance of the test *p* value is commonly set to 5 % (`p.level = 0.05`). Whilst, when using the Kolmogorov-Smirnov test (`test = "KS"`), which is highly sensitive to distribution differences, the significance of the test *p* value could be set to lower value, for instance, 1 % (`p.level = 0.01`).

Two CSV files will be written if the path to the save directory is given to the `save.dir` argument:

- 'Discriminant_pairs[_note].csv', generated if `save.discrim.tests = TRUE` (default), contains the *p* value of each two-samples KS tests for each property. Set `return.tests = TRUE` to return this table as `$result.KS` (default is `FALSE`). Of note, when using the KW test, the KS test results can also help verify the KW assumption of similar distribution shape across groups.
- 'Discriminant_tests[_note].csv' summarises the results from KS or KW tests.
  - For `test = "KW"` , the number of groups that follows a similar distribution shape(`n.similar.groups`) is reported. If this value matches the total number of source groups, the the assumption of similar distribution shapes is satisfied (`respect.KW.shape.assumption`). The table also includes the *p* value (`KW_p.value`) and its significance (`KW_signif`) for each properties.
  - For `test = "KS"` , the number of statistically different groups (`n.diff.groups`) is reported, and if it is at least equal to the threshold (`min.discriminant = 1`) required to identify a property as discriminant, the property is marked as discriminant in `KS_discriminant` .

Example for KW test:

```
KW.results <- fingR::discriminant.test(data = database,
                                       class = "Class_decontamination",
                                       mixture = "Target",
                                       test = "KW",
                                       properties = prop.values,
                                       p.level = 0.05,
                                       # min.discriminant = 1,
                                       # save.discrim.tests = TRUE,
                                       return.tests = TRUE,
                                       # save.dir = dir.example,
                                       # note = "example"
                                       )

KW.results$result.KS[1:3,]
```

```
>   Property Source_A Source_B n_source_A n_source_B KS_p.value KS_signif
> 1 TOC_PrC    Forest  Subsoil         24         10   1.01e-06        ***
> 2 TOC_PrC    Forest Cropland         24         24   4.57e-06        ***
> 3 TOC_PrC   Subsoil Cropland         10         24   1.34e-06        ***
```

```
KW.results$results.df[1:5,]
```

```
>   Property n.similar.groups respect.KW.shape.ass... KW_p.value KW_signif
> 1  TOC_PrC                0                   FALSE     0.00000        ***
> 2   TN_PrC                0                   FALSE     0.00000        ***
> 3 ...Al...                0                   FALSE     0.00000        ***
> 4 ...Ca...                1                   FALSE     0.00000         **
> 5 ...Fe...                3                    TRUE     0.79411
```

Example for KS test:

```
KS.results <- fingR::discriminant.test(data = database,
                                       class = "Class_decontamination",
                                       mixture = "Target",
                                       test = "KS",
                                       properties = prop.values,
                                       p.level = 0.05,
                                       # min.discriminant = 1,
                                       # save.discrim.tests = TRUE,
                                       return.tests = TRUE,
                                       # save.dir = dir.example,
                                       # note = "example"
                                       )

KS.results$result.KS[1:3,]
```

```
>   Property Source_A Source_B n_source_A n_source_B KS_p.value KS_signif
> 1 TOC_PrC    Forest  Subsoil          24          10   1.01e-06        ***
> 2 TOC_PrC    Forest Cropland          24          24   4.57e-06        ***
> 3 TOC_PrC   Subsoil Cropland          10          24   1.34e-06        ***
```

```
KS.results$results.df[1:5,]
```

```
>           Property n.diff.groups KS_discriminant
> 1          TOC_PrC             3            TRUE
> 2           TN_PrC             3            TRUE
> 3 EDXRF_Al_mg.kg.1             3            TRUE
> 4 EDXRF_Ca_mg.kg.1             1            TRUE
> 5 EDXRF_Fe_mg.kg.1             0           FALSE
```

The results from the KS test are used for the following guide.

Based on the `$results.df` data frame from `discriminant.test`, the `is.discriminant` function filter out the properties that passed the discriminant power tests according to the set *p* value (`p.level`) as list them in a vector. The function recognise the structure of the data frame produced by the `discriminant.test` function, however, it is possible to set it for other data frame format by setting its arguments.

```
prop.discrim <- fingR::is.discriminant(KS.results$results.df,
                                       # property = "Property",
                                       # test.format = "KS_p.value",
                                       # position = 1,
                                       # separator = "_",
                                       # p.level = 0.05,
                                       # note = "example"
                                       )

prop.discrim
```

```
> $KS
>  [1] "TOC_PrC"          "TN_PrC"           "EDXRF_Al_mg.kg.1"
>  [4] "EDXRF_Ca_mg.kg.1" "EDXRF_K_mg.kg.1"  "EDXRF_Pb_mg.kg.1"
>  [7] "EDXRF_Si_mg.kg.1" "EDXRF_Sr_mg.kg.1" "EDXRF_Zn_mg.kg.1"
> [10] "EDXRF_Zr_mg.kg.1"
```

A.3.3 - Identified tracers: conservative and discriminant properties

The properties that pass both the evaluation of conservative behaviour (`prop.cons` from `is.conservative`) and discriminant power (`prop.discrim` from `is.discriminant`) are compared by the `selected.tracers` function, which list in a vector.

```
tracers <- fingR::is.tracers(cons = prop.cons,
                             discrim = prop.discrim)
```

```

tracers
```

```
> $mean.sd_KS
> [1] "TOC_PrC"          "TN_PrC"           "EDXRF_Al_mg.kg.1"
```

A.3.4 - Discriminant Function Analysis stepwise selection

Frequently, a Discriminant Function Analysis (DFA) stepwise selection is applyed on the selected tracers. The DFA stepwise selection aims to retain the tracers that maximise source discrimination. Of note, the DFA stepwise selection has been criticised since its use is associated to a reduction of the number of tracers, especially since some studies showed that the use of a higher number of tracers decreases the sensitivity of sediment source fingerprinting modelling to non-conservative tracers (Martínez-Carreras et al., 2008; Sherriff et al., 2015). In addition, it is not useful for small selection of tracers, as it is the case here.

The `stepwise.selection` function allows to apply a forward stepwise selection based on the tracer selected, and returns a vector containing the retained tracers.

```
tracers.SW <- fingR::stepwise.selection(data = database,
                                        class = "Class_decontamination",
                                        tracers = tracers$mean.sd_KS,
                                        target = "Target"
                                        # save.dir = dir.example,
                                        # note = "example"
                                        )

tracers.SW
```

```
> [1] "EDXRF_Al_mg.kg.1" "TOC_PrC"          "TN_PrC"
```

Here, the stepwise selection did not remove any of the selected tracers. However, if the stepwise selection resulted in different tracers, examining the modelling results for both sets may provide useful insights. Both tracer selection vectors could be joint in a list as follows:

```
all.tracers <- list("mean.sd_KS" = tracers$mean.sd_KS,
                    "mean.sd_KS_DFA" = tracers.SW)
```

A.4 - Source Contribution Modelling

A.4.1 - Virtual Mixtures Generation

To evaluate the accuracy of unmixing models, virtual mixtures could be used as a reliable alternative to laboratory mixtures (Batista et al., 2022). These artificial mixtures (virtual or laboratory made) act as target samples with known contributions, enabling for the calculation of modelling accuracy metrics. In addition, the ease of virtual mixture generation allows to explore a wide range of source contribution combinations.

The `VM.contrib.generator` function allows a combination of source contributions to be generated. The contributions are designed to range from a minimum value (`min`) to a maximum value (`max`) by a specified step (`step`). The function first creates a contribution sequence for the first group of sources, from `min` to `max` according to the `step` (e.g. `min = 0` , `max = 100` , `step = 5` : 0, 5, 10, ... 100). The following sources are then defined as the remaining maximum after the specified step. The contributions can be generated as a percentage (e.g. `min = 0` and `max= 100`) or as a ratio (e.g. `min = 0` and `max= 1`). A small increment results in a higher number of virtual mixtures. For example, three sources with 5 % increment (`min = 0` , `max = 100` , `step = 5`) generated 231 contribution combinations, and 5151 contribution combinations with 1 % increment (`step = 1`).

The contribution combination data frame is saved ('VM_contributions[_note][number of virtual mixtures].csv') in the save directory specified by the `save.dir` argument.

```
VM.contrib <- fingR::VM.contrib.generator(n.sources = 3,
                                          min = 0,
                                          max = 100,
                                          step = 5,
                                          sources.class = c("Forest", "Subsoil", "Cropland"),
                                          save.dir = dir.example,
                                          # note = "example"
                                          # VM.name = "Sample_name",
                                          # fileEncoding = "latin1",
                                          # return = TRUE,
                                          # save = TRUE
                                          )

VM.contrib[1:5,]
```

```
>   Sample_name Forest Subsoil Cropland
> 1      VM-001      0       0      100
> 2      VM-002      0       5       95
> 3      VM-003      0      10       90
> 4      VM-004      0      15       85
> 5      VM-005      0      20       80
```

The property values for each virtual mixture are generated based on the source group property signatures (i.e. means). The property values are calculated as a simple mass balance, the mean value of each source group is multiplied by the theoretical contribution of each source group and the result is summed, as detailed

in the following equation:

$$p = \sum_{i=1}^{n} P_{Si} * C_{Si} \tag{A.1}$$

Where p is the property value of a virtual mixture, P_{Si} the mean value of the property for the source group i, C_{Si} the theoretical contribution of the source group i of the virtual mixture, and n the number of source groups.

The `VM.builder` function allows the calculation of the tracers values (`tracers`) of the virtual mixtures generated with `VM.contrib.generator` according to their respective theoretical source contribution combinations (`contributions`). The `VM.builder` function returns and, if `save.dir` is set, saves three data frames:

- `$property` - 'VM_properties[_note].csv': contains the values of the tracers for each virtual mixtures.
- `$uncertainty` - 'VM_properties_SD[_note].csv': contains the uncertainty of the tracers. If the actual measurement uncertainty are provided (`uncertainty`) they will be used, otherwise 5 % of the tracer values will be considered as measurement uncertainty.
- `$full` - 'VM_properties_full[_note].csv': contains the values of the tracers and their measurement uncertainty.

It is possible to add the property values data frame of the source samples to the one of the virtual mixture by setting `add.sources = TRUE` , which could be required when running unmixing models.

```
VM <- VM.builder(data = database,
                 material = "Material",
                 source.name = "Source",
                 class = "Class_decontamination",
                 tracers = tracers$mean.sd_KS,
                 uncertainty = unname(prop.uncertainties[tracers$mean.sd_KS])
                 contributions = VM.contrib,
                 VM.name = "Sample_name",
                 add.sources = TRUE,
                 save.dir = dir.example,
                 # note = "example"
                 )

VM$full[1:5,]
```

```
>   Sample_name Class_decontamination TOC_PrC TN_PrC EDXRF_Al_mg.kg.1
> 1      VM-001       Virtual Mixture    5.16   0.42         84858.53
> 2      VM-002       Virtual Mixture    4.97   0.40         86004.71
> 3      VM-003       Virtual Mixture    4.78   0.39         87150.90
> 4      VM-004       Virtual Mixture    4.60   0.38         88297.08
> 5      VM-005       Virtual Mixture    4.41   0.36         89443.26
```

It is also possible to generate virtual mixture contributions and tracer values in one step in the `VM.builder` function, by setting the contribution range as a vector (`VM.range`) and the step (`VM.step`), such as below:

```
VM <- VM.builder(data = database,
                 material = "Material",
                 source.name = "Source",
                 class = "Class_decontamination",
                 tracers = tracers$mean.sd_KS,
                 uncertainty = unname(prop.uncertainties[tracers$mean.sd_KS↩
    ]),
                 VM.range = c(0, 100),
                 VM.step = 5,
                 VM.name = "Sample_name",
                 add.sources = TRUE,
                 save.dir = dir.example,
                 # note = "example"
                 )
```

A.4.2 - Un-Mixing models

Running the models will generate numerous files, therefore we recommended to create a dedicated folder to organize them, and keep the directory with `dir.modelling` .

```
dir.create(file.path(dir.example, "Modelling/"), showWarnings = FALSE)
dir.modelling <- paste0(dir.example, "Modelling/")
```

A.4.2.1 - Bayesian Mean Model - BMM

Similarly, create a dedicated folder for Bayesian Mean modelling (BMM), and keep the directory with `dir.mod.BMM` .

```
dir.create(file.path(dir.modelling, "BMM/"), showWarnings = FALSE)
dir.mod.BMM <- paste0(dir.modelling, "BMM/")
```

The Bayesian Mean Model (BMM) is a statistical approach that uses Bayesian inference to estimate the mean of a population or dataset (Laceby and Olley, 2015; Batista et al., 2019). This approach incorporates prior knowledge and observed data to calculate a posterior distribution for the mean, providing a probabilistic framework that accounts for uncertainty in the estimates. The BMM approach that minimises the sum of square residuals of the mixing equation for each iteration of a Monte Carlo simulation.

A.4.2.1.a - Run BMM

The `run.BMM` function has been developed to allow to simplify the use of the BMM model. The number of iterations should be set in `n.iter` , between 2500 and 7500, to ensure convergence of the Monte Carlo chain. Setting `n.iter` to 30 allows the structure to be tested before the actual modelling is carried out.

Of note, it is not compulsory to provide the actual measurement uncertainty of tracers to `uncertainty`, although it is recommended.

The function returns a data frame containing the individual iteration source contributions for each mixture and, if `save.dir` is set, saves it as 'BMM_prevision[_note].csv'.

```
BMM.mix <- fingR::run.BMM(data = database,
                          class = "Class_decontamination",
                          mixture = "Target",
                          sample.id = "Sample_name",
                          tracers = tracers$mean.sd_KS,
                          uncertainty = unname(prop.uncertainties[tracers$mean.sd_KS]),
                          n.iter = 30, # as test value - to replace
                          save.dir = dir.mod.BMM,
                          #note = "example"
                          )
```

When dealing with isotopic ratios, which are non-linear properties, the residuals of the mixing equation for each iteration should be calculated taking into account the relative content of the related property (see Laceby and Olley (2015) for further explanation). Several isotopic ratios could be used, bearing in mind that the order must be identical between `isotope.ratio`, `isotope.prop` and `isotopes.unc`. For example, when using the δ^{13}C isotopic ratio in organic matter, the `run.BMM` function should be set as follows:

```
BMM.iso <- fingR::run.BMM(data = database,
                          class = "Class_decontamination",
                          mixture = "Target",
                          sample.id = "Sample_name",
                          tracers = tracers$mean.sd_KS,
                          uncertainty = unname(prop.uncertainties[tracers$mean.sd_KS]),
                          isotope.ratio = c("d13C_PrM"),
                          isotope.prop = c("TOC_PrC")
                          isotopes.unc = c("d13C_SD"),
                          n.iter = 30, # as test value - to replace
                          save.dir = dir.mod.BMM,
                          #note = "example_iso"
                          )
```

A.4.2.1.b - Collect and organise BMM contributions

Then, the predictions resulting from the BMM must be processed to determine the contribution values for each target mixture.

The `BMM.summary` function provides a summary of the predictions, including mean value, standard deviation, and various quantiles (2.5, 5, 25, 50, 75, 95, 97.5) for each target mixture (saves 'BMM_contrib[_note].csv'). From this summary, the `BMM.pred` function extracts the median and/or mean, `stats = "Median"`,

`stats = "Mean"`, or `stats = c("Median", "Mean")`, value of source contributions for each target mixture (saves 'BMM_ordered_contrib[_note].csv'). Finally, the **`ensure.total`** function ensures that the total of the predicted source contributions from all sources sum to 1 or 100 % (saves 'corrected_contrib[_note].csv').

```
## Summarise BMM model previsions
BMM.summary.mix <- fingR::BMM.summary(pred = BMM.mix,
                                      # sample.id = "mix.names",
                                      # source = "source",
                                      # value = "value",
                                      save.dir = dir.mod.BMM,
                                      # note = "example"
                                      )

## Extracts the median value of the previsions
BMM.preds.mix <- fingR::BMM.pred(data = BMM.summary.mix,
                                 stats = "Median",
                                 # sample.id = "mix.names",
                                 # source = "source",
                                 save.dir = dir.mod.BMM,
                                 # note = "example"
                                 )

## Ensure that the total predicted contribution sums to 1 or to 100%
BMM.preds.mixE <- fingR::ensure.total(data = BMM.preds.mix,
                                      sample.name = "mix.names",
                                      path = dir.mod.BMM,
                                      note = "BMM"
                                      )

BMM.preds.mixE[1:4,]
```

```
>        mix.names Median_Forest Median_Subsoil Median_Cropland total
> 1 MDd_2106_00-01         0.122          0.877           0.001 1.000
> 2 MDd_2106_01-02         0.029          0.814           0.157 1.000
> 3 MDd_2106_02-03         0.043          0.956           0.001 1.000
> 4 MDd_2106_03-04         0.006          0.496           0.497 0.999
```

The same sequence of functions is applied for the virtual mixture predictions, resulting in `BMM.summary.VM` from **`BMM.summary`**, `BMM.preds.VM` from **`BMM.pred`**, and `BMM.pred.VME` from **`ensure.total`**.

```
BMM.preds.VM[1:4,]
```

```
>   mix.names Median_Forest Median_Subsoil Median_Undecontam. total
> 1    VM-001         0.026          0.973              0.001     1
> 2    VM-002         0.001          0.998              0.001     1
> 3    VM-003         0.069          0.930              0.001     1
> 4    VM-004         0.001          0.811              0.188     1
```

A.4.2.2 - MixSIAR model

Create a dedicated folder for MixSIAR modelling, and keep the directory with `dir.mod.MixSIAR`.

```
dir.create(file.path(dir.modelling, "MixSIAR/"), showWarnings = FALSE)
dir.mod.MixSIAR <- paste0(dir.modelling, "MixSIAR/")
```

The MixSIAR package is designed to create and run Bayesian mixing models using Just Another Gibbs Sampler (JAGS). This package is widely used in the sediment source fingerprinting community to predict source contribution. To explore more about MixSIAR, including detailed tutorials, examples, and technical documentation, please visit the official MixSIAR website. Additionally, the source code and further resources can be found on the MixSIAR GitHub page (https://github.com/brianstock/MixSIAR/tree/3.1.9).

According to MixSIAR guide, installation should follow these steps:

- Download and install/update R (https://cran.r-project.org/bin/).
- Download and install JAGS (https://mcmc-jags.sourceforge.io/).
- Open R and run:

```
devtools::install.packages("MixSIAR", dependencies=TRUE)
```

  Or install the GitHub version:

```
#install.packages(remotes)
remotes::install_github("brianstock/MixSIAR", dependencies=TRUE)
```

- Load the MixSIAR package

```
library(MixSIAR)
```

A.4.2.2.a - Generate data for MixSIAR

To MixSIAR model requires data to be formated in a specific format to load the information of source and mixture samples. The `data.for.MixSIAR` function generates CSV files that conform to the format required by MixSIAR loading functions (i.e. `load_mix_data`, `load_source_data`, and `load_discr_data`). The function generates three files with the properties according to the specified tracer selection (in `tracers`):

- 'MixSIAR_mix[_note].csv': containing mixtures information.
- 'MixSIAR_sources[_note].csv': containing the mean and standard deviation (sd) of the source classes.
- 'MixSIAR_discrimination[_note].csv': containing is a matrix of zero as there is no trophic information in sediment source fingerprinting studies.

```
# Actual sediment samples
fingR::data.for.MixSIAR(data = database,
                        class = "Class_decontamination",
                        target = "Target",
                        tracers = tracers$mean.sd_KS,
                        sample.name = "Sample_name",
                        save.dir = dir.mod.MixSIAR,
                        # note = "exemple",
                        # fileEncoding = "latin1",
                        # show.data = FALSE,
                        )

# Virtual mixtures
fingR::data.for.MixSIAR(data = VM$full,
                        class = "Class_decontamination",
                        target = "Virtual Mixture",
                        tracers = tracers$mean.sd_KS,
                        sample.name = "Sample_name",
                        save.dir = dir.mod.MixSIAR,
                        note = "VM",
                        # fileEncoding = "latin1",
                        # show.data = FALSE,
                        )
```

A.4.2.2.b - Load mixture, source and discrimination data

The MixSIAR functions `load_mix_data`, `load_source_data`, and `load_discr_data` are used to load the corresponding CSV files for the actual mixtures: 'MixSIAR_mix.csv' (actual mixtures), 'MixSIAR_sources .csv' (sources), and 'MixSIAR_discrimination.csv' (discrimination matrix) that were generated previously.

```
# Load sediment samples data
MSIAR.mix   <- MixSIAR::load_mix_data(filename = paste0(dir.mod.MixSIAR, "↩
    MixSIAR_mix.csv"),
                                      iso_names = tracers$mean.sd_KS,
                                      factors = c("Sample_name"),
                                      fac_random = FALSE,
                                      cont_effects = NULL
                                      )

# Load source data
MSIAR.source <- MixSIAR::load_source_data(filename = paste0(dir.mod.MixSIAR,↩
     "MixSIAR_sources.csv"),
                                          source_factors = NULL,
                                          conc_dep = FALSE,
                                          data_type = "means",
                                          mix = MSIAR.mix
                                          )
```

```
16
17 # Load discrimination data
18 MSIAR.discr <- MixSIAR::load_discr_data(filename = paste0(dir.mod.MixSIAR, "↩
       MixSIAR_discrimination.csv"),
19                                         mix = MSIAR.mix)
```

The same functions are used to load the virtual mixtures information. The virtual mixtures properties ('MixSIAR_mix_VM.csv') are loaded using `load_mix_data` and the same source and discrimination matrix files as for the actual mixtures.

```
1  # Load virtual mixtures data
2  MSIAR.VM <- MixSIAR::load_mix_data(filename = paste0(dir.mod.MixSIAR, "↩
       MixSIAR_mix_VM.csv"),
3                                     iso_names = tracers$mean.sd_KS,
4                                     factors = c("Sample_name"),
5                                     fac_random = FALSE,
6                                     cont_effects = NULL
7                                     )
8
9  # Load source data
10 MSIAR.source.VM <- MixSIAR::load_source_data(filename = paste0(dir.mod.↩
       MixSIAR, "MixSIAR_sources_VM.csv"),
11                                            source_factors = NULL,
12                                            conc_dep = FALSE,
13                                            data_type = "means",
14                                            mix = MSIAR.VM
15                                            )
16
17 # Load discrimination data
18 MSIAR.discr.VM <- MixSIAR::load_discr_data(filename = paste0(dir.mod.MixSIAR↩
       , "MixSIAR_discrimination_VM.csv"),
19                                           mix = MSIAR.VM)
```

A.4.2.2.c - Write JAGS model file

The "JAGS is Just Another Gibbs Sampler. It is a program for analysis of Bayesian hierarchical models using Markov Chain Monte Carlo (MCMC) simulation not wholly" used in MixSIAR package (Stock et al., 2022). The `write_JAGS_model` writes the JAGS file to define the structure of the Bayesian model. The JAGS model is saved at the path set in `filename` and using the specified txt file name (e.g. 'MixSIAR_model.txt').

```
1 # Write JAGS model file for actual samples
2 MixSIAR::write_JAGS_model(filename = paste0(dir.mod.MixSIAR, "MixSIAR_model.↩
      txt"),
3                           resid_err = FALSE,
4                           process_err = TRUE,
```

```
                            mix = MSIAR.mix,
                            source = MSIAR.source
                            )
```

Another JAGS model is written for virtual mixtures since the the mixture samples and sources are set in `mix` and `source`.

```
# Write JAGS model file for virtual mixtures
MixSIAR::write_JAGS_model(filename = paste0(dir.mod.MixSIAR, "MixSIAR_model_VM.txt"),
                            resid_err = FALSE,
                            process_err = TRUE,
                            mix = MSIAR.VM,
                            source = MSIAR.source.VM
                            )
```

A.4.2.2.d - Run MixSIAR

When running MixSIAR model you must choose one of the MCMC run option (Stock et al., 2020):

run	Chain Length	Burn-in	Thin	Chains
"test"	1,000	500	1	3
"very short"	10,000	5,000	5	3
"short"	50,000	25,000	25	3
"normal"	100,000	50,000	50	3
"long"	300,000	200,000	100	3
"very long"	1,000,000	500,000	500	3
"extreme"	3,000,000	1,500,000	500	3

In this example MCMC is set to "test", which allows to quickly ensures that the code implemented is functional.

```
# Run MixSIAR model for sediment samples
jags.mix <- MixSIAR::run_model(run = "test",
                               mix = MSIAR.mix,
                               source = MSIAR.source,
                               discr = MSIAR.discr,
                               model_filename = paste0(dir.mod.MixSIAR, "MixSIAR_model.txt")
                               )

# note if "Error: .onload ... 'rgags' - R version is too old need >= 3.2.2
```

```
#> Compiling model graph
#>    Resolving undeclared variables
#>    Allocating nodes
```

```
#> Graph information:
#>    Observed stochastic nodes: 114
#>    Unobserved stochastic nodes: 93
#>    Total graph size: 2838
#>
#> Initializing model
```

```
# Run MixSIAR model for Virtual mixtures
jags.VM <- MixSIAR::run_model(run = "test",
                              mix = MSIAR.VM,
                              source = MSIAR.source.VM,
                              discr = MSIAR.discr.VM,
                              model_filename = paste0(dir.mod.MixSIAR, "MixSIAR_model_VM.txt")
                              )
```

```
#> Compiling model graph
#>    Resolving undeclared variables
#>    Allocating nodes
#> Graph information:
#>    Observed stochastic nodes: 693
#>    Unobserved stochastic nodes: 479
#>    Total graph size: 16541
#>
#> Initializing model
```

A.4.2.2.e - Collect and organise MixSIAR contributions

Then, similar to the BMM, the predictions from the MixSIAR must be processed to determine the contribution values for each target mixture.

Conversely to `fingR::run.BMM` function, the `MixSIAR::run_model` function does not same the Bayesian previsions directly. Therefore the `JAGS.summary` function saves the previsions ('JAGS_prevision[_note].csv') and provides a summary of the predictions, including mean value, standard deviation, and various quantiles (2.5, 5, 25, 50, 75, 95, 97.5) for each target mixture (saves 'JAGS_contrib[_note].csv'). From this summary, the `JAGS.pred` function extracts the median and/or mean, `stats = "Median"`, `stats = "Mean"`, or `stats = c("Median", "Mean")`, value of source contributions for each target mixture (saves 'JAGS_ordered_contrib[_note].csv'). Finally, the `ensure.total` function ensures that the total of the predicted source contributions from all sources sum to 1 or 100 % (saves 'corrected_contrib[_note].csv').

```
## Summarise MixSIAR model previsions
MixSIAR.summary.mix <- fingR::JAGS.summary(jags.1 = jags.mix,
                                           mix = MSIAR.mix,
                                           sources = MSIAR.source,
                                           path = dir.mod.MixSIAR,
                                           # note = "example",
```

```
                                        save_pred = TRUE
                                        )

## Extracts the median value of the previsions
MixSIAR.pred.mix <- fingR::JAGS.pred(path = paste0(dir.mod.MixSIAR, "contrib.csv"),
                                     stats = "Median",
                                     save = TRUE,
                                     # note = "example"
                                     )

## Ensure that the total predicted contribution sums to 1 or 100%
MixSIAR.pred.mixE <- fingR::ensure.total(data = MixSIAR.pred.mix,
                                         sample.name = "sample",
                                         path = dir.mod.MixSIAR,
                                         note = "MixSIAR"
                                         )

MixSIAR.preds.mixE[1:4,]
```

```
>           sample Median_Forest Median_Subsoil Median_Cropland total
> 1 MDd_2106_00-01         0.191          0.031           0.778 0.999
> 2 MDd_2106_01-02         0.070          0.032           0.898 0.999
> 3 MDd_2106_02-03         0.072          0.044           0.884 0.999
> 4 MDd_2106_03-04         0.073          0.063           0.864 0.998
```

The same sequence of functions is used for the virtual mixture predictions, resulting in `MixSIAR.summary.VM` from `JAGS.summary`, `MixSIAR.preds.VM` from `JAGS.pred`, and `MixSIAR.pred.VME` from `ensure.total`.

```
MixSIAR.pred.VME[1:4,]
```

```
>   sample Median_Forest Median_Subsoil Median_Cropland total
> 1 VM-001         0.150          0.398           0.451 0.999
> 2 VM-002         0.069          0.418           0.513 1.000
> 3 VM-003         0.084          0.452           0.464 1.000
> 4 VM-004         0.081          0.480           0.439 1.000
```

A.4.3 - Modelling accuracy statistics calculation

The accuracy of unmixing models is evaluated by comparing the theoretical source contribution values (`VM.contrib`), representing the known contributions of the virtual mixtures, with the predicted contributions of the virtual mixtures (`BMM.preds.VM`) generated by the unmixing model.

Several criteria can be used to evaluate the accuracy of the predictions:

- **Uncertainty**: Assessed using prediction interval widths (e.g., W50, W95; for Bayesian models).
- **Residual Error** or **Bias**: Evaluated using metrics such as mean error (ME).

- **Performance**: Measured using metrics such as the squared Pearson correlation coefficient (r^2), root-mean-square error (RMSE), Nash-Sutcliffe modeling efficiency coefficient (NSE), and continuous ranked probability score (CRPS; for Bayesian models).

Modelling accuracy statistics could be interpreted the following way (Chalaux-Clergue et al., 2024a): "Higher values of W50 indicate a wider distribution, which is related to a higher uncertainty. The sign of the ME indicates the direction of the bias, i.e. an overestimation or underestimation (positive or negative value, respectively). As ME is affected by cancellation, a ME of zero can also reflect a balanced distribution of predictions around the 1 : 1 line. Although this is not a bias, it does not mean that the model outputs are devoid of errors. The RMSE is a measure of the accuracy and allows us to calculate prediction errors of different models for a particular dataset. RMSE is always positive, and its ideal value is zero, which indicates a perfect fit to the data. As RMSE depends on the squared error, it is sensitive to outliers. The r^2 describes how linear the prediction is. The NSE indicates the magnitude of variance explained by the model, i.e. how well the predictions match with the observations. A negative RMSE indicates that the mean of the measured values provides a better predictor than the model. The joint use of r^2 and NSE allows for a better appreciation of the distribution shape of predictions and thus facilitates the understanding of the nature of model prediction errors. The CRPS evaluates both the accuracy and sharpness (i.e. precision) of a distribution of predicted continuous values from a probabilistic model for each sample (Matheson and Winkler, 1976). The CRPS is minimised when the observed value corresponds to a high probability value in the distribution of model outputs."

To illustrate, only predictions made using BMM are used, however, it also applies to predictions made using MixSIAR.

A.4.3.1 - General accuracy metrics

The `eval.groups` function calculates general accuracy metrics (ME, RMSE, r^2, NSE) by comparing the theoretical source contribution values (provided in `df.obs`) with the predicted values (provided in `df.pred`) (saves 'stats[_note].csv'). In `df.obs`, the virtual mixtures are identified by the column `Sample_name`, while in `df.pred`, they are identified by the column `mix.names`, which is specified in `by` (The resulting data frame is saved as 'ObsPred[_note].csv').

```
BMM.stats <- fingR::eval.groups(df.obs = VM.contrib,
                                df.pred = BMM.preds.VME %>%
                                            dplyr::select(-total),
                                by = c("Sample_name" = "mix.names"),
                                path = dir.mod.BMM,
                                # note = "example"
                                )

BMM.stats
```

```
>       Type         Source       ME RMSE   r2    NSE
> 1   Median         Forest    -0.14 0.22 0.58   0.22
> 2   Median       Subsoil     0.38 0.46 0.38 -2.34
> 3   Median      Cropland    -0.25 0.39 0.00 -1.36
```

A.4.3.2 - *Continuous ranked probability score*

The `CRPS` function calculates the continuous ranked probability score (CRPS). The predicted values of the virtual mixture (`prev`) are the previsions for each sample from the Bayesian models. Since a large number of previsions are made when running the Bayesian models, it is possible to specify the path to the file containing the previsions rather than loading them into the workspace in `path.to.prev` (previously saved by `BMM.summary`).

The function returns and, if `save.path` is set, saves two data frames at the `save.dir` direction or if `save = TRUE` is set, saves them at the direction indicated by `path.to.prev` :

- `$samples` - 'CRPS[_note].csv': contains the CRPS values for each source group for each virtual mixtures.
- `$mean` - 'CRPS[_note]_mean.csv': contains the values of the mean CRPS value per contribution source class group for each virtual mixtures.

```
# Calculate prediction CRPS values
BMM.CRPS <- fingR::CRPS(obs = VM.contrib,
                        path.to.prev = paste0(dir.mod.BMM, "BMM_prevision_VM.csv"),
                        source.groups = c("Forest", "Subsoil", "Cropland"),
                        mean.cal = TRUE,
                        # save = TRUE,
                        save.dir = dir.mod.BMM,
                        # note = "example"
                        )

BMM.CRPS$samples[1:5,]
```

```
>   Sample_name    Forest  Subsoil  Cropland
> 1      VM-001    0.0522   0.3848    0.5969
> 2      VM-002    0.0222   0.4576    0.5850
> 3      VM-003    0.0535   0.2822    0.4328
> 4      VM-004    0.0725   0.2435    0.4804
> 5      VM-005    0.0271   0.3478    0.4939
```

```
BMM.CRPS$mean
```

```
>         Source  CRPS.mean
> 1       Forest     0.1315
> 2      Subsoil     0.1619
> 3    Cropland     0.1889
```

A.4.3.3 - *Prediction interval width*

The `interval.width` function calculates two prediction interval widths: W50 and W95. The W50 contains 50 % of the previsions (Q75-Q25) and the W95 contains 95 % of the previsions (Q97.5-Q2.5). Since the interval width is only calculated on the Bayesian model previsions, it is possible to calculate them on actual

and virtual mixtures. Similarly to `CRPS`, it is possible to specify the path to the file containing the Bayesian model previsions, rather than loading them into the workspace with `path.to.prev` (previously saved by `BMM.summary`).

The function returns and, if `save.path` is set, saves two data frames at the `save.dir` direction or if `save = TRUE` is set, saves them at the direction indicated by `path.to.prev`:

- `$samples` - 'Interval_width[_note].csv': contains both interval width values for each source group for each virtual mixtures.
- `$mean` - 'Interval_width_mean[_note].csv': contains the mean of both interval width values per contribution source class group for each virtual mixtures.

```
# Calculate prediction interval width (W95, W50)
BMM.predWidth <- fingR::interval.width(path.to.prev = paste0(dir.mod.BMM, "BMM_prevision_VM.csv"),
                                       mean.cal = TRUE,
                                       # save = TRUE,
                                       save.dir = dir.mod.BMM,
                                       # note = "exemple"
                                       )

BMM.predWidth$samples[1:6,]
```

```
>   mix.names          Source      W50    W95
> 1    VM-001          Forest    0.271  0.946
> 2    VM-001         Subsoil    0.607  0.997
> 3    VM-001        Cropland    0.448  0.997
> 4    VM-002          Forest    0.102  0.675
> 5    VM-002         Subsoil    0.514  0.997
```

```
BMM.predWidth$mean
```

```
> # A tibble: 3 x 3
>     Source        W50.mean   W95.mean
>      <chr>           <dbl>      <dbl>
> 1   Forest           0.376      0.885
> 2  Subsoil           0.576      0.959
> 3 Cropland           0.416      0.924
```

A.4.3.4 - Encompassed sample predictions

The `ESP` function calculates the Encompassed Sample Prediction (ESP). The ESP is a newly introduced statistics in Chalaux-Clergue et al. (2024c) and was created to assess the transferability of the statistics calculated on virtual mixtures to actual sediment samples. The ESP was calculated as the percentage of actual samples for which the predicted contributions remained within the lowest and the highest predicted contributions obtained for the virtual mixtures. When expressed as a percentage, ESP ranges from 0 to 100 %, the latter providing an optimal value. Values close to 100 % indicate a higher transferability of modelling

evaluation statistics calculated on virtual mixture to actual sediment samples.

```
sources.lvl <- c("Forest", "Subsoil", "Cropland")

# Calculate encompassed sample predictions (ESP)
BMM.ESP <- fingR::ESP(obs = BMM.preds.VM,
                      pred = BMM.preds.mixE,
                      sources = paste0("Median_", sources.lvl),
                      count = "Both"
                      )

BMM.ESP
```

```
>                       Source   ESP.Number ESP.Percentage
> Median_Forest         Forest           33             87
> Median_Subsoil       Subsoil           38            100
> Median_Cropland     Cropland            20             53
```

A.5 - Citation

```
utils::citation(package = "fingR")
```

```
>  To cite the 'fingR' package in publications please use:
>
>    Chalaux-Clergue, T. and Bizeul, R. (2024). fingR: A package to support
>    sediment source fingerprinting studies, Zenodo [Package]:
>    https://doi.org/10.5281/zenodo.8293595, Github [Package]:
>    https://github.com/tchalauxclergue/fingR, Version = 2.1.1.
>
>  A BibTeX entry for LaTeX users is
>
>    @Manual{,
>      title = {fingR: A package to support sediment source fingerprinting ↩
    studies},
>      author = {{Chalaux-Clergue} and {Thomas} and {Bizeul} and {Rémi}},
>      year = {2024},
>      month = {6},
>      note = {R package version 2.1.1},
>      doi = {https://doi.org/10.5281/zenodo.8293595},
>      url = {https://github.com/tchalauxclergue/fingR},
>    }
```

References

Batista, P.V.G., Laceby, J.P., Evrard, O., 2022. How to evaluate sediment fingerprinting source apportionments. Journal of Soils and Sediments 22, 1315–1328. URL: https://link.springer.com/10.1007/s11368-022-03157-4, doi:10.1007/s11368-022-03157-4.

Batista, P.V.G., Laceby, J.P., Silva, M.L.N., Tassinari, D., Bispo, D.F.A., Curi, N., Davies, J., Quinton, J.N., 2019. Using pedological knowledge to improve sediment source apportionment in tropical environments. Journal of Soils and Sediments 19, 3274–3289. URL: http://link.springer.com/10.1007/s11368-018-2199-5, doi:10.1007/s11368-018-2199-5.

Chalaux-Clergue, T., Bizeul, R., Batista, P.V.G., Martínez-Carreras, N., Laceby, J.P., Evrard, O., 2024a. Sensitivity of source sediment fingerprinting to tracer selection methods. SOIL 10, 109–138. URL: https://soil.copernicus.org/articles/10/109/2024/, doi:10.5194/soil-10-109-2024.

Chalaux-Clergue, T., Bizeul, R., Foucher, A., Evrard, O., 2024b. A unified template for sediment source fingerprinting databases. URL: https://zenodo.org/doi/10.5281/zenodo.10725788, doi:10.5281/ZENODO.10725788.

Chalaux-Clergue, T., Evrard, O., Durand, R., Caumon, A., Hayashi, S., Tsuji, H., Huon, S., Vaury, V., Wakiyama, Y., Nakao, A., Laceby, J.P., Onda, Y., 2022. Organic matter, geochemical and colorimetric properties of potential source material, target sediment and laboratory mixtures for conducting sediment fingerprinting approaches in the Mano Dam Reservoir (Hayama Lake) catchment, Fukushima Prefecture, Japan. URL: https://zenodo.org/record/7081094, doi:10.5281/ZENODO.7081094.

Chalaux-Clergue, T., Foucher, A., Chaboche, P.A., Hayashi, S., Tsuji, H., Wakiyama, Y., Huon, S., Vandromme, R., Cerdan, O., Nakao, A., Evrard, O., 2024c. Impacts of farmland decontamination on 137Cs transfers in rivers after Fukushima nuclear accident: Evidence from a retrospective sediment core study. Science of The Total Environment 947, 174546. URL: https://linkinghub.elsevier.com/retrieve/pii/S0048969724046941, doi:10.1016/j.scitotenv.2024.174546.

Evrard, O., Batista, P.V.G., Company, J., Dabrin, A., Foucher, A., Frankl, A., García-Comendador, J., Huguet, A., Lake, N., Lizaga, I., Martínez-Carreras, N., Navratil, O., Pignol, C., Sellier, V., 2022. Improving the design and implementation of sediment fingerprinting studies: Summary and outcomes of the TRACING 2021 Scientific School. Journal of Soils and Sediments 22, 1648–1661. URL: https://link.springer.com/10.1007/s11368-022-03203-1, doi:10.1007/s11368-022-03203-1.

Laceby, J.P., Olley, J., 2015. An examination of geochemical modelling approaches to tracing sediment sources incorporating distribution mixing and elemental correlations. Hydrological Processes 29, 1669–1685. URL: https://onlinelibrary.wiley.com/doi/10.1002/hyp.10287, doi:10.1002/hyp.10287.

Martínez-Carreras, N., Gallart, F., Iffly, J.F., Pfister, L., Walling, D.E., Krein, A., 2008. Uncertainty assessment in suspended sediment fingerprinting based on tracer mixing models: A case study from Luxembourg. IAHS publication 325, 94. URL: https://iahs.info/uploads/dms/14500.16-94-105-11-325-Martinez.pdf.

Matheson, J.E., Winkler, R.L., 1976. Scoring Rules for Continuous Probability Distributions. Management Science 22, 1087–1096. URL: http://pubsonline.informs.org/doi/10.1287/mnsc.22.10.1087, doi:10.1287/mnsc.22.10.1087.

Sherriff, S.C., Franks, S.W., Rowan, J.S., Fenton, O., Ó'hUallacháin, D., 2015. Uncertainty-based assessment of tracer selection, tracer non-conservativeness and multiple solutions in sediment fingerprinting using synthetic and field data. Journal of Soils and Sediments 15, 2101–2116. URL: http://link.springer.com/10.1007/s11368-015-1123-5, doi:10.1007/s11368-015-1123-5.

Stock, B.C., Semmens, B.X., Ward, E.J., Parnell, A.C., Phillips, D.L., 2020. MixSIAR: Bayesian Mixing Models in R. URL: https://doi.org/10.5281/zenodo.1209993.

Stock, B.C., Semmens, B.X., Ward, E.J., Parnell, A.C., Phillips, D.L., 2022. JAGS: Bayesian Mixing Models in R. URL: https://doi.org/10.5281/zenodo.1209993.

Appendix B

A unified template for sediment source fingerprinting databases

Over the last few years, the sediment source fingerprinting community has been engaged in promoting best practices to improve the design and the implementation of sediment fingerprinting techniques (Evrard et al., 2022). Data sharing is a key part of open science making research more reliable and accessible to the community. To move forward and improve data sharing, we propose these templates for databases and metadata (Chalaux-Clergue et al., 2024).

These templates include: common metadata for samples (soil, river flood deposits, sediment core, etc.) description (name, IGSN, location, sampling date, etc.), list and description of common properties (elemental geochemistry, organic matter, radionuclides, etc.) used in sediment source fingerprinting studies. These templates are intended to evolve thanks to the participation of the community, as part of a collaborative project.

Chalaux-Clergue, T., Bizeul, R., Foucher, A., & Evrard, O. (2024).
A unified template for sediment source fingerprinting databases (Version 24.03.01) [Dataset].
Zenodo. https://doi.org/10.5281/zenodo.10725788

This template and all its updates can be cited using the DOI: https://doi.org/10.5281/zenodo.10725787. This DOI represents all versions, and will always resolve to the latest one.

Table B.I: Summary of CSV Files

File Name	Description
SSF_database_template_v24.03.01.csv	This file serves as a template for users to enter their own data. It contains the required structure, including predefined columns, to ensure data consistency and compatibility (i.e. IGSN, Sample_name, Sample_size, properties and uncertainties values).
SSF_metadata_template_v24.03.01.csv	This file contains metadata required to uniquely identify and describe the samples in the database, to ensure traceability of samples. (IGSN, Parent_IGSN, Sample_name, Material, Nature, Class, location information (geographic coordinates, country, city, etc.), etc.).
SSF_variable_description_v24.03.01.csv	This file provides a comprehensive description of the columns in File 1 and File 2, ensuring clarity and usability of the database. The column names as it appears in the database and/or metadata files, with a description of the column expected content and purpose, its class (e.g. numeric, character, factor, date, etc.), and examples to illustrate typical entries in the column.

Published databases following these templates are listed in the References section of the Zenodo page.

References

Chalaux-Clergue, T., Bizeul, R., Foucher, A., Evrard, O., 2024. A unified template for sediment source fingerprinting databases. URL: https://zenodo.org/doi/10.5281/zenodo.10725788, doi:10.5281/ZENODO.10725788.

Evrard, O., Batista, P.V.G., Company, J., Dabrin, A., Foucher, A., Frankl, A., García-Comendador, J., Huguet, A., Lake, N., Lizaga, I., Martínez-Carreras, N., Navratil, O., Pignol, C., Sellier, V., 2022. Improving the design and implementation of sediment fingerprinting studies: Summary and outcomes of the TRACING 2021 Scientific School. Journal of Soils and Sediments 22, 1648–1661. URL: https://link.springer.com/10.1007/s11368-022-03203-1, doi:10.1007/s11368-022-03203-1.

Appendix C

Analyses for Conducting Sediment Fingerprinting Approaches in the Mano Dam Reservoir (Hayama Lake) Catchment (Fukushima Prefecture, Japan)

The current dataset was compiled to study sediment fingerprinting practices, i.e. tracer selection and contribution modelling. Organic matter, elemental geochemistry, visible diffuse spectrocolorimetric properties, radiocesium properties, and grain size were analysed were analysed in potential source material that may supply sediment to coastal rivers, here the upper part of the Mano river, draining the main Fukushima radioactive pollution plume (Japan). Four potential soil source materials (n = 68) were considered: undecontaminated cropland (n = 24), as non-decontaminated soil before the application of local decontamination policies, remediated cropland (n = 10), as decontaminated soil after the application of local decontamination policies, forest soils (n = 24) and subsurface material originating from channel bank collapse or landslides (n = 10; referred to as subsoil). A sediment core was collected in the Mano Dam lake (Hayama lake) on the 6 June 2021 and was sectioned into 1-cm layers (n = 38). Laboratory mixtures (n = 27) were made to assess different contribution levels from the sources.

The current dataset comprises four CSV files including data and metadata information and their respective descriptions of variables. The data set is composed of soil samples, sediment core layer and laboratory mixtures. Laboratory mixtures were prepared to provide a dataset to calibrate/validate un-mixing models implemented to address this research question and analysed in the same conditions and using the same equipment as the source/target material.

Chalaux-Clergue, T., Evrard, O., Durand, R., Caumon, A., Hayashi, S., Tsuji, H., Huon, S.,Vaury, V., Wakiyama, Y., Nakao, A., Laceby, J. P., & Onda, Y. (2024). **Organic matter, geochemical, visible spectrocolorimetric properties, radiocesium properties, and grain size of potential source material, target sediment core layers and laboratory mixtures for conducting sediment fingerprinting approaches in the Mano Dam Reservoir (Hayama Lake) catchment, Fukushima Prefecture, Japan** (Version 2) [Dataset]. Zenodo. https://doi.org/10.5281/zenodo.10836974

All the update of this database can be cited using the DOI: https://doi.org/10.5281/zenodo.7081093. This DOI represents all versions, and will always resolve to the latest one. Two versions of this database were published, on 1 November 2022 (Version 1) and 19 March 2024 (Version 2), respectively used used in Chapter I and II.

This database was published as an example database of the unified template introduced in Appendix B (https://doi.org/10.5281/zenodo.10725787).

Appendix D

Diagnostic Properties of River Flood Deposit Sediment Collected Annually from 2011 to 2023 at Ten Sites across a Water Reservoir Catchment Contaminated after the Fukushima Daiichi Nuclear Accident Radiocesium Fallout (Mano Dam)

The current dataset was compiled to investigate sediment and radiocesium transfers in the Mano Dam reservoir catchment from 2011 to 2023, which was contaminated following the Fukushima Daiichi nuclear power plant accident in March 2011.

This dataset contains river flood sediments collected annually at ten sites in the Mano Dam reservoir catchment (n = 102) and on potential source soils. Potential source materials include forest soils (n = 24), farmland soils (n = 24) and subsoil (subsoil material and landslide; n = 10). The dataset allows the assessment of spatial heterogeneity in sediment dynamics, erosion processes and contaminant transfer, providing insights into landscape and management influences on sediment sources and deposition patterns. Flood sediment samples were collected in November following major flood events associated with the occurrence of extreme precipitation events such as typhoons or tropical storms.

The dataset consists of four CSV files containing data and metadata with variable descriptions.

Chalaux-Clergue, T., Tenaud, N., Durand, R., Caumon, A., Wakiyama, Y., Laceby, J. P., Lefèvre, I., Huon, S., Vaury, V., Mendes-Millan, M., Ogier, A., Onda, Y., Nakao, A., & Evrard, O. (2024). **Diagnostic Properties of River Flood Deposit Sediment Collected Annually from 2011 to 2023 at Ten Sites across a Water Reservoir Catchment Contaminated after the Fukushima Daiichi Nuclear Accident Radiocesium Fallout (Mano Dam)** (Version 1) [Data set]. Zenodo. https://doi.org/10.5281/zenodo.11609434

All the update of this database can be cited using the DOI: https://doi.org/10.5281/zenodo.11609433. This DOI represents all versions, and will always resolve to the latest one. This database is used in Chapter III.

This database was published as an example database of the unified template introduced in Appendix B (https://doi.org/10.5281/zenodo.10725787).

Appendix E

Diagnostic properties of three sediment cores collected in 2021-2022 from Three water reservoirs draining contaminated catchments after the Fukushima Daiichi Nuclear Power Plant accident (Mano dam, Ogaki dam, and Yokokawa dam)

The current dataset was compiled to investigate sediment and radiocesium transfers in three water reservoirs: Mano Dam reservoir, Ogaki Dam reservoir and Yokokawa reservoir, which were contaminated following the Fukushima Daiichi nuclear power plant accident in March 2011.

This dataset contains three sediment cores, collected in 2021 in the Mano Dam reservoir and in 2022 in the Ogaki and Yokokawa reservoirs, and on potential source soils. Potential source materials include forest topsoil (n = 42), farmland topsoil (n = 56) and subsoil (subsoil material and landslide; n = 17). The dataset allows the assessment of spatial heterogeneity in sediment dynamics, erosion processes and contaminant transfer, providing insights into landscape and management influences on sediment sources and deposition patterns. Flood sediment samples were collected in November following major flood events associated with the occurrence of extreme precipitation events such as typhoons or tropical storms.

The dataset consists of four CSV files containing data and metadata with variable descriptions.

Chalaux-Clergue, T., Chaboche, P.-A., Tenaud, N., Durand, R., Caumon, A., Hayashi, S., Tsuji, H., Funaki, H., Yoshimura, K., Wakiyama, Y., Laceby, J. P., Murayama, M., Matsuzaki, T., Lefèvre, I., Huon, S., Vaury, V., Mendes-Millan, M., Ogier, A., Nakao, A., & Evrard, O. (2024). **Diagnostic properties of three sediment cores collected in 2021-2022 from Three water reservoirs draining contaminated catchments after the Fukushima Daiichi Nuclear Power Plant accident (Mano dam, Ogaki dam, and Yokokawa dam)** (Version 1) [Dataset]. Zenodo.https://doi.org/10.5281/zenodo.14731789

All the update of this database can be cited using the DOI: https://doi.org/10.5281/zenodo.14731788. This DOI represents all versions, and will always resolve to the latest one. This database is used in Chapter III.

This database was published as an example database of the unified template introduced in Appendix B (https://doi.org/10.5281/zenodo.10725787).

Résumé Général

Résumé général

Introduction

Contexte

Le 11 mars 2011, le Japon a été touché par une série d'événements qui ont entraîné la catastrophe nucléaire la plus grave depuis Tchernobyl. À 14h46, heure locale, le Japon a été frappé par le "*Great East Japan Earthquake*" (Grand séisme de l'est du Japon; 東日本大震災 - '*higashi nihon daishinsai*' en japonais) ou "grand tremblement de terre du Tōhoku" - la région nord de l'île principale du Japon, Honshū -, d'une magnitude Mw de 7,3, sur l'échelle de Richter, bien que le séisme principal se soit produit à environ 130 km au large de la côte nord-est de l'île de Honshū avec une magnitude Mw de 9,0 (Simons et al., 2011). Il s'agit du tremblement de terre le plus puissant jamais enregistré dans le pays (Yagi and Fukahata, 2011; Zhao, 2015). Moins d'une heure après le séisme principal, un puissant tsunami a frappé les côtes japonaises, d'une hauteur allant de 4,1 m à Kamaishi (釜石市) à 40,5 m à Miyako (宮古市), toutes deux situées dans la préfecture d'Iwate (岩手県). Le tsunami a touché environ 2000 km de linéaire côtier et s'est engouffré jusqu'à 10 m à l'intérieur des terres, inondant environ 561 km^2. (JMA, 2011; NOAA, 2015). Les préfectures d'Iwate, de Miyagi (宮城県) et de Fukushima (福島県) ont été sévèrement touchées, la préfecture de Miyagi étant la plus affectée. Le bilan de ces deux catastrophes est particulièrement lourd, le gouvernement japonais ayant fait état de 19 579 morts, 6 242 blessés et 2 553 disparus (Fire and Disaster Management Agency, 2021; Emergency Disaster Preparedness Headquarters, 2021).

La centrale nucléaire de Fukushima Daiichi ("*Fukushima Daiichi Nuclear Power Plan*"; FDNPP), opérée par la *Tokyo Electric Power Company* (TEPCO) et située sur la côte de la préfecture de Fukushima, qui fonctionnait sur des générateurs de secours à la suite du tremblement de terre, a été inondée par une vague de 14 à 15 m de haut (IAEA, 2015), dépassant largement les 5,5 m du mur anti-tsunami. L'inondation des générateurs de secours a privé les quatre réacteurs en fonctionnement de leurs systèmes de refroidissement, ce qui a conduit à une augmentation de la température et de la pression d'hydrogène au sein des quatre réacteurs. Afin de contrôler la pression des réacteurs, les opérateurs ont procédé à des opérations de dépressurisation, qui ont entraîné le rejet d'hydrogène et d'éléments radioactifs à l'intérieur des bâtiments des réacteurs. La présence d'hydrogène dans les bâtiments a, par la suite, entraîné l'explosions des réacteurs 1 et 3 et des incendies dans le réacteur 4. Ces évènements ont conduit au rejet de grandes quantités de radionucléides dans l'environnement, estimées à 520 PBq (sans tenir compte des gaz nobles), dont 20 % se sont déposés sur la région nord-est de l'île de Honshū tandis que le reste a été emporté vers l'Océan Pacifique (Chino et al., 2011; Kobayashi et al., 2013; Steinhauser, 2014; Yamamoto, 2015). L'accident a finalement été qualifié d'accident majeur (niveau 7) sur l'échelle internationale des événements nucléaires et radiologiques ("*International Nuclear and Radiological Event Scale*"; INES) (IAEA, 2015).

Parmi les radionucléides rejetés dans l'environnement, deux éléments se sont principalement déposés sur les sols du Japon, l'iode (^{131}I) et le radiocésium (^{134}Cs et ^{137}Cs) (Kato et al., 2012; Hashimoto et al., 2012). En raison de leurs demi-vies respectives de 8 jours, 2 ans et 30 ans, la contamination liée au radiocésium, et en particulier au ^{137}Cs, constitue un enjeu à long terme pour le Japon, représentant un risque sanitaire actuel et futur pour la population, ce qui est encore le cas, plus de 10 ans après l'accident. Sur les 2,7 PBq de ^{137}Cs retombés sur les sols du Japon, la majeure partie, 2,0 PBq, s'est déposée dans la préfecture de Fukushima (74 %) (Fig. R.1.A) (Kato et al., 2019; Taniguchi et al., 2019). Au sein de la préfecture de Fukushima, 83 % de

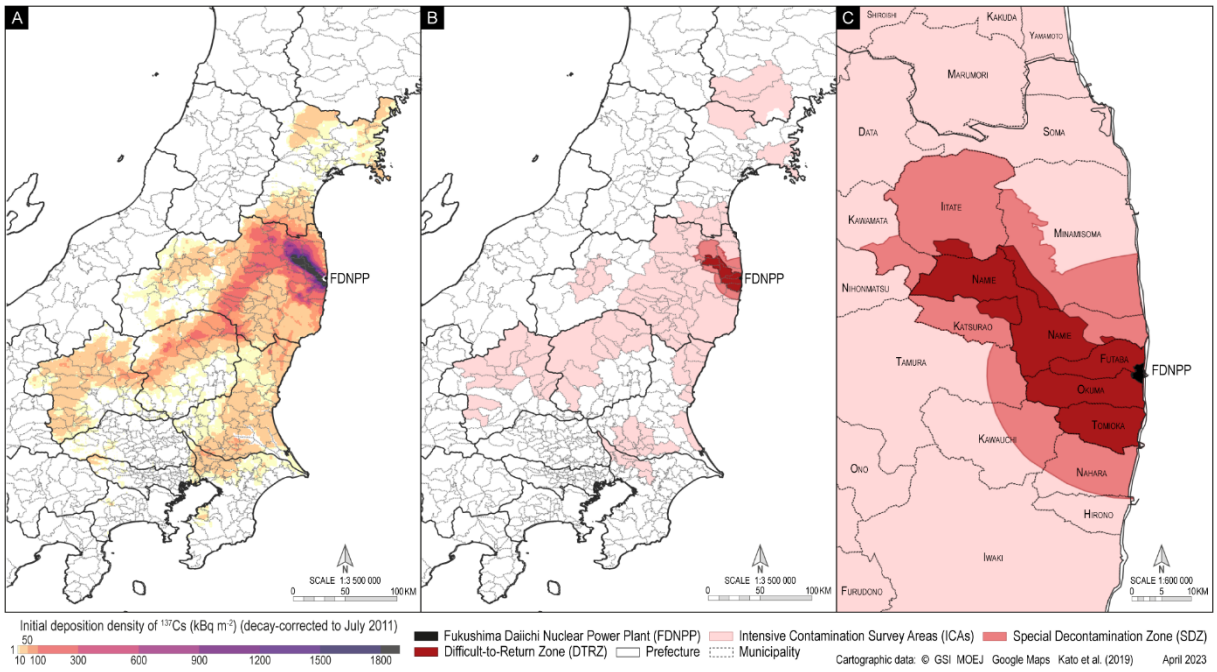


Figure R.1: (A) Carte des dépôts de ^{137}Cs dans la région du nord-est du Japon suite à l'accident de la FDNPP (d'après Kato et al. (2019)); (B) - (C) délimitation des zones où des travaux de décontamination ont été menés, comprenant les zones d'étude intensive de la contamination (*Intensive Contamination Survey Areas* - ICAs) (40 municipalités; 24 000 km^2), la zone de décontamination spéciale (*Special Decontamination Zone* - SDZ) (11 municipalités; 1 150 km^2) et la zone difficile au retour (*Difficult-to-Return Zone* - DTRZ) (tout ou partie de 8 municipalités; 335 km^2) (Source : Ministère japonais de l'environnement). Cartes réalisée dans le cadre de Evrard et al. (2023).

la préfecture ont reçu au moins 5 kBq $\cdot$ m^{-2} de ^{137}Cs (11,430 km^2), et 26 % au moins 100 kBq m^{-2} (3,520 km^2) (Kato et al., 2019). Les habitants vivant dans un rayon de 20 km autour de la centrale nucléaire (Zone d'évacuation, "*Evacuation Zone*") et ceux qui pourraient être exposés à un débit de dose radioactive supérieur à 20 mSv $\cdot$ yr^{-1} au moment de l'accident (Zone d'évacuation planifiée ou "*Planned Evacuation Zone*") ont été évacués en priorité (Fig. R.2). Au total, onze communes situées dans la préfecture de Fukushima ont reçu un ordre d'évacuation et ont été classées comme zone à habitat restreint ("*Residence Restriction Area*"), concernant 80 000 habitants et couvrant une zone de 1 150 km^2 (les villes de Futaba - 双葉町, Kawamata - 川俣町, Minamisōma - 南相馬市, Namie - 浪江町, Naraha - 楢葉町, Ōkuma - 大熊町, Tamura - 田村市, et de Tomioka - 富岡町 ainsi que les villages de Iitaté - 飯舘村, Katsurao - 葛尾村, et de Kawauchi - 川内村). Pour permettre le retour rapide de la population et la reprise des activités économiques et en particulier celle de l'agriculture, le gouvernement japonais a entreprise un programme de décontamination à grande échelle des sols contaminés au ^{137}Cs dans les zones résidentielles et cultivées touchées par le panache radioactif principal. Différentes zones ont été délimitées en fonction de la contamination radioactive mesurée en 2011, ainsi que de l'exposition des habitants et/ou des travailleurs au débit de dose qui en résulte. L'objectif à long terme du programme de décontamination était d'atteindre une exposition individuelle inférieure à 1 mSv yr^{-1} ou 0.23 μSv h^{-1}, en supposant que les personnes passent, par jour, 8 heures à l'extérieur et 16 heures dans une maison en bois avec un faible taux d' atténuation (niveau de référence de la dose d'exposition de la population générale dans des conditions normales selon la commission internationale de protection radiologiques; *International Commission on Radiological Protection* - IRCP) (MoE, 2013). Toutes les zones où le débit de dose dépassait ce seuil ont été considérées comme des "zone de contrôle intensif de la contamination" (Intensive Contamination Survey Area - ICAs) par le ministère japonais de l' environnement (*Ministry of Environemnt* - MoE), ce qui a concerné une zone de 24,000 km^2 et 6,9 million d'habitants qui

n'a pas été évacuée (Fig. R.1.B) (MoE, 2018). De plus, dans les conditions post-accidentelles, des débits de dose plus élevés ont été autorisés par le ministère, qui a augmenté le seuil maximum pour une zone d'habitat à 20 $mSv \cdot yr^{-1}$ ou 3.8 $\mu Sv \cdot h^{-1}$. Les onze municipalités où le débit de dose dépassait ce seuil au moment de l'accident ont été classées comme "zones de décontamination spéciale" (*Special Decontamination Zone* - SDZ; 除染特別地域). Les zones où le débit de dose dépassait encore ce seuil cinq ans après l'accident, soit en 2016, ont été classées comme "zone difficile au retour" (*Difficult-to-Return Zone* - DTRZ; 帰還困難区域) (Fig. R.1.B and C).

Une fois déposé sur le sol, le ^{137}Cs se fixe fortement et de manière quasi-irréversible aux particules fines, telles que les limon ou les argiles (Sawhney, 1972; He and Walling, 1996). Ainsi, 90 à 99 % du ^{137}Cs retombé se sont accumulés dans les 5 cm centimètres superficiels des sols non-perturbés (Kato et al., 2012; Lepage et al., 2015), ce qui pouvait justifier la mise en place d'un processus de décontamination par excavation des sols contaminées. En décembre 2011, le ministère de l'environnement a publié les directives sur la décontamination (MoE, 2011) (révisées par la suite en 2013; MoE (2013)), décrivant les méthodes de décontamination dans les zones résidentielles et cultivées, ainsi que les protocoles pour la collecte, le transport et le stockage des terres excavées. En janvier 2012, le ministère a publié la "politique de décontamination dans la zone de décontamination spéciale", présentant la feuille de route des activités de décontamination (Yasutaka and Naito, 2016).

Dans les zones agricoles, incluant les rizières ou autres terres arables, la procédure de décontamination dépendait de l'activité initiale en ^{137}Cs mesurée dans les sols (MoE, 2013, 2015, 2023). D'une part, si l'activité était inférieure à 5 $kBq \cdot kg^{-1}$, un labour d'inversion était réalisé sur une profondeur de 30-40 cm. D'autre part, si l'activité était supérieure à 5 $kBq \cdot kg^{-1}$, les quatre étapes suivantes étaient réalisées: (1) l'excavation des 5 cm superficiels de sol, (2) l'ajout de saprolite, dérivé du granite ou du grès, provenant de carrières locales ouvertes à cet effet, et qualifié de "sol sain" par les autorités japonaises (55,5 m^3 pour 1 000 m^2), (3) la restauration de la fertilité du sol à l'aide d'amendements, soit par l'ajout de carbonates (selon les besoins) et de silicate de phosphore (environ 0,8 $t \cdot ha^{-1}$), soit par l'ajout de zéolites (environ 0,5 $t \cdot ha^{-1}$), et (4) la préparation des sols par le mélange de la couche de "sol sain" avec le sol sous-jacent par un double labour profond (25-30 cm). La décontamination des forêts s'est limitée aux zones situées à moins de 20 m des habitations et le long des routes. Elle consistait à retirer la litière et la matière organique tombée (feuilles, branches) - qualifiées de "sédiment" par les autorités japonaises - sur une épaisseur d'environ 5 cm sans atteindre la couche de "sol minéral". Les forêts ont également été débroussaillées. De plus, les conifères ont été élagués jusqu'à une hauteur d'environ 4 m, s'ils se situaient à moins de 4 m de la lisière de la forêt. Les branches élaguées ont été collectées. La décontamination des prairies et bandes herbeuses situées autour des zones agricoles, des habitations ou des bâtiments et le long de routes, consistait à faucher et à retirer les herbes et les buissons.

Toute la matière organique collectée lors de la décontamination a été transportée vers des installations spéciales pour y être traitée. En mars 2020, 87 km^2 de terres agricoles, 78 km^2 de forêts et 15 km^2 de routes au sein de la SDZ avaient été décontaminées, ce qui représente environ 16 % de la superficie de la SDZ (MoE, 2023). Néanmoins, la décontamination a mobilisé un grand nombre de travailleurs et généré des quantités importantes de déchets, pour un total de 13,43 millions m^3 de déchets transportés vers des installations de stockage provisoires en 2020. Sur la période 2011-2020, 16 % des investissements consacrés à la reconstruction des dégâts du grand tremblement de terre du Tōhoku et de la pollution liée à l'accident de la FDNPP,

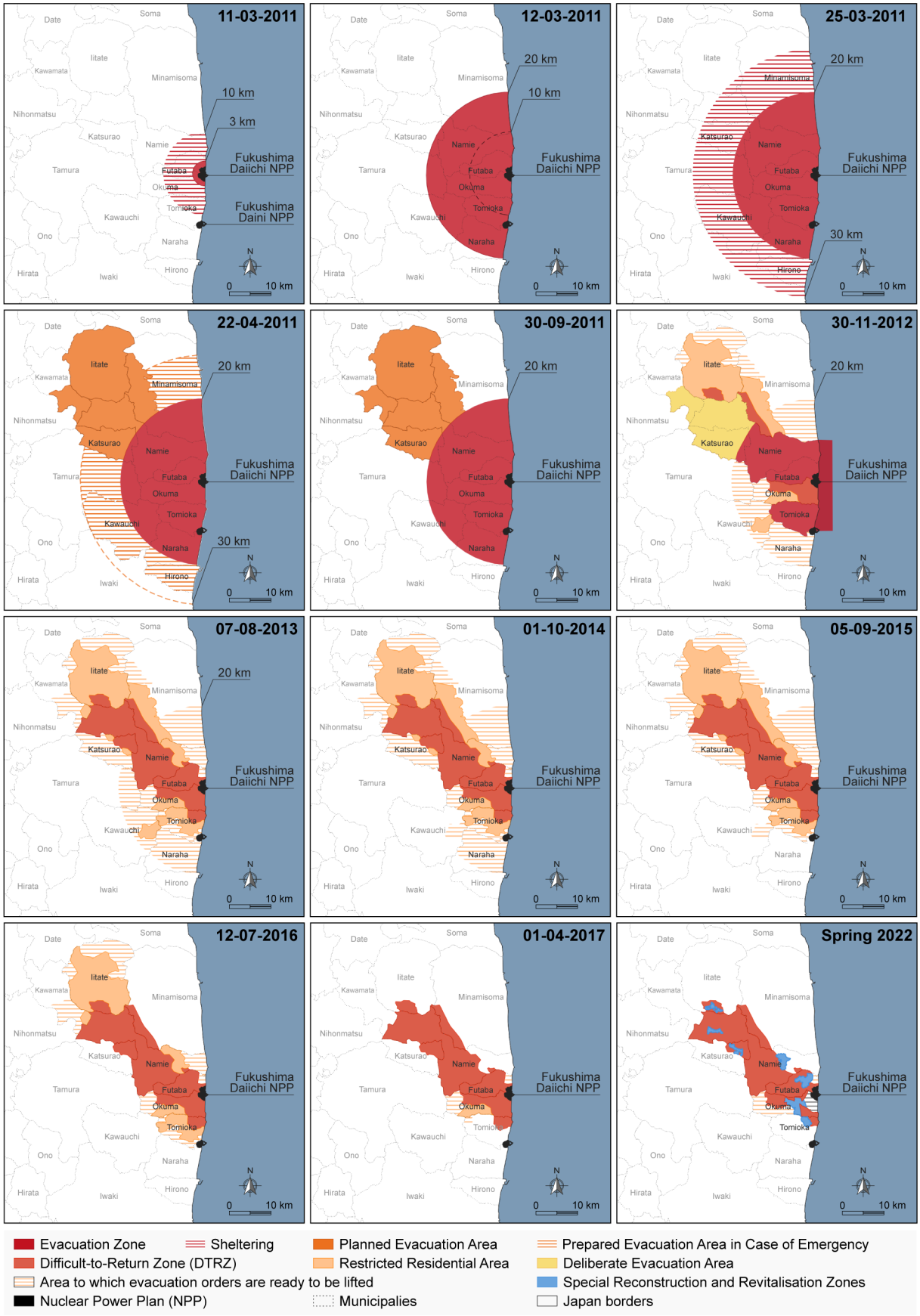


Figure R.2: Évolution des zones où les mesures de protection et d'évacuation ont été ordonnées ou recommandées depuis l'accident de la centrale nucléaire de Fukushima, le 11 mars 2011, jusqu'au printemps 2022 (adapté de IAEA (2015) pour l'année 2011 et mis à jour depuis lors).

ont été mobilisés pour la "*Nuclear Recovery Policy*" ("politique de reconstruction nucléaire"), soit 6 122,3 milliards de yens japonais (environ 50,9 milliards d'euros en prenant pour taux de change moyen en 2020, tel que 1 € = 120 ¥), dont environ 1 500 milliards ¥ et 1 400 milliards ¥ pour la décontamination dans la SDZ et les ICA, respectivement (MoE, 2018; Board of Audit of Japan, 2023; Evrard et al., 2023).

La progression de la décontamination, achevée entre 2017 et 2020 dans les ICA et la SDZ, ainsi que la décroissance radioactive ont conduit à une réduction des débits de dose radioactifs ambiants et des niveaux d'exposition individuels. Cela a permis la levée progressive des ordres d'évacuation entre avril 2014 (ville de Tamura) et mars 2020 (village de Futaba) (fig. R.2). L'ordre d'évacuation a été maintenu dans la DTRZ, car la zone n'a pas été ciblée en premier lieu par le programme de décontamination en raison de son haut niveau de contamination. Cependant, après une réouverture partielle de la DTRZ au printemps 2022, la zone a été progressivement accessible sans décontamination obligatoire, à l'exception des "zones spéciales de reconstruction et de revitalisation" ("*special reconstruction and revitalisation zones*") principalement localisées à proximité des zones résidentielles ou agricoles. Cependant, malgré l'investissement humain et financier considérable qu'ont représenté les travaux de décontamination, seule une proportion minoritaire des résidents évacués est revenue, estimée à environ 30 % en 2020 (Taira et al., 2020; Asanuma-Brice et al., 2023). Plusieurs facteurs ont contribué à ce faible taux de retour, notamment le changement des conditions de vie (séparation des familles et détérioration de la vie communautaire), le manque d'infrastructures et de services publics, les inquiétudes liées à l'exposition aux radiations et les restrictions imposées pour les activités en plein air, telles que la randonnée, la pêche en eau douce et la récolte traditionnellement pratiquée des légumes sauvages (山菜 - 'sansai') ou des champignons.

Le programme de décontamination ayant principalement ciblé les zones résidentielles et agricoles, celui-ci a été limité à une proportion minoritaire du l'ensemble de la région. Ainsi, la majorité du territoire, recouverte de forêts (70-80 %), n'a pas été décontaminée. De plus, si seuls 19 % des dépôts de ^{137}Cs ont eu lieu sur les zones agricoles, 74 % se sont produits sur des zones forestières (Kato et al., 2019). Selon Yasutaka et al. (2013), la décontamination de la zone tampon de 20-m de forêts autour des zones résidentielles et le long des routes a été estimée comme correspondant à environ 5 % de l'ensemble de la zone forestière au sein de la SDZ.

Par ailleurs, cette région du japon est touchée chaque année par au moins un épisode de précipitation intenses, tels que des typhons ou des tempêtes tropicales, principalement entre juillet et octobre. Ces évènements de précipitations intenses ont été identifiés comme le principal facteur du transfert de sédiments par érosion hydrique dans les bassins versants de ces régions (Laceby et al., 2016; Chartin et al., 2017). Par conséquent, la majorité du transfert de ^{137}Cs se produit lors de ces évènements (82 à 99 %; Yamashiki et al. (2014); Sakaguchi et al. (2015); Iwagami et al. (2017); Osawa et al. (2018)), en lien avec le transfert des particules fines de sol, et principalement avec la fraction limono-argileuse de celles-ci (3-63 μm; Sakaguchi et al. (2015)). Ainsi, sous l'influence de ces évènements, les zones qui n'ont pas été décontaminées, comme les forêts ou la DTRZ, pourraient constituer des sources à long terme de sédiments contaminés et pourraient aussi conduire à une recontamination des zones précédemment décontaminées en aval.

Néanmoins, parallèlement à la progression de la décontamination, une diminution des activités de ^{137}Cs dans les sédiments fluviaux a été observée dans la région au cours du temps. Divers facteurs ont été mis en avant pour expliquer cette diminution, notamment la décroissance radioactive, la réduction des stocks de ^{137}Cs liée aux événements érosifs répétés, la progression de la décontamination, ainsi que la réduction de l'érosion résultant du développement spontané du couvert végétal dans les zones agricoles abandonnées. Ainsi, des changement drastiques et rapides de l'occupation des sols ont eu lieu suite à l'évacuation des

zones contaminées, puis lors de la mise en œuvre du programme de décontamination et enfin, de la reprise de l'activité agricole dans les zones décontaminées. Par conséquent, des changements signifiants dans les dynamiques de transferts de sédiment et de radiocésium sont anticipés sur la période allant de l'accident de la FDNPP, en mars 2011, jusqu'à aujourd'hui.

Objectifs et démarche générale

Ce projet de thèse a pour principal objectif d'étudier l'impact de la décontamination et de la remise en culture des sols agricoles sur les transferts de sédiments et de radiocésium dans les fleuves côtiers drainant le principal panache radioactif généré par l'accident de la centrale nucléaire de Fukushima. Pour ce faire, il s'appuie sur l'analyse comparée de bassins versants contrastés caractérisés par des occupations du sol et des stratégies de gestion post-accidentelles différentes.

Ces travaux de recherche se concentrent ainsi sur la partie supérieure de trois fleuves côtiers (les fleuves Mano - 真野川, Ukedo - 請戸川 et Ota - 太田川), situés dans la partie nord-est de la préfecture de Fukushima et drainant le panache de radiocésium principal de l'accident de la FDNPP. Ces bassins versants présentent des caractéristiques topographiques similaires et peuvent être subdivisés en deux sections principales : une zone montagneuse, en amont, et une zone côtière, en aval, séparées par une zone de transition aux reliefs abrupts. Les sections montagneuses de ces bassins versants sont drainées par des réservoirs de barrages construits à des fins d'irrigation agricole et situés en bordure du plateau montagneux. Le réservoir du barrage Mano est localisé sur le fleuve homonyme, le réservoir du barrage Ogaki sur le fleuve Ukedo et le réservoir du barrage Yokokawa (横川) sur le fleuve Ota. Ces trois bassins versants montagneux sont typiques de cette région nord-est de la région de Fukushima en ce qui concerne leurs conditions environnementales et de topographie. Les deux bassins versant des barrages Mano et Ogaki drainent des bassins mixtes agricoles et forestiers, la forêt et les zones agricoles couvrant, respectivement, environ 90 % et 7-10 % de leur surface. Au contraire, le bassin versant du barrage de Yokokawa peut être considéré comme exclusivement forestier, la forêt y recouvrant 99 %. Dans les deux bassins des barrages Mano et Ogaki, en raison de leur topographie accidentée, les zones agricoles, comprenant les terres arables, des prairies et les rizières, sont principalement concentrées dans le fond des vallées, à proximité des cours d'eau. En raison de cette localisation en fond de vallées et suite à la mise en place d'un système d'irrigation/drainage, notamment pour la riziculture, les zones agricoles sont fortement connectées au système hydrographique. L'habitat est principalement composé de maisons isolées ou de hameaux, et ces zones recouvrent une surface très minoritaire des bassins versants (environ 1 %). Dans le bassin versant du barrage Mano, situé dans la partie nord du village de Iitate dans la SDZ, la décontamination a été initiée en juin 2014 et s'est achevée en décembre 2016. Au contraire, le bassin versant du barrage Ogaki, situé dans la ville de Namie dans la DTRZ, n'était initialement pas inclus dans le programme de décontamination. Cependant, la décontamination du bassin versant du barrage Ogaki a néanmoins finalement été initiée au printemps 2022, en parallèle de la réouverture progressive de la DTRZ, et après la décontamination obligatoire des "zones spéciales de reconstruction et de revitalisation", principalement situés autour de la ville de Namie et de la vallée agricole de la partie amont de la rivière Koidetani (小出谷川).

Cette thèse s'inscrit dans la continuité des travaux de recherche initiés par le Laboratoire des Sciences du Climat de l'Environnement (LSCE) entre 2011 et 2013 dans le cadre du projet TOFU ("*Traçage des conséquences environnementales du tsunami provoqué par le séisme de TOhoku et de l'accident de FUkushima*"). Ces travaux se sont poursuivis avec le projet AMORAD ("*Amélioration des MOdèles de prévision de la dis-*

persion et d'évaluation de l'impact des RADionucléides au sein de l'environnement") coordonné par l'Institut de Radioprotection et de Sûreté Nucléaire (IRSN) et financé dans le cadre du programme des Investissements d'Avenir en RadioProtection et Sûreté Nucléaire (RPSN) de 2014 à 2021. Au sein de celui-ci, le LSCE a coordonné l'axe "transfert continental de radionucléides" visant à améliorer la modélisation de l'érosion des radionucléides dans les paysages continentaux sur la base des retours d'expérience et des mesures effectuées dans la région affectée par l'accident de la FDNPP.

Dès la première campagne de terrain organisée en 2011 dans le cadre du projet TOFU, des sédiments fluviaux déposés après une crue, appelés "laisses de crue" (voir image R.3), ont été collectés lors de deux campagnes d'échantillonnage organisées chaque année pendant la phase post-accidentelle immédiate (2011-2016), une première campagne ayant lieu au printemps après la fonte des neiges (avril-mai) et une seconde campagne à l'automne après la saison des typhons (octobre-novembre). Ensuite, à partir de 2017, l'échantillonnage des dépôts de laisses de crue a été limité à la campagne d'automne. Par ailleurs, des échantillons de sol correspondant aux potentielles sources de sédiments, telles que les terres agricoles abandonnées, les terres agricoles décontaminées, le "sol sain" ajouté lors de la décontamination, les prairies, les forêts, les glissements de terrain, les berges et les matériaux d'horizons profonds du sol ("*subsoil*"), ont été prélevés au cours de trois campagnes d'échantillonnage spécifiques organisées en 2011, 2015 et 2019. En 2021, 19 campagnes d'échantillonnage de laisses avaient été menées. Dans un premier temps, toutes les analyses physico-chimiques effectuées sur les échantillons de sol et de laisses de crues (spectrométrie gamma, géochimie élémentaire, propriétés de la matière organique et spectrocolorimétrie dans le visible) ont été homogénéisées et compilées dans une base de données unique associée à 159 échantillons de sol et 911 échantillons de laisses de crues. De cette base de données, les échantillons de sol et de sédiments considérés comme pertinents pour le travail de recherche de la thèse ont été sélectionnés. Ils comprennent ainsi des échantillons de sol prélevés dans les bassins versants des réservoirs du barrage Yokokawa (n = 14) et du barrage Mano (n = 34), ainsi que des échantillons prélevés le bassin versant de la partie supérieure du fleuve Niida (n = 34 ; 新田川), un bassin versant limitrophe et très similaire au bassin versant du barrage Mano. De plus, les échantillons de laisses de crues prélevés annuellement entre 2011 et 2023 après la saison des typhons lors de la campagne d'automne (octobre-novembre) au niveau d'une dizaine de sites situés dans le



Figure R.3: Prélèvement de laisses de crue lors des campagnes de prélèvement d'automne des années 2022 et 2023 (© Olivier Evrard).

bassin versant du barrage Mano ont également été sélectionnés (n = 91). Dans la mesure où la base de données initiale ne comprenait pas d'échantillons de sol provenant du bassin versant du barrage Ogaki, en raison de sa localisation dans la DTRZ où l'accès était fortement restreint avant la pandémie de COVID-19, une campagne de terrain spécifique a été organisée en avril 2022 pour identifier les sources potentielles de sédiments dans la zone. Les échantillons de sol y ont ensuite été prélevés en juin/juillet 2022, le long du fleuve Ukedo (n = 36). Ensuite, deux autres campagnes de prélèvement post-typhons ont été menées en novembre 2022 et en novembre 2023, avec la collecte de 33 et 35 échantillons de laisses de crues. Ces 68 échantillons de laisses de crue supplémentaires ont ainsi pu être incorporés à la base de données générale. Parmi ces échantillons, 18 ont été collectés dans le bassin versant du réservoir de Mano Dam (total = 109). De plus, suite aux retours d'expérience relatifs à l'étude de trois carottes sédimentaires prélevées en amont, au milieu et en aval du réservoir du barrage Mano en novembre 2014 (Huon et al., 2018), deux carottes sédimentaires supplémentaires ont été prélevées au milieu et en aval de ce même réservoir en juin 2021. En complément, deux autres carottes de sédiments ont été prélevées dans les sections aval des réservoirs des barrages Ogaki et Yokokawa en septembre et en août 2022.

Dans un premier temps, la méthodologie du traçage sédimentaire, dite de "*sediment source fingerprinting*", a pu être révisée. La méthodologie du traçage sédimentaire consiste en deux étapes, la sélection des traceurs parmi les propriétés physico-chimiques analysées, suivie de la modélisation des contributions relatives des sources de sédiments par leur déconvolution au sein d'un mélange sédimentaire. Pour être sélectionnée comme traceur, une propriété doit respecter deux critères : elle doit rester stable lors du processus d'érosion, ce que l'on qualifie de "comportement conservatif", et elle doit permettre de différencier les sources potentielles, ce qu'on appelle sa "capacité de discrimination". L'identification correcte des traceurs représente une étape cruciale pour garantir une prédiction fiable des contributions relatives des sources de sédiments. Plusieurs méthodologies de sélection de traceurs existent, et notamment la plus courante, appelée "*Three-Steps Method*" (méthode en trois étapes - TSM), et la méthode récemment proposée par Lizaga et al. (2020), appelée "*Consensus Method*" (méthode du consensus - CM). Ces méthodes de sélection des traceurs sont utilisées en parallèle dans différentes études et n'avaient jamais été comparées dans la littérature scientifique. Il a donc été choisi de comparer leurs sélections respectives de traceurs sur un seul ensemble de données d'échantillons réels, issus des couches de sédimentation successives d'une carotte prélevée dans le réservoir du barrage Mano. Ces deux méthodes ont donc été comparées par rapport à leurs sélections de traceurs et, dans un second temps, l'impact de ces différentes sélection de traceurs a été évalué sur la prédiction des contributions sédimentaires. En outre, l'utilisation de mélanges virtuels, définis mathématiquement, pour évaluer la précision de la modélisation des contributions de sources sédimentaires a été formalisée et discutée. Parallèlement à ce travail, un package R a été développé et publié. Le package, nommé fingR, a été développé pour permettre une mise en application facilitée et pratique de l'approche la plus courante (càd. la TSM) ainsi que des outils permettant d'évaluer la précision des prédictions générées.

Dans un second temps, l'impact de la décontamination des sols sur les transferts de sédiments et de radiocésium a été étudié dans l'un des trois bassins versants contrastés susmentionnés. Des méthodologies de traçage sédimentaires ont été développées pour appuyer cette analyse et pour évaluer plus particulièrement l'impact potentiel de la décontamination sur les changements de contributions parmi les sources de sédiments au cours du temps. Cette approche a également été appliquée à différentes matrices de sédiments en fonction du site d'étude :

- Deux types de matrices sédimentaires ont été utilisés pour étudier l'impact de la décontamination des terres agricoles : des carottes sédimentaires prélevées dans des réservoirs de barrages et des laisses de crue prélevées après les typhons le long du réseau hydrographique. Ces échantillons ont été prélevés

dans le bassin versant du réservoir du barrage Mano, un bassin versant mixte agricole/forestier décontaminé de manière précoce pour la région. D'une part, les carottes sédimentaires ont fourni un enregistrement continu des transferts de sédiments qui ont eu lieu dans le bassin versant avant, pendant et après l'accident. La séquence de dépôts sédimentaires a été caractérisée et sa chronologie a été reconstruite à l'aide d'une série de propriétés diagnostiques mesurées sur les sédiments et d'autres informations contextuelles disponibles par ailleurs. Ensuite, les flux de sédiments et de radiocésium associés ont été reconstitués sur la période allant de l'accident de la FDNPP en 2011, à la collecte de la carotte sédimentaire (juin 2021). D'autre part, les laisses de crue, collectées annuellement au niveau de dix sites situés à travers le bassin versant du réservoir de Mano, ont permis de caractériser les variations spatiales et l'évolution temporelle des transferts de sédiments et de radiocésium à travers ce bassin versant.

- L'influence des différentes occupations du sol dominantes et de la gestion des bassins versants après l'accident de la FDNPP a été étudiée en comparant la situation des bassins versants des barrages Mano, Ogaki et Yokokawa. Cette analyse a permis d'évaluer l'impact du délai de mise en place des travaux de décontamination sur les transferts de sédiments et de radiocésium le long du réseau hydrographique.

La conjugaison des stratégies d'échantillonnage de carottes sédimentaires et celle des laisses de crue fournit un ensemble de données plus complet, permettant d'améliorer notre compréhension de l'hétérogénéité des processus d'érosion qui se produisent à travers un bassin versant, dans le contexte des changements majeurs d'utilisation des sols qui ont eu lieu au cours des phases successives d'abandon, de décontamination et de reprise de l'activité agricole depuis l'accident de la FDNPP jusqu'à aujourd'hui.

References

Asanuma-Brice, C., Evrard, O., Chalaux, T., 2023. Why did so few refugees return to the Fukushima fallout-impacted region after remediation? An interdisciplinary case study from Iitate village, Japan. International Journal of Disaster Risk Reduction 85, 103498. URL: https://linkinghub.elsevier.com/retrieve/pii/S2212420922007178, doi:10.1016/j.ijdrr.2022.103498.

Board of Audit of Japan, 2023. Status of Implementation of Projects Related to Recovery from the Great East Japan Earthquake. Technical Report. Board of Audit of Japan. URL: https://www.jbaudit.go.jp/pr/kensa/result/5/pdf/050203_01_zenbun.pdf.

Chartin, C., Evrard, O., Laceby, J.P., Onda, Y., Ottlé, C., Lefèvre, I., Cerdan, O., 2017. The impact of typhoons on sediment connectivity: Lessons learnt from contaminated coastal catchments of the Fukushima Prefecture (Japan): Typhoon Impact on Sediment Connectivity - Fukushima, Japan. Earth Surface Processes and Landforms 42, 306–317. URL: https://onlinelibrary.wiley.com/doi/10.1002/esp.4056, doi:10.1002/esp.4056.

Chino, M., Nakayama, H., Nagai, H., Terada, H., Katata, G., Yamazawa, H., 2011. Preliminary Estimation of Release Amounts of ^{131}I and ^{137}Cs Accidentally Discharged from the Fukushima Daiichi Nuclear Power Plant into the Atmosphere. Journal of Nuclear Science and Technology 48, 1129–1134. URL: http://www.tandfonline.com/doi/abs/10.1080/18811248.2011.9711799, doi:10.1080/18811248.2011.9711799.

Emergency Disaster Preparedness Headquarters, 2021. Police Activities and Damage from the 2011 Tohoku Earthquake. Technical Report 1. Emergency Disaster Preparedness Headquarters, Police Agency. URL: https://www.npa.go.jp/news/other/earthquake2011/pdf/higaijokyo.pdf.

Evrard, O., Chalaux-Clergue, T., Chaboche, P.A., Wakiyama, Y., Thiry, Y., 2023. Research and management challenges following soil and landscape decontamination at the onset of the reopening of the Difficult-To-Return Zone, Fukushima (Japan). SOIL 9, 479–497. URL: https://soil.copernicus.org/articles/9/479/2023/, doi:10.5194/soil-9-479-2023.

Fire and Disaster Management Agency, 2021. 2011 Tohoku-Pacific Ocean Earthquake (Great East Japan Earthquake). Technical Report 161. Disaster Management Headquarters, Fire and Disaster Management Agency. Japan. URL: https://www.fdma.go.jp/disaster/higashinihon/items/161.pdf.

Hashimoto, S., Ugawa, S., Nanko, K., Shichi, K., 2012. The total amounts of radioactively contaminated materials in forests in Fukushima, Japan. Scientific Reports 2, 416. URL: https://www.nature.com/articles/srep00416, doi:10.1038/srep00416.

He, Q., Walling, D., 1996. Interpreting particle size effects in the adsorption of 137Cs and unsupported 210Pb by mineral soils and sediments. Journal of Environmental Radioactivity 30, 117–137. URL: https://linkinghub.elsevier.com/retrieve/pii/0265931X96892757, doi:10.1016/0265-931X(96)89275-7.

Huon, S., Hayashi, S., Laceby, J.P., Tsuji, H., Onda, Y., Evrard, O., 2018. Source dynamics of radiocesium-contaminated particulate matter deposited in an agricultural water reservoir after the Fukushima nuclear accident. Science of The Total Environment 612, 1079–1090. URL: https://linkinghub.elsevier.com/retrieve/pii/S0048969717319083, doi:10.1016/j.scitotenv.2017.07.205.

IAEA, 2015. The Fukushima Daiichi Accident. Non-Serial Publications, International Atomic Energy Agency, Vienna, Austria. URL: https://www-pub.iaea.org/MTCD/Publications/PDF/SupplementaryMaterials/P1710/Languages/French.pdf.

Iwagami, S., Onda, Y., Tsujimura, M., Abe, Y., 2017. Contribution of radioactive 137Cs discharge by suspended sediment, coarse organic matter, and dissolved fraction from a headwater catchment in Fukushima after the Fukushima Dai-ichi Nuclear Power Plant accident. Journal of Environmental Radioactivity 166, 466–474. URL: https://linkinghub.elsevier.com/retrieve/pii/S0265931X16302557, doi:10.1016/j.jenvrad.2016.07.025.

JMA, 2011. Information on the 2011 Geart East Japan Earthquake. URL: https://www.jma.go.jp/jma/en/2011_Earthquake/Information_on_2011_Earthquake.html.

Kato, H., Onda, Y., Gao, X., Sanada, Y., Saito, K., 2019. Reconstruction of a Fukushima accident-derived radiocesium fallout map for environmental transfer studies. Journal of Environmental Radioactivity 210, 105996. URL: https://linkinghub.elsevier.com/retrieve/pii/S0265931X18303308, doi:10.1016/j.jenvrad.2019.105996.

Kato, H., Onda, Y., Teramage, M., 2012. Depth distribution of 137Cs, 134Cs, and 131I in soil profile after Fukushima Dai-ichi Nuclear Power Plant Accident. Journal of Environmental Radioactivity 111, 59–64. URL: https://linkinghub.elsevier.com/retrieve/pii/S0265931X11002426, doi:10.1016/j.jenvrad.2011.10.003.

Kobayashi, T., Nagai, H., Chino, M., Kawamura, H., 2013. Source term estimation of atmospheric release due to the Fukushima Dai-ichi Nuclear Power Plant accident by atmospheric and oceanic dispersion simulations: Fukushima NPP Accident Related. Journal of Nuclear Science and Technology 50, 255–264. URL: http://www.tandfonline.com/doi/abs/10.1080/00223131.2013.772449, doi:10.1080/00223131.2013.772449.

Laceby, J.P., Chartin, C., Evrard, O., Onda, Y., Garcia-Sanchez, L., Cerdan, O., 2016. Rainfall erosivity in catchments contaminated with fallout from the Fukushima Daiichi nuclear power plant accident. Hydrology and Earth System Sciences 20, 2467–2482. URL: https://hess.copernicus.org/articles/20/2467/2016/, doi:10.5194/hess-20-2467-2016.

Lepage, H., Evrard, O., Onda, Y., Lefèvre, I., Laceby, J.P., Ayrault, S., 2015. Depth distribution of cesium-137 in paddy fields across the Fukushima pollution plume in 2013. Journal of Environmental Radioactivity 147, 157–164. URL: https://linkinghub.elsevier.com/retrieve/pii/S0265931X15001484, doi:10.1016/j.jenvrad.2015.05.003.

Lizaga, I., Latorre, B., Gaspar, L., Navas, A., 2020. Consensus ranking as a method to identify non-conservative and dissenting tracers in fingerprinting studies. Science of The Total Environment 720, 137537. URL: https://linkinghub.elsevier.com/retrieve/pii/S0048969720310482, doi:10.1016/j.scitotenv.2020.137537.

MoE, 2011. Basic Principles on the Act on Special Measures Concerning the Handling of Environment Pollution by Radioactive Materials Discharged by the Nuclear Power Station Accident Associated with the Tohoku District-Off the Pacific Ocean Earthquake That Occurred on March 11, 2011. Technical Report. Ministry of the Environment. Japan. URL: https://josen.env.go.jp/en/framework/pdf/basic_principles.pdf.

MoE, 2013. Decontamination Guidelines. Technical Report 2. Japanese Ministry of Environment. Japan.

MoE, 2015. Decontamination Report - A Compilation of Experiences to Date on Decontamination for the Living Environment Conducted by the Ministry of the Environment. Technical Report. Japanese Ministry of Environment. Japan. URL: http://josen.env.go.jp/en/policy_document/.

MoE, 2018. Decontamination Projects for Radioactive Contamination Discharged by Tokyo Electric Power Company Fukushima Daiichi Nuclear Power Station Accident. Technical Report. Japanese Ministry of Environment.

MoE, 2023. Decontamination status. URL: http://josen.env.go.jp/area/.

NOAA, 2015. Great Tohokun Japan Earthquake and Tsunami, 11 March 2011. URL: https://www.ngdc.noaa.gov/hazard/11mar2011.html.

Osawa, K., Nonaka, Y., Nishimura, T., Tanoi, K., Matsui, H., Mizogichi, M., Tatsuno, T., 2018. Quantification of dissolved and particulate radiocesium fluxes in two rivers draining the main radioactive pollution plume in Fukushima, Japan (2013–2016). Anthropocene 22, 40–50. URL: https://linkinghub.elsevier.com/retrieve/pii/S2213305418300262, doi:10.1016/j.ancene.2018.04.003.

Sakaguchi, A., Tanaka, K., Iwatani, H., Chiga, H., Fan, Q., Onda, Y., Takahashi, Y., 2015. Size distribution studies of 137Cs in river water in the Abukuma Riverine system following the Fukushima Dai-ichi Nuclear

Power Plant accident. Journal of Environmental Radioactivity 139, 379–389. URL: https://linkinghub.elsevier.com/retrieve/pii/S0265931X14001519, doi:10.1016/j.jenvrad.2014.05.011.

Sawhney, B.L., 1972. Selective Sorption and Fixation of Cations by Clay Minerals: A Review. Clays and Clay Minerals 20, 93–100. URL: https://doi.org/10.1346/CCMN.1972.0200208, doi:10.1346/CCMN.1972.0200208.

Simons, M., Minson, S.E., Sladen, A., Ortega, F., Jiang, J., Owen, S.E., Meng, L., Ampuero, J.P., Wei, S., Chu, R., Helmberger, D.V., Kanamori, H., Hetland, E., Moore, A.W., Webb, F.H., 2011. The 2011 Magnitude 9.0 Tohoku-Oki Earthquake: Mosaicking the Megathrust from Seconds to Centuries. Science 332, 1421–1425. URL: https://science.sciencemag.org/content/332/6036/1421, doi:10.1126/science.1206731.

Steinhauser, G., 2014. Fukushima's Forgotten Radionuclides: A Review of the Understudied Radioactive Emissions. Environmental Science & Technology 48, 4649–4663. URL: https://pubs.acs.org/doi/10.1021/es405654c, doi:10.1021/es405654c.

Taira, Y., Matsuo, M., Yamaguchi, T., Yamada, Y., Orita, M., Takamura, N., 2020. Radiocesium levels in contaminated forests has remained stable, even after heavy rains due to typhoons and localized downpours. Scientific Reports 10, 19215. URL: https://www.nature.com/articles/s41598-020-75857-1, doi:10.1038/s41598-020-75857-1.

Taniguchi, K., Onda, Y., Smith, H.G., Blake, W., Yoshimura, K., Yamashiki, Y., Kuramoto, T., Saito, K., 2019. Transport and Redistribution of Radiocesium in Fukushima Fallout through Rivers. Environmental Science & Technology 53, 12339–12347. URL: https://pubs.acs.org/doi/10.1021/acs.est.9b02890, doi:10.1021/acs.est.9b02890.

Yagi, Y., Fukahata, Y., 2011. Rupture process of the 2011 Tohoku-oki earthquake and absolute elastic strain release: RUPTURE PROCESS OF TOHOKU-OKI EARTHQUAKE. Geophysical Research Letters 38, n/a–n/a. URL: http://doi.wiley.com/10.1029/2011GL048701, doi:10.1029/2011GL048701.

Yamamoto, M., 2015. Overview of the Fukushima Dai-ichi Nuclear Power Plant (FDNPP) accident, with amounts and isotopic compositions of the released radionuclides. Journal of Radioanalytical and Nuclear Chemistry 303, 1227–1231. URL: http://link.springer.com/10.1007/s10967-014-3639-3, doi:10.1007/s10967-014-3639-3.

Yamashiki, Y., Onda, Y., Smith, H.G., Blake, W.H., Wakahara, T., Igarashi, Y., Matsuura, Y., Yoshimura, K., 2014. Initial flux of sediment-associated radiocesium to the ocean from the largest river impacted by Fukushima Daiichi Nuclear Power Plant. Scientific Reports 4, 3714. URL: https://www.nature.com/articles/srep03714, doi:10.1038/srep03714.

Yasutaka, T., Iwasaki, Y., Hashimoto, S., Naito, W., Ono, K., Kishimoto, A., Yoshida, K., Murakami, M., Kawaguchi, I., Oka, T., Nakanishi, J., 2013. A GIS-based evaluation of the effect of decontamination on effective doses due to long-term external exposures in Fukushima. Chemosphere 93, 1222–1229. URL: https://linkinghub.elsevier.com/retrieve/pii/S0045653513009405, doi:10.1016/j.chemosphere.2013.06.083.

Yasutaka, T., Naito, W., 2016. Assessing cost and effectiveness of radiation decontamination in Fukushima Prefecture, Japan. Journal of Environmental Radioactivity 151, 512–520. URL: https://linkinghub.elsevier.com/retrieve/pii/S0265931X15001575, doi:10.1016/j.jenvrad.2015.05.012.

Zhao, D., 2015. The 2011 Tohoku earthquake (Mw 9.0) sequence and subduction dynamics in Western Pacific and East Asia. Journal of Asian Earth Sciences 98, 26–49. URL: https://linkinghub.elsevier.com/retrieve/pii/S1367912014004799, doi:10.1016/j.jseaes.2014.10.022.

université PARIS-SACLAY
ÉCOLE DOCTORALE
Sciences mécaniques et énergétiques, matériaux et géosciences (SMEMAG)

Titre : Impact de la décontamination et de la remise en culture des sols agricoles sur les transferts de sédiments et de radiocésium dans les rivières de Fukushima

Mots clés : pollution environnementale, érosion des sols, transfert de radiocésium, transfert de sédiment, traçage sédimentaire, source-to-sink

Résumé : D'importantes quantités de radionucléides (principalement du radiocésium) se sont déposées sur les sols du nord-est du Japon après l'accident de la centrale nucléaire de Fukushima Daiichi en mars 2011. Dès fin 2013, les autorités japonaises ont entrepris un programme sans précédent de décontamination à grande échelle dans les zones cultivées et résidentielles touchées par le panache radioactif (8953 km^2). L'objectif principal était de ne pas exposer les habitants à des doses radioactives supérieures à 1 mSv an^{-1} en plus du niveau naturel, afin de permettre un retour rapide des habitants et la reprise des activités agricoles. Dans ces zones, la décontamination a consisté à décaper sur 5-cm la couche supérieure de sol concentrant le radiocésium (90-99 %) et à la remplacer par du sable saprolitique extrait de carrières locales ouvertes à cet effet. Cependant, la décontamination n'a concerné qu'une petite partie du paysage, puisque les terres agricoles couvrent moins de 10 % de cette région. En outre, comme les terres agricoles ont commencé à être remises en culture, de nombreuses questions ont été soulevées quant à l'impact de ces travaux de décontamination sur le transfert du radiocésium dans les rivières et à travers les paysages. Une approche de traçage sédimentaire multi-proxy a été mis en place pour quantifier l'évolution des sources de sédiments et de radiocésium associé aux particules transitant par le système hydrographique drainant le panache radioactif depuis l'accident. Ce grâce à l'analyse combinée de carottes de sédiments et de dépôts de crues fluviales prélevés dans toute la région. En 2021, les autorités japonaises ont annoncé la réouverture potentielle de certaines parties de la zone de retour difficile (Difficult-to-Return zone) à partir du printemps 2023 sans décontamination obligatoire. Les recherches actuelles ont permis de reconstituer et de comparer les sources et les transferts de sédiments et de radiocésium dans trois bassins versants contrastés (barrage de Mano, barrage de Yokokama et barrage de Ogaki) où différents modes de gestion (et calendriers) ont été mis en œuvre. Cela permettra de mieux comprendre l'impact des différentes décisions de gestion et de leur calendrier (décontamination précoce ou tardive) sur les transferts de sédiments et de radiocésium dans ces conditions post-accidentelles uniques.

Title : Impact of decontamination and recultivation of agricultural soils on sediment and radiocaesium transfers in Fukushima rivers

Keywords : environmental pollution, soil erosion, radiocesium transfer, sediment transfer, sediment source fingerprinting, source-to-sink

Abstract : Significant quantities of radionuclides (mainly radiocesium) were deposited on the soils of Northeastern Japan after the accident of the Fukushima Daiichi Power Plant in March 2011. Starting from late 2013, the Japanese authorities initiated an unprecedented large-scale decontamination programme in cultivated and residential areas affected by the main radioactive plume (8953 km^2). The main objective was not to expose local inhabitants to radioactive doses exceeding 1 mSv yr^{-1} in addition to the natural levels, in order to allow a rapid return of the local inhabitants and the resumption of agricultural activities. In these areas, decontamination consisted of removing the uppermost 5-cm layer of soil that concentrated radiocesium (90-99 %) and then replacing it with saprolite sand extracted from local quarries opened for this purpose. Decontamination targeted a minor proportion of the landscape, as farmland covers less than 10 % of this region. Furthermore, as agricultural land started to be re-cultivated, many questions were raised regarding the impact of this decontamination work on the transfer of radiocesium into rivers and across landscapes. A multi-proxy sediment tracing approach was designed to quantify the evolution of sources of sediment and particle-bound radiocesium transiting river systems draining the main contamination plume since the accident, through the combined analysis of sediment cores and river flood deposits collected across the region. In 2021, Japanese authorities announced the potential reopening of parts of the Difficult-to-Return zone without obligatory decontamination from Spring 2023 onwards. The current research reconstructed and compared the sources and transfers of sediment and radiocesium in three contrasted catchments (i.e., Mano Dam, Yokokama Dam and Ogaki Dam) where different management modes (and schedules) were implemented. This will shed light into the impact of different management decisions and their timing (early-decontamination or late-decontamination) on sediment and radiocesium transfers in these unique post-accidental conditions.